COOL'09

Workshop on Beam Cooling and Related Topics

August 31 – September 4, 2009
Lanzhou, China
(Organized By IMP, Lanzhou, China)

The workshop will highlight the state of the art in electron cooling, stochastic cooling, laser cooling, muon cooling, and storage of particles in antiproton and heavy ion traps.

International Program Committee

Ilan Ben-Zvi (BNL), Brookhaven, USA
Håkan Danared (MSL), Stockholm, Sweden
Yaroslav Derbenev (TJNAF), Newport News, USA
Dan Kaplan (IIT), Chicago, USA
Kwang-Je Kim (ANL), Argonne, USA
Igor Meshkov (JINR), Dubna, Russia
Dieter Möhl (CERN), Switzerland
Yoshiharu Mori (KEK), Tokyo, Japan
Sergei Nagaitsev (FNAL), Batavia, USA
Akira Noda, Kyoto University, Japan
Vasily Parkhomchuk (BINP), Novosibirsk, Russia
Ralph Pasquinelli (FNAL), Batavia, USA
Dieter Prasuhn (IKP), Jülich, Germany
Andrew Sessler (LBNL), Berkeley, USA
Markus Steck (GSI), Darmstadt, Germany
Gérard Tranquille (CERN), Switzerland
Hongwei Zhao (IMP), Lanzhou, China

http://cool09.impcas.ac.cn

Institute of Modern Physics, CAS
www.impcas.ac.cn

Local Organizers at IMP

Xiaohong Cai
Zhenguo Hu
Qiang Liang(Secretary)
Lijun Mao(Scientific Secretary)
Junxia Wu(Scientific Secretary)
Jiawen Xia
Ming Xie
Xiaodong Yang(Co-Chair)
Youjin Yuan(Editor)
Hongwei Zhao(Chair)

Preface

The workshop on beam cooling and related topics, COOL 2009, was organized by Institute of Modern Physics, IMP, in succession to several precursor workshops on beam cooling and related techniques. It was held in the Ningwozhuang Hotel of Lanzhou, China, between August 31 and 4 September, 2009.

The workshop was attended by 48 participants from 8 countries in Europe, America, and Asia. About 33 contributions were presented in talk, 12 on poster. The workshop was structured in 12 sessions with 3 oral presentations each, two sessions in the morning and two sessions in the afternoon. One afternoon was reserved for the poster presentations.

The contributions gave a rather complete overview of recent developments in the field of beam cooling, but also some planned new projects and ideas for advanced cooling concepts were discussed. The presentations covered the range from high intensity antiproton stacking accumulated by stochastic cooling and now also supplemented by electron beam, down to low intensity crystalline beams achieved by means of electron and laser cooling. Beyond these well-established techniques, more advanced concepts like muon cooling and a stochastic cooling scheme based on the use of an electron beam were discussed.

A possibility to relax from the workshop and enjoy the vicinity was given on an excursion that took the participants to the Ta'er Lamasery in Qinghai. The excursion, as well as the reception and banquet near the Yellow River, gave plenty of time for intense and extended discussions.

The organizers would like to thank IMP, National Natural Science Foundation of China, Chinese Academy of Sciences and Kansai Electronics (Suzhou) Co. Ltd for sponsoring this workshop.

Special thanks should be given to the conference secretaries Qiang Liang, Lijun Mao, Xiaohong Cai, Zhenguo Hu, Honglian Chen, who prepared and managed the workshop with high efficiency and great enthusiasm. Great thanks go to the editors Volker R. W. Schaa, Christine Petit-Jean-Genaz, Youjin Yuan, Martin Comyn and Takashi Kosuge for successfully introducing the Scientific Programme Management System (SPMS) of Joint Accelerator Conference Website (JACoW) for the processing and publication of the workshop and for their editorial work.

Chair: Hongwei Zhao
Co-chair: Xiaodong Yang

March 20, 2010

Address at COOL 2009

Good morning! Distinguished Participants, colleagues,

My colleagues and I are very pleased that the Workshop on Beam Cooling and Related Topics takes place in Lanzhou.

First of all, please allow me on behalf of the Institute of Modern Physics as the host of this workshop to extend warmest welcome to all the participants, especially to our distinguished guests from other different countries and regions from afar. As registered, there are more than 40 Chinese scientists and 39 scientists from 6 other nations and regions, Germany, Japan, Russia, Sweden, Switzerland and the U.S.A, attending this workshop. This workshop will focus on the state of the art in the physics and engineering of beam cooling systems and related techniques, including electron, stochastic, laser and ionization cooling and so on. The program includes applications of beam cooling to traps, heavy ion and antiproton beams. Presentations of the latest developments and techniques as well as the status of existing and future facilities have been invited. I believe this workshop must be a very good opportunity for us to exchange information and expertise and it will play a very active role in promoting further developments in related fields.

The Institute of Modern Physics (IMP), affiliated to Chinese Academy of Sciences (CAS), was founded in 1957. Since its foundation, IMP has focused on basic researches of heavy ion nuclear physics and the interdisciplinary researches in related fields. The accelerator physics and technology as well as the applications of nuclear technology are developed. The National Laboratory of Heavy Ion Research Facility in Lanzhou was established in 1991. The main research facility at IMP is a heavy ion accelerator complex named Heavy Ion Research Facility in Lanzhou abbreviated as HIRFL, which consists of two cyclotrons, one heavy ion synchrotron and one cooling storage ring named as HIRFL-CSR. There are some other facilities in operation such as the Radioactive Ion Beam Line in Lanzhou, the 320kV high voltage heavy ion applied research facility and 1.5MeV/50mA electron accelerator and so forth. Particularly, successful construction and operation of the HIRFL-CSR have paved the way to many significant research opportunities for IMP, such as highly charged atomic physics, radioactive ion beam physics, hadron-nucleon physics, high energy density matter physics, irradiation material sciences and radio-biology. According to the program of this workshop, there will be 6 presentations by my colleagues

from IMP in addition to an organized tour of our laboratories, which may provide you with more information about us in details. I want to emphasize that IMP conducts wide scientific exchanges and collaboration with Chinese and foreign institutions and has established ties with research centers in 36 countries and regions. There are a number of long-term scientific cooperation agreements between IMP and noted domestic and foreign research centers, universities and enterprises. Since 1978 the IMP has received 1343 foreign visiting scientists and assigned more than 1000 scholars for scientific collaborations and exchanges abroad. IMP is quite willing to further strengthen ties with you all in future.

Finally, I would like to express my sincere appreciation to all the participants for your active participation in this workshop held in Lanzhou. The workshop is named COOL09, but I think the hospitality of IMP must be warm in contrary to COOL. We shall do our best to help make your stay in Lanzhou pleasant. In addition, I would like to thank all the colleagues, who have worked hard in preparing the workshop in order to make the workshop successful.

I hope that all of our guests will have a pleasant time in Lanzhou. I wish the workshop great success.

Thank you.

Deputy Director of IMP: Ming Xie

August 31, 2009

Contents

Preface i
Foreword iii
Contents vii
Committees ix
Pictures x
MOM1MCIO01 – Status of Antiproton Accumulation and Cooling at Fermilab's Recycler 1
MOM1MCIO02 – Antiproton Decelerator Status Report 6
MOM2MCIO01 – Electron Cooling for the Low-Energy RHIC Program 11
MOM2MCIO02 – Application of Cooling Methods to NICA Project 16
MOM2MCIO03 – Cooling Experiments at COSY in Preparation for the HESR 21
MOA1MCIO01 – All-Optical Ion Beam Cooling and Online Diagnostics at Relativistic Energies 22
MOA1MCCO02 – Operation and Upgrade of Stacktail Cooling System 27
MOA1MCIO03 – Prototype Pick-up Tank for CR Stochastic Cooling at FAIR 32
MOA2MCIO01 – Twenty-five Years of Stochastic Cooling Experience at Fermilab 36
MOA2MCIO02 – Numerical Design Study of Stochastic Stacking of 3 GeV Anti-Proton Beam in the RESR for the FAIR Project 41
TUM1MCIO01 – Muon Cooling R&D for the Muon Collider - A Five-year Plan for the US 46
TUM1MCIO02 – Enhanced Optical Cooling of Muon Beams 51
TUM1MCCO03 – Frictional Cooling Demonstration at MPP 55
TUM1MCIO04 – Six-Dimensional Cooling Simulations for the Muon Collider 59
TUM2MCIO01 – Compensation of Mean Energy Loss due to an Internal Target by Application of a Barrier Bucket and Stochastic Momentum Cooling at COSY 63
TUM2MCIO02 – Particle Accumulation with a Barrier Bucket RF System 67
TUA1MCIO01 – Status of the International Muon Ionization Cooling Experiment (MICE) 71
TUA1MCIO02 – Study of Collective Effect in Ionization Cooling 76
TUA1MCIO03 – Development of Helical Cooling Channels for Muon Colliders 81
TUA2MCIO01 – Status and Challenges in Beam Crystallization 86
TUA2MCIO02 – The Evolution of the Phase Space Density of Particle Beams in External Fields 91
TUA2MCCO03 – Wedge Absorber Simulations For The Muon Ionization Cooling Experiment 94
THM1MCIO01 – Status of the FAIR Project 98
THM1MCCO02 – Tevatron Electron Lens and its Applications 103
THM1MCCO03 – Electron Cooling Force Measurements with Variable Profile Electron Beam in HIRFL-CSRm 107
THM2MCIO01 – Transfer of CRYRING to FAIR 111
THM2MCIO02 – The Versatile NESR Storage Ring with Powerful Electron Cooling 115
THM2MCCO03 – Ultra Low Energy Electron Cooler for the Heidelberg CSR 119
THPMCP001 – Numerical Analysis of Low-Intensity Schottky Spectra Recorded as Time Series 123
THPMCP002 – Effective Luminosity Simulation for PANDA Experiment at FAIR 127
THPMCP003 – Prototype Pick-up Module for CR Stochastic Cooling at FAIR 130
THPMCP004 – Calculations of Electron Beam Motion in Electron Cooling System for COSY 134
THPMCP005 – Simulation Study of Simultaneous Use of Stochastic Cooling and Electron Cooling with Internal Target at COSY and HESR 138
THPMCP006 – Implementation of Longitudinal Dynamics with Barrier RF in Betacool and Comparison to ESME 142
THPMCP007 – Advance in the LEPTA Project 146
THPMCP008 – Muon Cooling in a Racetrack FFAG using Superfluid Helium Wedge Absorbers 150
THPMCP010 – Cooling Stacking Experiments at HIMAC 154
THPMCP011 – Application of BPM in HIRFL-CSR Electron Cooler 157
THPMCP012 – Study on the Oxide Cathode for HIRFL-CSR Electron Cooler 160
THPMCP013 – The Primary Plan of Stochastic Cooling at HIRFL-CSRe 164
FRM1MCIO01 – Electron Cooling for the Therapy Accelerator Complex 168
FRM1MCIO02 – Commissioning of Electron Cooling in CSRe 173
FRM1MCIO03 – Status of the 2 MeV Electron Cooler for COSY Juelich 178
FRM2MCCO01 – Electron Cooling for Future Electron-Ion Collide at JLAB 181
FRM2MCIO02 – Status of HIRFL-CSR Project 185

Appendices **191**
List of Authors 191
Institutes List 195
Participants List 198

International Program Committee

Ilan Ben-Zvi	Collider-Accelerator Department, Brookhaven National Lab (BNL)
Hånkan Danared	Manne Siegbahn Laboratory (MSL)
Yaroslav Derbenev	Center for Advanced Studies, Thomas Jefferson National Acc. Facility
Dan M. Kaplan	Illinois Institute of Technology (IIT)
Kwang-Je Kim	Argonne National Laboratory (ANL)
Igor Meshkov	Joint Inst. for Nuclear Research (JINR)
Yoshiharu Mori	Hign Energy Accelerator Research Organization (KEK)
Dieter Möhl	Europ. Org. for Nuclear Research (CERN)
Sergei Nagaitsev	Fermi National Acc. Laboratory (FNAL)
Akira Noda	Nuclear Science Reserch Facility, Kyoto University
Vasily V. Parkhomchuk	Budker Inst. of Nuclear Physics (BINP)
Ralph Pasquinelli	Fermi National Acc. Laboratory (FNAL)
Dieter Prasuhn	Institut für Kernphysik, Forschungszentrum Jülich
Andrew Sessler	Lawrence Berkeley National Laboratory(LBNL)
Markus Steck	Ges. für Schwerionenforschung (GSI)
Gérard Tranquille	Europ. Org. for Nuclear Research (CERN)
Hongwei Zhao(Chairman)	Institute of Modern Physics (IMP,CAS)

Local Organizing Committee

Hongwei Zhao(Chairman)	Institute of Modern Physics (IMP,CAS)
Xiaodong Yang(Co-Chairman)	IMP,Lanzhou,China
Youjin Yuan(Editor)	IMP,Lanzhou,China
Qiang Liang(Secretary)	IMP,Lanzhou,China
Xiaohong Cai(STD)	IMP,Lanzhou,China
Zhengguo Hu(STD)	IMP,Lanzhou,China
Lijun Mao(Sci. Secretary)	IMP,Lanzhou,China
Junxia Wu(Sci. Secretary)	IMP,Lanzhou,China
Jiawen Xia	IMP,Lanzhou,China
Ming Xie	IMP,Lanzhou,China


WARM WELCOME TO THE PARTICIPANTS OF COOL'09
August 31 - September 4, 2009 Lanzhou, China


COOL09
Welcome
International Workshop on Electron Cooling
and Related Topics


Calibration: 0.31 mm/kV


ulsed Laser System
s (including Schottky)
s at CSRe

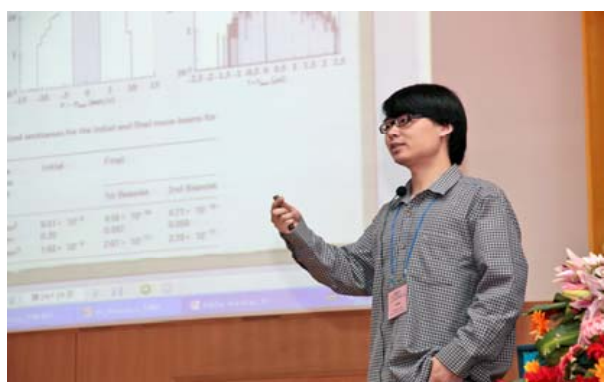

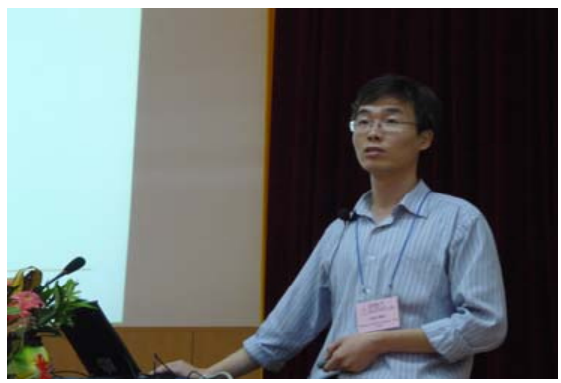

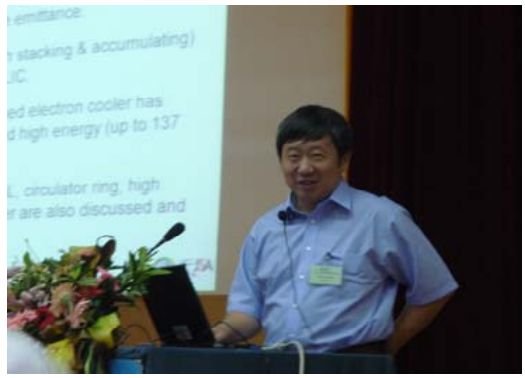

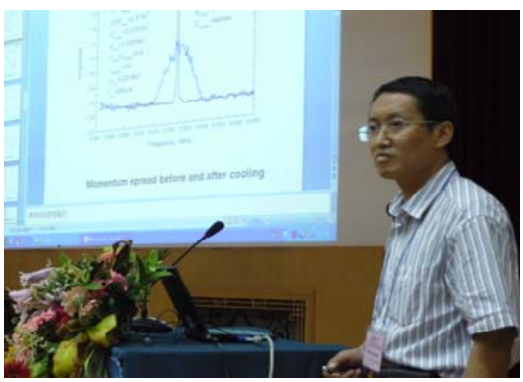
Momentum spread before and after cooling

STATUS OF ANTIPROTON ACCUMULATION AND COOLING AT FERMILAB'S RECYCLER*

L. R. Prost#, C. M. Bhat, D. Broemmelsiek, A. Burov, K. Carlson, J, Crisp, P. Derwent, N. Eddy, C. Gattuso, M. Hu, S. Pruss, A. Shemyakin, M. Sutherland, A. Warner, M. Xiao
FNAL, Batavia, IL 60510, U.S.A.

Abstract

The Recycler ring is an 8 GeV permanent magnet storage ring where antiprotons are accumulated and prepared for Fermilab's Tevatron Collider program. With the goal of maximizing the integrated luminosity delivered to the experiments, storing, cooling and extracting antiprotons with high efficiency has been pursued.

Over the past two years, while the average accumulation rate doubled, the Recycler continued to operate at a constant level of performance thanks to changes made to the Recycler Electron Cooler (energy stability and regulation, electron beam optics), RF manipulations and operating procedures. In particular, we discuss the current accumulation cycle in which ~400×10^{10} antiprotons are accumulated and extracted to the Tevatron every ~15 hours.

INTRODUCTION

Fermilab's Recycler was designed to provide an additional storage ring for the accumulation of 8 GeV antiprotons [1] and is now a critical component of the accelerator complex, without which the latest initial and integrated luminosity records for a hadron collider would not have been possible. The Recycler receives antiprotons from the Accumulator ring, and, through the combined use of stochastic [2] and electron cooling [3], stores up to 500×10^{10} particles, which are then extracted to the Tevatron collider. Over the past two years, the average antiproton accumulation rate more than doubled, imposing more stringent requirements for cooling and storing in the Recycler.

In this paper we characterize the Recycler performance by considering its ability to maintain the proper throughput of antiprotons in order to optimize the use of the whole accelerator chain, its efficiency storing the antiprotons, and the parameters of the bunches to be extracted to the Tevatron. In particular, we discuss the Recycler Electron Cooler (REC) [4] most recent improvements as well as modifications of the RF manipulations and procedures developed to limit losses.

RECYCLER PERFORMANCE

Accumulation & Cooling Scenario

At Fermilab, antiprotons are produced by striking an Inconel target with 120 GeV protons coming out of the Main Injector every 2.2 s. 8 GeV antiprotons are collected in the Debuncher ring where they are cooled stochastically and then transferred to the Accumulator ring. The rate at which antiprotons are accumulated in the Accumulator is referred to as the stacking rate.

Table 1 summarizes side by side the different running conditions between the summer of 2007 [5,6] and the summer of 2009. Antiprotons are transferred to the Recycler every 30 minutes in sets of two 'parcels' instead of 3 or 4 'parcels' every 2-3 hours two years ago. The transfer efficiency was kept >95%. In turns, the optimum collider store duration was found to be ~15 hours, during which a 'stash' (*i.e.* number of antiprotons stored in the Recycler as opposed to the 'stack' that refers to the Accumulator) of ~400×10^{10} antiprotons is built for extraction to the Tevatron [7].

Table 1: Summary of the Main Antiproton Production Parameters in the Summers of 2007 and 2009

	Summer '07	Summer '09
Average stacking rate, $\times10^{10}$ antiprotons per hour	19	26
Stack size for transfers	45-50$\times10^{10}$	25-30$\times10^{10}$
Frequency of transfers, hr	2-3	0.5
Average stash size	~300×10^{10}	~400×10^{10}
Collider store duration, hr	~25	~15

Figure 1 shows a comparison of the evolution of the number of antiprotons as well as the rms momentum spread during typical accumulation sequences in the Recycler in June 2007 and May 2009. It illustrates the move from larger transfers at large intervals to smaller transfers more often.

After the last transfer from the Accumulator, the longitudinal emittance is reduced to 60-70 eV s (95%) and 94-96% of the beam is 'mined'. Mining is the RF manipulation which takes the stored antiprotons from a single 6.1 μs-long bunch to 9 macro-bunches captured in mini barrier buckets while leaving high momentum particles in the so-called 'hot bucket' [8]. From there, each macro-bunch is successively divided into four 2.5 MHz bunches, which are then extracted to the Main Injector with >98% efficiency and from the Main Injector to the Tevatron for collisions. Note that the time between the last transfer from the Accumulator and extraction to the Tevatron was also diminished considerably as it currently lasts 1-1.5 hours, while 2-2.5 hours were typical 2 years ago.

* Operated by Fermi Research Alliance, LLC under Contract No. DE-AC02-07CH11359 with the United States Department of Energy
# lprost@fnal.gov

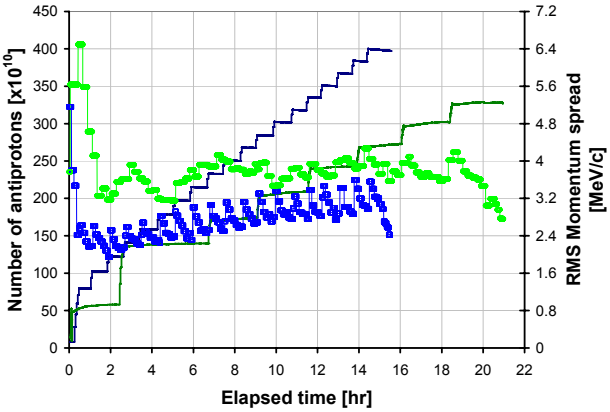

Figure 1: Typical accumulation and cooling cycle in the Recycler in Jun 2007 (green curves) and May 2009 (blue curves). Solid lines: number of antiprotons. Lines with circle or square data points: rms momentum spread. Note that the upward slopes between transfers for the 2007 data are due to the Recycler DCCT not working properly, and is not real.

Storage Efficiency

During both injections and extractions, the antiprotons travel through the Main Injector. By comparing the number of particles that come through during injections and extractions, we have a measure of the efficiency of the Recycler as a repository of antiprotons. Numerically, the storage efficiency is defined as

$$\frac{N_{\bar{p}\ \text{extracted to MI}} - N'_{\bar{p}\ \text{left in RR}}}{N_{\bar{p}\ \text{transferred from MI to RR}} + N'_{\bar{p}\ \text{left from previous extraction}}} \quad (1)$$

where $N_{\bar{p}}$ is the number of antiprotons measured by the Main Injector DC Current Transformer (DCCT) and $N'_{\bar{p}}$ is the number of antiprotons measured by the Recycler DCCT. Thus calculated, the storage efficiency includes injection and extraction efficiencies from and to the Main Injector, losses due to the antiprotons lifetime and accidental losses (*e.g.*: correctors' power supply trip, vacuum burst, and instability). A normal storage efficiency, where there is no accidental loss or operational issue, is ~93%. Out of the 7% of beam which is lost, ~3.5% is due to injection and extraction inefficiencies. The other ~3.5% comes from the antiprotons lifetime.

Figure 2 shows the evolution of the number of antiprotons and the associated beam loss between subsequent firing of a kicker for an accumulation and cooling cycle with typical storage efficiency. Note that the losses increase as a function of the number of stored antiprotons. Because of this, all cooling procedures were optimized in priority for when the number of antiprotons in the Recycler is large.

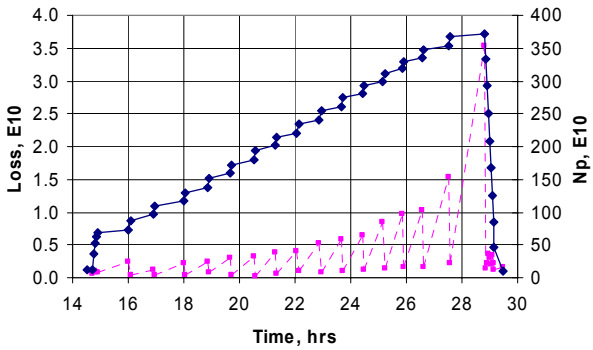

Figure 2: Beam intensity measured after a transfer (blue diamonds) and beam loss (pink squares) between injections/extractions during one cycle of accumulation. April 20 -21, 2009. Upper points on the loss curve correspond to time between two – parcel transfers, and the lower points are the loss between parcels. The life time drops with intensity from ~ 700 hrs to ~150 hrs.

Cooling Efficiency

In addition to storing antiprotons as efficiently as possible, the Recycler has to deliver the beam with adequate phase-space characteristics from larger average stash sizes and less time for cooling.

In practice, the fraction of the beam to be extracted from the stash (so-called mining efficiency) is determined by its longitudinal emittance during the mining process. Under normal conditions, the amount of beam which is extracted to the Main Injector reaches a near maximum of 95-96% for a longitudinal emittance of 65 eVs (95%), which is our nominal target emittance at this time. For fairly low numbers of antiprotons ($<200\times10^{10}$), mining efficiencies as high as 98-99% can be reached. Further decrease of the longitudinal emittance is limited by instabilities and poor lifetime.

Once the beam is mined and the 2.5 MHz bunches formed, the beam is cooled further and typically reached an equilibrium emittance of 1.0 eV s per bunch (95%, average of all bunches) and 2 π mm mrad (95%, normalized, flying wires). For a given RF structure, the final emittances depend weakly on the pre-history of beam or the number of particles (Figure 3) but this equilibrium is a good indication that the strength of the electron cooling force is not deteriorating. In addition, note that for these parameters, the intra beam scattering (IBS) makes the distribution of average velocities in the beam frame "spherical", *i.e.* $\langle v_L \rangle \approx \langle v_H \rangle \approx \langle v_V \rangle$. Consequently, emittances can only be decreased together for a given RF structure.

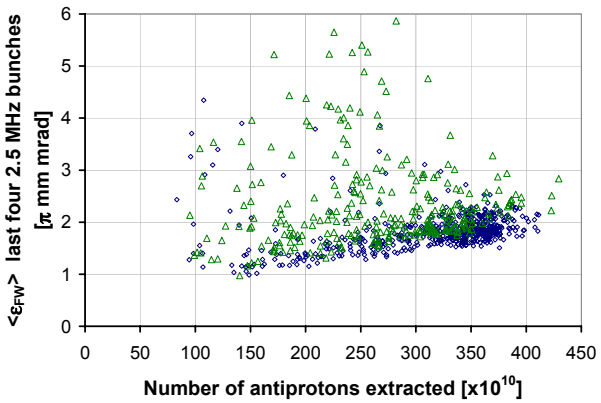

Figure 3: Average transverse emittances (flying wire, 95%, normalized) of the last 4 extracted bunches as a function of the stash size. Green triangles: June 2006-August 2007 data; Blue diamonds: November 2007-June 2009 data.

Contribution of stochastic cooling

While the increased frequency of transfers from the Accumulator and the larger average number of antiprotons stored in the Recycler are not favorable for stochastic cooling and diminish its overall efficiency, its role cannot be ignored for achieving high storage efficiencies.

First, after most of the beam has been extracted to the Tevatron, the Recycler is left with a fairly low number of particles (10-30×10^{10}) with large transverse emittance and momentum spread. In these conditions, the cooling efficiency of the electron beam is greatly diminished and the stochastic cooling system is essential for preparing the bunch to accept the first set of transfers from the Accumulator in a timely manner.

Most importantly, while the stochastic cooling rate decreases rapidly as the number of stored antiprotons increases (as ~1/N) and stochastic cooling is not needed to achieve the beam parameters required for extraction to the Tevatron, we found that it was important to keep it on, even with very little output power, in order to maintain decent lifetime at large stash sizes.

MAIN IMPROVEMENTS

Electron Cooling Optimization

Two major contributions to the effectiveness of electron cooling are the electron beam energy stability and the electron beam angles (*i.e.* rms transverse velocities over the length of the cooling section).

As already noted in Ref. [6], we found that the electron beam energy was drifting and we described how we use a large dispersion area in our beam line to provide a real-time beam-based measurement of the energy drift or relative error. This energy error is now used in a stand-alone software application, which makes the necessary adjustments to the Pelletron charging system in order to keep the electron beam energy to within 500 V of its nominal [9]. In parallel, a lot of attention has been paid to the temperature control of the Pelletron and the Generating Voltmeter (GVM), the instrument used to measure the terminal high voltage, because of their clear influence on the energy (true or measured). In steady state, the SF_6 cooling system keeps the Pelletron temperature within ±0.2 K. Because a large portion of the heat load is removed from the Pelletron tank through its walls, the ambient temperature affects the cooling efficiency of the tank and thus the voltage stability. Presently, three air conditioning units keep the temperature in the building within ±1 K. Finally, a thermal regulator was installed with the GVM, and now its temperature varies typically by ±0.5 K over several weeks, effectively eliminating this source of the energy drift [9].

One contribution to the total angles in the electron beam arises from deviations of the beam envelope from cylindrical in the cooling section. Such distortions can be studied by imaging the beam in the pulse mode on a removable scintillator (YAG crystal [10]) located at the exit of the cooling section and captured by a gated CID camera [11].

Dedicated measurements carried out in 2007 showed a large contribution from quadrupole oscillations in the cooling section, confirming the preliminary results of Ref. [6]. With a special procedure, the electron beam transverse distribution was brought closer to an ideal axially symmetrical shape using 6 upstream quadrupoles [12]. However, cooling rates with a DC beam did not improve. Qualitatively, a possible explanation for this result may be that, in DC mode, secondary ions, which accumulate in the beam potential, lead to a significantly different envelope than for the pulsed beam. Nevertheless, similarly to what was done in the pulsed mode with the YAG but using drag rate measurements instead of beam images, the quadrupoles were tuned with a DC beam and lead to higher cooling rates both longitudinally and transversely. In particular, for an electron beam offset of 2 mm with respect to the antiproton trajectories, the cooling rate increased by 1.5-2 times [12, Fig. 4].

The electron beam angles also deteriorate with time because of the tunnel ground motion that affects the relative position of the cooling solenoids with respect to one another, thus inducing dipole kicks along the cooling section [13]. To correct, a procedure based on drag rate or cooling rate measurements was developed and is described in Ref. [13]. Although the uncertainties of this procedure are large, it successfully improved the cooling efficiency in operation. At this time, we find that it needs to be repeated every ~6 months to avoid a noticeable deterioration of the cooling rate.

Finally, while in theory the cooling force should increase with the electron beam current, in our experience, the maximum drag/cooling rates were found at 100 mA, our present operating beam current. We do not have a satisfying explanation for this limitation at this time.

Cooling Procedures & RF Manipulations

The basic procedures for accumulating and cooling antiprotons in the Recycler have not changed and are

described in Refs [5,6,8]. They heavily rely on the REC, its performance, and its availability. However, the improvements highlighted above allowed for some operational simplifications without impairing the cooling and storage efficiencies. In addition, a RF manipulation during injections was revisited with beneficial results.

Because the portion of the time when the electron beam is not needed became relatively small (~15%), the electron beam is now on at all times. By leaving the electron beam on, the REC gained in stability, notably the electron beam energy. Then, instead of constantly moving the electron beam to adjust the cooling rate, we leave the electron beam at a constant position, namely 2 mm offset (vertically) from the antiprotons central orbit. With the improved cooling rate, we found that this position was adequate to cool all stashes up to the record number of 525×10^{10} antiprotons. While the optics solution with quadrupoles improved the cooling efficiency, the antiprotons lifetime still deteriorates when the cooling rate increases (*i.e.* when the electron beam is moved closer to the antiprotons central orbit). Thus keeping the electron beam at a constant offset might slightly deteriorate the antiprotons lifetime at low intensities ($<150\times10^{10}$). On the other hand, Figure 2 shows that the impact on the total beam loss is small because the total beam loss is mostly determined by the lifetime at high intensities where cooling cannot be traded for lifetime preservation.

The new cooling procedure also reduces the number of manipulations of the electron beam, which in turns limit the risk of overcooling the antiproton beam because of an operational mistake. Note that Operators still have the possibility of moving the electron beam in non-standard situations.

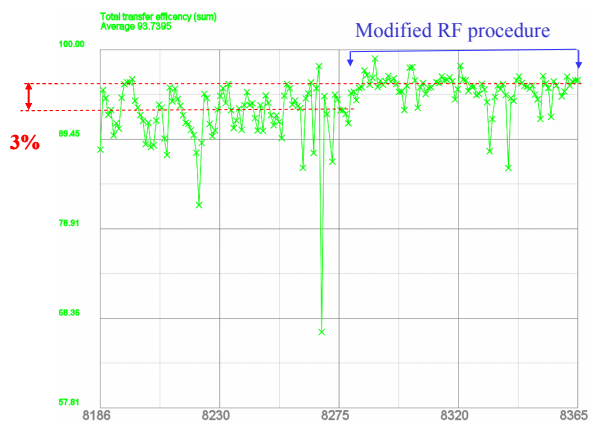

Figure 4: Transfer efficiency as a function of the transfer number. The RF change was made on June 9th, 2008 (transfer #8267). Note that the benefits from the RF modification may not be apparent right away because of the accelerator chain conditions and destructive studies taking place concurrently.

An important improvement for increasing the storage efficiency was the slight modification of the RF manipulations during the injection process. Just before injections, the potential well is deepened in order to capture as many DC particles (*i.e.* particles not contained by the RF bucket) as possible to avoid their loss when the injection kicker fires. Analyses found that this manipulation was done too rapidly for adiabatic capture, and it was slowed down. Figure 4 shows the transfer efficiency before and after the RF modification. On average, the transfer efficiency increased by 3% (thus increasing the storage efficiency). In particular, the modified RF manipulation significantly reduced the sensitivity of the transfer efficiency on the number of stored antiprotons.

RESISTIVE WALL INSTABILITY

One of the limitations on the Recycler beam's brightness is a resistive wall instability [14,15]. To first order, its threshold is determined by the 'phase density' of the bunch, which, we defined as:

$$D = \frac{N_{\bar{P}}}{4\varepsilon_{L\,rms}\cdot\varepsilon_T} \qquad (2)$$

where $N_{\bar{p}}$ is the number of antiprotons in units of 10^{10}, $\varepsilon_{L\,rms}$ is the root-mean-square longitudinal emittance in eV s and ε_T is the 95%, normalized transverse emittance in μrad. For the Recycler, a calculation of the phase density threshold for a Gaussian distribution gives 0.8 at the lowest sideband, and it was verified experimentally to within the uncertainties associated with the measurements.

This instability was dealt with by installing a transverse digital damper system in 2005 [16]. To address the increased brightness of the beam in the Recycler, the original system was upgraded, and the operational bandwidth increased from 30 MHz to 70 MHz [17,18]. Currently, we find that the beam remains stable up to D ~ 3.5, in line with expectations.

Recently, we only experienced instabilities once the antiproton beam had been mined. At this stage, lifetime preservation is no longer the main consideration and, the electron beam is moved closer to the axis of the antiproton beam, providing stronger cooling, thus increasing the brightness of the antiprotons further. Interestingly, only one of the macro-bunches goes unstable at a time, although we can have several instabilities in a row affecting different macro-bunches. By looking at the dampers pickups at the onset of the instability, we see that, as expected, it is always the tail of the bunch which starts oscillating at a frequency of ~70-100 MHz, above the dampers limit (Figure 5).

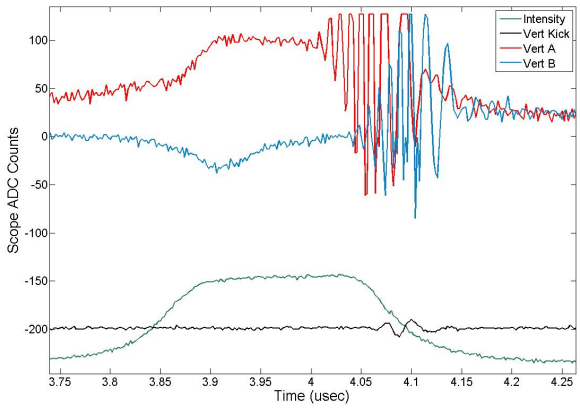

Figure 5: Example of an instability during extraction affecting a single macro-bunch. The black curve is the kicker response. The red and blue curves are the pickups signals. The green trace is the intensity profile.

All the latest instability events developed when the antiproton beam was cooled for several hours without injections before final cooling and mining. This may indicate a correlation with better cooling of the tails particles, thus diminishing the number of resonant particles ('Landau particles') that help maintain beam stability. Calculation of the instability threshold for the value of D, Eq. (2), for a Gaussian and a step-like distribution finds that it is ~2 times higher for the Gaussian distribution than for the step-like distribution [19]. Unfortunately, in operation, there is no measurement that can resolve quantitatively the amount of tail particles (at the level of ~ 0.0001) so that we could predict (and avoid) the instability to occur. We do however recognize that the lifetime gives a good indication of whether or not we might be near the instability threshold. Typically, this would be the case if the lifetime is greater than 500 hours for a stash of $>350\times10^{10}$.

While increasing the dampers bandwidth by a factor of 2 was entirely done through improving the electronics, going further would require hardware modifications in the vacuum chamber (kickers and/or pickups). There are no such plans for the remaining of the Tevatron running period.

CONCLUSION

Over the past two years, the average antiproton flux in the Recycler more than doubled. Nevertheless, the Recycler was able to accommodate these higher rates with the same efficiency as before. This was achieved merely through fine tuning of existing components and procedures in a context where only percent level improvements could be expected.

A better control of the REC electron beam envelope as well as of its energy, along with slightly modified RF manipulations permitted to streamline and simplify the cooling and accumulation procedures, making the operation of the Recycler more robust.

ACKNOWLEDGMENTS

We are grateful to the entire Recycler and Support departments for helping with many aspects of the work and measurements discussed in this paper and countless productive discussions.

REFERENCES

[1] G. Jackson, FERMILAB-TM-1991 (1996)
[2] D. Broemmelsiek, A.V. Burov, S. Nagaitsev and D. Neuffer, "*Bunched beam stochastic cooling in the Fermilab Recycler Ring*" in Proc. of the 2005 Part. Accel. Conf., Knoxville, Tennessee (2005) FFPAE009
[3] S. Nagaitsev, *et al*., Phys. Rev. Lett. **96** 044801 (2006)
[4] A Shemyakin *et al.*, AIP Conf. Proc. **821**: 280 (2006)
[5] P. Derwent, "*Status of the Recycler*", in Proc. of COOL'07, Bad Kreuznach, Germany (2007) MOM1I01
[6] L. Prost *et al.*, "*Electron Cooling Status and Characterization at Fermilab's Recycler*" in Proc. of COOL'07, Bad Kreuznach, Germany (2007) MOA2I06
[7] C. Gattuso, M. Convery & M. Sypher. "*Optimization of Integrated Luminosity in the Tevatron*", *to be published* in Proc. of the 2009 Part. Accel. Conf., Vancouver, BC, Canada (2009) MO4RAC03
[8] C.M. Bhat, Physics Letters A **330** (2004) 481-486
[9] A. Shemyakin, K. Carlson, L.R. Prost & G. Saewert. "*Stability of Electron Energy in the Fermilab Electron Cooler*", FERMILAB-CONF-08-425-AD
[10] Use of YAG for beam imaging in the cooler was proposed by W. Gai, and the crystal was provided by his ANU group.
[11] A. Warner *et al.*, IEEE Trans. Nucl. Sci. V**52** 5 (2005)
[12] A. Shemyakin *et al.*, "*Optimization of Electron Cooling in the Recycler*", *to be published* in Proc. of the 2009 Part. Accel. Conf., Vancouver, BC, Canada (2009)
[13] L. Prost & A. Shemyakin, "*Beam-based Field Alignment of the Cooling Solenoids for Fermilab's Electron Cooler*" in Proc. of COOL'07, Bad Kreuznach, Germany (2007) THAP09
[14] A. Burov & V. Lebedev, AIP Conf. Proc.**773**: 350-354 (2005)
[15] V. Balbekov, "*Transverse coherent instability of a bunch in a rectangular potential well*", FERMILAB-PUB-06-070-AD (2006)
[16] N. Eddy and J.L. Crisp, AIP Conf. Proc. **868**: 293-297 (2006)
[17] A. Burov, "*Analysis of Transverse Resistive Instability in the Recycler*", FERMILAB-TM-2336-AD (2005)
[18] N. Eddy, J.L. Crisp and M. Hu, "*Measurements and Analysis of Beam Transfer Functions in the Fermilab Recycler Ring Using the Transverse Digital Damper System*", in Proc. of the 11th European Part. Accel. Conf., Genoa, Italy (2008) THPC117
[19] A. Burov & V. Lebedev, PRSTAB **12** 034201 (2009)

ANTIPROTON DECELERATOR STATUS REPORT

Lajos Bojtár, CERN, Geneva, Switzerland*

Abstract

The Antiproton Decelerator (AD) has been delivering 5.3 MeV antiprotons to the experiments for 10 years now. Beam cooling is essential for the AD operation. We review the AD machine and in particular the cooling performance. We give an overview of the present and future experiments and also the possible further deceleration of the beam from 5.3 MeV to 100 keV kinetic energy.

INTRODUCTION TO AD

The Antiproton Decelerator (AD) started regular operation [1] in 2000. The AD has been constructed from the parts of the AC machine in order to provide 5.3 MeV antiprotons for initially 3 experiments, ASACUSA, ATRAP and ALPHA. The experiments have the ultimate goal to produce antihydrogen in their trap and measure its properties with spectroscopy in order to verify CPT symmetry with a high precision. ASACUSA has been doing spectroscopy with antiprotonic helium. Later a fourth experiment ACE joined. They have been studying living tissue irradiation with antiprotons in order to investigate the possibility to use antiprotons for cancer therapy. AEgIS is a recently approved fifth experiment aiming to measure directly the effect of the Earth's gravity on antihydrogen. This will be the first experiment of this kind.

THE DECELERATION CYCLE

Antiprotons are produced by sending a 26 GeV/c proton beam onto a water cooled iridium target. Antiprotons on the downstream are focused by a magnetic horn to collect as many as possible. Then a dogleg shaped part of the injection line separates the antiprotons from the other types of particles. Four bunches are injected into the AD ring by a magnetic septum and a kicker. The momentum spread of the beam is large at injection, about a $\pm 3\%$. In order to decrease the dp/p to fit more beam inside the momentum acceptance of the stochastic cooling, which is around $\pm 1\%$, a bunch rotation is applied. After bunch rotation the dp/p is $\pm 1.3\%$. There are two bunch rotation cavities in the ring, each gives about 500 kV at harmonic 6. The cavities are ramped up already when the beam is injected and after a quarter of synchrotron turn they are turned off. The AD cycle has 4 flat parts, these are introduced in order to cool the beam. After injection and the bunch rotation, stochastic cooling is applied at 3.57 GeV/c. The second stochastic cooling process takes place at the 2 GeV/c plateau. The machine operates with two different tunes, one for higher energies and one for lower energies. The tune is changed after the second stochastic cooling. The beam is decelerated to 300 MeV/c where electron cooling is applied. After further deceleration to the final momentum, electron cooling is applied for a second time at 100 MeV/c. Figure 1 shows the AD cycle.

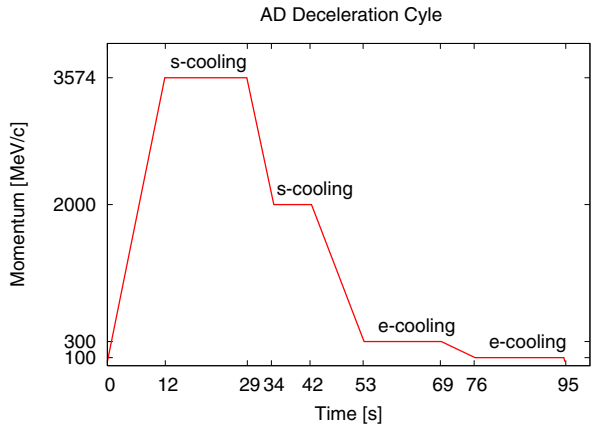

Figure 1: The AD deceleration cycle.

Table 1: AD Main Parameters

Circumference [m]	182
Prod. beam [protons/cycle]	1.3×10^{13}
Injected beam [pbars/cycle]	4×10^{7}
Momentum [GeV/c]	3.57-0.1
ϵ_{tr} $[\pi \times mm \times mrad]$	180-0.8
$\pm$dp/p	$3 \times 10^{-2} - 7 \times 10^{-5}$
Average vacuum [Torr]	4×10^{-10}
Cycle length [s]	96
Dec. efficiency [%]	85

OPERATIONAL PERFORMANCE

The AD operates non-stop during the entire run since 2004. Machine supervisors are working during the day and providing an on-call service outside working hours, including weekends. In the last two years AD suffered several major breakdowns. A consolidation budget and program has been approved in order to improve the reliability of the hardware and make the necessary maintenance and preventive actions. In 2008 the number of injected antiprotons has decreased by 30 %. Many things have been verified in order to find the cause of the lower injected intensity, like injec-

* on behalf of the AD team

tion line optics and matching, production beam parameters, AD acceptances, bunch rotation settings. At the end of the shutdown we discovered a mechanical fault of the target positioning system. The positioning mechanism has been repaired and the injected intensity is back to the normal values during the 2009 run. New optics have been put into operation in the ejection line leading to smaller beam size and lower transfer losses. The Table 2 shows the yearly statistics of the AD.

Table 2: AD Run Time by Year

Year	2003	2004	2006	2007	2008
Total [h]	2800	3400	2352	3800	3338
Physics [h]	2300	3090	2185	3760	3142
Md [h]	500	310	167	40	62
Uptime (%)	90	71	69	78	86

STOCHASTIC COOLING

The hardware for the stochastic cooling is recovered from the AC machine, but only the 0.9-1.6 GHz (nominal) band is kept due to space limitations. There are two stages of stochastic cooling in the cycle, the first at injection and a second at 2 GeV/c. Due to the two distinct momenta there are two separate signal paths for each plane. For longitudinal cooling the notch filter method is used. In order to increase the signal to noise ratio the transverse separation of the pickups is decreased during the cooling process. There is a kicker movement system too, but it is not used. Programmable gain invariant delays are used to optimize phase. Programmable static and dynamic phase invariant attenuators are used to optimize gain. These are controlled by function generators and the gain is decreased during the cooling. The performance figures are summarized in Table 3. Apart from recent problems with the pickup movement the stability of the stochastic cooling system is excellent since many years.

Table 3: Stochastic Cooling Performance

Momentum [GeV/c]	3.57	2.0
Duration [s]	17	7
$\epsilon_x/\epsilon_y[\pi \times mm \times mrad]$	5/5	3/3
dp/p	10^{-3}	10^{-4}

ELECTRON COOLING

The electron cooler was taken from the dismantled LEAR machine and with some modification was installed in the AD ring. The main parameters of the cooler are summarized in Table 4. The performance figures can be found in Table 5. Due to the very low momentum spread at 100 MeV/c even a small noise on the RF system can cause a significant increase of the longitudinal emittance during the capture process. In order to compensate this effect there is an overlap between the start of the capture and the end of the electron cooling. A longer overlap leads to shorter bunches, but with a higher percentage of the beam in the tails of the distribution. Another problem is the time jitter of the ejected bunch when the overlap is too big. In the last years electron cooling works well and the drag force has a significant effect on the RF system, disturbing the synchronization loop and causing about a 40 ns time jitter. Some attention is needed to find the correct setting. A typical beam profile is shown on Figure 2. The reason for the tail formation it not well understood. In many years during the AD operation the stability of the orbit was a major issue. Sudden jumps occurred, making difficult to keep electron cooling performance on the optimum. The source of the orbit jumps was identified as a faulty magnet coil. Since the coil has been replaced during the 2007 run the electron cooling performance is far more stable.

Table 4: Parameters of the Electron Cooler

Cooling length [m]	1.5
Electron beam energy [keV]	2.8-35
Electron beam current [A]	0.1-2.5
Field in solenoid [Gs]	590
Electron beam radius [cm]	2.5

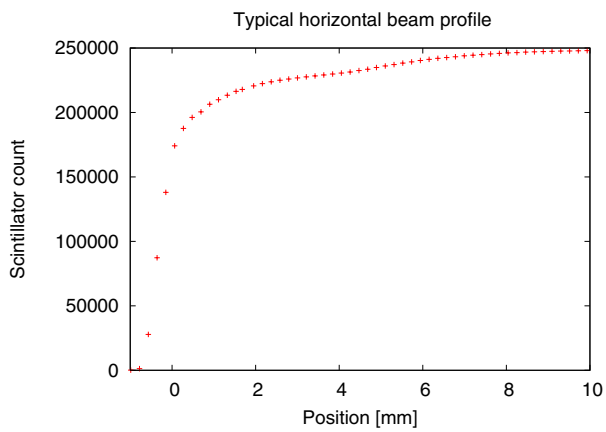

Figure 2: A typical horizontal beam profile obtained by the scraper at 100 MeV/c. The $\beta_h = 5m$ at the scraper position, ϵ_h = 0.5 π mm mrad with 80 % of the beam inside and with a long tail of the distribution.

FURTHER DECELERATION OF THE BEAM

The experiments can trap antiprotons with kinetic energy less than 10 keV. ALPHA and ATRAP use degrader foils to slow down antiprotons to this range. The foil method

Table 5: Performance of the Electron Cooler

Mom. [MeV/c]	300	100
Cooling time [s]	16	15
$\epsilon_x/\epsilon_y[\pi \times mm \times mrad]$	3/3	0.8/0.5
dp/p	10^{-4}	$< 7 \times 10^{-5}$

is very inefficient, 99.9 % of the beam is lost and the remaining part suffers a big emittance blow up due to the scattering on the foils. ASACUSA uses an RFQD with an adjustable output energy in the range of 10-100 keV. They also use a very thin degrader foil in order to isolate the trap vacuum from the rest of the system. With the RFQD about 25 % of the beam is decelerated and about 4% is kept in the trap.

During development sessions in 2008 a novel deceleration technique using the longitudinal drag force of the electron cooler was attempted. The idea is to ramp the AD magnetic field and the electron cooler energy synchronously such that the circulating antiprotons are continuously cooled as their energy changes. Due to limitations in the control of the AD cycle, a very modest first test was made decelerating 3.5×10^7 antiprotons from 46.5 MeV to 43.4 MeV in 56 seconds whilst keeping the transverse emittances below 1 [π mm mrad] during the whole deceleration. Additional measurements to measure the drag force at 5.3 MeV (100 MeV/c) were also performed in order to estimate the time needed to decelerate the beam below this energy.

This year experiments to go below 5.3 MeV have been made with the beam successfully decelerated to 4.8 MeV (95.37 MeV/c) in 33 seconds as expected from the measurements made in 2008. The control of the closed orbit, and more specifically the alignment of the antiproton beam with the electrons, proved to be more delicate than expected and hindered the progression of the experiments. The aim of future studies will be to optimize the deceleration of the beam to an energy of 4 MeV (87 MeV/c) and to measure the beam parameters during the ramp.

Another idea is to cool the beam at 100 MeV/c in a barrier bucket and obtain a much smaller longitudinal emittance than coasting beam cooling can provide. This is possible in the AD because the intensity is very low and even though the beam is confined longitudinally by a factor 20 the IBS and space charge effects remain acceptable. In the current scheme a coasting beam is cooled, captured into a single bunch, then a bunch rotation is applied and the beam is ejected. When the RFQD is used the 202 MHz bunch structure needed for deceleration is created by a buncher cavity 6 meters in front of the RFQD in the ejection line. This type of bunching limits the the deceleration efficiency to 50 % at best, in practice about 25 % is decelerated. The proposal is to cool the beam in a barrier bucket and capture it with 202 MHz already in the machine. This requires the installation of two 202 MHz cavities into the AD ring. This way there is no loss due to the buncher cavity and a factor

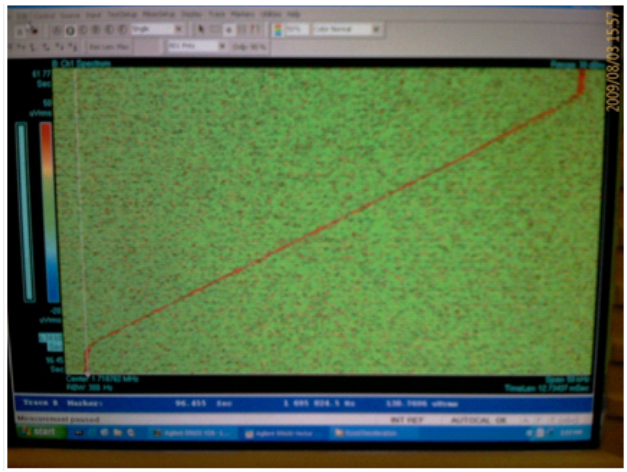

Figure 3: Beam deceleration using the the electron cooling drag force.

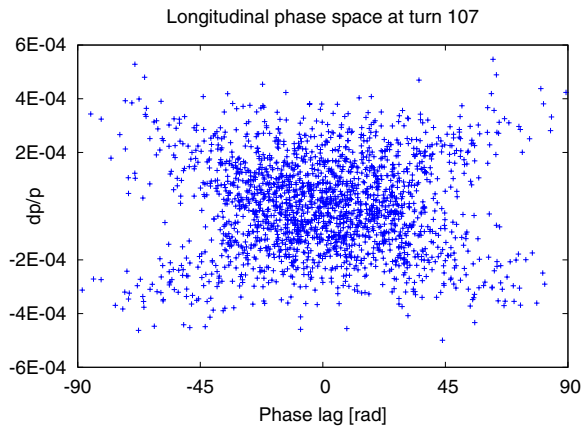

Figure 4: Longitudinal phase space plot at the end of the capture process with 202 MHz, with a 300 ns long barrier bucket. A starting dp/p =7 $\times$ 10^{-5} was assumed. This is a simulation result including longitudinal space charge forces.

2-3 in intensity can be gained. The longitudinal emittance of the beam is much lower in this case, because the large increase in momentum spread due to the h=1 bunching in the current scheme is not present. Due to the longitudinal space charge forces the beam can not be compressed enough to fit inside the ± 10 degree phase acceptance of the RFQD [2], therefore the buncher cavity is still needed to give a further longitudinal focusing, however it doesn't throw away a large part of the beam in this case. Figure 4 shows the longitudinal phase space plot at the end of the capture, Table 6 shows the ratio of the beam inside a given phase extent. If the RFQD can be modified to have a larger phase acceptance, maybe at the expense of an increased length then it would be possible to drop the buncher cavity and obtain a beam at 100 keV with with a much smaller momentum spread. This possibility needs further investigation. At the expense of installing two cavities in

Table 6: Percentage of the Beam Inside a Given Phase Extent

Phase [±deg]	25	30	35	40	45
Portion inside	61%	70%	78%	83%	87%

the AD ring the intensity can be multiplied by a factor 2-3 for ASACUSA. A preliminary test has been done with bunched beam cooling at 100 MeV/c with $V_{rf} = 500$V, h=3 to test this idea. These preliminary results are very promising. The tail structure similar to the profile shown on Figure 2 was observed. The bunch length was determined by the longitudinal space charge force and found to be dependent on the intensity. At lower intensity the transverse profile was better, the ratio of the beam in the tail of the distribution was smaller. This could indicate that an intensity dependent effect like IBS or tune shift due to space charge plays a role in the formation of the tail. The barrier bucket cooling can be tested with the existing equipment in the AD ring, the test is under preparation. A proposal [3] based on the idea described above will be published soon by the author.

EXTRA LOW ENERGY ANTIPROTON RING (ELENA)

The Motivation

ELENA is a compact ring [4] for further deceleration and cooling of 5.3 MeV pbars delivered by the CERN Antiproton Decelerator. The ultimate goal of ELENA is to increase the number of antiprotons in traps of AD experiments significantly. By using a ring equipped with beam cooling, high deceleration efficiency and important increases in phase-space density can be obtained, resulting in an increased number of trapped antiprotons. The low energy limit for this machine is 100 keV. It was chosen as a compromise between requirements from experiments of ultra low energy beam and constraints given by space charge limitations in machine and cooler, requirements to vacuum of few 10^{-12} Torr and others. For the ATRAP and ALPHA experiments, improvements of 2 orders of magnitude can be expected. ASACUSA on the other hand presently uses first an RFQD for deceleration to 100 keV, and then additionally an ultra-thin degrader (1 micron thick) for deceleration to 5 keV. Here, a 10-fold increase can be expected thanks to reduced transverse and longitudinal emittances.

Location of ELENA

With a circumference of about 26m, ELENA can be located in the AD hall where assembly and commissioning would not disturb current AD operation too much. AD experimental areas could be kept as they are now, but much lower beam energies require new transfer line elements (electrostatic) and diagnostics. Some reshuffle of AD Experimental Area has to be done to prepare the space for

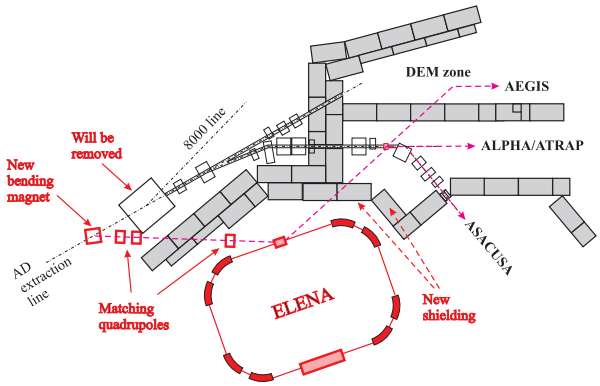

Figure 5: ELENA ring location in AD Experimental Area.

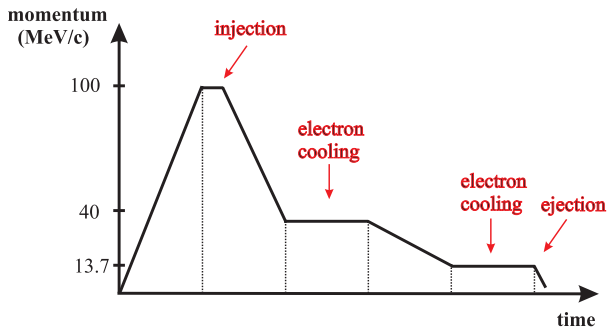

Figure 6: Schematic view of ELENA cycle.

ELENA, as well as modifications in shielding. The precise positioning of a new ring in AD Hall is dictated by optimal conditions for injection and for extraction [5] into existing experimental areas.

Machine Cycle

Due to the small emittance of a beam ejected from AD, beam in ELENA can be decelerated down to intermediate energy without cooling at injection energy. This makes design of electron cooler much easier. After the last cooling at 13.7 MeV/c, the beam is ejected

Ring Configuration and Machine Parameters

Two long straight sections are suited for electron cooler and for injection/ejection septa, see Figure 7. Two short straight sections will be used for injection/ejection kickers, diagnostics, RF and other equipment. The lattice includes 8 bending magnets and 8 quadrupoles. Quadrupoles will be built as multipoles which include in some of them skew quadrupolar and sextupolar components, in other horizontal and vertical steering elements. The main intensity limitation in ELENA is due to incoherent tune shift caused by space charge. It is negligible during deceleration and cooling of coasting beam. To deliver short bunch of 1.3 m to trap of experiment the bunch rotation in the longitudinal phase space is applied. At the end of this process the bunch is short and space charge effects have to be taken into ac-

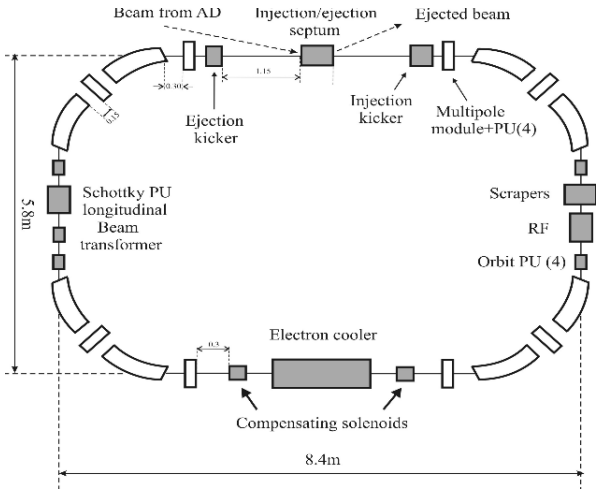

Figure 7: ELENA ring layout.

count. For the conservative value of tune shift ΔQ = 0.1 and beam emittances $\epsilon_{x,y}$=3 π mm mrad in ELENA intensity in one bunch is limited to 0.65×10^7 pbars. Therefore it is proposed to bunch the beam after cooling at 13.7 MeV/c at harmonic h = 4, thus increasing the maximum number of pbars available at least up to 2.6×10^7. Each of 4 experiments with trap (including AEgIS) will receive a quarter of total amount of pbars. Fast switching electrostatic magnet placed in a common part of extraction line allows to extract all 4 bunches during one turn. The main machine parameters are given in Table 7:

Table 7: ELENA Basic Parameters

Momentum range, MeV/c	100 - 13.7
Energy range, MeV	5.3 - 0.1
Circumference, m	26.062
Intensity of injected beam	3×10^7
Intensity of ejected beam	2.5×10^7
Number of extracted bunches	4
Em. at 100 keV, π.mm.mrad, [95%]	3 / 3
dp/p after cooling, [95%]	10^{-4}
Bunch length at 100 keV, m / ns	$1.3/300$
Required vacuum, Torr	3×10^{-12}

The ELENA Electron Cooler

For fast and efficient cooling special attention must be paid to the design of the electron gun and the quality of the longitudinal magnetic field guiding the electrons from the gun to the collector [6]. The electron gun has to be designed in a way to produce a cold ($T_\perp < 0.1$ eV, $T_\parallel < 1$ meV) and relatively intense electron beam ($n_e \approx 3 \times 10^{12}[cm^{-3}]$). The gun is immersed in a longitudinal field of 700 Gs which is adiabatically reduced to maximum field of 200 Gs in the transition between the gun solenoid and the toroid. Due to this, transverse temperature is reduced as well during beam adiabatic expansion. The main characteristics of the proposed device are summarized in Table 8.

Table 8: ELENA Electron Cooler Parameters

Cooling length [m]	1
Beam cooled at momentum [MeV/c]	35 and 13.7
Electron beam energy [V]	355 and 54
Electron beam current [mA]	15 and 2
Magnetic field in solenoid [Gs]	200
Electron beam radius [cm]	2.5

CONCLUSION

The AD is continuing to provide good quality beam to the physics community. Intensities are well above 3×10^7 pbars per shot since the repair of the target positioning system, with a repetition rate around 96 seconds. Deceleration efficiency is above 80 %. Ejected beam emittances are below 1 π mm mrad. The AD experiments have been producing interesting physics and pursuing their ultimate goal, the antihydrogen spectroscopy. The AEgIS experiment has been approved and will measure the strength of gravity on antimatter. The direction for improvements is to decelerate the beam to lower energy and increase the number of antiprotons in the traps by a large factor, even orders of magnitude.

ACKNOWLEDGMENTS

I would like to express my gratitude towards the members of the AD team, support personnel, members of the AD physics community and all people who gave their valuable comments.

REFERENCES

[1] P. Belochitskii, et al., “Commissioning and First Operation of the Antiproton Decelerator (AD)”, CERN-PS-2001-047-AE.

[2] A.M. Lombardi, W. Pirkl, Y. Bylinsky, “First Operating Experience with the CERN Decelerating RFQ for Antiprotons”, CERN-PS-2001-064-PP.

[3] L. Bojtár, “Intensity Improvement for AD Experiments Using Barrier Bucket Cooling”, to be published.

[4] T. Eriksson (editor) et. al., “ELENA – A Preliminary Cost and Feasibility Study”, CERN-AB-2007-079.

[5] P. Belochitskii, “ELENA Optics”, private communication.

[6] G. Tranquille, “Electron Cooler for ELENA”, private communication.

ELECTRON COOLING FOR LOW-ENERGY RHIC PROGRAM*

A.V. Fedotov#, I. Ben-Zvi, X. Chang, D. Kayran, V.N. Litvinenko, A. Pendzick, and T. Satogata
Brookhaven National Laboratory, Upton, NY 11973, U.S.A

Abstract

Electron cooling was proposed to increase luminosity of the RHIC collider for heavy ion beam energies below 10 GeV/nucleon. Providing collisions at such energies, termed RHIC "low-energy" operation, will help to answer one of the key questions in the field of QCD about existence and location of critical point on the QCD phase diagram [1-4]. The electron cooling system should deliver electron beam of required good quality over energies of 0.9-5 MeV. Several approaches to provide such cooling were considered. The baseline approach was chosen and design work started. Here we describe the main features of the cooling system and its expected performance.

EXPECTED PERFORMANCE

In a preparation for Low-Energy RHIC physics program, several short test runs were carried out at an intermediate energy point of interest, γ=4.9, for projections of future low-energy RHIC operations [5]. During the first test run with gold ions in June 2007, the beam lifetime was very short and dominated by machine nonlinearities. These nonlinearities were intentionally increased to suppress head-tail instabilities. During the latest test run in March 2008, beam lifetime was improved using a new defocusing sextupole configuration. The store length was extended from 15 minutes in 2007 to 1 hour in 2008 [5].

Some improvements in the useful luminosity are straightforward. For example, doubling the number of bunches (to the nominal 108) will double the event rate. We also expect some improvement in the machine performance with additional tuning. An estimate of run time needed for the proposed low-energy physics program is given in Ref. [6, 7]. Luminosity projections are relatively low for the lowest energy points of interest.

Luminosity decreases as the square of bunch intensity loss due to longitudinal intra beam scattering (IBS) and transverse emittance growth from transverse IBS. Both transverse and longitudinal IBS can be counteracted by electron cooling. This allows one to keep the initial peak luminosity constant throughout the store without beam loss. In addition, the phase-space density of the hadron beams can be further increased by providing stronger electron cooling.

*Work supported by Brookhaven Science Associates, LLC under contract No. DE-AC02-98CH10886 with the U.S. Department of Energy.
Author email: fedotov@bnl.gov

LUMINOSITY LIMITATIONS

Intra-beam Scattering

IBS is one of the major effects contributing to RHIC heavy ion luminosity degradation, driving bunch length and transverse beam emittance growth. IBS-driven bunch length growth causes beam losses from the RF bucket.

At these low energies, strong IBS growth can be counteracted with electron cooling [6, 8]. If IBS were the only limitation, one could achieve small hadron beam emittance and bunch length with the help of electron cooling, resulting in a dramatic luminosity increase. Unfortunately, the defining limitation is expected to be space charge at the lowest energy points in RHIC.

Space-charge Tune Shift

In circular accelerators, the figure of merit for space-charge effects is the shift of incoherent betatron oscillation frequencies. This is called the "space-charge tune shift". When the space-charge tune shift becomes significant, the beam overlaps many machine imperfection resonances, leading to large beam losses and poor lifetime. For machines where beam spends only tens of msec in high space-charge regime, and machines where the resonances are compensated, the tolerable space-charge tune shift can be as big as ΔQ=0.2-0.5. However the acceptable tune shifts are much smaller for long storage times. In some machines, lifetimes of a few minutes were achieved with tune shifts higher than 0.1. For RHIC, we are interested in much longer lifetimes. As a result, we take space-charge tune shift values of about 0.05 as a limit for our present estimate.

For a Gaussian transverse distribution, the maximum incoherent space-charge tune shift can be estimated:

$$\Delta Q = -\frac{Z^2 r_p}{A}\frac{N_i}{4\pi\beta^2\gamma^3\varepsilon}\frac{F_c}{B_f}, \qquad (1)$$

where F_c is a form factor which includes correction coefficients due to beam pipe image forces (the Laslett coefficients), r_p is the proton classical radius, N_i is the number of ions per bunch, A and Z are the ion atomic and charge numbers, γ, β are relativistic factors, ε is the un-normalized RMS emittance, and B_f is the bunching factor (mean/peak line density). Here we assume F_c =1.

For low-energy RHIC operations, the present RF bucket acceptance is relatively small due to limited RF voltage. The injected ion beam longitudinal emittance is comparable to or larger than the RF bucket acceptance. As a result, the RF bucket is completely filled after injection. For the estimate of the space-charge tune shift ΔQ in this full bucket case, we assume a parabolic ion beam longitudinal profile [9].

Beam-beam and Luminosity Limits

The linear part of the tune shift due to interaction with a colliding bunch is called the "beam-beam" parameter. If the beam-beam parameter exceeds some limiting value one can have a significant emittance increase due to diffusion processes. In hadron machines, typical limiting values for the beam-beam parameter per single IP are around 0.01. For a round beam, the beam-beam parameter for hadrons is:

$$\xi = \frac{Z^2 r_p}{A} \frac{N_i}{4\pi\beta^2\gamma\varepsilon} \frac{1+\beta^2}{2}. \qquad (2)$$

When the single-bunch luminosity is limited by the beam-beam effect it can be expressed in terms of ξ as:

$$L = \frac{A}{Z^2 r_p} \frac{N_i c}{\beta^* C_r} \frac{2\gamma\beta^2}{1+\beta^2} f\left(\frac{\sigma_s}{\beta^*}\right)\xi, \qquad (3)$$

where C_r is the ring circumference, β* is the beta-function at the IP, σ_s is the RMS bunch length, and the factor $f(\sigma_s/\beta^*)$ describes the "hourglass effect". For low-energy RHIC operations we presently use $\beta^*=10\text{m} >> \sigma_s$, so we neglect the hourglass effect by approximating $f(\sigma_s/\beta^*)=1$.

When the single-bunch luminosity is limited by the space-charge tune shift ΔQ, it can be expressed as:

$$L = \frac{A}{Z^2 r_p} \frac{N_i c}{\beta^*} \frac{B_f}{C_r} \gamma^3 \beta^2 f\left(\frac{\sigma_s}{\beta^*}\right)\Delta Q. \qquad (4)$$

For typical RHIC beam parameters and fixed ΔQ=0.05, ξ=0.01, the maximum achievable single bunch luminosity in RHIC is limited by space charge tune shift for γ<11, while for γ>11 the luminosity is limited by beam-beam [9]. In the energies where space charge dominates, luminosity and event rates scale with γ^3.

Beam-beam and Space Charge

An even more interesting and unexplored effect is the interplay of direct space-charge and beam-beam effects, which is the case when one wants to collide beams with significant space-charge tune shift. In such a case, a large beam-beam parameter can excite resonances which will be crossed as a result of space-charge tune spread.

We started to explore these effects in RHIC Accelerator Physics Experiments (APEX) in 2009 with proton beam and conditions where both beam-beam and space-charge tune shifts were large [10]. Some interesting behavior was observed, which was related to strong beam-beam effect. However, observed effects are not directly relevant for lowest energy points from RHIC energy scan. At lowest energies, when RHIC is space-charge limited, the beam-beam parameter is much smaller than the space-charge tune shift. Our plan is to continue this experiment during the next RHIC run with gold ion beams at low energies. Our main goal is to understand whether we can operate with ΔQ>0.05 under collisions, which would provide an additional luminosity improvement with electron cooling, compared to the estimates given in next section.

PERFORMANCE WITH COOLING

Initially we considered electron cooler with a maximum energy of 2.8MeV, this can provide cooling for c.m. ion beam energies of 5-12 GeV/nucleon. At c.m. energies > 12 GeV/nucleon luminosity is sufficiently high so the electron cooling is not really required, although it could significantly increase luminosity even further. However, our most recent cooling approach can provide cooling all the way up to c.m. energies of 20 GeV/nucleon. Since this latter energy also corresponds to the present RHIC injection energy of gold ions for the high-energy RHIC program, the use of such a cooler (with maximum electron energy of 4.9MeV) may be beneficial for the RHIC high-energy program.

In this section some examples of luminosity improvement for the lowest energies of interest are shown. Note that the bunch intensities at lowest energies may need to be reduced to respect the space-charge limit. As a result, the role of electron cooling for the lowest energy points is to counteract IBS: this prevents transverse emittance growth and intensity loss from the RF bucket due to the longitudinal IBS. As the energy is increased, space charge of the hadron beam becomes smaller (see Eq. (1)) which permits cooling of the transverse or longitudinal emittances of the hadron beams. This, in turn, allows us to reduce β*. Thus electron cooling provides a larger luminosity gain for higher energy points.

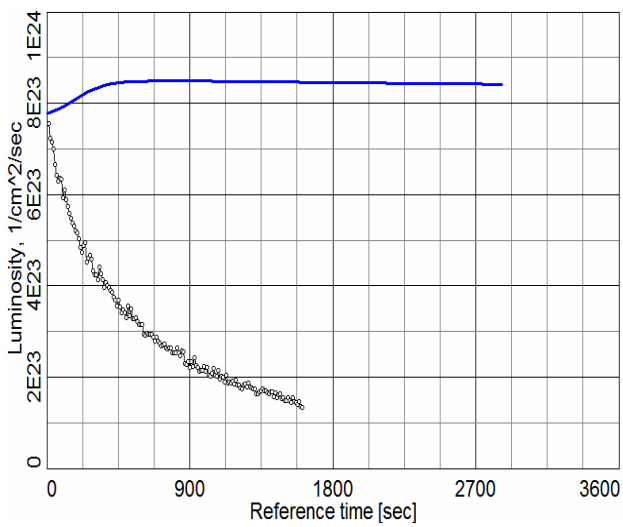

Figure 1: Simulation of luminosity with (blue line, upper curve) and without (black dots) electron cooling at γ=2.7.

Figure 1 shows results of a BETACOOL [11] simulation of luminosity evolution with and without electron cooling for γ=2.7. Simulations are done for ion bunch intensity $N_i=0.5\cdot10^9$, initial 95% normalized emittance of 15 mm-mrad, RMS momentum spread $\sigma_p=5\cdot10^{-4}$, RMS bunch length $\sigma_s=1.9$ m, and 56 bunches. There is an intensity loss as a result of the longitudinal IBS and particle loss from the RF bucket. There is also still a significant emittance increase due to transverse IBS even for a reduced bunch intensity of $N_i=0.5\times10^9$ per

bunch [9]. This results in the rapid luminosity drop shown in Fig. 1 with black circles. The resulting store length becomes relatively short – one has to refill RHIC every 10-15 minutes. The transverse emittance will be kept constant, and the longitudinal IBS will be counteracted with electron cooling. As a result, electron cooling will provide long store times with relatively constant luminosity. The overall gain in average luminosity with electron cooling, taking into account the time needed for refill between short stores without cooling, will be about a factor of 3. Larger luminosity gains may be possible if we can operate with space-charge tune shifts larger than $\Delta Q=0.05$. Operation with slightly larger tune shifts may be expected with the help of cooling.

Figure 2 shows a simulation of luminosity performance with and without electron cooling for $\gamma=6.6$. Simulations were performed for ion bunch intensity $N_i=1\times10^9$, 95% normalized emittance of 15 mm mrad, and $\sigma_p=5\times10^{-4}$. For these parameters we are not yet space-charge limited. In such a case, in addition to just counteracting IBS, electron cooling allows us to cool the transverse emittance to the space-charge limit, which in turn allows to decrease β^* at the IP: the effect of this can be seen by the luminosity jump in Fig. 2. Thereafter the luminosity remains constant. For the scenario shown in Fig. 2, electron cooling provides a factor of about 6 improvement in average luminosity.

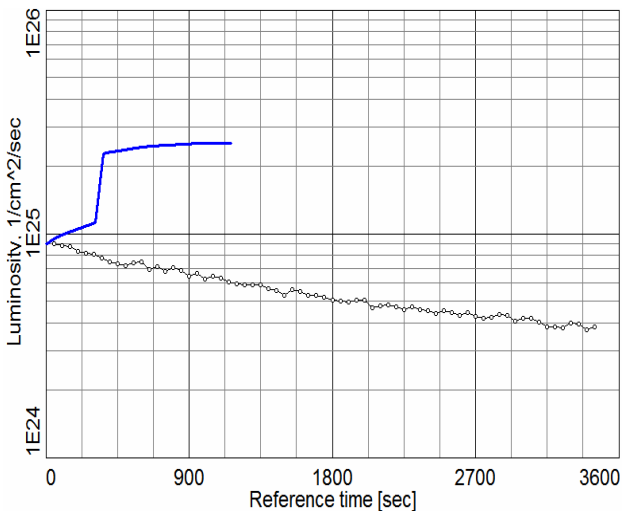

Figure 2: Simulation of luminosity with (blue line, upper curve) and without (black dots) electron cooling at $\gamma=6.6$.

ELECTRON COOLER CONSIDERATIONS

The required electron beam (0.9-5MeV) can be produced either using electrostatic or RF beam accelerators.

RF Based Cooler

The electron beam energies needed for low-energy RHIC are sufficiently high that we can consider cooling using bunched electron beam. The main problem for bunched electron beam is to provide beam transport without significant degradation of beam emittance and energy spread. Two approaches were considered and found feasible [6].

In the first approach a low-frequency RF gun was used to provide long electron bunches. As a result, even for high bunch charges, space-charge effects can be minimized, and one can deliver an electron beam of necessary quality to the cooling section. A prototype of such a 112 MHz SRF gun is presently under construction by Niowave Inc. in Michigan.

In the second approach a 703.75 MHz SRF gun, being built for the R&D ERL at BNL [12], was assumed. The length of electron bunches at this frequency is very short (about 1 cm rms) which would result in quick increase of momentum spread of electron beam due to longitudinal space charge. However, the length of the ion beam is very large with 1.9 meters rms. This allows us to put about 20 electron bunches on a single ion bunch. The charge needed for cooling can thus be divided between 20 electron bunches resulting in 50pC per bunch. With such a low charge the electron beam emittance is very small and is not an issue. The energy spread due to longitudinal space charge is also greatly reduced. The cooling in such a scenario is provided by a pulse/train of bunches with 20 bunches in the train spaced by 42.6 cm apart. More details about results of simulations based on RF approaches can be found in Ref. [6].

DC Approach

Electron cooling with electron beam kinetic energies $E_{k,e}=0.9$-5MeV can be performed using a DC electron beam, as is being done in the Recycler cooler at Fermilab [13, 14]. RHIC cooling times will be much shorter than those measured at the Recycler since we need to cool Au ions compared to antiprotons in the Recycler. The cooling time is thus reduced by a factor of $Z^2/A=31.7$, where $A=197$ and $Z=79$ are the atomic mass and charge of Au ions, respectively. In addition, due to strong dependence of electron cooling times on energy, operation at smaller energies results in much faster cooling times as well.

Apart from some modifications needed to address electron beam transport at low energies and recombination suppression in the cooling section, it appears that the existing Recycler cooler is ideally suited for low-energy RHIC cooling. As a result, our present baseline approach is based on DC electron beam produced with the FNAL Recycler's Pelletron. An evaluation of modifications to use the Recycler's Pelletron for RHIC is presently in progress.

Non-magnetized vs. Magnetized Approach

In low-energy electron coolers a magnetic field is required to provide transport of the electron beam. For energies of 0.9MeV and higher needed for our project, continuous magnetic field transport is no longer required.

However, in the cooling section, the interaction of the ion and electron beams results in ion beam loss due to recombination. Employment of strong magnetic field in

the cooling section allows one to incorporate a large transverse temperature of the electron beam for recombination suppression.

On the other hand, a novel idea of suppression ion recombination based on the use of an undulator field in the cooling section was proposed for RHIC [15]. In the presence of an undulator field, the trajectories of all the electrons have the same coherent azimuthal angle θ, determined by the undulator period λ and field value B at the axis:

$$\theta = \frac{eB\lambda}{2\pi pc}, \quad (5)$$

where p is the electron momentum. Since the recombination cross section is approximately inversely proportional to the electron energy in the ion rest frame, the ion beam lifetime can be sufficiently improved. Using an undulator to suppress recombination allows one to use non-magnetized electron beam with relatively small temperatures for cooling [16, 17]. To make sure that the representation of the friction force in the presence of an undulator field is accurate, an undulator field was implemented in the VORPAL code [18], and systematic numerical simulations were performed for different strength of the magnetic field B and pitch period λ [19]. A comprehensive study of magnetic field errors and their effect on cooling was also conducted [20].

For the low-energy cooler in RHIC both approaches of magnetized and non-magnetized cooling were considered. As for the case of high-energy RHIC-II cooler, it was found that one can use a rather weak undulator with a magnetic field of about 3-5G (8 cm period) to combat recombination in the cooling section, which makes use of the non-magnetized cooling attractive for low-energy RHIC operation as well.

Since non-magnetized cooling significantly simplified electron beam transport and reduced the cost of the cooler, it was chosen as our baseline approach.

COOLER DESIGN AND PARAMETERS

Luminosity improvement is needed mostly for low ion c.m. energies of 5-12 GeV/nucleon. This requires electron beam with a kinetic energy range of 0.86-2.8MeV. It turns out that with a present setup of two RHIC detectors and RF tuning limits, simultaneous operation of both detectors is not possible at some energy points without significant modifications [7]. On the other hand, use of cooling to improve luminosity in the c.m. energy range of 5-8.6 GeV/nucleon, where both detectors can operate simultaneously and where most luminosity improvement is needed, requires only a 0.86-1.8MeV cooler. As a result, the electron cooler should be able to operate at least up to 1.8MeV kinetic energy of electrons and preferably up to 2.8MeV.

Our present baseline cooler design is based on existing FNAL's Recycler Pelletron, which is operating at 4.36MeV. This 6MeV Pelletron in principle should be able to provide cooling of ions all the way up to the present RHIC injection energy. This will require operation of Pelletron up to 4.9MeV, which seems feasible since high-current operation is not required.

At low energy, RHIC ion bunches are very long (rms bunch length 1.5-1.9 m) with the full bunch length up to 30 nsec. DC electron beam is ideally suited for cooling of such long ion bunches. To counteract IBS for lowest energy point only 0.05A of DC current is required. To provide also additional cooling of beam emittance for higher energy points requires electron beam current of about 0.1A.

Depending on beam energy and longitudinal emittance, the ion beam will have rms longitudinal momentum spread in the range of σ_p=4-6×10^{-4}. This sets a limit on the rms momentum spread of electron beam of < 4×10^{-4}. Present relative rms energy spread in Recycler's electron beam is about 1×10^{-4} which satisfies this requirement.

The requirement on transverse angles of electron beam in the cooling section is given by the angular spread of the ion beam. For example, for rms normalized emittance of 2.5 mm-mrad at γ=2.7, and 30 m beta function in the cooling section, the ion beam rms angular spread in the lab frame is 0.18 mrad. This results in a requirement to have transverse angular spread of electrons in cooling section < 0.2 mrad. Since the ion bunch angular spread decreases with energy increase, even stricter control of electron angular spread will be needed at higher energy points to maintain cooling performance. Thus a careful consideration of various effects and estimate of full "angular budget" similar to what was done at FNAL will be needed for the full energy range of interest.

The most straightforward approach is to use the Recycler's cooling section "as is", where control of angular spread is accomplished by 2m long weak solenoids. Here small magnetization at the cathode is required, which is the present Recycler's cooler approach. Due to the relatively small required current, another approach with zero magnetic field on the cathode and thus no magnetic field in the cooling section is also feasible. In the latter case, only short corrector solenoids every 2m will be needed to provide needed focusing in the cooling section. This latter approach would correspond to a pure case of "non-magnetized" cooling. Experimental investigation of this approach is highly desired. Such an experiment can be conducted at existing Recyler's cooler at FNAL. Both approaches to the cooling section will be carefully considered during design.

The use of undulators for recombination suppression in the cooling section is also compatible with both approaches to the cooling section described above. However, the effect of undulators on cooling as well as engineering design should be carefully evaluated. For example, use of undulators together with present Recycler's cooler 2m long solenoids results in additional drift velocities of electrons. For baseline parameters, additional contribution to angular spread due to such drift was found to be within specifications. Regardless of the chosen approach, it appears that use of undulators may require significant engineering modification of the

cooling section while the expected benefit in luminosity with recombination suppression seems rather modest. A careful cost-benefit consideration will be done before including undulators in the baseline.

Some basic parameters of the cooler are summarized in Table 1. Electron beam requirements shown in Table 1 are given only for the lowest energy points of interest since cooling requirement at energies above 2.8MeV is not yet fully established. The value in brackets indicates the maximum possible energy of Pelletron-based cooler operation discussed here.

Table 1: Basic Parameters of Electron Beam

Electron kinetic energies, MeV	0.86-2.8 (4.9)
DC current, mA	50-100
Length of cooling section per ring, m	10
RMS momentum spread	<0.0004
RMS transverse angles, mrad	<0.2
Undulator magnetic field, G	3
Undulator period, cm	8

CHALLENGES

Some modification of the Recycler's Pelletron cooler will be needed to address the following issues: operation in a wide range of energies; use of the same electron beam to cool ions in two collider rings; suppression of recombination.

Besides some technical modifications, this will be the first cooler to cool directly beams under collisions. This puts special requirement on control of ion beam profile under cooling [21]. A careful study of interplay of space-charge and beam-beam effects within the hadron beams [10] is needed to understand the limits of cooling applicability.

SUMMARY

We have started design work on a low-energy RHIC electron cooler which will operate with kinetic electron energy range 0.86-2.8 (4.9) MeV. Several approaches to an electron cooling system in this energy range are being investigated. At present, our preferred scheme is to transfer the Fermilab Pelletron to BNL after Tevatron shutdown, and to use it for DC non-magnetized cooling in RHIC. Such electron cooling system can significantly increase RHIC luminosities at low-energy operation.

ACKNOWLEDGMENTS

We would like to thank W. Fischer, E. Pozdeyev, T. Roser and other members of Collider-Accelerator department at BNL for many useful discussions and help. We also thank A. Sidorin, A. Smirnov (JINR, Dubna) and K. Carlson, J. Leibfritz, S. Nagaitsev, L. Prost, A. Shemyakin (FNAL) for useful discussions and information.

REFERENCES

[1] Proc. of Workshop "Can we discover QCD critical point at RHIC?" (BNL, March 2006) RIKEN BNL Research Center Report No. BNL-75692-2006; http://www..bnl.gov/riken/QCDRhic.
[2] A. Cho, Science, V. 312, April 12, 2006, p 190.
[3] G. Stephans, "critRHIC: the RHIC low energy program", J. Phys. G: Nucl. Part. Phys. 32 (2006).
[4] M. Stephanov, K. Rajagopal, and E. Shuryak, Phys. Rev. Letters 81, p. 4816 (1998).
[5] T. Satogata et al., Proc. of PAC07 (Albuquerque, NM, 2007), p. 1877; Proc. of PAC09 (Vancouver, Canada, 2009).
[6] A. Fedotov, I. Ben-Zvi, X. Chang, D. Kayran, V. Litvinenko, E. Pozdeyev, T. Satogata, BNL Collider-Accelerator AP Note: C-A/AP/307 (April, 2008).
[7] T. Satogata et al., Proc. of Workshop on Critical Point and Onset of Deconfinement CPOD09 (June 8-12, BNL, USA, 2009).
[8] A. Fedotov, I. Ben-Zvi, X. Chang, D. Kayran, T. Satogata, Proc. of COOL07 (Bad Kreuznach, Germany, 2007), p. 243.
[9] A. Fedotov, I. Ben-Zvi, X. Chang, D. Kayran, V. Litvinenko, E. Pozdeyev, T. Satogata, Proc. of HB2008 (Nashville, TN, 2008), WGA10.
[10] A. Fedotov et al., "Interplay of space-charge and beam-beam effects", RHIC APEX 2009 experiments, unpublished.
[11] BETACOOL code: http://lepta.jinr.ru; A. Sidorin et al., NIM A 558, p. 325 (2006).
[12] V. N. Litvinenko et al., "Status of R&D ERL at BNL", Proc. of PAC07, p. 1347.
[13] S. Nagaitsev et al., Phys. Rev. Letters 96, 044801 (2006).
[14] L. Prost et al., these proceedings.
[15] Ya. Derbenev, "Electron cooling in solenoid with undulator", TJLAB Note 2001, unpublished.
[16] A. Fedotov et al., Proc. of PAC05 (Knoxville, TN, 2005), p. 4236.
[17] A. Fedotov et al., Proc. of PAC07 (Albuquerque, NM, 2007), p. 3696.
[18] C. Nieter, J. Cary, J. Comp. Phys. 196 , p.448 (2004); http://www.txcorp.com.
[19] G. Bell, D. Bruhwiler, A. Fedotov, A. Sobol, R. Busby, P. Stoltz, D. Abell, P. Messmer, I. Ben-Zvi, V. Litvinenko, Journal of Computational Physics 227 (2008), p. 8714.
[20] A. Sobol, D. Bruhwiler, G. Bell, A. Fedotov, V. Litvinenko, submitted for publication (June 2009).
[21] A. Fedotov, I. Ben-Zvi, D. Bruhwiler, V. Litvinenko, A. Sidorin, "High-energy electron cooling in a collider", New Journal of Physics 8 (2006) 283.

APPLICATION OF COOLING METHODS TO NICA PROJECT

E. Ahmanova, V. Bykovsky, A. Kobets, D. Krestnikov, I. Meshkov, R. Pivin,
A. Rudakov, A. Sidorin, A. Smirnov, S. Yakovenko, JINR, Russia
Jürgen Dietrich, FZJ, Germany
Takeshi Katayama, GSI, Germany

Abstract

The **N**uclotron-based **I**on **C**ollider f**A**cility (NICA) is a new accelerator complex being constructed at JINR aimed to provide collider experiments with heavy ions up to Uranium at maximum energy (center of mass) equal to 11 GeV/u. It includes new 6.2 MeV/u linac, 600 MeV/u booster synchrotron (Booster), upgraded superconducting (SC) synchrotron Nuclotron and collider consisting of two SC rings, which provide average luminosity of the order of 10^{27}cm^{-2}s^{-1}. A few cooling systems are proposed for the NICA project. The Booster will be equipped with an electron cooling system. Two cooling methods – stochastic and electron ones - will be used at the collider rings. Main parameters of the cooling systems and peculiarities of their design are presented here.

INTRODUCTION

The goal of the NICA project [1] is construction at JINR of the new accelerator facility that consists of (Fig.1)
- cryogenic heavy ion source KRION of Electron String Ion Source (ESIS) type,
- source of polarized protons and deuterons,
- the existing linac LU-20,
- a new heavy ion linear accelerator,
- a new Booster-synchrotron (that will be placed inside of the yoke of the decommissioned Synchrophasotron),
- the existing heavy ion synchrotron Nuclotron (being developed presently to match the project specifications),
- two new superconducting storage rings of the collider,
- new set of transfer channels.

The facility will have to provide ion-ion (1 ÷ 4.5 GeV/u), ion-proton collisions and collisions of polarized proton-proton (5 ÷ 12.6 GeV) and deuteron-deuteron (2 ÷ 5.8 GeV/u) beams. As a result of the project realization, the potential of the Nuclotron accelerator complex will be sufficiently increased in all the fields of its current physics program: both fixed target experiments with slowly extracted beams and experiments with internal target. The Booster will be equipped with a slow extraction system to provide medicine, biological and applied researches.

The collider will have two interaction points. The Multi Purpose Detector (MPD) aimed for experimental studies of hot and dense strongly interacting QCD matter and search for possible manifestation of signs of the mixed phase and critical endpoint in heavy ion collisions, is located in one of them. The second one is used for the Spin Physics Detector (SPD).

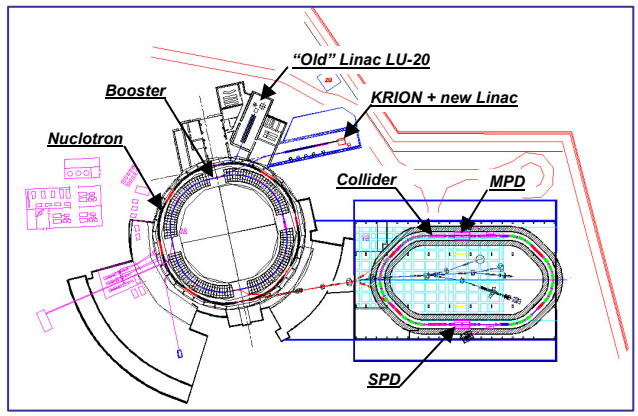

Figure 1: Schematics of the NICA accelerator complex.

Collider will be operated at a fixed energy without acceleration of an injected beam. Correspondingly the maximum energy of the experiment is determined by the Nuclotron magnetic rigidity that is equal to about 45 T·m. Main goal of the NICA facility construction is to provide collider experiment with heavy ions like Au, Pb and U at average luminosity above $1 \cdot 10^{27}$ cm^{-2}·s^{-1} (at the energy of 3.5 GeV/u). Therefore in this report we discussed the heavy ion mode of the facility operation only, and the Gold nuclei $^{197}Au^{79+}$ are chosen as the reference particles.

To reach the required parameters a beam cooling is proposed both in the Booster and in the collider rings. During R&D stage we plan to test a prototype of the stochastic cooling system at the Nuclotron on a magnetic field plateau.

BOOSTER ELECTRON COOLER

The maximum design ion energy of 4.5 GeV/u can be achieved in the Nuclotron with fully stripped ions only. To provide high efficiency of the ion stripping one has to accelerate them up to the energy of a few hundreds of MeV/u. For this purpose a new synchrotron ring – the Booster is planned to be used (Table 1). Heavy ion injector-linac is designed for acceleration of Au^{32+} ions. The Booster has maximum magnetic rigidity of 25 T·m that corresponds to about 600 MeV/u of the ion energy, and the stripping efficiency is no less than 80%.

The Booster is equipped with an electron cooling system that allows providing an efficient cooling of the ions in the energy range from the injection energy up to 100 MeV/u.

The magnetic system of the Booster is superconducting. Its design is based on the experience of construction of the Nuclotron SC magnetic system [2] and SC magnetic system of SIS-100 developed later at FAIR project.

Therefore to avoid connections between "warm" and "cold" sections in the ring the solenoids of the cooler located along the Booster circumference are designed in the SC version (Fig. 2). This is main difference of the Booster cooler from a conventional electron cooling systems.

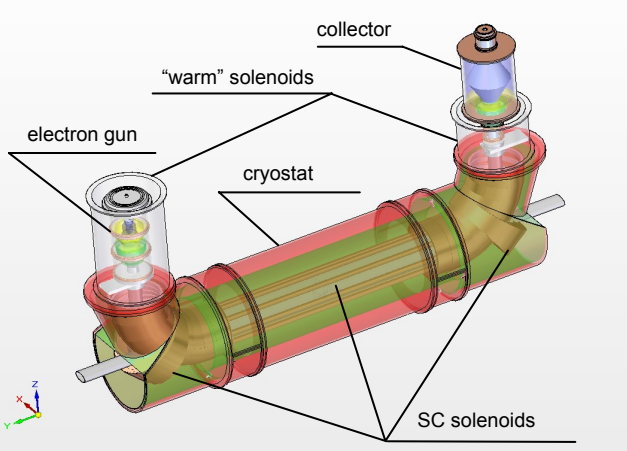

Figure 2: The Booster electron cooler.

The Booster cooling system will be used for two independent purposes:
- optimization of 6-dimentional phase space of a heavy ion beam to provide its effective acceleration in the collider injection chain and injection into the collider rings;
- formation of high quality beams when the Booster is used for medicine, biological and applied researches.

To cover total range of the ion energy in the Booster (600 MeV/u) the electron beam maximum energy has to be about 330 keV. However the cooling system at such energy is rather expensive, therefore the maximum electron energy (60 keV) is chosen as a compromise between the system price and its capability to fulfill the main project task – the ion colliding beams. A possibility to decrease the ion beam phase volume at low energy is restricted by space charge limitations.

Another criterion for the electron energy choice is related to the frequency variation range of the Booster RF system. The ion acceleration in the Booster is proposed to be performed in two steps: on the 4^{th} harmonics of the revolution frequency up to the cooler energy and on the 1^{st} one after the cooling. If the cooling is performed at the ion kinetic energy ≥ 100 MeV/u, one can use the same RF system on both steps of the acceleration.

All other parameters of the Booster cooler (Table 2) are typical for conventional electron cooling systems. Design of the cooler is performed by JINR electron cooling group and its construction is planned to be done at JINR workshop. Test of the cooler elements will be performed at existing test bench.

Main goal of the cooling of heavy ion beam is to decrease its longitudinal emittance to the value required for effective injection and acceleration in the Nuclotron and for the bunch compression in the Nuclotron before injection into the collider. Transverse beam emittance has to be stabilized at relatively large value to avoid space charge limitations in the Nuclotron and collider rings. To avoid overcooling of the transverse degree of freedom the electron beam misalignment in respect to the ion orbit can be used. Simulations of such a regime of the cooler operation performed with Betacool code showed that during 1 second of the cooling one can decrease the longitudinal beam emittance by about 3 times at practically constant transverse emittance. That is sufficient for our goal.

Table 1: Basic Parameters of the Booster and its Electron Cooling System

Ions	$^{197}Au^{32+}$
Booster circumference, m	211.2
Injection/extraction energy, MeV/u	6.2/600
Max. dipole field, T	1.8
Ion number	2×10^{9}
Beta functions in cooling section, m	8 / 8
Dispersion function in cooling section, m	0.6
Maximum electron energy, keV	60.0
Electron beam current, A	0 ÷ 1.0
Cooler overall length, m	4.0
Effective length of the cooling section, m	2.5
Magnetic field in the cooling section, kG	1.5
Magnetic field inhomogeneity in the cooling section, ΔB/B	$1\cdot10^{-4}$
Electron beam radius in the cooling section, cm	2.5
Transverse electron temperature, meV	200
Longitudinal electron temperature, meV	0.5
Cooling time, s	1
Residual gas pressure, Torr	10^{-11}

At the electron cooling of heavy ions one of the serious problems is the recombination - i.e. capture of cooling electrons by ions - resulting in loss of the ions due to change of their charge and deformation of the ion closed orbit. The recombination rate of Au^{32+} ions in the Booster cooler was extrapolated from the experimental data obtained at GSI and CERN. The estimation has shown that during 1 s of cooling the ion losses will be less than 10%. In any case the use of SC solenoid in the cooling section gives a possibility to provide the electron beam compression in order to suppress the recombination by increase of the temperature of transverse degree of freedom of the electron beam.

COLLIDER OPERATION

Two collider rings have a maximum magnetic rigidity of 45 Tm that is equal to the Nuclotron one. The rings are situated one upon the other by the scheme "twin bore magnets": bending and quadrupole magnets have two apertures in common yoke.

Estimations show that the required luminosity can be reached at the ion bunch intensity of 10^{9} ions per bunch.

The inter bunch distance (and, correspondingly, the maximum bunch number) is limited by requirement to avoid parasitic collisions in the vicinity of interaction point. At the collider and MPD parameters [3] the maximum bunch number is below 20. At such conditions one way to increase the luminosity is to decrease the bunch length. Also, the bunch length has to be as small as possible to avoid an "hour glass" effect and to provide the luminosity concentration in the central part of the detector. On other hand a small bunch length increases the bunch peak current that can provoke a coherent instability. Finally the bunch length was chosen as a compromise between these two contradicting effects (Table 2).

In the NICA energy range the luminosity is limited by incoherent tune shift. Correspondingly, the beam emittances (Table 2) are chosen to keep the tune shift below 0.05. Beam-beam parameter at all energies is below 0.005.

Table 2: Collider beam parameters and luminosity for Au-Au collisions

Ring circumference, m	251		
Ion number per bunch	$1 \cdot 10^9$		
Number of bunches	17		
Beta-function in the interaction point, m	0.5		
Rms bunch length, m	0.3		
Rms momentum spread	0.001		
Ion energy, GeV/u	1.0	3.5	4.5
Rms beam emittance (unnormalized), π·mm·mrad	3.9	0.27	0.14
Luminosity, 10^{27} $cm^{-2}s^{-1}$	0.06	1.05	1.9

Two schemes of the collider feeding with the ions are under consideration now:

- in accordance with the first one during the feeding the collider RF system is switched on at the working harmonics of the revolution frequency and bunch prepared by the injection chain is injected into corresponding separatrix;
- the second scheme presumes storage in the collider of a coasting beam initially. After storage of a required ion number an adiabatic bunching and bunch compression are performed.

At the first scheme application the ion bunch of required int14ensity and emittance has to be prepared by the injection chain. The required bunch emittance is formed using electron cooling in the Booster. To reach the design bunch length the bunch is compressed in the Nuclotron by RF phase "jump" after acceleration. In this regime the maximum bunch number in the collider ring is limited by the injection kicker pulse duration: one needs to avoid distortion of circulating bunches by inflector pulse at injection of a new bunch.

The second scheme simplifies significantly the requirements to the injection chain. The beam storage can be realized using RF stacking procedure or with application of RF barrier bucket technique. Intensity of the injected ion portion influences on the stacking process duration only and can be arbitrary in principle. The required beam emittance is formed during the stacking by the cooling application. The maximum bunch number in the collision mode is limited by requirement to avoid parasitic collisions in the vicinity of the interaction point and can be larger than at the first scheme. However at this scheme the collider has to be equipped with two RF systems. One of them is used for the beam stacking with the Barrier Buckets and bunching of the stacked beam with sinusoidal RF at the harmonics number coinciding with the bunch number. Another one is operated at the collisions. It is conventional RF system of significantly larger harmonics number that is necessary to keep a short bunch length at reasonable RF voltage. The second scheme is preferable for the facility operation but it requires additional space of the collider circumference for RF system placing. Therefore the final choice of the storage scheme will be done at the technical design of the collider rings.

The beam cooling application in the collider rings has two goals:

- beam storage using cooling-stacking procedure;
- luminosity preservation during experiment.

The first goal can be achieved with stochastic cooling system of reasonable technical parameters, because in this case the beam has rather low linear particle density.

BEAM COOLING DURING EXPERIMENT

Without a beam cooling, during the experiment the beam emittance and the bunch length increase due to intrabeam scattering (IBS) process. The expected IBS growth time values in the collider are of the order of 10 - 50 s at the ion energy of 3.5 GeV/u. The luminosity preservation is the general goal of the beam cooling in the collider. In equilibrium between IBS and cooling, the luminosity life-time is limited mainly by the ion interaction with residual gas atoms. The vacuum conditions in the collider rings are chosen to provide the beam life time of a few hours.

In the required energy range (from 1 to 4.5 GeV/u) the both electron and stochastic cooling method can be used. However there is presently a lack of the world experience of the cooling systems of required parameters.

On one hand, the electron energy for the ion beam cooling at 4.5 GeV/u is equal to about 2.45 MeV that is much higher than in conventional electron cooling systems. Indeed, the highest energy of the electron beam reached in the Recycler cooling system (FNAL) is equal to about 4.3 MeV (that corresponds to the ion energy of about 8 GeV/u) [4]. Unfortunately this system is operated at low magnetic field value that does not allow achieving short cooling time. The existing cooling systems with magnetized cooling are operated at the electron energy below 300 keV.

Concerning stochastic cooling there is no experience of the bunched ion beam cooling. Stochastic cooling of

bunched beam has been demonstrated a few years ago in pioneering work at RHIC [5] with Gold ion beam of a high energy and for longitudinal degree of freedom only. Due to some peculiarities of that cooling system design its design can not be applied directly to bunched beam cooling at low ion energy. And no experience exists yet for stochastic cooling of transverse degrees of freedom of bunched beam. Therefore design and construction of the cooling system (independently – electron or stochastic) require R&D stage of the work.

Stochastic cooling application looks very attractive because it does not lead to additional particle loss and keeps the shape of ion distribution close to Gaussian one. First simulations and feasibility study have shown the problems of both physical and technical character. Nerveless constriction of stochastic cooling system for the bunched beam of NICA parameters constitutes to be rather realistic.

Simulations of electron cooling process at cooler parameters listed in Table 3 (Fig. 3) demonstrate capability of the system to stabilize the luminosity at the required level during a long time. However, the electron cooling leads to formation of a small and dense core of the ion distribution function (Fig. 4) that determines the luminosity, and very long tails at relatively low intensity. The tails are not stabilized by the cooling and their development can lead to additional particle loss. The particle loss due to recombination in the cooling section is suppressed by increase of the electron beam temperature (to provide the beam lifetime longer then 1 hour the temperature has to be increased up to about 50 eV). Therefore, to keep sufficient value of the friction force the magnetic field in the cooling section has to be increased up to 2 T.

At the moment an optimum strategy of the beam cooling during experiment seems to be in combination of both cooling methods: electron cooling should be used to provide short cooling time for central part of the ion distribution and stochastic cooling – for stabilization of the distribution tails.

Table 3: Main Parameters of the Collider Electron Cooling System

Maximum electron energy, MeV	2.5
Cooling section length, m	6.0
Electron beam current, A	0.5
Electron beam radius, cm	0.5
Magnetic field in cooling section, T	2.0
Magnetic field inhomogeneity in cooling section	2×10^{-5}
Beta functions in cooling section, m	20
Transverse electron temperature, eV	50.0
Longitudinal electron temperature meV	5.0
Beam lifetime due to recombination, hour	1.0

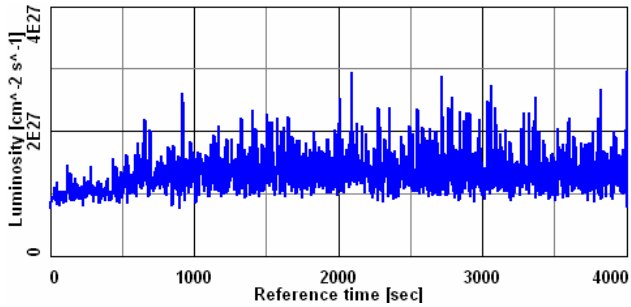

Figure 3: Luminosity variation during 1 hour of the experiment under action of the electron cooling. Ion beam energy is 3.5 GeV/u, initial ion beam parameters are taken from the Table 2. Simulations with Betacool program.

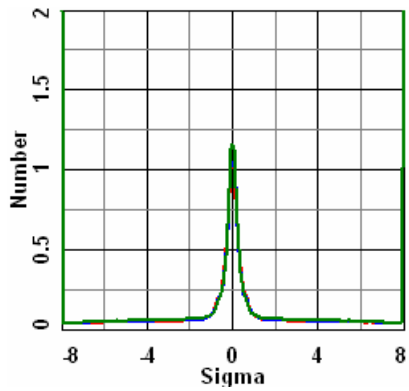

Figure 4: The ion beam profile under the electron cooling. Vertical axis is the relative particle number, horizontal – the beam profiles in the initial RMS value.

R&D FOR COLLIDER COOLING SYSTEMS

Preliminary design of the collider electron cooling system was performed in co-operation with All-Russian Electrotechnical Institute (VEI, Moscow) on the basis of dynamitron-type high voltage generator (Fig. 5). For the electron beam transport from the high-voltage vessels to the cooling section as well as for the cooling sections SC solenoids will be used. The electron beam transport inside the accelerating/decelerating columns is provided by normal conducting solenoids at relatively weak magnetic field. Such a scheme permits to provide electron beam compression in the cooling section and, correspondingly, increase the electron transverse temperature. That allows to suppress the ion recombination.

Design of the high voltage generator prototype has been started; it will be constructed in VEI and tested at total voltage.

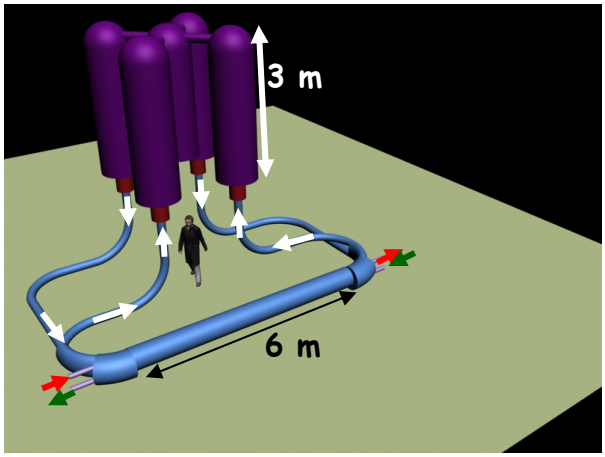

Figure 5. Artistic view of the collider electron cooling system.

For the stochastic cooling development one plans to perform the cooling experiment with ion beam circulating in the Nuclotron – cooling of longitudinal degree of freedom. Presently in the Nuclotron ring there are two free straight sections of the length of 3.5 m each one (one of them is reserved for the beam injection from the Booster, another one - for the spin control device). These sections will be used temporarily for experimental test of a prototype of the collider stochastic cooling system. The existing Nuclotron RF system can not provide the same large bunching factor for heavy ion beam as required for the collider operation. But the cooling system can be tested at the same linear particle density of a bunched deuteron beam, which has intensity by two orders of magnitude larger than expected one for the heavy ions.

The pick-up and kicker electrodes of the stochastic cooling system prototype will be elaborated in cooperation with COSY and will be similar to that one designed for the HESR of the FAIR project [6].

CONCLUSION

Application of the cooling methods is a key feature of the NICA project being developed at JINR. The project realization requires elaboration of novel cooling systems that can be done using both numerical simulations and experimental work with prototypes.

Numerical simulations of the beam dynamics in the collider under stochastic and electron cooling are in progress. The electron cooling system of the collider will be designed and constructed in collaboration with BINP, FZJ and VEI. Elaboration of the stochastic cooling system we plan to perform in collaboration with CERN, GSI, FZJ, FNAL and BNL. The prototype of the stochastic cooling will be tested at the Nuclotron.

REFERENCES

[1] G. Trubnikov, et.al., Project of the Nuclotron-based ion collider facility (NICA) at JINR, Proceedings of EPAC08, Genoa, Italy

[2] Khodzhibagiyan, H.G., and Smirnov, A.A., The concept of a superconducting magnet system for the Nuclotron, *Proc. of the 12th Int. Cryogen. Eng. Conf.*, 1988, pp. 841–844.

[3] NICA Conceptual Design Report, http://nucloserv.jinr.ru/nica_webpage/Nica_files/reports/CDR_07/, editors I.Meshkov and A.Sidorin, JINR, Dubna, 2008

[4] S. Nagaitsev, A. Bolshakov, D. Broemmelsiek, A. Burov, et al. Antiproton Cooling in the Fermilab Recycler Ring, Proceedings of COOL05, Galina, IL USA (2005). AIP 821 (2006) 39-47.

[5] J. M. Brennan, M. Blaskiewicz, Bunched Beam Stochastic Cooling at RHIC, Proceedings of COOL07, Bad Kreuznach, Germany, 2007.

[6] R. Stassen, P. Brittner, R. Grev Greven, H. Singer, H. Stockhorst, Recent developments of the HESR stochastic cooling system, Proceedings of COOL07, Bad Kreuznach, Germany, 2007.

CONTRIBUTION NOT RECEIVED

ALL-OPTICAL ION BEAM COOLING AND ONLINE DIAGNOSTICS AT RELATIVISTIC ENERGIES

M. Bussmann*, U.Schramm, Forschungszentrum Dresden-Rossendorf, D-01328 Dresden
W. Nörtershäuser, C. Novotny, C. Geppert, Johannes-Gutenberg-Universität Mainz, D-55099 Mainz
Th. Walther, G. Birkl, Technische Universität Darmstadt, D-64289 Darmstadt
D.F.A. Winters[a], Th. Kühl, C. Kozhuharov, M. Steck, F. Nolden, C. Dimopoulou, Th. Stöhlker[a]
GSI Helmholtzzentrum für Schwerionenforschung GmbH, D-64291 Darmstadt
[a] Ruprecht-Karls-Universität Heidelberg, D-69120 Heidelberg

Abstract

Recent experiments [1, 2] at the Experimental Storage Ring (ESR) at GSI have shown that relativistic Li-like C^{3+} ion beams can be cooled to an unprecedented momentum spread of $\Delta p/p \approx 10^{-7}$ using a single-frequency laser tuned to the Doppler-shifted $2S_{1/2} \rightarrow 2P_{1/2}$ and $2S_{1/2} \rightarrow 2P_{3/2}$ atomic transitions.
Although these results encourage the application of laser cooling to beams of other Li-like and Na-like ions at even higher energies as will be available at future storage rings at FAIR (Facility for Antiproton and Ion Research), two major concepts have to be demonstrated experimentally: First, efficient laser cooling of ion beams with large initial momentum spread, thus avoiding additional electron cooling to match the large momentum spread to the usually small momentum acceptance of the laser force. Second, all-optical measurements of the relevant beam parameters, thus overcoming the limited resolution of standard storage ring detectors such as the Schottky pickup electrode at ultra-low momentum spreads. The aim of this paper is to discuss the technical realization of these concepts as planned for an upcoming beam time at ESR.

PROSPECTS OF LASER COOLING ION BEAMS AT RELATIVISTIC ENERGIES

Future ion storage ring facilities such as FAIR will provide access to ultra-high energy beams of stable and rare ions for fundamental research. Many of the experiments planned at these facilities, such as in-ring mass spectrometry of short-lived rare nuclei, tests of strong-field quantum electrodynamics with highly-charged ions or in-beam x-ray spectroscopy of atomic transitions in heavy nuclei will greatly benefit from ion beams with ultra-low momentum spread. When considering relativistic ions at energies of several hundred MeV/u to GeV/u, however, cooling the ion beams to a momentum spread $\Delta p/p$ below 10^{-4} using electron cooling suffers from the fact that the energy transfer in Coulomb collisions between electrons and ions depends on their relative velocity v_{rel} as[1] $dE_{\mathrm{ecool}}/ds \propto v_{\mathrm{rel}}^{-2}$ [3]. At highly relativistic energies, efficient electron cooling thus requires the use of electron beams of several hundred mA and energies of several MeV [4, 5] - therefore electron cooling has been proposed only for the FAIR New Experimental Storage Ring (NESR) and High Energy Storage Ring (HESR) and not for the Schwerionen-Synchrotron SIS100/300.
With laser cooling of ion beams in storage rings, the situation changes drastically. For increasing beam energy the laser cooling force increases both due to the relativistic Doppler shift as well as the properties of the atomic cooling transition of the ion of interest [6, 7]. Unlike to the laser cooling of ions in traps, which is limited to a few ion species due to the lack of suitable laser sources, tuning the laser frequency ω_l in the laboratory frame to the cooling transition frequency in the rest frame $\omega_r = (1+\beta)\gamma\omega_l, \beta = v_{\mathrm{beam}}/c$ via a change in beam energy γ provides for laser cooling of a variety of Li-like and Na-like ions using a single laser system [8]. The saturation of cooling transitions exploiting this relativistic Doppler frequency shift allows for precision spectroscopy for a wide range of wavelengths up to the x-ray spectrum [7, 9, 10].

CHALLENGES OF LASER COOLING ION BEAMS AT RELATIVISTIC ENERGIES

Besides the benefits of laser cooling ion beams, recent results [1, 11] indicate several challenges when considering laser cooling to be applied at future high energy storage rings[2]:

1. Laser cooling is efficient only along the direction of the propagation of the laser beam.

2. Thus, additional coupling between the longitudinal motion of the ions along the beam axis to their transverse betatron motion is required to efficiently cool all three degrees of freedom of the ion motion.

3. At previous beam times at ESR, initial moderate electron cooling of the beam was required to yield enough fluorescence for optical detection, although laser cooling proved to be efficient.

* m.bussmann@fzd.de

[1] Here and in the following text we omit the energy dependence of the Coulomb logarithm for the sake of simplicity.

[2] For an in-depth discussion see [8]

4. The momentum acceptance of the laser force is usually orders of magnitude smaller than the initial momentum spread of the ion beam.
5. At high ion currents intra-beam scattering counteracts the laser force and close encounters of ions in the beam can force ions outside the momentum acceptance of the laser force.
6. Consequently, at previous experiments, the laser force could only counteract intra-beam scattering when the ion beam current was about 10 μA.
7. At low currents, when the transition to the space charge dominated regime occurs, all ion charge based detection devices such as the beam profile monitor or the Schottky pickup electrode are close to or reach their resolution limit.

Although items 1 and 2 have been addressed both in experiment [12, 13] and in theoretical works [14], up to now, no feasible approach to three-dimensional laser cooling at highly relativistic energies has been demonstrated. In the following, we will thus focus on the experimental approach towards all-optical beam cooling and characterization planned for the upcoming ESR beam time, thereby concentrating on items 3 to 7 in detail.

INCREASING THE MOMENTUM ACCEPTANCE OF THE LASER FORCE AND COUNTERACTING INTRA-BEAM SCATTERING

At previous ESR beam times, detuning the bunching frequency relative to the frequency of a single-mode single-frequency Ar+ ion laser [15] has been used to subsequently address all ions in the phase space of the bucket [9]. This required a stepwise change of the bunching frequency which at each step caused a replacement of the bucket center in momentum space relative to the mean momentum of the ions and thus lead to an oscillation of the ion bunch in the bucket [2].

We will follow a two-stage approach to enhance the laser force acceptance. Firstly, we will replace the Ar+ ion laser by a single-frequency diode laser system that will allow for scanning the laser frequency over a broad range without mode hopping.. The scanning range can be estimated by $\Delta f_\mathrm{l} = (c/\lambda_\mathrm{l}) \times \Delta p_\mathrm{b}/p_\mathrm{b}$ and one finds with $\lambda_\mathrm{l} = 514$ nm $\Delta f_\mathrm{l} \approx 12$ GHz. Recently, a solid-state laser system has been introduced which is based on an external-cavity diode laser for which both the grating position and diode current are simultaneously controlled to avoid mode-hopping during frequency-tuning [16], providing several ten GHz of tuning range [16]. Such a system will require two times the doubling of the laser frequency via second harmonic generation. This in turn leads to a reduction in laser beam power. For laser cooling to become efficient one needs a laser intensity equal or greater than the saturation intensity $I_\mathrm{sat} = \pi ch\Gamma/(3\lambda_0^3) \approx 1.475$ Wcm^{-2} for the $2S_{1/2} \rightarrow 2P_{3/2}$ transition in C^{3+} at $\lambda_0 = 154.81$ nm. This can be easily achieved using fiber amplifiers which deliver multi-Watt narrow line width output [17, 18].

In the future, simultaneous cooling of all ions in the bucket could be achieved using a pulsed laser system in addition to the continuous wave laser tuned close to the cooling transition [19]. The spectral bandwidth $\Delta\lambda_\mathrm{bw}$ of the pulsed laser should be large enough to address about half of the momentum acceptance of the bucket, giving $\Delta f_\mathrm{bw} = 6$ GHz. For a Gaussian-shaped pulse this results in a pulse duration of $\tau_\mathrm{l} = 0.44/\Delta f_\mathrm{bw} \approx 73$ ps. With a laser beam radius $r_\mathrm{beam} = 1$ mm matching the ion beam radius the required cooling power to saturate the cooling transition with a single-frequency laser can be estimated to[3] $P_\mathrm{sat} = I_\mathrm{sat} \times (\pi r_\mathrm{beam}^2) \approx 47$ mW. However, to saturate the transition with a pulsed laser, the spectral density of the pulse must be at least I_sat/Γ. Since the spectral bandwidth of the pulse must be at least 6 GHz, we find a minimum pulse intensity of $I_\mathrm{pulse} = I_\mathrm{sat}\Delta f_\mathrm{bw}/\Gamma \approx 34$ Wcm^{-2}. This is a very moderate intensity. The required pulse intensity is in our case thus not determined by the atomic transition but instead by the requirement for doubling the center frequency of the pulse twice. For efficient second harmonic generation at a beam radius[4] of 100 μm we estimate a minimum pulse energy of about 50 μJ following [20] which gives a conversion efficiency of about 15 %, this means that for the second SHG stage focusing to a beam radius of 30 to 40 μm is required. At optimum, the repetition rate of the laser will be of the same order of the revolution frequency to achieve permanent temporal overlap. From these considerations the ideal laser system would be a 50 ps, 50 μJ laser system with a repetition rate of 1 MHz. This leads to a peak power of 1 MW and an average power of 50 W. Such systems are in reach of current technology [21], and, most importantly, can be built using fibre amplifier technology [22] as will be used for the scanning laser setup.

OPTIMIZING THE FLUORESCENCE DETECTION SYSTEM

At previous laser cooling beam times at ESR the only optical window which allowed for transmission of the fluorescence light at 154 nm was placed in a dedicated, field-free cavity section of the ring. Initial moderate electron cooling was required to detect fluorescence light using a VUV photomultiplier (VUV-PM) that was placed outside the beam tube with viewing direction perpendicular to the beam pipe. The fluorescence light was transmitted through a MgF_2 viewport attached to the experimental section of the ESR as shown in 1. High fluorescence yields can only be expected at small momentum spread when most ions in the beam can absorb the laser photons [23]. A variety of ef-

[3] Please note that this is the power required at a central wavelength of 257 nm.

[4] In the following the laser beam radius is decreased to lower the constraints on the pulsed laser system¡ without sacrificing cooling efficiency at low momentum spread.

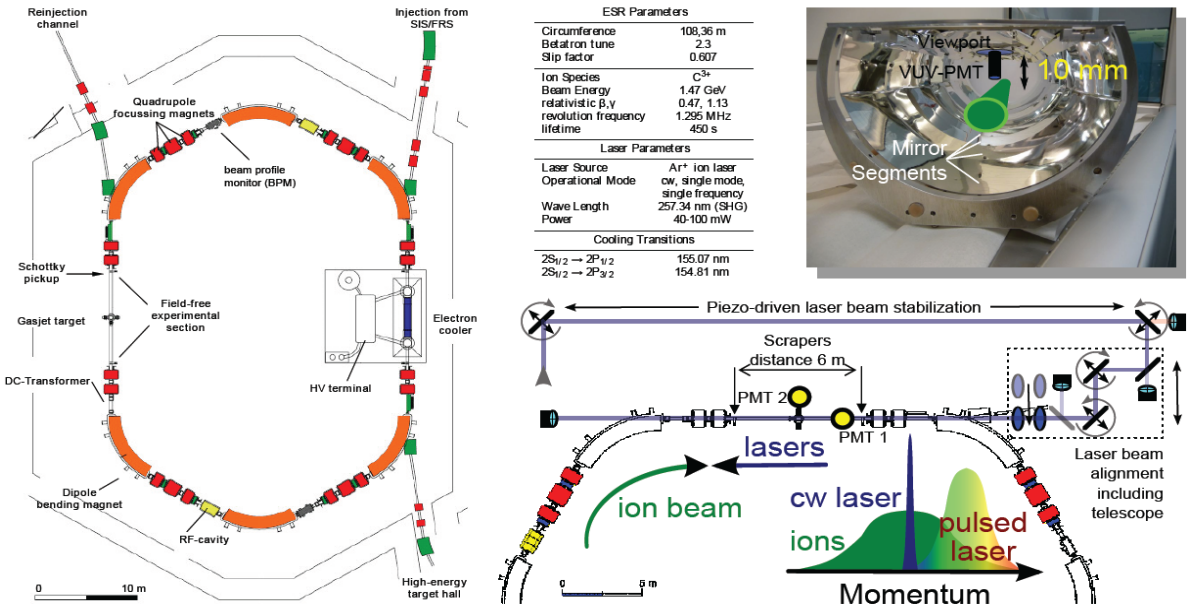

Figure 1: **Left:** Overview of the Experimental Storage Ring ESR at GSI. Ions are injected in the upper right part, revolving clockwise. The electron cooler system is found on the right, while the field-free experimental section is found opposite to the electron cooler on the left. Also shown are the two main diagnostic systems, the beam profile monitor (BPM, upper left) for measuring the beam width and the Schottky pickup electrode (field free section, left) for measuring the momentum spectrum of the ion beam. The parameters used for the 2004 and 2006 ESR experiments on laser cooling C^{3+} ion beams are listed in the table located on the right of the ESR overview. **Upper right:** Picture of the drift tube cavity after it has been dismantled in 2009. One can see the reflecting mirrors on the bottom of the tube opposite to the viewport windows, where a schematic drawing of a photomultiplier (PMT) that can be lowered into the tube using a motor-driven linear vacuum feedthrough has been added. The laser beam is indicated in green. **Lower right:** Detailed view of the field-free experimental section. A second PMT is added to the setup. Please note that the final position of the PMT has not yet been determined. Also shown are the scrapers that allow for the off-line positioning of the laser beam relative to the ion beam orbit. The laser beam line includes a newly developed Piezo-driven laser beam stabilization as well as a new beam alignment setup which will be used to optimize the overlap between laser beam and ion beam and to measure the ion beam width as explained in the text. A telescope can be put into the optical path, allowing for stronger focusing at small ion beam diameters. In the lower part, the overlap of the single-frequency laser and the broadband laser with the ion momentum distribution is indicated schematically.

fects can limit the fluorescence rate observed, most of them are related to the geometrical acceptance of the detector as well as relativistic effects, see [24] for an exhaustive discussion. These limitations can be overcome by installing an in-vacuum detector system which can be moved close to the ion beam.

A serious limitation to the fluorescence yield observed in the last two beam times was caused by using a single photomultiplier instead of at least two. With a single photomultiplier, only off-line alignment of ion beam and laser beam is possible, using the ESR beam scrapers as markers for the ion beam orbit to center the laser beam inside the beam tube. A second MgF_2 viewport will be added to the ESR beam line. This will make online beam overlap optimization possible by measuring the intensity of the fluorescence light detected at two different places along the region of overlap between ion and laser beam. In addition, we plan to add a motor-driven linear vacuum feedthrough to the ESR beam tube. It will allow to move the photomultiplier close to the beam in order to increase the collection efficiency of the detector. Such a setup will require to add shielding to the detector that blocks stray light from the laser which otherwise would lead to unwanted background light seen by the detector.

OPTICAL DIAGNOSTIC OF LASER COOLED ION BEAM PROPERTIES

In the following we will discuss new diagnostic methods to determine the beam properties of laser-cooled ion beams. Since a high fluorescence yield is only to be expected at small momentum spread, the methods listed here cannot replace the standard beam diagnostics available at ESR. They should rather be seen as an extension of the existing diagnostic tools for precision measurements with ultra-cold ion beams interacting with laser light.

When considering laser cooled ion beams, very low momentum spreads severely limit the use of Schottky pickup measurements of the momentum spread. At ESR, the Schottky signal power decreases by orders of magnitude for momentum spreads below $\Delta p/p < 10^{-6}$, while the momentum resolution is essentially limited by the length of the Schottky pickup electrode to about $\Delta p/p < 10^{-6}$ [11]. The transition of the beam dynamics from the intra-beam scattering dominated regime to the space-charge dominated regime has, yet, only been observed for low beam currents on the order of 10 μA and below, since only at low ion currents the laser force was able to counteract intra-beam scattering. At such low beam currents however, the transverse beam size cannot be determined with great accuracy.

With the new diagnostics setup, beam width, bunch length and longitudinal momentum spread can be determined using all-optical techniques. Beam width measurements require precise alignment of laser and ion beam. With a new mirror setup using motor-driven translation stages, we will be able to not only align the laser beam using the fast, Piezo-driven beam stabilization system used in previous beam times, but can control the horizontal laser beam position on the complete interaction length, thus being able to scan over the horizontal ion beam profile. During a fast scan of the horizontal displacement $\Delta x_{\mathrm{radial}}$ of the laser beam relative to the ion beam the fluorescence signal rate $R_{\mathrm{fluo}}(\Delta x_{\mathrm{radial}}) \propto \exp(-\Delta x^2_{\mathrm{radial}}/2\sigma^2_{\mathrm{radial}})$ can be recorded. From this measurement one can deduce the radial ion density beam profile and thus the beam width σ_{radial}.

The method of optical bunch length measurement used at the PALLAS storage ring [25] can be almost directly transferred to the ESR. At PALLAS, the bunching frequency is used as a trigger to start a multi-hit time-to-digital converter (TDC). The TTL-converted photomultiplier signal is used as a stop signal. The probability $P_{\mathrm{fluo}}(\tau_{\mathrm{delay}})$ to detect a photon after a certain delay time τ_{delay} is proportional to the axial local ion bunch density $n_{\mathrm{axial}}(z)$. By choosing the phase relative to the bunching frequency one can deduce the axial ion density $n_{\mathrm{axial}}(\beta \times \tau_{\mathrm{delay}}) \propto P_{\mathrm{fluo}}(\tau_{\mathrm{delay}})$.

Optical measurements of the momentum spread have already been tested in the 2004 ESR beam time [9]. A fast voltage ramp is applied to the drift tube electrodes, locally changing the ion momentum inside the drift tube. In order to scan the distribution, one finds for the scan range $U_{\mathrm{scan}} > \Delta p/p \times E_{\mathrm{beam}}/e$. For the C^{3+} beam energy of $E_{\mathrm{beam}} = 1.47$ GeV we find a fast voltage supply with a scanning range of -5 kV to +5 kV suitable for cold beams with $\Delta p/p \leq 7 \times 10^{-6}$. The time for one complete ramping cycle should be fast enough to not alter the velocity distribution by the laser force. The scanning time thus has to be smaller than the cooling time estimated by

$$\tau_{\mathrm{cool}} = \frac{\Delta p}{p} \times \frac{\beta \hbar \omega_r}{m_{\mathrm{C}^{3+}} c^2} \times \frac{2}{\Gamma} \, .$$

When taking into account the length of the interaction region between laser and ion beam, incomplete saturation and the ratio of the Doppler-broadened saturation transition line width to the laser line width, cooling times of 20 ms could be reached at ESR. This means, the voltage ramp should be scanned in about 1 ms while simultaneously recording the fluorescence rate. With a scanning single-frequency laser system as described above, changing the laser frequency rather than changing the local beam velocity will give the same effect. Fast, mode-hop free scanning of the laser frequency on the order of 1 GHz/ms is in reach with modern laser systems, which would allow to resolve much larger momentum spreads.

As discussed, slow scanning of the laser frequency alters the velocity distribution. When the beam is very cold, this effect can be used to probe for the phase transition to the crystalline state as shown in [26]. At first, the laser frequency is detuned far from the cooling transition frequency and then constantly scanned towards the transition frequency. The fluorescence rate grows with decreasing detuning. If beam crystallization occurs, the fluorescence rate shortly decreases before sharply rising to its maximum. This short decrease is caused by a sudden decrease in ion velocity spread due to the crystallization. At small detuning, almost all ions are then out of resonance with the laser. With further reduction of the detuning all ions come in resonance with the laser, leading to a sharp increase in the fluorescence. For bunched beams, fluorescence peaks are observed for each harmonic h of the revolution frequency [27], but the general evolution of the fluorescence rate with detuning is universal and an unambiguous proof for beam crystallization.

Beam ordering can be detected without having to resort to optical methods [28, 29, 30], but long-range correlations as expected in beam crystallization cannot be easily resolved by Schottky measurements [31]. The situation changes if the interaction of ions with laser light is considered [32]. In the following we briefly discuss using the TDC setup mentioned before to measure the longitudinal ion dynamics. As in the case of the optical bunch length measurement, the TDC is used to record multiple photomultiplier signals. The temporal distribution of signals is then Fourier-transformed using a fast FFT algorithm to acquire the spectral distribution of the photomultiplier signals. This spectral distribution is directly related to the momentum distribution of the ions.

For the case of a crystalline coasting beam with N particles in which the particles are arranged in a string-like pattern, one would observe a strong peak in the Schottky spectrum at the $h = N$ harmonic of the revolution frequency. Even with very dilute beams of $N = 10^3$ ions this would lead to a frequency in the GHz range, which cannot be resolved

by the Schottky pickup electrode. Using a fast photomultiplier with ns rise time and a TDC with sub-100 ps time resolution, high-frequency components in the signal spectrum up to GHz could be measured directly. Such a measurement would demand high fluorescence rates even at very low beam currents and thus does not seem feasible. However, due to the high temporal resolution of the optical detection, the transition to an ordered state could be resolved without ambiguity even for high ion beam currents. This is due to the fact that unlike in an ordinary Schottky measurement, the signal power does not decrease with decreasing momentum spread. In fact, the fluorescence signal is expected to rise at smaller momentum spread. The optical measurement of the momentum spectrum of the ion beam is thus complementary to the standard Schottky measurement.

SUMMARY

In the upcoming ESR beam time we will focus on replacing the scanning of the bunching frequency by scanning the laser frequency over a range of several GHz. Recent developments in diode laser technology make it possible to scan large frequency ranges without any mode hopping. Combining such a system with a pulsed broadband laser will enable us to address the complete phase space volume of the ion beam simultaneously without the need for initial electron cooling.

Optical detection systems to measure bunch width, length, momentum spread and momentum spectrum will complement the existing beam diagnostics at ESR and expand the resolution limits that have constrained precision measurements of the properties of ultracold ion beams in the past. With the fast scanning laser system an unambiguous determination of the phase transition from a liquid-like space-charge dominated beam to a crystalline state will be available.

This work is partially supported by GSI FuE Laserkühlen DRSCHR, Helmholtz VH-NG 148 and BMBF within the framework of of the research program 'Hadronen- und Kernphysik'.

REFERENCES

[1] U. Schramm, M. Bussmann, D. Habs et al., PAC05, Knoxville, May 2005, FOAD004, p. 403. http://www.JACoW.org

[2] M. Bussmann, U. Schramm, D. Habs et al, J. Phys. Conf. Ser. 88, 012043.

[3] G. Zwicknagel , C. Toepffer , P.-G. Reinhard, Phys. Rep. 309 (1999) 117.

[4] I. Augustin et al., Nucl. Instr. Meth. B 261(1-2) (2007) 1014.

[5] V. Litvinenko et al., PAC07, Albuquerque, June 2007, TUPMS076, p. 1347. http://www.JACoW.org

[6] U. Schramm , M. Bussmann , D. Habs Nucl. Instr. Meth. A 532(1-2) (2004), 348.

[7] H. Backe, Hyperfine Interactions 171(1-3) (2006), 93.

[8] U. Schramm, D. Habs, Progr. Part. Nucl. Phys. 53(2) 2004, 583.

[9] U. Schramm, M. Bussmann, D. Habs et al., Hyperfine Interactions 162(1) (2005), 181.

[10] U Schramm., M. Bussmann, D. Habs et al., STORI-2005, Bonn, May 2005, p. 324. http://www.fz-juelich.de/ikp/stori05/

[11] M. Bussmann, D. Habs, U. Schramm et al., COOL07, Bad Kreuznach, September 2007, FRM1C02, p. 226, http://www.JACoW.org.

[12] I. Lauer, U. Eisenbarth, M. Grieser et al., Phys. Rev. Lett. 81 (1998), 2052.

[13] U. Schramm, M. Bussmann, D. Habs et al., COOL05, Galena, September 2005, AIP Conf. Proc. 821 (2006), 509.

[14] H. Okamoto, A. M. Sessler, D. Möhl, Phys. Rev. Lett. 72(25) (1994), 3977.

[15] J. S. Hangst, J. S. Nielsen, O. Poulsen, P. Shi, J. P. Schiffer, Phys. Rev. Lett. 74(22) (1995), 4432.

[16] T. Führer, T. Walther, Opt. Lett. 33(4) (2008), 372.

[17] R. Nicolaescu, T. Walther, E. S. Fry, M. Muendel, Appl. Opt. 38(9) (1999), 1784.

[18] A. Seifert, M. Sinther, T. Walther, E. S. Fry, Appl. Opt. 45(30) (2006), 7908.

[19] S. N. Atutov, R. Calabrese, R. Grimm et al., Phys. Rev. Lett. 80(10) (1998), 2129.

[20] A. Borsutzky, R. Brnger, C. Huang, R. Wallenstein, Appl. Phys. B 52(1) (1991), 55.

[21] T. Omatsu, K. Nawata, M. Okida, K. Furuki, Opt. Express 15(15) (2007), 9123.

[22] A. Galvanauskas, M.-Y. Cheng, K.-C. Hou, K.-H. Liao, IEEE J. Sel. Top. Quant. Electr. 13(3) (2007), 559.

[23] U. Schramm, T. Schätz, M. Bussmann, D. Habs, J. Phys. B 36(3) (2008), 561.

[24] C. Novotny, PHD-Thesis, GSI Diss. 2009-06 March (2009), 82-97.

[25] U. Schramm, T. Schätz, M. Bussmann, D. Habs Physica Scripta T104 (2003), 189.

[26] T. Schätz, U. Schramm, D. Habs, Nature 412 (2001) 717.

[27] U. Schramm, T. Schätz, D. Habs, Phys. Rev. Lett. 87(18) (2001), 184801.

[28] M. Steck, K. Beckert, H. Eickhoff et al., Phys. Rev. Lett. 77 (1996) 3803.

[29] H. Danared, A. Källberg, K.-G. Rensfeld et al., Phys. Rev. Lett. 88 (2002), 174801.

[30] T. Shirai, M. Ikegami, S. Fujimoto, H. Souda, M. Tanabe, H. Tongu, A. Noda, K. Noda, T. Fujimoto, S. Iwata, S. Shibuya, A. Smirnov, I. Meshkov, H. Fadil, M. Grieser, Phys. Rev. Lett. 98(20) (2007), 204801.

[31] R.W. Hasse, COOL07, Bad Kreuznach, September 2007, THAP21, p. 213, http://www.JACoW.org.

[32] S. Atutov, V. Biancalana, R. Calabrese, T. Clauser, D. Diacono, V. Guidi, G. Lamanna, P. Lenisa, E. Mariotti, L. Moi, Nucl. Inst. Meth. A 430(1) (1999), 10.

IMPROVEMENTS TO THE STACKTAIL AND DEBUNCHER MOMENTUM COOLING SYSTEMS*

V. Lebedev†

Fermilab, Batavia, IL 60510, U.S.A.

Abstract

Upgrades and improvements to the stacktail and Debuncher momentum cooling systems have contributed to the success of Tevatron Run II. This paper describes measurements and simulations that facilitated achievement of peak stacking rates of $30{\cdot}10^{10}$ hour^{-1} as well as a better understanding of the principles of the system design and operation. The heating of the antiproton core by the stacktail system is a serious limiting factor to the maximum stacking rate. The paper also discusses heating mechanisms and ways to mitigate them.

INTRODUCTION

Antiprotons are produced by a 120 GeV Main Injector proton beam hitting the antiproton production target every 2.2 s. The antiprotons coming out of the target are focused by the lithium lens to the AP-2 line and transported to the Debuncher where they are stochastically precooled. They are then transferred to the Accumulator where they are momentum-cooled into a dense core by stochastic cooling systems. The stacking rate decreases with stack size, therefore after achieving a stack size of about $30{\cdot}10^{10}$ antiprotons, they are transferred to the Recycler. In the Recycler, the antiprotons are cooled using both stochastic and electron cooling, to be used for collider operations.

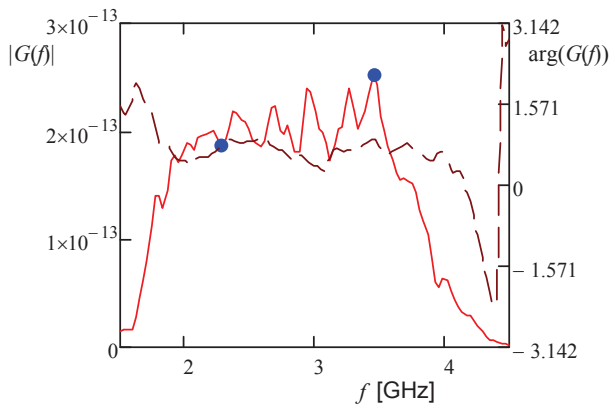

Figure 1: Dependence of the magnitude and phase of the total stacktail gain on frequency after equalizer installation for the revolution frequency 628830 Hz.

The sequence of upgrades carried out over the last 3 years and their results are presented in Refs. [1] and [2]. Here we mention only two the most important ones: a correction of the system gain with an equalizer and an increase of the lattice slip factor [4]. The magnitude and phase of the total stacktail gain after the equalizer installation are shown in Figure 1. The slip factor increase resulted in the bands being close to overlap at the high frequency end. The upgrades resulted in an increase of the peak stacking rate from $20{\cdot}10^{10}$ to $30{\cdot}10^{10}$ hour^{-1}. That is quite close to expectations based on model prediction. Recent developments of the stochastic cooling theory [3, 4] have been extremely useful in choosing the upgrade path and to follow up the problems encountered along the way. In this paper we discuss the present stacking rate limitations and possible ways to overcome them.

STACKING IN THE ACCUMULATOR

Figure 2 presents measured and simulated particle distributions during the first 100 s of stacking in the Accumulator. The measurements were performed by recording the beam Schottky noise of the longitudinal Schottky monitor operating at the 126th harmonic of the revolution frequency (~79 MHz). The signal was mixed down and digitized during the 100 s period by an 8 bit digital scope with a sampling rate of 156 kHz. The data were split into arrays belonging to different stacking cycles (2.2 s long). Then, each stacking cycle data were additionally split into 160 arrays with a length of 2048 words and subjected to the FFT. Averaging 16 consecutive spectra resulted in 10 Schottky noise spectra per stacking cycle. A low pass filter installed before the digitizer reduced the core signal and allowed us to achieve the required dynamic range with only an 8 bit scope resolution. The effect of the filter is visible in Figure 2 as a noise floor that increases with frequency.

The stacking process has the following steps. First, antiprotons precooled in the Debuncher are transferred to the Accumulator. They arrive at the deposition orbit with a revolution frequency of 628756 Hz. There are ~$2.3{\cdot}10^8$ antiprotons in one transfer with rms revolution frequency spread of 3 Hz. Then, the injected antiprotons are RF displaced to the deposition frequency of 628831 Hz. The width of the RF bucket is chosen to maximize the stacking rate. This results in about ~2% of the injected particles being left at the deposition orbit. They are presented as a small peak in the spectrum at the frequency of 628750 Hz. The large peak represents the injected beam. The stacktail system pulls the injected particles into the core located at 628897 Hz. One can see a step by step propagation of particles to the core in Figure 2. The particles which were not moved out of the deposition region before the next pulse arrives are RF displaced in

* Work supported by the U.S. Department of Energy under contract No. DE-AC02-76CH03000

† val@fnal.gov

the direction of the injection orbit and lost for further stacking. One can see the build-up of such particles on the left from the deposition orbit. Experiments show that a higher stacking rate is achieved if the stacktail is on during RF displacement of the beam from the injection to the deposition orbit. The presence of RF strongly distorts the Schottky spectra making the last spectrum of each stacking cycle unusable for analysis (0.22 s out of 2.2 s.)

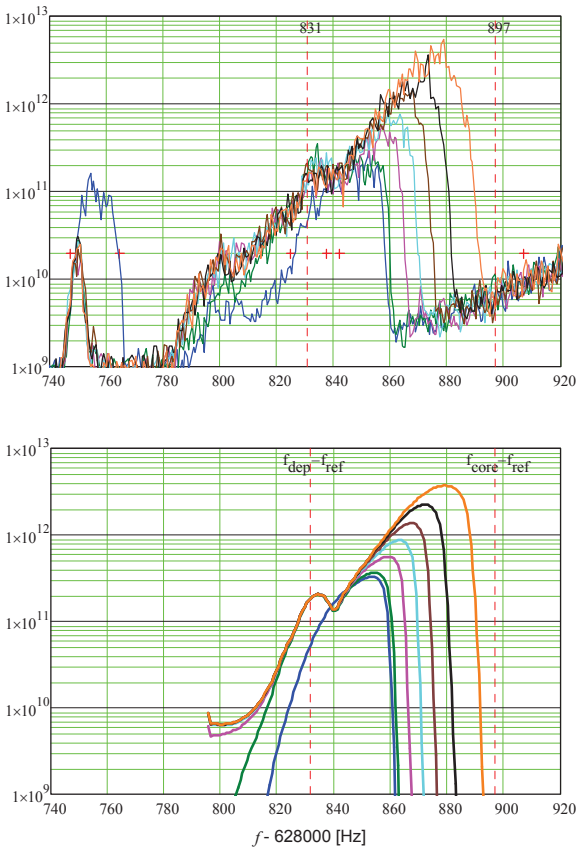

Figure 2: Evolution of particle distribution over revolution frequency during the first 100 s of stacking; top - measurements, bottom - simulations. Curves are built at 1.54 s in cycle 2, and 0.22 s in cycles 3,5,8,13,23 and 47.

The major goal of the measurements presented in Figure 2 was to make a direct measurement of the system gain. Previous measurements [4] were performed with narrow momentum spread, low intensity beams. They provided a measurement of gain dependence on frequency and beam momentum with good accuracy (≤10%) and resulted in a credible model which guided us through the upgrades. However, it was impossible to measure the absolute value of the gain with comparable accuracy because we could not control or measure with sufficient accuracy the longitudinal distribution of this narrow beam. One can see a good correlation between the measurements and simulations in Figure 2. The only free parameter in the model was the absolute value of the gain.

The simulations are based on solving the Fokker-Planck equation where all system parameters came from the beam-based measurements [4]. To accelerate the simulations, we presently neglect in calculations the particle interaction through the cooling system, which modifies the cooling force and diffusion. That allowed us to simulate a complete 1 hour stacking cycle in about 20 minutes on a single-processor computer. Correct accounting of the particle interaction would increase computational time by at least 2 or 3 orders of magnitude resulting in a many hour simulation on a multiprocessor computer. There are a few reasons which make simulations so extensive. First, in contrast to a normal stochastic cooling system where computation of a single cooling cycle completely characterizes the system, characterization of the stacktail system requires simulations of about 1000 cycles. It lengthens computations proportionally. Second, taking into account the particle interaction for the stacktail requires much more computations than for a general cooling system where this interaction is only important at the end of the cooling cycle. In this case the band overlap can be neglected and a computation of beam dielectric functions for all harmonics requires a computation of single integral over the distribution function:

$$\varepsilon_n(y)=\begin{cases}1+\dfrac{G_{PC}(\omega_n)}{2\pi i\eta n}\displaystyle\int_{\delta\to 0_+}\frac{x\,d\psi_0(x)/dx}{x-y-i\delta}dx\\ 1+\dfrac{1-A(\omega)e^{-i\omega T_0}}{2\pi i\eta n}G_{FC}(\omega_n)\displaystyle\int_{\delta\to 0_+}\frac{d\psi_0(x)/dx}{x-y-i\delta}dx\end{cases}, \quad (1)$$

Here the top and bottom equations correspond to the cases of the Palmer and filter cooling, with their gains parameterized as follows: $G_{PC}(x,\omega_n)=xG_{PC}(\omega_n)$ and $G_{FC}(x,\omega_n)=G_{FC}(\omega_n)$, $A(\omega)$ describes the depth and dispersion of the notch filter, η is the slip factor, T_0 is the revolution time, and $y=-(\omega-n\omega_0)/n\eta$. In contrast, the stacktail operates very close to band overlap. That requires using an expression which takes into account the band overlap in computations of the dielectric function[1] [3]:

$$\varepsilon(\omega)=1+\left(1-A(\omega)e^{-i\omega T_0}\right)\int_{\delta\to 0_+}\frac{d\psi_0(x)}{dx}\frac{G(x,\omega)e^{i\omega T_2\eta_2 x}}{e^{i\omega T_0(1+\eta x)}-(1-\delta)}dx\,. \quad (2)$$

This integral differs at different harmonics resulting in the need to make the computation for a large number of harmonics. This drastically increases the time of computation. To demonstrate the strength of band overlap effect, the dielectric functions and stability diagrams computed with and without it taken into account are presented in Figure 3. For both cases, the wiring of the system (multiple pickup legs and notch filters) was correctly accounted [4]. One can see that the difference is close to the total value of the effect. In particular, ignoring the band overlap results in a decrease of the stability region by almost a factor of 2. Thus if one wants to have a correct accounting of signal suppression, it has to be done with band overlap taken into account. This left us with no choice but to neglect the signal particle interaction in solving the Fokker-Planck equation. To estimate the effect of particle interaction on the computation results, ε

[1] Eq. (2) is justified for the case of a system with one pickup leg and one notch filter. Taking into account multiple legs and notch filters would make this equation lengthier and therefore we omit it. A corresponding expression is presented in Ref. [4].

was computed for a number of time steps and frequencies after a solution of the Fokker-Plank equation is obtained. Figure 4 presents the changes in ε within the time of cycle 47 (~103 s) for the simulations presented in Figure 2. The beam is close to the stability boundary at the beginning of the cycle when the injected beam has narrow distribution; but in 100 ms smoothening the beam distribution in the vicinity of the deposition orbit results in a reduction of particle interaction by more than a factor of two. Consequently, as long as the stack size is small, the effect of particle interaction is also small during most of cycle time resulting in relatively small (≤10-20%) overall correction for the stacking rate. Figure 4 also shows that in the stacktail region (628840-628890 Hz) the $|\varepsilon$ -1| does not exceed 0.25, i.e. the particle interaction has a small effect on the speed of the stack front propagation and, consequently, on the value of the gain deduced from the experimental data. Note that for a well-tuned cooling system, its operation in a regime with strong particle interaction also implies that the system operates close to its optimal gain, when the particle heating power due to diffusion is equal to half of the cooling power due to cooling force. In this case the signal suppression (amplification) due to particle interaction reduces (increases) both the cooling force and diffusion yielding a comparatively small effect of the particle interaction if $|\varepsilon - 1| \le 0.5$.

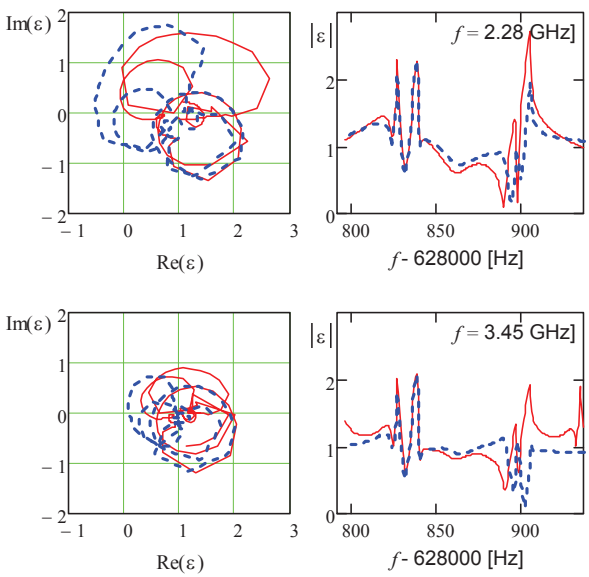

Figure 3: The beam stability diagrams (left) and the dependencies of $|\varepsilon|$ on the revolution frequency (right) computed at 55 ms of stacking cycle 800 for different revolution frequency harmonics: top - n=3626 (2.28 GHz), bottom - n=5486 (3.45 GHz); red solid lines – computed with band overlap taken into account, blue dashed lines –band overlap is neglected.

Further accumulation of antiprotons results in an increased contribution of core particles to the dielectric function, so that it will be making a dominant contribution after approximately 500 cycles (20 min). In this case the particle interaction for the core is strong during the entire cycle and cannot be neglected. Figure 3 presents a comparison of contributions for the particles in the core and fresh beam delivered to the deposition orbit.

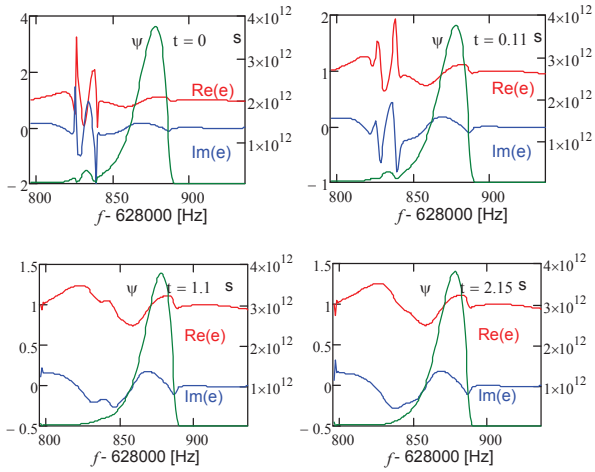

Figure 4: The real (red) and imaginary (blue) parts of ε computed at different times in cycle 47 for stacking simulations presented in Figure 2. The particle distribution is shown with a dark green line.

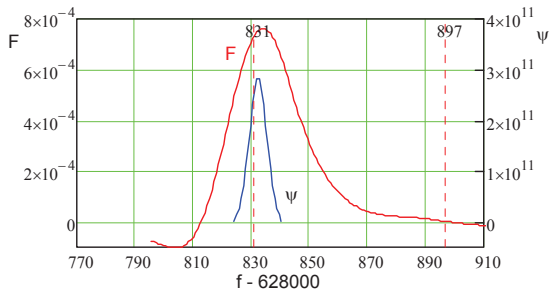

Figure 5: Dependences of cooling force and the distribution of particles delivered to the deposition orbit on the revolution frequency.

Both the experimental data and simulations presented in Figure 2 show that the stacktail is not capable of clearing the deposition orbit before next pulse arrival. It is mainly related to the narrow flattop of the cooling force as can be seen in Figure 5. Both the simulations and experimental results show that the optimum deposition orbit is in the vicinity of 628831 Hz or, as the simulations show, at a frequency slightly below the frequency where the cooling force achieves its maximum. This results in the low frequency tail of the beam delivered to the deposition orbit seeing about half of the cooling force. Consequently, a significant fraction of these particles do not clear the deposition orbit before the next pulse arrives and is lost.

The present model, where the particle interaction through the stacktail is not taken into account, yields that the stacking rate continues to grow with a decrease in momentum spread. However, as shown above, the system is close to the stability boundary and it is unclear how such decrease can affect the stacking rate. Recent reductions in the Debuncher beam momentum spread by about 10% yielded a ~5-10% increase in stacking rate.

This suggests that a further decrease should result in an increase in stacking rate. If required, the system stability can be supported by ramping the stacktail gain within stacking cycles.

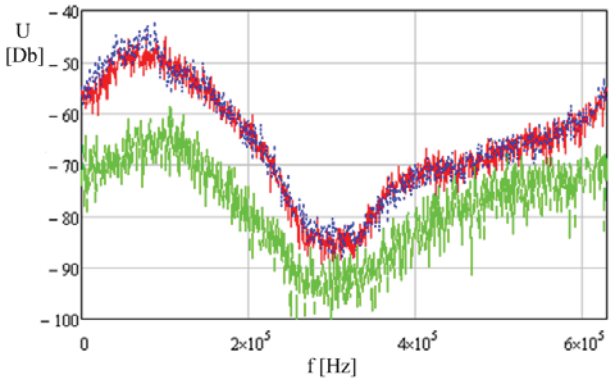

Figure 6: Spectral density for stacktail TWT 16; green line – no stacking, blue line – beginning of the stacking cycle, red line – end of the stacking cycle.

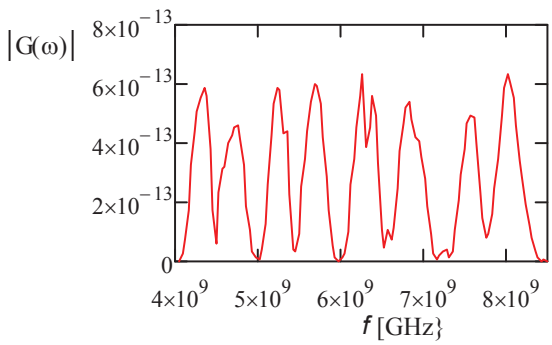

Figure 7: The dependence of gain on frequency for Debuncher longitudinal cooling.

Another problem affecting stacktail operation is related to the intermodulation signal distortion (IMD) by TWTs. It reduces the depth of the notch introduced by the notch filters on harmonics of the core particles resulting in core heating. Figure 6 presents a typical spectral power for one of the revolution harmonics. The green line corresponds to the case of no stacking. In this case, the noise consists of two contributions: the thermal noise of preamplifiers and the noise of the core particles. Both are shaped by the notch filters. It is unclear whether the minimum spectral density is determined by the noise floor of the spectrum analyzer, by TWT noise or by something else; but in the absence of IMDs, this value should not change when stacking is resumed. The red and blue curves represent the spectral density during stacking. One can see that stacking results in a 10 Db increase in the spectral density on the core due to IMDs. The measurements were performed for all TWTs. They showed that IMDs are larger at high frequencies and that they are different for different TWTs. The notch depth (ratio of maximum to minimum spectral densities) drops from 31-37 Db range at 2.4 GHz to 22-28 Db at 3.5 GHz. Figure 6 also demonstrates that the notch depth hardly depends on the stacktail power in the range of operational power variations (~6 Db). Simulations show that if the spectral density of the kicker voltage was determined by thermal and particle noise, the notch depth would be about 20 Db deeper. Core heating by IMDs necessitates gain reduction with increased stack size to prevent longitudinal core blowup. It results in a reduction of stacking rate with stack size. This additional heating due to IMDs was taken into account in the numerical model described above resulting in reasonable agreement between simulations and measurements.

DEBUNCHER LONGITUDINAL COOLING

In contrast with the Accumulator, where all stochastic cooling systems operate close to the optimum gain, all Debuncher systems are power limited during most of the cooling cycle. In this case, the cooling decrement has comparatively weak dependence on the effective bandwidth of the system. Instead of growing as W^2 it grows proportionally to $\sqrt{W}$ resulting in that the bandwidth increase yields four times smaller gain than for a system operating close to the optimal gain. Analysis of possible equalization schemes revealed that only a few percent cooling rate improvement could be achieved. Therefore, we did not pursue this option.

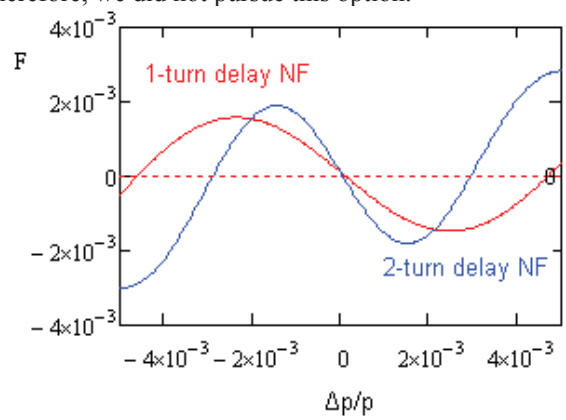

Figure 8: Dependence of cooling force on momentum for one-turn and two-turn delay notch filters in Debuncher.

Longitudinal Debuncher cooling is a filter cooling system with its frequency band split into four sub-bands whose signals are wired through a common notch filter. Each band has 2 additional pickup sub-bands combined into a kicker band. Figure 7 presents the gain of the system reconstructed from measurements of each sub-band. To improve the longitudinal cooling, we made an upgrade of its notch filter; so that during the first half of the cooling cycle the long leg of the notch filter has one turn delay (as before the upgrade) and in the second half of the cycle the delay is switched to two turns. It effectively doubles the small amplitude cooling rate for the same electronic gain. The two-turn delay notch filter also reduces the momentum acceptance of the cooling system. However, it is engaged after 1 s of normal cooling, when the beam is already sufficiently cold. Therefore, switching in the two-turn delay notch filter improves momentum cooling while not causing additional

particle loss from the distribution tails. Figure 8 presents the cooling force for the cases of one and two-turn delay notch filters computed from the measured beam response functions. Engaging the two-turn notch filter effectively increases the power of the system by a factor of 4 and results in the system staying on the optimum gain for the second half of the cooling cycle. The optimum gain is proportional to the square of beam momentum spread. Therefore, to stay at optimal gain, the gain is gradually decreased by 6 Db to the end of the cooling cycle.

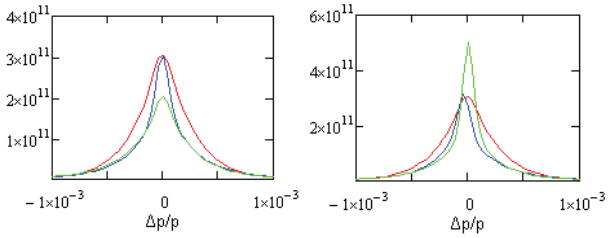

Figure 9: Simulated distortion of the Schottky spectrum at the end of Debuncher cooling cycle depending on the value of $\delta A = A - 1$: red lines - undistorted spectrum, blue line (left) - $\delta A = 0$; green line (left) - $\delta A = -0.05$, blue line (right) - $\delta A = 0.05i$; green line (right) - $\delta A = 0.05$.

Computer simulations have been based on solving the Fokker-Planck equation [3] with measured cooling system parameters. Taking into account that the particle interaction is important only at the end of the cooling process, ε was computed neglecting band overlap using the bottom equation of Eq. (1). The computation of the integral over the distribution function was reduced to a matrix multiplication to accelerate the computations. It can be presented in the following form:

$$\varepsilon(\omega_k, x_n) = 1 + \left(1 - A(\omega_k) e^{-i\omega_k T_0}\right) G(\omega_k) \Xi_{nm} \psi_m , \qquad (3)$$

where indices n and m numerate dependencies on the momentum, index k numerates the revolution frequency harmonics, and we omitted the time dependent index. Matrix Ξ_{nm} is computed once at the beginning of calculations. It was obtained by a piece-wise integration of the distribution interpolated by the second order polynomial between nodes. That yields:

$$\Xi_{nm} = a(n-m+1) - a(n-m-1) + b(n-m+1) + b(n-m-1) - 2b(n-m) , \qquad (4)$$

$$a(n) = \frac{1}{2}\ln\left(\frac{k+1/2}{k-1/2}\right), \quad b(n) = n\ln\left(\frac{k+1/2}{k-1/2}\right) - 1 .$$

The integral ($\Xi_{nm}\psi_m$) was computed once at every time step resulting in fast computations of $\varepsilon(\omega_k, x_n)$ for multiple revolution frequency harmonics. Because the cooling system has 8 sub-bands its gain oscillates repeatedly with frequency (see Figure 7). To achieve an accurate description, 120 harmonics uniformly distributed through its frequency band are used.

Simulations predicted ~10% improvement in beam momentum spread at the end of cooling cycle with the installation of the two-turn delay notch filter. The observed cooling improvement is in agreement with numerical simulations. The final rms momentum spread is $3.2 \cdot 10^{-4}$. The simulations also proved that the result depends strongly on the notch depth of the filter. Therefore special attention was paid to amplitude balancing of the notch filter legs. Although predicted and measured evolutions of the distribution are quite close, there are still minor inconsistencies. In particular, there is a difference in the signal suppression by the cooling system. The spectral density measured from the cooling pickup is:

$$S_n(y) \propto \psi_0(y) \Big/ \left|\varepsilon_n(y)\right|^2 . \qquad (5)$$

As it follows from Eq. (1), there is no signal suppression in the distribution center for a perfect notch filter, $A(\omega)=1$. However the notch filter of Debuncher longitudinal cooling is far from being perfect. The rms value of $\delta A_n = \left|A(\omega_n) - 1\right|$ weighted with the system gain is equal to 0.08. Figure 9 presents possible spectrum distortions depending on δA_n for a given harmonic. One can see that that the real part of δA results in the signal suppression or amplification depending on its sign, while the imaginary part shifts the spectrum. The reason that there are discrepancies between the measurements and simulations is not quite clear. A systematic offset in measuring the real part of $A(\omega)$ is the most probable one.

DISCUSSION

Improvements to the stacktail and Debuncher momentum stochastic cooling systems resulted in a stacking rate close to its theoretical limit. Presently, the stacking rate is ~75% of the Debuncher flux. ~5% of the antiprotons are outside of Debuncher cooling range and remain in the Debuncher; ~2% are left at the deposition orbit in Accumulator; and ~15% are back-streamed from the stacktail. The amount of back-streamed particles grows to ~25% at the end of a stacking interval. There has been considerable progress in understanding cooling system operations.

The stacktail numerical model shows that clearing of the deposition orbit is the major limitation in the stacking rate. It predicts that the rest of the stacktail allows significantly larger flux (~20-30%). It is unclear how much stacking can be improved by reducing the momentum spread of injected beam but it looks like as the most promising path to pursue.

The author is grateful to J. Morgan, V. Nagaslaev, R. Pasquinelli, D. Vander Meulen and S. Werkema for their contributions to the development of the stochastic cooling systems described in this paper.

REFERENCES

[1] V. Lebedev, "Status of Tevatron Run II," PAC2009.

[2] R. Pasquinelli, *et al.*, "Progress in Antiproton Production at the Fermilab Tevatron Collider," PAC-2009.

[3] V. Lebedev, "Stochastic Cooling with Schottky Band Overlap," COOL'05, AIP Conf. proc., v. 821, p. 231.

[4] V. Lebedev, "Antiproton accumulation and production," COOL'07, p. 39.

PROTOTYPE PICK-UP TANK FOR CR STOCHASTIC COOLING AT FAIR*

F. Nolden, R. Hettrich, U. Jandewerth, C. Peschke, P. Petri, M. Steck, GSI, Darmstadt, Germany

Abstract

A prototype pick-up tank for stochastic precooling in the CR storage ring of the FAIR project at GSI was built. It will be equipped with movable electrodes driven by linear motors. The electrodes can be operated at cryogenic temperatures. The design of the tank and first test measurements are presented.

INTRODUCTION

The Collector Ring CR [1, 2] is a storage ring within the FAIR project at GSI which has three purposes: stochastic cooling of radioactive ion beams, stochastic cooling of antiproton beams, and nuclear mass measurements of short-lived nuclei in an isochronous optical setting. These beams are injected at high emittances and momentum spreads immediately after production. They have a short bunch length of about 50 ns; their momentum spread is therefore reduced by bunch rotation and subsequent adiabatic debunching. Two different optical settings are required for ions and antiprotons. Due to their different energies, the frequency slip factors must be different in order to achieve optimum conditions for stochastic cooling.

Table 1: Basic Parameters of the CR

	rare isotopes	antiprotons
circumference	216.25 m	
max. magnetic rigidity	13 Tm	
energy	740 MeV/u	3.0 GeV
Lorentz β	0.83	0.97
Lorentz γ	1.80	4.20
max. number of particles	$1 \cdot 10^9$	$1 \cdot 10^8$
charge state	up to 92	-1

The beam parameters after adiabatic debunching and at the end of the cooling process are listed in Table 1. Three pick-up tanks and three kicker tanks will be installed at locations of zero dispersion in the long straight sections. A further pick-up tank is needed for Palmer cooling of radioactive beams, which is located in an arc at high dispersion.

Here we discuss the prototype design of a pick-up tank at zero dispersion. The design is made such that it could serve as either a horizontal pick-up or, after rotation by 90 degrees, as a vertical pick-up.

Table 2 displays the initial and final beam parameters for rare isotope and antiproton beams. In order to reach the required final emittances, a good signal-to noise ratio is indispensable. Therefore a tank design with movable (plunging) electrodes was adopted.

Table 2: Initial and Final Beam Parameters for CR

	rare isotopes	
	$\delta p/p$ (2σ)	ϵ_{xy} [mm mrad]
injected	1.5 %	200
debunched	0.4 %	200
cooled	0.05 %	0.5
total cooling time [s]	1.5	
	antiprotons	
	$\delta p/p$ (2σ)	ϵ_{xy} [mm mrad]
injected	3.0 %	240
debunched	0.7 %	240
cooled	0.1 %	5
total cooling time [s]	10	

The layout of the straight sections in the CR follows a FODO design [3]. Along the length of the 2m long pick-up tank, the slope of the betatron function is non-negligible, and the beam envelopes change substantially. Table 3 lists the vertical radius inside the pick-ups P1 and P2 in the beginning and at the end of cooling, both at the entrance and the exit of the tank. Table 4 shows the analogous data for the tank P3, where the electrodes are arranged horizontally. The signal from these tanks is produced by electrodes arranged above and below the beam (vertical pick-up). In the course of the cooling process the beam size decreases substantially, in particular for the radioactive beams.

Table 3: Vertical Beam Radius (in mm) for Pick-ups P1 and P2

	P1			
	initial		final	
	entrance	exit	entrance	exit
pbar	56	41	8	6
RIB	58	49	3	3
	P2			
	initial		final	
	entrance	exit	entrance	exit
pbar	37	43	6	6
RIB	42	52	2	3

Table 4: Horizontal Beam Radius (in mm) for Pick-up P3

	initial		final	
	entrance	exit	entrance	exit
pbar	52	40	7	6
RIB	57	47	3	2

* Work supported by EU design study (contract 515873 - DIRAC-secondary-Beams)

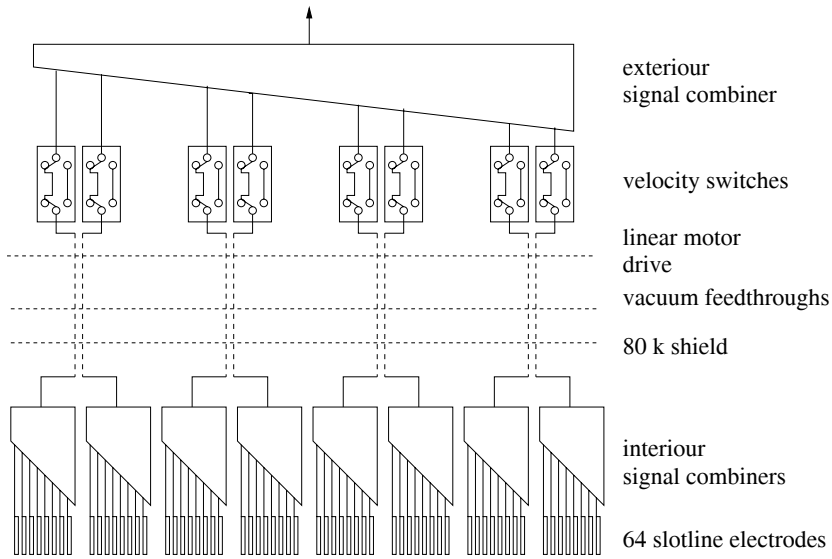

Figure 1: Sketch of signal paths in pick-up.

TANK ARCHITECTURE

The signals arise from slotline electrodes. Their design has been developed in the past years through a series of optimization procedures [4]. Eight of these electrodes are arranged on a single pcb (printed circuit bord). Because the beam velocities of radioactive ions and antiprotons are different, one has to pay attention to the phase-correct combination of the signals from each electrode. Because of their low charge state, the signal to noise ratio is most critical for antiprotons. We assume in the following that each slotline delivers a voltage U_0. The signal combiner is optimized with respect to to the velocity β_1 of the antiprotons. If the beam velocity β_2 is different from this velocity, and if one uses n_p pick-up electrodes arranged at a distance d_p, then one gets from an ideal power combiner a sum voltage

$$\begin{aligned} U &= \frac{U_0}{\sqrt{n_p}} \sum_{n=0}^{n_p-1} e^{-i\omega t_m} \qquad (1) \\ &= \frac{U_0}{\sqrt{n_p}} \frac{\sin\left(n_p \omega t_m/2\right)}{\sin\left(\omega t_m/2\right)} e^{-i(n_p-1)\omega t_m/2} \end{aligned}$$

with the mismatching time between electrodes

$$t_m = \frac{d_p}{c}\left(\frac{1}{\beta_1} - \frac{1}{\beta_2}\right) \qquad (2)$$

Taking the signal from eight electrodes in a row with a distance d_p of 25 mm between electrodes, the phase error for radioactive ions leads to an acceptable maximum combination loss of 0.8 dB at the upper band limit of 2 GHz. The electrode pcb is mounted to the front side of an aluminum body. Inside this body eight chambers exist, inside which the signal is transported to the rear side. Here the signal from eight electrodes is power combined. Then the signal is transported by coaxial lines attached to a solid carrier rod towards the outside of the tank. Each carrier rod transports the signal of two neighbouring eight-slot pcbs. This mechanism is mechanically movable with a maximum amplitude of 60 mm. There are four movable mechanical systems on each side of the tank. The aluminum body inside the tank is cooled to a temperature of 20 K. The thermal contact between the helium cold heads and the aluminum body is maintained by movable silver-coated copper-beryllium sheets.

These cold parts are shielded from the room temperature surroundings by means of a gilded copper cylinder which is kept at a temperature of 80 K. The gold surface is 4 μm thick and has an extremely low thermal emissivity. Between the copper body and the gold surface there is a thin intermediate nickel layer which prevents diffusion of copper into the gold.

After passing coaxial ceramic feedthroughs, the signal is fed into high quality movable cables outside the vacuum tank. Here the signal will be amplified by cryogenic low-noise preamplifiers at a temperature of 80 K. Between these cables and the final eight-fold combiner, switches are mounted which add a proper delay to the radioactive beam signal, if needed.

JERK FREE MOVEMENT PROFILES

For the linear drives a maximum movable path of 60 mm is foreseen. The fastest movement occurs when the device is driven in order to admit a fresh injection of secondary radioactive beams. In this case a distance of $S = 60$ mm must be covered within a time interval $T = 200$ ms.

Such movements have a typical path scale S, a typical time scale T, a typical velocity scale $V = S/T$, and a typical acceleration scale $A = S/T^2$. The velocity vanishes at the beginning and at the end of the movement. One can easily see that such a movement requires at least an acceleration of $4A$. To avoid excitation of mechanical resonances

inside the structure the acceleration profile $a(t)$ should be as smooth as possible, because the mechanical excitations are expected to be caused by the Fourier components $a(\omega)$ of the acceleration profile at the mechanical resonances ω. For such jerk-free profiles one requires in addition that the acceleration must vanish in the beginning and at the end of the motion, as well. A well-known example of such a profile is the fifth order polynomial

$$s(t) = S\left[\frac{1}{2} + \frac{1}{16}\left(15\tau - 10\tau^3 + 3\tau^5\right)\right] \qquad (3)$$

with the normalized time variable

$$\tau = \frac{2t}{T} - 1, \;\; -1 \le \tau \le 1 \qquad (4)$$

Several movement profiles were investigated theoretically. As long as the resonances are unknown, the following criteria can be useful for optimized profiles:

1. The accelerating 'energy' $E_{\mathrm{acc}} = \int |a(t)|^2 dt$ of the movement should be minimized. By Parseval's theorem, this quantity can be expressed by the Fourier transform $a(\omega)$, as well: $E_{\mathrm{acc}} = (2\pi)^{-1} \int |a(\omega)|^2 dt$.

2. The maximum acceleration $a_{\max}$ should be minimized.

3. The excitation frequency $a(\omega)$ should decay rapidly towards high frequency.

It turned out that harmonic profiles of the form

$$s(t) = S\left[\frac{1}{2} + \frac{1}{2}\tau + \sum_{n=0}^{N} b_n \sin\left((2n+1)\pi\tau\right)\right] \qquad (5)$$

$$a(t) = -4A\pi^2 \sum_{n=0}^{N} b_n \left(2n+1\right)^2 \sin\left((2n+1)\pi\tau\right) \qquad (6)$$

have very convenient properties. Their acceleration spectrum decreases much faster at high harmonics than profiles using polynomial approaches, such as the 5th order polynomial. Their 'energy' E_{acc} values as well as their minimum accelerations are also rather small.

The Fourier transform of the acceleration profile must be calculated using the condition that it vanishes outside the time interval $\tau \in \{-1, +1\}$. This is taken into account by multiplication with a function $p_1(\tau)$ which is equal to one in this interval and vanishes outside:

$$\begin{aligned} & \mathcal{F}\left\{\sin((2n+1)\pi\tau)\, p_1(\tau)\right\} \qquad (7) \\ = \;& \int_{-1}^{1} \sin\left((2n+1)\pi\tau\right) e^{-i\omega\tau} d\tau \\ = \;& \frac{1}{i}\left[\frac{\sin\left((2n+1)\pi - \omega\right)}{(2n+1)\pi - \omega} - \frac{\sin\left((2n+1)\pi + \omega\right)}{(2n+1)\pi + \omega}\right] \\ = \;& \frac{\sin\omega}{i} \frac{2(2n+1)\pi}{\left((2n+1)\pi\right)^2 - \omega^2} \end{aligned}$$

These spectra decrease proportionally to ω^{-2} for large frequencies, therefore the spectral energy of the acceleration is well concentrated around frequencies $f = \omega/2\pi = 1/T$. In contrast the spectra of polynomial-type profiles decay proportionally to ω^{-1} only. This can be derived from the recursion relations ($\omega \neq 0$)

$$\begin{aligned} & \mathcal{F}\left\{\tau^n p_1(t)\right\} = \int_{-1}^{1} \tau^n e^{-i\omega\tau} d\tau \qquad (8) \\ = \;& \frac{-1}{i\omega} \tau^n e^{-i\omega\tau}\Big|_{-1}^{1} + \frac{n}{i\omega} \int_{-1}^{1} \tau^{n-1} e^{-i\omega\tau} d\tau \\ = \;& \begin{cases} \frac{2\sin\omega}{\omega} + \frac{n}{i\omega}\mathcal{F}\left\{\tau^{n-1} p_1(t)\right\} & n \text{ even} \\ \frac{2i\cos\omega}{\omega} + \frac{n}{i\omega}\mathcal{F}\left\{\tau^{n-1} p_1(t)\right\} & n \text{ odd} \end{cases} \end{aligned}$$

Table 5: Harmonic Coefficients

	b_0	b_1
sinusoidal profile ($N = 0$)	0.15915	-
$N = 1$, minimum $a_{\max}$	0.14957	0.003195
$N = 1$, minimum E_{acc}	0.14324	0.005305

Table 5 shows the coefficients of a purely sinusoidal profile, and of two profiles with a higher harmonic, namely the one with minimized maximum acceleration, and the one with minimum 'energy'. It is obvious that one gets a substantialy lower maximum acceleration and also a lower 'energy' by adding a small third harmonic to the path profile.

Table 6: Maximum Velocity, Acceleration and Energy of Harmonic Profiles

	$\frac{v_{\max}}{V}$	$\frac{a_{\max}}{A}$	$\frac{E_{\mathrm{acc}}}{A^2 T}$
sinusoidal profile ($N = 0$)	2.00	6.28	19.74
$N = 1$,minimum $a_{\max}$	2.00	5.13	18.08
$N = 1$, minimum E_{acc}	2.00	5.32	17.77

LINEAR MOTOR DRIVES

The linear drives (see fig. 3) use a Bobolowski DTL 85/205 motor. The primary and secondary parts of this motor are not coupled mechanically. The absence of friction inside the linear motor promises to be a good condition for long lifetime. The motor can deliver a maximum force of 280 N along a maximum length of 85 mm. Compression springs help accelerating the movable parts when the device is to be moved outside.

Different forces act on the drive:

- inertial forces due to the acceleration of the 25 kg support structure with rod and aluminum body,

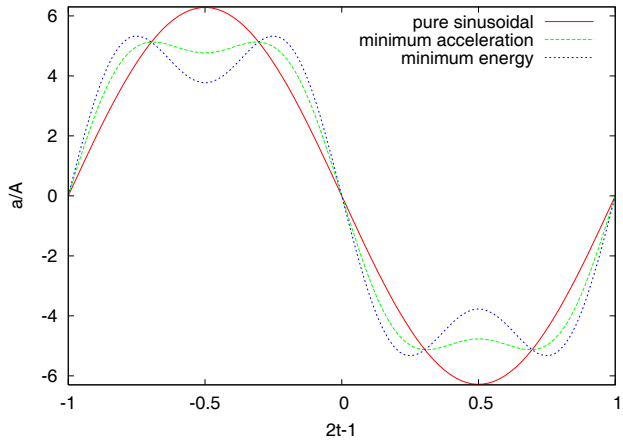

Figure 2: Harmonic acceleration profiles.

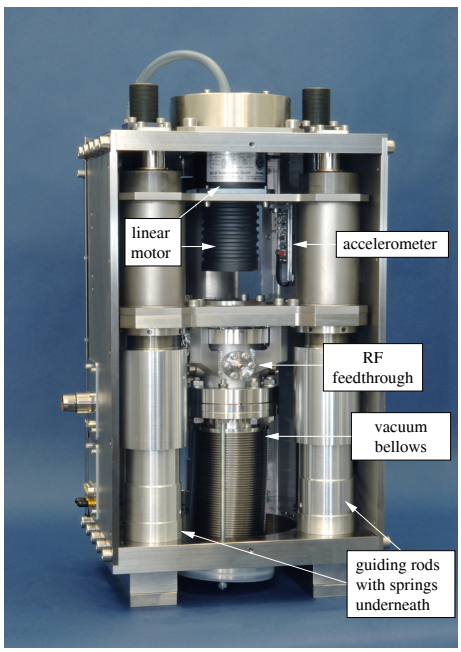

Figure 3: Linear drive before installation.

- the vacuum pressure of about 420 N,
- the force of the compression springs (about 100N),
- spring-like forces of the vacuum bellows,
- friction forces,
- gravitational forces in case of vertical mounting.

The springs are dimensioned such that they move the device to an outer stand-by position in case of a motor failure. The motor can keep the electrodes close to the beam (e.g. 10 mm) at the end of a cooling cycle. The fast outward directed movement is performed by the motor with effective assistance from the compression springs.

Each linear motor is controlled by a motor controller. The currents delivered to the motor depend on digital settings of the PI control parameters. If these are set correctly, a smooth motion of the motor can be established. The device is equipped with an optical position measurement system informing the controller at a rate of about 20 ks with a precision of less than ten μm. The controllers of the 8 different drives are synchronized via an ethercat bus system.

Figure 3 shows a photograph of the motor drive unit. The springs are mounted on each of three guiding rods providing the alignment of the primary and secondary parts of the motor. In order to detect unwanted vibrations an accelerometer is installed, which is sensitive in all three space directions. Its signals can interlock the motor controller as soon as their amplitude exceeds a predefined threshold.

MECHANICAL TANK DESIGN

The prototype vacuum tank has a length of 2.2 m and an inner diameter of 450 mm. A photography is shown in Fig. 4. The tank has four flanges for the linear drives on each side. There are two large flanges for Helium cold heads. In order to mount equipment inside, the tank has eight large flanges on each side, which are opened only for assembly or disassembly of electrodes, cables etc.

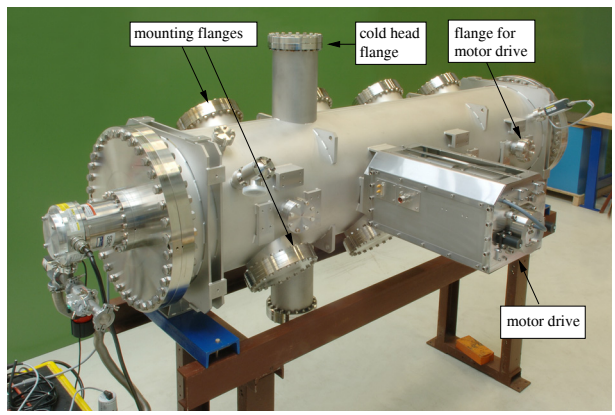

Figure 4: Tank prototype.

The vacuum vessel was delivered by end of 2008, two linear drives were installed by spring 2009. At present we are performing various movement studies. Both drives can be run simultaneously.

REFERENCES

[1] F. Nolden et al., "Stochastic Cooling Developments at GSI", *AIP Conference Proceedings*, **821** (2005), 177-184.

[2] F. Nolden, et al., "The Collector Ring CR of the FAIR Project", MOPCH077, *Proc. EPAC'06* (2006) 208-210

[3] A. Dolinskii, F. Nolden, M. Steck, "Lattice Considerations for the Collector and the Accumulator Ring of the FAIR Project", TUA2C08, *Proc. Cool 200*), 106-109

[4] C. Peschke, U. Jandewerth, F. Nolden, P. Petri, M. Steck, "Prototype Pick-up Module for CR Stochastic Cooling at FAIR", THPMCP003, *Proc. Cool 2009* (2009)

TWENTY-FIVE YEARS OF STOCHASTIC COOLING EXPERIENCE AT FERMILAB*

Ralph J. Pasquinelli#, Fermilab, Batavia, IL 60510, U.S.A.

Abstract

In the early 1980s, it was decided that Fermilab would build a proton antiproton collider to search for the top quark following the success at CERN with the discovery of the W and Z bosons in the SPS pbar p collider. The effort was designated the Tevatron I project. Design of the antiproton source began in earnest in 1981 with a construction start in 1983. The Tevatron started fixed target operations that same year. The first antiprotons were delivered to the Tevatron in October of 1985 and first collisions were observed in the CDF detector. The Antiproton Source consists of two 8 GeV kinetic energy accelerators, the Debuncher and Accumulator. The Debuncher ring performs bunch rotation and pre-cooling, the Accumulator ring utilizes stochastic cooling for antiproton collection. The addition of the Recycler ring (also 8 GeV) in 2003 as a depository for antiprotons changed the scope of cooling in the Accumulator. This paper will present the chronology of the cooling systems development from those early days to the current record setting performance.

DEBUNCHER COOLING SYSTEMS

The original design of the stochastic cooling systems in the Debuncher included only transverse cooling operating from 2-4 GHz.[1, 2] Incoming flux was predicted to be $3x10^7$ pbars per second, but was significantly lower due to insufficient protons on target. Bunch rotation and longitudinal cooling takes the incoming 4.25% momentum spread and reduces it to 0.037%. The acceptance of the Debuncher was designed at 20π mm-mrad in both planes and has been improved with lattice modifications and careful placement of aperture restricting devices to 35π. The horizontal and vertical cooling reduces the beam to under 2π mm-mrad. With the expected flux, it was clear from the outset that front-end effective noise temperature of the stochastic cooling systems would need to be significantly below tunnel temperature of 311^OK. The original Debuncher stochastic cooling systems employed liquid nitrogen to cool the pickups and amplifiers to 80^OK. Total front-end effective noise temperatures were of the order of 120^O K.

A significant upgrade to the cooling system was begun in 1996 and completed in 1998 with increased bandwidth to 4-8 GHz. [3] The octave band is split into eight 500 MHz wide bands for the pickups then combined to four 1 GHz bands for the kickers utilizing slotted waveguide structures. [4] This decision was based on minimizing the number of cold to warm transitions on the cryogenic pickups, and the need for more kicker drive ports. The slotted waveguide structure bandwidth is dependent on the length of the array, facilitating this requirement. Liquid helium cooled pickups, amplifiers, and components [5] are responsible for a front-end effective noise temperature ranging from 10^OK to 30^OK. [6] This four to ten fold decrease in effective noise temperature dramatically improved cooling performance. With an enhanced S/N ratio, it was now possible to make beam transfer function measurements with pbars. Prior to this upgrade, the only way transfer functions could be measured was to reverse magnet polarity and inject forward protons, a cumbersome effort taking two to three days to complete.

Momentum cooling was realized by using the same pickups and kickers simultaneously in sum and difference mode. Unlike the accumulator, where high dispersion straights are available for utilizing Palmer cooling, notch filter cooling was implemented for momentum cooling. The first notch filter consisted of four independent Bulk Acoustic Wave (BAW) delays. Momentum spread now became sufficiently narrow that small drifts in notch filter frequency between the four systems became problematic limiting the asymptotic momentum spread. A solution was to combine all four bands of momentum cooling into one trunk, then passing through an octave wide optical notch filter, splitting back into separate bands, effectively eliminating notch frequency drift between bands. The Debuncher Momentum system has been upgraded to a single/double turn optical notch filter. After the first second of the cooling cycle, a single turn delay is switched to a double turn increasing the gain near the central momentum. The resulting momentum spread being 3.26 MeV/c (0.037%). An automated tuning program is run periodically to adjust the filter to the correct revolution frequency, typically only a few picoseconds of adjustment.

Because the tune of the Debuncher is close to the three quarter integer, it is possible to improve system signal to noise in the transverse cooling with the addition of two turn delay notch filters. These filters suppress any common mode signal from the pickup and notch thermal noise between bands where no Schottky signal exists, all while providing balanced gain and phase to the desired transverse Schottky signal.

The upgrade consists of eight each cryogenically cooled pickup tanks and water-cooled kicker tanks. Sixty-four 200 Watt traveling wave tube amplifiers (TWT) running at the 1 dB compression point drive the kicker tanks.

*Work supported by the Fermi Research Alliance, under contract DE-AC02-76CH03000 with the U.S. Dept. of Energy.

#pasquin@fnal.gov

ACCUMULATOR COOLING SYSTEMS

The Accumulator cooling consists of the Stacktail [7, 8] and core cooling systems. [9] The original Stacktail system operated from 1-2 GHz and core systems operated from 2-4 GHz. Stacktail horizontal and vertical transverse systems were also part of the original design operating from 1-2 GHz. The pickups for the Stacktail betatron system were the same as the momentum system by taking the difference signal from the medium energy pickup plates for vertical and edge coupling for horizontal. Pickups for the Stacktail are located in high dispersion and momentum cooling uses the Palmer method of energy dependent pickup response. Due to the high momentum spread of the beam in the Stacktail, the Stacktail betatron system had difficulty resolving betatron motion from momentum spread. This coupled with the nonlinear distribution of beam in the stack made the betatron system more of a momentum cooling system. It was never very effective for stacking and was abandoned when the Stacktail was upgraded to 2-4 GHz in 1999. [10]

Core cooling consists of two transverse and two momentum cooling systems. The original 2-4 GHz momentum system was augmented with the addition of a 4-8 GHz core momentum system in 1989. Pickup to kicker delay for this momentum system is half the revolution period. The gain slope and dispersive effects of this length of coaxial cable were detrimental to system bandwidth. An equalizer was designed to relieve some of this effect, but the required 40 dB gain slope compensation also negatively affected system signal to noise. In 2006, this system was upgraded to optical fiber transmission between pickup and kicker, which eliminated gain slope and dispersion. This is the only cooling system that has sufficient beam transition time between pickup and kicker that would allow for the slow propagation velocity of fiber (67% velocity of light). The 4-8 GHz momentum system is now being upgraded by the addition of two new planar loop kicker arrays.

When the Stacktail was upgraded to 2-4 GHz, the core transverse cooling was also upgraded to 4-8 GHz. The initial 4-8 GHz upgrade utilized planar loops in one octave band. Gain slope and phase dispersion due to cable delays across the ring reduced system performance. As an R&D project for signal transmission in the Recycler, a free space optical link was installed between pickups and kickers in the Accumulator. [11] This proved successful and eliminated the need for equalizers. With the recent success of slotted waveguide arrays in the Debuncher, it was decided in 2000 to upgrade core transverse cooling to the higher sensitivity of slotted waveguides and transverse cooling became six separate cooling systems in three bands covering the frequency span. These narrower bands did not have the gain slope or dispersion extremes of the full octave and the optical free space link could be decommissioned. Core transverse heating from the Stacktail kicker power was a considerable problem with the 1-2 GHz system and was overcome by taking four of the kickers and adding transverse feedback to combat the heating. Transverse kickers were also included in the 2-4 GHz Stacktail upgrade, but proved un-necessary in operations due to Stacktail kicker centering (eight short vacuum vessels as opposed to three long tanks from the original system) and improved transverse core cooling.

The accumulator exhibits saturation effects as the stack size approaches an excess of $1x10^{12}$ antiprotons. This was mitigated by increasing the stacking cycle time and reducing Stacktail power resulting in a commensurate decrease in stacking rate. Cores of that size exceed a system dynamic range of 60 dB and notch filters lose their effectiveness. With the addition of the Recycler, stacks rarely exceed $4x10^{11}$ and the stacking rate is maximized. The Stacktail system continues to be the most complicated of all cooling systems and has taken considerable effort to optimize.[12]

RECYCLER COOLING

At the outset of Recycler commissioning, only stochastic cooling was available. [13] Due to the lattice of the synchrotron and a low revolution frequency, the cooling frequency bands are limited to avoid Schottky signal band overlap. The Recycler has the original four cooling systems: two longitudinal systems covering 0.5-1 GHz and 1-2 GHz plus two transverse systems H&V 2-4 GHz.

The Recycler is seven times the circumference of the Accumulator and required a transmission scheme other than optical fiber (propagation too slow) or coaxial cable (insertion loss to large) to connect the pickups to the kickers. Two choices were pursued: an over-moded circular waveguide transmission line or free space laser link.

AT&T developed the over-moded waveguide years before optical fiber systems were practical. Low loss at a very high carrier frequency (60-80 GHz) and several GHz wide bandwidths were obtainable. A proof of principle was the signal collection for the VLA radio telescope in Socorro New Mexico. [14] Some two kilometers of "spare" waveguide was made available to FNAL from NRAO for the Recycler link, but after twenty years of outside storage, inspection showed only 10 percent of the waveguide was not corroded. The fabrication of new waveguide was financially impractical.

With the success of the Accumulator free space link, it was decided this was the best scheme to span the 550-meter chord between pickups and kickers. With the use of expanding lenses and telescopes, three links were built in temperature controlled environments and the laser beam transmitted in an evacuated 24 inch diameter pipe buried between pickup and kicker. One of the laser links has the 0.5-1 GHz longitudinal and the 2-4 GHz vertical system multiplexed. The lack of gain slope and phase dispersion allows for maximum cooling bandwidth. Free space optical transmission has proven to be robust and requires only periodic remote control alignment of the laser beams to compensate for mechanical/thermal laser beam drift.

PICKUPS/KICKERS

The initial electrode design for pickups and kickers consisted of a three dimensional antenna with a pocket ground plane. [15,16] These arrays proved functional for the first years of operations, but did experience several difficulties. The arrays were delicate and expensive to fabricate. Kicker overheating caused the solder connections to fail on several occasions, resulting in a loop falling into the beam aperture.

As higher frequency systems were designed, three-dimensional technology proved less sensitive at frequencies above 4 GHz. With the advent of improved computer aided microwave design tools, it was possible to develop printed circuit planar antennas. [17,18,19] The 4-8 GHz core momentum system first employed three-dimensional loops but has since been modified with planar kickers. The Stacktail system uses planer loops throughout. An added benefit with this technology is the combiner/splitter network is integrated into the same circuit board, providing an inexpensive and robust design. Planar arrays (as they became known) are fabricated in octave bands from 0.5 to 8 GHz.

When it was decided to replace the Debuncher cooling electronics in 1996, the required sensitivity of the pickups to achieve the required cooling rates left two options. The first was to use plunging planar arrays, the plunging necessary to follow beam size to maintain S/N as the beam cooled rapidly. This technique had been successfully implemented in the CERN ACOL ring.[20] Mechanical requirements of a moving pickup at cryogenic temperatures did not appeal to the FNAL design team. With octave bandwidths still required, it was decided that the frequency response could be met with multiple narrower bands. The innovation of slotted waveguide arrays was chosen for the upgrade. Bandwidths of in excess of 500 MHz were attainable with sensitivities an order of magnitude greater than previously used methods. No moving parts allowed for easier cryogenic cooling to $4^{O}K$. These same slotted structures are used for the kickers. In the Debuncher, two 200-Watt TWTs are used to drive each array one each transversely and longitudinally. The absorptive loads in the waveguide were brazed to water cooled heat sinks and cooled with $13^{O}C$ water to minimize any out gassing due to heating.

Slotted waveguide technology was utilized in the Accumulator core 4-8 GHz transverse cooling systems in 2002. These waveguide pickups were also employed in 2003 for 1.7 GHz Schottky systems in both the Recycler and Tevatron and four 4.8 GHz Schottky systems in the CERN LHC in 2005. [21,22,23]

ELECTRONICS

The electronics for stochastic cooling are required to gain/phase shape signals, provide amplification, and precisely control timing delays between pickups and kickers. Front-end signal to noise is critical with the only free parameter (once bandwidth has been chosen) being the effective noise temperature. Commercially available low noise amplifiers did not meet the necessary effective noise temperature requirements in 1983 and LBL was commissioned to work on cryogenically cooled front end amplifiers and components.[24] These amplifiers operated from 1-4 GHz in two separate octave bands. Due to the nature of limited electron mobility in silicon at cryogenic temperatures, physically separate bias networks were required. By the time of the Debuncher cooling upgrade, commercially available cryogenic amplifiers with effective noise temperatures in the range of $5^{O}K$ to $25^{O}K$ in the 4-8 GHz band were purchased from Miteq Inc. During the initial testing, it was discovered that these amplifiers were not stable at all temperatures between room and liquid helium temperatures. The ensuing instability destroyed the amplifiers, requiring Fermilab to implement a redundant interlock system to ensure amplifiers were not powered during cool down or warm up. Since the interlocks were installed, no amplifiers have failed due to this unstable operating mode.

Signal processing requires taking the sum and difference of both pickup and kicker signals. Commercial hybrids perform admirably, but did not provide adequate common mode rejection performance. A Fermilab patented hybrid [25] has been included in many cooling applications with excellent difference mode performance and power handling capabilities.

After the first few years of operations, it became clear that system equalization could improve cooling performance at very low cost. Today, most systems have a custom equalizer designed in-house and fabricated at local circuit board vendors.[26,27]

The Antiproton Source tunnel is quite warm and power dissipation in electronics became a subtle problem. Driver amplifiers heat sunk to ambient temperatures would endure a graceful decline in gain over a period of years. A simple fix was chilled water-cooling of all such amplifiers. Once implemented, stable gains have resulted in worry free operation.

Power amplifiers are the most expensive electronic part of a cooling system. The cost per watt can be as high as several hundred dollars. Fermilab has one of the largest installations of TWT amplifiers at 112 with a total power capacity of 22.4 kilowatts. The critical timing required for stochastic cooling necessitates having the TWTs located very close to the kickers to minimize insertion loss and transmission delay. The TWT power supply is the weakest link in reliable operations. All supplies are located in service buildings as far as 100 meters from the TWT. The added cable capacitance and regulation requirements required tight tolerance on the power supply design. Ready access is required to facilitate supply replacement.

NOTCH FILTERS

Fermilab has pioneered a variety of technologies for the fabrication of recursive notch filters required for Stochastic Cooling. The original design for the Stacktail system was based on superconducting delay lines. [28,29]

The availability of coaxial cables made from superconducting material was very limited. The first cable used consisted of a niobium center conductor and a lead outer conductor. The 83-meter length available was not commensurate with the delay required for the accumulator filter, but was adequate for initial testing. In collaboration with KEK, negotiations with Furukawa industries of Japan produced required quantities of 1.6 mm diameter lead plated copper coax. At the outset of development, it was known that intermodulation distortion from the TWT power amplifiers would be detrimental to cooling. A significant effort was directed to passing power through the superconducting cable in an effort to put the notch filter after the power source, mitigating the intermods. The maximum achievable power transfer was twenty-five watts before inducing a quench. Forty watts minimum was required, so this approach was abandoned. Superconducting notch filters have the best performance of all filter technologies. Due to low insertion loss and wide bandwidth, these notch filters produce the deepest notches with the maximum dynamic range and low dispersion due to lack of skin effects. The operational costs of the liquid helium plant is the only draw back.

A subsequent notch filter technology was the use of BAW delay lines, [30] a technology developed for radar applications after World War II. The BAW consists of a quartz or sapphire crystal with surface printed antenna to transform electrical energy to acoustic waves in the crystal. The slower propagation velocity of acoustic waves yields a delay on the order of one microsecond per centimeter of crystal. Sapphire is the preferred material due to its lower temperature coefficient. The impedance match to the crystal has a very high voltage standing wave ratio (VSWR) as is typical with all piezo electric materials, hence the manufacturer supplied the delay line with circulators and an equalizer. BAW notch filters are realized with a passive circuit requiring only temperature stability of the oven that housed the device. Operating costs are significantly below that of superconducting filters, but have the limitation of a high insertion loss (40-60 dB) and a limited dynamic range of 30-50 dB set by signal to noise ratio. BAW filters are best suited to frequencies below 6 GHz and delays less than a few microseconds.

The last notch filter technology implemented was the use of fiber optic delays. [31] With the expansion in telecommunications hardware, wide band fiber optic links became commercially available as a viable means of creating longer delays than achievable with either coax or BAW techniques. This was particularly necessary for notch filters in the Recycler, where delays approached 12 microseconds. Fiber optic links operate in the communication wavelengths of 1330 and 1550 nanometers. The first optical notch filters were fabricated for the Debuncher cooling systems. [32] Optical links have bandwidths exceeding the cooling system requirements, but the higher the bandwidth utilized, a reduced dynamic range is incurred. For filters with octave bandwidths between 1-8 GHz, dynamic range is limited to approximately 40 dB or less. Optical links have both an active laser transmitter and photo diode receiver. For applications requiring location in the tunnel due to beam time of flight requirements, radiation shielding is a prudent precaution for extending link life.

Fourteen notch filters are now in use: one Debuncher momentum (optical), eight Debuncher transverse (four BAW, four optical), three Stacktail (two BAW, one superconducting), two Recycler (both optical).

PBAR ACCUMULATION PERFORMANCE

The original accumulation specifications were for a stack size of 4.3×10^{11} pbars and a stack rate of 1×10^{11} per hour. [33] This lofty goal for stack rate was not achieved until August 2001. Most recent records are a maximum stack size of 3.13×10^{12} in February 2008 and stacking rate of 2.85×10^{11} per hour in December 2008. Run II operations routinely have stack sizes less than 4×10^{11} at stacking rates exceeding 2.5×10^{11} per hour with transfers to the Recycler every hour. [34] Current plans are to continue the collider experiments through 2010 and perhaps 2011 depending on operations at CERN with the LHC.

ACKNOWLEDGEMENTS

Work on stochastic cooling at Fermilab began in 1981 and has been operational since 1985. From the collaborators at LBL and Argonne in the early days, to the Accelerator Division, Technical Division, and Particle Physics Divisions at Fermilab, hundreds have contributed to building and maintaining the twenty-five Stochastic Cooling systems now in operation. Our colleagues at CERN AA and ACOL have been a source of information, support, and inspiration. It is a tribute to this team that this Nobel technique of Simon van der Meer has supported high-energy physics research at Fermilab for the last 24 years.

REFERENCES

[1] R. Shafer, "The Fermilab Antiproton Debuncher Betatron Cooling System", Proceedings of the 12th International Conference on High Energy Accelerators, August 11-16, 1983, pages 581-583, Fermilab.

[2] D. Peterson, W. Kells, J. Marriner, G. Mayer, S. Mtingwa, R. Pasquinelli, R. Shafer, "Measurement and Performance of the Fermilab Antiproton Source Debuncher Betatron Stochastic Cooling System", IEEE Transactions on Nuclear Science, 87CH2387-9, No. 4, March 1987, pages 1728-1730. Washington D.C.

[3] J. Marriner, "Debuncher Stochastic Cooling Upgrade for Run II and Beyond", Pbar note 573, http://www-bdnew.fnal.gov/pbar/documents/pbarnotes/pbar_notes_501-600.htm.

[4] D. McGinnis, "Slotted Waveguide Slow Wave Stochastic Cooling Arrays", paper TUP100, IEEE Transactions on Nuclear Science, 0-7803-5573-3/99, March 1999, pages 1713-1715. New York.

[5] D. McGinnis, "The 4-8 GHz Stochastic Cooling Upgrade for the Fermilab Debuncher", paper MODL5, IEEE Transactions on Nuclear Science, 0-7803-5573-3/99, March 1999, pages 59-61. New York.
[6] R. J. Pasquinelli, "Noise Performance of the Debuncher Stochastic Cooling Systems", Pbar note 661, http://www-bdnew.fnal.gov/pbar/documents/pbarnotes/pbar_notes_601-700.htm.
[7] R. J. Pasquinelli, et al, "Stacktail Momentum Cooling in the Fermilab Antiproton Source", IEEE Transactions on Nuclear Science, 87CH2387-9, No. 4, March 1987, pages 1132-1134. Washington D.C.
[8] J. Marriner, "The Fermilab Antiproton Stacktail System", Proceedings of the 12th International Conference on High Energy Accelerators, August 11-16, 1983, pages 579-580, Fermilab.
[9] W. Kells, et al, "Performance of Tevatron I Core Stochastic Cooling Systems", IEEE Transactions on Nuclear Science, 87CH2387-9, No. 4, March 1987, pages 1090-1092. Washington D.C.
[10] R.J. Pasquinelli, D. McGinnis, "Performance of the Upgraded Stacktail Momentum Cooling System in the Fermilab Antiproton Source", IEEE Transactions on Nuclear Science, 0-7803-1203-1/93, May 1993, pages 2361-2363. Washington D.C.
[11] R.J. Pasquinelli, "Wide Band Free Space Transmission Link Utilizing a Modulated Infrared Laser", paper TUA12, 1999 PAC IEEE Nuclear Science, April 1999, New York.
[12] V. Lebedev, "Operation and Upgrade of Stacktail Cooling System", COOL09 this workshop.
[13] Broemmelsiek, R.J. Pasquinelli, "Fermilab Recycler Stochastic Cooling Commissioning and Performance", paper FPAB070, IEEE Transactions on Nuclear Science, 0-7803-7739-9, May 2003, pages 3431-3433. Portland.
[14] S. Weinreb, et al, "Waveguide System for a Very Large Antenna Array", Microwave Journal March 1977
[15] D. A. Goldberg, G. R. Lambertson, F. Voelker, Loren Sharlz, "Measurement of Frequency Response of LBL Stochastic Cooling Arrays for TeV-I Storage Rings", IEEE Transactions on Nuclear Science, 0018-9499/85, March 1985, pages 2168-2170. Vancouver BC
[16] J.K. Johnson, Ross Nemetz, "Power Combiners for Loop Pickup and Kicker Arrays for FNAL Stochastic Cooling Rings", IEEE Transactions on Nuclear Science, 0018-9499/85, May 1985, pages 2171-2173. Vancouver BC.
[17] J. Petter, D. McGinnis, J. Marriner, "Novel Stochastic Cooling Pickups/Kickers", IEEE Transactions on Nuclear Science, CH2669-0/89, March 1989, pages 636-638. Chicago.
[18] D. McGinnis, J. Petter, J. Marriner, J. Misek, S. Y. Hsueh, "Frequency Response of 4-8 GHz Stochastic Cooling Electrodes", IEEE Transactions on Nuclear Science, CH2669-0/89, March 1989, pages 639-641. Chicago.
[19] J. Petter, D. McGinnis, J. Marriner, J. Misek, "New 4-8 GHz Core Cooling Pickups and Kickers for the Fermilab Accumulator", IEEE Transactions on Nuclear Science, CH2669-0/89, March 1989, pages 648-650. Chicago.
[20] B. Autin et al, "ACOL Stochastic Cooling Systems", IEEE Transactions on Nuclear Science, 87CH2387-9, No. 4, March 1987, pages 1549-1551. Washington D.C.
[21] R. J. Pasquinelli, "A 1.7 GHz Waveguide Schottky Detector System", 2003 PAC Proceedings IEEE Nuclear Science, June 2003, Portland.
[22] A. Jansson et al, "Experience with the 1.7 GHz Schottky Pickups in the Tevatron", Paper THPLT135, EPAC 2004, Lucerne Switzerland.
[23] F. Caspers et al, "The 4.8 GHz LHC Schottky Pick-up System", Paper FRPM068, Proceedings of PAC07, IEEE transactions on Nuclear Science, Albuquerque, NM.
[24] C.C. Lo, "Stochastic Beam Cooling Amplifier System Front End Components Performance Characteristics", IEEE Transactions on Nuclear Science, 0018-9499/85, May 1985, pages 2174-2176. Vancouver BC.
[25] J. Petter, "Planar Slot Coupled Microwave Hybrids", U.S. Patent #5,075,647. December 1991.
[26] D. McGinnis, J. Marriner, "Design of 4-8 GHz Stochastic Cooling Equalizers for the Fermilab Accumulator", IEEE Transactions on Nuclear Science, 0-7803-0135/91, May 1991, pages 1392-1394. San Francisco.
[27] D. Sun et al, "New Equalizers for Antiproton Stochastic Cooling at Fermilab", paper THAP16, COOL 07, Bad Kreuznach, Germany.
[28] M. Kuchnir, et al, "Superconducting Delay Line for Stochastic Cooling Filters", IEEE Transactions on Nuclear Science, Vol. NS-30, No. 4, March 1983, pages 3360-3362.
[29] R. J. Pasquinelli, "Superconducting Notch Filters for the Fermilab Antiproton Source", Proceedings of the 12th International Conference on High Energy Accelerators, August 11-16, 1983, pages 584-586, Fermilab.
[30] R.J. Pasquinelli, "Bulk Acoustic Wave (BAW) Devices for Stochastic Cooling Notch Filters", IEEE Transactions on Nuclear Science, 0-7803-0135/91, May 1991, pages 1395-1397. San Francisco.
[31] R. J. Pasquinelli, "Electro Optical Technology Applied to Accelerator Beam Measurement and Control", IEEE Transactions on Nuclear Science, 0-7803-1203-1/93, May 1993, pages 2081-2085, Washington D.C.
[32] R. J. Pasquinelli et al, "Optical Correlator Notch Filters for Fermilab Debuncher Betatron Stochastic Cooling", IEEE Transactions on Nuclear Science, CH2669-0/89, March 1989, pages 696-698, Chicago.
[33] Design Report Tevatron 1 Project, September 1983, section 1-1.
[34] R.J. Pasquinelli et al, Progress in Antiproton Production at the Fermilab Tevatron Collider, Paper TU6PFP75, Proceedings of the PAC 2009, Vancouver BC.

NUMERICAL DESIGN STUDY OF STOCHASTIC STACKING OF 3 GEV ANTI-PROTON BEAM IN THE RESR FOR THE FAIR PROJECT

T. Katayama, O. Dolinskyy, B. Franzke, S. Litvinov, F. Nolden, M. Steck, GSI, Germany
D. Moehl, L. Thorndahl, CERN, Switzerland

Abstract

The accumulation of anti-proton beam up to the 1e11 particles with high density in longitudinal phase space is planned at the FAIR project. Following the experiences at CERN and FNAL, the accumulation with stochastic stacking method will be employed at the accumulator ring RESR. In the present paper, firstly the characteristics of incoming anti-proton beams are given as well as the basic design parameters obtained from the analytical method. Then the stochastic stacking process is numerically investigated with use of Fokker-Planck approach. The key elements for the stacking process are explained and then some results of simulation of stacking are described.

INTRODUCTION

At the FAIR project, the sequence of anti-proton production, cooling and stacking is as follows. Proton beam is accelerated at the SIS100 up to 29 GeV with the intensity of 2e13 per 10 sec. After passing through the production target of nickel, the anti-proton flux of 4e8 is produced within the transverse emittance of 240 π mm.mrad and the momentum spread of +/- 3% (uniform). The bunch length from the SIS100 is +/- 25 n sec. Thus produced anti-proton beam is injected into the Collector Ring (CR) with the circumference of 216.25 m and the ring slipping factor of 0.0107. In the CR the injected bunch is rotated to reduce the momentum spread from +/- 3 % (uniform) to 2.45e-3 (rms) with use of harmonic=1 RF of 100 kV. Subsequently the stochastic cooling is applied to further reduce the momentum spread to 5.0e-4 (rms) with the notch filter cooling system of band width 1-2 GHz and the microwave power 1.2 kW. The transverse cooling system is also envisaged to reduce the emittance from 240 π mm.mrad to 5 π mm.mrad.

The stacking ring, RESR, has a little bit larger circumference 239.9 m comparing with that of CR, and the ring slipping factor is adjustable from 0.03 to 0.11. The stochastic stacking system is in principle similar to those at CERN AAC and FNAL AS. The anti-proton beam is injected on the injection orbit of the RESR, and is accelerated to the deposit orbit which aparts from the injection orbit by around Δp/p=1.0 %. There prepared a stochastic stacking system, being composed of radial aligned two tails and core cooling system.

The goal of the RESR stacking system is to stack the 1e11 particles in the core region with the deposited particle number 1e8 from the CR Ring. While the cycle time is planned at 10 sec at the 1st phase of the project, it will be shortened to 5 sec at the goal. Then all the stacking system have to be designed to accommodate this final goal.

SIMPLIFIED ANALYTICAL APPROACH

A simplified theoretical model of the stacking process was developed by van der Meer [1]. It is based upon the assumptions that the voltage on the kicker is exactly in phase with the particles, and the diffusion terms by electronic noise, and intra-beam scattering effects are neglected. In addition the beam feedback effects and the difficulty of achieving the designed coherent term is not taken into account. While these assumptions are not fulfilled in the real stacking system, the simplified approach could give some basic parameters of the stacking system.

The stacked beam profile and the required voltage gain/turn to attain this profile are given as

$$\Psi(E)=\Psi_1 \exp(E-E_1)/E_d]$$
$$V(E)=2\phi_0 T/\Psi_1 \exp[(E_1-E)/E_d] \quad (1)$$

where E_1 and Ψ_1 are the deposit energy and particle density. At the numerical calculation, Ψ_1 is given by $N/\Delta E_1$ where N is the deposited particle number and ΔE_1 is energy width (4 sigma) of the newly deposited batch. Ed is the characteristic energy defining the exponential profile of density and voltage gain.

$$E_d=4A\phi_0 T^2=\beta pc\Lambda\phi_0/TW^2\eta \quad (2)$$

with the particle flux which can be transported

$$\phi_0=TW^2\eta E_d/\beta pc\Lambda \quad (3)$$

where

$$A=\beta pc\Lambda/4T^3W^2\eta$$
$$\beta=v/c,\ W=Bandwidth\ (f_{min}\text{-}f_{max}),\ \Lambda=ln(f_{max}/f_{min})$$
$$T=Revolution\ period,\ \eta=1/\gamma^2-1/\gamma_t^2$$

The required total width of the stack region is given by

$$\Delta E_{stack}=E_d \ln(\Psi_2/\Psi_1) \quad (4)$$

where Ψ_2 is a particle density at the core region. Thus obtained exponential profile of density and gain

determines the minimum width for the stack region, namely the sharpest particle density. However many important effects increase the required width, and then the analytic approach is just the simple estimation while it gives the basic feeling of the stacking parameters.

The other important factor which should be taken into account for the determination of voltage gain is the minimum voltage at the deposit position. Suppose that the energy width of deposited beam σ_1 and its distribution is Gaussian. The deposited beam should be cleared off the deposited position by the next deposit time to clear up the space for the next batch. Then the minimum voltage is given as

$$V_{deposit} > 6\sigma_1 / f_0 T_{cycle} \quad (5)$$

.

In Table 1, the obtained parameters from the analytical method are tabulated for the cycle time 5 sec. The momentum spreads of deposited beam are 2.5e-4 and 5.0e-4. Following values are used in the calculation.

Beam energy E=3 GeV, N(deposited)=1e8, η=0.032, f_0=1.19e6, N(core)=1e11, $\Delta p/p$(core)=+/-2.5e-4, W=1-2 GHz.

Table 1: Parameter List from the Analytical Solution

Cycle Time	5 sec	
Deposit Δp/p (rms)	2.5e-4	5.0e-4
4 Δp/p (rms)	1.0e-3	2.0e-3
4 ΔE (rms) [eV]	3.71e6	7.42e6
Psi(1)=N_1/4ΔE [/eV]	26.9	13.45
ΔE(core) [eV]	1.86e6	1.86e6
Psi(core)=Ncore/ΔE(core) [/eV]	5.38e4	5.38e4
Psi(core)/Psi(1)	2.0e3	4.0e3
Flux [/sec]	2.0e7	2.0e7
Ed [eV]	1.9e6	1.9e6
Tail Width (ΔE) [eV]	14.4e6	15.7e6
Tail Width (Δp/p)	3.88e-3	4.23e-3
V(1) [Volt]	1.25	2.50
V(core) [Volt]	6.26e-4	6.26e-4
V(1)/V(core)	2.0e3	4.0e3
Min V(1) [Volt]	0.94	1.87

The last column shows the minimum voltage at the deposit position to clear up the space for the next batch.

From the results it is found that the required width of stacked region is around 16 MeV.

In Fig. 1 the schematic layout of tails and core system are illustrated as well as the typical calculated beam density (/eV) after 1000 stacking and the coherent term (eV/sec) in log scale. The beam is deposited in the middle of Tail1 plates, and is shifted towards the stacking area due to the coherent term, around 3e6 [eV/sec] generated by Tail1, Tail2 system. At the core center, 3 GeV energy, beam is sharply populated due to the core cooling system and the notch filter characteristics. In the following chapter, simulation parameters and main factors which determines the required coherent term, are described.

STACKING SIMULATION PARAMETERS

Considering the beam size at the deposit region, and partly from the numerically calculated results, for example the core PU positioning, the parameters for the simulation for Fokker-Planck approach are as follows.

Table 2: Simulation Parameters

	Tail1	Tail2	Core
Frequency band (GHz)	1-2	1-2	2-4
PU and Kicker Type	Loop	Loop	Loop
Positioning (MeV)	-22.9	-16.9	+/- 8.6
PU gap (mm)		20 or 30	
Number of PU units	64	64	64
PU Coupling Impedance/unit (Ohm)			
	25	25	25
Kicker gap (mm)		40	
Number of Kicker unit		16	
Kicker Impedance/unit (Ohm)		100	

Note that we define that the middle of two core plates is 0 MeV.

Key factors for the design of stacking system are as follows.

1) Construct the exponential type gain shape.

2) Optimal shape of coherent term in the concerned energy range.

3) Suppression of the Schottky noise and thermal noise as large extent as possible.

To attain the goal of these purposes, the positioning of Tail and Core PUs, the PU heights, the notch depth, the system delay and amplifier gain are adjusted.

System Structure of the Stacking System

To achieve the required coherent term, we plan to compose the system as given in Fig. 2. Two Tail systems are prepared to form the desired coherent term. Output signal from each Tail PU is pre-amplified and is followed by Delay, Notch filter and Main-Amplifier. Finally it is powered into the kicker as well as the amplified signal from the core system. The transfer function $TF(E,T_d)$ of the chain of Tail system is given as

$$TF(E, T_d) = Z_{pu}\, G_{pu}(E)\, F(T_d)\, H(E)\, G_{amp}\, G_k(E)\, Z_k \quad (6)$$

where Z_{pu}, and Z_k are the coupling impedances of pickup and kicker, G_{pu} and G_k are the geometric factors as a function of beam position or the beam energy as the PU are located at the position of large dispersion 13 m. $F(Td)$ and $H(E)$ are the function of system delay and the transfer function of notch filter.

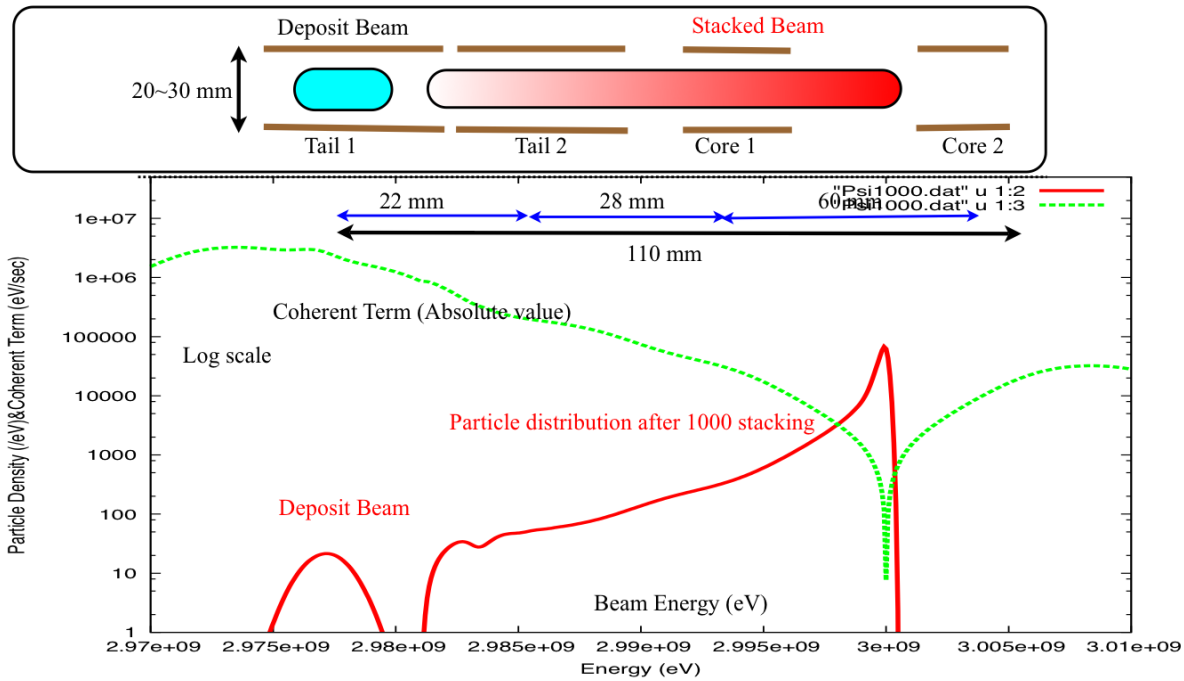

Figure 1: Schematic layout of the stochastic stacking system. The injection orbit (not illustrated in the figure) is around 1 % (Δp/p) left from the deposit position.

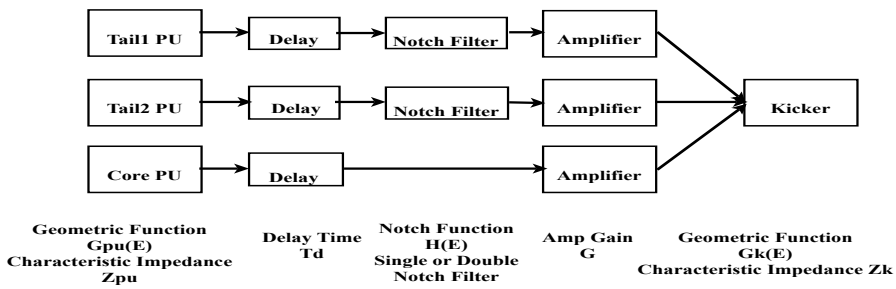

Figure 2: System structure of stacking system.

Geometric Factor

The sensitivity of each PU plate is given by

$$g(x,h,w)=2/\pi \arctan[\sinh(\pi w/2h)/\cosh(\pi x/h)] \quad (7)$$

where w is a width of plate (40 mm), h the gap height (20 or 30 mm) and x the horizontal beam position relative to the center of plate. For the large x, this sensitivity function has an asymptotic form $\exp(-x/h)$ which is required exponential shape as a function of energy E.

Notch Filter

The transfer function of correlator single notch filter with depth a is given as a function of frequency f by

$$H(f)=[1.0-a\ \exp(-j2\pi\Delta f/f_0)\ ]/(1+a) \quad (8)$$

where f_0 is a notch frequency and Δf the frequency difference from the notch frequency. The double notch filter is a series of single notch filter. The typical shapes of amplitude of single and double notch filters are illustrated in Figure 3.

The horizontal scale is a frequency, vertical scale is an amplitude. The upper curve is corresponding to the single notch and the lower line the double notch case. It is apparently shown that the double notch reduces the central part signal, the Schottky and thermal noise. But it is noted that the signal between the notch frequency and the edge frequency is also reduced, namely the required coherent signal is also reduced.

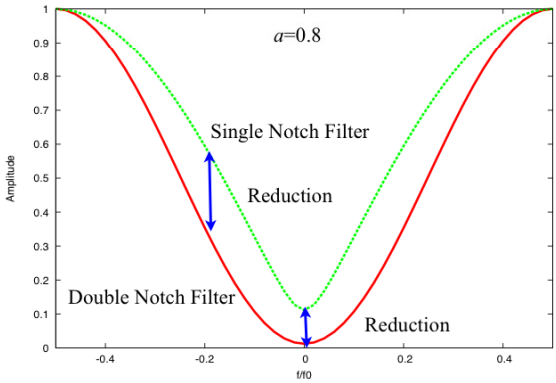

Figure 3: The amplitude shape of the single and double notch filters. Depth parameter a is 0.8.

Coherent Function

The coherent function plays a key role of the design of coherent term which is a function of ring slipping factor η, the band width W, the notch depth a, and the system delay T_d. Typical example of the calculated coherent function is given in Fig. 4 where each line corresponds to the delay time difference of 20 psec. The horizontal scale is the energy in MeV. Note that the position of Tail1 PU is -22.9 MeV and Tail2 PU is -16.6 MeV and the Core PUs are +/- 8.6 MeV. The system delay has to be chosen to give the required value of coherent function.

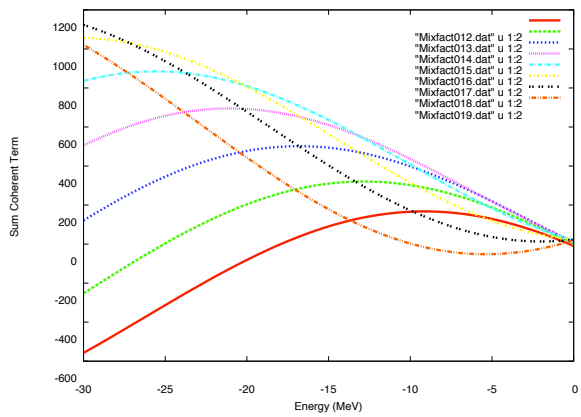

Figure 4: The coherent function as a parameter of system delay. Horizontal scale is energy in MeV. Each line corresponds to the delay time of 20 psec difference. η=0.03 and W=1-2 GHz and the notch depth=30 dB.

Coherent Term

Including the above described elements, the coherent term is calculated as a function of energy. The typical result is given in Fig. 5. The horizontal scale is beam energy and the vertical scale is absolute value of coherent term. The top curve is a sum of the coherent terms. The second line is the produced by Tail1, and the 3 rd line is due to the Tail2 and the bottom line is due to the Core system. The sharp dip at 3 GeV is mainly due to the notch filter.

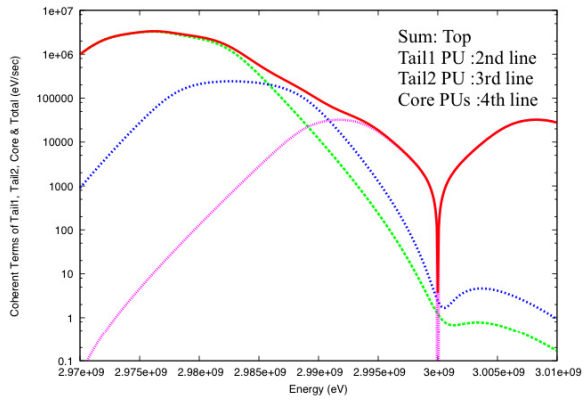

Figure 5: Typical coherent term as a function of energy.

INTRA BEAM SCATTERING EFFECTS

Main source of the diffusion of the stacked particle is an Intra-Beam Scattering, IBS effect. There were several formalism of the growth rate calculation. Among them we use the Matini formula [2] to obtain a numerical results. The lattice structure of RESR is included to calculate the growth rate at each accelerator segment and they are averaged over the ring. In the present estimation, the transverse emittance is assumed as constant of 2π mm.mrad for both the horizontal and vertical betatron freedom. At each computing cycle the rms value of Δp/p of the stacked beam is calculated which is varied around 3e-4 to 9e-4 during the stacking number up to 1000.

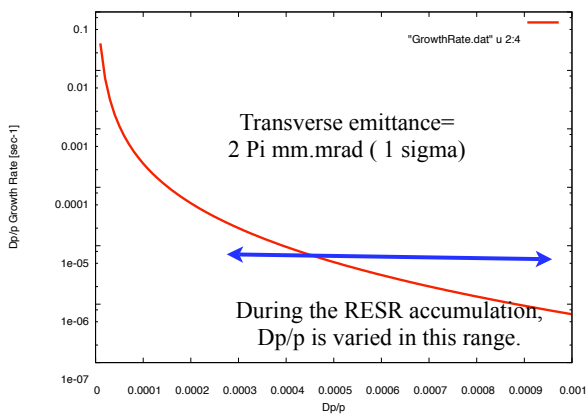

Figure 6: IBS growth rate during the stacking up to 1000 times. Transverse emittances are kept at 2 π mm.mrad.

The calculated growth rate is given in Fig. 6. The stacked particles are populated almost 90 % in the core region within Δp/p value of +/- 2.5e-4. Then in the simulation, the IBS heating term is approximated as 10 times larger than the calculated growth rate.

RESULTS OF STACKING SIMULATION

We have investigated many cases of stacking parameters including beam feedback effects and intra-beam scattering. Typical example of the stacked beam profile is given in Fig. 7.

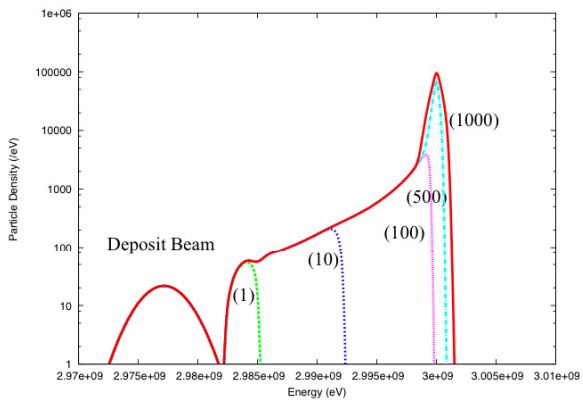

Figure 7: Beam profile during the stacking.

In the Fig. 7, the horizontal scale is the beam energy, the vertical scale is a particle density per unit energy. The figures in the bracket represent the number of stacking. Other parameters in this simulation are as follows.

Cycle time=10 sec, N(deposit)=1e8, Ring slipping factor=0.03, Deposited Beam $\Delta p/p$=5e-4 (rms), Tail1 Gain=130dB, Tail2 Gain=106dB, Core Gain=90dB, Notch Depth=20dB, IBS factor=10.0, Tail & Core Gap Height=30 mm, Tail1 Delay Time = -0.500 ns, Tail2 Delay Time = -0.320 ns, Core Delay Time = -0.167 ns

The required microwave power are calculated at 210 Watt for Tail1, 0.9 Watt for Tail2 and 0.1 Watt for Core system.

As is clear in the figure the stacked particles are populated mainly in the core region. The number of particles in the whole stacked area and the one in the window momentum spread (+/-2.5e-4) around the core center, and their ratio are given in the Figure 8. The top line is a ratio (right scale) and the 2nd and the 3rd lines show the particle number in the whole stacked region and in the window momentum spread around the core center of the energy 3.0 GeV. Almost 90 % particles are stacked in the window energy.

In the stacking simulation, we have assumed the momentum spread of the deposited beam as 2.5e-4 or 5.0e-4 (rms). The cycle time is 5 or 10 sec. In most cases the beam feedback effects do not seriously deteriorate the stacking performance except for extreme parameters when say η=0.03 and cycle time 5 sec, Nyquist plot of Tail1 can dangerously approach the unstable territory just after the deposit for the large Tail1 gain.

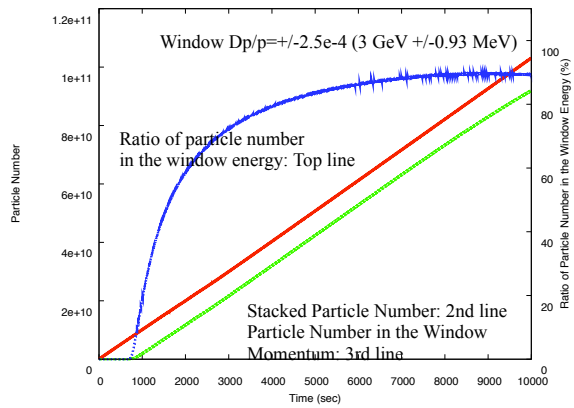

Figure 8: The stacked particle number in the whole stacked area and in the window energy at the core center.

PRE-COOLING AT RESR

The pre-cooling at the RESR injection orbit with the band system 2-4 GHz could cool the momentum spread of the beam from Collector Ring 5.0e-4 to 1.0 e-4 within 5 sec with moderate cooling system of room temperature. Thus pre-cooled beam of the momentum spread Δp/p=1e-4 (rms) can be stacked in the stacked region with Tail1 gain of 120 dB, which results in the reduction of microwave power order of magnitude smaller (Tail1: 32 Watt) than the case without pre-cooling. On the other hand the small momentum spread gives the large signal suppression via a beam feedback effect. The real and imaginary parts of Open Loop Gain reach to around +/-0.5. The careful choice of ring slipping factor and the gain of Tail1 are required.

SUMMARY AND OUTLOOK

1). We have numerically designed a stochastic stacking system of RESR with a Fokker Planck approach where IBS effects and beam feedback effects are included.

2). Two tails and a core cooling/stacking system allow us the stacking of the deposited beam, N=1e8 up to the 1000 stacking, N=1e11. The deposited momentum spread, 2.5e-4 or 5e-4 (rms), both are acceptable for the stacking of cycle time 5 sec and 10 sec.

3). Ring slipping factor, η is a key parameter of the design of the system. In the present design it is assumed as 0.03 or 0.05 which is optimal for the Tail1 system of band width 1-2 GHz.

4). Transverse cooling system for the core region is a forthcoming subject.

REFERENCES

[1] S. van der Meer, "Stochastic Stacking in the Antiproton Accumulator", CERN/PS/AA/78-22, 1978

[2] M. Martini, "Intrabeam Scattering in the ACOL-AA Machines", CERN PS/84-9, 1984

MUON COOLING R&D FOR THE MUON COLLIDER - A 5 YEAR PLAN FOR THE US *

A. D. Bross#, Fermi National Accelerator Laboratory, P.O. Box 500, Batavia, IL 60510, U.S.A.
for the US Neutrino Factory and Muon Collider Collaboration and Fermilab Muon Collider Task Force

Abstract

The Neutrino Factory and Muon Collider Collaboration and the Fermilab Muon Collider Task Force have recently submitted a proposal to the US Department of Energy Office of High Energy Physics to deliver a Design Feasibility Study for a Muon Collider after a 5 year R&D program. This paper presents a brief physics motivation for and the description of a Muon Collider facility and then discusses in some detail the technical components of the proposal with respect to the muon ionization cooling R&D needed for an Energy-Frontier, high luminosity Muon Collider.

INTRODUCTION

The physics potential of a high-energy lepton collider has captured the imagination of the high energy physics community. Understanding the mechanism behind mass generation and electroweak symmetry breaking, searching for, and perhaps discovering, supersymmetric particles and confirming their supersymmetric nature, and hunting for signs of extra space-time dimensions and quantum gravity, constitute some of the major physics goals of any new lepton collider. In addition, making precision measurements of standard model processes will open windows on physics at energy scales beyond our direct reach. Sensitivity to the unexpected is, of course, of fundamental importance. The Muon Collider (MC) provides a possible realization of a multi-TeV lepton collider, and hence a way to explore new territory beyond the reach of present colliders. A muon accelerator facility also presents the opportunity to explore new physics within in a number of programs.

A schematic that shows the evolution of a muon accelerator complex which ultimately reaches a multi-TeV Muon Collider [1] is shown schematically in Fig. 1. The front-end of the facility provides an intense muon source that can perhaps support both an energy-frontier Muon Collider and a Neutrino Factory (NF). The muon source is designed to deliver $O(10^{21})$ low energy muons per year within the acceptance of the accelerator system, and consists of (*i*) a multi-MW proton source delivering a multi-GeV proton beam onto a liquid Mercury pion production target, (*ii*) a high-field target solenoid that radially confines the secondary charged pions, (*iii*) a long solenoidal channel in which the pions decay to produce positive and negative muons, (*iv*) a system of RF cavities in a solenoidal channel that capture the muons in bunches and reduce their energy spread (phase rotation), and (*v*) a muon ionization cooling channel that reduces the transverse phase space occupied by the beam by a factor of a few in each transverse direction. At this point the beam will fit within the acceptance of an accelerator for a Neutrino Factory. However, to obtain sufficient luminosity, a Muon Collider requires a great deal more muon cooling. In particular, the 6D phase-space must be reduced by $O(10^6)$, which requires a longer and more complex cooling channel. Finally after the cooling channel, the muons are accelerated to the desired energy and injected into a decay (NF) or storage ring (MC). In a Neutrino Factory the ring has long straight sections in which the neutrino beam is formed by the decaying muons. In a Muon Collider, positive and negative muons are injected in opposite directions and collide for about 1000 turns before the luminosity becomes marginalized due to the muon decays.

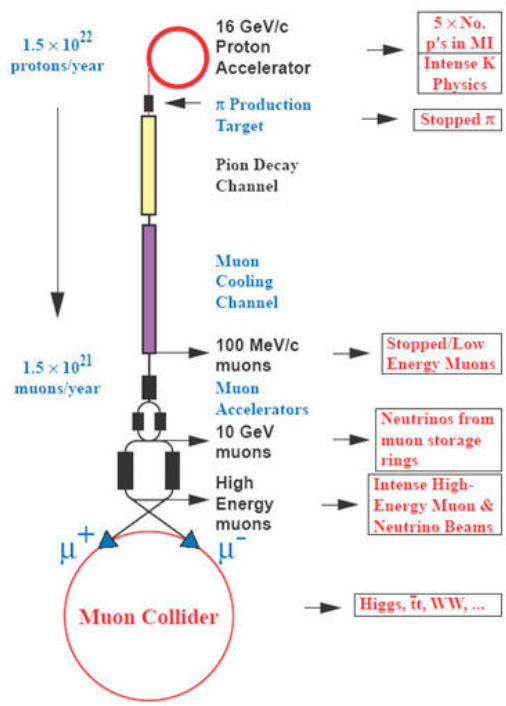

Figure 1: Schematic of muon acceleration complex.

6 D COOLING FOR THE MUON COLLIDER

Overview

Intense 6D cooling for the Muon Collider is not yet under experimental study, but is being modeled, studied with theoretical and computation tools and an

* This work was supported by the Fermi National Accelerator Laboratory, which is operated by Universities Research Association, under contract No. DE-AC02-76CH03000 with the U.S. Department of Energy
#bross@fnal.gov

experimental program exploring some of the major component parts of the system is being developed. At this point in time, we do not have a full end-to-end simulation for the cooling needed for a muon collider, but a self-consistent end-to-end cooling scheme has been developed and is shown schematically in Figure 2 [2].

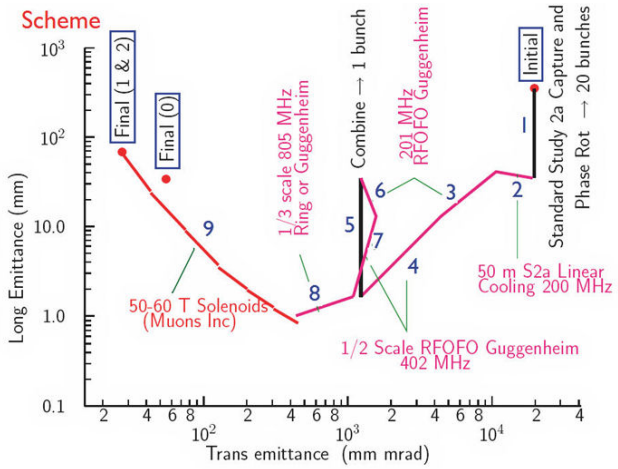

Figure 2: Cooling scheme for the muon collider.

This scheme utilizes the initial transverse cooling scheme from the Neutrino Factory Study 2a [3], the "Guggenheim" ring-FOFO (see P. Snopok's paper in these proceedings) and final cooling with 50T solenoids and LH_2 absorbers. Other alternate concepts being considered for parts of the cooling include: the Helical Cooling Channel (HCC) [4], the FOFO-Snake [5] and Parametric Resonance Ionization Cooling (PIC) [6]. As seen from above, the bulk of the muon cooling for the MC is done in the 6D cooling channels. To date the R&D has lent its primary focus on three main schemes for doing the 6D cooling for the Muon Collider and these concepts remain the central focus of 6D cooling in our R&D proposal. These are the Guggenheim channel, the Helical Cooling Channel (HCC) and the FOFO-Snake channel. However, additional subsystems for charge separation and charge recombination are required, and low-energy bunch merging may also be needed and other cooling schemes are also being explored.

Guggenheim Channel

The Guggenheim channel uses a large-pitch helical lattice (see Figure 3) in order to avoid the injection and extraction problems with a Ring-FOFO. The component parts of the Guggenheim are the same as that for the Ring-FOFO and include vacuum 201 MHz normal-conducting RF cavities, liquid hydrogen absorbers and solenoids. This approach has been under study for a number of years, but much work remains to be done which is incorporated into the 5 Year R&D program. Code must be developed and comparisons must be made between alternative ways of modeling the fields, either using 3D field maps or a multipole expansion. The benefits of a "tapered" channel must also be assessed. Matching sections must be designed and realistic parameters for absorbers and windows must be used in the simulations. If magnetic shielding is needed between "turns" in the lattice, its effect must also be evaluated.

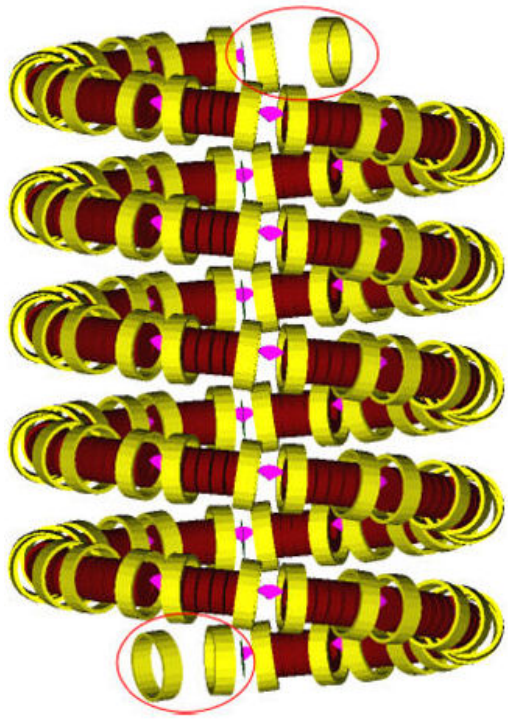

Figure 3: Schematic of the Guggenheim Cooling Channel. The RF cavities are in red, the solenoids in yellow and the LH_2 wedge-absorbers in pink.

Helical Cooling Channel

The basic HCC is composed of solenoidal, helical dipole, and helical quadrupole current coils to provide focusing and dispersion needed for emittance exchange as the beam follows an equilibrium helical orbit. Dense hydrogen gas fills the channel and acts as the energy absorber for ionization cooling and also is expected to suppress RF breakdown (see K. Yonehara's talk in these proceedings). A tight-pitched HCC made up of a series of solenoids with their centers arranged along a helical path (see Figure 4), however, effectively produces the magnetic field required for the HCC and is now the favored solution. The implementation of such a channel with embedded RF cavities is extremely challenging. A model incorporating realistic cavity parameters still needs to be developed and tested via simulations and a model of the helical magnet must be fully developed and its properties incorporated into the simulations. These tasks are part of the 5 Year R&D plan. Matching sections between the HCC and the rest of the front end need to be designed and simulated. In addition, overall optimization of the entire system must be carried out. Work needs to be done modeling space-charge effects at the end of the channel to make sure collective effects are benign. These space charge studies will have to be done for all cooling schemes, of course. As this system is pressurized with H_2

gas, we will need a structural analysis of the isolation windows and a detailed safety analysis.

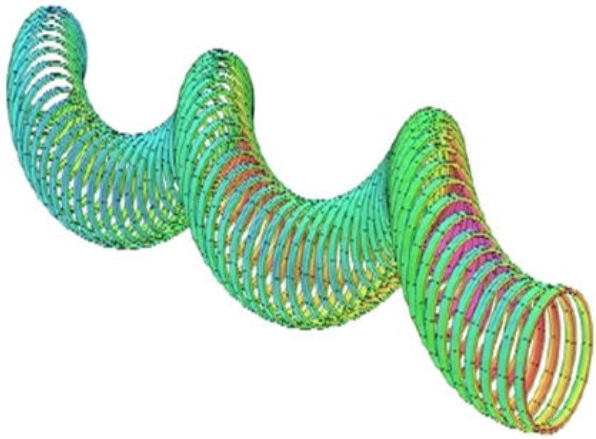

Figure 4: Schematic of the favored coil system proposed for the HCC.

FOFO-Snake Channel

The FOFO-snake channel consists of a series of tilted, translated solenoids following a straight path [11]. It acts like a planar wiggler and has the great advantage that both muon charges can be cooled in the same channel. There are several possible implementations of this design that will be studied in the 5 Year plan and include a gas-filled cavity version, a vacuum cavity version, and a magnetically insulated version. The other activities required to assess this approach are the same as those for the other cooling channel options, namely, studies of the matching sections, space-charge effects, and error sensitivity.

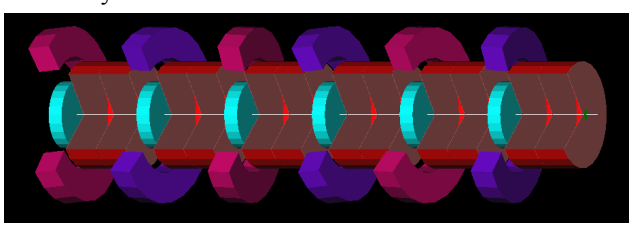

Figure 5: Schematic of FOFO-Snake Cooling channel. The cavities are in red, the solenoids in magenta and purple and the LH_2 absorbers in teal.

Final Cooling

One of the most challenging goals in the cooling for Muon Collider is to get a final normalized transverse emittance on the order of 2–25 μm. The strategy used in the cooling channel design is to end the 6D cooling section when the longitudinal emittance is well below the value needed by the collider. Then, either brute force transverse cooling or reverse emittance exchange can be used to obtain the required transverse emittance. Four alternatives are being considered for the final stage of cooling. Some schemes use an additional subsystem for high-energy bunch merging.

One of these schemes is the 50T channel which uses a straight lattice of very high field high-temperature superconductor (HTS) solenoids (Figure 6) to do the final cooling [7]. Development of this channel requires an optimization

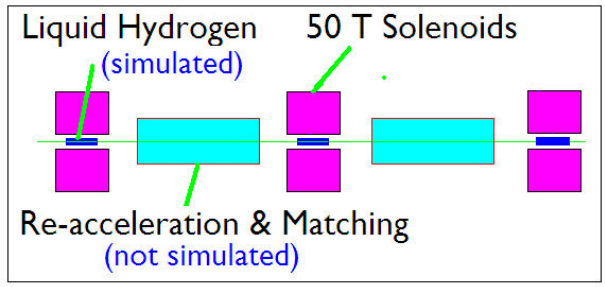

Figure 6: Conceptual diagram of final cooling channel utilizing 50T solenoids and LH_2 absorbers.

of the lattice parameters for various assumed maximum values of the solenoid strength. Lattices must also be matched on both ends and these sections need to be designed and simulated. Studies of collective effects, especially space charge, will be a component of the R&D in the 5 Year plan. As part of the 5 Year plan work, the selected design will be subjected to an error sensitivity study to validate its performance. The Very High Field Superconducting Magnet Collaboration [8] will study HTS wire and cables in order to gain a better understanding of the technology needed to fabricate the very-high-field solenoids needed in this application.

Finally, two novel concepts that would collect muons at low energy and then bring them almost to rest are also being studied. These are the "Particle Refrigerator" [9] shown in Figure 7 and the Inverse Cyclotron [10]. The "Particle Refrigerator" uses the concept of frictional cooling which has long been known (at least conceptually) to be capable of producing very-low emittance beams. Frictional cooling works for muons with very low kinetic energy (<10 keV), so the idea presented in Figure 7 requires muons to climb a few mega-volt potential, stop and then reverse direction in order to enter the frictional cooling channel. This increases the acceptance of the system from a few keV to a few MeV.

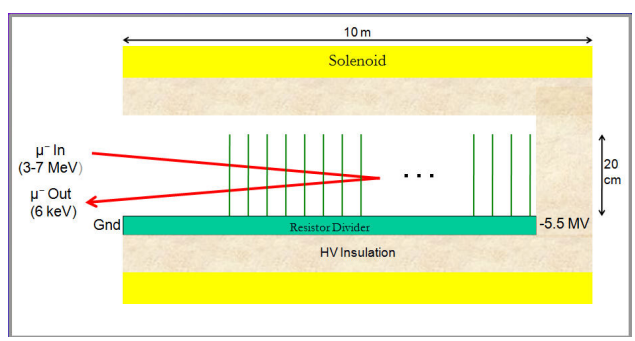

Figure 7: Concept for the particle refrigerator.

In the inverse cyclotron, a large admittance sector cyclotron filled with LiH wedges surrounded by helium or hydrogen gas is utilized. Muons are cooled (and slowed) as they spiral inward into the center of the cyclotron after they are injected at the outer rim of the cyclotron. As the muon momentum approaches zero, the momentum spread also approaches zero and long bunch trains coalesce. Finally when the bunch train has coalesced into a central swarm, it is ejected axially with an electric kicker pulse.

CRITICAL TECHNOLOGIES

As can be seen from the previous section, many possibilities are being pursued with respect to 6D cooling for a Muon Collider. Many of these concepts are quite elegant, but at present no scheme can be realized without the development of new technologies. Two areas that are of critical importance are operation of high-gradient RF cavities in a magnetic field of up to approximately 3T and the fabrication of ultra-high field (50T) solenoids.

A crucial challenge for the Neutrino Factory and Muon Collider Front-End Design and cooling channels is the operation of high-gradient normal-conducting RF (NCRF) in the presence of high magnetic field. This problem has been the primary focus of the MuCool [11] program. What has been observed in MuCool is that the safe operating gradient limit degrades significantly when a NCRF cavity is operated in magnetic field (see figure 8).

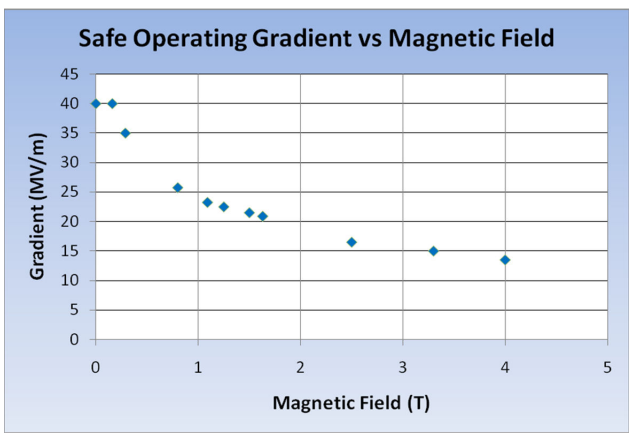

Figure 8: Safe operating gradient vs. B field.

The data shown in Figure 8 are for an 805 MHz pillbox test cavity and seem to follow a universal curve. The maximum stable gradient degrades quickly with increasing B field. The cause of this effect is understood and comes from field emission from emitters (surface field enhancements in the regions of high gradient) in the cavity. The field emission is focused to spots by the B field when B is parallel to E, as is the case with a pillbox cavity. These beamlets then initiate the breakdown event in the cavity.

In order to address this problem, three approaches are being investigated. The first is to eliminate field emission by processing the NCRF copper cavities using superconducting RF techniques. This has been done in MuCool for a 201 MHz copper cavity with promising results. This cavity reached a stable operating gradient of 21 MV/m (the design gradient was 16 MV/m) in the absence of B field. Initial tests of this cavity with applied external B (B<0.5T) field have shown a B field degradation, but in comparison with the results from the 805 MHz pillbox cavity, the B field effect is qualitatively different. Much more work needs to be done in this area and is part of the 5 Year R&D program. A new concept in processing for SCRF which can, in principle, also be applied to NCRF is Atomic Layer Deposition (ALD) [12]. Initial tests of a superconducting cavity coated with 5 nm of ZrO2 plus 30 nm of Pt were performed at TJNL. The ALD treatment greatly reduced the dark current while maintaining the achievable cavity gradient. The next step will be to test a similarly treated normal conducting cavity in a magnetic field to evaluate its performance. To this end, the 5 Year R&D plan contains an option to build an 805-MHz cavity for ALD coating and testing in the 5-T solenoid at the MuCool Test Area (MTA).

The second approach for abating the magnetic field effect is to prevent the magnetic focusing. In this case an open cell geometry is required and additional coils are added in the lattice to modify the B field direction and thus eliminate the B field focusing effect. However, the open-cell structure does mean that additional power (X2) is needed in order to reach the same on-axis accelerating gradient.

The third approach to dealing with the magnetic field effect is to operate RF cavities filled with high pressure H_2 gas (an underlying principle of the Helical Cooling Channel). The results from tests in the MuCool Test Area done by researchers at Muons Inc [13] using a RF test cell filled with H_2 gas are quite promising. In these data no degradation in maximum stable operating gradient was observed at B fields up to 3.5T for Mo electrodes. However, such a cavity has never been tested with beam. In pure hydrogen, ionization electrons will remain in the gas for a significant portion of the RF pulse, being accelerated back and forth by the RF fields, and transferring the electromagnetic energy stored in the cavity to the gas through collisions. Depending on the intensity of the incident beam, the Q of the cavity could be reduced by several orders of magnitude. It is possible that introducing another gas species may capture these free electrons. However, a good candidate gas has not yet been found. (SF6 is frozen at LN2 temperature, and also may form hydrofluoric acid.) In addition, it must be demonstrated that the large numbers of ions created do not present a problem. A beam test of a HPRF test cavity is presently being prepared at the MTA. If successful, this initial test would be followed by the design, construction and testing of a prototype 805-MHz HPRF cavity having entrance and exit windows more suitable for beam passage.

THE US 5-YEAR PLAN PROPOSAL

A proposal that presented a 5-year R&D program aimed at completing a Design Feasibility Study (DFS) for a Muon Collider and, with international participation, a Reference Design Report (RDR) for a muon-based Neutrino Factory has been submitted to the US Department of Energy as a joint proposal from US Neutrino Factory and Muon Collider Collaboration and the Fermilab Muon Collider Task Force [14]. The goal of the R&D program is to provide the HEP community with detailed information on future facilities based on intense beams of muons and give clear answers to the questions of the expected capabilities and performance of these muon-based facilities, while providing defensible estimates for their cost. This information, together with the physics insights gained from the next-generation neutrino and LHC experiments, will allow the HEP community to make well-informed decisions regarding the optimal choice of new facilities.

With regard to muon ionization cooling (or more generally speaking, the Front-End of the facility), the R&D plan will embark on both design and simulation and hardware efforts. The design and simulation work will study and optimize:

- Pion capture and decay, bunching and phase rotation.
- Precooling.
- 6D Cooling.
- Final Cooling.

A full end-to-end simulation of muon production and cooling (through final cooling) with all interfaces between cooling sections will be a major component of the effort. The hardware effort on cooling has 3 main objectives:

- Established the operational viability and engineering foundation for the concepts and components incorporated into the Muon Collider Design Feasibility Study and the Neutrino Factory Reference Design Report.
- Establish the engineering performance parameters of these components.
- Provide the basis for a defendable cost estimate.

The most critical technical challenge for the Muon Collider is the demonstration of a viable cooling scenario. To this end, the R&D proposal will support the MICE experiment (see Derun Li's talk, these proceedings) which will study the initial transverse muon ionization cooling, and will strive to develop a single scheme for 6D cooling that is backed by rigorous component testing for this chosen scheme. The various candidate cooling schemes that have been outlined in this paper will become more or less attractive as viable options depending on the results of component testing within this program. We anticipate critical results from the RF tests in the first two years of our R&D program, at which time we will proceed with building a short cooling section for one, and only one, cooling scheme. It is not envisioned that during this 5 year R&D program a 6D muon ionization cooling demonstration experiment will be performed. Figure 9 presents what we believe will be the Muon Collider Technical Foundation after the 5 Year program is completed, relative to where we believe the technology is today.

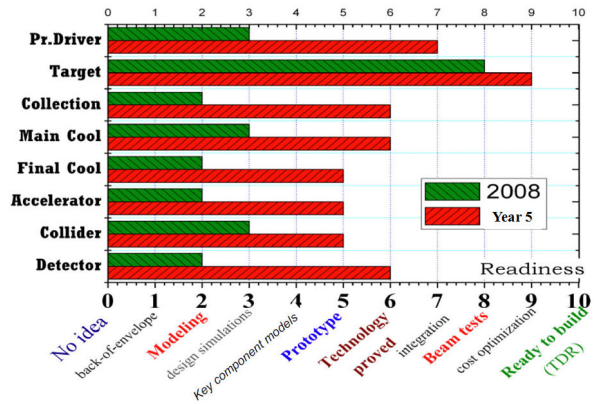

Figure 9: Technical foundation of the various sub-systems in the Muon Collider complex after the 5 Year R&D program.

REFERENCES

[1] M. Alsharo'a et al., (Muon Collider Collaboration), Phys. Rev. ST Accel. Beams, 6 081001 (2003).
[2] R. B. Palmer *et al.*, "A complete scheme of ionization cooling for a muon collider," in Proc. PAC 2007, p. 3193.
[3] S. Geer and M. Zisman (Eds.), "The neutrino factory and beta beam experiments and development," APS Neutrino Study, BNL-72369-2004, FERMILAB-TM-2259, Nov 2004. 115pp., e-Print: physics/0411123.
[4] K. Yonehara *et al.*, "Simulations of a Gas-Filled Helical Muon Beam Cooling Channel, in Proc. PAC 2005, p. 3215.
[5] D. Newsham *et al.*, "Simulations of parametric resonance ionization cooling," in Proc. PAC 2007, p. 2927.
[6] Y. Alexahin *et al.*, "6D ionization cooling channel with resonant dispersion generation," in Proc. PAC 2007, p. 3477.
[7] S. A. Kahn et al., "A high field HTS solenoid for muon cooling," in Proc. PAC 2007, p. 446.
[8] See http://www.cap.bnl.gov/mumu/conf/MUTAC-080408/talks/09AM/ATollestrup1-080408.pdf
[9] T.J. Roberts and D. Kaplan, "The Particle Refrigerator," Proceedings of PAC09, paper WE6PFP096.
[10] D.J. Summers, Stephen B. Bracker, L.M. Cremaldi, R. Godang, R.B. Palmer, "*6D muon ionization cooling with an inverse cyclotron*," AIP Conf.Proc.821:432-436,2006.
[11] MuCool WEB page: http://mice.iit.edu/mta/
[12] Norem *et al., "Results from Atomic Layer Deposition and Tunneling Spectroscopy for Superconducting RF Cavities,"* in the Proceedings of 11th European Particle Accelerator Conference (EPAC 08), Magazzini del Cotone, Genoa, Italy, 23-27 Jun 2008, pp WEPP099
[13] Muons Inc. WEB page: http://muonsinc.com
[14] NFMCC web page: http://www.cap.bnl.gov/mumu/
MCTF web page: http://apc.fnal.gov/
5-Yr. proposal: http://apc.fnal.gov/groups2/MCCC/

ENHANCED OPTICAL COOLING OF MUON BEAMS

E.G. Bessonov, M.V. Gorbunkov, Lebedev Phys. Inst. RAS, Moscow, Russia,
A.A. Mikhailichenko, Cornell University, Ithaca, NY 14853, U.S.A.

Abstract

The possibility of the Enhanced Optical Cooling (EOC) of muon beams in storage rings is investigated.

INTRODUCTION

Muon in motion has a lifetime $\tau_\mu = \tau_{\mu,0}\gamma$, where $\tau_{\mu,0} \cong 2.2\mu\, s$ is the muon lifetime at rest, $\gamma = \varepsilon / m_{\mu,0}c^2$, ε stands for muon energy. During this time, muons can develop $N_\mu\big|_{\gamma>>1} = \tau_\mu c / C \cong 297\overline{B}(T)$ revolutions in a storage ring having the orbit circumference *C* and average magnetic field strength $\overline{B}$. Damping time of the muon beam in a storage ring must be much smaller than the muon decay time: $\tau < \tau_\mu$. This is the most severe limitation on the muon cooling in storage rings. Enhanced (fast) Optical Cooling methods must be used in this case.

Below we investigate the possibility of muon cooling in a storage ring using version 1, section 3 of EOC [1].

COOLING SCHEME

Stochastic cooling (SC) and optical stochastic cooling (OSC) of particle beams in rings were considered in [2] - [4]. Our scheme is close to the OSC one. It includes a storage ring, pickup and kicker undulators installed in straight sections of the ring, an optical system which includes an optical filter, an optical parametric amplifier (OPA) [1]. It also includes a procedure and adequate hardware for selection of undulator radiation (UR) wavelets (URW) emitted by particles in the pickup undulator. This selection is arranged by means of a screen installed at the image plane of the optical system connecting the pickup and kicker undulators.

Maximal rate of energy loss for a particle in the combined fields of one helical kicker undulator and URW amplified in OPA is

$$P_{loss}^{\max} = -eE_w^{cl} L_u \beta_{\perp m} f\, \Phi(N_{ph}^{cl})\sqrt{\alpha_{ampl}} \quad \text{or}$$

$$P_{loss}^{\max} = \frac{2\sqrt{2}\pi e^2 \gamma f K^2 \sqrt{M}\,\Phi(N_{ph}^{cl})\sqrt{\alpha_{ampl}}}{(1+K^2)^{3/2}\sigma_w}, \qquad (1)$$

where $E_w^{cl} = \sqrt{2} r_\mu \gamma^2 \sqrt{\overline{B^2}} / (1+K^2)^{3/2}\sqrt{M}\sigma_w$ is the electric field strength related to the first harmonic of the undulator radiation emitted by a particle in the pickup undulator within the frequency band $\Delta\omega/\omega = 1/2M$ calculated in the framework of the classical electrodynamics (CED), $K = e\sqrt{\overline{B^2}}\lambda_u / 2\pi m_\mu c^2$, $\sqrt{\overline{B^2}}$ is the undulator r.m.s. magnetic field strength, $\beta_{\perp m} = K/\gamma$, $\Phi(N_{ph}^{cl})|_{N_{ph}^{cl}<1} = \sqrt{N_{ph}^{cl}}$, $N_{ph}^{cl} = \pi\alpha K^2/(1+K^2)$ is the number of photons emitted by one particle in the URW, M is the number of the undulator periods, $L_u = M\lambda_u$, λ_u is the undulator period, α_{ampl} is the gain in OPA, f is the revolution frequency, σ_w is the waist size of the URW. Function $\Phi(N_{ph}^{cl})$ takes into account the quantum nature of the particle emission of the electromagnetic radiation. It radiates on average one photon per $1/N_{ph}^{cl}$ pass throw pickup undulator in the photon energy interval $\Delta(\hbar\omega)/\hbar\omega = 1/2M$ near the maximum photon energy $\hbar\omega_{\max}$. Contrary, in this case the electric field strength and the stimulated energy transfer in the kicker undulator are only $1/\sqrt{N_{ph}^{cl}}$ times bigger than the ones calculated in the framework of CED.

We suggested that the density of the energy in the URW emitted by a particle, is approximated by Gaussian distribution with a waist size $\sigma_w > \sigma_{x,z}^{\mu}$, $\sigma_{w,c}$ within the length $2M\lambda_{1\min}$, where $\sigma_{x,z}^{\mu}$, are the transverse beam dimensions; a value $\sigma_{w,c} = \sqrt{L_u\lambda_{1\min}/8\pi}$ is the waist size corresponding to $Z_R = L_u/2$; the Rayleigh length $Z_R = 4\pi\sigma_w^2/\lambda_{1\min}$, $\lambda_{1\min} = \lambda_1|_{\theta=0}$, $\lambda_1 = \lambda_u(1+K^2+\vartheta^2)/2\gamma^2$ is the wavelength of the first harmonic of the UR emitted at the angle θ, counted between the vector of particle average velocity in the undulator and the direction to the observation point, $\vartheta = \gamma\theta$.

The damping times for the particle beam in the longitudinal and transverse planes are [1]

$$\tau_\varepsilon = \frac{6\sigma_{\varepsilon,0}}{P_{loss}^{\max}\cdot N_k} = \frac{3\sqrt{2}(1+K^2)^{3/2} T\sigma_w\sigma_{\varepsilon,0}}{2\pi r_e mc^2\gamma K^2\sqrt{M}\,\Phi(N_{ph}^{cl})N_k\sqrt{\alpha_{ampl}}},$$

$$\tau_x = \tau_\varepsilon \frac{\sigma_{x,0}}{\sigma_{x_\eta,0}}, \qquad (2)$$

where $\sigma_{\varepsilon,0}$ is the initial energy spread of the particle beam, $\sigma_{x_\eta,0} = \eta_{x,k}\beta^{-2}(\sigma_{\varepsilon,0}/\varepsilon_s)$, $\sigma_{x,0} = \sqrt{\beta_{x,k}\in_x}$ are the initial radial beam sizes in kicker undulator determined by the energy spread and the spread of betatron amplitudes, $\eta_{x,k}$, $\beta_{x,k}$ are the ring dispersion and beta functions at the kicker undulator, $\in_{x,0}$ is the initial radial emittance of the beam, N_k is the number of kicker undulators, $T = 1/f$, the product $r_e m_e c^2 = e^2$ of the electron radius and mass are introduced for the convenience. Note, that the damping time for the transverse direction is proportional to $\beta_{x,k}/\eta_{x,k}$. Factor 6 in (2) takes into account a

This work was supported by RFBR under Grant No 09-02-00638-a.

circumstance that the initial energy spread is $2\sigma_{\varepsilon,0}$, the particles meet with their URWs 2 times less often (half of URWs are absorbed by the screen) and that the jumps of the particle closed orbit in average lead to lesser jumps of the amplitudes of synchrotron and betatron oscillations. The path between pickup and kicker undulators must be isochronous to the fraction of operational wavelength.

When $N_{ph}^{cl} < 1$, $N_{mix} = N_k$, the equilibrium energy spread and the beam dimensions at the location of kicker undulator are

$$\sigma_{\varepsilon,\,eq} = \frac{N_{ph,\Sigma}}{2\sqrt{2}N_{ph}^{cl}}\Delta\varepsilon_{loss}^{\max},\ \sigma_{x,\,eq} = \sigma_{x_\eta,\,eq} = \frac{\eta_{x,k}}{\beta^2}\frac{\sigma_{\varepsilon,\,eq}}{\varepsilon}. \quad (3)$$

where $N_{ph,\Sigma} \cong N_{ph}^{cl}(N_{p,s}-1) + N_n > 1$ is the number of photons in the sample produced by $N_{p,s}-1$ extraneous particles and N_n noise photons at the amplifier front end, $N_{p,s} = 2M\lambda_{1,\min}N_p/\sigma_{s,0}$ is the number of particles in the URW sample, N_p stands for the number of particles in the bunch, $\Delta\varepsilon_{loss}^{\max} = P_{loss}^{\max}/fN_{ph}^{cl}$ is the particle energy jump in the fields of one kicker undulator and the amplified URW (if one photon of the energy $\hbar\omega_{1,\max}$ in the URW), N_{mix} is the number of mixers in the ring, $\sigma_{s,0}$ is the initial length of the particle bunch. The energy jump $\Delta\varepsilon_{loss}^{\max}$ corresponds to the energy loss by each particle in the pickup undulator if URW contains a single photon only. Note, that if the number of noise photons in the equation (3) set to $N_n = 0$, then N_{ph}^{cl} in the equation will disappear as well. It means that classical and quantum expressions for equilibrium beam dimensions in this case are identical (differences stay only in the energy jumps $\Delta\varepsilon_{loss}^{\max}$ for classical and quantum cases). For one particle in the URW sample the equilibrium beam dimensions would be limited only by one energy jump.

The equations (3) determine the particle energy jump through the equilibrium energy spread and dimensions of the beam. Below we introduce the dimensionless coefficients $k_\varepsilon = \sigma_{\varepsilon,0}/\sigma_{\varepsilon,eq}^{EOC} > 1$, $k_x = \sigma_{x,\,0}/\sigma_{x,\,eq}^{EOC} > 1$. The values $k_{\varepsilon,x} - 1$ present the degree of cooling for the longitudinal and transverse directions respectively. In this case the energy jump (3) corresponding to the equilibrium beam parameters can be represented in the form $\Delta\varepsilon_{loss,\varepsilon,x}^{\max} = 2\sqrt{2}N_{ph}^{cl}\sigma_{\varepsilon,0}/k_{\varepsilon,x}N_{ph,\Sigma}$. The corresponding power loss is

$$P_{loss,\varepsilon,x}^{\max} = fN_{ph}^{cl}\Delta\varepsilon_{loss,\varepsilon,x}^{\max} = \frac{2\sqrt{2}f\,(N_{ph}^{cl})^2\sigma_{\varepsilon,\,0}}{k_{\varepsilon,x}N_{ph,\Sigma}}. \quad (4)$$

We took into account that from the equation $\sigma_{x,\,eq} = \sigma_{x_\eta,\,eq}$ follows the equation $P_{loss,x}^{\max} = P_{loss,\varepsilon}^{\max}$.

In this case, according to (2), the damping time (the time necessary to decrease the initial beam dimensions to the equilibrium ones) is

$$\tau_{\varepsilon,x} = \frac{6\sigma_{\varepsilon,0}}{P_{loss,l}^{\max}\cdot N_k} = \frac{3\sqrt{2}N_{ph,\Sigma}k_{\varepsilon,x}}{2(N_{ph}^{cl})^2 N_k}T. \quad (5)$$

According to the expression (5), the damping time is proportional to the degree of cooling, to the revolution period over the number of kicker undulators and to the number of noise photons at the amplifier front end plus the number of muons in the URW sample.

If the degree of cooling and the equilibrium beam parameters are chosen, then according to (1) and the condition $P_{loss}^{\max} = P_{loss,\varepsilon,x}^{\max}$, the gain corresponding to the equilibrium beam parameters is

$$\sqrt{\alpha_{ampl}} = \frac{(1+K^2)^{3/2}(N_{ph}^{cl})^2\sigma_w}{\pi r_e m_e c^2\gamma K^2\sqrt{M}\Phi(N_{ph}^{cl})k_{\varepsilon,x}N_{ph,\Sigma}}\sigma_{\varepsilon,eq}. \quad (6)$$

It follows from (5) that one can set an arbitrary degree of cooling if the gain of the OPA and equilibrium dimensions of the beam are chosen according to (6). Higher initial beam dimensions require higher gain in OPA, the rate of cooling ($\Delta\varepsilon_{loss}^{\max}$) and the equilibrium beam dimensions. In the case of fast muon cooling the conditions could be very hard to satisfy in practice.

If we set the damping time equal to the muon decay time ($\tau_\mu = \tau_{\varepsilon,\,x}$) then the equation (5) determines the relativistic factor of the being cooled muons for this case:

$$\gamma_\mu = \frac{\tau_\mu}{\tau_{\mu,0}} = \frac{\tau_{\varepsilon,x}}{\tau_{\mu,0}} = 4.5\cdot 10^5\tau_{\varepsilon,x}. \quad (7)$$

The deflection parameter of the undulator is determined by the given values γ_μ, $\lambda_{1,\min}$ and λ_u:

$$K_1^2 = 1 + \frac{2\gamma_\mu^2\lambda_{1,\min}}{\lambda_u}. \quad (8)$$

The average power of an optical amplifier is determined by the power of its URW beam and by its noise power:

$$P_{ampl} = P_{ampl}^{URW} + P_{ampl}^{n}, \quad (9)$$

where $P_{ampl}^{URW} = \hbar\omega_{1,\max}N_{ph}^{cl}\alpha_{ampl}fN_\mu N_b/2$, $P_{ampl}^{n} = l_b\alpha_{ampl}\hbar\omega_{1,\max}fN_nN_b/2M\lambda_{1\min}$, $\omega_{1,\max} = 2\pi c/\lambda_{1,\max}$, l_b is the length of the particle bunch and N_b is the number of bunches. The powers correspond to the case in which a half of total number of particles are involved in the cooling process (screening is introduced) and the amplification time interval of the amplifier is equal to the duration time of the particle bunch [1].

The transverse resolution of the particle within the bunch is

$$\delta x_{res} \cong 0.86\sqrt{\lambda_{1\min}L_u}. \quad (10)$$

To have the smallest possible damping time, we must choose small beta-function value in vicinity of kicker undulators (limited by condition $\beta_{x,k} > L_u/2$) to have smallest transverse beam dimension in a damping ring.

The number of revolutions performed by muon in a ring during one period of phase oscillations comes to

$$N_{rev}^{ph} = \sqrt{2\pi\varepsilon_s / h\alpha_c e V_m}\ , \qquad (11)$$

where h is the harmonic number, α_c is the momentum compaction factor, V_m is amplitude of the RF accelerating voltage.

EXAMPLE

To appreciate the efficiency of the EOC, we will consider below an example of the EOC of muon beam in a storage ring with the equal number of pickup and kicker undulators, mixers, OPAs, isochronous bends between pickup and kicker undulators and non-isochronous residual part of the orbit. Let the revolution period be $T = 15\mu s$, the undulator period $\lambda_u = 1$ m, the number of the undulator periods M=10, the number of undulators $N_p = N_k = 10$, limiting degree of cooling $k_{\varepsilon,x} - 1 = 10$, number of muons per a bunch $N_\mu = 10^7$, the number of bunches $N_b = 10^2$, the length of the muon bunch $l_b = 2$ m, the wavelength of the OPA $\lambda_{1\min} = 4 \cdot 10^{-5}$ cm, the waist size of the URW at kicker undulator $\sigma_w = 1$ mm, the number of noise photons at the amplifier front end $N_n = 1$, the equilibrium beam energy spread $\sigma_{\varepsilon,\,eq} = 1.84 \cdot 10^6$ eV ($\sigma_{\varepsilon,\,eq} / \varepsilon = 10^{-6}$), the equilibrium transverse dimensions of the beam at kicker undulator $\sigma_{x_\eta,k\,eq} = \sigma_{x,k,eq} = 0.3$ mm.

In this case, according to (5)-(8), the muon decay time $\tau_\mu = 38.1$ ms, the muon energy $\varepsilon_\mu \cong 1.836$ TeV ($\gamma_\mu = 17.4\,10^3$), the deflection parameter of the undulator $K = 22$, the gain of OPA $\alpha_{ampl} = 5.13 \cdot 10^{10}$, the undulator magnetic field strength $\sqrt{\overline{B^2}} = 48.7$ T, the initial energy spread $\sigma_{\varepsilon,0} / \varepsilon = 10^{-5}$, the photon energy $\hbar\omega_{1,\max} = 3.1$ eV, $\sigma_{w,c} = 0.378$ mm, $\delta x_{res} \cong 2$ mm, $P_{ampl}^{URW} = 1.76$ kW, $P_{ampl}^{n} = 3.82$ W, $P_{ampl} = 5.58$ kW, $T_\varphi = 21.8$ ms.

If we choose the dispersion functions of the ring at pickup and kicker undulators equal to $\eta_{x,\,p} = 10^3$ m, $\eta_{x,\,k} = 30$ m, the beta functions $\beta_{x,p} = 50$ m, $\beta_{x,k} = 5$ m, then the transverse initial dimensions of the beam at the pickup undulator $\sigma_{x_\eta,p,0} = 10$ mm, $\sigma_{x,p,0} = 10$ mm, the total transverse initial dimensions of the beam at the pickup undulator $\sigma_{\Sigma,p,0} = \sqrt{\sigma_{x_\eta,p,0}^2 + \sigma_{x,p,0}^2} = 14$ mm (amplitudes will be $\sqrt{2}$ times larger).

We took into account that $N_{ph}^{cl}|_{K>>1} = \pi\alpha = 2.3 \cdot 10^{-2}$, $N_{\mu,s} = 40$, $N_{ph,\Sigma} = 1.9$, $1/N_{ph}^{cl} = 43.6$, $\Phi(N_{ph}^{cl}) = 0.151$.

DISCUSSION

Short muon lifetime together with presence of noise at the amplifier front end, quantum nature of the emission of URWs (small probability of photon emission by muon in pickup undulators) in all schemes of optical cooling impose severe limitations on the minimal rate of cooling, OPA gain, its average power, on the number of muons being cooled. High rate of cooling at moderate initial beam energy spread and transverse beam dimensions leads to high muon energy in a damping ring, big jumps of muon energy, position of closed orbit and amplitude of betatron oscillation. It leads also to big values for equilibrium beam dimensions at modest degree of cooling ($k_{\varepsilon,x} \sim 10$), high power of OPAs at small number of particles in the sample and hence in the bunch, high magnetic field strength (high temperature SC magnets with ~50T field for undulators to shorten their length could be used here). High length of pickup undulator leads to low resolution of particles in the beam necessary for the EOC scheme and to high dispersion and beta functions in the location of the pickup undulator.

Note that quantum nature of URW emission at $N_{ph}^{cl} << 1$ leads to small number $N_{ph}^{cl} << 1$ of emitted URWs per a turn and to fewer ($\sim\sqrt{1/N_{ph}^{cl}}$) degree times increase of the energy transfer in the process of stimulated interaction of the URW with the muon at kicker undulator [1].

In the EOC scheme a non-exponential cooling regime is realized when the beam dimensions are decreased much more than *e*=2.7 times for one damping time.

According to (5), (7), the damping time and the energy of the beam necessary for cooling at given revolution period are proportional to the number of the being cooled particles (number of particles in the sample) and the degree of cooling. In our example the degree of cooling $k_{\varepsilon,x} - 1 = 10$ and at the number of particles in the sample $N_{\mu,s} = 40$ lead to the muon beam energy $\varepsilon_\mu \cong 1.836$ TeV and the muon beam damping time is $\tau_\mu = 38.1$ ms, which is equal to the muon lifetime at this energy. If the phase advance between pickup and kicker undulators is equal to π then the beam is cooled both in longitudinal and transverse dimensions simultaneously. The degree of cooling of the 4-dimensional phase space is 10^4. If the screen in the optical system is transparent, produce phase advance π for the URW and overlaps half of the beam in the image plane along the position of the synchronous orbit then all particles both with positive and negative deviations of their energy from synchronous one will take part in the cooling process. In this case the damping time will be 2 times smaller.

SUMMARY

We have demonstrated the possibility of EOC of muons in storage rings. In contrast to the publication [4] we took into account the quantum nature of the photon emission in the pickup undulator. According to (1) and (5), (7) it leads to the decrease of the rate of cooling by the coefficient $N_{ph,\Sigma}/(N_{ph}^{cl})^2$ for each degree of freedom (longitudinal

and transverse horizontal) and to the increase of the energy necessary for cooling.

The rate of the energy loss by muons for the EOC scheme stays constant. It does not depend on the deviation of their energy from the energy of given reference muon. In this case the smaller initial maximal transverse and longitudinal amplitudes of oscillations of particles in the beam the smaller the equilibrium beam dimensions at the same damping time could be reached.

Despite what we underlined in our previous publication [1] the importance of quantum effects in case when the number of radiated photons is less than one, (or in other words–the energy radiated, when calculated by classical formula, is less than the energy of quanta) this fact has not attracted adequate attention. All publications of other authors on optical cooling (including recent one [5]) need to be corrected for the rate of cooling which actually is $(N_{ph}^{cl})^2 / N_{ph,\Sigma}$ only of what they are claiming for each degree of freedom. The equilibrium beam dimensions must be corrected as well. We would like to attract attention once again that these limitations manifest themselves at the *kicker* undulator, as the stimulated processes here are proportional to the *electric field* value in a wavelet (not to its energy). Additional remarks one can find in the Appendix.

EOC and other schemes of OSC can be used effectively for cooling of stable particles (protons, ions). EOC scheme has faster non-exponential rate of cooling but it requires optics with high resolution and OPAs with shorter wavelengths.

The possibility of EOC and other schemes of OSC for muons in storage rings requires additional investigations.

APPENDIX

In external fields of bending magnets and undulators installed in the storage rings, relativistic particles emit electromagnetic radiation in the form of synchrotron radiation (SR) and UR wavelets directed in the narrow range of angles ($\sim 1/\gamma$) along their velocities. The spectral-angular distribution of the emitted energy and polarization characteristics of the URWs can be calculated in the framework of classical electrodynamics (CED). More correct quantum approach leads to the same characteristics of the emitted radiation if we accept that the energy is emitted in the form of photons with the energy $\varepsilon_{ph} = \hbar\omega$ and if the energy of these photons is much less than the energy of the particle. Distribution of the number of photons emitted by the particle in the bending magnet or in the undulator is determined by the distribution of the energy of the emitted radiation

$$\frac{\partial N_{ph}}{\partial\omega\partial o} = \frac{1}{\hbar\omega}\frac{\partial^2\varepsilon}{\partial\omega\partial o} .$$

The forms of the SR and UR wavelets and their properties are different. The loss of the energy (friction) leads to damping of betatron and phase oscillations of particles in the rings. In CED the energy is emitted continuously. In the quantum electrodynamics (QED) particles propagate along trajectory some distance without the energy loss and then emit instantaneously the URW with the energy $\hbar\omega$ and at the same time they loose the energy $\Delta\varepsilon = \hbar\omega$. The radiation in the QED has random nature. In average the energy emitted in the framework of CED and QED are equal. The emission of the energy in the form of finite quanta leads to jumps of the closed orbit of the particles. Joint action of the quanta excitation and damping leads to rms equilibrium transverse and longitudinal dimensions of particle beams in the rings. The value of these dimensions is proportional to the value of the jumps (the energy of URWs) and in strict accordance with the experiment. The URW length, special and time dependence, polarization and other characteristics of radiation are determined by the type of undulators and in agreement with the experiment.

Note that stable particles exist in the ring for many hours. It is possible to inject in the ring one particle and produce experiments [6]. Experimentally we can detect the particle (reduction of the particle state), observe its Brownian motion in the equilibrium volume. If we use laser undulator then we can have very hard radiation and lose the particle if the jump of the particle orbit will be larger than the dynamic aperture of the ring [7]. URW consists of a whole number of photons (never parts of photons).

REFERENCES

[1] E.G. Bessonov, M.V. Gorbunkov, A.A. Mikhailichenko, “Enhanced Optical Cooling System Test in a Muon Storage Ring”. Phys. Rev. ST Accel. Beams **11**, 011302 (2008).

[2] A.G. Ruggiero, “A Muon Collider Scenario Based on Stochastic Cooling”, Nucl. Instr. Methods A 350 (1994) 45- 52.

[3] A.A. Mikhailichenko, M.S. Zolotorev,” Optical Stochastic Cooling”, Phys. Rev. Lett.71: 4146-4149, 1993.

[4] A.A. Zholents, M.S. Zolotorev, W. Wan “Optical Stochastic Cooling of Muons”, Phys. Rev. ST Accel. Beams **4**, 031001, (2001).

[5] A.E. Charman and J.S. Wurtele, “Quantum Mechanical Treatment of Transit-Time Optical Stochastic Cooling of Muons”, arXiv:0905.0485v1 [physics.acc-ph] 4 May 2009. http://arxiv.org/PS_cache/arxiv/pdf/0905/0905.0485v1.pdf

[6] A.N. Aleshaev, I.V. Pinaev, V.M. Popik, S.S. Seredniakov, T.V. Shaftan, A.S. Sokolov, N.A. Vinokurov, P.V. Vorob’ev, “A Study of Influence of Synchrotron Radiation Quantum Fluctuation on the Synchrotron Oscillations of a Single Electron Using Undulator Radiation”, http://arXive:acc-phys/9503001v2 .

[7] V.N. Litvinenko, “High Intensity γ-Rays Source Driven by the Duke Storage ring FEL”, proceed. of the 2001 FEL Conference, p.II-79.

FRICTIONAL COOLING DEMONSTRATION AT MPP

Bao Yu*, Institute of High Energy Physics, Chinese Academic of Science, Beijing, China
Allen Caldwell, Daniel Greenwald, Christian Blume,
Max Planck Institute for Physics, Munich, Germany

Abstract

Frictional Cooling holds promise for delivering beams with a very narrow energy spread. At the Max Planck Institute for Physics (MPP), a demonstration experiment based on this scheme will soon take data. In this paper, the experimental setup and the Monte-Carlo simulation results based on Geant4 are described. The use of frictional cooling as an efficient scheme for producing a low energy muon beam is also simulated yielding a beam with mean energy of 3 keV and an RMS of ~300 eV with an efficiency significantly improved from the current scheme.

FRICTIONAL COOLING

The idea of Frictional Cooling is to bring charged particles into a kinetic energy range where the faster particles lose more energy per distance traveled than slower ones [1]. This is done by passing the beam through a gas. Fig. 1 shows the stopping power for μ^+ in Helium as a function of kinetic energy. For kinetic energies below 10 keV, the stopping power increases with increasing energy. Applying

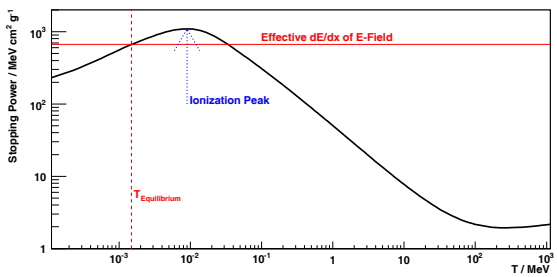

Figure 1: Stopping power of μ^+ in Helium (scaled from the NIST data [2] for protons).

an electric field to restore kinetic energy in the longitudinal direction will bring the particles to an equilibrium energy: particles with kinetic energies less than the equilibrium energy are accelerated because they gain more energy from the electric field than they lose to the gas. Particles with kinetic energies greater than the equilibrium energy are decelerated because they lose more energy than they gain. Thus the phase space is reduced. Additionally, since energy is restored only in the longitudinal direction, the beam divergence is reduced, cooling the beam in the transverse direction.

In this energy regime, energy is lost through excitations, elastic scattering on nuclei and charge exchange interactions. Multiple scattering places a lower limit on the emittance achievable by the two cooling effects described above. The cooled beam has an energy spread of ~ 300 eV, which can be preserved during reacceleration, yielding high energy beams with small relative momentum spreads.

EXPERIMENTAL DEMONSTRATION AT MPP

The Frictional Cooling Demonstration (FCD) experiment at MPP is undertaking verification of the principal behind frictional cooling using protons, which are stable and more easily produced than muons.

Experiment Setup

We have constructed a basic cooling cell consisting of a Helium gas cell and a 10 cm long accelerating grid (Fig. 2). The aim of the experiment is to verify that protons starting from rest are accelerated up to an equilibrium energy. The proton source produces protons at rest at one end of accelerating grid. A Silicon Drift Detector (SDD) at the other end of the grid measures the energy of the protons.

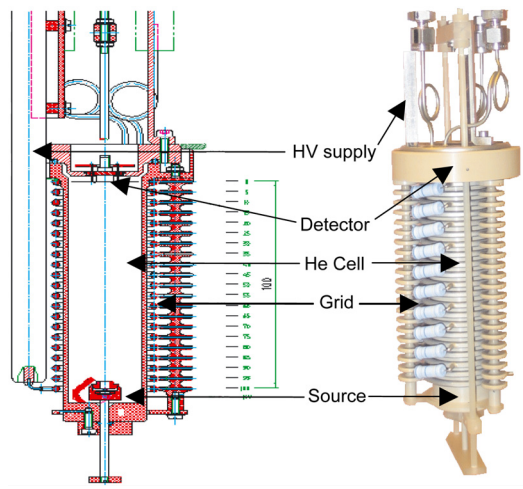

Figure 2: FCD experimental setup.

The Helium gas cell is a PEEK cylinder with two feedthroughs for flowing gas in and out. The flow rate is controled by an electronic valve to maintain a constant gas pressure in the cell. Both the detector and the source are inside the cell, so no windows are required.

The gas cell is mounted inside the accelerating grid. The grid consists of 21 metal rings connected in series by 64 MΩ resistors.The detector-side ring is grounded, and

* Now studying at Max Planck Institute for Physics, Munich, Germany, Email: baoyu@ihep.ac.cn

the source-side ring is connected to a high-voltage supply capable of providing up to 100 kV. Calculation of the electric field created by the accelerating grid shows that it is very uniform. The results of this calculation were implemented in the whole experiment simulation.

The proton source is contained inside the gas cell. It consists of an alpha source covered by a mylar foil. The alpha particles break the bonds between the Hydrogen and Carbon nuclei of the Mylar molecule, leaving the Hydrogen nuclei free to be accelerated out of the foil by the electric field. The thickness of the foil was chosen carefully according to the results of simulation of the source to maximize the proton production rate.

The SDD was built by the Max Planck Institute Semiconductor Laboratory. The detector can achieve an energy resolution of 500 eV at 5.9 keV at room temperature and better than 150 eV when the detector is cooled to −25 °C.

First Results

To verify the production of protons and characterize the detector's response to protons, we record the spectra of protons with no gas in the cell and with various strengths of the electric field.

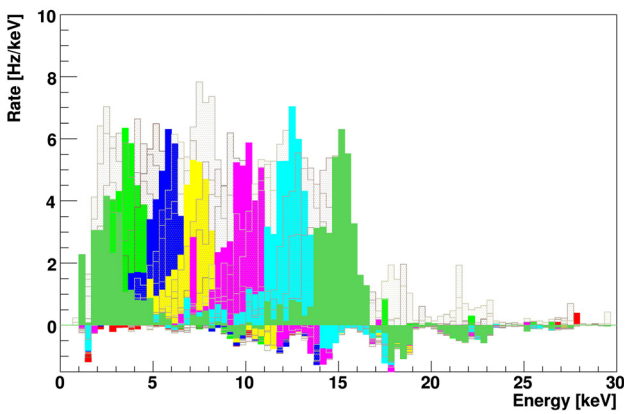

Figure 3: Energy spectra (with background x-rays subtracted) for strengths of the electric field from 10 kV/m to 300 kV/m in 10 kV/m steps (lines) with an evacuated gas cell. The six highlighted spectra are spaced 50 kV/m apart.

Figure 3 shows the energy spectra taken for strengths of the field from 10 kV/m to 300 kV/m, in 10 kV/m steps. The proton source was placed 80 mm from the detector, resulting in energies of 5.6 keV to 24 keV in 800 eV steps, however only a fraction of the energy of a proton is measured by the SDD. Figure 4 shows the mean energies of the spectra plotted as a function of the incoming energies of the protons. The incoming energy is taken from numerical calculation of the electric field. This data is used to characterize the dead layers of the detector and the detector's response to protons.

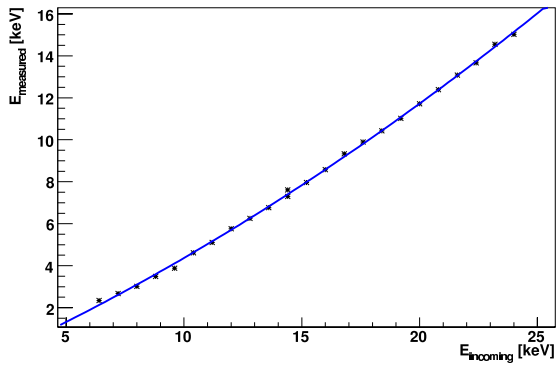

Figure 4: The mean energies of the proton spectra as a function of the incoming energy of the protons.

Status

The gas cell has been commissioned using gas together with high-voltage. The regions of stable operation for high-voltage and gas pressure have been determined. As a next step, proton spectra in various pressures of gas and various strengths of electric field will be taken. The resulting spectra will be compared to Monte-Carlo simulation.

MONTE-CARLO SIMULATION

We have developed a program called CoolSim [3] based on Geant4 [4], in which geometries can be implemented easily by a macro-command interface. We have added new low-energy physics processes to the Geant4 frame work such as Hydrogen formation for protons, Muonium formation for μ^+ and charge exchange interactions for both protons and μ^+.

For simulating frictional cooling, the G4hLowEnergyIonisation and G4MultipleScattering processes are instan-

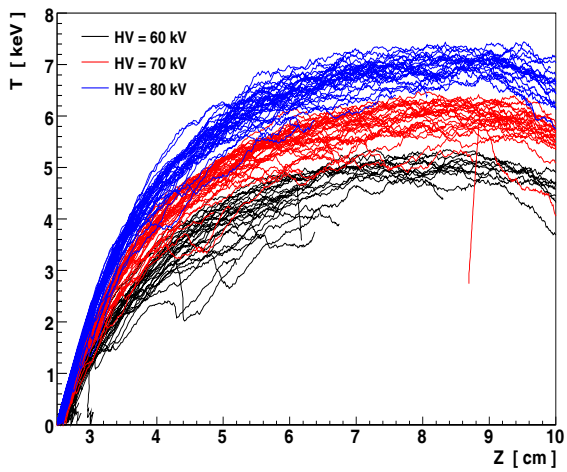

Figure 5: Kinetic energy versus depth in the gas cell for a few representative protons.

tiated in the physics list to determine energy loss and the spatial displacement.

Figure 5 shows the kinetic energies of protons as a function of the depth in the cooling cell for three different High-Voltages [5]. The kinks in the plot are due to sudden large losses of energy from large angle scattering off of gas nuclei.

The corresponding energy distributions at the detector are shown in Fig. 6 [5]. Multiple scattering causes the tail to lower energies in the distributions. The cross section for large angle scattering increases with decreasing particle energy. The mean kinetic energy increases with electric field strength. Therefore the low energy tail in the energy distributions diminishes and the survival rate increases with increasing electric field strength.

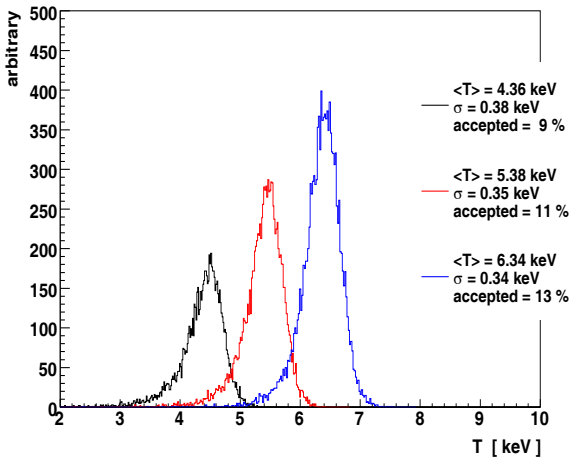

Figure 6: The energy distributions at the detector for three different strengths of the electric field: 600 kV/m (black), 700 kV/m (red), and 800 kV/m (blue)

Figure 7 is a summary of the simulation results under different conditions [5]. By varying the gas density and electric field strength in the experiment, we can vary the equilibrium energy protons attain. The experimental results will be used to test the simulation results.

FRICTIONAL COOLING FOR A LOW-ENERGY MUON BEAM

As an example use of frictional cooling, we consider producing a cold muon beam from a surface muon source. For the simulation, we take the input parameters to be those of the muon beam at the Paul Scherrer Institute (PSI), Switzerland, up to the point where the slow muons are produced [6]. We then compare the efficiency of our scheme to the current scheme at PSI.

The μ^+ Beam at PSI

The new μE4 beam line at PSI delivers the world's highest surface-μ^+ flux of 228×10^8 /mAs with a momentum of

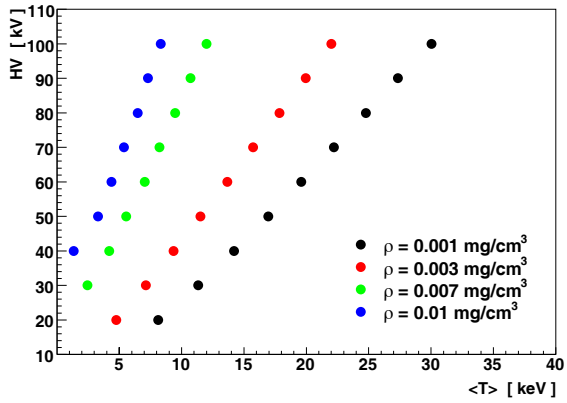

Figure 7: Simulation results: equilibrium energies for different high-voltages (E = HV/10 cm) and gas densities.

28 MeV/c and $\Delta p/p$ (FWHM) of 5.0–9.5%. It has a spatial divergence of x/x' (FWHM) of 6.5 cm/150 mrad and y/y' (FWHM) of 2.6 cm/300 mrad [6].

Cooling Scheme Based on Frictional Cooling

Figure 8 shows the layout of the proposed cooling scheme. Muons pass through a foil for an initial energy loss. The thickness of the foil is optimized to be 110 μm to increase the number of muons that can be cooled by the gas cell with the lowest possible electric potential. A 10 cm

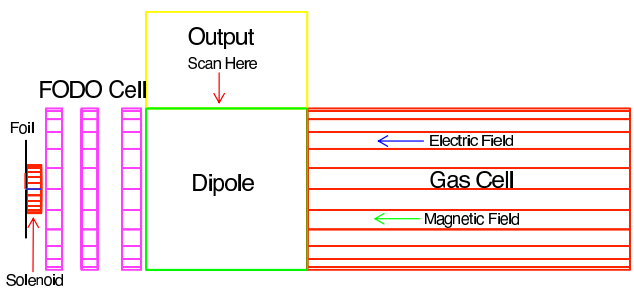

Figure 8: Outline of the scheme based on Frictional Cooling.

long solenoidal magnetic field with strength 1 T collects the muons after the foil. They then pass through a FODO cell to reduce the beam divergence.

After the quadrupoles, a weak dipole of 0.005 T will let the high-energy input beam get through unaffected.

The beam then enters a 2 meter long gas cell filled with Helium at a density of 0.01 mg/cm^3. An electric field of 1.8 MV/m in the opposite direction against the incoming beam is present. A Van de Graff generator may be needed to provide an electric potential of 3.6 MV. Discharge in the Helium gas caused by field configuration may be a serious issue and has to be investigated. The muons will spiral in the gas in a 1 T solenoidal magnetic field. They are slowed down by the gas and the electric field, and turned back by

the electric field with an equilibrium energy around several keV.

The cooled muons exit the gas cell and are turned into the output channel by the dipole. We scan the beam on the edge of the dipole as the output.

Figure 9 shows the longitudinal and transverse momentum distributions of the beam before entering the cooling scheme and after the FODO cell (but before entering the gas cell). It also shows the momentum distribution before entering the gas cell for the subset of the beam which can ultimately be cooled. Muons with transverse momenta

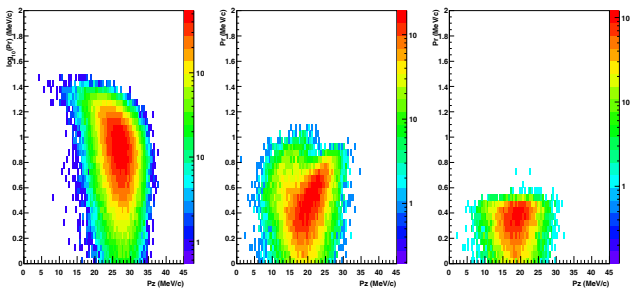

Figure 9: Transverse and longitudinal momentum of source (left), after the quadrupoles (middle) and those can be cooled (right).

greater than 3 MeV/c cannot be cooled because they are not in the coolable region of the stopping power curve (Fig. 1) when they turn around and begin to exit out of the gas cell; they will be accelerated to higher energies by the electric field. The FODO cell has been optimized to increase the number of muons with low transverse momentum.

Simulation Results

This scheme was simulated in the CoolSim program. Ideal fields without fringe fields were used. Figure 10 shows the input and output energy spectra. The energy spread is compressed from 734 keV to 0.263 keV with an efficiency of 5%. With different gas densities and electric field strength, we can attain different equilibrium energies from 1 keV to 8 keV.

The efficiency of this scheme based on frictional cooling is 2 to 3 orders of magnitude higher than that of the existing moderation method, which uses thin cryosolid layers to convert a surface-muon to a low energy μ^+ with an efficiency of 10^{-5} to 10^{-4} [7]. Simulation of a simplified scheme, which requires voltages of only 500 kV (attainable by a common high-voltage supply) and is without the FODO cell, still yields an efficiency of 0.5%.

CONCLUSION

The CoolSim simulations show that frictional cooling holds promise as a scheme for both high-energy accelerator beams, for use in a muon collider [8] or neutrino factory [9], and low-energy muon experiments [10]. In particular, frictional cooling could significantly improve the efficiency for producing slow muons. The FCD experiment is nearing the final data taking stage and hopes to verify the principle behind frictional cooling very soon.

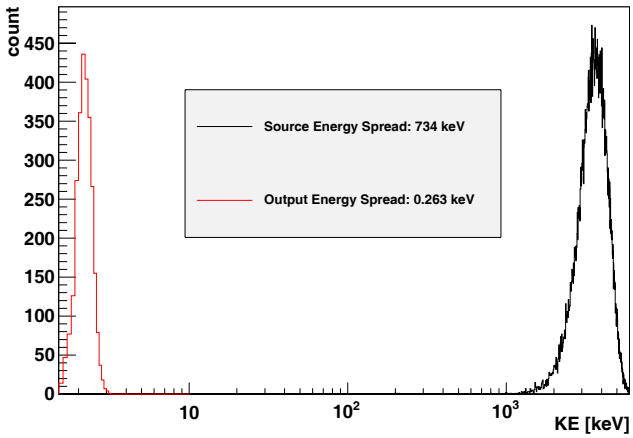

Figure 10: Output energy spectrum compared to the PSI's surface muon beam spectrum. The beam is cooled to 2.7 keV with a narrow spread of 0.263 keV.

REFERENCES

[1] M. Muhlbauer, et al., Nucl. Phys. Proc. Suppl. 51A (1996) 135.

[2] http://physics.nist.gov/PhysRefData/Star/Text/PSTAR.html

[3] http://wwwmu.mpp.mpg.de/coolsim

[4] Geant4 toolkit: http://geant4.cern.ch

[5] C. Blume, diploma thesis, Tech. University of Munich, Munich 2009, http://mpp.mpg.de/~cblume/fcdSimDoc/thesis.pdf

[6] T. Prokscha, et al., Nucl. Instr. and Meth. A 595 (2008) 317.

[7] T. K. Paraiso, et al, Physica B 374-375 (2006) 498.

[8] H. Abramowicz, A. Caldwell, R. Galea, S. Schlenstedt, Nucl. Instr. and Meth. A 546 (2005) 356.

[9] J. Aysto, et al., hep-ph/0109217v1 24 sep 2001.

[10] Pavel Bakule and Elvezio Morenzoni, Contemporary Physics, May-June 2004, Vol. 45, No. 3, 203.

SIX-DIMENSIONAL COOLING SIMULATIONS FOR THE MUON COLLIDER*

P. Snopok†, G. Hanson‡
University of California, Riverside, CA 92521, USA

Abstract

The two cooling channels based on the RFOFO ring concept are considered and simulated. One of them is the RFOFO helix, also known as the Guggenheim. The helical shape of the channel resolves the injection and extraction issues as well as the absorber overheating issue. The issue of the RF breakdown in the magnetic field is addressed in the so-called open cavity cooling channel lattice with magnetic coils in the irises of the RF cavities. The details of the tracking studies of both channels are presented and compared to the performance of the original RFOFO cooling ring design.

RFOFO COOLING RING

In a Muon Collider design the muon beam 6D phase space volume must be reduced several orders of magnitude in order to be able to further accelerate it. Ionization cooling is currently the only feasible option for cooling the beam within the muon lifetime ($\tau_0 = 2.19$ μs). The RFOFO ring [1, 2] is one of the feasible options currently under active investigation along with other designs [3, 4, 5]. The RFOFO ring provides a significant reduction in the six-dimensional emittance in a small number of turns with a relatively low particle loss factor. 6D cooling is achieved by employing the concept of emittance exchange. When a dispersive beam passes through a wedge absorber in such a way that higher momentum particles pass through more material, both the longitudinal and the transverse emittances are reduced. However, the design of the injection and extraction channels and kickers is very challenging for the RFOFO, and the ring could not be used as is, because the bunch train is too long to fit in the ring. Both problems would be removed in the RFOFO helix, also known as the Guggenheim channel [6]. In addition, using the helix solves another important issue, namely, the overheating in the absorbers.

The main parameters of the original RFOFO design are summarized in Table 1 and compared to the parameters of the Guggenheim channel. The layout of the RFOFO ring is shown in Fig. 1. The results of particle tracking through the RFOFO channel in the code G4Beamline [7] are used as the point of reference while comparing the RFOFO and Guggenheim channel efficiencies.

* Work supported by the United States Department of Energy under Grant No. DE-FG02-07ER41487.

† pavel.snopok@ucr.edu
‡ gail.hanson@ucr.edu

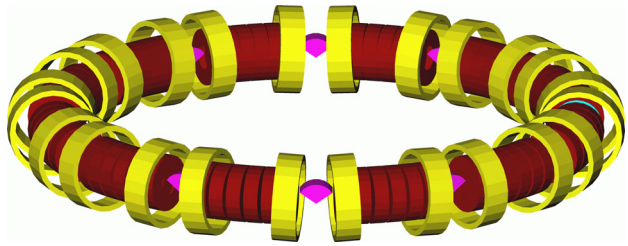

Figure 1: RFOFO ring layout. Yellow—tilted magnetic coils with alternating currents to provide necessary bending and focusing, and generate dispersion, purple—wedge absorbers for cooling and emittance exchange, brown—RF cavities for restoring the longitudinal component of the momentum.

Table 1: Parameters of the RFOFO Ring Compared to the Guggenheim Helix

		RFOFO	Guggenheim
RF frequency	[MHz]	201.25	201.25
RF gradient	[MV/m]	12.835	12.621
Maximum axial field	[T]	2.77	2.80
Pitch	[m]	0.00	3.00
Pitch angle	[deg]	0.00	5.22
Circumference	[m]	33.00	32.86
Radius	[m]	5.252	5.230
Coil tilt (wrt orbit)	[deg]	3.04	3.04
Average momentum	[MeV/c]	220	220
Reference momentum	[MeV/c]	201	201
Absorber angle	[deg]	110	110
Absorber vertical offset	[cm]	9.5	9.5
Absorber axial length	[cm]	27.13	27.13

GUGGENHEIM HELIX

The layout of the Guggenheim channel to a large extent repeats the one of the RFOFO ring, except for the three meters of separation between the layers of the helix. As a result, the circumference of the helix has to be slightly smaller than that of the ring to keep the arclength of one revolution intact.

Figure 2 shows the 5-turn layout which has been simulated. Along with the unshielded case with all the magnetic coils of all layers contributing to the magnetic field guiding muons, another scheme has been considered, with shielding between individual layers. Both layouts include safety windows around absorbers and Be windows in the RF cavities.

The simulation details can be found in [6]. Here we show only the six-dimensional emittance reduction (see Fig. 3), and the transmission (see Fig. 4) as functions of the num-

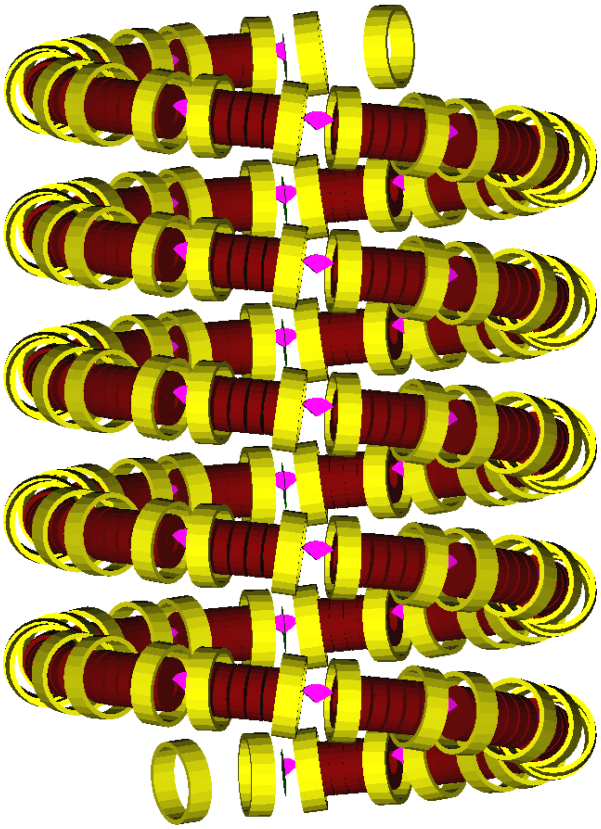

Figure 2: Multilayer Guggenheim channel layout. Color-coding is the same as for Fig. 1.

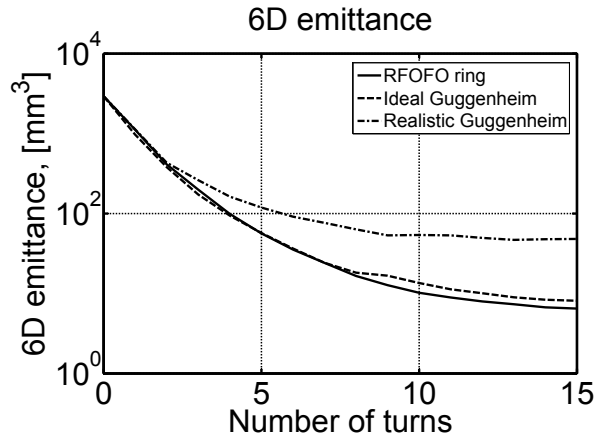

Figure 3: Six-dimensional emittance reduction vs number of turns.

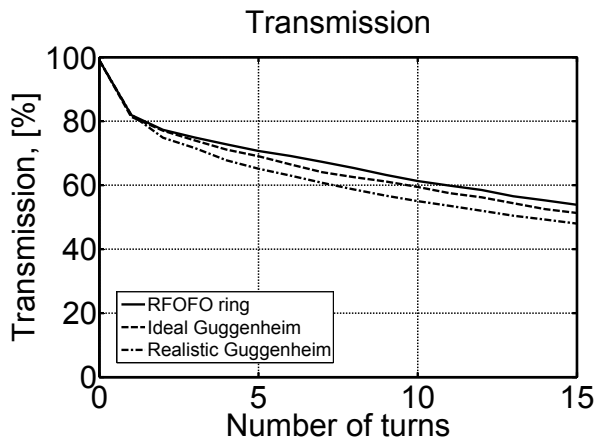

Figure 4: Transmission—percent of surviving muons vs number of turns.

ber of turns. The transmission is measured as the ratio of the number of particles at a certain arclength to the initial number of particles. The muon decay and stochastic processes are taken into account. The solid line is used for the RFOFO ring, which serves as a reference, the dashed line is the Guggenheim channel with shielding between layers and no windows in absorbers or RF cavities (the idealized Guggenheim, the performance of which should not differ significantly from the RFOFO ring, which is indeed the case), and the dash-dotted line is for the realistic Guggenheim with shielding between layers and windows in both absorbers and RF cavities.

Figure 3 clearly demonstrates significant six-dimensional cooling; however, the performance of the cooling channel is seriously affected by the use of absorber and RF windows. These results are in agreement with earlier studies for the RFOFO ring [1].

RF BREAKDOWN AND THE OPEN CAVITY LATTICE

Various studies suggest that the presence of the magnetic field disrupts the performance of RF cavities by causing breakdown [8, 9]. Thus, it was proposed to consider an alternative layout of the cooling channel, the so-called open cavity lattice [10]. The concept itself consists of two parts: a) moving the solenoidal coils from over the RF cavities into the irises; and b) shaping the RF cavities such that the walls of the cavities are predominantly parallel to the magnetic field lines (see Fig. 5), which hopefully solves the problem of the breakdown. Current layout illustrated in Figure 6 does not include specifically shaped RF cavities; instead a simplified pillbox geometry is used. If the layout is proven viable in terms of transmission and six-dimensional emittance reduction, the next step will be to import RF cavity shapes from Poisson/Superfish into G4Beamline for simulations.

The new cooling ring has 12 cells with three RF cavities in each and four solenoidal coils in the irises. These coils bear currents with the following densities: 63 A/mm^2, 45 A/mm^2, -45 A/mm^2, -63 A/mm^2.

The circumference of the ring is 30.72 meters. The idea of tipping the solenoids, similar to the RFOFO ring concept, is employed in this layout to generate an average vertical magnetic field of 0.136 T providing necessary bending. Solenoid axes are tilted 4.9° above or below the or-

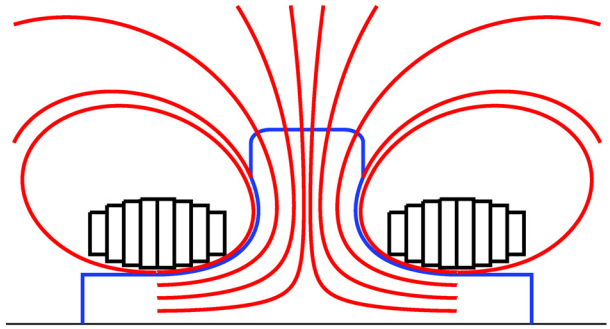

Figure 5: Open cavity shape. Black—coils generating the magnetic field, blue—walls of the RF cavity, red—magnetic field lines.

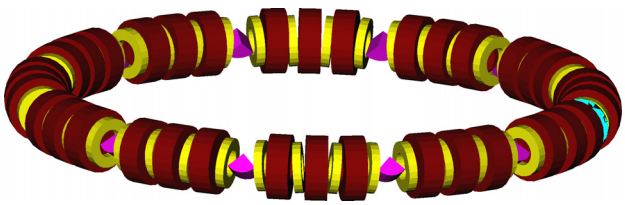

Figure 6: Open cavity layout, color-coding is the same as for Fig. 1.

bital midplane depending on the direction of the current. The centers of the solenoids are displaced radially outward from the reference circle by 21 mm to minimize the integrated on-axis radial field, thus, vertical beam deviations. This technique allows to save 2% of the beam that would be lost with no offset.

The fact that the solenoids are tilted leads to the reduction of the amount of space available for the RF system; hence, the energy gain per cell is limited, which, in turn, limits the angle of the wedge absorber to approximately 90° (compared to 110° in RFOFO).

Figures 7–9 illustrate the difference between field components for the original RFOFO design and the new design with coils in irises. Since there are four coils per cell, all field profiles have more complicated shapes; however, the overall magnitudes are similar.

The peak in the longitudinal field is still approximately 3 T; the radial component is more pronounced, but still small compared to both the vertical and the longitudinal components. The vertical component is everywhere positive providing an average bending field of 0.136 T.

The dispersion calculation (Fig. 10) shows that the dispersion at the absorber plane (beginning of the cell) is primarily in the vertical direction, at an angle of $\sim 20°$ from the vertical axis. This fact suggests the orientation of the absorbers. The dispersion in the the center of the cell is negative, again mainly in the vertical direction.

Preliminary simulations of the dynamics in the magnetic field with RF cavities and absorbers turned off show that the transmission (Fig. 11) is 90% with no decay and 65.4%

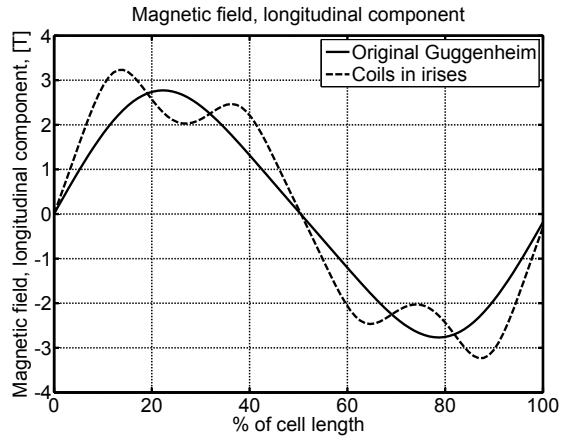

Figure 7: Longitudinal field component. Solid line—original RFOFO ring or Guggenheim helix lattice, dashed line—open cavity lattice.

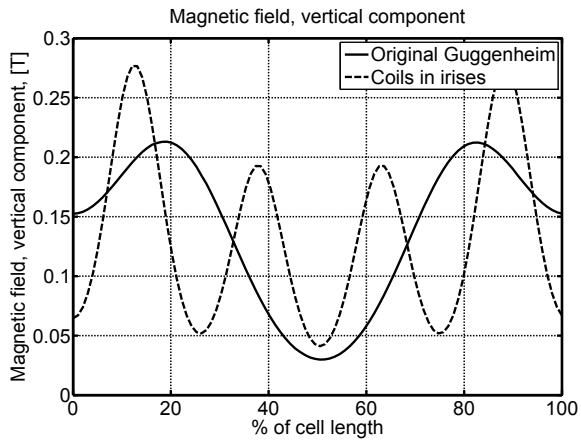

Figure 8: Vertical field component. Solid line—original RFOFO ring or Guggenheim helix lattice, dashed line—open cavity lattice.

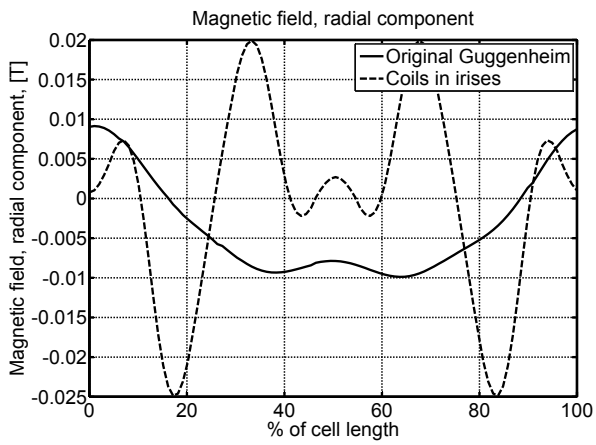

Figure 9: Radial field component. Solid line—original RFOFO ring or Guggenheim helix lattice, dashed line—open cavity lattice.

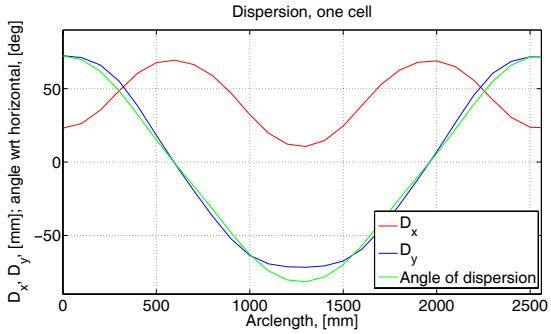

Figure 10: Dispersion plot. Red line—horizontal, blue line—vertical, green—orientation of dispersion with respect to the horizontal axis.

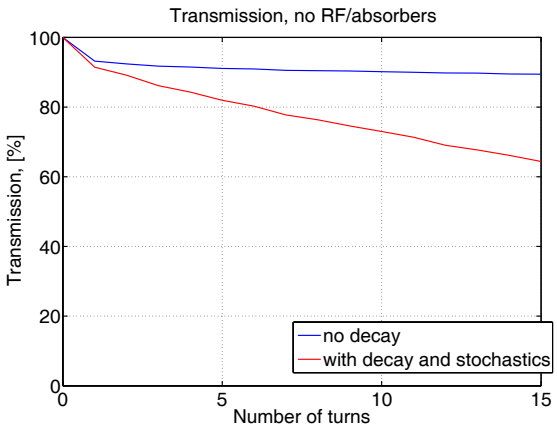

Figure 11: Transmission in the open cavity lattice with no RF and absorbers with decay and stochastics on and off.

with decay after 15 turns in the ring (461 m). These results are consistent with tracking results in the RFOFO ring or the Guggenheim helix with RF and absorbers turned off. However, the situation differs dramatically when absorbers and RF cavities are turned on. There is no conclusive statement on the overall performance of the open cavity lattice compared to the original RFOFO lattice so far. However, a number of ongoing studies suggest that the open cavity lattice is less efficient both in terms of transmission and the 6D cooling.

An alternative approach to using the open cavity or any other type of magnetically insulating lattice is to research the techniques allowing RF cavities withstand more magnetic field without breaking down. Such techniques include atomic layer deposition creating a thin layer of material on the cavity walls [11], high-pressure gas filled cavities [12], dielectric-loaded cavities [13], and using other materials such as Al or Be and low temperatures [14].

REFERENCES

[1] R. Palmer et al. Ionization cooling ring for muons. *Phys. Rev. ST Accel. Beams*, 8(6):061003, Jun 2005.

[2] J. S. Berg, R. C. Fernow, and R. B. Palmer. RFOFO ring cooler. *Journal of Physics G: Nuclear and Particle Physics*, 29:1657–1659, 2003. DOI: 10.1088/0954-3899/29/8/325.

[3] D. Kaplan. MANX: A 6D ionization cooling experiment. arXiv: 0711.1523v1, 2007.

[4] Y. Alexahin, K. Yonehara, and R. Palmer. 6D ionization cooling channel with resonant dispersion generation. In *Proceeding of Particle Accelerator Conference*, 2007.

[5] C. Johnstone, M. Berz, and K. Makino. Linear quadrupole cooling channel for a Neutrino Factory. In *Proceedings of Particle Accelerator Conference*, pages 3526–3529, 2005.

[6] P. Snopok, G. Hanson, and A. Klier. 6D simulations of the Guggenheim cooling channel for the Muon Collider. *IJMPA*, 24(5):987–998, 2009.

[7] T. Roberts. G4Beamline, a "swiss army knife" for Geant4, optimized for simulating beamlines. http://www.muonsinc.com.

[8] J. Norem et al. A model of RF breakdown arcs. Technical Report NFMCC-doc-527-v1, NFMCC, 2008.

[9] R. Palmer et al. RF breakdown with and without external magnetic fields. Technical Report NFMCC-doc-528-v2, NFMCC, 2008.

[10] R. Palmer et al. Cooling with magnetic insulation. presentation at the 2009 NFMCC collaboration meeting. http://www.cap.bnl.gov/mumu/conf/MC-090125/talks/RPalmer1-090125.pdf, 2009.

[11] J. Norem et al. Recent results from tests of atomic layer deposition (ALD) for superconducting RF. In *Proceeding of Particle Accelerator Conference*, 2009.

[12] M. Chung et al. Mitigation of plasma effects in high pressure RF cavity for ionization cooling. Technical Report NFMCC-doc-532-v2, NFMCC, 2009.

[13] M. Popovic, A. Moretti, and M. L. Neubauer. Dielectric loaded RF cavities. In *Proceeding of Particle Accelerator Conference*, 2009.

[14] R. Palmer et al. Material and temperature dependence in RF cavities. Presentation at the MuCool RF Workshop, 2009.

COMPENSATION OF MEAN ENERGY LOSS DUE TO AN INTERNAL TARGET BY APPLICATION OF A BARRIER BUCKET AND STOCHASTIC MOMENTUM COOLING AT COSY

H. Stockhorst, R. Stassen, D. Prasuhn and R. Maier (Forschungszentrum Jülich GmbH)
T. Katayama (Tokyo) and L. Thorndahl (Geneva)

Abstract

The High Energy Storage Ring (HESR) of the future International Facility for Antiproton and Ion Research (FAIR) at the GSI in Darmstadt will be built as an anti-proton cooler ring in the momentum range from 1.5 to 15 GeV/c. An important and challenging feature of the new facility is the combination of phase space cooled beams with internal targets. Theoretical investigations have demonstrated that the strong mean energy loss due to an internal target can not be compensated by cooling alone. A barrier bucket cavity can be used for mean energy loss compensation while cooling will reduce the momentum spread. Experimental results at COSY to compensate the large mean energy loss induced by an internal pellet target similar to that being used by the PANDA experiment at the HESR with a barrier bucket cavity (BB) will be presented. Experimental cooling results using the Time-Of-Flight (TOF) method are shown in comparison with Filter cooling. TOF cooling is found to be very effective to cool the momentum spread prior to Filter cooling. Main focus of attention is the presentation of the experimental results.

HESR BEAM REQUIREMENTS

The High-Energy Storage Ring (HESR) [1] of the future International Facility for Antiproton and Ion Research (FAIR) at the GSI in Darmstadt will be built as an antiproton cooler ring in the momentum range from 1.5 to 15 GeV/c. Two operational modes will be available for the users. A pellet target with a thickness of $4 \cdot 10^{15}$ atoms cm^{-2} provides the high luminosity mode (HL) with 10^{11} antiprotons yielding the required luminosity $2 \cdot 10^{32}$ cm^{-2} s^{-1}. The HL-mode has to be prepared in the whole energy range and beam cooling is needed to particularly compensate beam heating by the beam-target interaction. Much higher requirements have to be fulfilled in the high resolution mode (HR) with 10^{10} antiprotons. The same target thickness yields here the luminosity $2 \cdot 10^{31}$ cm^{-2} s^{-1}. This mode is requested up to 8.9 GeV/c with an rms-relative momentum spread down to about $4 \cdot 10^{-5}$.

Both, transverse and longitudinal cooling is foreseen at the HESR. Transverse cooling is mainly applied to compensate a transverse beam blow up due to the beam-target interaction. The highest demands are made on longitudinal cooling, especially in the HR-mode. To fulfil this goal the bandwidth of the cooling system will be increased from (2 – 4) GHz to (2 – 6) GHz in the final stage. High sensitive pickup/kicker structures are being developed and tested at COSY [2]. The filter cooling technique [3] is applied for longitudinal cooling in the momentum range above 3.8 GeV/c. Below 3.8 GeV/c the Time-Of-Flight momentum (TOF-) cooling technique [4] will be used.

MOMENTUM COOLING METHODS

In the Filter cooling method a pickup in sum mode measures the beam current and the discrimination of particles with different momentum deviations is obtained by inserting a notch filter in the signal path before it drives a kicker in sum mode. The advantage of this method is that Schottky particle noise is substantially suppressed in the centre of the particle momentum distribution. A severe restriction in the practical cooling bandwidth comes from mixing between pickup and kicker. Large mixing from pickup to kicker will reduce the maximum momentum spread that can be cooled for a given upper cooling frequency without particle losses. Strong unwanted mixing from pickup to kicker especially prevents filter cooling below 3.8 GeV/c in the HL-mode. In the low momentum range 1.5 GeV/c up to 3.8 GeV/c TOF cooling is therefore envisaged. In this method the filter in the cooling chain is removed and the signal transit time from pickup to kicker is adjusted to the time-of-flight of a particle with nominal momentum. Mixing from pickup to kicker can now be used to discriminate between particles of different momenta. This method attains a larger cooling acceptance which is especially preferable for the HL-mode. Larger initial momenta can thus be cooled without particles losses. The main disadvantage of this method is however that due to the absence of the notch filter strong particle noise diffusion occurs in the distribution centre. The gain of the cooling system should be then reduced to avoid too much Schottky heating in the center of the distribution. Beam equilibrium values are consequently larger as for filter cooling.

MOMENTUM COOLING EXPERIMENTS

At COSY momentum as well as transverse cooling is available. The system consists of two bands. Band I covers the frequency range (1 – 1.8) GHz and band II the range (1.8 – 3) GHz. The pickup and kicker electrode bars are movable to achieve a maximum in sensitivity. In these experiments only momentum cooling in band II is considered. The proton beam was accelerated to 2.6 GeV/c. To avoid transition crossing during acceleration the optics in the arcs is manipulated so that the transition energy is shifted upwards. When the flat top momentum is reached the acceleration rf-cavity is switched off and the optics is changed again so that now

the machine is operated above transition energy. By this both straight sections of COSY attain zero dispersion. The pellet target of the WASA installation [5] is located at a dispersion free position in the target straight section. A flat top time of about 1000 was chosen and the particle number was about 1 to 2 $\cdot 10^9$.

TOF and Filter Cooling

Beam transfer function measurements have been carried out to optimize the gain and the delay of the momentum cooling system when the internal target was switched off and no cavity was operated. An example of an open loop gain measurement at harmonic number n = 1367 is shown in figure 1 for TOF-cooling operation.

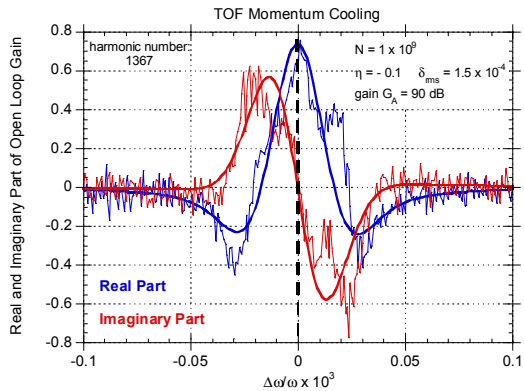

Figure 1: Open loop gain at n = 1367 for TOF cooling.

The imaginary part has a zero crossing and negative slope as desired for cooling. The real part is not zero as compared to filter cooling [6]. As a consequence Schottky noise heating is not suppressed in the center of the distribution. In comparison to the measurement a simulation result from a Fokker-Planck equation model [7] is shown in good agreement.

In order to benefit from TOF cooling the initial momentum spread of the beam was then increased from $\delta_{rms} = (\Delta p / p)_{rms} \approx 1 \cdot 10^{-4}$ to $\delta_{rms} = 1 \cdot 10^{-3}$ by applying band-limited white noise ($\Delta W = 500\,Hz$) at harmonic number one with a momentum kicker. The nearly rectangular beam distribution was cooled with the TOF cooling method as depicted in figure 2. The figure shows the initial particle density at harmonic number 1000 as well as at time t = 200 s and 900 s where the beam is close to equilibrium. It is visible that the initially unsymmetrical distribution became more symmetric when the cooling time proceeded. The variance of the distributions exhibits an exponential decrease towards an equilibrium value $\sigma^2 = 805\,kHz^2$. A relative momentum spread $\delta_{rms} \approx 1 \cdot 10^{-4}$ is deduced with the measured frequency slip factor $\eta = 1/\gamma^2 - 1/\gamma_{tr}^2 = -0.1$.

In the above measurements the delay was adjusted so that the beam could be kept nearly at the center of the initial distribution. The measurements showed that a delay length change of 7.5 mm (≈ 30 ps delay change) resulted in a negative shift of the center of the equilibrium distribution of -150 kHz corresponding to the negative frequency slip factor.

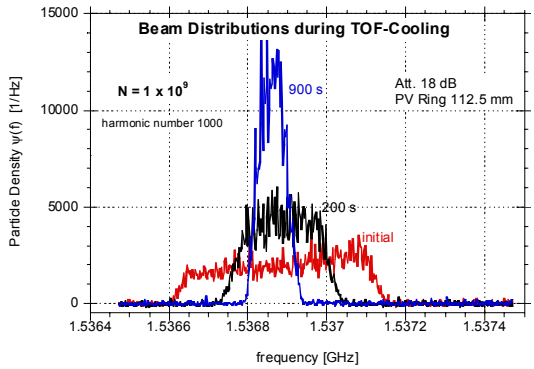

Figure 2: Particle densities at n = 1000 during TOF cooling.

In accordance to theoretical predictions this shift turned out to be linear in a delay change. This method allows to adjust the beam momentum in a range of $\delta \approx 1 \cdot 10^{-3}$.

In the next experiments the beam was initially heated by applying band-limited white noise with $\Delta W = 700\,Hz$ at harmonic number one in order to show the larger cooling momentum acceptance of TOF cooling as compared to Filter cooling. In figure 3 the result of only Filter cooling is displayed. After 200 s the distribution is cooled but exhibit still tails towards lower and higher frequencies. This indicates that Filter cooling is more effective in the center. Particles with lower or higher frequencies in the tails see a wrong sign in the cooling force and are driven further out of the center.

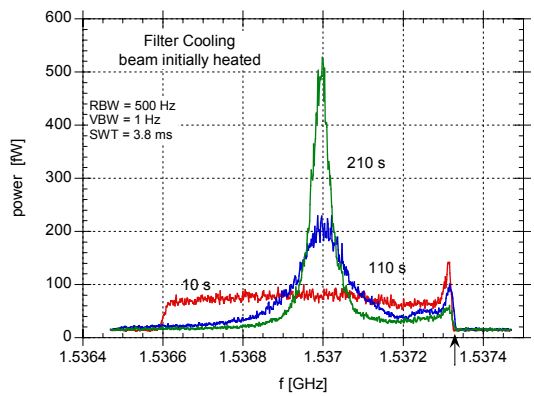

Figure 3: Filter cooling of an initially heated beam.

As a result a part (28 %) of the beam particles in the tails is heated by the cooling system and is lost at the momentum acceptance of the machine.

At 1.53734 GHz a small peak (see arrow in figure 3) is visible which is due to a vanishing local frequency slip factor. The available particle frequency attains here a maximum value. Particles which loose energy due to the heating can not have frequencies beyond that value. They enhance the density in the vicinity of this value leading to

asymmetric distributions. As seen in figure 3 the tails are reduced by cooling and heating as time proceeds.

In order to avoid initial particles losses the beam was pre-cooled with the TOF method for 200 s. After pre-cooling the cooling system was switched to Filter cooling: The Filter part that contains the delay by one revolution was closed and the gain was inverted.

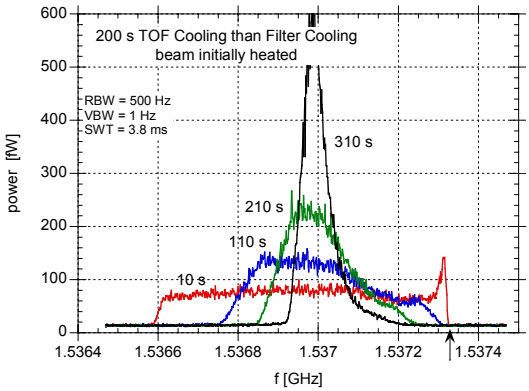

Figure 4: Power spectra at n = 1000 during cooling. The beam is pre-cooled with TOF cooling for 200 s. Cooling is then switched to the Filter cooling method.

The result is shown in figure 4 where one observes that the tails are reduced by only cooling. Particles are moved to the center during pre-cooling (t = 210 s). Also the particle enhancement at the small peak is reduced by TOF cooling. In this case almost no particle losses were observed. The final relative momentum spread after 900 s of cooling was $1 \cdot 10^{-4}$ (FWHM).

Filter Cooling with Synchrotron Motion

Theoretical predictions [7] have shown that the mean energy loss due to the beam-target interaction can be compensated by a barrier bucket cavity. Experimental tests of stochastic momentum cooling of particles subject to the synchrotron motion induced by a barrier bucket [2] or h = 1 cavity have been therefore carried out. Figure 5 compares from top to bottom Filter cooling without synchrotron motion and cooling with a barrier bucket cavity and the h = 1 cavity operation.

The maximum available barrier bucket peak voltage $U_0 = 175\,\mathrm{V}$ was used. The h = 1 cavity was operated with $U_0 = 200\,\mathrm{V}$. The target was switched off for this study. Figure 5a shows Filter cooling of the initially not heated beam. A significant cooling is visible after 310 s. The filter frequency is slightly above the initial center frequency. The influence of the synchrotron motion of the protons in a barrier potential becomes visible in figure 5b. After 310 s the beam width is reduced by cooling. The resulting width is however broader as compared to only Filter cooling in figure 5a. While in figure 5a the filter determines the center of gravity of the distribution it is determined by the barrier frequency.

Momentum cooling becomes less effective with synchrotron motion induced by the h = 1 cavity. Particle losses occur and the momentum spread is only slightly reduced (figure 5c).

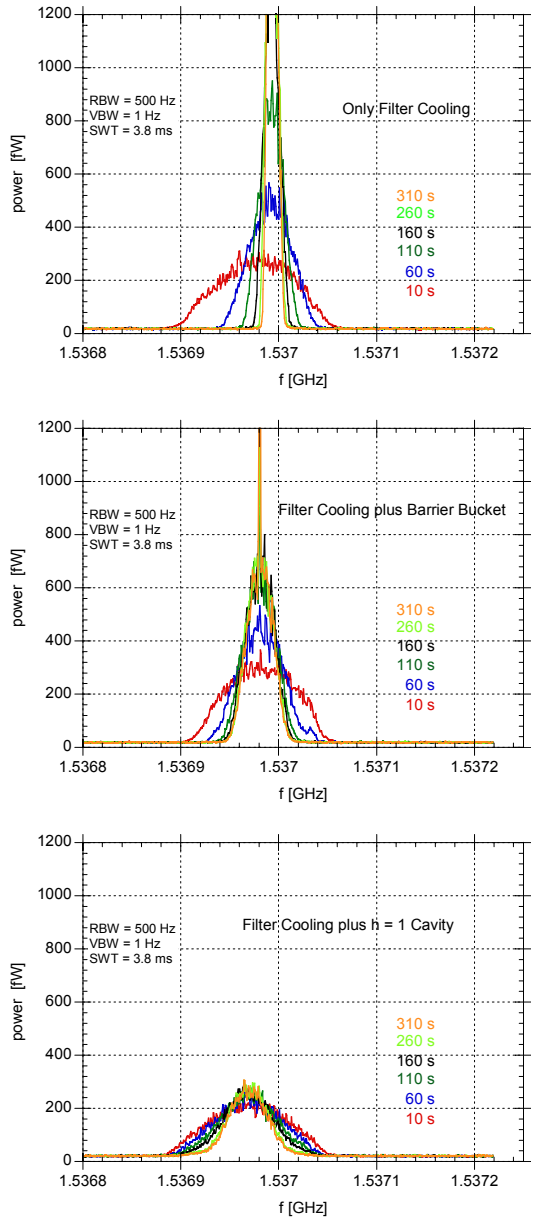

Figure 5: Filter cooling without/with synchrotron motion.

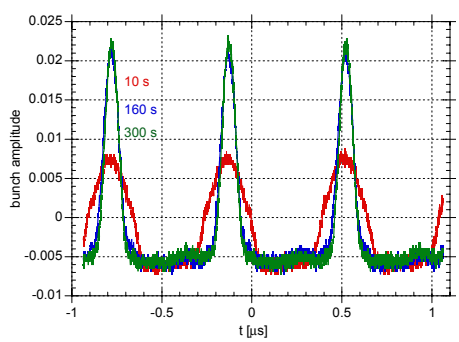

Figure 6: Bunch evolution during Filter cooling.

While in the barrier bucket case the bunch is nearly DC the beam is bunched when the h = 1 cavity is operated. The bunches become shorter during cooling (figure 6).

Mean Energy Loss Compensation

First the mean energy loss in the pellet deuterium target of the WASA installation [5] has been deduced by measuring the linear time dependence of the frequency shift of the spectral Schottky line at n = 1000. The mean energy loss ΔE is determined from a measurement of the linear frequency shift per unit time and the frequency slip factor $\eta = 1/\gamma^2 - \alpha$: ΔE ≈ -12 meV/turn. The effective target thickness is then calculated with the Bethe-Bloch formula yielding $N_T \approx 2 \cdot 10^{15} \text{atoms/cm}^2$. The target thickness is thus comparable to that in the PANDA experiment at the HESR. The cooling result is displayed in figure 7. The target is switched on at t = 14 s. The barrier extends from 1.53692 GHz to 1.537015 GHz. It is seen that at t = 10 s a fraction of 29 % of the particles visible as a hump are outside the barrier. At t = 110 s this hump becomes smaller and is moved closer to the center. At the same time the density in the barrier is increased (figure 8) and the width of the distribution is reduced by cooling. For t > 300 s the peak density attains a maximum for a while and then drops down. The maximum is reached when the particle losses start to become stronger than the increase in peak density due to cooling, figure 8. Figure 7 shows that the particles losses can only be due to a transverse emittance increase caused by the beam-target interaction. Particle losses in the longitudinal phase space would be visible in a similar enhancement of particles as in figure 3 at frequency 1.5374 GHz, see arrow in figure 7. Note that the center of gravity of the distributions keeps the same which means that the mean energy loss is compensated.

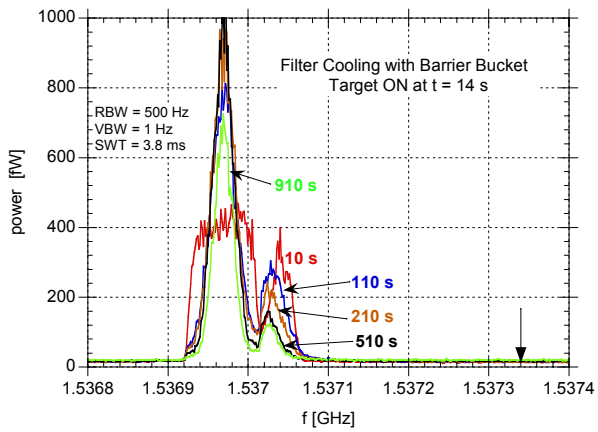

Figure 7: Power spectra at n = 1000 during Filter momentum cooling and barrier bucket operation. The pellet target is switched ON at t = 14 s.

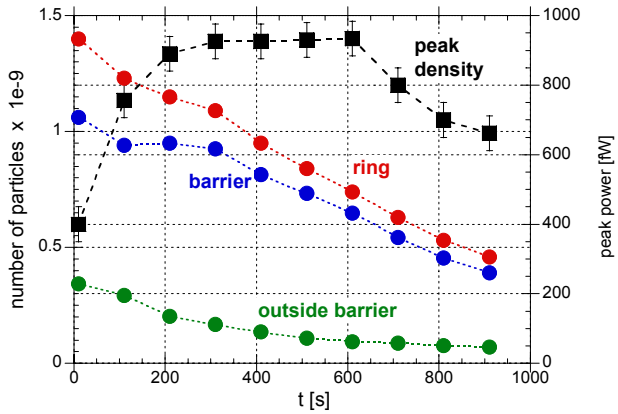

Figure 8: Peak power of particles in the barrier, number of totally stored particles and stored particles in as well as outside the barrier region during cooling.

SUMMARY AND OUTLOOK

The experiments have verified that the TOF cooling method as theoretically predicted is feasible and can be successfully applied to reduce the initial momentum spread for Filter cooling. The Filter or TOF technique for a proton beam with synchrotron motion induced either by a barrier or a h = 1 cavity has been investigated experimentally. Cooling with a barrier bucket turned out to be more efficient since the beam is similar to a DC-beam. The barrier bucket cavity was applied to compensate the mean energy loss induced by the WASA pellet target with a thickness comparable to that in the PANDA experiment at the HESR. The beam momentum spread could be cooled but particle losses probably caused by a transverse emittance increase reduced the life time of the beam. Further experimental and theoretical investigations are necessary to gain experience and to determine the optimal barrier voltage and cooling system quantities.

REFERENCES

[1] HESR, “Baseline Technical Report”, http://www.fz-juelich.de/ikp/hesr/2-11-HESR.pdf, and update April 2008

[2] R. Stassen et al., “COSY as Ideal Test Facility for HESR RF and Stochastic Cooling Hardware”, PAC09, Vancouver, Canada, May 4-8, 2009

[3] D. Möhl et al., Phys. Rep. Vol. 58, No.2, Feb. 1980

[4] W. Kells, “Filterless Fast Momentum Cooling”, Proc. of the 11th Int. Conf. on High-Energy Accelerators, Geneva, Switzerland, July 7-11, 1980, p. 777

[5] C. Ekstroem et al., Nucl. Instrum. Meth. Phys. Res. A 371, 572-574 (1996)

[6] J. M. Brennan et al., “Bunched Beam Stochastic Cooling at RHIC”, COOL07, Bad Kreuznach, Germany, Sept. 10-14, 2007, p. 25

[7] H. Stockhorst et al., “Stochastic Cooling for the HESR at the FAIR Facility”, PAC09, Vancouver, Canada, May 4-8, 2009

PARTICLE ACCUMULATION USING BARRIER BUCKET RF SYSTEM

D. Krestnikov, I. Meshkov, R. Pivin, A. Sidorin, A. Smirnov#, JINR, Dubna, Russia
C.Dimopoulou, G.Schreiber, M.Steck, GSI, Darmstadt, Germany.

Abstract

Using of the RF burrier bucket system for the accumulation process was proposed for a few accelerator projects (FAIR, NICA). This rather new idea can bring new advantages to the accelerator physics. The principle possibility of this accumulation method with moving and stationary barrier bucket in the presence of the electron cooling was successfully demonstrated in the ESR storage ring last year. The article presents results of the numerical simulation and comparison with the experimental data. The aim of this work is an investigation of the accumulation process and optimization of the parameters of the cooling and barrier bucket systems. The numerical simulation of the accumulation process with barrier bucket systems for the ESR and NESR storage rings was done with BETACOOL code.

INTRODUCTION

One of the main goals of barrier buckets application at the New Experimental Storage Ring (NESR) of the FAIR project is to reach the high intensity of RIBs required by the internal experiments in the NESR and in particular by the electron-ion collider [1]. It is planned to stack the RIBs longitudinally at injection energy i.e. in the range 100-740 MeV/u. The stacking will be supported by electron cooling.

The Nuclotron-based Ion Collider fAcility (NICA) is a new accelerator complex being constructed at JINR aimed to provide collider experiments with heavy ions in the energy range from 1 to 4.5 GeV/u. To provide designed average luminosity of the order of 10^{27}cm^{-2}s^{-1} one needs to store in each ring of the collider of about $2\cdot10^{10}$ ions [2]. Injection chain of the collider permits to accelerate a single heavy ion bunch at intensity of the order of 10^9 particles. More attractive scheme of the beam storage in the collider ring relates to barrier buckets application and stacking under support by stochastic cooling system.

Presently two general schemes of the particle accumulation are discussed: with moving or with fixed barrier RF bucket.

In the scheme with moving barrier RF bucket (which is effectively used, for instance, in Fermilab's Recycler) the ion bunch is injected in the longitudinal gap prepared by two barrier pulses. The injected beam becomes coasting after switching off the barrier voltages and merges with the previously stacked beam. After the momentum spread is well cooled by electron or stochastic cooling, the barrier voltages are switched on and moved away from each other to prepare the empty space for the next beam injection. This process is repeated to attain the required intensity.

In the fixed barrier bucket scheme, one prepares a stationary (fixed in phase) voltage distribution consisting of two barrier pulses of opposite sign. The resulting stretched rf potential separates the longitudinal phase space into a stable and an unstable region. After injection onto the unstable region (potential maximum), the particles circulate along all phases and cooling application leads to their capture in the stable region of the phase space (potential well). After some time of the beam cooling the unstable region is free for a next injection without losing of the stored beam.

In an ideal case the maximum intensity of the stored beam is limited by intrabeam scattering (IBS) process. In equilibrium between IBS and cooling the stack momentum spread increases with increase of the stored particle number. When the momentum spread becomes to be larger than the barrier height the particles from the stack can penetrate into the injection region where they are killed by injection kicker pulse. The stacking efficiency depends on relation between injection repetition period and cooling time. In the real life the stacking efficiency can be seriously restricted by quality of the injection kicker pulse and imperfection of the barrier voltage pulse shape.

To investigate the stacking efficiency of the storage process both schemes (with moving and fixed barrier buckets) were experimentally tested at ESR with electron cooling of the ion beam [3]. The experimental results were used for benchmarking of computer codes developed for design of new storage rings. One of them, dedicated to simulation of the particle accumulation with barrier RF bucket at FAIR rings was developed in [4]. To compare predictions of different models new algorithms were implemented into BETACOOL program also [5]. In this article we discuss the results of the BETACOOL simulations.

PARTICLE ACCUMULATION WITH FIXED BARRIER BUCKET

Experiments with fixed burrier buckets were performed at beam and cooler parameters listed in the Table 1. Electron beam current was varied from 150 to 300 mA, injection repetition period t_{inj} was 3, 5 or 8 s. The revolution period of about 700 ns was separated by two sinusoidal burrier pulses into a stable region of duration of about 100 ns and unstable one, where the injection was taking place. For simplicity, the stacking process was simulated in BETACOOL with rectangular shape of the barrier pulses shown in Fig. 1 by red line.

#smirnov@jinr.ru

Table 1: Parameters of the ESR Experiments

Ion kind	$^{124}Xe^{54+}$
Particle number	10^7 / injection
Energy	154,4 MeV/u
Circumference	108.5 m
Initial momentum spread	5×10^{-4}
Initial hor./vert. emittance	0,7 mm mrad
RF voltage	120 V
Electron cooler length	1.8 m
Electron beam radius	2.5 cm
Effective electron temperature	10^{-3} eV
Cooler magnetic field	0.08 T
Beta functions in cooler hor./vert.	16 / 7 m

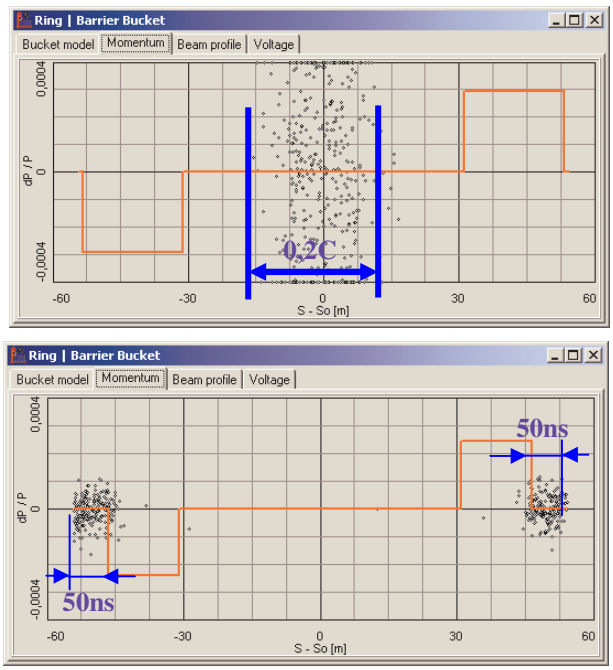

Figure 1: Particle positions in the longitudinal phase space. a) initial injection (0.2 C – means 20% of Circumference), b) after cooling.

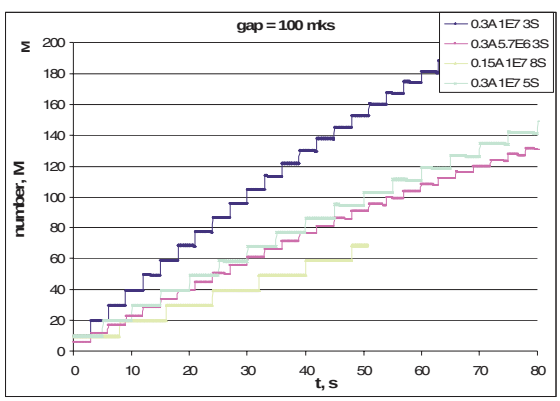

Figure 2: Stacking in 100 ns gap
a) I_e = 0.3 A, N_i = 1,0×10^7 , t_{inj} = 3 s;
b) I_e = 0.3 A, N_i = 5,7×10^6 , t_{inj} = 3 s;
c) I_e = 0.15 A, N_i = 1,0×10^7 , t_{inj} = 8 s;
d) I_e = 0.3 A, N_i = 1,0×10^7 , t_{inj} = 5 s;

The simulation show that the stacking rate is scaled with the intensity of the injection pulse at fixed injection repetition period (Fig. 2) and almost independent on the electron beam current. The last result follows to the fact that even the period of 3 s is sufficient for cooling of the injected beam. The ion life time was restricted by interaction with residual gas and approximately equal to 1000 s. At such conditions the stacking efficiency was closed to 100% up to the stack intensity of about 10^9 particles. So, the simulations demonstrate good capability of the stacking scheme for effective storage of intensive ion beams.

COMPARISON WITH EXPERIMETS

In the experiments at ESR the stack intensity saturated after a few tens of injections at the level of 10^8 particles (Fig.3). So large difference between simulations and experimental results can be explained by peculiarities of technical realization of the stacking scheme.

First of all, the kicker field does not equal zero after completion of the injection, but it oscillates with sufficient amplitude during a few ns. The kicker field distorts the stacked beam and leads to loss of the stored ions.

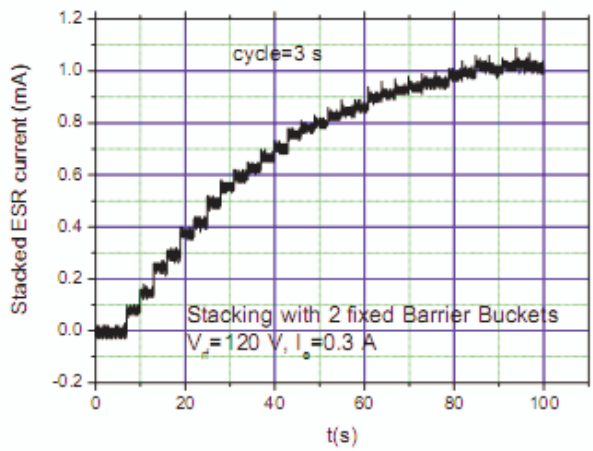

Figure 3: Example of the stacking process in experiment.

The stacking life time measured by switching off the injection and repeated kicker pulses was about 50 – 60 s. Simulation results of accumulation process with the lifetimes of 1000 and 50 sec are presented on Fig. 4. Red curve corresponds to experimental lifetime value and can be described by equation

$$N(t) = \frac{N_{inj}}{T_{inj}} \tau_{life} \left(1 - e^{-\frac{t}{\tau_{life}}} \right) \qquad (1)$$

In the case of τ_{life} = 50 sec the Formula (1) well reproduce the experimental dependence of the particle number on time during accumulation process. It means that in the experiments the particle losses are determined by the kicker pulse quality.

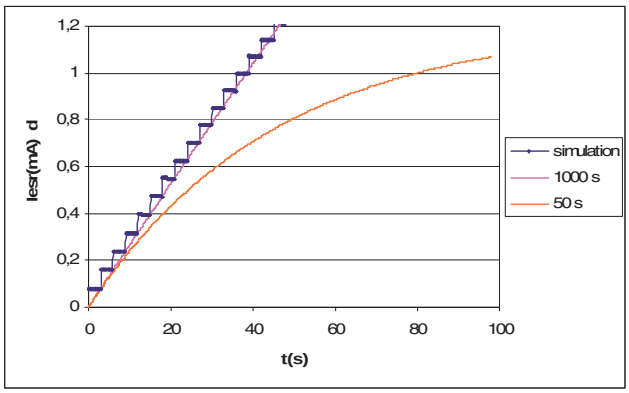

Figure 4: Simulation of the stacking process at different beam life time.

STACKING IN PRESENCE OF PARASITIC POTENTIAL WELL

Another possible limitation of the stacking efficiency relates to the shape of the burrier voltage pulse. In the experiment the imperfection of the barrier pulse formed a parasitic potential well in the injection region. The particles trapped in this well are lost at new injection. To investigate this effect the stacking process was simulated at the RF shape shown in the Fig. 5, the corresponding RF potential is shown in the Fig. 6.

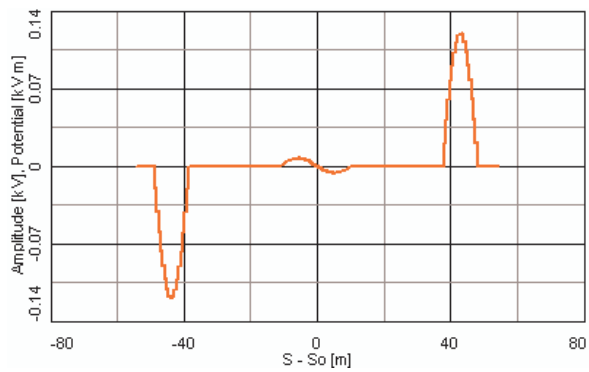

Figure 5: Barrier pulse shape with parasitic potential well with amplitude 7 V.

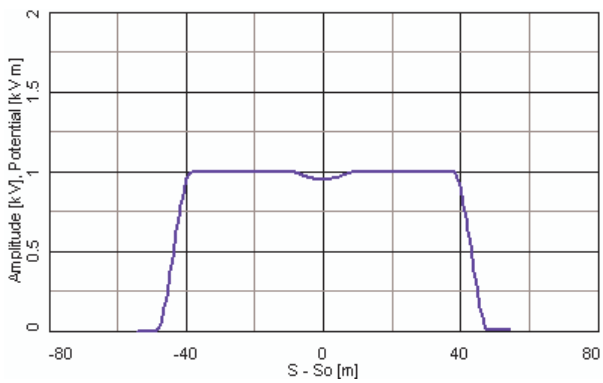

Figure 6: The potential distributions with additional potential well in the injection region.

The losses during new injection of the particles trapped in this additional well lead to 60% decrease of the stack intensity after completion of the accumulation process (Fig. 7). However, the situation can be improved by small shift of the electron energy. In this case the electron cooling removes the particles from the additional well and the stacking efficiency is not less than for an ideal barrier pulse shape.

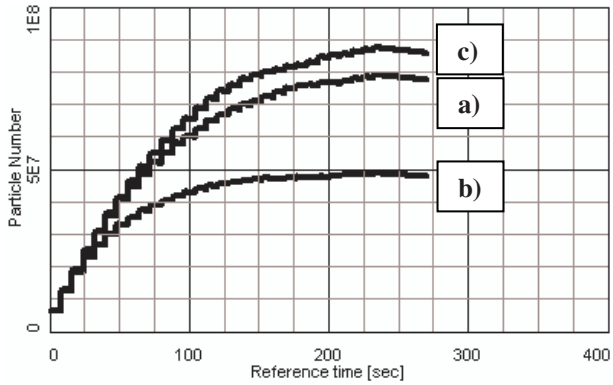

Figure 7: The stacking process without additional potential well (a), with the additional well (b) and tuned electron energy (c), with the potential well and electron momentum shifted by $\Delta p/p = 5\times10^{-5}$. Injection pulse intensity is $6{,}5\times10^{6}$ ions, interval between injections is 8 s.

SIMULATIONS FOR NESR

Stacking of RIBs in the NESR using fixed barrier buckets was simulated for Sn isotope (Table 2). The longitudinal phase space was divided by equal parts with help of two barrier pulses of half-sinusoidal shape.

Table 2: NESR Parameters

Ion kind	$^{132}Sn^{50+}$
Particle number/ injection	$1{,}0\times10^{8}$
Energy	740 MeV/u
Circumference	222.8 m
Initial momentum spread	$6{,}5\times10^{-4}$
Initial hor./vert. emittance	0,125 mm mrad
RF voltage	2000 V
Interval between injection	2 sec
Electron cooler length	5 m
Electron beam current	1 A
Electron beam radius	0.5 cm
Effective electron temperature (Parkhomchuk's formula)	10^{-3} eV
Cooler magnetic field	0.2 T
Beta functions in cooler hor./vert.	10 / 22 m

The stacking process develops at constant time constant up to about $3.6\cdot10^{9}$ ions. At this intensity the beam momentum spread reaches the barrier height and IBS pushes the ions to unstable region, where injections are performed. After that the intensity of the stacked beam tends to saturation (Fig. 8).

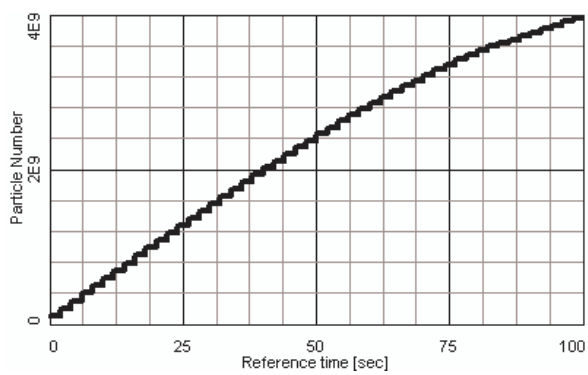

Figure 8: Storage process in NESR with fixed barrier buckets.

At the same conditions the stacking process with moving barrier buckets of rectangular shape was simulated. The stacking efficiency in this case is slightly less than with fixed one. It does not relate to IBS process and can be explained by technical realization of the stacking process. When the coasting stack circulates in the ring and the barrier voltages are switched on in order to prepare free space for a new injection, some part of the beam is trapped in a stable region between the pulses (Fig. 9). When the pulses are moved away from each other to prepare the empty space these particles oscillate between the pulses and part of them is lost at the new injection. For the pulse shape shown in the Fig.9 the stack intensity saturates at the level of about $8 \cdot 10^8$ particles.

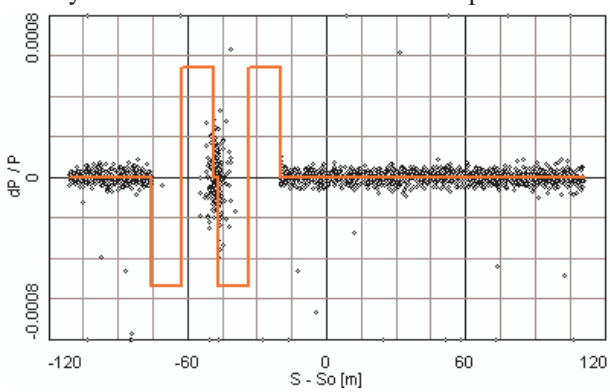

Figure 9: Particle distribution in the longitudinal phase plane after switching on the barrier voltage.

The stacking efficiency can be improved by accurate optimization of the barrier pulse shape and the simulations show that it can reach almost the same level as at fixed buckets.

CONCLUSIONS

Simulations and experiments showed high efficiency of a beam stacking using the barrier bucket technique. Further investigation of the stacking procedure using the RF barrier bucket method is related to the improvement of the BETACOOL code, new experiments at ESR, numerical simulation of the experimental results and optimization of the accumulation process for NESR. Simulations of the ion stacking in the NICA collider are in progress now.

REFERENCES

[1] FAIR Baseline Technical Design Report, GSI (2006). http://www.gsi.de/fair/reports/.

[2] NICA Conceptual Design Report, http://nucloserv.jinr.ru/nica_webpage/Nica_files/reports/CDR_07/

[3] C. Dimopoulou, B. Franzke, T. Katayama, F. Nolden, G. Schreiber, M. Steck, D. Moehl, Experimental Demonstration of Longitudinal Ion Beam Accumulation with Electron Cooling, Proceedings of EPAC08, Genoa, Italy

[4] T. Katayama, C. Dimopoulou, B. Franzke, M. Steck, D. Moehl, T. Kikuchi, Simulation Study of Ion beam Accumulation with Moving Barrier Bucket and Electron Cooling, Proceedings of COOL 2007, Bad Kreuznach, Germany

[5] A. Smirnov, A. Sidorin, D. Krestnikov, R. Pivin, Simulation Study of Stable and Moving Barrier Buckets Using Betacool Code, Proceedings of RuPAC 2008, Zvenigorod, Russia

STATUS OF THE INTERNATIONAL MUON IONIZATION COOLING EXPERIMENT*

Derun Li#, Lawrence Berkeley National Laboratory, Berkeley, California 94720, U.S.A.

Abstract

Muon ionization cooling provides the only practical solution to prepare high brilliance beams necessary for a neutrino factory or muon colliders. The **m**uon **i**onization **c**ooling **e**xperiment (MICE) is currently under development at the Rutherford Appleton Laboratory in UK. The experiment comprises a dedicated beam line to generate a range of input emittance and momentum of a muon beam, with time-of-flight and Cherenkov detectors to ensure a pure muon beam. A first measurement of emittance is performed in the upstream magnetic spectrometer with a scintillating fiber tracker. A cooling section will then follow, alternating energy loss in liquid hydrogen and RF acceleration. A second spectrometer identical to the first one and a particle identification system provide a measurement of the outgoing emittance. In September 2009, it is expected that the beam and some detectors will be in the final commissioning phase and the time of the first measurement of input beam emittance only months away. The plan of steps of measurements of emittance and cooling that will follow in the rest of 2009 and later.

INTRODUCTION

Neutrino **f**actory (NF) and **m**uon **c**ollider (MC) offer high potential physics opportunities, but both NF and MC are difficult to build. Muon beams are produced with very large six-dimensional emittance and have short lifetime (~ 2.2 micro-second at rest). One of the main challenges is how to effectively manipulate intense muon beams, in particular to reduce the transverse emittance of the muon beams, namely cooling. Ionization cooling is considered to be the only practical cooling scheme for muons. No one has ever demonstrated the muon ionization cooling yet. MICE is such a demonstration experiment where a section of real ionization cooling channel hardware (based on the US Feasibility Study-II design) will be built and tested. The experiment is currently under construction at the Rutherford Appleton Laboratory (RAL) in UK [1]. The experiment comprises a dedicated beam line to generate a range of input emittance and momentum of a muon beam, with time-of-flight and Cherenkov detectors to ensure a pure muon beam. The emittance of the incoming muon beam will be measured in the upstream magnetic spectrometer with a scintillating fiber tracker. A cooling section will then follow. The cooling section consists of three liquid hydrogen absorbers and eight 201-MHz normal conducting RF cavities surrounded by two superconducting solenoid magnets. Muon beams lose energies in the liquid hydrogen absorber and gain longitudinal energies only from RF cavities, therefore a net reduction in transverse emittance. A second spectrometer that is identical to the first one and a particle identification system provide a measurement of the outgoing emittance. Figure 1A & 1B show an engineering model of the MICE experiment setup and the ionization cooling channel.

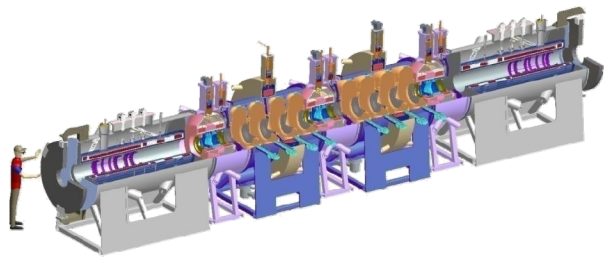

Figure 1A: MICE experiment layout: two spectrometer solenoids with particle ID and timing for emittance measurement and a section of cooling channel in between.

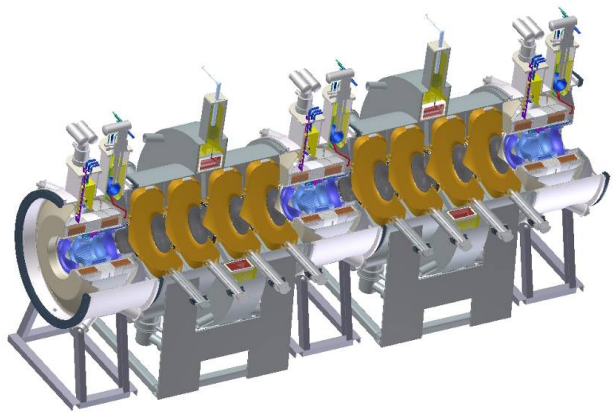

Figure 1B: MICE cooling channel consists of three liquid hydrogen absorbers (blue) and eight 201-MHz normal conducting RF cavities (yellow) surrounded by five superconducting solenoid magnets.

The aim of MICE is to measure ~ 10% cooling of 140 - 240 MeV/c muons with a measurement precision of $\Delta\varepsilon/\varepsilon$ of 10^{-3}. In addition, it is also necessary to explore and demonstrate that we can design, engineer and fabricate the hardware needed for MICE and place them in a muon beam and measure their performance. Moreover, MICE will help to validate design tools (simulation codes) we have developed and check agreements with the experiment.

MICE collaboration has over 150 collaborators from Belgium, Bulgaria, China, Holland, Italy, Japan,

*This work was supported by the Director, Office of Science, Office of High Energy Physics, of the U.S. Department of Energy under Contract Nos. DE-AC02-05CH11231

DLi@lbl.gov

Switzerland, UK and USA, respectively. Responsibilities of each participating country are illustrated in Figure 2.

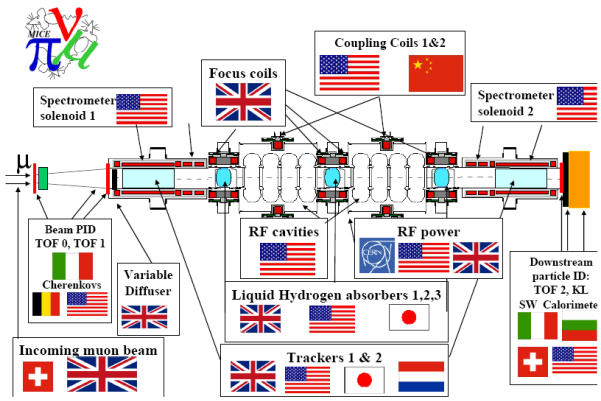

Figure 2: As an international collaboration experiment, MICE hardware is contributed by participating countries and the responsibility of each participating country is illustrated above with its national flag.

EXPERIMENTAL HALL

A dedicated MICE experimental hall has been assigned at RAL and is currently under construction, its location is shown in Figure 3. Necessary infra-structures for hosting the experiment are being implemented by MICE collaborators at RAL.

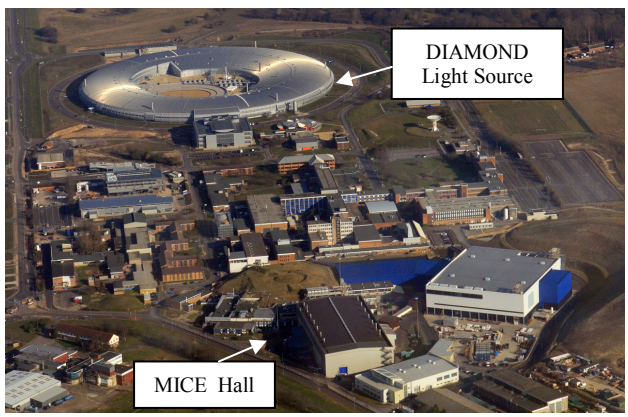

Figure 3: MICE experimental hall at RAL, UK

MICE BEAMLINE

The MICE muon beamline will be extracted from ISIS synchrotron at RAL. All magnets for MICE beamline have been installed, as shown in Figure 4 and the beamline location relative to ISIS is illustrated in Figure 5.

Figure 4: Magnets in MICE beamline (fish-eye lens view)

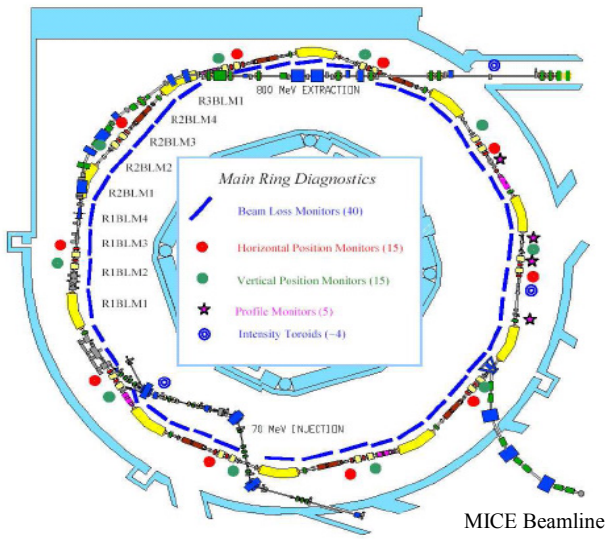

MICE Beamline

Figure 5: MICE beamline at ISIS of RAL

MICE TARGET

The MICE target is a thin slab of titanium with dimensions 35mm × 10mm × 1mm attached to the end of a cross shaped shaft 565mm long. The target is dipped into the beam at a rate of 1.0 Hz where it is assumed to interact with 1.4×10^{12} incident protons per pulse. The beam is assumed to be incident on the target 15mm from the base on the narrow face, a schematic of the MICE target insertion mechanismis illustrated in Figure 6. The first target was installed at ISIS in August 2009. It has been tested and successfully used for the MICE beamline commissioning.

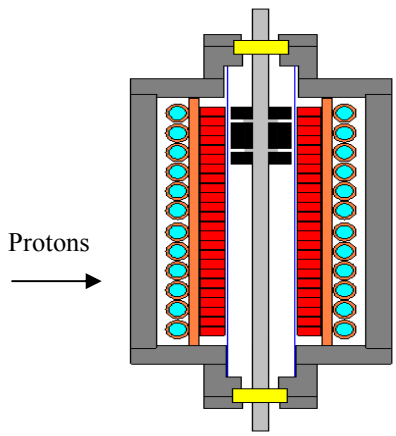

Figure 6: Schematic of MICE target insertion mechanism

MICE ABSORBER

There are three AFC (Absorber and Focusing Coil) modules in the MICE cooling channel. Each module has one liquid hydrogen absorber surrounded by a superconducting solenoid magnet, as shown in Figure 7. The AFC module design is complete; and a production readiness review was held recently. Fabrication contract

of the AFC modules has been awarded. The first AFC module could be delivered to RAL as early as July 2010.

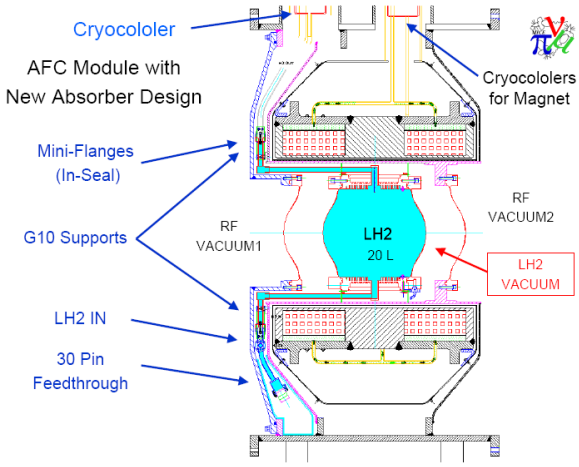

Figure 7: Schematics of the MICE AFC module

RFCC MODULE

There are two RFCC (**RF** cavity and **C**oupling **C**oil) modules. Each RFCC module consists of four 201-MHz normal conducting RF cavities surrounded by one superconducting solenoid (coil) magnet, as shown in Figure 8.

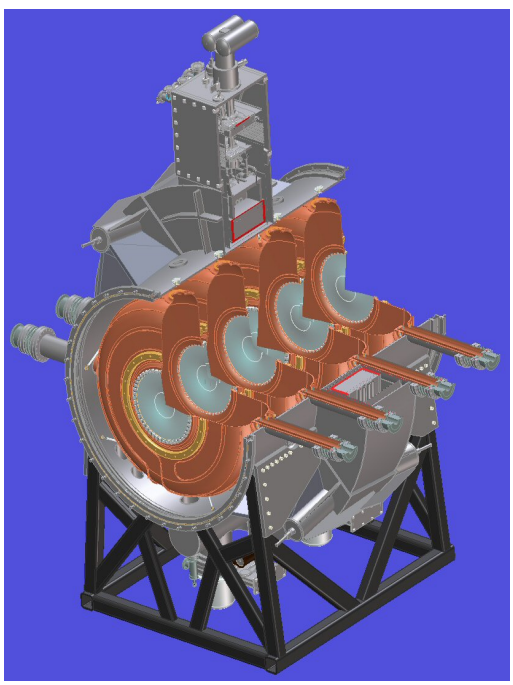

Figure 8: RFCC module: four 201-MHz normal conducting cavities and one superconducting solenoid (coil) magnet.

201-MHz Normal Conducting RF Cavity

MICE cavity design and fabrication techniques are based on a 201-MHz prototype cavity developed for the US MuCool program. Cavity body is formed by e-beam welding at the equator of two pre-spun half shells from ~ 6-mm copper sheets. The first 5-cavity fabrication contract was awarded to Applied Fusion, a company in California in early 2009. The fabrication has been progressing well; the first five cavities are nearly complete and could be delivered to LBNL in December 2009. Figure 9 is a photo taken in the summer of 2009 showing the fabrication progress. Each cavity has two coaxial loop couplers with integrated SNS type ceramic RF windows, and two curved thin beryllium (0.38-mm thickness) to cover the 42-cm open beam irises. Four cavities will be installed in a vacuum vessel, as shown in Figure 8. Therefore both the cavities and beryllium windows do not have differential pressures. Due to limited available RF power sources for MICE, each cavity will provide an accelerating gradient of 8 MV/m, corresponding to 1 MW peak RF power per cavity with 1-ms pulse length and 1 Hz repetition rate.

Figure 9: First five MICE cavities in fabrication.

Superconducting Coupling Coil Magnet

There are two superconducting coupling coil magnets in MICE cooling channel. The magnet design and fabrication are conducted through collaboration between Lawrence Berkeley National Laboratory (LBNL) and Harbin Institute of Technology (HIT) in China. A series of design reviews have been held. The engineering design is complete, contract bidding is in process. Each magnet is being cooled by cry-coolers. Three test coils have been winded. Figure10 and 11 show the engineering design model and a photo of hardware fabrication.

Fabrication of the MICE coupling magnets expects to start soon; the first magnet could be delivered in middle of 2011.

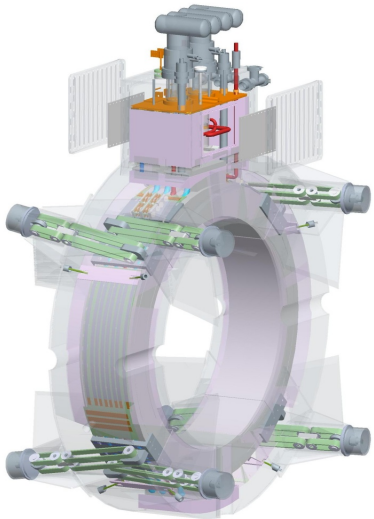

Figure 10: The MICE superconducting coupling coil magnet design (engineering model)

Figure 11: Coil mandrel under welding.

BEAMLINE COMMISSIONING

Beamline commissioning started in March 2008. We have successfully observed rates in beam counters versus the ISIS beam loss. Muon particles were observed using TOF/CKOV counters, as shown in Figure 14.

DETECTOR SYSTEM

The MICE detector system consists of two spectrometer solenoid magnets; one upstream and one downstream of the cooling channel. The system is designed to measure the full set of the muon emittance parameters. Each of the spectrometers provides a high-resolution measurement of the five parameters of the muon helix in a tracker embedded in a 4 T solenoid and a precise time measurement. Moreover, muon/pion/electron identifiers (a t_0 timing station and a small Cherenkov) are situated in front of the upstream detector and muon-electron identifiers (a larger Cherenkov and an electromagnetic EM-Calorimeter) are situated beyond the downstream spectrometer. The spectrometer magnet design and fabrication progress are shown in Figure 12 and 13, respectively.

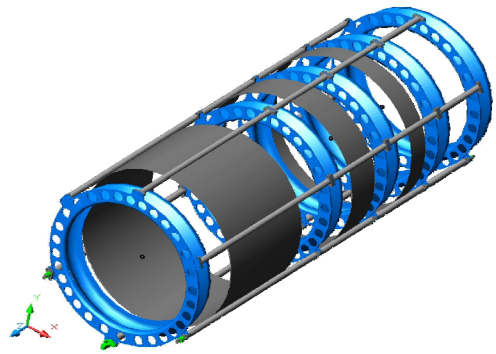

Figure 12: MICE spectrometer: Two trackers in 4-Tesla solenoid, with 5 SciFi tracking stations in each tracker.

Figure 13: One of the spectrometer solenoid magnets is being tested at the fabrication company.

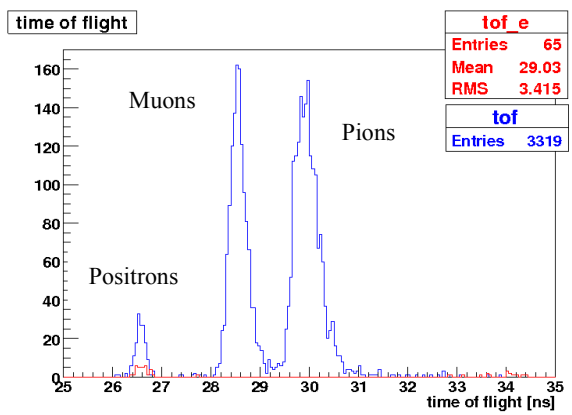

Figure 14: Particles were observed using TOF/CKOV counters at MICE beamline.

MICE SCHEDULES

MICE schedule has been delayed due some technical difficulties in hardware delivery and available funding. Figure 15 is the latest schedule for MICE with stepped approaches. The first emittance measurement with muon ionization cooling will occur in 2011 (STEP V).

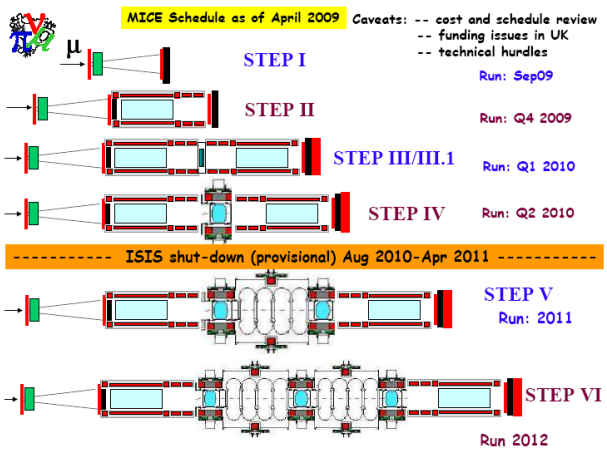

Figure 15: The latest schedule for MICE

SUMMARY

MICE target and detectors are all working now. MICE beamline has been commissioned successfully. The Experiment Hall for MICE and associated infrastructures, RF distribution design are nearly complete. Fabrication of hardware components for the MICE cooling channel are in progress. The first emittance measurement with muon ionization cooling will occur in 2011 (STEP V).

REFERENCES

[1] Technical notes and publications on MICE can be found at: http://www.mice.iit.edu

STUDY OF COLLECTIVE EFFECT IN IONIZATION COOLING *

D. Huang, Illinois Institute of Technology, Chicago, IL 60616, USA
K.Y. Ng, Fermilab Batavia, IL 60510, USA
T.J. Roberts, Muons Inc., Batavia, IL 60510, USA

Abstract

As a charged particle passes through a non-gaseous medium, it polarizes the medium and induces wake fields behind it. The interaction with wake fields perturbs the stopping power for the beam particles that follow. The perturbation strongly depends on the densities of both the incident beam and the medium. To understand this collective effect, detailed studies have been carried out. Both analytic and simulation results are obtained and compared.

INTRODUCTION

The study of the physics of a charged particle passing through a non-gaseous medium is of long history [1, 2, 3]. For a single particle, if its momentum is high enough, it will lose energy through both ionization process and density effect. The latter has been systematically studied. For a beam consisting of a large number of particles, the interaction among the beam particles should also be taken into account in order to describe the process correctly.

Essentially, the density effect is introduced by the polarization of the medium. The electric fields from the polarized medium molecules generate wake fields behind the incident particle, which perturb the motion of the beam particles following. If the particle density of the beam is high enough, the wake will enhance the stopping power for beam particles, and may possibly increase the rate of ionization cooling.

In this article, we derive the expressions for the wake electric field introduced by a single incident charged particle and its perturbation on the stopping power. This is extended to a two-particle system and a multi-particle system with various distributions. The comparison with simulations is next demonstrated. Finally, the damping mechanism on the wake is discussed, and its effect on the stopping-power enhancement is found to be important.

WAKE ELECTRIC FIELD

First, let us focus on a single particle of charge e moving with velocity v in the z direction, where $-e$ is the electron charge. The particle is at longitudinal position $z = z_1$ at time $t = 0$. Cylindrical coordinates are used with $\vec{\rho}$ denoting the transverse directions. The scalar potential generated by both the incident particle and polarized medium in the Coulomb gauge is given by

$$\phi(\vec{r},t) = \frac{e}{\pi v}\int d\omega \int \frac{\kappa d\kappa J_0(\kappa\rho)}{\kappa^2+\omega^2/v^2}\frac{e^{i\frac{\omega}{v}(z-z_1-vt)}}{\varepsilon(k^2,\omega)}, \quad (1)$$

where J_0 is the Bessel function. The wave number vector is denoted by $\vec{k} = (\vec{\kappa}, k_z)$ and the frequency by ω. In the above, the integration over k_z and $\vec{\kappa}\cdot\vec{\rho}$ have already been carried out. The polarization of the medium is described by the dielectric constant, which in a dispersive medium takes the form

$$\varepsilon(k^2,\omega) = 1 - \omega_p^2 \sum_j \frac{f_j}{\omega^2-\omega_j^2+i\omega\Gamma_j}, \quad (2)$$

where f_j is the fraction of bound electrons that oscillate with the bound frequency ω_j and damping rate $\frac{1}{2}\Gamma_j$, with $\sum_j f_j = 1$. In the above, $\omega_p = \sqrt{4\pi n_e e^2/m_e}$ is the plasma frequency, where m_e is the electron mass and n_e the electron density. We make the assertion that ω_p is much larger than the bound frequencies and damping rates.[1] Then $\frac{1}{2}\Gamma_j$ can be replaced by the infinitesimal positive number ϵ, leading to

$$\frac{1}{\varepsilon} = \frac{\omega^2}{(\omega+i\epsilon)^2-\omega_p^2} = \frac{\omega^2}{(\omega-\omega_p+i\epsilon)(\omega+\omega_p+i\epsilon)}. \quad (3)$$

Contour integration over ω can now be performed giving

$$\phi(\vec{r},t) = e\int d\kappa \frac{\kappa^2 J_0(\kappa\rho)}{\kappa^2+\omega_p^2/v^2} e^{-\kappa|z-z_1-vt|} + \frac{2e\omega_p}{v}\int d\kappa \frac{\kappa J_0(\kappa\rho)}{\kappa^2+\omega_p^2/v^2}\sin\frac{\omega_p}{v}(z-z_1-vt)\theta(z_1+vt-z). \quad (4)$$

The limits of integration are from $\kappa = 0$ to

$$\kappa = \frac{\omega_p}{v}\sqrt{x_m^2-1} \quad \text{with} \quad x_m = \frac{2\gamma m_e v^2}{\hbar\omega_p}, \quad (5)$$

which corresponds to the maximal momentum transfer in a collision. In the above, $\gamma = 1/\sqrt{1-v^2/c^2}$, c is the velocity of light, and $\hbar$ is the reduced Planck constant. The second term in Eq. (4) is the potential coming from the polarization of the medium, and the first term is the *medium-modified self-field* of the incident charged particle. The longitudinal and transverse electric fields derived from the second term vanish in front of the particle and are therefore the wake fields. Behind the particle, they take the form:

$$E_z^w(\vec{r},t) = -\frac{2e\omega_p^2}{v^2}\int d\kappa \frac{\kappa J_0(\kappa\rho)}{\kappa^2+\omega_p^2/v^2}\cos\frac{\omega_p(z-z_1-vt)}{v},$$
$$E_\rho^w(\vec{r},t) = +\frac{2e\omega_p^2}{v^2}\int d\kappa \frac{\kappa^2 J_1(\kappa\rho)}{\kappa^2+\omega_p^2/v^2}\sin\frac{\omega_p(z-z_1-vt)}{v}. \quad (6)$$

Evaluating at the particle location ($z = z_1+vt, \rho = 0$), we obtain the longitudinal field on axis,

$$E_z^w = -\frac{2e\omega_p^2}{v^2}\ln x_m. \quad (7)$$

* Work supported by USDOE Grant DE FG0292ER40747 and USDOE STTR Grant DE FG02 08ER86281.

[1] We believe the bound frequencies are one order of magnitude smaller than ω_p in liquid hydrogen.

The corresponding energy loss per unit time or stopping power is

$$\frac{dW}{dt} = evE_z^w = -\frac{2e^2\omega_p^2}{v}\ln x_m. \quad (8)$$

Behind the particle, the electric wake can be very well approximated by extending the upper limit of the κ integrations to infinity, resulting in

$$E_z^w = \frac{2e\omega_p^2}{v^2}K_0\left(\frac{\omega_p\rho}{v}\right)\cos\left[\left(\frac{z-z_1}{v}-t\right)\omega_p\right],$$
$$E_\rho^w = \frac{2e\omega_p^2}{v^2}K_1\left(\frac{\omega_p\rho}{v}\right)\sin\left[\left(\frac{z-z_1}{v}-t\right)\omega_p\right], \quad (9)$$

with $K_{0,1}$ the modified Bessel functions of the second kind.

The vector potential contributes only to the medium-modified self-field when bound frequencies are neglected. The electric field derived from it consists of two parts: one part cancels the medium-modified stationary self-field from the scalar potential in Eq. (4), while the other represents the medium-modified self-field of a moving charge. The total self-field can be written as

$$E_z^s = e\int d\kappa\,\frac{\kappa^3 J_0(\kappa\rho)}{\kappa^2+\frac{\omega_p^2}{v^2}}e^{-\gamma\sqrt{\kappa^2+\frac{\omega_p^2}{c^2}}|z-z_1-vt|},$$

$$E_\rho^s = e\int d\kappa\,\frac{\gamma\kappa^2 J_1(\kappa\rho)}{\kappa^2+\frac{\omega_p^2}{v^2}}\sqrt{\kappa^2+\frac{\omega_p^2}{c^2}}e^{-\gamma\sqrt{\kappa^2+\frac{\omega_p^2}{c^2}}|z-z_1-vt|}.$$

In the absence of the medium ($\omega_p = 0$), it reduces to the familiar pancake self-field,

$$E_z^s = \frac{e\gamma Z}{(\rho^2+\gamma^2Z^2)^{3/2}},\quad E_\rho^s = \frac{e\gamma\rho}{(\rho^2+\gamma^2Z^2)^{3/2}}, \quad (10)$$

where $Z = z - z_1 - vt$. In the presence of the medium, the self-field decays very much faster with respect to Z. For a bunch with longitudinal and transverse radii $\gg v/\omega_p$, the self-field has almost no influence compared with the wake fields. Therefore we ignore it in the rest of our discussions.

TWO-PARTICLE SYSTEM

Now let us discuss the stopping power for a two-particle system. The particles are denoted by 1 and 2, respectively, with the charge density

$$\rho(\vec{r},t) = e\left[\delta(\vec{r}-\vec{r}_1-\vec{v}_1t)+\delta(\vec{r}-\vec{r}_2-\vec{v}_2t)\right]. \quad (11)$$

The electric field at $(\vec{r},t)$ is

$$\vec{E}(\vec{r},\,t) = -\frac{i2e}{4\pi^2}\int d^3k\int d\omega\,\frac{\vec{k}e^{-i\omega t}}{\varepsilon k^2}\times$$
$$\times\left[e^{i\vec{k}\cdot(\vec{r}-\vec{r}_1)}\delta(\vec{k}\cdot\vec{v}_1-\omega)+e^{i\vec{k}\cdot(\vec{r}-\vec{r}_2)}\delta(\vec{k}\cdot\vec{v}_2-\omega)\right]. \quad (12)$$

The energy gained per unit time by the two particles are

$$\frac{dW_{1,2}}{dt} = -\frac{i2e^2}{4\pi^2}\int d^3k\frac{\vec{k}\cdot\vec{v}_j}{k^2\varepsilon(k^2,\vec{k}\cdot\vec{v}_{1,2})}\times$$
$$\times\left[1+e^{\pm i\vec{k}\cdot(\vec{r}_1-\vec{r}_2)\pm i(\vec{k}\cdot(\vec{v}_1-\vec{v}_2)t)}\right]. \quad (13)$$

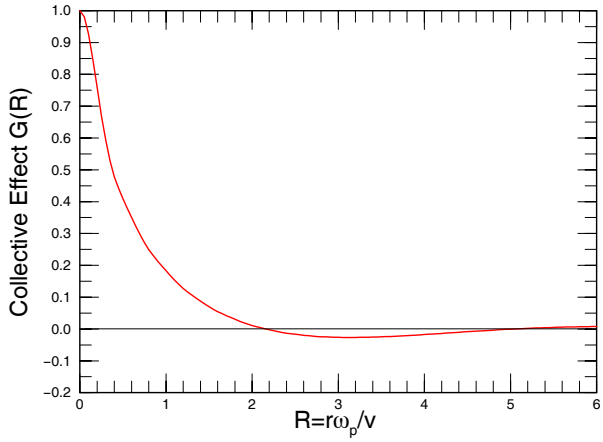

Figure 1: Stopping power enhancement due to collective wake effect on a two-particle system as a function of $R = r\omega_p/v$, where r is the separation between the two particles.

For the special case where $\vec{v}_1 = \vec{v}_2 = \vec{v}$, we have the *average* energy loss per particle per unit time or stopping power

$$\frac{dW}{dt} = -\frac{ie^2}{2\pi^2}\int d^3k\,\frac{\vec{k}\cdot\vec{v}}{k^2\varepsilon(k^2,\vec{k}\cdot\vec{v})}\left[1+\cos(\vec{k}\cdot\vec{r})\right],$$

where $\vec{r} = \vec{r}_1 - \vec{r}_2$. Here, only the imaginary part of $1/\varepsilon$ contributes. After averaging over all orientations of this two-particle system, we arrive at

$$\left\langle\frac{dW}{dt}\right\rangle_{\text{angles}} = -\frac{e^2\omega_p^2}{v}\ln x_m\left[1+G(R)\right], \quad (14)$$

where the correlation function or stopping power enhancement is defined as

$$G(R) = \frac{-\frac{\sin Rx_m}{Rx_m}+\frac{\sin R}{R}-\mathrm{Ci}(Rx_m)+\mathrm{Ci}(R)}{\ln x_m}, \quad (15)$$

and $\mathrm{Ci}(x) = -\int_x^\infty dy\,\cos y/y$ is the cosine integral. Here, the distance of separation of the two particles, $R = r/a_I$, has been normalized to $a_I = v/\omega_p$ or the *interaction length*. The correlation function [4] as depicted in Fig. 1 shows that $G(R) = 1$ at $R = 1$ and decreases rapidly when $R \gg 1$ with oscillation period equal to the plasma wavelength $\lambda_p = 2\pi a_I$. It is interesting to point out that the averaging over all orientations cancels out all self-field contribution.

VARIOUS BEAM DISTRIBUTIONS

In this section we will discuss the stopping power enhancement for a particle in the center of a bunch as a result of the polarization wake. Various bunch distributions are used and their importance analyzed.

Uniformly Distributed Sphere

Let us start with a uniformly distributed spherical N_b-particle bunch of radius r_0. The extra collective stopping power G_t received by the particle at bunch center is obtained by integrating the two-particle correlation function $G(R)$ of Eq. (15) over all the particles in the bunch. We get

$$G_t = \frac{3N_b}{R_0^3}\int_0^{R_0} R^2 G(R)dR = N_b \frac{f(R_0) - f(R_0 x_m)}{\ln x_m}, \quad (16)$$

with $R_0 = r_0\omega_p/v$, the reduced bunch radius and

$$f(u) = \left(\frac{1}{u^3} + \frac{1}{u}\right)\sin u - \frac{\cos u}{u^2} - \mathrm{Ci}(u). \quad (17)$$

Since x_m is usually a very big number, the above can be readily approximated as

$$G_t \approx \frac{3N_b \sin R_0}{R_0^3 \ln x_m}. \quad (18)$$

As an example, consider a $\gamma = 2.2$ bunch containing $N_b = 1\times10^{12}$ muons going through liquid hydrogen of density $\rho_{H_2} = 0.07099$ g/cm^{-3}. The electron density is $n_e = \rho_{H_2} N_A = 4.275\times10^{28}$ m^{-3}, where N_A is Avogadro's number. The plasma frequency is therefore $\omega_p = 1.166\times10^{16}$ s^{-1} leading to $x_m = 2.323\times10^5$. If bunch is a uniformly distributed sphere of radius $r_0 = 1$ mm, $R_0 = 4.369\times10^4$ and the envelope of G_t is ±0.0029. However, since the bunch edge can never be made sharper than the interaction length $a_I = 2.289\times10^{-8}$ m, the rapid oscillation of G_t with R_0 with period λ_p implies the enhancement of stopping power from correlation is essentially zero.

Cylindrical Bunch

Let us consider next distributions having the separable form $f(z,\rho) = f_z(z)f_\rho(\rho)$. One example is a bunch with uniform distribution in the transverse direction, but that is tapered at both end longitudinally, or

$$f_z(z) = \frac{A_n}{\hat{z}}\left(1 - \frac{z^2}{\hat{z}^2}\right)^n, \quad f_\rho(\rho) = \frac{2\pi\rho}{\pi\hat{\rho}^2}, \quad (19)$$

where $A_n = \Gamma(n+\frac{3}{2})/[\sqrt{\pi}\Gamma(n+1)]$ for any $n > -1$, $\hat{\rho}$ is the transverse radius of the bunch, and $\pm\hat{z}$ are the longitudinal extents of the bunch. We can no longer apply the expression of the all-orientation-averaged correlation function $G(R)$ of Eq. (15), because the distribution is now different in different directions. Instead, we start from Eq. (9) to compute G_t, the collective stopping power enhancement for a particle at the center of the bunch, by the integration,

$$G_t \ln x_m = N_b \int_0^{\hat{z}} dz\, f(z,\rho)\cos\left(\frac{z}{a_I}\right)\int_0^{\hat{\rho}} d\rho f_\rho(\rho) K_0\left(\frac{\rho}{a_I}\right), \quad (20)$$

and obtain easily

$$G_t \ln x_m = \frac{\sqrt{\pi}A_n}{(\omega_p\hat{\rho}/v)^2}\left(\frac{2v}{\omega_p\hat{z}}\right)^{n+\frac{1}{2}} J_{n+\frac{1}{2}}\left(\frac{\omega_p\hat{z}}{v}\right). \quad (21)$$

We see clearly that there is an oscillation in the Bessel function $J_{n+\frac{1}{2}}$ which gives positive or negative enhancement depending very sensitively on the half bunch length $\hat{z}$. In fact, when n is an integer, the Bessel function reduces to sine and cosine with period λ_p, and the result will be similar to that of the uniform distribution in a sphere discussed earlier. We learn from Eq. (21) that the longitudinal and transverse beam sizes behave very differently, and it is the longitudinal that introduces the oscillations. To avoid oscillations, we need to go to a distribution without finite longitudinal boundaries.

Lorentzian Distribution

Let us keep the transverse distribution to be finite and uniform, but let the longitudinal distribution be

$$f_z(z) = \frac{z_1}{\pi}\frac{1}{z^2 + z_1^2}, \quad (22)$$

where z_1 is the half longitudinal length at half maximum. The correlation stopping power enhancement G_t for a particle at the bunch center is found to be

$$G_t \ln x_m = \frac{N_b e^{-z_1/a_I}}{(\hat{\rho}/a_I)^2}. \quad (23)$$

If $\hat{\rho} = z_1 = 1$ mm, $\hat{\rho}/a_I = z_1/a_I = 4.37\times10^4$. Then the stopping-power enhancement is $G_t = 45.3\times10^{-19000}$, which is essentially zero. In order to have a more reasonable effect at the bunch intensity of 1×10^{12}, we require $\hat{\rho}/a_I = z_1/a_I = 20$. Then $G_t = 0.417$. If $\hat{\rho}/a_I = z_1/a_I = 25$, $G_t = 0.0018$ instead. However, one must remember that at $a_I = v/\omega_p = 2.289\times10^{-8}$ m, these examples correspond to $z_1 = 4.6\times10^{-7}$ and 5.7×10^{-7} m, or bunches of sub-micron lengths. At this moment, the most aggressive cooling scheme proposed by Neuffer [5] is to have an eventual bunch length of 30 cm and transverse radii $r_0 = 50$ μm.

Tri-Gaussian Distribution

Let

$$f_z(z) = \frac{e^{-z^2/(2\sigma_z^2)}}{\sqrt{2\pi}\sigma_z} \quad \text{and} \quad f_\rho(\rho) = \rho\frac{e^{-\rho^2/(2\sigma_\rho^2)}}{\sigma_\rho^2}. \quad (24)$$

The stopping power enhancement can be integrated readily to the exponential function. However, when $\sigma_\rho/a_I \gg 1$, it can be neatly reduced to

$$G_t \ln x_m = \frac{N_b e^{-(\sigma_z/a_I)^2/2}}{(\sigma_\rho/a_I)^2}, \quad (25)$$

which is much smaller than the case of the Lorentzian distribution. Here, we again see that the transverse and longitudinal behave every differently. Although both are Gaussian distributed, the longitudinal decay of the collective stopping power enhancement is Gaussian, while the transverse decay is $(a_I/\sigma_\rho)^2$, which is very much milder.

Exponential Distribution

In order to achieve a larger stopping power enhancement, the distribution must roll off very rapidly from the center of the bunch. A possible distribution is the exponential

$$f_z(z) = \frac{e^{-|z|/z_1}}{2z_1} \quad \text{and} \quad f_\rho(\rho) = \frac{e^{-\rho/\rho_1}}{\rho_1}. \quad (26)$$

When $z_1/a_I \gg 1$ and $\rho_1/a_I \gg 1$, G_t is given by

$$G_t \ln x_m \approx \frac{\pi N_b}{8(\rho_1/a_I)(z_1/a_I)^2}. \quad (27)$$

Or $G_t = 3.81\times10^{-4}$ at $\rho_1 = z_1 = 1$ mm. If either the bunch sizes are each reduced 5 times or the bunch intensity is increased by a factor of 125, the collective effect enhancement will become 4.8%, and thus more significant.

In Neuffer's scheme [5] with transverse bunch radii $\rho_1 = 50$ μm and bunch length $z_1 = 30$ cm, we get a stopping power enhancement of $G_t = 8.47 \times 10^{-8}$, which increases rapidly to 7.62×10^{-3} when the bunch length is reduced to $z_1 = 1$ mm. Here, again we notice that the longitudinal bunch length is the most important factor that determines the enhancement. For example, if we divide a bunch up longitudinally into bunchlets of shorter lengths but with the particle density unchanged, the stopping power enhancement for the bunch particles will be increased.

COMPARISON WITH SIMULATION

OOPICPro [6] developed by Tech-X Corporation is able to simulate a charged particle beam passing through matter. We simulate a $\gamma = 2.2$ tri-Gaussian muon bunch with rms radii 1 mm traveling through a plasma medium of electron density $n_e = 4.28 \times 10^{18}$ m^{-3} (which is very much less than that in liquid hydrogen). The peak beam density is 5×10^{19} m^{-3}, corresponding to total bunch intensity $N_b = 0.787 \times 10^{12}$. The longitudinal wake is shown in Fig. 2. The same wake can be computed by integrating our derived wake in Eq. (9) over all the particles in the bunch in a fake liquid hydrogen medium of the same low density. The field patterns in both the longitudinal and transverse directions agree with the simulation results. For example, the oscillation wavelength is $\lambda_p = 1.43$ cm corresponding to the plasma frequency of $\omega_p = 1.17 \times 10^{11}$ s^{-1}. However, OOPICPro gives the peak longitudinal wake electric field 1.02×10^8 V/m, while the computed one in Fig. 3 gives 4×10^8 V/m. The discrepancy may come from the fact that OOPICPro treats the medium as a fully ionized plasma while we treat the medium as a liquid with polarized molecules. This difference will be examined next.

RELAXATION AND DAMPING

We need to address the question of relaxation or damping of the plasma oscillation to determine whether the oscillatory wake can be established and sustained.

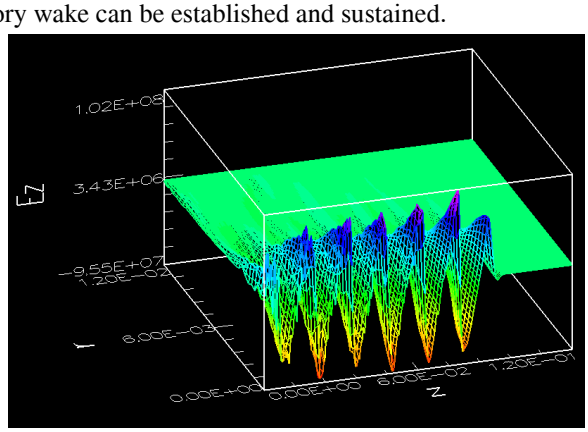

Figure 2: (Color) The longitudinal wake electric field behind an incident muon bunch simulated by OOPICPro with electron density 4.28×10^{18} m^{-3} and peak particle density 5×10^{19} m^{-3}. The bunch is tri-Gaussian distributed of rms radii 1 mm in all directions with $\gamma = 2.2$ muons. Both the longitudinal and transverse axes (z and r) are in m while E_z is in V/m.

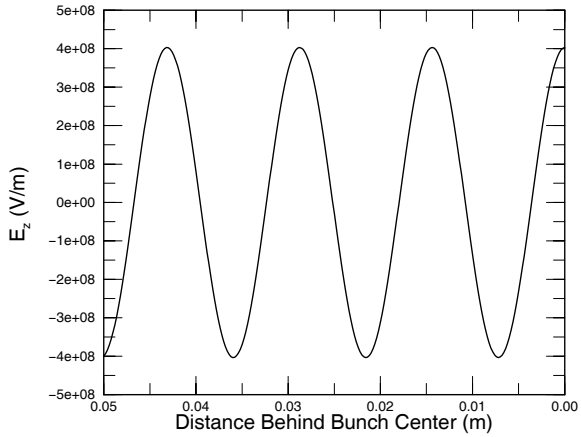

Figure 3: Computed longitudinal wake behind a tri-Gaussian bunch. Bunch sizes and medium density are the same as in the OOPICPro simulation in Fig. 3. The bunch center is at the origin and 2×10^5 macro-particles have been used.

Cold Plasma

In a fully ionized plasma, electrons are free to move around as a thermal gas. In the presence of the incident muon beam, the electrons are driven into oscillations about the background ions at plasma frequency. At the same time these electrons collide with the ions. If a collision takes place within one period of plasma oscillation, the plasma oscillation will be disturbed. Thus collision with ions serves as a damping mechanism. The collision frequency of an electron with the ionic background is given by [7] $\nu_e = 2.9 \times 10^{-9} n_i T_e^{-3/2} \ln \Lambda$ s^{-1}, where n_i is the ionic density in m^{-3}, $\ln \Lambda \approx 10$ is the cutoff logarithm, and T_e is the thermal temperature of the electrons in eV. For the above OOPICPro simulation, we substitute $n_i = 4.28 \times 10^{18}$ m^{-3} and $T_e = 1.72 \times 10^{-3}$ eV (corresponding to 20 K) to obtain $\nu_e = 1.74 \times 10^{12}$ s^{-1}, which is comparable to the plasma frequency of $\omega_p = 1.17 \times 10^{11}$ s^{-1}. So the wake will be heavily perturbed. We do see some damping of the simulated wake in Fig. 2, but not as heavy as estimated. The discrepancy may come from the relatively higher temperature of the ionized electrons, which may not even be in thermal equilibrium. Since the collision frequency increases as n_i while the plasma frequency increases with $\sqrt{n_i}$, the damping of plasma oscillation will become more severe as the plasma density increases. Such a simulation has been carried out using OOPICPro with the plasma density increased 10^4-fold to $n_i = 4.28 \times 10^{22}$ m^{-3} while all other parameters remain unchanged. The result in Fig. 4 shows that the on-axis longitudinal wake is damped almost immediately as soon as it is generated. The maximum $|E_z|$ is less than 8.5×10^5 V/m as compared with 1×10^8 V/m in Fig. 2.

Liquid Hydrogen

In producing Fig. 3, we employed the wake expression without consideration of damping and the electron density lowered to $n_e = 4.28 \times 10^{18}$ m^{-3} so as to compare with simulation. Now let us come back to the case of real liquid hydrogen where the bound-electron density is

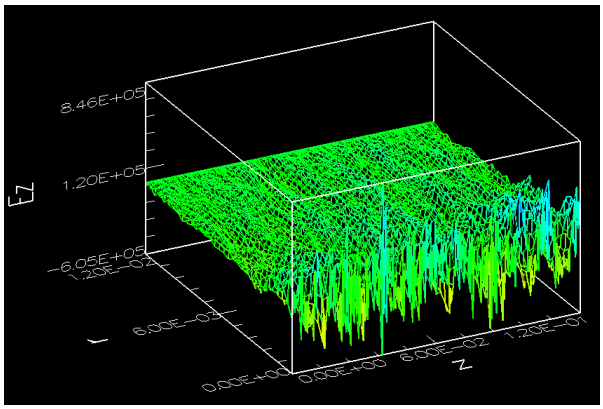

Figure 4: (Color) OOPICPro simulation for a muon beam in a plasma. All parameters are the same as in Fig. 2, except that the plasma density has been increased to 4.28×10^{22} m^{-3}. The z- and r-axes are in m, while E_z is in V/m.

$n_e = 4.270 \times 10^{28}$ m^{-3} and study possible damping of the wake. At $\gamma = 2.2$, the energy loss in liquid hydrogen is $dW/dx = -4.5$ MeV-cm^2-g^{-1}. For a bunch with cross-sectional radii $r = 1$ mm, consisting of 1×10^{12} muons, the density of ionized electrons is

$$n_{ei} = -\frac{\rho_{H_2} N_b dW/dx}{\pi r^2 I}, \qquad (28)$$

where the medium density is $\rho_{H_2} = 0.07099$ g/cm^3 and the ionization energy is $I = 35$ eV. We obtain $n_{ei} = 2.9 \times 10^{23}$ m^{-3}, which is five orders of magnitude less than the density of the bound electrons and can therefore be neglected. The damping of the wake can come from collisions between the neutral polarized hydrogen molecules, since directional changes of the polarized molecules will disturb the plasma oscillations. The mean thermal velocity of the H_2 molecules at 20 K is $v_{H_2} = 235$ m/s (3 degrees of freedom considered). The typical cross section for the hydrogen molecule in the hard-ball model is $\sigma_{H_2} \approx 3 \times 10^{-20}$ m^2. Thus the collision frequency is $\nu_{H_2} \approx 4 n_{H_2} \sigma_{H_2} v_{H_2} \approx 45 \times 10^{11}$ s^{-1}, with n_{H_2} the density of the H_2 molecules. This is still many order smaller than the plasma frequency of $\omega_p = 1.17 \times 10^{16}$ s^{-1}.

Another possibility of damping comes from the damping rates of the bound frequencies of the H_2 molecules. We asserted earlier that the bound frequencies ω_j are an order of magnitude smaller than ω_p. It is reasonable to assume that the damping rates $\frac{1}{2}\Gamma_j$ of the bound frequencies are the same order of magnitude as ω_j. Let us simplify the problem by including only one damping rate $\frac{1}{2}\Gamma$. Then ϵ in Eq. (3) will be replaced by $\frac{1}{2}\Gamma$, and there will be the extra factor of $e^{-\Gamma Z/2v}$ in the wake expressions of Eqs. (6) and (9), where $Z = z - z_1 - vt$. Since $2v/\Gamma \ll \sigma_z$, the bunch length, in the computation of stopping power enhancement in Eq. (20), the longitudinal beam distribution can be replaced by the peak beam density. Taking the tri-Gaussian distribution as an example, instead of Eq. (25), we obtain

$$G_t \ln x_m \approx \frac{N_b}{\sqrt{2\pi}(\sigma_\rho/a_I)^2(\sigma_z/a_I)} \frac{\Gamma}{2\omega_p}. \qquad (29)$$

For a beam with $\sigma_\rho = \sigma_z = 1$ mm and $N_b = 1 \times 10^{12}$, $\Gamma/2\omega_p \sim 0.1$ implies $G_t \sim 3.9 \times 10^{-5}$. In addition, if the transverse distribution is exponential, $(\sigma_\rho/a_I)^2$ in the denominator is replaced by $4(\sigma_\rho/a_I)/\sqrt{2}\pi$ and we have $G_t \sim 190\%$ instead. In short, the enhancement becomes much larger in the presence of some amount of damping.

CONCLUSIONS

The perturbation of stopping power due to collective effect as a charged particle beam traverses a medium is studied in detail. This effect is introduced by the polarization of the medium and depends on a variety of factors such as beam distribution, beam density, and medium density.

The magnitude of the collective perturbation is fundamentally determined by the ratio of the separation of beam particles and the interaction length in the polarized medium, which is also a function of the velocity of incident particles. As this ratio decreases, the collective effect becomes more significant.

The damping of the wake also plays an important role in the wake field. Without any damping consideration, the wake oscillates sinusoidally with period $\lambda_p = 2\pi a_I$. Since the average separation of the incident beam particles is usually much larger than the interaction length, the wake field perturbation on stopping power is negligibly small. Damping comes from two sources: one is the collision rate between absorber molecules, which is slow and insignificant, the other is the damping rates of the bound frequencies of absorber electrons. Under certain circumstances, a shorter damped wake enhances collective perturbation.

The model used in the analysis employs the dielectric constant ε in the form of Eq. (3) where bound frequencies are considered small and neglected. Further analysis should take account of the contribution of bound frequencies to the wake and their effects on the stopping-power enhancement should be fully investigated.

Whether an enhancement of stopping power will increase the ionization-cooling rate has not been proven. In our future analysis, we will study the perturbation on the stopping power for particles traveling at various angles relative to the traveling direction of the bunch center. This will allow us to determine precisely the effect on the cooling rate of the beam due to interaction with the wake generated in the medium.

REFERENCES

[1] E. Fermi, Phys. Rev. **57**, (1940) 485.

[2] J. Neufeld and R.H. Ritchie, Phys. Rev. **98**, (1955) 1632.

[3] W. Brandt, A. Ratkowski and R.H. Ritchie, Phys. Rev. Lett. **33**, (1974) 1325.

[4] N.R. Arista and V.H. Ponce, J. Phys. C **8** (1975) L188. Results depicted in Fig. 3 of Ref. [3] are incorrect.

[5] D. Neuffer, LEMC09 presentation.

[6] OOPICPro, Tech-X Corp., `http://www.txcorp.com`.

[7] J.D. Huba, NRL Plasma Formulary, 2009, p.33.

DEVELOPMENT OF HELICAL COOLING CHANNELS FOR MUON COLLIDERS

Katsuya Yonehara, Fermilab, Batavia, IL 60510, U.S.A.

Abstract

The biggest technical challenge problem for muon colliders is to cool of the six-dimensional (6D) muon beam phase sufficiently within the muons' short lifetime to permit acceleration. The Helical Cooling Channel (HCC) has been proposed as a means to obtain exceptional cooling performance in a short channel length. A number of experimental, design and simulation studies of the HCC have been completed recently. Results and current activities for the HCC are presented.

INTRODUCTION

The P5 committee compiled a road map for future facilities for high-energy physics (HEP) in May, 2008 [1]. According to their road map, muon colliders will be an appropriate long-term project for HEP community if progress is made on the necessary breakthrough technologies. Muons are an attractive for acceleration in future colliders because 1) muons emit no synchrotron radiation in circular accelerators even at TeV energies, whereas it severely limits the energies of circular electron-positron accelerators, and requires linear accelerators that are much larger than muon colliders, and 2) muon colliders have much less beamsstrahlung than electron-positron colliders, which results in better energy resolution, 3) muons have no internal structure, whereas that is a drawback in proton-proton and other hadron colliders. On the other hand, there are some challenges to make muon colliders. First, muons must be accelerated to high energy within their short lifetime. Half of the muons decay weakly into electron (positron) and anti-neutrino (neutrino) within 2.2 μs at rest. Second, rapid 6D muon beam phase space cooling is required to make practical muon colliders. Muons are generated in a pion decay channel. Without phase space cooling the initial muon beam phase space is too large to be accepted in a conventional RF accelerator system. A compact muon accelerating and cooling system is an essential requirement. Because high gradient RF is preferred for quick acceleration, SRF cavities are the most feasible solution for muon acceleration. To this end, the beam phase space needs to be cooled down to levels that are acceptable by the SRF system.

The most effective method of muon beam phase space cooling is by ionization cooling. Ionization cooling of a muon beam involves passing a magnetically focused beam through an energy absorber, where the muon transverse and longitudinal momentum components are reduced, and through RF cavities, where only the longitudinal component is regenerated. After some distance, the transverse components shrink to the point where they come into equilibrium with the heating caused by multiple Coulomb scattering. However, this process only makes 4D phase space cooling, called transverse cooling. Recently, a novel 6D phase space cooling channel based on ionization cooling called a helical cooling channel (HCC) was proposed [2]. It consists of a helical dipole and solenoid magnetic components to make a helical beam path as shown in Figure 1. The dense hydrogen gas is homogeneously filled in the beam path. In a helical dipole magnet, a high (low) momentum muon passes with longer (shorter) path length. As a result, the momentum distribution after the magnet with a continuous cooling absorber becomes uniform. This process is called emittance exchange. A helical quadrupole component is required to stabilize the beam phase space. To compensate for energy loss, a continuous RF acceleration field is needed. A high pressurizing hydrogen gas filled RF (HPRF) cavity can be used a homogeneous cooling absorber and a continuous acceleration at the same time. The HPRF cavity has been successfully tested and investigated for the cooling applications [3]. Integrating the HPRF cavity into the HCC is a major issue. The HCC is the most compact type of cooling channel of the various types of cooling channel.

In this paper, we discuss the latest results of 6D cooling simulation studies of the HCC. Then, we discuss the beam elements in the HCC. This study will lead to the question of how to incorporate the RF system into a compact helical cooling magnet.

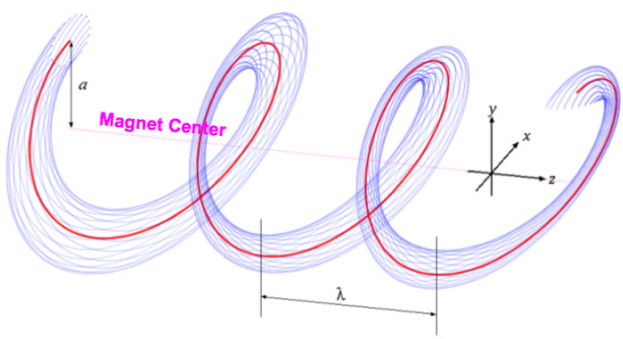

Figure 1: Helical particle tracking in the HCC. The red line indicates the trajectory of the reference design particle and the blue lines are the beam envelope. The particle track has a position offset from magnet center ("*a*" in picture). λ is a helical period.

HCC SIMULATION

From past HCC simulation studies, we noticed that an HCC with a lower RF frequency channel has larger longitudinal phase space stability [4]. The most plausible reason is because the momentum slip factor is not well

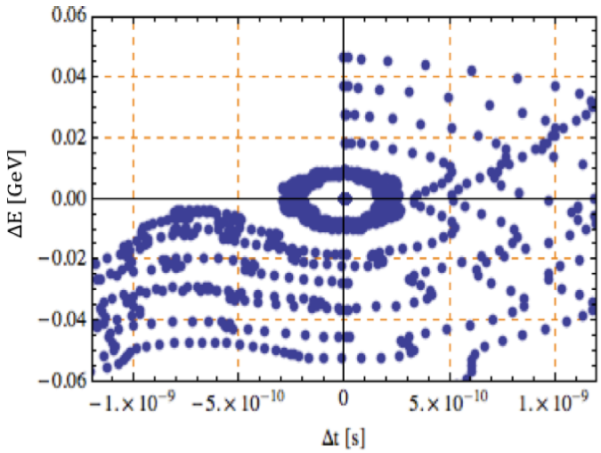

Figure 2: An RF bucket in a $E_0 = 16.0$ MV/m with $\phi_0 = 140.0^\circ$ at $\nu = 400.0$ MHz HCC.

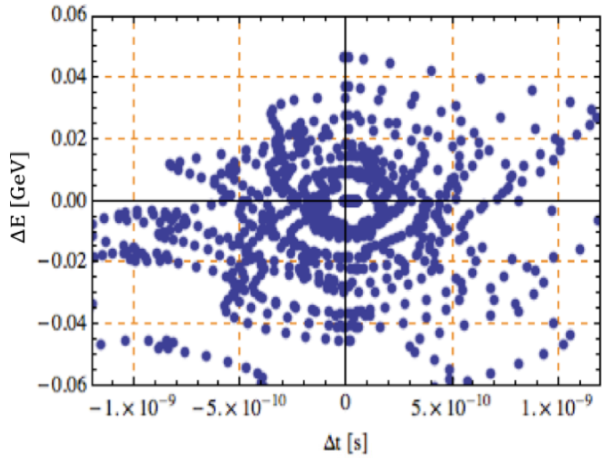

Figure 3: An RF bucket in a $E_0 = 31.4$ MV/m with $\phi_0 = 160.0^\circ$ at $\nu = 400.0$ MHz HCC.

matched to capture muons in the RF bucket, i.e. the time of flight of high (low) momentum muon traversing the HCC is too short (long) to stay in the RF bucket. The maximum RF bucket amplitude (ΔE_{max}) is given by

$$\Delta E_{max} \propto \left(\frac{1}{\nu} E_0(\phi_0 \cos\phi_0 - \sin\phi_0)\right)^{1/2}, \quad (1)$$

where ν is the RF frequency, E_0 is the amplitude of the acceleration field, and ϕ_0 is the RF phase, respectively. From this equation, one can expect that by applying a higher RF amplitude and setting a larger RF phase the RF bucket size becomes larger. Figures 2 and 3 show the RF buckets in an HCC with a small E_0 and ϕ_0 (Fig. 2) and with a large E_0 and ϕ_0 (Fig. 3), respectively. The former RF parameter is used in the conventional HCC design as in Ref.[4]. The plots in figures 2 and 3 clearly show an increase in RF bucket size.

In the conventional muon collider cooling scheme, the initial cooling channel must have a low frequency RF structure, i.e. usually starting with a 200 MHz RF system. By increasing the longitudinal phase space acceptance, the HCC will start with 400 MHz RF system. Figure 4

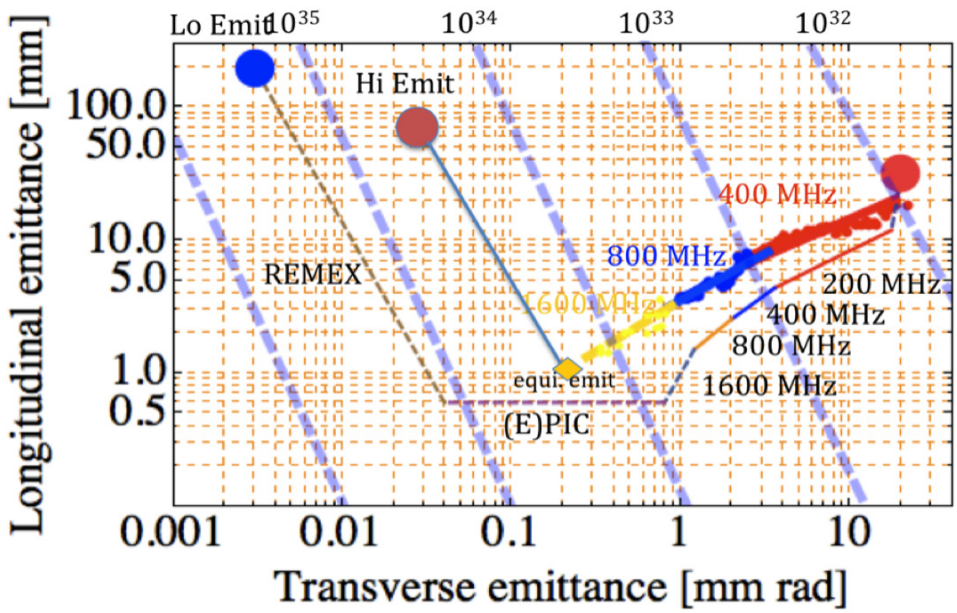

Figure 4: Fernow-Neuffer plot of transverse and longitudinal emittance evolutions in a series of HCCs for a muon collider. A thin line shows the result in an old HCC design while a thick line shows the result in a new HCC one with the optimized RF parameters. The big red point is the initial phase space after the frontend channel. The beam phase space goes down to the diamond point, which is the equilibrium emittance in the HCC. The big brown and blue points show the goal in "high emittance" and "low emittance" schemes, respectively [5]. To realize the low emittance scheme, some extra cooling channel is required. We propose to add (Epycyclic) Parametric Resonance Ionization Cooling channel (PIC) and Reverse Emittance EXchange channel (REMEX) [6]. The light blue broken line shows the expected luminosity under the assumption of no beam loss.

shows the plot of an evolution of transverse and longitudinal phase spaces (Fernow-Neuffer plot) in a series of HCCs, i.e. a 400 MHz HCC, an 800 MHz HCC, and a 1600 MHz HCC, respectively. The idea of incrementing the frequency in the series of HCCs is that more RF power can be put into higher frequency RF cavities. In the cooling simulation, optimizing the HCC parameters, the cooling factor for a 300 meter long HCC is ~ 3×10^5 in 6D phase space. This amount of cooling corresponds to a beam luminosity of more than 10^{34} $cm^{-2}s^{-1}$ for a muon collider, assuming that there is no beam loss in the entire system, including cooling, acceleration, and beam storing in a collider ring.

Table 1: HCC Parameter in Design Simulation

Parameter	Unit	Value		
RF frequency	MHz	400	800	1600
Helix period	m	1.0	0.6	0.3
Helix tangential pitch		1.0	1.0	1.0
Helix dipole field, b	Tesla	1.60	2.67	5.33
Helix quadrupole, b'	T/m	-0.55	-1.53	-6.10
Solenoidal field	Tesla	-5.30	-8.84	-17.7
RF field amplitude	MV/m	31.5	32.5	32.5
RF phase	Degree	160	160	160
RF cavity length	mm	100	60	30

Table 1 shows the beam element parameter in a series of HCCs as shown in Figure 4. These parameters are for a positive muon beam with a left-handed (anticlockwise) helicity beam, hence the sign of the field is sensitive. The mean momentum is 250 MeV/c. The direction of acceleration field is the global z direction, i.e. solenoid direction of the magnet. It should also be paid attention that the strength of the fields is stronger at higher RF frequency. A smaller beam phase space can be achieved in a stronger magnetic field because it makes a lower beta function. Stronger magnetic fields can be generated more easily in smaller bore magnets, which accommodate the smaller higher frequency RF cavities. This is another reason why a series of HCCs is needed to make lower emittance beams. Integrating of RF cavities into the helical magnet will be discussed later.

Currently we are working on the design of a phase space matching channel in the HCC simulation study. The action angle and canonical variables are well known from analytical investigation [2]. Now the issue is how to translate these parameters from one canonical coordinate system to the other by using the conventional beam elements.

STUDY OF BEAM ELEMENT IN HCC

In the rest of the paper, we discuss the beam elements, which consist of the helical magnet and the RF system. These modules cannot be designed separately because they will be integrated into the 6D cooling channel. This task is the main goal current HCC design study.

Helical Magnet

The design of helical magnet has already been created and prototyped at Fermilab. Figure 5 shows an innovative design for an optimum helical field by using coils arranged along a helical axis, a helical solenoid (HS). The HS coil can produce the required helical dipole and solenoidal fields, and can be tuned. The coil diameter is an additional parameter, which can be used to adjust the helical quadrupole component. However, this geometric effect is too weak to optimize the field gradient. Besides, an 80 mm gap requirement for infrastructure limits the maximum field gradient. Adding the helical correction conductors around the HS structure is currently the main

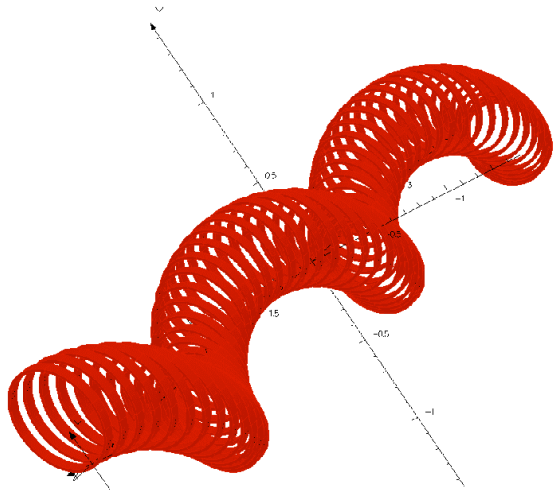

Figure 5: Design of helical solenoid magnet.

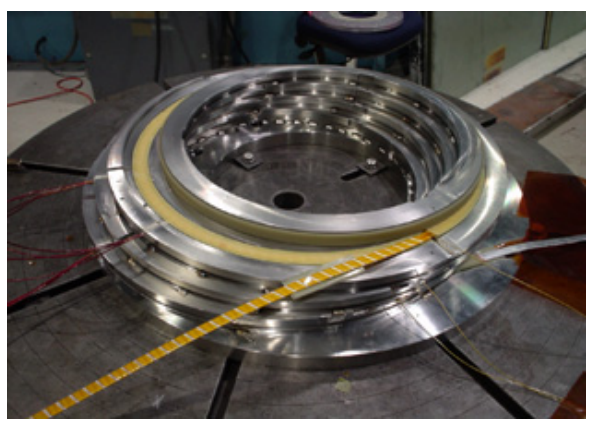

Figure 6: Winding the helical solenoid coil.

activity of optimization of the helical field. A detailed description is represented in Ref. [7]. A four coil test section of a helical solenoid has been made (see Figure 6) and it has been confirmed that the field simulation is accurate enough to design the HS coil of a full-length HCC magnet [8].

RF Cavity

As discussed above, the size of HS coil is fixed so as to generate the optimum helical magnetic field. Also the size of the RF cavity is inflexible. The radius of a pillbox type RF cavity is inversely proportional to the resonant frequency, which is determined by a boundary condition in the solution of Maxwell equations. In order to make a flexibly sized RF cavity, a high dielectric material loaded RF cavity has been proposed [9]. In this cavity, the velocity of light in the dielectric material is reduced and, as a result, the radial distribution of field in the dielectric material shrinks in the radial direction.

Figure 7 shows a conceptual picture of a dielectric-loaded RF cavity. The field calculation has been done in Superfish. In this example, the radius of the dielectric-loaded 400 MHz cavity can be about 9 cm, which is less than half the radius of a conventional vacuum RF cavity. The big issue for the dielectric loaded RF cavity is the RF power dissipation in the dielectric material. This issue may be resolved by using state of the art ceramics. There are many ceramics that have very low dielectric loss rates, around 10^{-5}. The required RF power will be a couple of MW. Finding the proper ceramics and doing the demonstration tests are planned in the dielectric loaded RF cavity R&D.

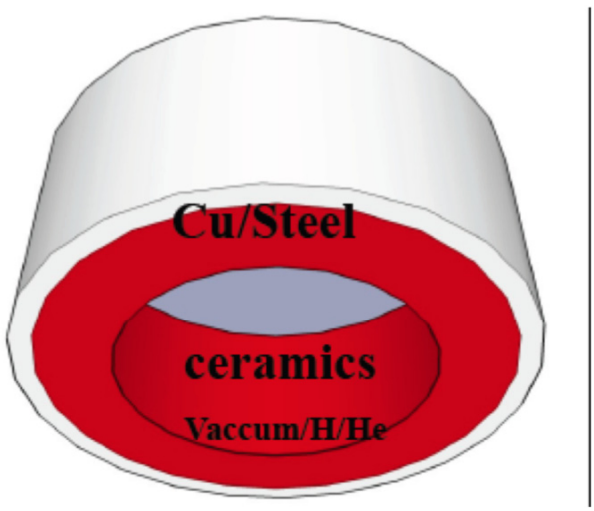

Figure 7: Conceptual drawing of dielectric-loaded RF cavity.

Figure 8 shows a series of dielectric-loaded RF cavities designed to be inside the HCC. Each RF cavity is a high-pressure pillbox-type, with a window between cavities and an RF power feed-through to the high pressure interior. The size of the RF power coupler will be determined when we optimize the RF parameters in simulation, which will be tested in the demonstration test in the current R&D.

The possibility of employing traveling wave helical RF structure is also being studied. Figure 9 shows a helical RF system within the HS coil magnet. A big advantage in the traveling wave RF structure is that there is no window between RF cells. Hence, the interference of the helical field caused by the RF power port will be minimized. The wedge shape RF cavity can generate an electric field along the helical beam path. The RF cavity has a coupling port to adjust the phase velocity in the RF cell to match to the beam velocity. In addition, the coupling port is needed to reduce the RF power by magnetic coupling. To this end, the coupling port can be located far from the cavity center, which is the beam path area. Hence, it can have a large aperture at the beam entrance and exit. A detailed discussion for this design is in Ref. [10].

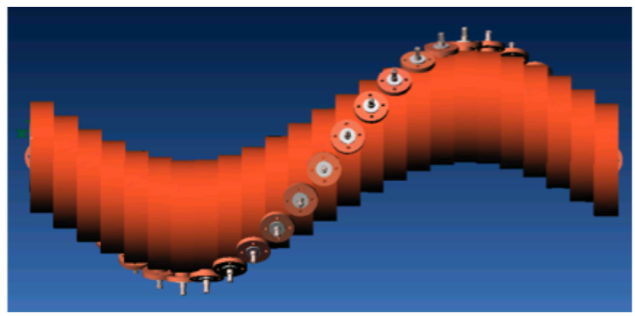

Figure 8: Conceptual design of RF cavities in arranged in a helical structure for use in an HCC.

HPRF cavity under high radiation conditions

RF cavities that are pressurized with hydrogen gas have been shown to operate at higher electric gradients in strong magnetic fields than vacuum cavities. The dense gas in the cavity absorbs the dark currents and suppresses breakdown. In addition the hydrogen gas acts as the energy absorber needed for ionization cooling, and occupies the same space as the RF cavities for a more compact cooling channel. This clever idea was first brought up by Muons Inc. and now the project is promoted by Muons Inc., NFMCC, and Muon Collider Task Force (MCTF).

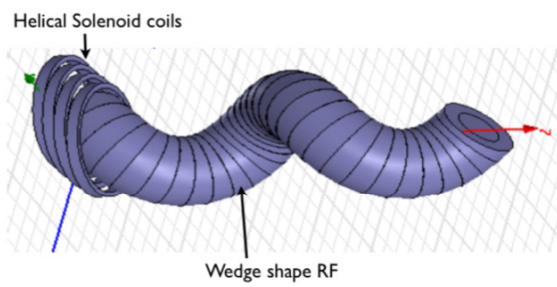

Figure 9: Traveling wave helical RF structure.

The results of these tests in the absence of beam have made a big impact, and continuation of the studies with high intensity proton beam now have a higher priority at Fermilab. The beam test will be done by 2010. One can expect that a high intensity charged beam will generate an electron swarm via the ionization interaction with a dense hydrogen gas, which will absorb a large amount of RF power and reduce the quality factor of the cavity. This process will be substantial if the recombination time is longer than the RF cycle [11]. By adding a very small amount of electronegative gas, this problem can be

resolved. In last HPRF test without beam, 0.01 % of SF6 was mixed in pure hydrogen gas in the HPRF Test Cell. The observed maximum field gradient is increased about 20 % in the linear proportional region. Figure 10 shows that the experimental results are well reproduced in numerical simulation, in which the electron attachment by SF6 is added [12]. Further simulation efforts have been made for future beam tests and have shown that filling the HPRF cavity with 0.01 % SF6 dopant gas will allow the HPRF to operate with a 10^{12} protons/pulse beam [13], which is comparable with the muon beam intensity expected in a muon collider.

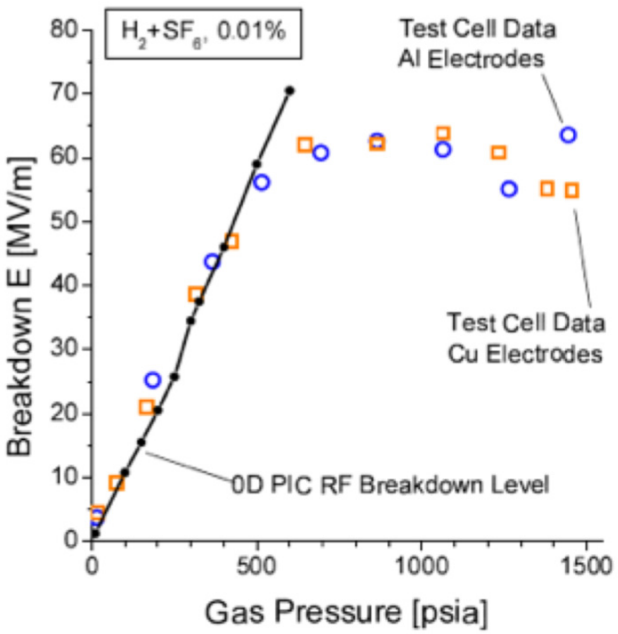

Figure 10: Comparison of experimental and simulation results. Square and circle points show the observed maximum electric field gradient with Copper and Aluminum electrodes in hydrogen gas with 0.01 % SF6 dopant gas and the solid line is the simulation result for this condition

SUMMARY

The HCC study has progressed in both experimental and simulation studies. In the simulation study, it is shown that the longitudinal phase space acceptance can be increased by tuning the RF parameters, with an initial RF frequency raised to 400 MHz. This can significantly mitigate the cost and space issues. One drawback in this design is that the HCC needs much greater RF power.

In experimental study, a 4-coil prototype of an HS has been built and tested and compared with the simulation results. The excellent agreement in both results shows that the HS coil magnet is feasible. Now, we endeavor to make a high field HS magnet, which will be used for the final HCC section as shown in Table 1.

HPRF testing without beam has been done in September, 2008. In this test, the effect of electronegative gas in high gradient RF fields was observed. The experimental results are well reproduced by the numerical simulation as shown in Figure 10. It indicates that the simulation tool will be able to predict the HPRF phenomena under high radiation conditions. According to the simulation study, the quality factor in the HPRF cavity with pure hydrogen gas will significantly drop, by two orders of magnitude. This reduction isl avoided if we add only 0.01 % of SF6 as a dopant gas. This will be tested at Fermilab in 2010.

REFERENCES

[1] P5 report 2008, http://www.er.doe.gov/hep/files/pdfs/P5_Report%2006022008.pdf
[2] Y.S. Derbenev and R.P. Johnson, PRSTAB 8, 041002 (2005)
[3] K. Yonehara et al., PAC09, TU5PFP020
[4] K. Yonehara and V. Balbekov, EPAC08, THPC110
[5] Muon Accelerator R&D program proposal for the next 5 years, https://mctf.fnal.gov/annual-reports/muon-5-year-documents-r5.pdf/download
[6] A. Afanasev et al., PAC09, FR5RFP012
[7] K. Yonehara et al., PAC09, MO6PFP062
[8] M. Yu et al., PCEC09
[9] M. Popovic and M. Neubauer, PAC09, TU5PFP017
[10] K. Yonehara, PAC09, TU5PFP021
[11] A. Tollestrup et al., FERMILAB-TM-2430-APC
[12] D. Rose et al., Voss Scientific report, VSL-0909
[13] D. Rose et al., Voss Scientific report, VSL-0812

STATUS AND CHALLENGES IN BEAM CRYSTALLIZATION*

Jie Wei and Peicheng Yu, Department of Engineering Physics, Tsinghua University, China
Hiromi Okamoto, Graduate School of Advanced Sciences of Matter, Hiroshima University, Japan
Yosuke Yuri, Takasaki Advanced Radiation Research Institute, JAEA, Gumma, Japan
Xiao-Ping Li, Skyworks Inc., USA
Andrew M. Sessler, Lawrence Berkeley National Laboratory, USA

Abstract

During the past several decades, beam crystallization has been studied both theoretically and experimentally. Theoretical investigations have been numerical, mainly using computer modeling based on the method of molecular dynamics (MD), and analytical, based on phonon theory. Experimental investigations involve both ion storage rings and ion traps using both electron and laser beam cooling. Topics of interests include crystal stability in various accelerator lattices and under different beam conditions, colliding crystalline beams, crystalline beam formation in shear-free ring lattices with both magnets and electrodes, experimental simulation of alternating-gradient conditions with an ion trap, tapered cooling and coupled cooling, and beam dynamics at different temperature regime as the beam is cooled from high to low temperature. In this paper, we first review theoretical approaches and major conclusions pertaining to beam crystallization. Then, we analyze conditions and methods of the various major experiments. Finally, we discuss, both theoretically and experimentally, some improvements, open questions, and challenges in beam crystallization.

INTRODUCTION

Beam crystallization has been a topic of interests since first evidence of experimental anomaly was observed on an electron-cooled proton beam at the storage ring NAP-M [1]. Since then, strong space-charge dominated phenomena and one-dimensional (1-D) ordering states were reported with both proton and heavier ions at storage rings ASTRID [2], TSR [3], CRYRING [4], ESR [5], and S-LSR [6]. Electron and laser beam cooling methods were used in attaining such states. On the other hand, attempts to achieve beam ordering beyond 1-D have not been successful, unlike the situation with ion traps where multi-dimensional crystalline structures were attained [7].

Theoretically, two main approaches were pursued: for the low-temperature regime, the molecular dynamics (MD) method was used to predict the ground-state structure [8–11] and the low-temperature dynamics [11–13]; for the intermediate temperature, high density regime the more conventional beam dynamics methods including envelope-equation resonance analysis [14, 15], space-charge particle-in-cell simulations, and intra-beam scattering analysis.

To attain an ordered state, effective beam cooling is needed to overcome beam heating caused by coherent resonance crossing and intra-beam scattering. Furthermore, the cooling force must conform to the dispersive nature of a crystalline ground state in a storage ring for 3-D structures. Experimentally, electron cooling has been used at NAP-M [1], ESR [4], CRYRING [5], and S-LSR [6] to cool beams of protons and heavier ions in all three directions, successfully reaching 1-D ordered states. With laser cooling, which has been used at ASTRID [2] and TSR [3], the beam can be cooled to ultra-low temperature in the beam rest frame in the longitudinal direction along the beam motion. However, to effectively reduce the transverse beam temperature methods like resonance coupling needs to be adopted [16]. With either cooling approach, the ideal "tapered cooling" effect is yet to be realized to move beyond 1-D ordering towards forming high-density crystalline structures in an actual storage ring.

CRYSTALLIZATION CONDITIONS

There are several necessary conditions for the formation of high-density, 3-D crystalline beams in storage rings.

Ground State Existence Condition

The storage ring is alternating-gradient (AG) focusing operating below the transition energy, γ_T,

$$\gamma < \gamma_T \tag{1}$$

where γ is the Lorentz factor of the beam. This condition is due to the criterion of stable kinematic motion under Coulomb interaction when particles are subject to bending in a storage ring [11].

Phonon Spectrum and Resonance Condition

The bare transverse phase advances per lattice period need to be less than 90°, i.e.,

$$\nu_{x,y} < \frac{N_{\rm sp}}{4} \tag{2}$$

where ν_x and ν_y are the bare horizontal and vertical tunes, and $N_{\rm sp}$ is the lattice super-periodicity of the storage ring. Note that the lattice elements consists of every device that

* Work supported by the "985 Project" of the Ministry of Education of China and the National Natural Science Foundation (10628510) and by the U.S. Department of Energy, Office of Basic Energy Sciences, under Contract No. DE-AC02-05CH11231.

† weij@tsinghua.edu.cn

interacts with the beam including magnetic fields (magnets), electric fields (accelerating and deflecting cavities), and cooling forces (cooling devices). This condition arises from the criteria that there is no linear resonance between the phonon modes of the crystalline structure and the machine lattice periodicity (requesting the left-hand-side of Eq. 2 to be less than $\sqrt{2}/4$) [13], and that linear resonance stopbands are not crossed during the entire cooling process as the 3-D beam density is increased [14, 15].

Cooling Force Condition

The cooling force needs to be applied in all three directions with cooling rates higher than the maximum heating rate of various mechanisms including intra-beam scattering, resonance heating, and diffusive processes, and the cooling force needs to conform to the dispersive nature of a crystalline structures, i.e. generally the cooling force needs to be "tapered" along the horizontal direction so that upon cooling particles' momenta p_z is linearly proportional to their horizontal displacements x [12],

$$\Delta p_z = \quad f_z(p_z \quad C_{xz}x) \tag{3}$$

where p_z is the longitudinal momentum component, f_z indicates the cooling strength, and C_{xz} is the tapering factor dependent on the lattice property.

Relaxed Conditions for a Low-density Beam

The above mentioned conditions may be relaxed if the beam density in the storage ring is adequately low so that the crystalline ground state is 1-D or 2-D: the maximum bare transverse phase advances per lattice period may be relaxed, and tapered cooling may not be necessary. At low beam density, cooling rate needed to overcome intra-beam scattering heating is also low. Naturally, with conditions on the machine lattice (Eq. 2) and cooling force (Eq. 3) relaxed, 1-D ordering is the first step towards full-density 3-D crystallization.

CRYSTALLINE PROPERTIES

It is convenient to use normalized units to describe the equations of motion [11] so that the ordering state of the system is mainly described by the dimensionless temperature T. The dynamic is determined by the essential quantities like the beam energy γ and the storage ring parameters (strengths of the magnetic field, electric field, and cooling force). Quantities like the charge state and mass of the particles are contained in the normalization; they do not change the dynamics of the crystalline state.

Characteristic Length, Normalized Temperature

For a system of particles with charge Ze and mass Am_0, the characteristic length ξ is given by [11]

$$\xi = \left(\frac{Z^2 r_0 \rho^2}{A\beta^2\gamma^2}\right)^{1/3} \tag{4}$$

where $r_0 = e^2/4\pi\epsilon_0 m_0 c^2$ is the proton classical radius, βc and $\gamma A m_0 c^2$ are the velocity and energy of the reference particle, and ρ is the radius of curvature of the main bending region of the storage ring.

The normalized beam-frame temperature of the crystalline beam system is defined to be proportional to the deviations of momentum from their ground-state values, then squared and averaged over the distance and over all the particles [12]. For systems of 1-D crystalline ground state, this normalized temperature T is related to the conventional temperature T_B by the relation

$$T = \frac{k_B \rho^2}{A m_0 c^2 \beta^2 \gamma^2 \xi^2} T_B \tag{5}$$

where k_B is the Boltzmann constant. Components of the temperature T_B is related to storage ring laboratory-frame parameters by

$$k_B T_{Bx,y} = A m_0 c^2 \beta^2 \gamma^2 \left(\frac{\nu_{x,y}}{R_0}\right) \epsilon_{x,y} \tag{6}$$

$$k_B T_{Bz} = A m_0 c^2 \beta^2 \left(\frac{\delta p}{p}\right)^2 \tag{7}$$

where $\epsilon_{x,y}$ are the un-normalized rms emittance, and $\delta p/p$ is the rms momentum spread.

Ground State Structure

When all three conditions (Eqs. 1 – 3) are satisfied, the crystalline ground states can be reached. At these states, motion of the circulating particles is periodic in time with the period of the machine lattice. As shown in Fig. 1, particle trajectory in the transverse direction conforms to AG focusing (breathing), and in the longitudinal direction conforms to the change in bending radius (shear). In the presence of a longitudinal electric field, momentum p_z also varies periodically conforming to the energy gain at the cavity.

The ground state structure is a 1-D chain when the beam line density is low. The structure becomes 2-D lying in the plane of weaker transverse focusing if the line density λ in the machine is

$$\lambda > 0.62\gamma\xi^{-1}[\min(\nu_y^2, \nu_x^2 \quad \gamma^2)]^{1/3} \tag{8}$$

For even higher density, the particles arrange themselves into 3-D crystals, becoming helices and then helices within helices. Fig. 2 shows such a multi-shell structure at a de-focusing location of the lattice. The maximum spatial density in the laboratory frame is approximately $\gamma\nu_y\sqrt{\nu_x^2 \quad \gamma^2}/(2\xi^3)$. If a sinusoidal electric field is present, the crystalline structure can be bunched azimuthally.

Beam and Lattice Heating

The minimum cooling rate needed for beam crystallization corresponds to the intra-beam scattering heating in an

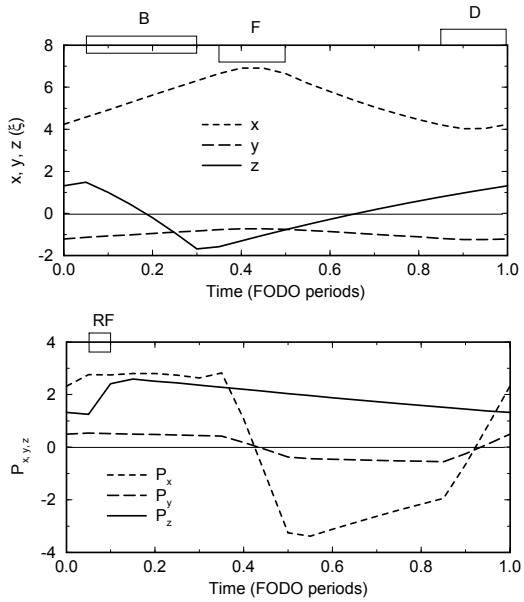

Figure 1: Particle trajectory of a bunched crystalline beam. The machine consists of 10 FODO cells with $\nu_x = 2.8$, $\nu_y = 2.1$, and $\gamma = 1.4$. Lattice components in each cell are displayed on the figure: B is a bending section, F and D are focusing and de-focusing quadrupoles, and RF is the bunching rf cavity.

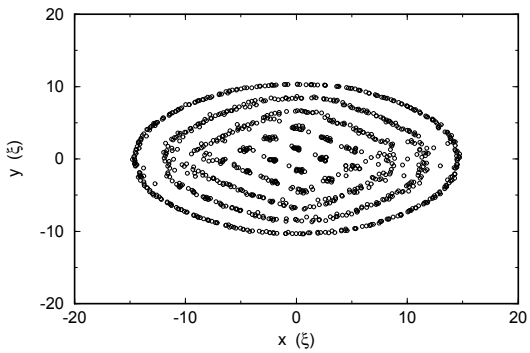

Figure 2: A multi-shell structure with particle positions projected into the x y plane ($\lambda = 25\gamma\xi^{-1}$).

AG-focusing lattice. At any non-zero temperature the beam absorbs energy and heats up under time-dependent external forces caused by variations in lattice focusing and bending. In the high temperature limit, this intra-beam scattering results in a growth rate proportional to $\lambda T^{-5/2}$. The peak heating rate occurs at the temperature of about $T \approx 1$ when the ordering starts to occur, as shown in Fig. 3. Typically, strong spatial correlation appears in all directions when the temperature is below $T \approx 0.05$. Lattice shear and AG focusing have similar effects on beam heating. Heating behavior is similar for both bunched and coasting beams. Effects of machine lattice imperfection, ion neutralization, and envelope instability have been studied.

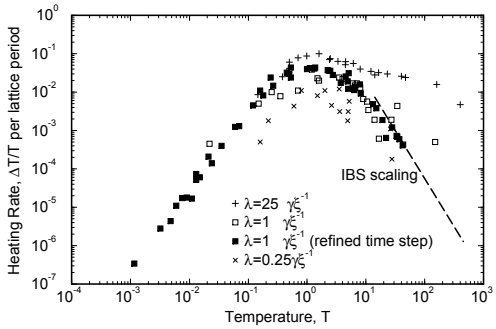

Figure 3: Typical heating rates as functions of temperature obtained by MD simulation at various line densities λ.

Cooling Methods

In order to attain a crystalline state, the beam must be effectively cooled in 3-D with a sufficient speed to overcome the heating. Both electron and laser cooling provide high cooling efficiency in the longitudinal direction but not in the transverse directions. "Sympathetic cooling" due to intra-beam scattering does produce transverse cooling. Coupling cavities operating on a synchro-betatron resonance or regular rf cavities in a dispersive region can provide effective 3-D cooling [16]. Realization of crystalline beams requires cooling that provides the ions with constant angular velocity, rather than constant linear velocity (tapered cooling) [12].

EXPERIMENTAL OBSERVATIONS

Experimental efforts on beam cooling and crystallization were made at several storage rings including NAP-M [1], TSR [3], ASTRID [2], ESR [4], CRYRING [5], and S-LSR [6]. In this section, we review the experimental results and provide theoretical estimates.

Table 1 lists experimental parameters and observations of these storage rings. All the experiments were performed at beam energies below transition (Eq. 1). On the other hand, every machine violates the crystallization condition Eq. 2. Furthermore, cooling forces were applied without a tapering factor (Eq. 3). Therefore, we do not expect the formation of 3-D crystalline states in these experiments.

With ASTRID and TSR, laser cooling was used to reduce the longitudinal temperature to a low level. Even though the longitudinal temperature could be extremely low, there was no clear indication of ordering aside from some anomaly in the longitudinal Schottky signal. With NAP-M, ESR, CRYRING, and S-LSR, electron cooling was used to cool the beam three dimensionally. A clear signature of these experiments was an abrupt drop of the momentum spread (and the longitudinal Schottky signal level) of the electron-cooled beam to very low values when the particle number decreased in the storage ring indicating possible ordering towards a 1-D chain in the longitudinal direction even though the transverse temperature may still be high. Not surprisingly, proton and heavier ion beams

Table 1: A compilation of experimental parameters and observations at existing storage rings.

	NAP-M	**TSR**	**ASTRID**	**ESR**	**CRYRING**	**S-LSR**
E_u [MeV/u]	65.7	2.43	0.00417	400	7.4	7
Circumference	47.25	55.4	40	108.36	51.63	22.557
γ	1.07	1.003	1.00000444	1.43	1.00789	1.00746
γ_T	1.18	2.96	4.34	2.6	2.33	1.41
$N_{\rm sp}$	4	2	4	6	6	6
$\frac{\nu_x}{N_{\rm sp}}$ / $\frac{\nu_y}{N_{\rm sp}}$	0.34 / 0.32	1.29 / 1.11	0.66 / 0.28	0.38 / 0.38	0.38 / 0.38	0.27 / 0.2 [§]
Species	Proton	$^{3}Be^{+}$	$^{24}Mg^{+}$	$^{238}U^{92+}$	$^{129}Xe^{36+}$	Proton
Cooling Method	EC	LC	LC	EC	EC	EC
ξ [μm]	4.61	5.1	21.8	12.7	11.2	4.83
$T_{Bx,y}$ / T_{Bz} [K] [*]	50 / 1	- - / 6	1000 / 0.001	10.8 / 57.9	11.6–34.8 / 0.58–1.74	5.7 / 0.31
$T_{x,y}$ / T_z	13.9 / 0.28	- - / 1.84	1300 / 0.0013	0.001 / 0.005	0.006–0.018 / 0.0003–0.0009	1.67 / 0.09
N_0 (anomaly) [†]	2×10^7	- -	5.5×10^8	1000	1000–10000	2000
N_0 (1-D to 2-D) [‡]	6.0×10^6	1.2×10^7	1.2×10^6	7.8×10^6	4.7×10^6	3.3×10^6
Observations	Schottky anomaly	Indirect transverse cooling	Schottky anomaly	1-D ordering	1-D ordering	1-D ordering

[*] $T_{Bx,y,z}$: the observed lower temperature limit of the corresponding ion species in the machine.
[†] N_0 (anomaly): the ion number when anomalies in the Schottky signal were observed.
[‡] N_0 (1-D to 2-D): the theoretical estimate (Eq. 8) of the intensity threshold when the ground state structure changes from 1-D to 2-D.
[§] $\nu_x/N_{\rm sp}$ and $\nu_y/N_{\rm sp}$ of the S-LSR can be made to be below 0.25 simultaneously.

exhibited similar behaviors.

NAP-M

When the proton beam was electron-cooled to reach a steady state, the momentum spread of the beam was measured from the Schottky bandwidth. As the number of protons N_0 in the machine varied from 10^8 to 2×10^6 [1], the momentum spread first decreased with the decreasing beam intensity. However, when N_0 was reduced to 2×10^7, the equivalent momentum spread became independent of the beam intensity.

MD study [17] indicates that at the intensity of $N_0 = 2 \times 10^7$ the ground state is 3-D. The observed Schottky anomaly thus does not correspond to ordering. In fact, at intensities higher than the anomaly point the scaling between the momentum spread and intensity indicated the equilibrium between intra-beam scattering and electron cooling. At intensities below the anomaly point, the observed constant momentum spread (Schottky signal) could be due to machine hardware issues [18].

On the other hand, the NAP-M machine lattice is appropriate for the formation of 1-D ordered states, should N_0 be below about 6×10^6.

TSR

TSR was the first storage ring where longitudinal laser cooling was applied on an ion beam. Transverse cooling was achieved indirectly through intra-beam scattering [3]. A drawback of the TSR machine lattice is its low lattice periodicity. Even though theoretically 1-D or 2-D ordering (a transversely rotating zig-zag structure with periodicity of the machine lattice) may be formed [17], in practice the large phase advance per lattice period makes beam crystallization nearly impossible.

ASTRID

At ASTRID, extremely low ($T_{Bz} \sim 1$ mK) temperature was achieved longitudinally through laser cooling [2]. Anomalies in Schottky signal were observed. However, the transverse temperature was too high to allow the formation of ordered structures during the experiments. MD studies indicate that 1-D and 2-D crystals may be formed if transverse temperature is reduced [17].

ESR

Systematic electron cooling studies were performed at ESR with various types of ion species at different densities [4]. For highly charged ions (Ar^{18+} and above), the momentum spread of the cooled ions dropped abruptly to very low values when the particle number in the machine decreased to 10000 and less indicating 1-D ordering in the longitudinal direction [19].

CRYRING

Ordering phenomena similar to those at ESR were observed at CRYRING [5]. Even though the beam energy is quite different, both lattice properties and predicted crystalline properties are similar.

S-LSR

Among the machines listed in Table 1, lattice design of the newly constructed and commissioned S-LSR is best suited for beam crystallization [6]. With the proton beam,

similar 1-D ordering phenomena were observed: the momentum spread of the cooled protons dropped abruptly to very low values when the particle number in the machine decreased to 2000 and less [20].

The bare transverse phase advance per period of lattice main magnets can be made to be below 90°. However, condition of Eq. 2 is rigorously satisfied only if rf cavities, cooling stations, and deflecting cavities are all placed symmetrically.

DISCUSSIONS AND SUMMARY

During the past three decades, both experimental and theoretical efforts were made in attaining crystalline beams in storage rings. Experimentally, states of 1-D ordering were realized using electron cooling on both proton and heavier ion beams at low density. Higher density, 3-D crystalline structures were only realized in ion traps; efforts to form 3-D crystalline beams in storage rings have not been successful. Theoretical approaches based on the molecular dynamics method and phonon spectrum analysis at low temperature and beam envelope resonance analysis at higher temperature were adequate in understanding the basic experimental findings of most machines (except for NAP-M case). More comprehensive analysis is needed especially for the intermediate temperature regime, and on the modeling of various cooling processes.

Challenges in beam crystallization are to design and construct storage rings with high lattice periodicity and low transverse phase advance (Eq. 2) to avoid linear resonances, and to implement effective beam cooling that conforms to the dispersive nature of the beam (Eq. 3).

Difficulties in attaining crystalline beams are due to the stringent necessary conditions (Eqs. 1 – 3) originating from the beam dynamics in a circular accelerator. Attempts were made to effectively compromise these conditions. For example, machine lattices of high or imaginary transition energy γ_T were proposed so that high-energy or colliding crystals may be realized in storage rings of moderate circumference [21]. Shear-free ring lattices consisting of both magnets and electrodes were designed at S-LSR so that 3-D crystalline structures may be formed without using tapered cooling forces [22].

Ion traps have been used to experimentally simulate features of an AG-focusing storage ring [23]. Combination of a storage ring and an ion trap may simulate the environment of colliding crystals.

Some fundamental questions remain to be answered. Crystalline beam corresponds to a new state of matter of one-component plasma where particles are confined by a periodic, time-dependent external potential with finite transverse boundary. Basic condensed-matter physics of such a system including phase-transition properties remains to be studied.

We thank H. Danared, N. S. Dikanski, D. Habs, J. S. Hangst, A. Noda, V. V. Parkhomchuk, and M.Steck for discussions on experimental results at various storage rings.

REFERENCES

[1] E.E. Dement'ev et al, Zh. Tekh. Fiz. 50 (1980) 1717; N.S. Dikanskii, D.V. Pestrikov, Proc. Workshop on Electron Cooling and Related Applications, KfK 3846 (1984); V.V. Parkhomchuk, A.H. Skrinsky, Reports on Progress in Physics, 54 (1991) 919

[2] J.S. Hangst et al, PRL 67 (1991) 1238, Phys. Rev. Lett. 76, 1238 (1991); N. Madsen, et al, Phys. Rev. Lett. 83, 4301 (1999); J. S. Hangst, et al, Phys. Rev. Lett. 74, 86 (1995)

[3] S. Schroder et al. Phys. Rev. Lett. 64, 2901 (1990); H.-J. Miesner et al, Phys. Rev. Lett. 77, 623 (1996)

[4] M. Steck et al, Phys. Rev. Lett. 77, 3803 (1996); M. Steck et al., Nucl. Instrum. Meth. A 532, 357 (2004)

[5] H. Danared et al, Phys. Rev. Lett. 88, 174801 (2002)

[6] T. Shirai et. al. Phys. Rev. Lett. 98, 204801 (2007); T. Shirai et al., Proc. Workshop on Beam Cooling and Related Topics, Bad Kreuznach (2007) 139

[7] F. Diedrich et al., Phys. Rev. Lett. 59, 2931 (1987); D. J. Wineland et al., Phys. Rev. Lett. 59, 2935 (1987); M. Drewsen et al, Phys. Rev. Lett. 81, 2878 (1998); T. Schätz, et al, Nature (London) 412, 717 (2001); U. Schramm et al, Nucl. Instrum. Meth. A 532, 348 (2004)

[8] J.P. Schiffer, P. Kienle, Z. Phys. A 321, 181 (1985); J.P. Schiffer, O. Poulsen, Europhys. Lett. 1, 55 (1986)

[9] A. Rahman, J. P. Schiffer, Phys. Rev. Lett. 57, 1133 (1986)

[10] R.W. Hasse, J.P. Schiffer, Ann. Phys. 203 (1990) 419

[11] J. Wei, X.-P. Li, A. M. Sessler, Phys. Rev. Lett. 73, 3089 (1994)

[12] J. Wei, H. Okamoto, A. M. Sessler, Phys. Rev. Lett. 80, 2606 (1998)

[13] X.-P. Li et al, Phys. Rev. ST-AB, 9, 034201 (2006)

[14] I. Hofmann, J. Struckmeier, Proc. Workshop on Crystalline Ion Beams (1988) 140; B. Yang et al, Phys. Plasmas, 3, 688 (1996)

[15] K. Okabe, H. Okamoto, Jpn. J. Appl. Phys. 42, 4584 (2003)

[16] H. Okamoto, A. M. Sessler, and D. Möhl, Phys. Rev. Lett. 72, 3977 (1994)

[17] J. Wei et al, in "Crystalline Beams and Related Issues", ed. D.M. Maletic A.G. Ruggiero, World Scientific (1996) p. 229; J. Wei, X. P. Li, A. M. Sessler, Proc. 1995 Part. Accel. Conf., (1995) 2946

[18] Similarly, a constant level of momentum spread (Schottky signal) was observed at ESR for low intensity beams. The phenomena were attributed to the stability issues of the magnet power supply [4].

[19] R. W. Hasse, Phys. Rev. Lett. 83, 3430 (1999); H. Okamoto et al, Phys. Rev. E 69, 066504 (2004)

[20] A. Noda et al, New J. Phys. 8, 288 (2006)

[21] J. Wei et al, Proc. Workshop on Beam Cooling and Related Topics, Bad Kreuznach (2007) 91

[22] M. Ikegami et al., Phys. Rev. ST-AB 7, 120101 (2004)

[23] H. Okamoto, Y. Wada, R. Takai, Nucl. Instrum. Meth. A 485 (2002) 244

THE EVOLUTION OF THE PHASE SPACE DENSITY OF PARTICLE BEAMS IN EXTERNAL FIELDS

E.G. Bessonov, Lebedev Physical Institute of the Russian Academy of Sciences, Moscow, Russia

Abstract

In this paper the evolution of the phase space density of particle beams in external fields is presented proceeding from the continuity equation in the six-dimensional (6D) phase space (μ-space). Such a way the Robinson theorem, which includes the Liouville theorem as a special case, was proved in a more simple and consistent alternative way valid for arbitrary external fields, averaged fields of the beam (self-generated electromagnetic fields except intrabeam scattering) and arbitrary frictional forces (linear, nonlinear). It includes particle accelerators as a special case. The limits of the applicability of the Robinson theorem in case of cooling of excited ions having a finite living time are presented.

INTRODUCTION

In 1958 K.W.Robinson derived at once the sum of damping rates (decrements) of three particle oscillation modes in circular accelerators in the relativistic case [1]. He did an expansion of the power of frictional forces over the particle energy for the private case of radiative reaction force. That is why his final formulae do not include the term with the derivative of the power. Later, A.A.Kolomensky derived the formulae in the general form for the relativistic case and applied it to the ionization cooling [2]. He calculated separately damping rates for three directions in the curvilinear coordinate system and then took their sum.

In order to derive damping increment, K.W.Robinson evaluated the determinant of the transfer matrix of the infinitesimal element of length of a particle orbit. The determinant determines the evolution of a 6D phase space volume of the beam or its density along the trajectory. P.Csonka for this purpose evaluated the infinitesimal 6D phase space volume as well and used some additional conditions to prove the theorem [3]. H.Wiedemann in the textbook [4] presented the proof of the theorem following Robinson's idea but keeping the derivative of the power losses over the energy. Now the theorem in the particle accelerator community is named by Robinson theorem or Robinson's damping criterion.

EVOLUTION OF PARTICLE BEAM DENSITY IN THE EXTERNAL ELECTROMAGNETIC FIELDS

Let us proceed from the continuity (Liouville's) equation in the 6D phase space coordinate-momentum $(\vec{r},\vec{p})$:

$$\frac{d\rho}{dt}+\rho\ div\ \vec{v}=0\,. \qquad (1)$$

Here components of the 6D velocity $\vec{v}=(\vec{v}_r,\vec{v}_p)$ are $\dot{x},\dot{y},\dot{z},\dot{p}_x,\dot{p}_y,\dot{p}_z$, where $\dot{r}_i=dr_i/dt$, $\dot{p}_i=dp_i/dt$. The equation (1) or equivalent equation $\partial\rho/\partial t+div\ (\rho\vec{v})=0$ expresses the number of particles conservation law. In our case the form of the equation (1) is preferable as it presents the total derivation of the density in the coordinate system moving with the beam. It can be presented in the integral form $\rho=\rho_0\exp[-\int div(\vec{v})dt]$, where ρ_0 is the initial phase space density.

The divergence $div\ \vec{v}=div_r\vec{v}_r+\ div_p\vec{v}_p$, $div_r\vec{v}_r=0$ as the velocity $\vec{v}_r=c\vec{p}/\sqrt{p^2+m^2c^2}$ does not depend on spatial coordinates (r_i, p_i are independent variables). The value $\vec{v}_p=\dot{\vec{p}}=\dot{\vec{p}}_H+\dot{\vec{p}}_{Fr}=\ \vec{F}_H+\vec{F}_{Fr}$ is the force acting upon the particle. The conservative force $\vec{F}_H=e\vec{E}(\vec{r},t)+\ (e/c)[\vec{v}\ \vec{H}(\vec{r},t)]$ is determined by external fields and the fields of the particle beam ($div_p\vec{F}_H=0$), while $\vec{F}_{Fr}$ is the frictional force. That is why $div_p\vec{v}_p=div_p\vec{F}_{Fr}$, and the equation (1) can be presented in the integral form $\rho=\rho_0\exp[-\int div_p\vec{F}_{Fr}dt]$.

The frictional force can be written in the form $\vec{F}_{Fr}=-\chi_{Fr}(\vec{r},p,t)\cdot\vec{n}$, where $p=|\vec{p}|$, $\vec{n}=\vec{p}/p$, $\chi_{Fr}(\vec{r},p,t)$ is the frictional coefficient. In this case $div_p\vec{F}_{Fr}=-\chi_{Fr}div_p\vec{n}-\vec{n}\cdot grad_p\chi_{Fr}=-\ 2\chi_{Fr}/p\ -\partial\chi_{Fr}/\partial p$. We took into account, that $div_p\vec{n}=2/p$ and $\vec{n}\cdot grad_p\chi_{Fr}\ (\vec{r},p,t)=(\partial\chi_{Fr}/\partial p)=v_r(\partial\chi_{Fr}/\partial\varepsilon)$, where $\varepsilon=\sqrt{p^2c^2+m^2c^4}$ is the energy of the particle.

The frictional power $P_{Fr}=\vec{F}_{Fr}\cdot\vec{v}_r=\chi_{Fr}(\vec{r},p,t)\cdot\vec{n}\cdot\vec{v}_r=c\ \beta\cdot\chi_{Fr}(\vec{r},p,t)$, where $\beta=v_r/c$. It follows that $\chi_{Fr}=\ P_{Fr}(\vec{r},p,t)/c\beta$, and the equation (1) become

$$\rho=\rho_0\exp[-\int\alpha_{6D}(\vec{r},p,t)\ dt]\,, \qquad (2)$$

where $\alpha_{6D}(\vec{r},p,t)=-div_p\vec{F}_{Fr}=2\chi_{Fr}/p+\partial\chi_{Fr}/\partial p$ or:

$$\alpha_{6D}(\vec{r},\varepsilon,t)=(1+\frac{1}{\beta^2})\frac{P_{Fr}(\vec{r},\varepsilon,t)}{\varepsilon}+\ \frac{\partial P_{Fr}(\vec{r},\varepsilon,t)}{\partial\varepsilon}\,.$$

The integral (2) along a trajectory of a particle is the solution of the equation (1). According to (2), the 6D rate of the beam density change is determined by the frictional

This work was supported by RFBR under Grant No. 09-02-00638a

power and its derivative with respect to the particle energy. The integral (2) is valid for the arbitrary systems (linear, nonlinear, coupled). We did not use a curvilinear coordinate system, the Jacobee's formula for the system of linear differential equations, matrices; any additional conditions (see [3]). In our case the expression (2) is valid for the nonrelativistic case as well. In general case ($\alpha_{6D} \neq const$) the solution is not exponential function. The equation (2) is valid for infinitesimal parts of the beam. The damping of different parts of the beam in some methods of cooling should be distinguished.

If $P_{Fr}(p) = 0$, then $\alpha_{6D}(\vec{r}, p, t) = 0, \quad d\rho / d\,t = 0$ and, according to (2), we come to the Liouville's theorem [4]–[7]. It states that for conservative systems the particle density ρ in the 6D phase space, the number of particles in the phase space volume occupied by the beam and hence the volume stay constant. In this case the volume is named the 6D normalized emittance. The volume divided by the factor $(\beta\gamma)^3$ is named the unnormalized emittance accordingly. The normalized emittance is invariant for conservative systems. 2D and 4D phase space volumes can be exchanged by conservative external fields. It follows from private examples (see e.g. [1]).

Robinson and Liouville theorems are valid for identical particles (electrons, protons, muons and so on). The Robinson theorem is valid if frictional forces exist only at the moment of their interaction with media or external fields and there is no time delay between the interaction time and the frictional force. Excited ions have higher rest mass then unexcited ones and have finite lifetime. It means that in general case the above theorems are not valid for ion cooling (excited ions are not identical to unexcited ones and have finite lifetime). The theorems works well if the lifetime of excited ions is less then some characteristic time for the processes of the beam evolution determined by concrete conditions. E.g., in the case of particle accelerators the delay time between the moment of the ion excitation by a laser beam and following photon reemission must be less then the period of betatron oscillations. Otherwise, the additional cooling or heating of the ion beam is possible.

It is supposed above that the particle beam is a continuous media (there is no free space between particles). On practice it means that the distance between particles is much less then dimensions of any instrument, which is used to move a particle from a peripheral region of the 6D volume of the beam to the central one and that the instrument do not disturb another particles of the beam (otherwise, the stochastic cooling is possible).

APPLICATION OF ROBINSON THEOREM TO PARTICLE ACCELERATORS

The equation (2) can be applied to the beam transport lines, linear and circular accelerators, storage rings, betatrons, recirculators and so on. If the motion of particles of a beam in the limits of the occupied 6D volume is described by linear differential equations, then all parts of the beam density and the total phase space volume occupied by the beam change identically.

If the energy losses are compensated by induction or RF fields in cavities of the circular machines, the average energy of particles is kept constant, power loss of particles of the beam in the limits of its phase space volume is a linear function of the energy, then, according to (2), the rate of the beam density change in these machines is determined by the 6D-damping increment

$$\overline{\alpha_{6D}} = -\overline{div\ \vec{F}_{Fr}} = (1 + \frac{1}{\beta^2}) \frac{\overline{P}_{Fr}(\varepsilon)}{\varepsilon}\Big|_{\varepsilon=\varepsilon_s} + \frac{\partial \overline{P}_{Fr}(\varepsilon)}{\partial \varepsilon}\Big|_{\varepsilon=\varepsilon_s} \quad ,(3)$$

where $\overline{P}_{Fr}(\varepsilon)$ is the average rate of the particle energy loss due to friction, ε_s is the energy of the reference particle. Reference particle can be synchronous particle if the radiofrequency accelerating field is switched on or some central particle if the induction accelerating field is used. If the increment α_{6D} is positive then in this case they say that 6D cooling occurs. The expression (3) can be negative, if the second term $\partial \overline{P}_{Fr}(p)/\partial\varepsilon$ is negative and larger by the value then the first one (beam heating).

Note that 6D cooling is a necessary but not sufficient condition for production of the high density beam in 3D space. Untidamping of synchrotron [8] or betatron [9] oscillations can occur under 6D cooling conditions. The emittance exchange can be used to remove the case of untidamping [1], [4], [9].

The following kinds of the charged particle energy looses can be used for cooling: electromagnetic radiation losses in the external electromagnetic fields (synchrotron radiation, undulator radiation, backward Compton and backward Rayleigh scattering) and in matter (ionization and excitation losses, bremstrahlung radiation).

If the energy of particles is maintained at constant level, $\overline{P_{Fr}}(p) \neq 0$, and $\partial \overline{P_{Fr}}(p)/\partial\varepsilon \sim \overline{P_{Fr}}(p)/\varepsilon$ then, according to (3), the density of the particle beam will increase by $e = 2.7$ times after particles of the beam will lose the energy $\Delta\varepsilon \sim \varepsilon$ (e.g., synchrotron radiation damping). If $\partial \overline{P_{Fr}}(p)/\partial\varepsilon \sim \overline{P_{Fr}}(p)/\Delta\varepsilon_b$ ($\Delta\varepsilon_b << \varepsilon$) then the same increase of the density will be after particles of the beam lose the energy $\Delta\varepsilon = \Delta\varepsilon_b$, where $\Delta\varepsilon_b$ is the initial energy spread of the beam. This case is possible for the radiative cooling of ion beams by the broadband laser beam [10]. In this case the power loss must increase with the energy from zero to maximal value in the limits of the energy spread $\Delta\varepsilon_b$ (fast, enhanced, stimulated cooling) [11]-[12].

To separate the longitudinal component p_s of the momentum from the transverse components p_x , p_z we must find the closed trajectory of a reference particle, direct the longitudinal unit vector along the trajectory and direct two other transverse unit vectors in the directions transverse to each other and to the longitudinal one. In such a way we will pass on to a curvilinear coordinate system for particle accelerators. In this system the 6D increment is the sum of two transverse (radial, vertical)

and longitudinal increments: $\alpha_{6D} = 2\alpha_x + 2\alpha_z + 2\alpha_s$. The increments for longitudinal and uncoupled vertical oscillations are found without a problem by direct calculations and the radial one is determined from the equation (3). In the relativistic case:

$$\alpha_x = \frac{1}{2}\left[\frac{\overline{P}_s}{\varepsilon_s} + \frac{\partial \overline{P}}{\partial \varepsilon}|_s - \frac{d\overline{P}}{d\varepsilon}|_s\right], \quad \alpha_z = \frac{1}{2}\frac{\overline{P}_s}{\varepsilon_s}, \quad \alpha_s = \frac{1}{2}\frac{d\overline{P}}{d\varepsilon}|_s \cdot \quad (4)$$

The total momentum and the energy of a particle are coupled with its components p_x, p_z, p_s by the relations $p^2 = p_x^2 + p_z^2 + p_s^2$, $\varepsilon = p^2 + mc^2$. That is why we could pass from μ-space to the new space (x, p_x, z, p_z, s, ε), which is usually used in the theory of accelerators. We can name it the ε-space. Particles in the accelerators and storage rings are subjected to fast transverse vertical and radial betatron oscillations. Moreover they participate in longitudinal oscillations of two types: fast oscillations of momentum with the betatron frequencies in accordance with the equation $p_s^2 = p^2 - p_x^2 - p_z^2$ and, if the accelerating radiofrequency field is switched on, slow synchrotron oscillations of the momentum $p(t)$ and energy $\varepsilon(t)$.

Note that frictional cooling goes through the energy losses of particles, particle beam can stay monoenergetic, its energy spread and 6D volume are equal to zero (particle beam is on the 6D hypersphere), but the spread of the longitudinal oscillations of particles will not be zero if the transverse emittances are nonzero.

CONCLUSION

The evolution of the phase space density of particle beams in external fields is presented proceeding from the continuity equation in the six-dimensional phase space. The Robinson theorem, was proved in an alternative way valid for arbitrary external fields, averaged fields of the beam (self-generated electromagnetic fields except intrabeam scattering) and arbitrary frictional forces. It includes particle accelerators as a special case. The limits of the applicability of the Robinson theorem in case of cooling of excited ions having a finite living time are presented.

The author thanks R.M. Feshchenko for usefull discussions.

REFERENCES

[1] K.W. Robinson, Radiation effects in Circular Electron accelerators, *Physical Review*, 1958, v.111, No 2, p. 373-380; Electron radiation at 6 BeV, CEA Report No 14 (1956).

[2] A.A. Kolomenskii, On the oscillation decrements in accelerators in the presence of arbitrary energy losses, Sov.Atom.Energ.19:1511-1513,1965, (translated from *Atomnaya Energiya*, v.19, No6, 1965, p.534-535, FSU); http://www.springerlink.com/content/x471033782340l1u/fulltext.pdf .

[3] P.L. Csonka, Proof of a generalized Robinson's theorem on beam damping, Physical Review A, v. 46, No 4, p.2101-2105(1992).

[4] H. Wiedemann, *Particle Accelerator Physics*, 3rd Edition, Springer-Verlag Berlin Heidelberg 1993, 1999, 2007.

[5] A.M. Sessler, "*Methods of beam cooling*", LBL-38278 UC-427, February 1996; 31st Workshop: "*Crystalline Beams and Related Issues*", November 11-21, 1995.

[6] D. Mohl, A.M. Sessler, Beam cooling: Principles and Achievement, Nuclear Instruments and Methods, A532, 2004, p.1-10.

[7] Klaus G. Steffen, High energy beam optics. Interscience publishers, New York-London-Sydney, 1985.

[8] D. Bohm, L. Foldy, The theory of the synchrotron, *Physical Review*, v.70, No 5&6, 1946, p. 249-258.

[9] D. Neuffer, Principles and applications of muon cooling, *Particle accelerators*, v.14, 1983, p.75-90.

[10] E.G. Bessonov, Kwang-Je Kim, Radiative cooling of ion beams in storage rings by broad band lasers, Phys. Rev. Lett., 1996, v.76, No 3, p.431-434; Preprint LBL -37458, UC-414, June 1995.

[11] E.G. Bessonov, On violation of the Robinson's damping criterion and enhanced cooling of ion, electron and muon beams in storage rings: Proceedings of RuPAC XIX, Dubna 2004, p.62-64. Published in http://cern.ch/AccelConf/r04/papers/THBO09.pdf.

[12] E.G. Bessonov, R.M. Feshchenko, Stimulated radiation cooling: Proceedings of RuPAC XXI, Dubna 2008, p.91-92. Published in: http://cern.ch/AccelConf/r08/papers/MOCAU03.pdf

WEDGE ABSORBER SIMULATIONS FOR THE MUON IONISATION COOLING EXPERIMENT

C. T. Rogers*, Rutherford Appleton Laboratory, Didcot, OX11 0QX, UK
P. Snopok†, University of California, Riverside, CA 92521, USA

Abstract

In the Muon Ionisation Cooling Experiment (MICE), muons are cooled by ionisation cooling. Muons are passed through material, reducing the total momentum of the beam. This results in a decrease in transverse emittance and a slight increase in longitudinal emittance, but overall reduction of 6D beam emittance.

In emittance exchange, a dispersive beam is passed through wedge-shaped absorbers. Muons with higher energy pass through more material, resulting in a reduction in longitudinal emittance as well as transverse emittance. Emittance exchange is a vital technology for a Muon Collider and may be of use for a Neutrino Factory.

In this paper, we show that even in the straight solenoidal lattice of MICE, emittance exchange can be demonstrated. In order to achieve this, a muon beam is passed through a wedge shaped absorber; the input beam distribution must be carefully selected to accomodate strong non-linear effects due to chromatic aberrations in the solenoid lattice, which we achieve using a polynomial weighting function to select beam moments.

EMITTANCE EXCHANGE IN THE MUON IONISATION COOLING EXPERIMENT

Ionisation cooling is achieved in the Muon Ionisation Cooling Experiment (MICE) [1] baseline by the placement of absorbing material in the beamline. The absorbing material removes beam momentum, which is replaced only in the longitudinal direction by RF cavities, resulting in a net reduction of emittance. Low-Z materials must be used as absorbers together with carefully designed beam optics. This minimises the effects of multiple Coulomb scattering, which tend to reduce the cooling effect. Overall, transverse emittance is reduced to some equilibrium point while longitudinal emittance stays the same or increases slightly due to stochastic processes in the energy loss.

In this note we consider using MICE to observe a phenomenon known as emittance exchange. In emittance exchange a dispersive beam is passed through a wedge-shaped absorber. Muons with higher energy pass through more material and experience greater momentum loss. In this way the longitudinal emittance of the beam can be reduced either in addition to, or even instead of transverse emittance reduction. Emittance exchange is vital to a Muon Collider and has been considered as an upgrade option to the Neutrino Factory. Ring coolers [2], Helical coolers [3] and Guggenheim coolers [4] have been proposed to perform emittance exchange and longitudinal cooling using a simple wedge or a truncated wedge.

In MICE muons will be passed one-by-one through a short section of ionisation cooling equipment and the six-dimensional phase space vector of each muon will be measured to high precision, enabling the measurement of reduction in 2D, 4D and 6D emittance due to ionisation cooling. The position and momentum of individual muons is determined by high resolution scintillating fibre spectrometers before and after the cooling apparatus. Fast time-of-flight counters measure time-of-flight between the upstream and downstream spectrometers, which together with the spectrometers enables reconstruction of the full 6D phase space vector of individual muons. Rejection of beam impurity before the cooling channel will be achieved using a pair of time-of-flight counters together with a threshold Cherenkov counter. After the cooling channel decay electrons will be identified using the time-of-flight through the experiment together with an Electron-Muon-Ranger.

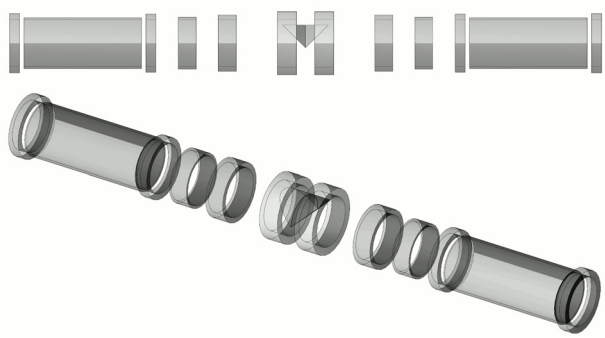

Figure 1: The geometry as simulated in G4MICE code: side and 3D view. The wedge absorber and coils are shown. The total length of the Step IV layout is just over 7.5 m, inner radius of the coils is 258 mm. A steel, cylindrical beam pipe with a 232 mm aperture was also included in simulations but is not shown in these figures.

Wedge Geometry

We study the use of a simple wedge-shaped absorber in a straight solenoid channel. The geometry considered is shown in Figure 1. The case considered here is MICE Step IV, where MICE is operated in a mode without RF cavities. RF cavities will be added to MICE at a later stage, but

* chris.rogers@stfc.ac.uk
† pavel.snopok@ucr.edu

it is expected that the non-linearities discussed below will be worse for a longer cooling section and swamp any cooling measurement. In addition, the thin end of the wedge absorbers will enable dark currents emerging from the RF cavities to enter the detector systems, which may swamp any muon signal.

NON-LINEARITY OF BEAM TRANSPORT

Solenoids have natural chromatic aberrations at 2nd order and spherical aberrations at 3rd order that are significant for the large emittances typical of MICE ($\varepsilon_\perp = 7$ mm, $\varepsilon_\parallel = 0.3$ ns). By carefully matching the input beam β function to the lattice β function and using a cylindrically symmetric beam, emittance growth from these non-linearities is suppressed in transverse phase space, and in longitudinal phase space tightly packed RF cavities and damping from the absorbers prevents emittance growth from getting out of hand.

In this context, introducing a dispersion into the beam might be expected to ruin the cooling performance of the lattice and indeed this can be observed. As expected, in the linear approximation the dispersion D undergoes a Larmor rotation between x and y spaces in addition to the usual evolution of D and D'. Unfortunately this Larmor rotation is momentum-dependent in second order leading to the loss of dispersion from the beam and large emittance growth for energy spreads typical of MICE (20 MeV rms).

The situation is worse when we consider a non-ideal beam. In MICE, we attempt to generate muons from pions generated by a target dipping into the ISIS proton synchrotron. These particles are transported through a system of quadrupoles, dipoles and a single 5 T solenoid to the entrance of the MICE cooling apparatus. While this beamline allows us some flexibility in the muon distribution that is presented to the cooling channel, the control over input dispersion is limited, and the selection of appropriate Twiss parameters may be challenging.

One solution to this issue is to carefully select a set of particles at input to MICE such that the beam is well behaved at the absorber and emittance growth is minimised, and this is the method that we study in this note.

NO MATERIAL

We consider tracking of several cases through the MICE magnetic fields in the absence of material. In the first instance, we take an input beam typical of simulations of the MICE beamline and pass it through the cooling channel. The beam transverse and longitudinal β functions are not well-matched to the cooling channel and the dispersion vector is poorly controlled, as shown by the *Mismatched* curve in Figure 2. This leads to roughly 10% emittance growth in each dimension due to non-linear effects in the beamline, which is enough to mask any cooling signal.

In order to find an ideal beam that does not suffer from these effects, we generate a perfect, Gaussian beam at the

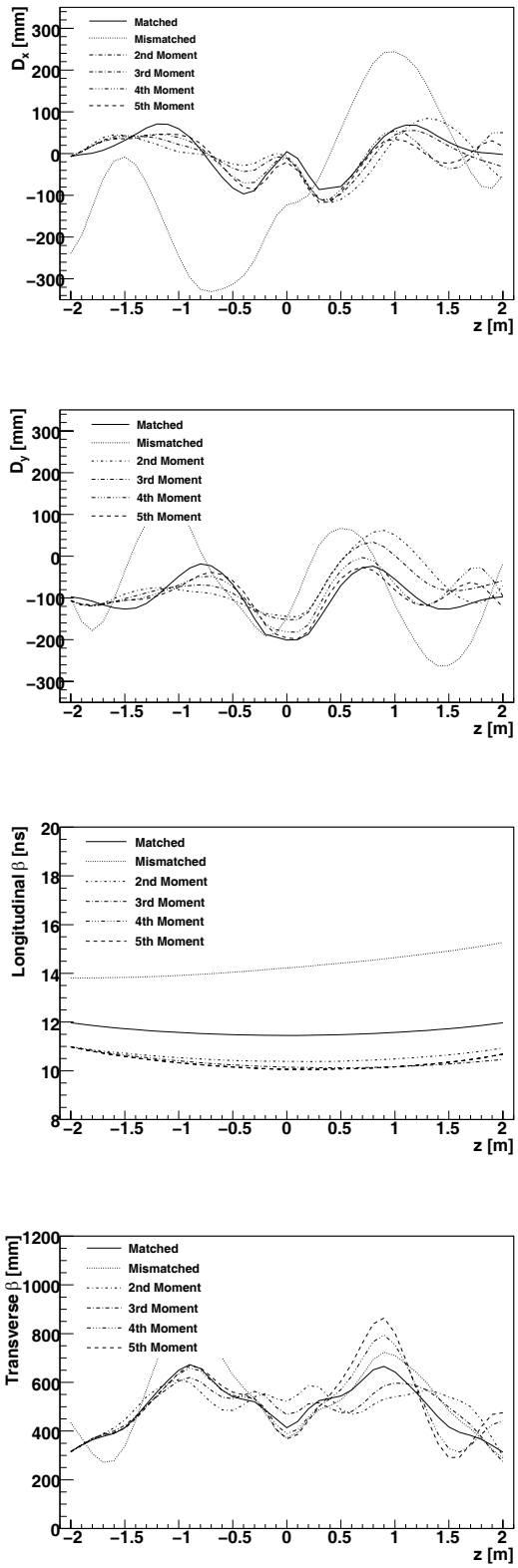

Figure 2: Dispersion in x and y, longitudinal β function and transverse β function vs position in the cooling channel. Plots are made for the ideal beam, a realistic (but mismatched) beam, and the realistic beam with selection of moments up to various orders.

centre of the cooling channel and then pass it to the downstream end. We then apply a z and t parity operation in order to transform the beam to a forward-going beam at input to the cooling channel. By selection of an initial beam with $D' = 0$ and $\beta' = 0$, the evolution of the beam is ensured to be symmetric about the centre of the magnetic lattice. Indeed, it can be seen from the *Matched* curve in Figure 2 that the evolution of linear and non-linear terms is symmetric in this case, such that the optical functions are symmetric about $z = 0$.

Statistical Weighting

In order to demonstrate the cooling channel experimentally, we need to select a beam that matches the parameters outlined above, from experimental data. We achieve this by applying a set of statistical weightings that map the input beam distribution from the beamline to the ideal input beam distribution detailed above. The idea is to count some particles several times to enhance the beam density in certain regions of phase space at the upstream detector, so that the probability distribution of the realistic beam is similar to the probability distribution of the ideal beam at input.

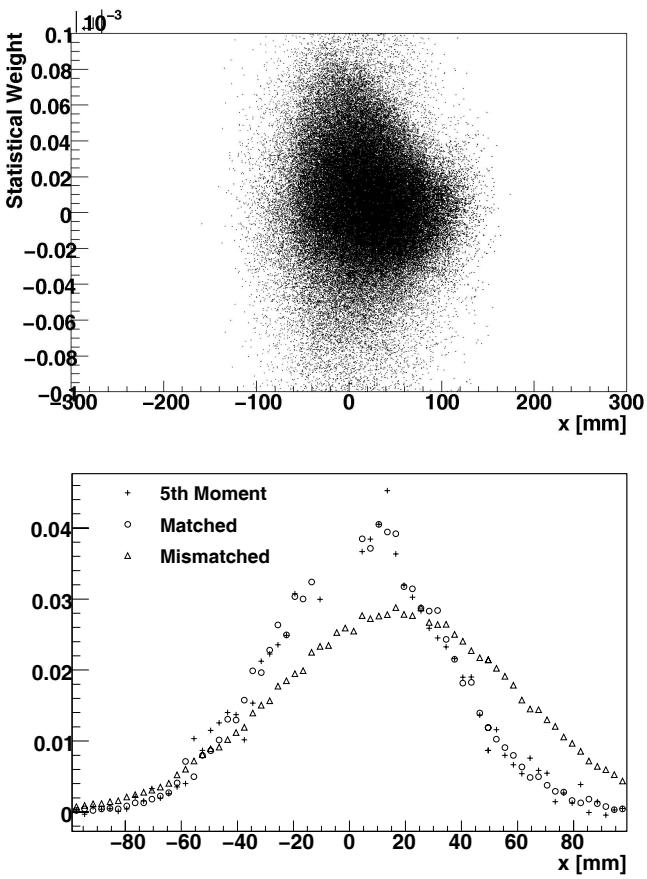

Figure 3: (top) The statistical weights applied as a function of x and (bottom) the ideal distribution in x and the mismatched distribution in x before and after weighting with a 5th order polynomial.

In this case, we attempt to select the moments of the beam using a polynomial weighting function [5]. Statistical weights are found by comparing the moments of the realistic beam with the moments of the ideal beam. We apply a weighting to each particle w^i, where $w(\vec{u})$ is a polynomial in the six-dimensional phase space vector, such that the weighting w^i of the i^{th} particle with phase space vector $\vec{u}^i = (x^i, y^i, t^i, p_x^i, p_y^i, E^i)$ is given by

$$w^i = a_0 + \sum_j a_j u_j^i + \sum_{k_1 k_2} a_{k_1 k_2} u_{k_1}^i u_{k_2}^i + \dots \quad (1)$$

Applying this weighting to each particle gives us a set of weights that maps the moments of the realistic beam to the moments of the ideal beam, and by extension the distribution of the realistic beam to the distribution of the ideal beam. The projection of the beam distribution to the x axis is shown in Figure 3, together with a scatter plot of the weightings as a function of x. The statistical weights are generally higher in the negative x region, indicating that a statistical enhancement of the beam is required in this region. This is confirmed when we study the x distribution, where we see that the realistic beam is statistically depleted in the negative x region. After weights are applied to select 5th moments, the realistic beam distribution matches the ideal beam distribution rather more closely.

In principle this technique enables us to select moments up to arbitrary order, although in this note we only work up to 5th moments due to computational constraints. The results are satisfactory although not quite ideal - the optical functions evolve in a more controlled manner, and importantly the considerable emittance growth has been avoided.

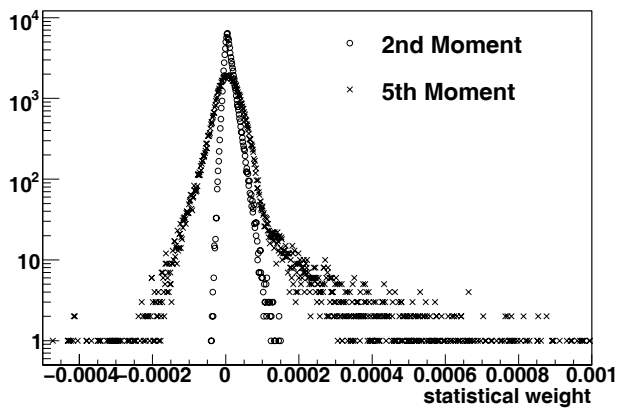

Figure 4: Distribution of statistical weightings required to select a beam for 1st through 2nd moments and for 1st through 5th moments. Note the long tail when higher moments are selected.

The weighting required for selection of 2nd and 5th moments is shown in Figure 4. At higher moments, rather large weightings are required, and it is expected this will have a detrimental effect on the statistical error of the measurement. The magnitude of this error is still to be determined.

WEDGE INCLUDED

Finally the case where a wedge is included is studied. The cooling performance of the various beams discussed above is assessed for a polyethylene wedge with a 90° opening angle. The on-axis length of the wedge has been chosen so that particles lose energy of about 11 MeV/c, which is similar to the energy gain that can be restored by the full MICE experiment.

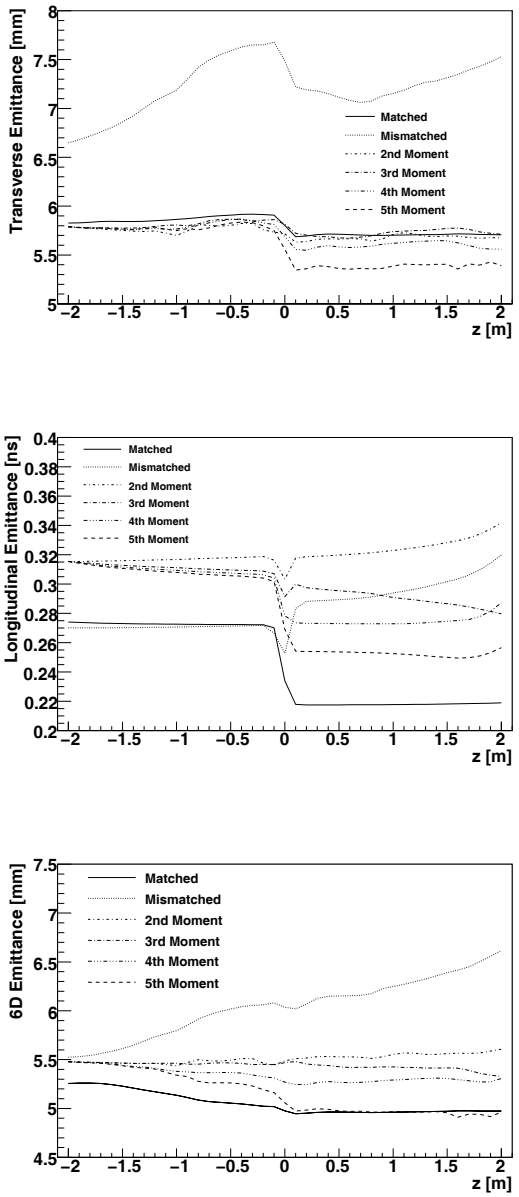

Figure 5: Evolution of transverse, longitudinal and 6d emittance as a function of z. Plots are made for the ideal beam, a realistic (but mismatched) beam, and the realistic beam with selection of moments up to various orders. Note that the realistic beam sees significant optical emittance growth when no statistical weighting is applied.

The emittance evolution is shown in Figure 5. It is clear that for the unweighted beam, the non-linearities ruin the cooling in both transverse and longitudinal phase space. After the weightings are applied there is now a clear cooling signal in both transverse and longitudinal phase spaces, that can be clearly attributed to the wedge. The full six dimensional emittance change is obscured slightly by emittance reduction due to non-linear terms in the optics, although a signal can still be observed in addition to the emittance evolution due to non-linearities. It may be possible to improve the weighting algorithm used here to achieve a closer match between the real beam, after selection, and the ideal case.

CONCLUSION

Emittance exchange is a powerful technique that may be of use for a Neutrino Factory and is vital to a Muon Collider. Observation of this phenomenon in the MICE setup would normally be impossible due to the presence of catastrophic beam blow up from non-linearities in the beam optics. The use of beam selection or statistical weighting presents us with the opportunity to make measurements over a wider range of parameters than can be generated with the MICE beam, and in this case it even enables us to take some control over the non-linear beam optics that is inherent in high emittance beams in solenoidal lattices. This enables us to observe emittance exchange.

REFERENCES

[1] D. Li, Status of the International Muon Ionization Cooling Experiment (MICE), Proc. COOL 2009.

[2] V. Balbekov, Solenoid-Based Ring Coolers, MUCOOL Note 232, 2002.

[3] K. Yonehara, Progress of Helical Cooling Channel Design for Muon Colliders, Proc. COOL 2009.

[4] P. Snopok, G. Hanson, A. Klier, Recent Progress on the 6d Cooling Simulations in the Guggenheim Channel, International Journal of Modern Physics A, Volume 24, Issue 05, 2009.

[5] C. T. Rogers, Statistical Weighting of the MICE Beam, Proc. EPAC 2008.

STATUS OF THE FAIR PROJECT*

M. Steck for the 'FAIR Project Team'
GSI Darmstadt, Germany

Abstract

The acceleration of high intensity primary beams and the preparation of high quality secondary beams are the main goals of the accelerators of the FAIR project. Primary beams are either heavy ions used for the production of rare isotope beams or protons which are converted to antiprotons. Various cooling systems are planned which allow the preparation of the secondary beams for high precision experiments. The system of accelerators which has been recently documented in a set of technical design reports is passing through a final review. This report gives an overview of the FAIR accelerators and the status of the design of various systems and components.

INTRODUCTION

Acceleration of high intensity primary beams and their conversion to secondary beams is the main mission of the proposed Facility for Antiproton and Ion Research (FAIR) [1]. The existing GSI accelerator system with the UNILAC linear accelerator and the heavy ion synchrotron SIS18 will serve as injector complex for the new synchrotron SIS100. Two production targets, one for antiproton production using a primary proton beam and one for rare isotope production by fragmentation or fission of heavy ions, in combination with subsequent magnetic separators, will provide the secondary beams. In a complex of storage rings the secondary beams will be prepared for the users. Beam cooling will be crucial to prepare high quality secondary beams. Stochastic cooling will provide pre-cooling of the hot secondary beams, for antiprotons it is also employed in beam accumulation. Electron cooling is mainly a tool to perform experiments with high quality stored beams. Moreover, it is also employed in the accumulation of rare isotopes and in the deceleration of ions and antiprotons in order to increase the efficiency of these manipulations. Details of the new accelerators of the FAIR project were documented in technical design reports which are the basis for further planning of the accelerators and the general machine concepts [2].

UPGRADE OF THE EXISTING FACILITY

The main activity at the existing GSI accelerator facility is devoted to the improvement of the machines for high intensity operation. The low energy part of the UNILAC is being modified in order to increase the transverse acceptance and therefore to accelerate beams with larger efficiency. This is achieved by installation of new electrodes in the RFQ and new matching sections between RFQ and DTL section. The goal is the acceleration of beam intensities for the heaviest ions which are sufficient to fill the synchrotron SIS18 up to the space charge limit. Installation of new power converters in the linear accelerator as well as the recent addition of a large acceptance charge state separator between linear accelerator and synchrotron will significantly improve the performance with intense heavy ion beams.

The upgrade of SIS18 comprises various aspects. The problem of the dynamic vacuum has attracted high attention. The increase of the residual gas pressure during high intensity operation with low charge states at the SIS18 injection energy of 11.4 MeV/u is counteracted by various measures. Amongst others the pumping speed was increased by NEG coating of vacuum chambers, additional collimators for localized and defined beam loss at surfaces designed with special orientation and low desorption materials were installed. Various technical modifications will allow an increase of the ramping rate of SIS18 to 10 T/s which is beneficial with respect to high average intensity and which will reduce the losses in the residual gas during injection and acceleration. A new connection to the power mains has been installed. Some weak corrector magnet power converters are being replaced, an additional acceleration cavity operating at $h = 2$ will allow faster acceleration. A dedicated machine development program with beam dynamics investigations and hardware improvements is aiming at filling the synchrotron SIS18 with heavy ion beams up to the space charge limit.

NEW SYNCHROTRONS

It is planned to install two new synchrotrons with a circumference of 1083 m in a common tunnel. They can be either used for the acceleration of highest intensity beams of relatively low charge states, e.g. U^{28+} from SIS18 without any stripping between UNILAC and SIS18 or for acceleration to highest energies at the expense of intensity due to unavoidable losses in the stripper foil.

SIS100

For the achievement of high average intensities SIS100 is designed as a fast ramping synchrotron with a magnetic bending power of 100 Tm using super-ferric magnets [3]. With a maximum ramp rate of 4 T/s it can provide 5×10^{11} U^{28+} ions at 2.7 GeV/u every 1.5 s. With the same cycle time 2×10^{13} protons can be accelerated to 29 GeV.

* Supported by BMBF and the federal state of Hesse

SIS100 is designed for slow and fast extraction. The fast extracted beams will be compressed into a short bunch of less than 50 ns length prior to extraction. For heavy ions a bunch compression scheme is applied at extraction energy. However, for protons at full energy the synchrotron period is too long, therefore a bunch merging scheme at intermediate energy resulting in a single bunch, which is accelerated to the final energy, is favorable.

The machine design is based on super-ferric magnets of the NUCLOTRON type [4]. Two straight full length dipole magnets of this type are available for testing and optimization at GSI. The manufacturing of a curved dipole prototype and of a quadrupole prototype is in progress. The cold vacuum chamber of this magnet concept will provide ultra-high vacuum conditions.

In order to alleviate the outgassing and dynamic vacuum problems during heavy ion operation the lattice is designed for controlled loss of ionized particles in specially designed beam catchers. A dedicated program to study desorption effects which will also guide the SIS100 design has been launched at the existing SIS18.

To accelerate the beam with the maximum ramp rate a total rf voltage of 400 kV at harmonic $h = 10$ will be needed. Ferrite loaded cavities operating in the frequency range 1.1 to 2.7 MHz are used for acceleration. The final bunch compression of heavy ions will be performed by magnetic alloy filled cavities operating in the frequency range 0.395 to 0.485 MHz. A total of 16 cavities with a voltage of 40 kV each will be needed to generate the required single short bunch for the injection of rare isotope beams into the collector ring and for plasma physics experiments.

SIS300

The second synchrotron SIS300 is aiming at highest energies for highly charged ions. The cos(θ)-dipole magnets are foreseen to be ramped with a rate of 1 T/s up to the maximum field of 4.5 T. A maximum energy of 34 GeV/u can be reached with highly charged ions. For lower charge states SIS300 can be used as a stretcher ring operated at fixed field delivering a nearly continuous beam by slow extraction of the ion beam from SIS300 after fast acceleration in SIS100 and transfer to SIS300. The present project schedule assumes that SIS300 will be added in a later stage of the project. Therefore the main activity is the design of the ring tunnel which can accommodate both synchrotrons. Hardware developments for SIS300 have a lower priority.

SECONDARY BEAM PRODUCTION AND SEPARATION

Antiprotons

Proton Linac The existing UNILAC accelerator is designed for the acceleration of heavy ions, the performance with protons is insufficient to serve as injector of high intensity proton beams which are needed for antiproton production. A new proton linac will accelerate protons from an ECR source to an energy of 70 MeV, which will be the energy for injection into SIS18 filling the two transverse acceptances by multiturn injection up to the space charge limit. A low energy RFQ section accelerates the protons to 3 MeV, a section with 12 Crossed-bar H-mode accelerating cavities (CH-DTL) operating at 325 MHz will allow the acceleration of short pulses ($\lessapprox 40\mu$s) with a maximum proton current of 70 mA to the energy of 70 MeV.

Antiproton Target A single bunch of 29 GeV protons from SIS100 will impinge on a nickel target of 60 mm length in order to produce antiprotons. Up to 2×10^{13} protons will be compressed into a bunch of less than 50 ns length in order to minimize the longitudinal heating in the subsequent target. The antiprotons which exit from the target with an energy of 3 GeV and large divergence will be first focussed by a magnetic horn and then be selected by a large acceptance magnetic separator. Chromaticity corrections as well as special collimators are part of the separator concept. The cycle of proton acceleration for antiproton production will be repeated every 10 s, which is close to the thermal limit of the target. The expected production rate is at least 1×10^8 antiprotons per pulse in the phase space volume which can be accepted by the magnetic separator and the subsequent Collector Ring. As the production target and the proton dump are located in close vicinity to the fragment separator for RIBs and some experimental installations, detailed FLUKA simulations have been performed in order to reduce the radiation during operation, but also to minimize the radiation level by activation of the target and proton beam dump area.

Rare Isotopes

For rare isotope production a heavy ion beam with an energy of about 1.5 GeV/u from SIS100 will be directed to the production target. The large acceptance of the fragment separator SuperFRS [5] for beams of divergence $\pm 40/20$ mrad horizontally/vertically and momentum spread ± 2.5 % requires the use of large acceptance superconducting magnets. Both slow extraction for fixed target experiments and fast extraction of a short bunch for experiments with rare isotopes in the storage ring complex of FAIR, can be provided. The combination of a preseparator and a main separator with a bending power of 20 Tm provides high selectivity for fragment separation. If highest purity of the rare isotope beam is required, an additional degrader can be inserted between the two separator stages, thus allowing a $B\rho - \Delta E - B\rho$ separation technique. Three branches, for low and high energy experiments and a branch transferring the rare isotopes to the storage ring complex are foreseen after the fragment separator.

COLLECTOR RING CR

The Collector Ring (CR) has a circumference of 216 m and offers large acceptance which is important for the efficient use of the secondary beams injected from the production targets and separators. The design considerations of the CR are governed by the stochastic cooling system which will be applied to ions and antiprotons. The ion optical functions are chosen differently, such that proper mixing conditions are provided for both beams [6]. As the ring will be operated for both beam species at the maximum bending power of 13 Tm, the particle velocity is different for antiprotons ($\beta = 0.97$) and rare isotopes ($\beta = 0.84$). Consequently, different ion optical settings will be used, which give the best momentum slip factor for the respective beam species. Common to both ion optical modes are dispersion free straight sections for injection and extraction and for the installation of the rf system. The rf system is designed to perform a fast bunch rotation and debunching of the incoming short bunch. This longitudinal phase space manipulation reduces the momentum spread by about a factor of 5 which results in a reduction of the total cooling time for stochastic cooling.

The rf system of the CR is designed to provide the high voltage gradient over some hundred turns of the beam. The operation with high electric field in the frequency range 1.17 to 1.37 MHz is achieved by filling the cavity with magnetic alloy material. The 1 m long cavity has to be operated with a maximum voltage of 40 kV, but due to the short pulse needed for bunch rotation the average power dissipation is below 2 kW which requires only forced air cooling. Five such cavities are needed for the fast bunch rotation.

Stochastic cooling in the CR is used for a large range of beam parameters [7]. The velocity of rare isotopes and antiprotons and correspondingly the revolution time differs by 15 %. The cooling system also has to deal with a wide range of intensities, e.g. for rare isotope beams the intensity can vary from nearly single ions up to some 10^8. The signal from antiprotons, even if the full intensity of 10^8 is injected, is rather weak due to the low charge. A total cooling time of 1.5 s is needed for ions in order to make full use of the fast cycle of SIS100. This can only be reached for lower intensities due to the usual increase of the cooling time with particle number, if a certain beam intensity is exceeded. The cooling time for antiprotons should be 10 s at most, 5 s total cooling time will result in doubling the antiproton production rate. For cost reasons the bandwidth of the stochastic cooling system is presently limited to the range 1 to 2 GHz, an optional extension to 1-4 GHz will reduce the cooling time.

For the cooling of the low intensity ion beams and for the antiproton cooling high sensitivity of the pick-ups is indispensable. A new slot line structure for the band 1-2 GHz coupled to a micro-strip circuit has been developed [8]. The pick-ups can be cooled inside the vacuum tank to 20 K with cold heads mounted outside. A prototype tank is presently assembled in order to test the concept [9]. Pick-ups and kickers will be moved during the cooling process synchronously with the decreasing emittance of the beam in order to have best signal to noise ratio. Switchable delays allow matching the traveling time of the correction signal to the time of flight of the particles from pick-up to kicker. The designed system has been proven to provide good amplitude and phase flatness in the band from 1 to 2 GHz.

ACCUMULATOR RING RESR

The concept of antiproton production with high average rate requires a second ring after the pre-cooling ring for the accumulation of high intensity stacks. It has been shown at the former antiproton complex at CERN, particularly at the accumulator ring AA [10], and at FNAL with the Debuncher and Accumulator ring [11], that the combination of two rings results in highest production rate.

In order to make most efficient use of buildings and technical infrastructure the accumulator ring RESR and the pre-cooling ring CR will be installed in a common tunnel. The ion optical lattice of the RESR is optimized for the requirements of a dedicated stochastic cooling system which mainly manipulates the incoming pre-cooled beam from the CR. The concept is based on a large dispersion at the stochastic cooling pick-ups in order to adjust the cooling strength for injected particles and the accumulated stack. Different pick-up systems have high sensitivity either to the incoming beam on an inner orbit (lower momentum) or to the stack which is accelerated to an outer orbit (larger momentum).

The requirements to the ion optical layout of the RESR are best matched by a lattice with a hexagonal ring shape. The circumference of 240 m allows the installation of the RESR around the CR, conflicts between neighboring ring components of the two rings are avoided by installing the two beam axes with a vertical offset of 1.2 m. A dispersion free beam transport system between the two rings has been designed.

The required large momentum acceptance of $\Delta p/p = \pm 1\%$ for the accumulation of antiprotons is dominating the ring design. Another feature are small vertical beta functions at the location of the longitudinal cooling pick-ups in order to minimize an unwanted interference between injected beam and stack. The injected beams are pre-cooled in the CR, thus the required transverse acceptance of 25 mm mrad is very moderate. For the tuning of the stochastic accumulation system the transition energy can be varied by adjusting the focussing strength of the nine groups of quadrupole magnets, yielding a range for the transition energy γ_t from 3.3 to 6.4 [12]. This flexibility of the lattice has been used in simulations of the accumulation process and will also allow optimization during ring commissioning.

A detailed concept for the antiproton accumulation system of the RESR has been worked out [13]. The ion optical

properties of the ring are integral part of the concept. It is foreseen to inject from the CR, which is located inside the RESR, onto an inner orbit of the RESR with a momentum offset $\Delta p/p = -0.8\%$. From the inner orbit the antiprotons are transported with the rf system to a central orbit. Finally, the stochastic cooling system drives the particles to an outer orbit at $\Delta p/p = +0.8\%$, where a high intensity stack is built up. The longitudinal cooling system in a basic version comprises two stack tail cooling systems in the band 1-2 GHz and a longitudinal core cooling system with the band width 2-4 GHz. For transverse core cooling two systems for horizontal and vertical cooling in the frequency range 2-4 GHz are foreseen. The small vertical beta function of 2 m allows the use of a vertical gap of only 20 mm in the momentum pick-ups which results in a well localized field distribution. The dynamic range of the cooling system is determined by the number of injected antiprotons of 1×10^8 per cycle and the maximum stack intensity of 1×10^{11}. According to simulations the influence of beam feedback for up to 10^{11} stored antiprotons is weak and should not adversely affect the beam stability.

The proposed accumulation mode requires C-shaped injection kickers which allow a displacement of particles in horizontal direction. A design with a ferrite yoke installed inside a vacuum tank can fulfill the requirements. The proposed injection of a single bunch from the CR can be achieved with rise times of the kicker field of 150 ns and a flat top time not exceeding 1 μs.

The RESR is not exclusively used with antiprotons, but is also a link in the chain of rare isotope accelerators. It can serve as a decelerator ring and as such it will be useful for both ions and antiprotons. For injection of antiprotons at the higher energy the transition energy of the RESR can be increased and consequently no crossing of the transition energy occurs during deceleration. For the much lower energy of ions this is achieved for the whole range of possible ion optical modes.

If rare isotopes below the production energy of 740 MeV/u are needed in the subsequent NESR, the RESR can decelerate them to energies between 100 and 740 MeV/u. This is most important for the collider mode of the NESR, when highest stability of the ion orbit is required and consequently deceleration in the NESR is not recommendable. The RESR therefore is equipped with magnets which allow a ramp rate of 1 T/s, the dipole magnets are identical with the NESR dipoles and also the other magnets have common design features with the NESR magnets. The power converters support the fast ramp rate. The rf system is based on the existing SIS18 system, installation of additional capacitors will allow an operation at harmonic $h = 1$ with a frequency range from 0.53 to 1.21 MHz. For the lowest ion energies a debunching and rebunching to harmonic $h = 2$ at an intermediate energy is necessary during the deceleration cycle.

STORAGE RING NESR

The NESR is designed for storage and internal experiments with ions, stable and unstable. It also allows a large variety of beam manipulations with ions and antiprotons which are supported by a powerful electron cooling system [14]. The strong requirement by experiments to study highly charged ions at lowest possible energy resulted in a concept of the NESR which allows fast ramping from the high injection energy needed for the production of highly charged and rare isotope beams to low energies. The present design of components is aiming at deceleration with a rate of 1 T/s. The fast ramp rate is most important for experiments with short-lived rare isotopes. The lowest energy for all kinds of ions is 4 MeV/u. The magnetic bending field is changed by a factor of about 25 from injection to lowest energy. The low energy beams are not only stored, they can also be extracted from the NESR.

Fast extraction is used for transfer into another low energy storage ring (the LSR of the FLAIR experiment). Slow extraction by resonant excitation of the beam or knockout with rf noise, and charge changing extraction by electron capture in the NESR internal target or its electron cooler are the available options, which governed the design of extraction components. The extraction components are designed for beams of a maximum magnetic rigidity of 4 Tm, that means that beam extraction is only available for decelerated beams. The extraction of decelerated beams is required for secondary beams or highly charged ions, all other ion beams can be provided directly from the synchrotron.

Antiprotons injected at 3 GeV from the RESR can be decelerated to a minimum energy of 30 MeV, which corresponds to the same variation of magnetic field strength as during ion deceleration. The low energy antiprotons can be extracted with slow resonance extraction or an adjustable fraction of the circulating low energy antiprotons can be transfered after fast extraction to FLAIR.

The NESR is designed with four 18 m long straight sections for the installation of special components and experimental equipment in the ring of 222.8 m circumference. The ion optical structure provides large acceptance, 150 mm mrad horizontally and 40 mm mrad vertically, for a momentum acceptance of $\Delta p/p = \pm 1.5\%$. Seven families of quadrupole magnets in the fourfold symmetric standard lattice result in horizontal and vertical tunes of $Q_x = 4.20$ and $Q_y = 1.87$. Twelve individually powered sextupole magnets are foreseen to achieve the required dynamic aperture, also taking into account higher order field errors in the main magnets. The large acceptance is required for experiments which need to simultaneously store particles with different momentum or, equivalently, particles with the same velocity, but different charge and mass. A large dispersion in the arcs results in a spatial separation of particles with different momentum, detectors can be placed in the dispersive sections for the observation of these particles.

The injection system is matched to the acceptance of the beamline from the fragment separator and allows direct injection of rare isotope beams from the SuperFRS with emittances of 50/20 mm mmrad, horizontally/vertically, and a momentum spread $\delta p/p = \pm 0.5$ %. This allows injection of fragments with large momentum spread or of multi-component beams with a corresponding range of charge to mass ratio.

For all operational modes of the NESR the availability of electron cooling over the whole range of ion energies is crucial, antiprotons can be cooled at energies below 800 MeV. Electron cooling provides high beam quality for experiments with stored beams. The deceleration profits from electron cooling, as the small beam emittance after cooling will allow almost loss free deceleration.

The NESR concept foresees the accumulation of heavy ion beams by longitudinal accumulation in combination with electron cooling. A wide band rf system which can be operated with variable voltage will compress the stored beam into a fraction of the circumference with a gap which can be filled with a new injection. The feasibility of such schemes has been confirmed in simulations and experimental investigations at the existing ESR storage ring [15].

For short-lived ions the cooling system is optimized to cool down beams, which were pre-cooled in the CR, with a total cooling time shorter than 1.5 s. The main application for this mode will be Schottky mass spectrometry [16], the determination of the mass of rare isotopes by measurement of their revolution frequency employing non-destructive Schottky noise detection. With momentum spreads of the cooled beam below 1×10^{-6} a mass resolution of at least the same order of magnitude can be achieved.

The NESR has long straight sections for the installation of the electron cooler, an electron target and an internal gas jet target, with additional space for detector systems. The northern straight section is reserved for collision experiment of rare isotopes with electrons circulating in an adjoining smaller storage ring. This electron ring allows collisions of rare isotope beams in a bypass of this straight section with electrons of up to 500 MeV energy. Although not funded in the start version of the FAIR project, this option is taken into account in all space considerations for the building concept and the preparation of infrastructure. The collision in the bypass is achieved by switching off the dipole magnets at the end of the straight section and installing two additional dipole magnets which bend the ion beam into and out of the bypass section.

HIGH ENERGY STORAGE RING HESR

The High Energy Storage Ring (HESR) with a circumference of 575 m and a magnetic bending power of 50 Tm will be the main user of the antiprotons accumulated in the RESR [17]. The antiprotons will be injected at 3 GeV and then be prepared according to the requirements of the experiment. The energy ranges from a maximum of 14.1 GeV down to a minimum of 0.83 GeV. The antiprotons are accelerated or decelerated in the HESR to the required energy with a ramp rate of 0.025 T/s. Experiments use an internal hydrogen target with a maximum thickness of 4×10^{15} atoms/cm^2. Stochastic and electron cooling are foreseen. The stochastic cooling supports operation in a high luminosity mode with 10^{11} stored antiprotons (luminosity 2×10^{32} cm^{-2}s^{-1}). For high resolution experiments electron cooling, which is presently planned for a later upgrade, would be operated at an order of magnitude smaller luminosity.

REFERENCES

[1] FAIR Baseline Technical Report, GSI, Darmstadt, 2006, http://www.gsi.de/fair/reports/btr.html.

[2] FAIR Technical Design Reports, GSI, Darmstadt, 2008. http://indico.gsi.de.

[3] P. Spiller et al., EPAC'08, Genoa, Italy, June 2008, MOPC100, p. 298, http://www.jacow.org.

[4] A.M. Baldin et al., IEEE Trans. on Applied Superconductivity, 1995, 5, 875-877.

[5] H. Geissel et al., Nucl. Instr. Meth. B204 (2003) 71.

[6] A. Dolinskii, F Nolden, M. Steck, COOL07, Bad Kreuznach, Germany, September 2007, TUA2C08, p. 106, http://www.jacow.org.

[7] F. Nolden, A. Dolinskii, B. Franzke, U. Jandewerth, T. Katayama, C. Peschke, P. Petri, M. Steck, D. Möhl, EPAC'08, Genoa, Italy, June 2008, THPP051, p. 3479, http://www.jacow.org.

[8] C. Peschke et al., COOL09, Lanzhou, China, September 2009, THPMCP003, http://www.jacow.org.

[9] F. Nolden et al., COOL09, Lanzhou, China, September 2009, MOA1MCIO03, http://www.jacow.org.

[10] H. Koziol, S. Maury, CERN-PS 95-15 (AR/BD), 1995.

[11] R. Pasquinelli, W, Hyslop. W. Kells, M. Kuchnir, J. Marriner, G. Mayer, J. MacCarthy, S. Mtingwa, D. Peterson, R. Shafer, PAC'87, Washington D.C., March 1987, p. 1132, http://www.jacow.org.

[12] S. Litvinov, A. Dolinskii, O. Gorda, F. Nolden, M. Steck, PAC'09, Vancouver, May 2009, FR5REP118, http://www.jacow.org.

[13] T. Katayama et al., COOL09, Lanzhou, China, September 2009, MOA2MCIO02, http://www.jacow.org.

[14] C. Dimopoulou et al, COOL09, Lanzhou, China, September 2009, THM2MCIO02, http://www.jacow.org.

[15] C. Dimopoulou, B. Franzke, T. Katayama, F. Nolden, G. Schreiber, M. Steck, D. Möhl, EPAC'08, Genoa, Italy, July 2008, THPP048, p. 3470, http://www.jacow.org.

[16] B. Franzke, K. Beckert, H. Eickhoff, F. Nolden, H. Reich, A. Schwinn, M. Steck, T. Winkler, EPAC'98, Stockholm, Sweden, June 1998, p. 256, http://www.jacow.org.

[17] A. Lehrach et al., Intern. Journal of Mod. Phys. Vol. 18, No. 2 (2009).

TEVATRON ELECTRON LENS AND IT'S APPLICATIONS*

X.L. Zhang, V. Shiltsev, A. Valishev, FNAL, Batavia, IL 60510, U.S.A.
V. Kamerdzhiev, FZ-Jülich, IKP, Germany.
A. Romanov, BINP, Novosibirsk, Russian.

Abstract

The Tevatron Electron Lenses (TELs) are designed for the purpose of the Beam-beam tuneshift compensation. Now they are the vital parts of the Tevatron. In this report, their daily operations and beam study results are presented. Their possible future applications are discussed as well.

INTRODUCTION

Fermilab's Tevatron is a 980 GeV particle collider ring in which tightly focused beams of protons and antiprotons collide in two dedicated interaction points (IPs). Both beams share the same beam pipe and magnet aperture by placing the beams on separated helical orbits everywhere except the main IPs using high-voltage (HV) electrostatic separators. However, the effects due to electromagnetic beam-beam interactions at the main IPs together with long-range interactions between separated beams limit the collider performance, reducing the luminosity integral per store (period of continuous collisions) by 10-30%[1]. The long-range effects which (besides being nonlinear) vary from bunch to bunch are particularly hard to treat. To compensate these beam-beam effects, the electron lenses were proposed [2] and installed at the Tevatron [3]. An electron lens employs space-charge force of a low-energy beam of electrons that collides with the high-energy bunches over an extended length L_e. Such a lens can be used for linear and nonlinear force compensation depending on electron current-density distribution $j_e(r)$ and on the ratio of the electron beam radius a_e to the rms size σ of the high-energy beam at the location of the lens. The electron transverse current profile (and thus the radial dependence of electromagnetic (EM) forces due to electron space-charge) can easily be changed for different applications. The electron-beam current can be adjusted between individual bunches, equalizing the bunch-to-bunch differences and optimizing the performance of all bunches in a multi-bunch collider by using fast high voltage modulator [6].

A shift of the betatron frequency (tune) of high-energy particles due to EM interaction with electrons is a commonly used "figure of merit" for an electron lens. A perfectly steered round electron beam with current density distribution $j_e(r)$, will shift the betatron tunes $Q_{x,y}$ of small amplitude high-energy (anti-)protons by [2]:

$$dQ_{x,y} = \pm \frac{\beta_{x,y} L_e r_p}{2\gamma e c} \cdot j_e \cdot \left(\frac{1 \mathrm{m} \beta_e}{\beta_e} \right) \qquad (1),$$

where the sign reflects focusing for protons and defocusing for antiprotons, $\beta_e = v_e/c$ is the electron beam velocity, $\beta_{x,y}$ are the beta-functions at the location of the lens, L_e denotes the effective interaction length between the electron beam and the protons or antiprotons, $r_p = e^2/mc^2 = 1.53 \times 10^{-18}$ m is the classical proton radius, and $\gamma_p = 1044$ the relativistic Lorentz factor for 980GeV protons.

TEVATRON ELECTRON LENSES

Both Tevatron Electron Lenses (TELs) direct their beam against the antiproton flow. The TELs operate at up to 10kV electron energy and can shift the betatron tune by as much as $dQ_{x,y}^{max} \approx 0.008$ [4] depending on the type of the electron gun design. The layout of the Tevatron Electron Lens 2 (TEL2) is shown below. TEL2 is installed in the Tevatron at the location where β_x/β_y=68m/150m whereas TEL1 is installed at the different location where β_x/β_y=104m/29m. The design difference between the two lenses is that the TEL1 bending section has a 90° angle between the gun solenoid and the main solenoid while this angle is about 57° in TEL2.

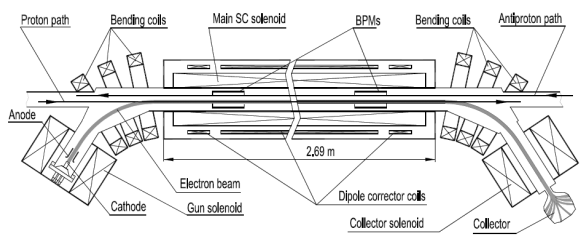

Figure 1: TEL2 layout.

The designed and measured electron beam profiles are flattop, smooth edge flattop (SEFT) and Gaussian, which are shown below:

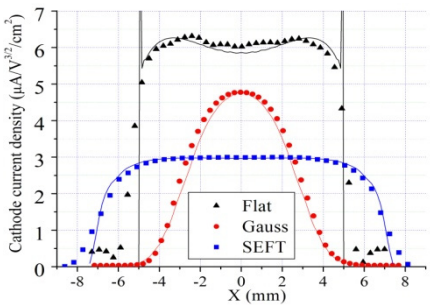

Figure 2: Three profiles of the electron current density at the electron gun cathode: black, flattop profile; red, Gaussian profile; blue, SEFT profile. Symbols represent the measured data and the solid lines are simulation results. All data are scaled to refer to an anode–cathode voltage of 10 kV.

*Work supported by the Fermi Research Alliance, under contract DE-AC02-76CH03000 with the U.S. Dept. of Energy.
#zhangxl@fnal.gov

The SEFT gun has been designed and built in order to generate much less nonlinearity than the flattop gun at the transit edges so that it causes much less proton loss when electron beam is not perfectly aligned with proton beam it acted on. The Gaussian gun was installed recently and hasn't been studied for beam-beam compensation effects yet.

BEAM-BEAM COMPENSATION STUDIES

The experimental beam-beam compensation (BBC) studies[4] were carried out at the Tevatron for either dedicated machine time or parasitically during the High Energy Physics (HEP) store and mostly done with protons. The tune shift, beam lifetime and halo loss rate at both physics detectors are measured and some typical data is presented in the following sections.

Tune Shift

Figure 3 presents the vertical tune shift induced by the TEL2 electron current from the SEFT gun. There is an excellent agreement between the tune shift measured by the 1.7 GHz Schottky tune monitor and the theory. The dependence of the tune shift on the electron energy also agrees with the theoretical predictions

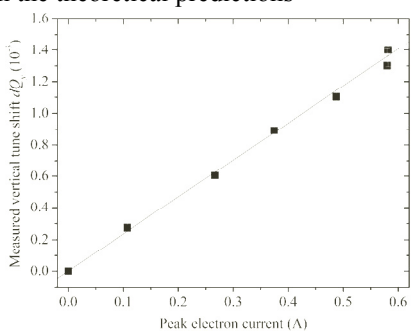

Figure 3: Vertical betatron tune shift of the 980 GeV proton bunch vs. the peak electron current in TEL2.

The results displayed in Figure 4 show the 980 GeV antiproton tune shift measurements at various cathode voltages U_c, ranging from -6 to -13 kV. As the total electron beam current (which is determined by the gun cathode–anode voltage difference and shown by the dashed line) was kept constant, the total electron space-charge Q_{SC} grew for smaller values of U_c, inducing correspondingly larger tune shift.

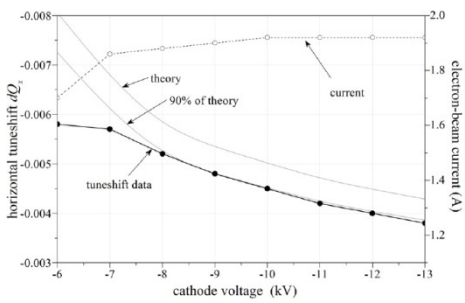

Figure 4: Horizontal tune shift of 980 GeV antiprotons versus TEL1 cathode voltage (electron energy). This data was obtained using the flattop electron gun.

Beam Lifetime

Improvement of the proton intensity lifetime (up to 40%) has been observed in experiments performed with TEL1. TEL1's large horizontal beta-function produce mostly horizontal proton tune shifts up. As the proton horizontal tunes are lower by $\Delta Q_x \approx$ -(0.002 - 0.003) for the bunches at the beginning of the bunch trains, P1, P13, and P25 [1], the TEL1 can effectively compensate for those. Figure 5 shows the dependence of D0 proton halo loss rate on the TEL1 electron current. These halo loss rates are measured bunch-by-bunch and are inversely proportional to the proton bunch lifetime. In this experiment, TEL1 was acting on P13 which has the lowest horizontal tune. Bunch neighbour bunch P14 unaffected by TEL1 was chosen as a reference bunch because its behaviour in terms of halo and lifetime was very similar to P13 in case without TEL. The loss rate of P13 dropped by about 35% once a 0.6 A-peak electron current was turned on, while the P14 loss rate stayed unaffected. After about 12 min the e-current was turned off which made the P13 loss rate return to the reference level. The loss reduction has been repeated several times over the next 4 h in this store and it was confirmed in several other HEP stores

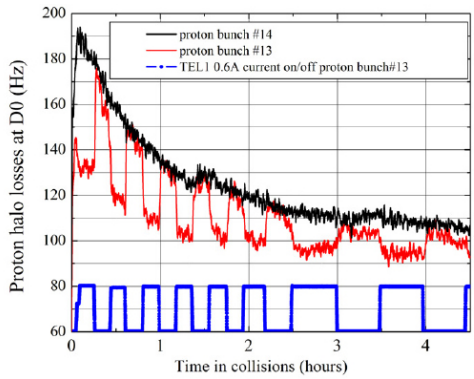

Figure 5: Proton beam halo rates as measured by D0 counters: black, for reference bunch 14; red, for bunch no. 13 affected by TEL1 (first 4 h in store #5352 L=197 × 10^{30} $cm^{-2}s^{-1}$).

The TEL-induced improvements in the luminosity lifetime of about 10% are significantly smaller than the corresponding changes in the proton intensity lifetime (about a factor of 2) because the luminosity decay is driven mostly by other factors, the strongest being the proton and antiproton emittance increase due to intra-beam scattering and the antiproton intensity decay due to luminosity burnout.

Usually, the proton lifetime, dominated by beam–beam effects, gradually improves with time in a HEP store and reaches about 50–100 h after 6–8 h of collisions. This is due to the decrease of the antiproton intensity and increase of antiproton emittance. In store #5119, we studied the effectiveness of the BBC by repeatedly turning on and off TEL2 on a single bunch P12 every half-an-hour for 16 h. The relative bunch intensity lifetime improvement R is plotted in Figure 6.[5]

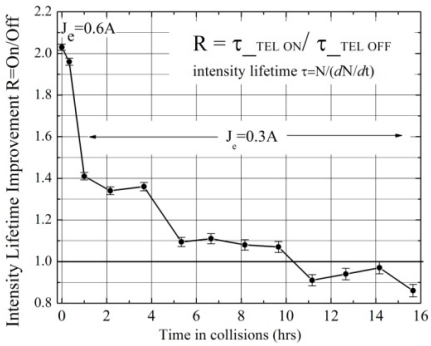

Figure 6: Relative improvement of the TEL2 induced proton bunch #12 lifetime vs. time (store #5119, Dec. 12, 2006, initial luminosity $L = 159 \times 10^{30}$ cm^{-2} s^{-1}).

The first two data points correspond to $J_e = 0.6$ A, but subsequent points were taken with $J_e = 0.3$ A to observe the dependence of the compensation effect on the electron current. The change of the current resulted in a drop of the relative improvement from $R = 2.03$ to 1.4. A gradual decrease in the relative lifetime improvement is visible until after about 10 h, where the ratio reaches 1.0 (i.e. no gain in the lifetime). At this point, the beam–beam effects have become very small, providing little to compensate. Similar experiments in several other stores with initial luminosities ranging from 1.5×10^{32} to 2.5×10^{32}cm^{-2}s^{-1} reproduced these results.

Collimation Effect

There are always particles with amplitudes beyond the electron beam cross section. For such particles with oscillations larger than the size of the electron beam, the electric field due to the electron space charge is no longer linear with the transverse displacement and the resulting nonlinearities may significantly change the particle dynamics depending on the electron current distribution. As we found experimentally, in the worst case of the flattop electron beam, the electron beam edges act as a `gentle' collimator, since the outlying particles are slowly driven out of the bunch until they eventually hit the collimators.

In Figure 7, one bunch was monitored over 100 min as the TEL1 was `shaving' the bunch size. The current of the TEL was initially set to 1 A for the first 45 min. After a 10 min respite, the current was increased to 2 A (these settings are shown above the plot). After about 85 min, the TEL1 was purposefully mis-steered in order to observe a `blowup' in the bunch sizes. The upper data in Figure 7 show the horizontal and vertical beam sizes measured many times during this process. Also indicated is the longitudinal bunch size.

The open circles show the intensity of the bunch during this process. One can see a fast initial decreasing of sizes, but after about 10 min, the rate of decrease drops significantly; this implies that the large-amplitude particles have been removed, and the core is more stable inside the electron beam. In addition, the increase of the TEL1 current to 2 A was expected to worsen the bunch-size lifetime, but the smaller bunch was well preserved for the remaining time that the TEL1 electron beam was on and centered on the proton beam. The stability of the bunch size is remarkable, suggesting that the flattop profile was ideal for the small bunch size.

The bunch intensity decay rate also decreases significantly after a short interval of faster losses, and when the electron current is doubled, the decay rate is nearly unchanged. After the bunch was observed for a while, the electron beam was moved transversely so that the bunch intercepted the edge of the electron beam. As expected, the particles were suddenly experiencing extremely nonlinear forces, causing emittance (and size) growth, shown by the bump in the upper plot of Figure 7, and heavy losses, shown by the fast decline of the lower plot.

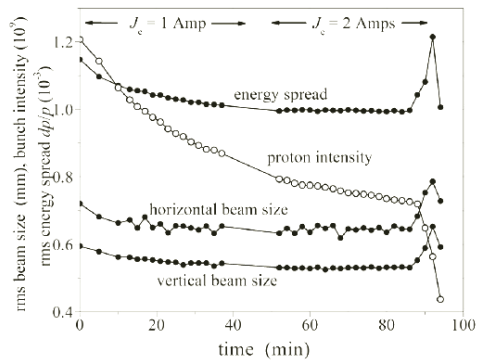

Figure 7. Scraping of a proton bunch due to interaction with the TEL1 electron beam (flattop electron current distribution).

OTHER APPLICATIONS

There have been a few studies carried out trying to use the unique and powerful electron beam creatively [8], such as to excite or scrap away the proton beam in more controlled fashion. But the most important application of the TEL is removing the un-captured beam from the abort gaps.

Removing Uncaptured Beam

Coalescing in the MI typically leaves a few percent of the beam particles outside RF buckets. These particles are transferred together with the main bunches. In addition, single intra-beam scattering, diffusion due to multiple intra-beam scattering (IBS), and phase and amplitude noise of the RF voltage, drive particles out of the RF buckets. The uncaptured beam is lost at the very beginning of the Tevatron energy ramp. At the top energy, uncaptured beam generation is mostly due to the IBS and RF noise while infrequent occurrences of the longitudinal instabilities or trips of the RF power amplifiers can contribute large spills of particles to the uncaptured beam. Uncaptured beam particles are outside of the RF buckets, and therefore, move longitudinally relative to the main bunches to fill the beam abort gap. If the number of particles in the uncaptured beam is too large and eventually lost due to energy ramp, beam abort or fallout,

usually causing large background in physics detector, damage their components even lead to quenches of the superconducting (SC) magnets by the corresponding energy deposition.

To remove the uncaptured beam, the TEL electron beam is timed to the abort gaps and placed 2-3 mm away from the proton beam orbit horizontally and about 1 mm down vertically [7]. Then the TEL1 is turned on and train of three electron pulses is generated every 7th turn for the purpose of excitation of the 4/7 resonance to effectively remove the uncaptured proton beam particles quickly. The electron pulse width is about 1 μs and the peak amplitude is about 250 mA in operation.

In Figure 8, the TEL was turned off during a store (average electron current is shown in black) at about t = 20 min. Accumulation of the uncaptured beam started immediately and can be measured as an excess of the total uncaptured beam current with respect to its usual decay. The blue line shows the excess measured by the Tevatron DCCT, $\delta N_{DCCT}(t)=N_{TEL\ on}(t) - N_{decay\ fit\ TEL\ off}(t)$. The uncaptured beam intensity measured by the Abort Gap Monitor (AGM) plotted in red. The DCCT excess grows for about 30 minutes before reaching saturation at intensity of about 16×10^9 protons.

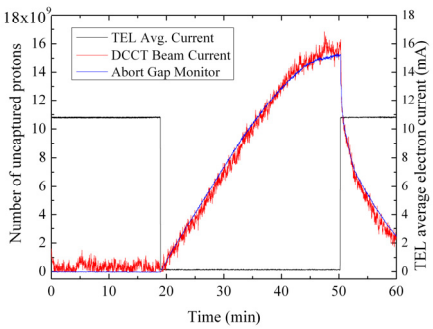

Figure 8: Uncaptured beam accumulation and removal by the TEL. The black line represents the average electron current of the TEL; the red line is the uncaptured beam estimated from the DCCT measurement; the blue line is uncaptured beam in the abort gap measured by the AGM.

Electron Columns

The space charge effect is one of the main factors to limit intensity of proton beam in proposed high current proton storage rings. It could be compensated by sufficient number of devices which are capable of trapping electrons, generated from the ionization of residual gas by proton beam, to form "electron columns" [9]. The longitudinal magnetic field of a solenoid which is supposed to be strong enough to keep electrons from escaping from the transverse position they are born at and suppress the e-p instability, but at the same time weak enough to allow ions escape and not affect the process of charge compensation. The ring electrodes at both ends of the solenoid supply electric field to trap the electrons longitudinally.

The preliminary studies with the Tevatron Electron Lens configured to work as "electron column" had shown significant accumulation of electrons inside an electrostatic trap in 3T longitudinal magnetic field with intentionally increased vacuum pressure. These negatively charged electrons moved vertical tune of 150 GeV proton beam upward by as much as +0.005.

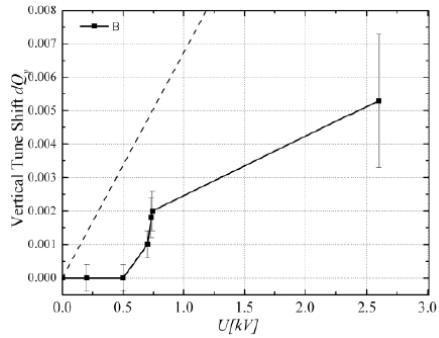

Figure 9: Summary of tuneshift vs. U[kV] measurements. The theoretical estimation is shown by the dashed line.

However, at the nominal vacuum pressure in the TEL of about 3×10^{-9} Torr no tuneshift is observed with any voltage on the electrodes up to -2.6 kV. And the significant vacuum instability was observed accompanied by the proton beam instability, which led either to the emittance growth or even to a proton beam loss, presumably, due to beam scraping. Further theoretical and bench studies are needed to understand the dynamic processes inside the ionized and magnetized "electron column".

SUMMARY

The successful demonstrations of the BBC prompted the BBC project for RHIC and R&D studies on LHC [11]. And the collimation effect also lead to the proposal of using hollow electron beam to do the collimation for LHC [10]. Once the new Gaussian electron gun is installed in the TEL2, its nonlinear beam-beam compensation abilities will be studied further in detail.

REFERENCES

[1] V.Shiltsev *et al.,* Phys. Rev. ST Accel. Beams 8, 101001 (2005)
[2] V.Shiltsev, *et al.,* Phys. Rev. ST Accel. Beams 2, 071001 (1999)
[3] V.Shiltsev, *et al.,* Phys. Rev. ST Accel. Beams 11, 103501 (2008)
[4] V.Shiltsev, *et al.,* New J. Phys. 10 (2008) 043042
[5] V.Shiltsev, *et al.,* Phys. Rev. Lett. 99 244801 (2007)
[6] G.W. Saewert, *et al.,* PAC09, TU6RFP079, 2009
[7] Xiao-long Zhang, *et al.,* Phys. Rev. ST Accel. Beams 11, 051002 (2008)
[8] X. Zhang, et al., Proceedings of the 2003 Particle Acc. Conf. pp 1778-1780, Portland, USA. 2003
[9] V.Shiltsev, *et al.,* PAC09, TH5PFP020, 2009
[10] J. C. Smith, *et al.,* PAC09, WE6RFP031, 2009
[11] A. Valishev, *et al.,* PAC09, WE6PFP034, 2009

COOLING FORCE MEASUREMENTS WITH VARIABLE PROFILE ELECTRON BEAM AT HIRFL-CSR *

L.J.Mao#, G.H.Li, J.Li, Y.Liu, X.M.Ma, J.W.Xia, T.L.Yan, J.C.Yang, X.D.Yang, Y.J.Yuan,
IMP, Lanzhou, 730000, China

Abstract

Two electron coolers have been operated at HIRFL-CSR for fast phase space cooling of heavy ion beams. The variable profile electron beam can be produced by these coolers. This should be one of the solutions for electron heating problems. In order to demonstrate the particularity of variable profile electron beam cooling, the longitudinal cooling force has been measured by electron energy-step method. In this paper, the measurement results were presented. It's clear that the cooling force is function of the electron beam density at ion orbit for variable profile electron beam. Moreover, parameter dependence on the alignment angles between the ion and electron beam was investigated.

INTRODUCTION

HIRFL-CSR is a new heavy ion cooling-storage-ring in IMP [1]. It consists of a main ring (CSRm) and an experimental ring (CSRe). The two existing cyclotrons SFC and SSC are used as injectors. The heavy ions were accumulated in CSRm with the help of electron cooling at injection energy, then, accelerated and extracted to CSRe for nuclear and atomic physical experiments. Two electron coolers were installed at CSRm and CSRe respectively.

Electron cooling is a well-established method to improve the phase space quality of ion beams in storage rings [2]. However, the ultra cooled ion beam leads to the formation of a core with extremely high density and gets lost easy. This sort of phenomena has been found at CELSIUS and COSY called electron heating. Using variable profile electron beam is one of the possible solutions for this problem. The variable profile electron beam is adopted in the electron coolers installed at HIRFL-CSR for first time.

The most important characteristics of the electron cooler are the attainable values of the cooling force as well as the dependencies of the cooling force on electron parameters. The electron coolers at HIRFL-CSR offer the opportunity to study cooling force with variable profile electron beam. The longitudinal cooling force was measured by the electron energy-step method with the aid of Schottky spectra system.

ELECTRON COOLERS AT HIRFL-CSR

The 35keV electron cooler was installed at CSRm for beam accumulation and the 300keV electron cooler was installed at CSRe for improving the luminosity even with strong heating effects of internal targets. The main parameters are listed in table 1.

The electron beam is generated in a gun which is immersed in a longitudinal magnetic field. With the help of a 2kV power supply connected between the cathode and grid electrode one can produce the negative electric field at the cathode edge thereby suppressing the emission of electrons at this place. By varying the potential of gird it is possible to obtain the electron beam with parabolic, flat or hollow profile, which is shown in fig 1.

Table 1: Parameters of the E-cooler at HIRFL-CSR

Parameters	CSRm	CSRe
Maximum electron energy [keV]	35	300
Maximum electron current [A]	3.0	3.0
Cathode diameter [mm]	29.0	25.0
Maximum magnetic field in gun section [T]	0.24	0.5
Maximum magnetic field in cooling section [T]	0.15	0.15
Magnetic expansion factor	1 - 4	1-10
Effective cooling section length [m]	3.4	3.4
Parallelism of cooling solenoid field	10^{-5}	10^{-5}
Maximum potential between the cathode and grid electrode [kV]	2.0	2.0
Maximum potential between the cathode and anode electrode [kV]	5.0	5.0

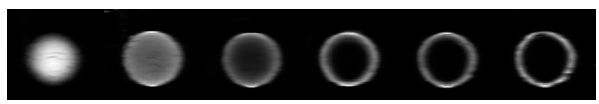

Figure 1: Electron beam profiles at grid potential U_{grid}=0V, 100V, 200V, 350V, 400V and 600V, the anode potential U_{anode}=500V.

LONGITUDINAL COOLING FORCE MEASUREMENT TECHNIQUE

The electron energy-step [3] method is one of the straightforward techniques for measuring the longitudinal cooling force. After the ion beam was cooled to equilibrium, the electron energy was changed rapidly by changing the cathode potential, creating a well defined velocity difference between ions and electrons. The ions will be accelerated or decelerated toward the new electron velocity. The acceleration is determined via Schottky spectra from the change in revolution frequency per unit time. The longitudinal cooling force at each time can be calculated in accordance with the relation

$$F_{\parallel}(t) = \gamma A \frac{1}{n}\frac{1}{\eta}\frac{C_{ring}^2}{L_{cooler}}\frac{E_0}{c^2}\left.\frac{df}{dt}\right|_{f(t)} \quad (1)$$

where A is the mass number of measured ion, n is harmonic number, η is the off-momentum factor, C_{ring} is the ring circumference and L_{cooler} is the cooling section effective length, E_0 is the atom mass unit equal to 938 MeV, c is the speed of light, $\frac{df}{dt}$ is variation of the n harmonic centre frequency. Correspondingly, the relative velocity between ion and electron is

$$v_{ion-electron}(t) = \frac{\beta c}{\gamma^2}\frac{1}{\eta}\frac{f(t) - f_{final}}{f_{final}} \quad (2)$$

Where β and γ are Lorenz factor, $f(t)$ and f_{final} are the n harmonic centre frequency at t time and final equilibrium, respectively.

The Tektronix RSA3303A real-time spectrum analyzer was used in the measurement. This method was applicable to relative velocities from 10^3 to 10^6 m/sec. The behaviour of a cooled 400MeV/u $^{12}C^{6+}$ beam at CSRe after applying a step of 300eV was illustrated in fig 2.

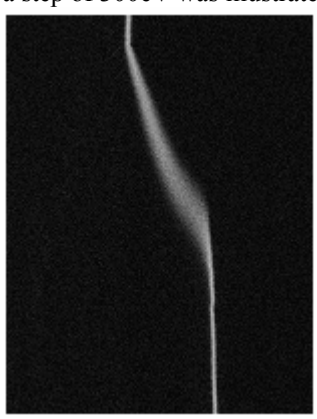

Figure 2: The spectra a cooled 400MeV/u $^{12}C^{6+}$ beam at CSRe shift after increasing electron energy 300eV rapidly.

The central frequency is calculated by formula,

$$f = \frac{\sum_{n=0}^{50}\sum_{is} f_{is} * Amp_{is,n}}{\sum_{n=0}^{50}\sum_{is} Amp_{is,n}} \quad (3)$$

It means the "barycentre" of spectra. Amp is the amplitude of Schottky signal.

The differentiation of frequency is calculated using Taylor expansion,

$$\left.\frac{df}{dt}\right|_{t0} = \frac{\sum_{k=-n}^{n} f(t_0 + k\cdot\Delta T)\cdot k}{\Delta T\sum_{k=-n}^{n} k^2} \quad (4)$$

EXPERIMENTAL CONDITIONS

The experimental conditions were summarized as table 2. These parameters were determined by HIRFL-CSR optimization. The longitudinal cooling force has been measured for $^{12}C^{6+}$ and $^{36}Ar^{18+}$ ions at various energies from 7.0 to 400.0MeV/u. At CSRm, the longitudinal magnetic field in cooling section is 0.039T, which is a quarter of design value, because of the coupling effect and compensation. The energy step is determined by the momentum acceptance of storage ring.

Two capacitive pickups are used as Schottky noise probes at CSRm and CSRe respectively. The electrodes have a length of 150mm in beam direction and distances of 170mm and 100mm in horizontal and vertical direction.

Table 2: Experimental Conditions

Ions	**$^{12}C^{6+}$**			**$^{36}Ar^{18+}$**
Storage ring	CSRm	CSRe	CSRe	CSRm
Circumference [m]	161.0	128.8	128.8	161.0
Cooler effective length [m]	3.4	3.4	3.4	3.4
Ion energy [MeV/u]	7.0	200.0	400.0	21.7
Electron energy [keV]	3.84	109.71	219.43	11.90
γ_t	5.168	2.629	2.629	5.168
B_cooling section [T]	0.039	0.078	0.078	0.039
B_gun [T]	0.12	0.14	0.21	0.12
Electron beam radius [mm]	25.4	16.8	20.5	25.4
Energy step [eV]	30	100	300	50

RESULTS

Figure 3 shows the longitudinal cooling force measured for $^{12}C^{6+}$ and $^{36}Ar^{18+}$ ions at standard operational parameters in table 2. The solid lines in the figure were calculated using the Parkhomchuk's semi-empirical formula [4]

$$\vec{F}(\vec{v}) = \frac{4\pi Z^2 n_e r_e^2 m_e c^2 (\vec{v} - \vec{v}_e)}{\left(|\vec{v} - \vec{v}_e|^2 + v_{eff}^2\right)^{\frac{3}{2}}} L_c \quad (5)$$

where Z is ion charge state, $\vec{v}$ and $\vec{v}_e$ are ion and electron velocity respectively, n_e is electron beam density, r_e is classical electron radius, L_c is Coulomb logarithm. Fitting the cooling force by Eq (5) can estimate the effective electron beam temperature. Best agreement with the experimental results corresponds to the effective electron beam temperature 0.003eV, the transverse electron beam temperature 0.05eV and the longitudinal one 10-5eV. According to the definition of effective velocity,

$$V_{eff} = \sqrt{< (c\beta\gamma\Delta\theta_B)^2 >} \quad (5)$$

where $\Delta\theta_B$ is the magnetic field homogeneity in the cooling section. Due to Eq (6) we estimated the homogeneity is about 8.0×10^{-5} , which was good agreement with measurement data [5].

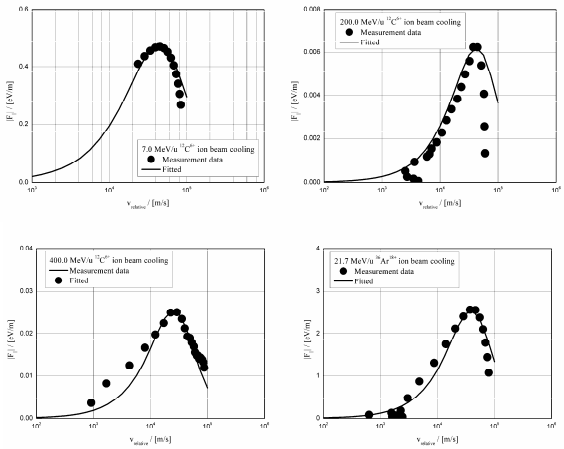

Figure 3: The longitudinal cooling force measured at CSR.

The electron beam profile is determined by the ratio between grid and anode potential. Further experiments studied the influence of the electron beam intensity and profile on the longitudinal cooling force. Table 3 and 4 show the electron beam conditions in experiments. Figure 4 and 5 show the results respectively. These show the force increases with increased density at electron beam centre.

Table 3: Electron Beam Parameters for 21.7 MeV/u $^{36}Ar^{18+}$ Cooling at CSRm

U_{grid} [kV]	0.2124	0.2490	0.2808	0.1909	0.0317
U_{anode} [kV]	1.4258	1.6690	1.8896	1.1426	1.1426
U_{grid}/U_{anode}	0.1489	0.1492	0.1486	0.167	0.0277
I_e [mA]	136	172	204	82	55
J_e at centre [mA/cm^2]	26.6	33.7	40.6	18.3	17.2

Table 4: Electron Beam Parameters for 200.0 MeV/u $^{12}C^{6+}$ Cooling at CSRe

U_{grid} [kV]	0.4834	0.5127	0.7227	0.8008	1.1157
U_{anode} [kV]	4.7998	5.1123	2.4023	1.6016	1.1133
U_{grid}/U_{anode}	0.1	0.1	0.3	0.5	1.0
I_e [mA]	382	416	422	431	427
J_e at centre [mA/cm^2]	38.8	42.2	22.2	15.2	7.9

Because the electron beam profile is variable, both the electron beam current and profile should be considered during optimization. After consider the ion-electron capture and space charge effect, the ratio between the grid and anode potential is set 0.2 to 0.5 and the current is 100 to 300mA usually at CSRm.

The cooling force is normalized by the factor $\beta^4\gamma^5$ shown in figure 6. Because of the low energy of argon ions, the cooling force decreased when the density is higher.

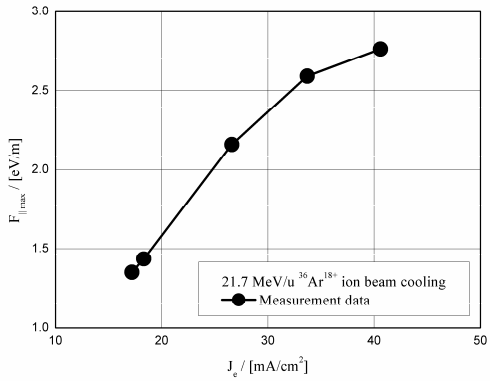

Figure 4: The longitudinal cooling force depends on the density at electron beam centre measured by 21.7 MeV/u $^{36}Ar^{18+}$.

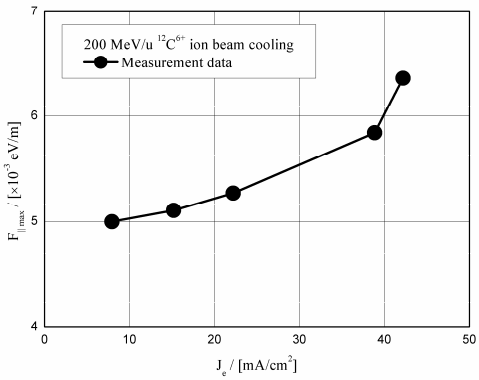

Figure 5: The longitudinal cooling force depends on the density at electron beam centre measured by 200.0 MeV/u $^{12}C^{6+}$.

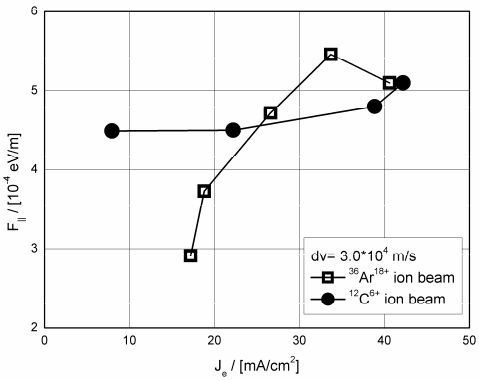

Figure 6: The longitudinal cooling force normalized by $\beta^4\gamma^5$.

The dependence of the longitudinal cooling force on the alignment angles between the ion and the electron beam in horizontal direction was measured also. In electron cooling, the energy spread of the ion beam is given to electron s having the same speed as the ions and moving parallel to them [6]. If the ion and electron beams are not perfectly aligned, cooling still occurs, but is less efficient. For this reason, we should optimize this angle in operation. The longitudinal cooling force as function of the alignment angle was shown in figure 7. It's obvious that perfectly alignment is good for obtaining maximum longitudinal cooling force; therefore the maximum cooling efficiency would be obtained.

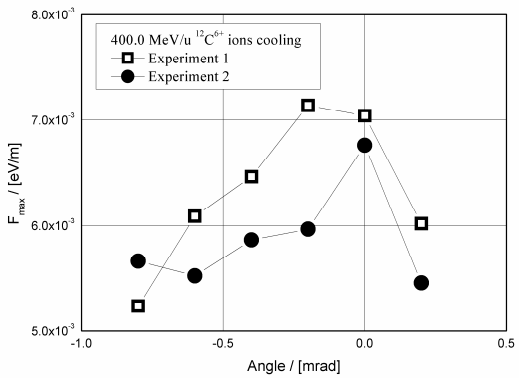

Figure 7: Longitudinal cooling force at different horizontal alignment angles between the ion and electron beams

CONCLUSION

Longitudinal cooling forces were obtained for $^{12}C^{6+}$ and $^{36}Ar^{18+}$ by electron energy-step method. The experimental results were best agreement with semi-empirical formula. The longitudinal cooling force increases with increasing electron beam current or decreasing the alignment angle between ion and electron beams. According the experiment results, the best cooling and accumulation efficiency were obtained in HIRFL-CSRm. For $^{12}C^{6+}$ beam, the stored beam current reached 3.5mA and for $^{36}Ar^{18+}$ beam reached 0.75mA.

REFERENCES

[1] J.W.Xia, W.L.Zhan, B.W.Wei et al. The heavy ion cooler storage ring project at Lanzhou. Nuclear Instruments and Methods in Physics Research A, 2002, 488(1):12-15

[2] H.Poth. Electron cooling: theory, experiment, application. Physics Reports, 1990, Vol 196(3&4): 135-297

[3] T.Winkler, K.Beckert, F.Bosch et al. Electron cooling force measurements for highly charged ions in the ESR. Hyperfine Interactions 99(1996): 277-283

[4] V.V.Parkhomchuk. New insights in the theory of electron cooling. Nuclear Instruments and Methods in Physics Research A, 2000, 441:9-17

[5] YANG Xiao-Dong, V.V.Parkhomchuk, ZHAO Hong-Wei et al. Test results of HIRFL-CSR main ring electron cooling device. High Energy Physics and Nuclear Physics, 2003, 27(8):726-730

[6] H.Danared, G.Andler, L.Bagge et al. Studies of transverse electron cooling. Proceedings of EPAC 2000, Vienna, Austria: 301-303

MODIFICATIONS OF CRYRING FOR TRANSFER TO FAIR

H. Danared, A. Källberg and A. Simonsson, Manne Siegbahn Laboratory, Stockholm, Sweden
D. Reistad, Intégro Utbildnings AB, Sigtuna, Sweden

Abstract

FLAIR will be the next-generation facility for physics with low-energy antiprotons, providing antiprotons at energies from tens of MeV down to rest. Also highly charged ions at very low energies will be available at FLAIR. A key component of the FLAIR facility will be the Low-energy Storage Ring LSR which will decelerate antiprotons from 30 MeV to 300 keV. The LSR will consist of the present CRYRING at the Manne Siegbahn Laboratory, which is being modified mainly with respect to injection and extraction, to allow injection of 30 MeV antiprotons and to provide it with both fast (single-turn) and slow (resonant) extraction at a variable energy. We here describe some aspects of the design of these modifications.

FLAIR AND CRYRING

FLAIR [1,2], the Facility for Low-energy Antiproton and Ion Research at FAIR [3], is expected to become the next-generation facility for physics with low-energy antiprotons, providing the world's highest fluxes of antiprotons at energies from tens of MeV down to rest. It will also offer unique possibilities for physics with highly charged ions at very low energies.

FLAIR will obtain beams of already decelerated antiprotons and ions from the NESR ring. The particles will then be further decelerated in one magnetic deceleration ring, the Low-energy Storage Ring LSR, which will be the modified CRYRING, and in one electrostatic ring, the Ultralow-energy Storage Ring USR, such that antiprotons can be delivered to experiments at a kinetic energy of only 20 keV. Also ions can be decelerated to low energies, limited in many cases by the increasing rate of recombination in collisions with residual-gas atoms as the energy is reduced, and by the consequent rapid reduction of the lifetime of stored beams of highly charged ions at low energies. Furthermore, antiprotons and ions can be decelerated by HITRAP for other experiments at very low energies or sent directly to experiments from the NESR or the LSR.

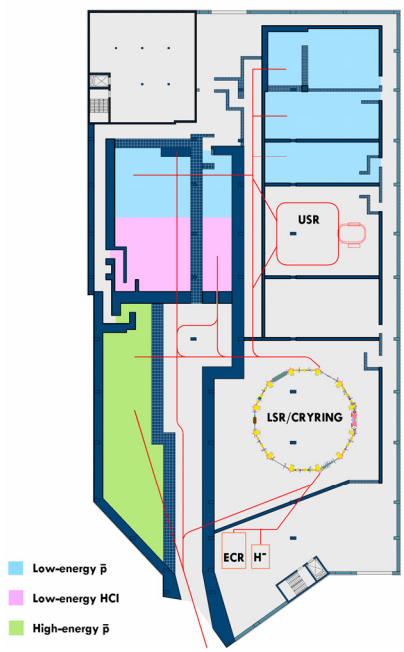

Figure 1: Proposed layout of the FLAIR hall.

The perhaps most important new feature at FLAIR, as compared to the Antiproton Decelerator, AD, at CERN, is that antiprotons will be phase-space cooled at lower energies during the deceleration process. The high production rate of antiprotons at FAIR, similar to that at CERN at the time of proton–antiproton collisions in the SPS but much higher than today's rate at CERN, can thus be combined with beams that have the smallest possible emittance and results in unprecedented beam intensities at low energies. Another difference is that the AD does not have the slow extraction that will be available at FLAIR.

A preliminary layout of the FLAIR hall is seen in fig. 1. Antiprotons will be delivered from NESR to the LSR at a kinetic energy of 30 MeV. In the LSR, the antiprotons can be decelerated down to 300 keV, or possibly somewhat lower if this is desirable. At 300 keV, the antiprotons are extracted to the electrostatic Ultralow-energy Storage Ring, USR, for further deceleration down to, at minimum, 20 keV. At that energy the particles can be trapped electrostatically and brought to rest by lowering the trap potential to zero. The LSR will, however, not be limited to extraction at the lowest energy, but antiprotons can be extracted at any energy between 30 MeV and 300 keV. For example, antiprotons will be delivered to HITRAP at 4.2 MeV.

Ions will be injected into the LSR at the same magnetic rigidity $B\rho$ of 0.80 Tm as 30 MeV antiprotons have, or at an energy of 30 Z^2/A^2 MeV/u, where Z is the charge state of the ion and A is its mass number. The ions can be decelerated and extracted over the same range of rigidities as the antiprotons, although the lowest limit may in practice be determined by the beam lifetime as already mentioned.

LSR will consist of the present CRYRING at the Manne Siegbahn Laboratory. This is a 1.44 Tm synchrotron and storage ring with 52 m circumference. CRYRING's properties closely match those required by the LSR as has been discussed earlier [4], and in that paper it was also shown that CRYRING already as it looks today is able to decelerate protons from 30 MeV to 300 keV with intensities close to the space-charge limit

and in excess of the commissioning goal of 1×10^8 particles being decelerated to 300 keV.

The major modifications that have to be made to CRYRING before it can be used as the LSR ring concern injection and extraction.

INJECTION

At present, CRYRING has a 10-turn horizontal electrostatic multiturn injection designed to match the output of the RFQ that serves as a pre-accelerator for the ring. The RFQ delivers particles with charge-to-mass ratios of 0.25 or higher at a fixed velocity corresponding to 300 keV per nucleon. Also particles with lower charge-to-mass ratios can be injected into the ring, but these are only focused by the RFQ, not accelerated.

In order for the ring to accept higher-energy antiprotons and ions from the NESR, a new injection system has to be developed. Antiprotons will be delivered from the NESR at an energy of 30 MeV, which is equal to a magnetic rigidity of $B\rho$ = 0.80 Tm, and highly charged ions will be delivered at the same magnetic rigidity irrespective of their charge or mass.

LSR will, however, retain a low-energy injector similar to the injector for singly charged ions at CRYRING today. This will be used for commissioning of the ring and the beamlines in the FLAIR hall with, e.g., protons or H^- ions, and possibly also for tests of experiments, such that physics can start as soon as possible after antiprotons and/or ions are available from the FAIR accelerator chain. For these low-energy ions, a multiturn injection resembling the present injection at CRYRING is foreseen.

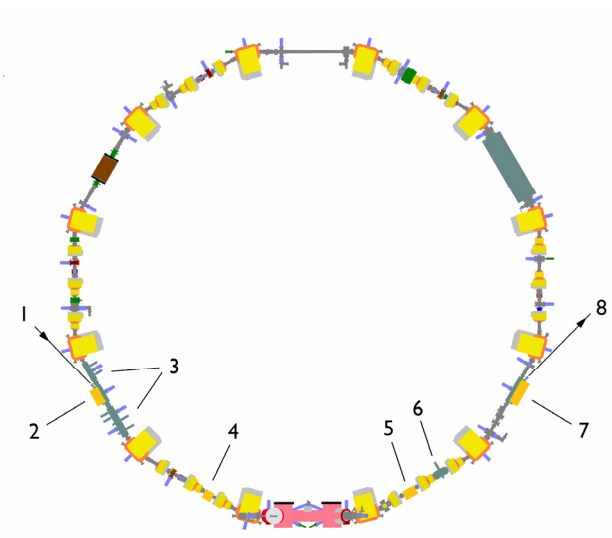

Figure 2: Schematic illustration of new components for injection and extraction. 1) Injected beam from NESR, 2) Injection septum magnet, 3) Electrostatic kickers for multiturn injection, 4) Injection kicker magnet, 5) Extraction kicker magnet, 6) Electrostatic extraction septum, 7) Extraction septum magnet, 8) Extracted beam.

To save space in the FLAIR building, the beamlines from the NESR and from the low-energy injector should be merged upstream of the LSR, and both kinds of particles should use the same injection channel in the ring. The system will consist of a septum magnet, a fast injection kicker for the NESR antiprotons and ions, as well as electrostatic deflector plates similar to the ones used at present to produce the closed-orbit bump for the multiturn injection. The closed-orbit bump will remain local to the injection-straight section while the kicker magnet will be positioned at the end of the magnet section following the injection, where the horizontal betatron phase advance with respect to the injection point is close to $\pi/2$. The new components for injection and extraction and their approximate position are shown in fig. 2, where also the straight sections have been rearranged compared to the current layout of CRYRING in order to match the geometry of the FLAIR building.

The magnetic septum and the multi-turn injection are being designed at present. The kicker magnet will be similar to the extraction kicker and is discussed further in the following section.

EXTRACTION

CRYRING at present does not have an extracted beam, although extraction was foreseen when the ring was designed. This means that there is a straight section available for an extraction septum magnet, sextupole magnets that can drive a third-integer resonance, etc. The LSR will, in contrast to the Antiproton Decelerator at CERN, implement both slow resonant extraction and fast single-turn extraction. New components for the extraction are the septum magnet, an electrostatic septum for the resonant extraction and a fast kicker for the single-turn extraction, and their positions are indicated in fig. 2.

Ideally, both the kicker and the electrostatic septum should be positioned at a betatron phase advance close to $\pi/2$ before the extraction septum which means in the first half of the magnet straight section before the septum magnet. However, there is not room for both devices at that position, and in addition the limited horizontal aperture through the quadrupole magnets prevents the electrostatic septum from being too far away from the magnetic septum. (The aperture is a more severe restriction for particles deflected by the electrostatic septum than by the kicker magnet since the former already have a horizontal displacement when they are deflected.) For these reasons, the electrostatic septum is positioned after the kicker magnet as seen in fig. 2.

Both the slow and the fast extraction will cover the energy range up to the injection energy both for antiprotons and for ions. Although LSR is a low-energy ring, its rather small circumference makes the rise or fall time of the kicker magnets quite short, and the space available in the ring for these is also quite short. Injection and extraction kickers will be similar although the injection kicker operates only at $B\rho$ = 0.80 Tm while the extraction kicker has to work for all rigidities between $B\rho$

= 0.80 Tm and the 0.079 Tm corresponding to 300 keV antiprotons. The extraction kicker needs to have a longer pulse length for lower energies and slower particles, but then the rise time can also be longer. Preliminary parameters of the kicker magnets which are now being procured are shown in tab. 1.

Table 1: Preliminary Parameters for Injection and Extraction Kicker Magnets

Parameter	**Value**
Beam rigidity (injection)	0.80 Tm
Beam rigidity (extraction)	0.079 – 0.80 Tm
Nominal deflection angle	17 mrad
Aperture (width × height)	107 mm × 87 mm
Length	457 mm
Fall time (injection)	280 ns
Rise time (extraction)	280 − 4140 ns

The slow extraction takes place near the third-order resonance Q_x = 2 1/3, where sextupole magnets are excited to divide the horizontal phase space into a stable area for particles with small betatron amplitudes and an unstable area for larger betatron amplitudes. Noise is applied to a transverse electrostatic kicker to excite the particles into the unstable part of phase space. Particles on unstable trajectories move further and further out from the equilibrium orbit until they cross a thin electrostatic septum. There they are deflected by an electrostatic field such that they can cross also the magnetic septum and end up in the extraction channel.

At the electrostatic septum, the particles need to be deflected by 11 mrad in order not to hit the magnetic septum, translating into an electrostatic septum voltage of less than 30 kV for 30 MeV antiprotons.

Several conditions have to be fulfilled for the particles to reach the extraction channel with minimum losses apart from the $\pi/2$ betatron phase advance which determines the relative position between electrostatic and magnetic septa: 1) The stable phase-space area inside the separatrix has to have the right size. The betatron amplitude growth from turn to turn increases with smaller stable area, decreasing the probability of particles hitting the septum foil but increasing the size of the extracted beam. 2) The outgoing leg of the separatrix has to have the right orientation so that particles cross the electrostatic septum with an angle x' that leads them into the extraction channel. 3) The Hardt condition should be fulfilled so that particles with different momentum offsets Δp cross the electrostatic septum at the same x', which again minimizes the number of particles hitting the electrostatic septum. 4) The sextupole fields should not be unnecessarily strong to avoid higher-order nonlinearities.

CRYRING has six focusing and six defocusing sextupoles and thus a more than sufficient number of free parameters to allow all four conditions to be satisfied simultaneously. Details will be presented elsewhere, and in this paper we just show in fig. 3 an example of the output from a particle-tracking code for a set of sextupole values that gives the desired result. Here the chromaticities are first controlled such that the Hardt condition gets satisfied using the focusing and defocusing sextupoles as two families. Superimposed on that, two focusing and two defocusing sextupoles are excited to optimize the other three conditions.

In fig. 3, the gray area in the centre is the area of stable motion for particles with reference momentum. The tracking is made with the assumption that the beam is cooled longitudinally to a relative momentum spread of $\Delta p/p = \pm 5 \times 10^{-4}$, and the blue and red triangles are stable

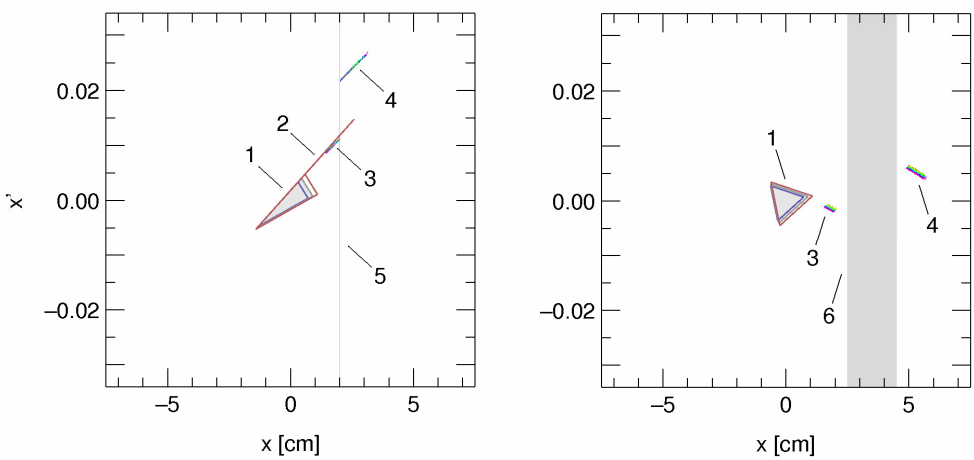

Figure 3: Particle distributions in phase-space at the electrostatic septum (left plot) and magnetic septum (right plot), illustrating resonant extraction. Particles are colour-coded according to momentum. 1) Area of stable motion for different particle momenta (see text), 2) Outgoing part of separatrix, 3) Particles to be extracted three turns before deflection in electrostatic septum, 4) Particles after deflection in electrostatic septum and (to the right) after deflection in magnetic septum, 5) Position of electrostatic septum, 6) Position of magnetic septum.

areas for particles with the lowest and highest momentum offsets respectively. At the location of the electrostatic septum, the dispersion and its derivative are D = 1.8 m and D' = 0.53, and with horizontal tune Q_x = 2.326 and the chromaticity adjusted to Q'_x = −1.6, the Hardt condition is fulfilled. As seen in the left part of the figure, all particles then reach the electrostatic septum at virtually the same x', although not exactly on the calculated line due to higher-order non-linearities. This condition cannot be fulfilled simultaneously at the magnetic septum, resulting in the slightly wider particle distributions in the right plot of fig. 3.

With a septum foil that is 0.1 mm thick, an extraction efficiency of 98.5% is obtained in this example, the remaining 1.5% of the particles hit the septum foil.

The electrostatic septum is now being manufactured and tests to extract the particles in CRYRING into a particle detector sitting at the future position of the magnetic septum will take place during the autumn of 2009.

REFERENCES

[1] FLAIR Technical Proposal, unpublished, www.oeaw.ac.at/smi/flair/TechnicalProposal/TP.htm.

[2] C.P. Welsch and H. Danared, Proc. EPAC 2006, Edinburgh, p. 220 (2006).

[3] FAIR Baseline Technical Report, Eds. H. H. Gutbrod et al., GSI 2006

[4] H. Danared, A. Källberg and A. Simonsson, Proc. Workshop on Beam Cooling and Related Topics, COOL 07, (Gesellschaft für Schwerionenforschung mbH 2007) p. 234.

THE VERSATILE NESR STORAGE RING WITH POWERFUL ELECTRON COOLING

C. Dimopoulou, O. Dolinskyy, R.G. Heine, T. Katayama,
U. Laier, F. Nolden, G. Schreiber, M. Steck, GSI, Darmstadt, Germany

Abstract

The large-acceptance New Experimental Storage Ring (NESR) at FAIR has two main operation modes: storage of ion beams for internal experiments and deceleration of highly charged ions and antiprotons before transfer to a low-energy area. The heavy ion beams can be stable or rare isotopes selected in a magnetic separator. Antiprotons come at 3 GeV from the production target, they are stochastically pre-cooled and accumulated in a dedicated complex. The NESR operation relies on a performant electron cooler designed for up to 500 keV electron energy, 2 A electron current and with the option of magnetic expansion/compression. Electron cooling provides highest phase-space density of the stored beams and compensates beam diffusion during deceleration, so that high efficiency can be reached. For low-abundant isotopes, it also supports the longitudinal RF-accumulation, e.g. by means of barrier bucket pulses. For short-lived isotopes the cooling and deceleration time is optimized to a few seconds. Selected results of beam dynamics studies and benchmarking experiments from the existing ESR are presented in connection with the requirements of the users.

INTRODUCTION

The NESR of the FAIR project [1, 2] will store highly charged radioactive and stable ion beams for internal experiments and decelerate ions and antiprotons for transfer to the low-energy experimental facility FLAIR. The beams stored in the NESR are provided from various sources. Stable ions can be injected at magnetic rigidity up to 13 Tm, energy and charge state are chosen according to their availability after acceleration in the synchrotrons SIS18 or SIS100. Secondary rare isotope beams (RIBs) emerge from a production target and are selected in the magnetic separator SuperFRS. There are two ways of injecting RIBs into the NESR. The first is to inject a short bunch directly from the SuperFRS. The second, ensuring a better injected beam quality, makes use of stochastic pre-cooling in the CR. Then, in the RESR, beams can be optionally fast decelerated and transferred to the NESR. Antiprotons at 3 GeV will be injected from the RESR, where they are accumulated after pre-cooling in the CR.

OPERATION MODES

The operation modes and experimental performance in the NESR rely on the availability of powerful beam cooling and dedicated RF systems. An electron cooling system is installed in one of the four straight sections (Fig. 1). It covers the full energy range (740-4 MeV/u) for ions and

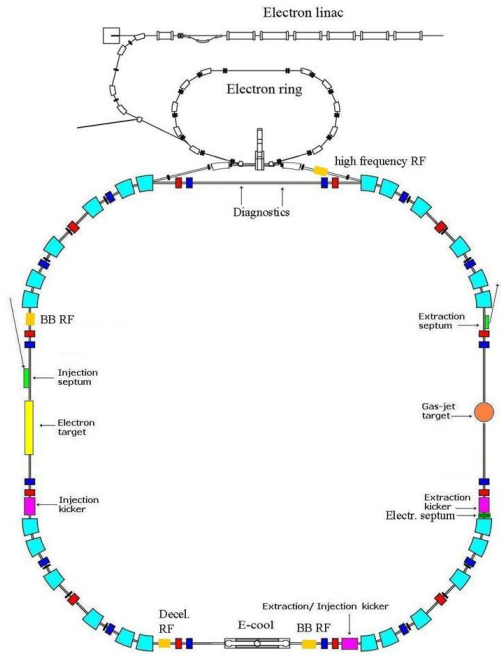

Figure 1: Layout of the NESR with experimental insertions.

allows for intermediate cooling in the range 800-30 MeV during the deceleration of antiprotons. It provides highest phase space density of the stored beams for the experiments and compensates the diffusion of the beams during deceleration. This ensures high efficiency and small losses during the deceleration cycle. For experiments with short-lived isotopes, the cooling time and the time of deceleration can be optimized to a few seconds. In addition, electron cooling will vitally support all RF manipulations: (i) the longitudinal accumulation at injection energy of RIBs produced at low abundancies, (ii) (re)bunching of the beams before each deceleration ramp, (iii) bunching at lowest energy for beam transfer to FLAIR and (iv) the generation of very short bunches in order to achieve maximum luminosity in the electron-ion collider mode. Three different RF systems are foreseen. A ferrite-filled RF cavity is responsible for bunching and decelerating the stored beams by successively changing the harmonic number. A broadband barrier bucket (BB) system is used for longitudinal compression of RIBs at injection energy and for the preparation of a single low-energy bunch for FLAIR. A high harmonics RF cavity produces short ion bunches for the electron-ion collider.

Table 1: NESR Beam Parameters

	Ions	**Antiprotons**
Injection energy [MeV/u]	100-740	3000
Lowest extraction energy[MeV/u]	4	30
Max. number of particles	10^{10}	10^{9}
Δp/p at injection	$\leq 5 \times 10^{-4}$	$\leq 1 \times 10^{-3}$
Δp/p after cooling	$\leq 10^{-4}$	$\leq 10^{-4}$
Transverse emittance injection [mm mrad]	≤ 0.5	≤ 5
Transverse emittance after cooling [mm mrad]	0.1-1	1

EXPERIMENTAL SETUPS

Experiments with stored ion beams will be performed mainly in the straight sections (Fig. 1). It is foreseen to install a dense internal target (e.g., gas-jet, pellet target, microdroplets), which is part of the nuclear and atomic physics program. Detector setups surround the interaction volume and special detectors for projectile-like particles are installed downstream. The latter provide 100 % efficiency, if the scattered particles stay within the acceptance of the ring between target and detector. Another straight section accommodates an electron target, which is practically an electron cooler dedicated to the investigation of ion-electron interactions at variable relative velocity. It is designed for electron energies below 40 keV, i.e. lower than the typical ones in the standard electron cooling system. Thus, the electron target may be used for cooling at low beam energy, where it could be even superior to the standard cooler. One straight section is bypassed with a separate collision section, the so-called bypass section, which will be employed in the investigation of electron scattering on radioactive nuclei [3]. Electrons are provided by a complex consisting of an electron linac and a separate electron storage ring. When operating the electron-ion collision mode, the stored ion beam is sent into the bypass section by switching off the two adjacent ring dipoles. Matching optics around the interaction point in the bypass allows focusing of both beams to a size below 0.1 mm. In longitudinal phase space, the beams can be compressed into bunches with a r.m.s. length of about 10 cm in order to reach high luminosity.

Table 2: NESR Ring Parameters

Circumference	222.8 m
Maximum magnetic rigidity Bρ	13 Tm
Minimum Bρ after deceleration	0.52 Tm
Maximum A/Z	2.7
Horiz./vert. acceptance	150/40
for Δp/p=$\pm$1.5 %	mm mrad
Momentum acceptance (ϵ_H=0)	$\pm$ 2.5 %
Horizontal/vertical tune	4.20/1.87
Transition energy γ_t	4.59
Vacuum pressure	$\leq 10^{-11}$ mbar

ION OPTICAL LAYOUT

The NESR (Table 2) has a maximum magnetic bending power of 13 Tm and uses normal conducting magnets. The basic lattice layout, not including the bypass section nor special focusing sections for the experiments, has a four-fold symmetry with 4 straight sections of 18 m length. The location and strength of sextupoles for chromaticity correction have been defined. Studies of the dynamic aperture have been performed with the PTC code taking into account the worst case of higher order multipole components in the main dipole and quadrupole magnets [2]. The simulations confirm that the required acceptance can be maintained. By means of closed orbit correction calculations with MADX, (i) the location of the orbit corrector magnets and the beam position monitors was defined and (ii) the strength of the corrector magnets was specified in order not only to compensate the closed orbit distortion but also to create the commonly required local orbit bumps in the experimental setups.

ELECTRON COOLING

For the antiprotons intermediate cooling is foreseen after deceleration from 3 GeV to 800 MeV. Therefore, a cooling system in the electron energy range from 2 to 450 keV has been designed [4]. Its parameters are given in Table 3. A homogeneous electron beam with variable diameter for an optimal overlap with the different ion beam sizes can be produced by adiabatic expansion or compression of the guiding longitudinal magnetic field. The option of a hollow electron beam, which seems to be advantageous for reducing ion-electron recombination losses, is also included. A straightness of the magnetic field lines better than $B_\perp/B_\parallel = 2\times10^{-5}$ at a maximum strength of 0.2 T and a fast ramping within 1.5 s during beam deceleration are stringent requirements on the magnet system. Electron currents of up to 2 A will allow fast cooling of short-lived isotopes. Fast ramping of the high voltage during deceleration is necessary. This calls for an active method of discharging and charging the high voltage section between upper (400 keV) and lower (a few keV) values within 1.5 s.

Beam dynamics studies have been performed to estimate the electron cooling performance for ring design studies as well as for the users. The BETACOOL code [5] was used to investigate the dependence of the cooling time and

Table 3: NESR Electron Cooler Parameters

Energy range	2-450 keV
Maximum voltage	500 kV
Voltage ramping rate	250 kV/s
Maximum current	2 A
Length of cooling section	5 m
Cathode radius	1 cm
Beam radius in cooling section	0.5-1.4 cm
Magnetic field:	
Gun	up to 0.4 T
Cooling section	up to 0.2 T
Collector	up to 0.23 T
Straightness $B_\perp/B_\parallel$	$\leq 2\times10^{-5}$
Maximum power in the collector	15 kW

the equilibrium parameters (transverse emittances and momentum spread) of the electron cooled beams on the initial beam parameters, for realistic operation parameters of the electron cooler [6]. Parkhomchuk's formula [7] with an effective electron velocity corresponding to magnetic field misalignments of 5×10^{-5} is used for the cooling force and the Martini model [8] for intrabeam scattering, which is the main heating source at these moderate intensities.

For ion beams at the maximum injection energy of 740 MeV/u, cooling times of less than 0.5 s were calculated, if the pre-cooled beam from the CR. is cooled with an electron beam of 1 A. An example is shown in Fig. 2. Even if momentum spread and emittance are twice as large as the design value of the CR, the cooling time does not exceed 1.5 s. Thus, the experiments can fully benefit from the planned cycle time of 1.5 s of SIS100.

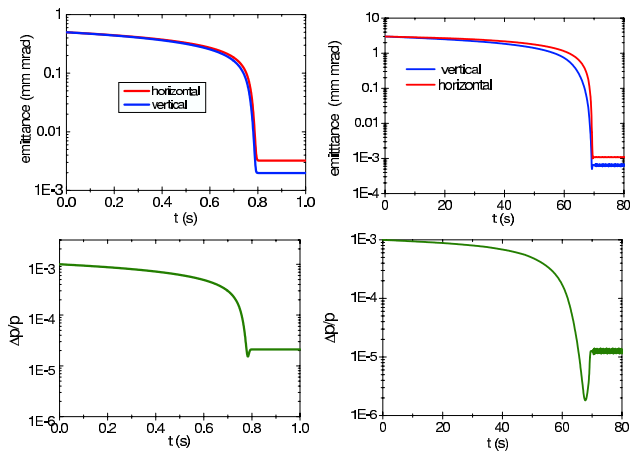

Figure 2: Simulations of electron cooling of coasting beams in the NESR with the BETACOOL code. Left: 10^8 $^{132}Sn^{50+}$ ions at 740 MeV/u, electron density n_e=1.4×10^8 cm^{-3}; Right: 10^8 antiprotons at 800 MeV, electron density n_e=1.6×10^8 cm^{-3}. The magnetic field strength in the cooling section was 0.2 T.

The conditions for electron cooling are less favorable for antiprotons which are injected at 3 GeV, at larger Δp/p and emittance (Table 1). Due to their low charge the cooling time can be of the order of minutes as shown in Fig. 2. An adiabatic growth of the beam parameters is assumed during the deceleration from 3 GeV to 800 MeV. The cooling time for antiprotons with a deviation of 1σ of the distribution after stochastic pre-cooling in the CR is 150 s, even with an electron beam current of 2 A. If the experiments request deceleration cycles below 1 minute, better pre-cooling must be achieved. This should be possible by additional stochastic cooling in the RESR.

For the deceleration mode, similar calculations were made at intermediate and lowest energies at which electron cooling is applied [6]. Indicative results are shown in Table 4. Due to space charge limitations for highly charged ions at the lowest energy of 4 MeV/u, a maximum intensity of 5×10^7 cooled ions is estimated. This intensity limit is further reduced, if the beam is compressed into a short bunch for transfer to FLAIR.

Table 4: Equilibrium Parameters (2σ values) for Electron-cooled Ion and Antiproton Beams in the NESR

Coasting beam of 10^8 $^{238}U^{92+}$

Kinetic energy (MeV/u)	Electron current (A)	$\epsilon_{H,V}$ (mm mrad)	Δp/p
740	1	2×10^{-2}	5×10^{-5}
100	1	6×10^{-2}	6×10^{-5}
4	0.1	2	6×10^{-4}

Coasting beam of 10^8 antiprotons

Kinetic energy (MeV)	Electron current (A)	$\epsilon_{H,V}$ (mm mrad)	Δp/p
800	1.5	2×10^{-3}	2×10^{-5}
30	0.5	5×10^{-2}	6×10^{-5}

RF MANIPULATIONS WITH ELECTRON COOLING

The beam manipulations in longitudinal phase space have been investigated by analytical estimates and computer simulations. In most cases, the relevant beam parameters reached after application of electron cooling were studied independently, as explained above, and used as input. The results constitute the basis for the design of the RF systems [2].

A ferrite-filled RF cavity with a frequency swing between 1 and 2.3 MHz and a peak voltage of 15 kV in c.w. operation can decelerate all beams over the whole energy range by changing the RF harmonic number in the course of the deceleration between h=2, 4, 8. It also allows debunching of hot single injected bunches in order to reach minimum momentum spread for fast cooling. Bunching and subsequent deceleration of the electron cooled coasting beams after injection or at intermediate energies has been simulated in the longitudinal phase space. Application of

electron cooling during the (re)bunching of ions (within the whole energy range) and antiprotons (below 800 MeV) before each deceleration ramp, is advantageous to counteract the dilution of the longitudinal emittance. As a result, the minimum required RF voltage was set to 50 V.

For longitudinal stacking of RIBs at injection energy, i.e. in the range 100-740 MeV/u, two compression schemes have been investigated with beam dynamics studies [9, 10] and successfully tested in dedicated experiments in the existing ESR [11, 12]. The first scheme uses barrier bucket RF pulses to confine the beam to a fraction of the circumference and free a part of the circumference for the injection of additional particles. The second makes use of a sinusoidal RF pulse at h=1 to compress the beam to a fraction of the circumference. Then, without affecting the stored beam, new beam is injected onto the unstable fixed point of the stationary RF bucket. In both schemes, electron cooling maintains the stack and merges it with the freshly injected bunch. It is planned to provide both possibilities in the NESR by means of the barrier bucket RF system. This broadband system provides single sine waves of 200 ns period. Four cavities, each driven by a 3.5 kW solid state amplifier, result in a total voltage of 2 kV, sufficient to compress cooled beams. In addition, the barrier bucket system has a c.w. operation mode at harmonic number one (h=1) at low frequencies in the range from 0.125 to 1.5 MHz. This mode enables accumulation by means of the h=1 scheme. Experience in operating a test version of a barrier bucket system for both stacking schemes was already acquired in the ESR. For realistic performance of the NESR electron cooling and RF systems the simulations predict a stacking cycle time i.e. time between two successive injections of about 2 s [9]. Thus one can achieve fast stacking of short-lived RIBs and fully profit from the cycle time of 1.5 s of SIS100.

It has been demonstrated by ESME simulations [6, 13] that the barrier bucket RF system in its low-frequency c.w. operation mode can compress the decelerated cooled beam of highly charged ions down to 4 MeV/u or antiprotons down to 30 MeV in a bunch with the required total length (4σ) of 30 m for transfer to FLAIR (Fig. 3). Furthermore, it still offers the option of bunch rotation at h=1 to produce the short bunch for extraction.

For the operation of the NESR in the collider mode, a high harmonics narrowband RF system operating at a fixed frequency of about 45 MHz is foreseen. The concept is based on a disk-loaded quarter wave resonator. The cooled coasting beam has to be adiabatically bunched into very short ion bunches matched to the relativistic electron bunches. Simulations with BETACOOL show that application of electron cooling during adiabatic bunching can decrease the bunch length by a factor of 4. Inversely, electron cooling during bunching is necessary in order to reach the required short bunch lengths, typically $\leq$ 10 cm r.m.s., with acceptable RF voltages of up to 150 kV [14].

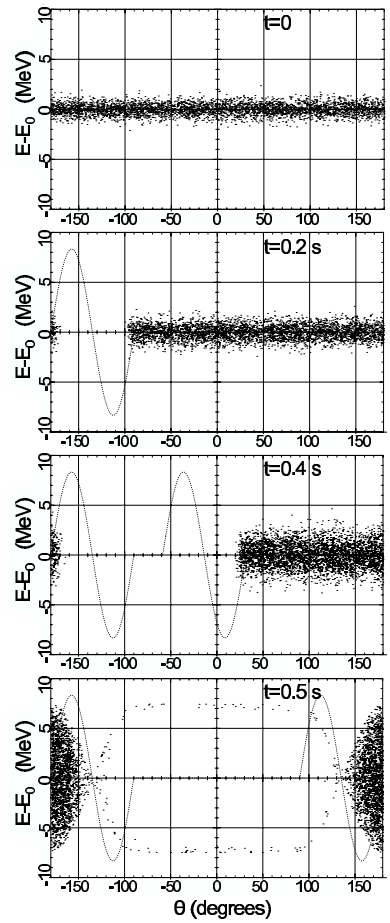

Figure 3: Compression of the 4 MeV/u $^{238}U^{92+}$ beam with initial Δp/p=6 $\times$ 10^{-4} (Table 4) into a bunch of 30 m by barrier bucket pulses at peak voltage of 2 kV (dotted lines). The dots represent the particle distribution in the longitudinal phase space. No electron cooling nor space charge is included in the ESME simulation.

REFERENCES

[1] FAIR Baseline Technical Design Report, GSI 2006.

[2] NESR Technical Design Report, GSI 2008.

[3] I.A. Koop et al., Conceptual Design of an Electron-Nucleus Scattering Facility at GSI, BINP 2006.

[4] V.V. Parkhomchuk et al., GSI-Acc-Report-2005-04-001.

[5] A.O. Sidorin et al., NIM A 558 (2006) 325.

[6] C. Dimopoulou et al., PRST-AB 10 (2007) 020101.

[7] V.V. Parkhomchuk, NIM A 441 (2000) 9.

[8] M. Martini, CERN-PS-84-9 (1984).

[9] T. Katayama et al., COOL07 JACoW Proceedings, 2007.

[10] A. Smirnov et al., these proceedings.

[11] C. Dimopoulou et al., COOL07 JACoW Proceedings, 2007.

[12] C. Dimopoulou et al., THPP048, EPAC08 Proceedings, http://jacow.org, 2008.

[13] http://www-ap.fnal.gov/ESME/.

[14] R. Heine et al., MOPP088, EPAC08 Proceedings, http://jacow.org, 2008.

ULTRA-LOW ENERGY ELECTRON COOLER FOR THE HEIDELBERG CSR

A. Shornikov, D. A. Orlov, M. Grieser, K. Blaum and A. Wolf

Max-Planck-Institut für Kernphysik, Heidelberg, Germany

Abstract

As a part of the low energy electrostatic Cryogenic ion Storage Ring (CSR) an ultra-low energy electron cooler is under construction at the MPIK in Heidelberg. The cooler shares the basic CSR ultra-high-vacuum and 2 K cryogenic concept and uses a magnet system installed inside of the CSR isolation vacuum for the electron confinement. Cold electron beams will be provided for both phase space cooling of 300 keV stored ions and for recombination merged beam experiments with typical electron energies of 1-20 eV. A cryogenic photocathode electron source, developed for the Heidelberg Test Storage Ring, is used to achieve the beam quality required for electron cooling at such low energies. A new electron-ion merging scheme together with a decelerating electron optics suitable for both low energy electrons and slow ions will be applied. The production of high-quality electron beams of sub eV energies was studied at the TSR photocathode electron target.

INTRODUCTION

The Heidelberg CSR (see Fig. 1) is an electrostatic ring to be built at the Institute, with no mass limitation and with the capability of storing 20-300 keV ions. The circumference of the ring is about 35 m and it is designed to have a large ring acceptance of about 100 mm mrad.

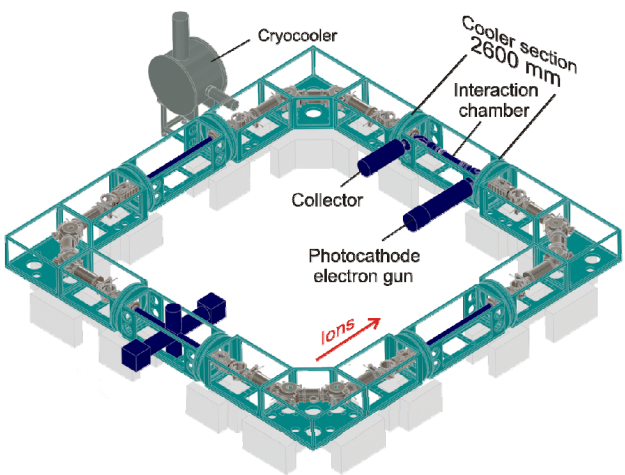

Figure 1: Schematic view of the CSR showing the electron cooler.

The key feature of the ring is the possibility of phase-space cooling of heavy, 100-200 a.m.u., molecular ions. To provide both phase space cooling with a velocity matched electron beam and cold electrons for merged beam recombination experiments, the CSR will be equipped with a dedicated ultra-low-energy electron cooler/target. The ring optics gives us the range of cooling energies we are interested in. The upper limit is given by 300 keV protons and corresponds to 163 eV electrons. For heavier single-charged ions the cooling energy decreases linearly as $1/M_i$ with M_i the ion mass, and corresponds to about 0.8 eV for M_i=200 a.m.u.; the typical electron cooling is foreseen to be a few eV. It is very difficult to cool these slow molecular ions because of the heavy mass and the low density of the electron beam, limited by the gun perveance. Thus, the lowest boundary is defined by the electron beam properties, including electron beam temperature and density.

The cooler will fit in one of the straight 2.6 m long experimental sections (see Fig. 1) and share the basic mechanical and cryogenic concept of the CSR with a two-level vacuum system. The first level is an isolation vacuum protecting the cryogenic environment from convection heat transfer and reducing radiation heat flux by thermal shields and by multilayer thermal isolation [1]. The second one is the 2K cryo-pumped beam vacuum volume at 10^{-13} mbar room temperature density equivalent pressure. The heat emission for the electron cooler has to be minimized and it should withstand bakeout up to 200-300^0 C. The magnetic electron optics of the cooler installed inside of the isolation vacuum has to be compatible with the electrostatic ring optics.

The CSR basic mechanical concept has been tested at the large scale 3-m long cryogenic electrostatic ion trap (Cryogenic Trap for Fast ion beams - CTF) that has been built as a part of the CSR project in 2007-2008. The CTF brought us practical knowledge about design and operation of large-scale cryogenic devices and proved our ability to achieve and measure vacuum with only 1000 rest gas particles per cubic centimetre specified for the CSR [1,2].

In this paper we discuss in more detail the results of numerical simulations, the mechanical and cryogenic concept of the cooler, and recent experiments on ultra-low energy electron beams [3], we have performed at the TSR e-target [4] with the same electron source and at energies we plan to use at the CSR.

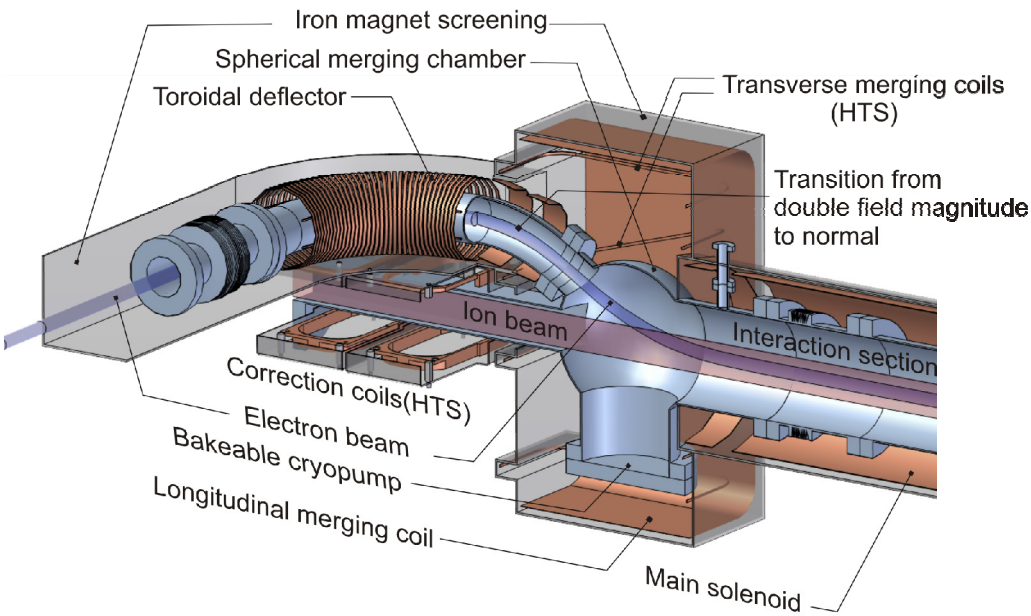

Figure 2: The new mechanical layout of the CSR electron cooler including magnet system inside of the isolation vacuum. The positions of copper magnets (toroidal deflector, main solenoid, longitudinal merging coil) and HTS magnets (correction and transverse merging coils) are also shown.

GEOMETRY AND SIMULATIONS

Recently [5] we have shown that the conventional merging scheme, with ion and electron beams merged in a toroidal section, is not applicable for the CSR because of strong and non-uniform deflection that slow ions suffer in the toroidal region.

The maximum magnetic field allowed in this geometry to keep 20 keV protons within the ring acceptance is below 1-2 Gauss that is not enough to provide a velocity matched high-quality electron beam. A new layout (see Fig. 2), where ions do not pass through the non-uniform toroidal field, has been proposed and numerically simulated by the TOSCA code [5]. In this merging scheme electrons start 140 mm above the ring plane. Then the electron beam is 90^0 deflected in a magnetically screened volume and only after that it is bent down in a rather uniform magnetic field produced by longitudinal and transverse merging coils (see Fig.2). In this geometry ion deflection does not depend on the position of an ion in relation to the beam axis and can be properly compensated by two pairs of magnetic correction coils placed before and after the interaction region. Trying to exclude any possible source of electron beam heating, the merging scheme has recently been designed in detail including the real beam lines, magnets, beam diagnostic tools and other auxiliary equipment. This realistic field geometry has been modelled by the TOSCA code and studied by tracking test electron beams through it. To avoid harmful influence of the magnetic field on the ion beam, the bending regions were completely iron-screened. We also keep the field magnitude in the toroidal sections twice higher than in the merging and interaction regions (see Fig. 2), which allows us to reduce the magnetic field seen by the ions while in the same time we prevent heating of the electron beam in the toroidal sections during bending.

The results on electron beam heating for the optimized cooler design are presented in Fig. 3 where the transverse beam temperature is shown as a function of electron energy for different magnetic fields.

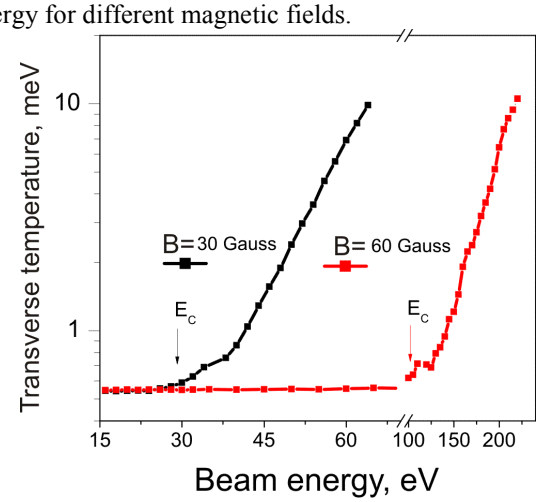

Figure 3: Transverse electron temperature as a function of beam energy for two values of the solenoidal field strength B. Due to non-adiabatic transport at high energies the transverse heating starts at critical energies E_C.

The initial transverse electron temperature of 0.5 meV is defined by the temperature of the electrons emitted from

the cryogenic photocathode (about 10 meV) reduced by the factor of magnetic expansion α=20. It is seen that for a fixed guiding magnetic field the transverse heating becomes important in comparison to the initial temperature at critical energies E_c at ~ 30 eV and 100 eV for B=30 Gauss and B=60 Gauss. Above these energies the heating rises exponentially and at higher beam energies a stronger magnetic field is required to provide adiabatic beam transport. As a function of the electron beam energy E the scaling rule for the minimum guiding magnetic field, required to suppress the heating for the considered cooler geometry, is found to be

$$B_{MIN}(E) = 30\ G \times \sqrt{\frac{E}{30\ eV}}$$

The effective length of the cooler for the planned magnetic field geometry is obtained from the points where the angle between the electron beam and the cooled ion beam, due to the magnetic field angle, amounts to about 0.5 mrad, that is much below the natural electron beam divergence $\sqrt{kT_\perp/E}$ for E≤20 eV and $kT_\perp$ =0.5 meV. This way the effective cooling length of the CSR electron cooler is found to be at least 780 mm that is 2.2 % of the ring circumference.

MECHANICAL AND CRYOGENIC CONCEPT

The basic mechanical concept of the electron cooler is the same as for the entire ring. The CSR is a double vacuum system, where the XHV beam line is housed in a cryostat kept under 10^{-6} mbar pressure. The cooling system of the CSR is based on a commercial refrigeration system [6] with helium cooling lines of 2 K, 5 K, 40 K and 80K going around the ring inside the CSR cryostat volume, and with a 5 K line available for room temperature operation of the CSR. For cryogenic operation the XHV beam line is kept below 10 K with some stations cooled below 2 K to provide good pumping of hydrogen from the residual atmosphere. The distribution of the cooling power for the 10 K inner chambers will be realized by thermal conductivity of stainless steel-chamber walls with thin copper coating or oxygen-free copper foil attached to the chamber connected to the 2 K line by oxygen-free copper bands. At room temperature ultra-high vacuum will be reached by high temperature (200-300°C) bakeout of the inner chamber and with a help of NEG, cryo- and ion-getter pumps [7].

The electron cooler consists of the photocathode chamber, the gun chambers, the toroid and merging chambers, the interaction region, and the collector chamber (see Fig. 1). The toroid, merging and interaction regions are placed inside of the 2600 mm long 800×800 straight section of the CSR cryostat with 800*800 mm cross-section and will be cooled together with the ring. All magnets in these sections will be also inside of the cryostat and have to fit cryogenic and 10^{-6} mbar vacuum requirements.

To produce the magnetic field, high-temperature superconductor (HTS) coils and cryogenic cooled oxygen-free copper coils will be used. The space to build the correction and transverse merging coils (see Fig. 2) is strongly limited leading to the use of HTS coils. Both resistive and superconductive magnets will be cooled to about 30-40 K using a separate low-pressure 30 W Ne-refrigerator developed for the electron cooler [8] and powered by a commercial Leybold cold head. The basic idea for the superconductor magnets is that the HTS coil is mounted inside of a compact welded titanium vessel flooded with Ne cooling gas. Resistive 50 A magnetic coils are made of a 6 mm thin-wall copper tube combining conductor and cooling-line functions. Due to the low resistance of oxygen-free copper at 30-40 K, the resistive power is strongly reduced. This solution in particular strongly simplifies the design of the solenoids and reduces the required space. It should be also mentioned that the copper magnets have higher bakeout temperature of about 200°C (defined by the used isolation coating) whereas the temperature of the superconductor wire should not exceed 150°C. This allows us to keep the bakeout temperature of the inner chamber at about 200-300°C (depending on position), which is crucial for achievement of XHV conditions.

ULTRA LOW ENERGY BEAM

To cool 300 keV atomic and molecular beams stored at the CSR, electron beams with energies down to <1 eV are required. For successful operation at such low energies, properties of the electron beam such as temperature and intensity are crucial.

To deliver ultra-cold electron beams the cryogenic photocathode electron source, developed for the TSR electron target [3,9], will be used together with dedicated electron optics providing adiabatic electron transport. Transverse temperatures below 1 meV for magnetically expanded (α=30) electron beams from GaAs photocathode sources were demonstrated [10]. We also have shown that the longitudinal temperature from this source is below 30 meV, which can be further reduced by acceleration due to kinematic transformation to about 0.05-0.1 meV in the used energy range [10]. In contrast, the broad energy distribution of 100-120 meV from thermocathode source causes the longitudinal temperature of slow (≤10 eV) electron beams to be about a few meV, which increases strongly the cooling time of the stored ions.

Another key point is the electron beam density. It goes down linearly with electron energy and is limited by the gun perveance which is typically $1\text{-}2\times10^{-6}$ $A/V^{3/2}$. To improve the beam perveance we performed the measurements with decelerated beams using the TSR electron target (Fig. 4). Here the electrons are extracted at

higher voltages (typically ~ 20 eV) and decelerated by a drift tube in the interaction region down to sub-eV energies. Behind the interaction region the electron beam is accelerated to its original energy and transported to the collector where its 2D current density profile was analyzed. We implemented beam deceleration as a diagnostic and experimental tool to calibrate the electron kinetic energy taking into account space charge effects and the difference of contact potentials with an accuracy of 0.1 eV.

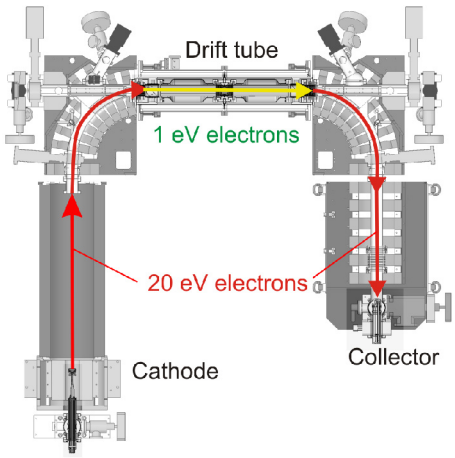

Figure 4: Scheme of the beam deceleration experiment at the TSR e-target with typical electron energies of a few eV

In these measurements, monitoring the electron beam profile, we found that the electron beam perveance could be increased by a factor of 10 up to 9-12×10^{-6} A/$V^{3/2}$, keeping a high quality of the electron beam. At higher deceleration voltages (with a threshold found to be very sensitive on the level of 10-20 meV) reflection of electrons caused strong inhomogeneity in the beam profile as well as a decrease of the photocathode lifetime. The measurements demonstrated that a strong increase of the electron current at a given low beam energy can be achieved using the deceleration scheme, which will strongly improve performance of the CSR electron cooler at lowest energies to be used.

CONCLUSIONS

The design concept of the ultra-low energy electron cooler for the CSR has been developed. Numerically and experimentally studied electron beam transport and field geometry allow us to foresee that electron cooling down to 1 eV can be provided by the photocathode electron beams for stored 300 keV molecular and atomic ions. Construction of the CSR electron cooler and the cryogenic magnetic optics is in progress.

REFERENCES

[1] M. Froese et al., "The Cryogenic Storage Ring project at Heidelberg", PAC 2009 Proceedings, (Vancouver) to be published
[2] M. Lange et al., "Commissioning of the Heidelberg Cryogenic Trap for Fast Ion Beams (CTF)" MOPC110, EPAC08 Proceedings, 2008.
[3] D.A. Orlov et al., "Ultra-cold electron beams for the Heidelberg TSR and CSR ", COOL05 Proceedings, p. 478, 2005.
[4] D.A. Orlov et al., "Photocathodes as electron sources for high resolution merged beam experiments", Journal of Physics: Conference Series 4, p. 290, 2005.
[5] H. Fadil et al., "Design of a low energy electron cooler for the Heidelberg CSR", EPAC06 Proceedings, TUPLS061, p. 1631, 2006.
[6] R. von Hahn et. al., "Cryogenic Concept for the low-energy electrostatic cryogenic storage ring (CSR) at MPI-K in Heidelberg", International Cryogenic Engineering Conference Proceedings, p. 1187, 2005.
[7] D.A. Orlov et. al., "Cryogenic and vacuum technological aspects of the low-energy electrostatic Cryogenic Storage Ring", AIP 985, p. 1233, 2008.
[8] Internal MPI-K technical report in collaboration with A. Vasiliev, L. Kochenda, M. Vznuzdaev, PNPI, Gatchina, Russia
[9] D.A. Orlov et al., "Electron cooling with photocathode electron beams applied to slow ions at TSR and CSR", COOL07 Proceedings, p. 230, 2007.
[10] F. Sprenger et. al., "The high-resolution electron-ion collision facility at TSR", COOL03 Proceedings, p. 298, 2003.

NUMERICAL ANALYSIS OF LOW-INTENSITY SCHOTTKY SPECTRA RECORDED AS TIME SERIES

F. Nolden, GSI, Darmstadt, Germany

Abstract

Schottky spectra of extremely well cooled low-intensity ion beams suffer from a low signal-to-noise ratio. Their digital post-processing is neither well prescribed nor trivial. The paper presents a comparison of the use of Hanning windows with overlapping samples on one hand, and of multitaper analysis, on the other hand. It is shown that the area under the Schottky peak is better defined if the multitaper method is used.

INTRODUCTION

Modern Spectrum spectrum analyzers nowadays usually offer several types of measurements. One of these measurement modes records the digitized data in the time domain after down conversion of the central frequency, as well as digital and analog filtering in a predetermined frequency span which is directly coupled to the sampling frequency. The digital data consist of in-phase and quadrature (IQ) components which are stored on disk. Because the data are stored without any gap in the time domain it is possible to analyze data packages of any desired size.

This article describes a set of first results which were gained with an RSA3303B analyzer from Tektronix. Two types of data evaluation are presented:

1. Evaluation using the classical averaging method with overlapping averages using a cosine (von Hann or Hanning) window.

2. Evaluation using the more advanced multitaper method.

MATHEMATICAL MODELLING OF SCHOTTKY SPECTRA

Single Particle Signal

The classical picture of Schottky spectra of coasting beams assumes a beam of N particles with constant revolution frequecies ω_n (or revolution periods $T_n = 2\pi/\omega_n$) which are positioned azimuthally in a random fashion. In order to take account of this position, one assumes a time lag τ_n, $0 \leq \tau_n < T_n$ for each particle. Any interaction among the particles or with other particles (internal gas jet target, cooling of any kind etc.) is neglected.

In the limit of an infitite number of passages through the Schottky probe, the Fourier transform of the resulting signal of each particle can be written

$$\tilde{U}(\Omega) = \frac{Z_L Q e \omega}{2} \sum_{m=-\infty}^{+\infty} S(\Omega) e^{-i\Omega\tau_n} \delta(\Omega - m\omega_n) \quad (1)$$

where $S(\Omega)$ is the Fourier transform of the sensitivity $s(t)$. The spectrum has peaks at every harmonic of the revolution frequency. As the phases $\omega_n \tau_n$ are random, one has to describe somehow its statictical properties.

Schottky Spectrum

The 'process' $U(t)$ is characterized by its autocorrelation function

$$R(t,\tau) = \langle U(t+\tau/2)U(t-\tau/2)\rangle \quad (2)$$

where $< \cdots >$ denotes a sample average. If the process $U(t)$ is stationary, then R is independent of t, i.e. $R(t,\tau) = R(\tau)$. The Fourier $S(\Omega)$ transform of $R(\tau)$ is then called the power spectrum of U. If the unit of U is volts, then $S(\Omega)$ has the unit $\mathrm{V}^2\mathrm{s}$. In the case of the Schottky spectrum, it is given by

$$S(\Omega) = \frac{N(Qe)^2}{m} \Psi(\Omega/m) \quad (3)$$

where $\Psi(\omega)$ is the revolution frequency distribution, assuming that there is no Schottky band overlap. It is assumed that $\Psi(\omega)$ is normalized to one.

Due to its statistical origin, the power spectrum can only be *estimated* from a single measurement.

ANALOG SIGNAL PROCESSING

Figure 1 shows how the analog signal from the Schottky pick-up is processed. The mixer can be modeled mathematically as a multiplier with the input signal U_i

$$U_n(t) \propto \cos(\omega_n t + \phi_n) = \cos\left((\omega_{\mathrm{LO}} + \delta\omega_n)\, t + \phi_n\right) \quad (4)$$

and the local oscillator (LO) signal

$$U_{\mathrm{LO}} \propto \cos(\omega_{\mathrm{LO}} t) \quad (5)$$

yielding signals at $\omega_i \pm \omega_{\mathrm{LO}}$. If this is done by using first the LO frequency directly and secondly after a 90 degree phase shift, one gets the in-phase (I) and quadrature phase (Q) low-frequency signals

$$U_I \propto \cos(\delta\omega_n t - \phi_n) \quad (6)$$

$$U_Q \propto \sin(\delta\omega_n t - \phi_n) \quad (7)$$

If both signals are available, one can decide which parts of the low frequency signal arise from rf components at either $\omega_{\mathrm{LO}} + \delta\omega_n$ or $\omega_{\mathrm{LO}} - \delta\omega_n$. This can be done either by using another 90 degree shift of the quadrature signal and adding or subtracting this signal from the in phase signal (image reject mixer) or by digitizing both signals and treat them numerically as a complex number $U_I + iU_Q$. After a digital Fourier transform (DFT) one gets different components below and above zero frequency.

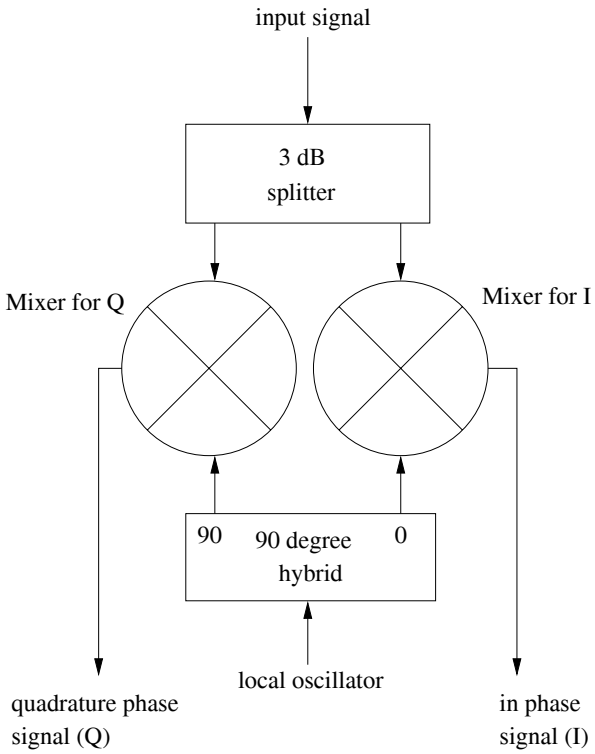

Figure 1: Signal processing in vector spectrum analyzer IQ mixer.

DIGITAL SPECTRUM ANALYSIS

We assume a digital complex dataset U_n, $0 \leq n < N-1$, sampled at a rate $1/\Delta t$. In the frequency domain this corresponds to a spectrum $\tilde{U}_n$ with frequency steps $\delta f = 2N/\Delta t$ The digital signal has two essential drawbacks, which may lead to problems:

1. It is of finite length, leading to spectral leakage, which can be overcome by tapering at the expense of spectral resolution.

2. It is sampled at a finite rate, which limits the spectral width and can cause aliasing.

While aliasing can normally be overcome by using a sufficiently high number of points in the DFT, the effect of leakage is more difficult to handle.

Leakage occurs because the measurement time interval T is finite. If an infinite set of measurements is cut abrubtly, one can represent the resulting frame as the product of the infinite set with a rectangular function. In the frequency domain this is equivalent to performing a convolution of the Fourier transform of the time series with a $\sin(\Omega T/2)/\Omega$ function which would cause sidelobes around every sharp frequency.

These sidelobes must be decreased by windowing. One multiplies the time series U_i with a series exhibiting w_n soft edges.

$$U_n \mapsto U_n w_n \tag{8}$$

A typical window used is the so called Hanning window (a name that was introduced in the anglo-saxon literature in order to refer to a German engineer called von Hann).

$$w_n = h_n = \left(\frac{2}{3(N+1)}\right)^{1/2}\left[1-\cos\left(\frac{2\pi n}{N+1}\right)\right] \tag{9}$$

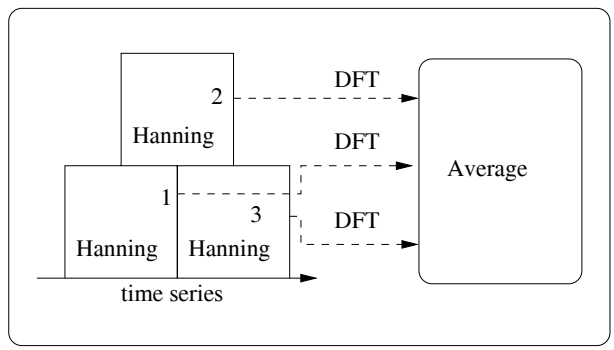

Overlapping Sample Averaging

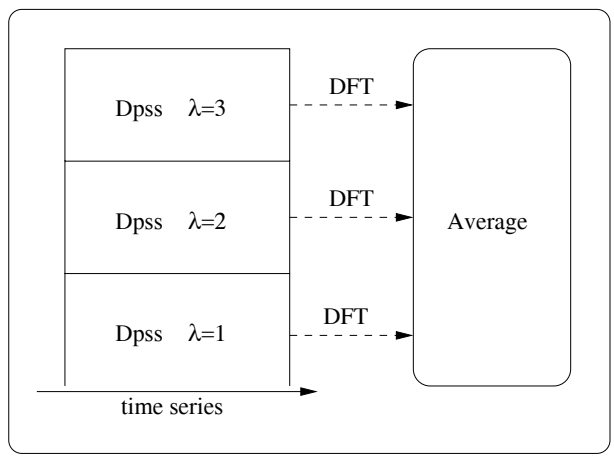

Multitaper Averaging

Figure 2: Overlapping sample averaging versus multitaper averaging.

Overlapping sample averages

Because windowing is equivalent to throwing away data at the edges of the time series one can use overlapping samples in order to include all of the data.

For each sequence U_i one gets the spectral estimate

$$S_j = \left|\sum_{n=0}^{N-1} U_n w_n \exp\left(-2\pi i j\right)\right|^2 \tag{10}$$

If one is not interested in temporal resolution, it is a common practice to average over these overlapping samples. An averaged estimate can be caculated by taking the mean over single overlapping sequence estimates. In the following we call this kind of averaging Walsh overlapping sample averages (wosa, according to the textbook [1]), although we do not use any explicit averaging.

Multitaper Analysis

In contrast to overlapping averages, the multitaper method [1] uses orthogonal sequences $v_{n,k}$ as tapers on the same finite dataset:

$$\sum_n v_{n,k} v_{n,l} = \delta_{k,l} \tag{11}$$

In particular one uses the DPSS tapers (Disctrete Prolate Spheroidal Sequences) $v_{n,k}(W)$, which are eigensolutions to the eigenvalue equation

$$\sum_{n=0}^{N-1} \frac{\sin\left(2\pi W(n-m)\right)}{\pi(n-m)} v_{n,k}(W) = \lambda_k(W) v_{m,k}(W) \tag{12}$$

with eigenvalue $\lambda_k(W)$. These sequences depend on a parameter W called the resolution bandwidth. The decisive property of DPSS sequences is that their use as windows minimizes spectral leakage. The spectral estimate is then calculated using the average

$$S_m = \sum_{k=0}^{K-1} \left| \sum_{n=0}^{N-1} U_n v_{n,k} e^{2\pi i n m} \right|^2 \tag{13}$$

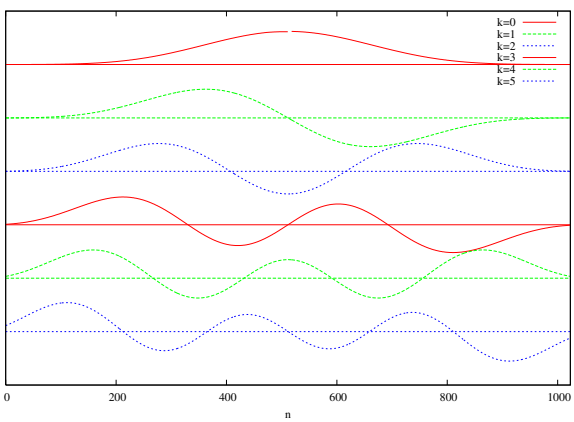

Figure 3: Series of DPSS tapers.

Figure 3 shows the DPSS tapers used in this paper with $N = 1024$ and the bandwidth parameter $W = 4/N$. This bandwidth appears to be an optimum choice for the simplification of peak identification. The tapers are numbered towards decreasing eigenvalues $\lambda_k(W)$, i.e. the $k = 0$ taper is the one with the largest eigenvalue. Multitapering has some remarkable features:

- The tapers can be non-zero (except for $k = 0$).
- Whereas the $k = 0$ taper is non-zero only in the middle of the time series, the following tapers more and more approach its edges. The $k = 5$ taper is even non-zero at the edges, which leads to some spectral leakage.
- Because the edges are used, the information contained in the time series is used effectively, in contrast to singe windowing where the information at the edges is effectively thrown away.
- Because the tapers are orthogonal, the spectra used in the averaging process are independent.

The tapers shown in Figure 3 have been calculated from a recipe presented in chapter 8 of [1], where a different eigenvalue equation by Slepian [2] is used with a tridiagonal matrix which has to be inverted. Furthermore the different eigenvectors are calculated by forced orthogonalization.

COMPARING SPECTRAL ESTIMATES WITH DIFFERENT EVALUATION ALGORITHMS

Figure 4 shows two spectral series calculated from identical time domain data. These data were measured at the 30^{th} harmonic (59.220875 MHz) of the Schottky spectrum of a 1 nA beam of $^{40}\text{Ar}^{18+}$ ions (about 180 particles) at an energy of 400 MeV/u. The momentum spread was reduced by electron cooling to extremely low values (see [3], [4] and [5]). The spectra on the left-hand side are single spectra with Hanning windowing and 50 % overlap. The spectra are taken from records (sometimes also called frames) in the time domain containing 1024 points. The distance between independent (non-overlapping) records is 128 ms.

The spectra on the right-hand side were calculated from the same data using the multitaper method with the first six of the $N = 1024$, $W = N/4$ tapers as presented in the previous section. Because there is no overlap, the number of spectra on the left-hand side is roughly twice as large as on the right-hand side.

In both cases one can see in many spectra a distinct peak at frequencies around 59,330,875 MHz. However, there are also many cases where the peak seems to hop or to be smeared out. The physical reason of this behaviour is not yet very clear. In any case, it leads to a substantial difficulty in interpreting such spectra. It is therefore crucially important to have meaningful spectral estimates.

When comparing both estimates, one has the impression that the peaks are somwhat better distinguished in the multitaper estimates. This impression can be confirmed numerically. To this purpose the area under the peak in an interval with a span of 10 Hz was determined and the background was subtracted. These areas are shown in figure 5.

It is visually obvious that the variation of the curve areas from the multitaper estimates is less than the variation due to the wosa estimates. Table 1 shows the average peak area $< F >$, its standard deviation $\sigma(F)$ and the relative deviation $\sigma(F)/ < F >$. Obviously for the wosa spectra the standard deviation is roughly as large as the mean value, for the multitaper estimates the standard deviation is two-thirds of the mean value.

One can therefore conclude that an evaluation using multitapers is superior to the usual overlapping sample es-

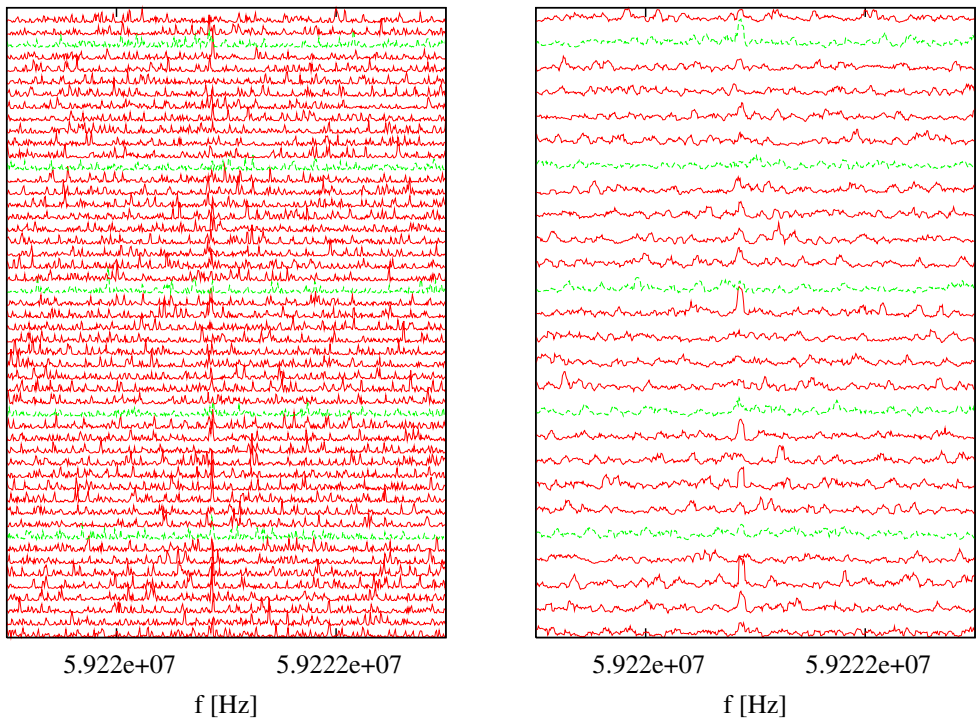

Figure 4: Estimated spectra with Hanning window and 50% overlap (left) and multitapering without overlap (right).

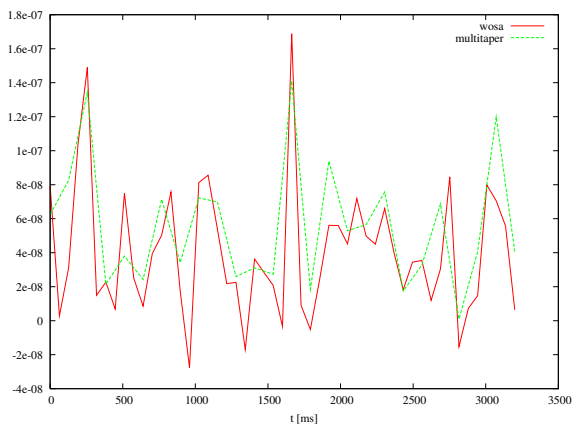

Figure 5: Calculated peak areas with wosa and multitapering.

timates with Hanning windows. Furthermore it should be noted that the spectra seem to feature intrinsic shifts or temporary heating effects, which prevent a smaller $\sigma(F)/ < F >$ value.

Table 1: Basic Parameters of the CR

	$< F >$	$\sigma(F)$	$\sigma(F)/ < F >$
wosa	$4.05 \cdot 10^{-8}$	$3.85 \cdot 10^{-8}$	0.95
multitaper	$5.60 \cdot 10^{-8}$	$3.64 \cdot 10^{-8}$	0.65

REFERENCES

[1] D. B. Percival, A. D. Walden, Spectral Analysis for Physical Applications, Cambridge University Press 1993

[2] D. Slepian, Prolate Spheroidal Wave Functions, Fourier Analysis, and Uncertainty, *Bell System Technical Journal*, **57**, 1371-1430

[3] M. Steck, K. Beckert, H. Eickhoff, B. Franzke, F. Nolden, H. Reich, B. Schlitt, T. Winkler, Anomalous Temperature Reduction of Electron Cooled Heavy Ion Beams in the Storage Ring ESR, *Phys. Rev. Lett.*, **77** (1996), 3803

[4] M. Steck, K. Beckert, P. Beller, B. Franzke and F. Nolden, New evidence for one-dimensional ordering in fast heavy ion beams, *J. Phys. B: At. Mol. Opt. Phys*, **36** (2003), 991-1002.

[5] M. Steck, P. Beller, K. Beckert, B. Franzke and F. Nolden, Electron Cooling Experiments at the ESR,
Nucl. Inst. Meth. A, **532** (2004), 357-365

[6] Yu.A. Litvinov et al., Observation of Non-Exponential Electron Capture of Hydrogen-Like ^{140}Pr and ^{142}Pm ions *Physics Letters B*, **664**, Issue 3, 162-168.

EFFECTIVE LUMINOSITY SIMULATION FOR PANDA EXPERIMENT AT FAIR

A. Smirnov#, A. Sidorin, D. Krestnikov, JINR, Dubna, Russia

Abstract

In last years at GSI (Germany) the new accelerator complex project FAIR is being realized. One of the most important goals of this project is caring out an experiment with internal target PANDA [1]. One of ways to achieve the design luminosity value is to use a pellet target. However, such target is coming up with the short-scale luminosity variation. Peak to mean luminosity ratio can reach a big value unacceptable for detectors. If a detector is overloaded its count rate is not proportional to the luminosity, but depends on electronics design. In this case one can define so called "effective luminosity" as a ratio of the detector count rate to cross-section of the reaction.

Dependencies of the effective luminosity on the pellet target parameters for PANDA experiment simulated using BETACOOL code [2] are presented in this article.

INTRODUCTION

A numerical simulation of the experiment with a pellet target is connected to two different time-scale processes. The first one is the short-time process, which describes luminosity variations while one pellet is crossing the beam. This process can be about a few tenths microseconds long. The long-time process of the beam parameter evolution (particle number, transverse and longitudinal profiles) are defined by the beam losses and equilibrium between target heating and electron cooling. Characteristic time of this process can be of a few minutes or even hours.

The long-time process simulation is the general goal of the BETACOOL program. In the case of a pellet target simulation the algorithm is based on assumption that during one step of the integration over the time a large number of the pellets cross the beam. In the frame of the PANDA collaboration an additional algorithm was developed and implemented into the BETACOOL. It calculates luminosity time dependencies at the time scale sufficiently shorter then time that takes a pellet to get through the beam.

For benchmarking of the BETACOOL algorithms, results of experiment with the pellet target WASA at the COSY storage ring were used. During the COSY run from June 21 to July 5 2008 a luminosity value and different beam parameters were recorded as functions of time. Modeling of the experiment using the BETACOOL program showed a good agreement with the recorded data [3].

This article presents results of the PANDA experiment simulations using the developed algorithms.

#smirnov@jinr.ru

DESCRIPTION OF THE ALGORITHM

In the process of the long-time BETACOOL algorithm working, profiles of the antiproton beam are saved to hard disk drive at each step of integration over the time. Typically the integration step is of the order of a few seconds. The beam profile (horizontal or vertical) is a normalized particle density distribution along the corresponding co-ordinate. The beam profiles are calculated from array of model particles by averaging over their betatron oscillations. The new short-time algorithm generates a flux of pellets and propagates the pellet flux through the antiproton beam. When the pellet flux crosses the beam the profiles are considered to be constant on each integration step. The integration step of this algorithm is about 1 μs. At every step of the algorithm the density of the particles in the current pellet position is calculated for every pellet using the beam profiles.

Initially the short-time algorithm generates a pellet array. The pellets from the array are located in a long cylinder which has radius equal to the pellet flux radius. The cylinder height is chosen in accordance with the pellet vertical velocity in order to have required time of the simulation. For instance, the cylinder of 1 m of the height (see Fig. 1, the vertical position of the pellet is indicated as a "longitudinal distance" inside the cylinder) at the pellet velocity of 60 m/s (typical value for the pellet target) the pellet array will cross the antiproton beam during about 15 ms. Across the cylinder the pellets are distributed uniformly. Along the cylinder the pellets distributed in accordance with mean distance between pellets in vertical direction with a given dispersion.

After generation of the pellet array the algorithm propagates this array through the antiproton beam in the vertical direction from top to bottom with given step over time.

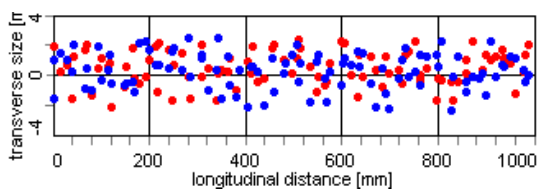

Figure 1: The pellet distribution along the flux: red – horizontal coordinate, blue – vertical.

During the propagation a "weight" value P_{xy}, which is proportional to the antiproton areal density in the pellet position, for each pellet is calculated. The pellet "weight" is evaluated as a product of the horizontal and vertical beam profile magnitudes in the pellet position:

$$P_{xy} = P_x(x_p) \cdot P_y(y_p), P_\alpha(\alpha) = \frac{1}{N}\frac{dN}{d\alpha},\ \alpha = x, y \quad (1)$$

Here P_x , P_y are horizontal and vertical beam profile magnitudes, x_p and y_p are the horizontal and vertical co-ordinates of the pellet. If a pellet is outside of the antiproton beam the pellet weight is equal to zero. It the current version of the algorithm realization it is assumed that all the pellets have the same dimensions, correspondingly the weight values from all pellets are simply summing up:

$$P = \sum_{i=1}^{n} P_{xy_i}\ , \quad (2)$$

here P_{xy_i} - "weight" value of the i-th pellet, n – number of the pellets in the pellet array. The luminosity is linearly proportional to this value:

$$L = \rho_p P \pi r_p^2 f_{rev}, \quad (3)$$

where ρ_p is the mean pellet area density in atoms/cm^2, r_p is the pellet radius, f_{rev} is the antiproton revolution frequency.

EFFECTIVE LUMINOSITY

The short-time luminosity variation (Fig.2) is calculated on each integration step of the long-time luminosity calculation (Fig.3). The black curve in the Fig. 2 presents the function $P(t)$ calculated by the short-time algorithm, this signal averaged over the time (blue line on Fig.2) is proportional to the luminosity calculated with the long-scale algorithm in the corresponding moment of time (blue line on Fig.3).

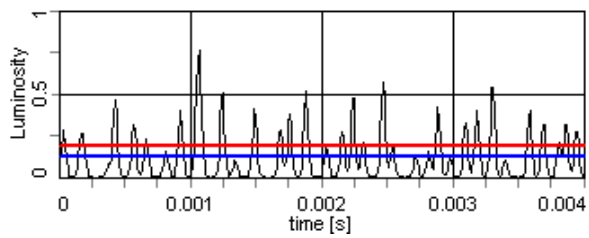

Figure 2. Short-scale signal from pellets: blue line – average value, red line – detector limit.

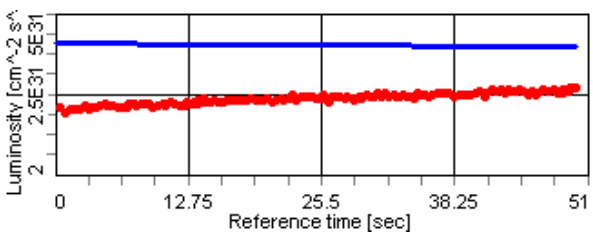

Figure 3: Long-scale luminosity evolution on time and effective luminosity for "top cut" model of detector limit (red line).

The detector is designed for some maximum acceptable event rate. Dividing this event rate by the reaction cross-section one can calculate the maximum acceptable luminosity (or detector limit). An example of the detector limit level is shown by the red line on Fig.2. If the luminosity exceeds this value the detector is overloaded.

In these simulations we consider two ultimate variants of the detector response when it is overloaded: the count rate value is saturated and equal to the detector limit ("top-cut" model on Fig.4 b), the detector is completely closed and can not accept any event – the count rate is zero ("full-cut" model on Fig.4 c). The response of real detector can be in between of these two ultimate cases.

If a detector is overloaded its count rate is not proportional to the luminosity. Ratio between event rate and the detector count rate can be characterized by the effective luminosity. Numerically the effective luminosity is calculated with the following expression:

$$L_{eff} = L_{aver}\frac{I_{cut}}{I_{aver}} \quad (4)$$

where L_{aver} – average luminosity calculated with the long-time algorithm (fig.3, blue line) in the corresponding moment of time, I_{aver} – integral of the total pellet signal (fig.3), I_{cut} – integral of the pellet signal for chosen model of the detector response. An example of the effective luminosity time dependence is presented on fig. 3 (red line) for the "top-cut" model of the detector response.

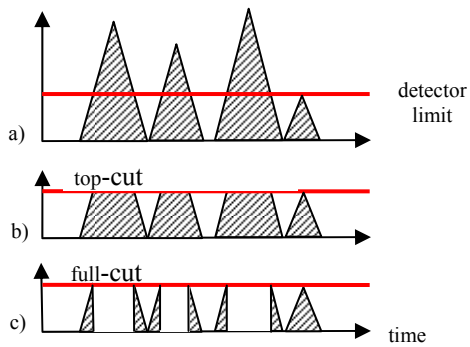

Figure 4: Count rate time dependence: a) event rate from the pellets, the red line is the detector limit b) and c) the detector count rate for two models of the detector response when it is overloaded.

SIMULATION OF PANDA EXPERIMENT

The numerical simulation of the effective luminosity was done for two operational regimes of the PANDA experiment: with high-luminosity (HL) and high-resolution (HR) modes. The typical parameters of the pellet target and antiproton beam are presented in the table 1.

The dependence of the effective luminosity on the pellet size in micrometers for the different detector limit is presented on Fig.5 a, b (HR) and Fig.5 c, d (HL). The detector limit was chosen in the range from the value of the mean luminosity to the value in 10 times larger. The distance between pellets was chosen in accordance with the pellet size to keep the same effective target density.

Simulation results show that for the HR mode the effective luminosity equal to the mean luminosity if the detector limit is defined by the mean luminosity for the

HL mode 2×10^{32} $cm^{-2}s^{-1}$. A reduction of the effective luminosity for the HR mode can exist if some detectors will be designed especially for the HR mode and the detector limit will exceed the mean luminosity in two times only.

Table 1: The Typical Parameters of PANDA Experiment

Pellet target		
Hydrogen density, atom/cm^3	$4{,}26\times10^{22}$	
Pellet size (diameter), mm	0,028	
Pellet flux radius, mm	1,25	
Distance between pellets, mm	5	
Effective target density, cm^{-2}	4×10^{15}	
Antiproton beam		
Beam energy, GeV	8	
Operation mode	HR	HL
Particle number	10^{10}	10^{11}
Momentum spread	10^{-5}	10^{-4}
Mean luminosity, $cm^{-2}s^{-1}$	2×10^{31}	2×10^{32}

In the case of the high luminosity mode the effective luminosity is rather different at "top-cut" and "full-cut" models. For the "top-cut" model the maximum pellet size has to be less than 20 μm if the detector limit exceeds the mean luminosity in two times only. For the "full-cut" model the pellet size has to be less than 10 μm and detector limit is sufficiently higher than 2×10^{33} $cm^{-2}s^{-1}$.

CONCLUSION

Simulation results show that for the high resolution mode the effective luminosity can be equal to the mean luminosity if the pellet size is less than 20 μm and all detectors are designed for the maximum luminosity value of 2×10^{32} $cm^{-2}s^{-1}$ which corresponds to the high luminosity mode. For the high luminosity mode the pellet target can be used for the detector design with "top-cut" mode only. The detector design with "full-cut" mode can not be used for the high luminosity mode due to very large reduction of the effective luminosity.

REFERENCES

[1] The PANDA experiment at FAIR. GSI Scientific Report 2004. http://www-panda.gsi.de

[2] A. Sidorin, I. Meshkov, I. Seleznev, A. Smirnov, E. Syresin, A. Smirnov, and G. Trubnikov. BETACOOL program for simulation of beam dynamics in storage rings. Nucl. Instrum. Methods, A, 558, 325 (2006).

[3] A. Smirnov, A. Sidorin, D. Krestnikov, R. Pivin, D. Prasuhn, M. Wolke. Simulation of Pellet Target Experiments with Betacool Code. Proceedings of RuPAC 2008, Zvenigorod, Russia. http://jacow.org

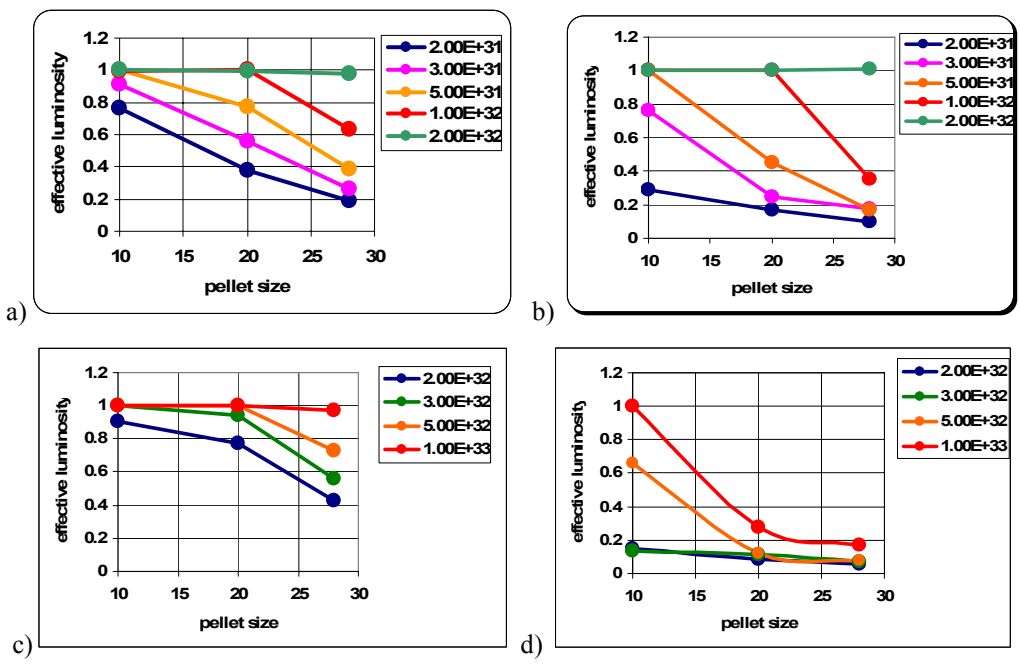

Figure 5: Effective luminosity simulation for different limits of detectors: high resolution (HR) mode - a) "top-cut" model, b) "full-cut" model; high luminosity (HL) mode - c) "top-cut" model, d) "full-cut" model.

PROTOTYPE PICK-UP MODULE FOR CR STOCHASTIC COOLING AT FAIR*

C. Peschke, U. Jandewerth, F. Nolden, P. Petri, M. Steck, GSI, Darmstadt, Germany

Abstract

The performance of the collector ring (CR) of the FAIR project will strongly depend on a stochastic cooling system which is designed for fast pre-cooling of rare isotope and antiproton beams injected at different velocities. A prototype of the cryogenic movable pick-up module has been built. It consists of four circuit boards on an aluminum body and includes two times eight slotline electrodes, combiners and test electronics. It has been optimized for high sensitivity and flat frequency response. Measurements of the electric near-field over frequency and position will be presented.

INTRODUCTION

The collector ring (CR) will be a storage ring in the FAIR project at GSI which has three different operating modes.

The first mode is stochastic cooling of rare isotope beams. The rare isotope beams have a velocity of 0.83c. After bunch rotation and adiabatic debunching, they will be cooled down from ε_{xy} = 200 mm·mrad and $\delta p/p$ = 0.4% (2σ) to ε_{xy} = 0.5 mm·mrad and $\delta p/p$ = 0.05% within 2 s.

The second mode is stochastic cooling of antiproton beams with a velocity of 0.97c. After bunch rotation and adiabatic debunching, they will be cooled down from 240 mm·mrad and 0.7% to 5 mm·mrad and 0.1% within 10 s. Due to the low charge, this is the most demanding mode for the stochastic cooling system.

The last mode uses an isochronous optical setting for nuclear mass measurements of very short-lived nuclei. In this mode, no stochastic cooling will be used.

In the CR, four pick-up and three kicker tanks are foreseen. Three pick-up tanks will be placed in straight sections without dispersion for horizontal, vertical, and longitudinal cooling. Each of this pick-up tanks will be equipped with eight movable, cryogenic pick-up modules described in this paper. A fourth pick-up tank is foreseen for Palmer cooling of rare isotope beams. This one will be located in an arc with high dispersion. It will use the same slotline electrodes in a different arrangement. The three kicker tanks, foreseen in straight sections without dispersion will use the same slotline electrode board and a similar module body, but a different power splitter board.

SLOTLINE PICK-UP MODULE

To meet the requirements for large bandwidth, high signal to noise ratio and large aperture, a planar slotline electrode has been developed [1]. The stochastic cooling system for the CR is designed for a band from 1 GHz to 2 GHz. A pick-up module consists of a milled aluminum (Al) body, two alumina (Al_2O_3) pick-up boards, two combiner boards, and a lot of small electrical and mechanical parts. Figure 1 shows the aluminum body with one pick-up and one combiner board. Each module will be mounted with a steel tube to a linear motor drive outside the vacuum. It will be individually movable to any distance between 10 mm and 70 mm from beam axis. Two times four of such modules will be mounted in one cryogenic tank. This will allow us to have a large, non-uniform aperture along the tank for the incoming hot beams and a small aperture with high sensitivity for the cooled beam [2].

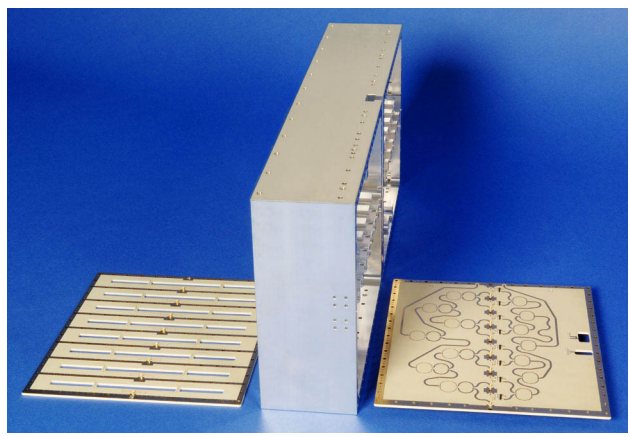

Figure 1: Main components of the pick-up module.

Each pick-up board (Fig. 2, top, left) consists of eight slotline electrodes. Each electrode consist of a slotline perpendicular to the beam and a microstrip circuit on the rear side of the Al_2O_3 board. The mirror currents of the charged particles induce traveling waves in both directions of the slotline. At approximately $\lambda/4$ from the end of the slotline, the signal is coupled out to the microstrip line. The $\lambda/4$-section at the beginning of the microstrip is a virtual short to one of the two conductors of the slotline. The exact length of these sections has been optimized to get large signals and a flat frequency response in magnitude and phase [3]. The two signals are coupled out to microstrip lines and are combined in the first stage 100 Ω to 50 Ω Wilkinson combiner. For the wanted signal, this combiner could also be replaced by a simple parallel connection, but it helps to damp unwanted modes in the pick-up system.

Behind the first combiner, the signal goes through a coaxial line in the module body (Fig. 2, bottom) to the combiner board or an optional low noise amplifier. The slotline electrode with the first combiner stage have a high reflection factor. An amplifier at this position would see its own

* Work supported by EU design study (contract 515873 -DIRACsecondary-Beams)

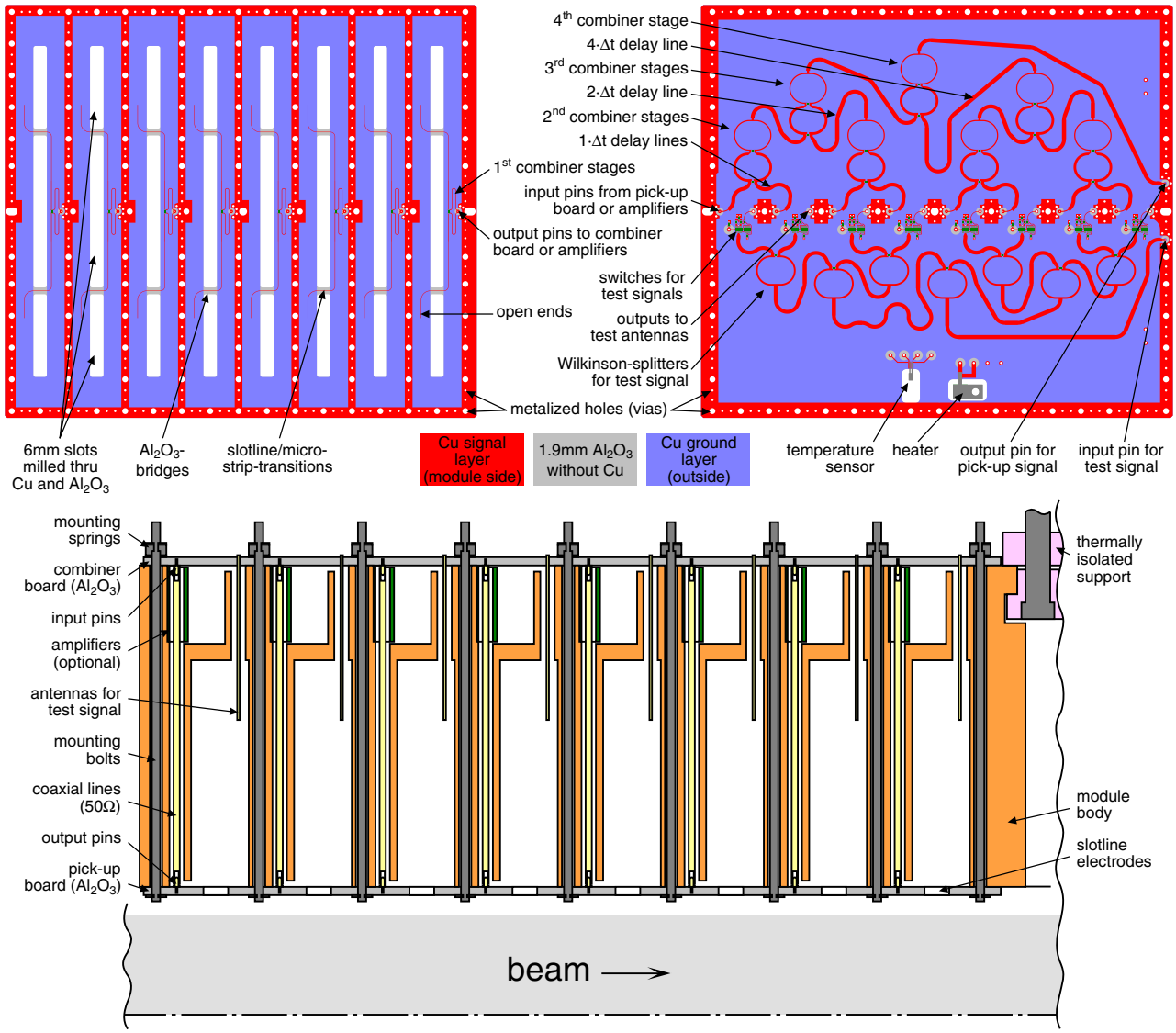

Figure 2: Layout of a two times eight slot pick-up module prototype

input, which could have an equivalent noise temperature below the physical temperature of the module and the amplifier. This in addition to the low losses from the slotline to the amplifier would result in a much lower noise temperature of the pick-up system. The disadvantage is, that defective amplifiers cannot be replaced without opening of the vacuum tank. Also, 128 amplifiers per tank instead of 16 are quiet expensive. The amplifiers would have separate power supply lines, so defective amplifiers can be switched off and do not prevent the operation of the remaining system. In the pick-up module analyzed in this paper, the foreseen amplifiers are replaced by aluminum dummies, which only exists as outer conductor of the coaxial lines. The dimensions of the coaxial lines and the connection pins are compatible to PC-3.5 connectors. This simplifies bench measurements and allows us, to use some standard parts.

On the combiner board (Fig. 2, top, right), three additional combiner stages form an eight to one power combiner. For a flat frequency response, the combiners are a two stage Wilkinson type. The resistors are standard SMD metal film parts (type 0603). The particles pass the slots one after another with a delay of $\Delta t = \Delta z / \beta c$ with the distance between the slots $\Delta z = 25$ mm (center to center). To get a phase-correct signal combination, the different delay lines before the combiners are necessary. The combiner board is designed for the velocity of the antiprotons with a β of 0.97. The rare isotopes with $\beta = 0.83$ deliver much stronger signals. Therefore, the slight amplitude degradation of 0.4 dB at 1.5 GHz is acceptable. The combination of the signals from two combiner boards would result in a unacceptable degradation of 1.8 dB at 1.5 GHz for rare isotopes. Therefore, the signals from the combiner boards go in separate coaxial lines to the vacuum feedthroughs at the

other end of the support tube. The two times eight signals will be combined outside the vacuum using switchable delay lines.

There will also be two other coaxial lines for test signals from outside the tank. These test signals are split with single stage Wilkinson splitters on the combiner board into separate signals for each slotline. The signals are coupled with antennas into the pockets in the module body above the slotlines. This signals can be used to test whether each component and connection is working. This is also possible in shutdown periods without beam and even with poor vacuum. With installed low noise amplifiers inside the module, we could measure each slot separately by powering only a single amplifier. Without amplifiers, the semiconductor switches on the combiner board are necessary to address single slots.

The aluminum body of the module and the alumina printed circuit boards have a different thermal expansion coefficient. To prevent cracks in the alumina, there is only a single alignment dowel pin in the middle of each board. The outer edge of the board can move up to 500 µm during cool down. Two slot holes prevent rotation around the alignment pin. A good electrical contact between the module body and the circuit boards will be achieved by the tension of 133 mounting springs and bolts.

To lower the thermal noise, the module will be cooled down to approximately 20 K by the second stage of two Gifford-McMahon type two stage cold heads per tank. The support tube is thermally connected to the shield temperature of approximately 80 K from the first stage of the cold heads. A polymer isolator prevents a high thermal flux from the support tube to the module.

Two other parts on the combiner board are a temperature sensor diode and a resistive heater. The heater can help to drive out gas from the module, but the temperature is limited by the electronic components and the cold heads. It is not decided, whether it is needed for operation.

FIELD MEASUREMENTS

For three-dimensional field measurements, an electric near-field probe moved by a computer controlled mapper has been used. The near-field probe consists of a small electric dipole (8 mm) at the end of two thin semi-rigid cables. The two half dipoles are fed with opposite phases by an wide band 180° hybrid (Anzac H-183-4). The complex transmission S_{21} between the probe and the module output has been measured versus position and frequency using a vectorial network analyzer (R&S ZVA40). The transmission of the hybrid and all cables as well as the coupling of the dipole has been measured over the frequency. All following measurements have been corrected by this calibration values.

Figure 3 shows the voltage integrated along trajectories in different heights y above the center of the slotlines versus frequency f.

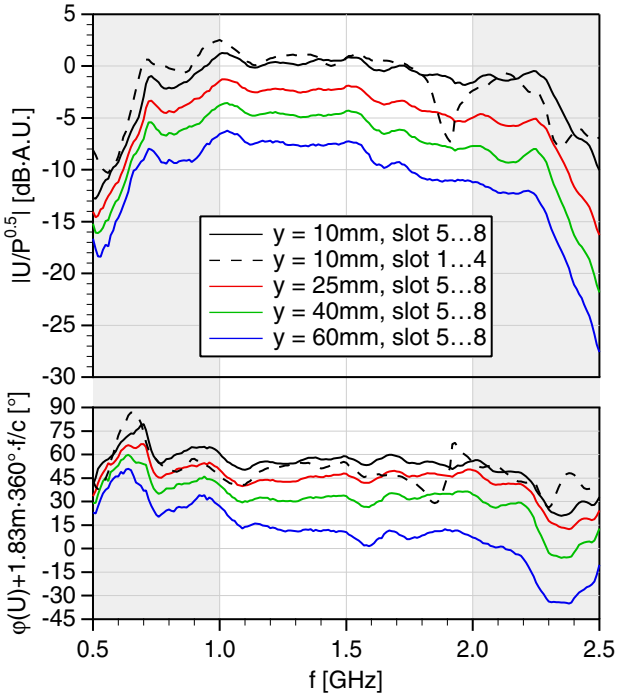

Figure 3: Normalized voltage and phase in different heights versus frequency.

The plotted value is the integral of the transmission from pick-up to near-field probe with a transit time factor for antiprotons ($\beta = 0.97$). This value is proportional to the voltage over the square root of power loss

$$\frac{U}{\sqrt{P_V}} \propto \int_{z_1}^{z_2} S_{21} \cdot e^{i\frac{\omega}{\beta c}} dz \,, \qquad (1)$$

proportional to the sensitivity, and proportional to the square root of the shunt impedance. An electrical length of 1.83 m has been subtracted from the phase. So, the lower part of the diagram shows only the phase nonlinearity. The solid lines represent integrals from the center between slot 4 and 5 (z_1) to the end of the module, 12.5 mm behind slot 8 (z_2) in beam direction. The dashed line represent an integral from the front of the module, 12.5 mm in front of slot 1 to the center. The voltages from slot 5 to 8 looks promising. The voltage in a height of 10 mm above the pick-up is flat within ±1.5 dB and ±5° from 1 GHz to 2 GHz. The out-of-band response is also very good. There is no frequency point with high sensitivity and wrong phase nearby the operating band, which can heat up the beam. On the other hand, the voltage from slot 1 to 4 has more ripple and a nasty resonance at 1.9 GHz. This resonance is present at each of the slots 1 to 4 and none of slots 5 to 8. It can be explained as the result of a coupling between the output microstrip line and the two microstrip arcs nearby on the combiner board. The next combiner board will have an larger distance at these two critical points at the expense of a larger electrical length.

Figure 4 shows the voltage along trajectories from slot 1 to 8 versus the displacement in slotline direction in an height of $y = 10$ mm above the pick-up for different frequencies. At 1 GHz the response is very flat. The pick-up is usable for very wide beams of more than 100 mm. As expected, the effective width of the pick-up gets smaller for higher frequencies but is still wider then 50 mm for 2 GHz. The phase deviation is also very small between 1 and 1.5 GHz. Also at 2 GHz, the phase deviation is small enough to cool the beam.

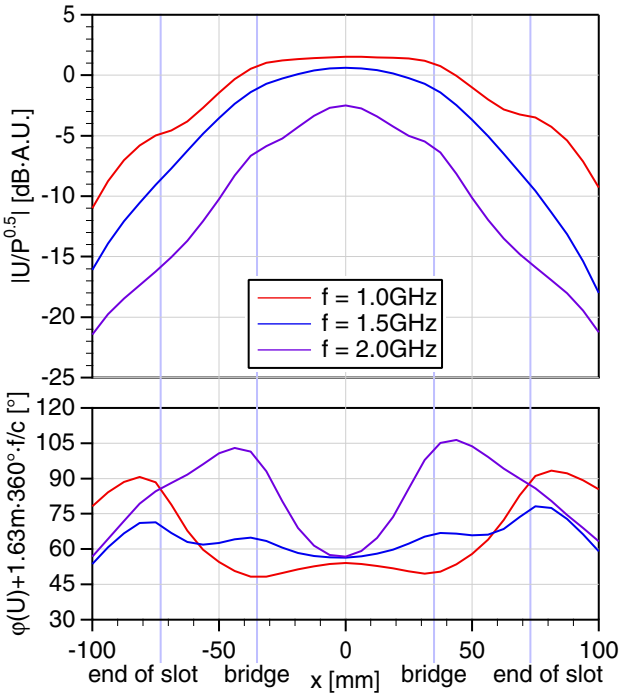

Figure 4: Normalized voltage and phase at different frequencies versus x-displacement.

The last diagram (Fig. 5) shows the dependence on the height y of the trajectory above the pick-up at different frequencies for slot 1 to 8. As expected for the open pick-up, the voltage drops exponentially with the distance. The phase deviation is relatively flat for all frequencies. Please note, that this behavior will change slightly if there is a second pick-up module at the opposite side of the beam, because the fields of the two modules will add up. This diagram demonstrates the necessity of movable pick-ups for fast cooling. The sensitivity at 1.5 GHz drops by 8.1 dB between 5 mm and 65 mm distance.

SUMMARY AND OUTLOOK

A complete pick-up module for the stochastic cooling in the CR with all electrical and mechanical aspects has been designed and a first prototype has been built up. The field measurements show a good behavior of sensitivity and phase linearity versus frequency and displacement for the slots five to eight. In the next step, we will slightly modify the wiring of the output line to fight against the resonance

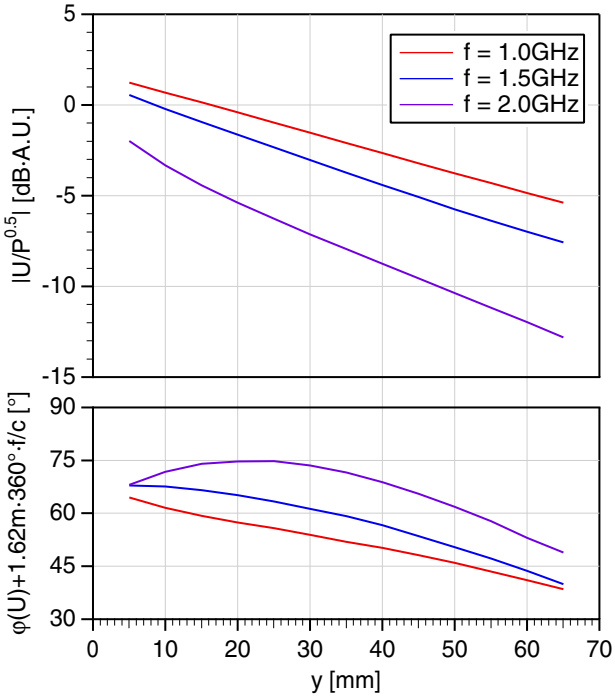

Figure 5: Normalized voltage and phase at different frequencies versus height y.

of the combiner for slot 1 to 4. If the behavior is the same as for slot 5 to 8 after the modification, the module fulfills all electrical requirements.

After the modification, two of these modules will be mounted in the new prototype tank for tests with movable electrodes, vacuum and in the next step with cryogenic temperatures.

REFERENCES

[1] C. Peschke, F. Nolden, M. Balk: “Planar Pick-Up Electrodes for Stochastic Cooling”; Nuclear Instruments and Methods A 532 (2004), pages 459–464

[2] F. Nolden, R. Hettrich, U. Jandewerth, C. Peschke, P. Petri, M. Steck: “Prototype Pick-up Tank for CR Stochastic Cooling at FAIR”; this conference

[3] C. Peschke, F. Nolden: “Pick-Up Electrode System for the CR Stochastic Cooling System”; Proceedings of the Workshop COOL 07, JACoW, http://www.jacow.org/cl07

CALCULATIONS OF ELECTRON BEAM MOTION IN ELECTRON COOLING SYSTEM FOR COSY

M.I. Bryzgunov, V.M. Panasyuk, V.B. Reva (BINP, Novosibirsk)

Abstract

Results of calculations of electron beam motion in cooler for COSY (Juelich, Germany) are shown. The aim of the calculations is to study excitation of the beam galloping due to magnetic and electric field ripples, imperfection of bending field in toroids, transverse electric field in the end of accelerating tube etc. Dependences of the beam temperature on different parameters of magnetic and electrostatic systems are presented. Methods of correction of electron beam motion in order to decrease its transverse velocity are shown.

INTRODUCTION

In low energy electron coolers temperature (transverse velocity) of electron beam is not very important parameter because motion of electrons is adiabatic along full length of coolers from electron gun to collector and there is no significant excitation of transverse velocity. But in electron cooling systems for high energy, longitudinal Larmor length for electrons is high. Because of this, motion is not adiabatic and strong excitation of transverse temperature of the beam in possible. In such case investigation of electron motion in order to prevent strong increasing of electron transverse temperature is important task.

There are several one-particle effects which can increase transverse temperature of electron during the flight in magnetic field of the electron cooler:

1) magnetic field ripples,
2) electric field ripples,
3) excitation on transverse electric field in the end of the acceleration tube,
4) excitation on transverse magnetic field in transition between different values of magnetic field,
5) entry and leaving from bending parts.

In linear approximation, transverse beam motion in the system can be divided to for modes. First one is transverse shift of the beam relatively the reference line of the system without transverse velocity. Second one is dipole mode, in which all electrons of the beam with the same longitudinal coordinate move in transverse direction synchronously in the same direction, i.e. centre of mass of the beam moves, but there is no motion of electrons relatively the centre of mass. Third mode is synchronous motion of electrons relatively the centre of mass, but centre of mass doesn't move. In literature such motion is called galloping. And the fourth mode appears in systems where quadruple component of transverse magnetic field exists. This mode changes transverse profile of the beam by compressing it in one direction and stretching in perpendicular direction.

In systems with axial symmetry only galloping (third mode) can exist. Since in points 1-4 from the list above we suppose axial symmetry, only galloping can be excited there. In point 5 excitation of all modes is possible.

Influence of quadruple component on the temperature of the beam is very weak and it can be adjusted by field index in bends of the cooler. According to this, we need only two different types of additional correctors: dipoles and axial lenses, for correction of beam motion.

ELECTRON COOLER FOR COSY

Electron cooler for COSY (Juelich, Germany) is constructed to work in wide range of operating electron energy: 25 keV (injection) – 2 MeV (maximum energy for the ring) [1]. Magnetic field in cooling section is 2 kG. Cooling time ~10 sec.

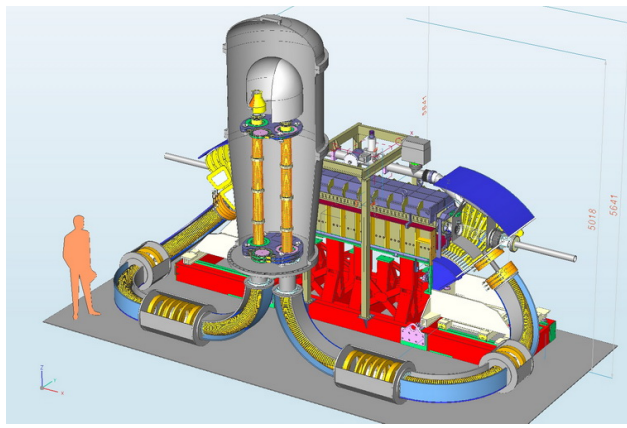

Figure 1: Electron cooler for COSY.

Strict requirements on size of the cooler, forces us to make its shape so complicated (fig. 1). In such shape acceleration and deceleration tubes are placed in one high voltage vessel. Length of acceleration tubes is 2 m. Along full trajectory from gun to collector electrons move in longitudinal magnetic field.

Magnetic system of high voltage vessel consists of two sets of identical coils, producing longitudinal magnetic field in acceleration and deceleration tubes. Transport line between high voltage vessel and cooling section consists of three 90° bends, one 45° toroid, two straight sections for technical purposes and two sections with variable profile of magnetic field for minimization of excitation of transverse motion in transition between different values of magnetic field. Cooling section consists of special coils with possibility to adjust straightness of magnetic force line by rotating each coil independently [2]. Bending field in 90° bends (82 G for 2 MeV electrons) is made with special coils (fig. 2). Each bend includes 4 coils. We are

planning to change current in every coil independently, so one can regulate both value of the field and field index.

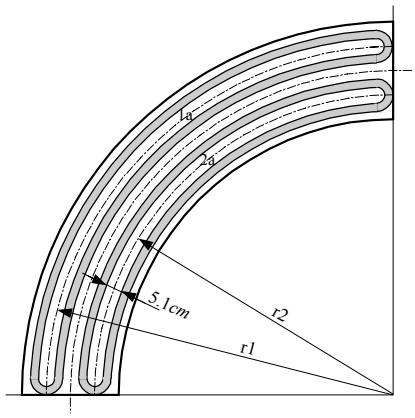

Figure 2: Bending coils in 90° bends.

HEATING ON DIFFERENT ELEMENTS

All main effects which can heat electron beam were calculated. We suppose that strong heating of the beam should be avoided but small excitation will be compensated with special correctors.

Magnetic Ripples

The dynamic of electron in electrostatic column can be described with equations:

$$\begin{cases} x'' + \dfrac{\gamma'}{\gamma\beta^2}x' - \dfrac{qB}{\gamma\beta m_e c^2}y' - \dfrac{qB'}{2\gamma\beta m_e c^2}y = 0 \\ y'' + \dfrac{\gamma'}{\gamma\beta^2}y' + \dfrac{qB}{\gamma\beta m_e c^2}x' + \dfrac{qB'}{2\gamma\beta m_e c^2}x = 0 \end{cases} . \quad (1)$$

Here we suppose that there is only longitudinal electric field and no transverse electric field. Transverse magnetic field is calculated in paraxial approximation of the first order. Making substitutions $\eta=x+iy$, $k=qB/(m_e c^2)$, $\eta = \eta_1(w)\cdot\exp\left(-\dfrac{i}{2}\int_0^w \kappa(w')dw'\right)$, $w = \int \dfrac{dz}{\gamma(z)\beta(z)}$, one can rewrite the system in form of equation for complex amplitude $\eta_1(w)$

$$\frac{d^2\eta_1}{dw^2} + \frac{\kappa(w)^2}{4}\eta_1 = 0 . \quad (2)$$

From the theory of Mathieu equation there is a condition on resonance. In terms of w variable it means that frequency of changing of k is equal to $2k$. Higher order resonances are weak and can be neglected. In terms of s variable it means that period of magnetic system is equal to the length of Larmor spiral. During the acceleration, Larmor length is changing and resonance occurs only in small region of acceleration part. Calculation of trajectory shows that increasing of temperature of the beam on magnetic ripples during acceleration is small (less than $5\cdot10^{-6}$ cm/s) and can be neglected.

Electrostatic Tube

In the end of acceleration tube, strong defocusing transverse electric field appears. This field can increase transverse temperature of the beam. Transverse velocity of electron after transition through the thin final lens can be estimated using formula:

$$V_T = \frac{eE}{2p}r , \quad (3)$$

here E – electric field in tube, r – radius of electron, p – momentum of the electron.

Such estimations give good coincidence with precise calculations of electron trajectory calculated with SAM program (fig. 3). For energy U=2 MeV transverse velocity after transition for electron with r=1.5 cm is about $9\cdot10^7$ cm/s . In longitudinal magnetic field 500 G it corresponds to transverse Larmor radius 0.5 mm.

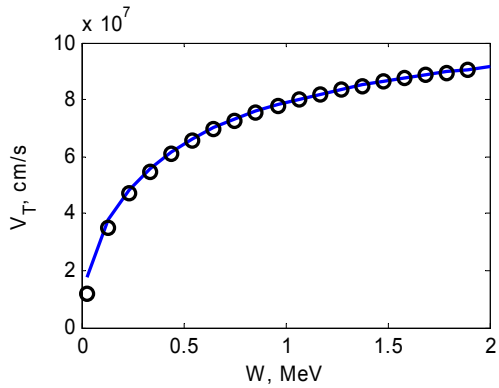

Figure 3: Transverse velocity of the electron started with r=1.5 cm after transition through the end of acceleration tube (solid line – estimation using (3), circles – calculation).

Since electric field for acceleration of beam is made with separated electrostatic plates with different potential, resulting electric field is not homogenous and transverse electric field can increase transverse temperature of the beam. To estimate influence of this effect, electric field in acceleration column was calculated using SAM program (BINP, Novosibirsk). These calculations show that the highest effect in electric filed ripples introduces flange region between different sections. But for chosen construction, influence of such ripples is very weak in comparison with effect in the end of tube.

Bends

In the general case, magnetic force line which starts in center of acceleration column doesn't coincide with centre of the bend. Because of this, transverse magnetic field can appear in transition from liner part to the bend. To decrease heating of the beam after transition through a bend, the length of the bend should be equal to integer number of Larmor length. In such a case kick on entry to bend in compensated by kick on leaving (fig. 4).

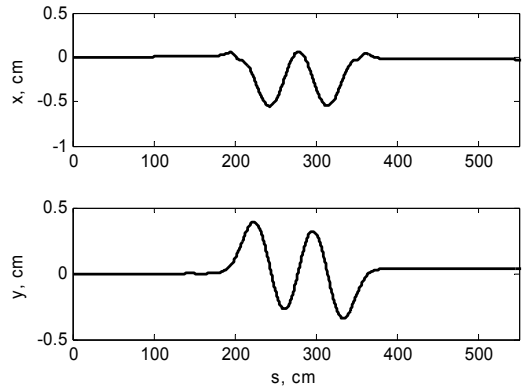

Figure 4: Trajectory of electron with energy 2 MeV in 90° bend. Bend starts in s=200 cm, radius R=100 cm.

The worst situation, which one should avoid, occurs when length of bend is equal to $n+1/2$ of Larmor length. In such a case two kicks are added and resulting transverse velocity of electrons is very high.

Matching Section

Transition between two different values of magnetic field leads to increase of transverse temperature of the beam. In transition from 1 kG to 2 kG for 2 MeV electrons transverse velocity increases for $3\cdot10^9$. To avoid this, special matching is needed. There are different methods of matching (for example see [3-5]). In this work it is made using special profile of magnetic field.

To calculate magnetic field profile one can transform (2) to equation on envelope W:

$$W'' + \frac{k^2}{4}W - \frac{1}{W^3} = 0\,. \qquad (4)$$

Supposing that acceleration is absent, one can turn back from variable w to s in (4) just replacing w by s and k by k_N which is equal to $k_N = \frac{k}{\gamma\beta}$. From (4) value of W function without oscillations is

$$W = \sqrt{\frac{2}{k_N}}\,. \qquad (5)$$

Any envelope function can be set and shape of magnetic field can be restored

$$B(z) = \frac{\gamma\beta mc^2}{e}k_N(z) = \frac{2\gamma\beta mc^2}{e}\sqrt{\frac{1}{W^4} - \frac{W''}{W}}\,. \qquad (6)$$

Using this method any W function which haven't oscillations in the beginning and in the end of matching section and equal there to the values calculated by (5) can be set and shape of magnetic field can be restored.

The section (fig. 5) is made as an addition insertion in beam line between acceleration tube and first bend (and between final bend and deceleration tube). The insertion includes some additional coils with one current source for every coil. Current in every coil is set in order to make shape of magnetic field calculated from (6).

In fig. 5 the profile is made for 2 MeV electrons using 11 additional coils. Form of envelope function is

$$W(s) = W_1 + \frac{W_2 - W_1}{2}\left(erf\left(\frac{s}{a}\right) + 1\right), \qquad (7)$$

with a=15 cm. Values of magnetic field in the beginning and in the end are 500 G and 1000 G correspondingly.

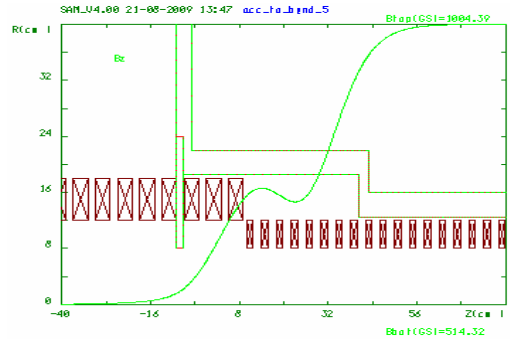

Figure 5: View of the matching section and magnetic field shape for electrons with energy W=2 MeV.

It was said above, that the cooler works in wide range of electron energy. Therefore we need to make its own shape of magnetic field in the matching section for every value of energy. Because of this,, the section consists of so many coils.

Since it is impossible to make ideal shape, there is small galloping of the beam after transition, which should be corrected.

Similar matching section is used in transition between 3-rd 90° bend and 45° toroid with field 2 kG.

Straight Section

There are two straight sections between 90° bends (fig. 6).

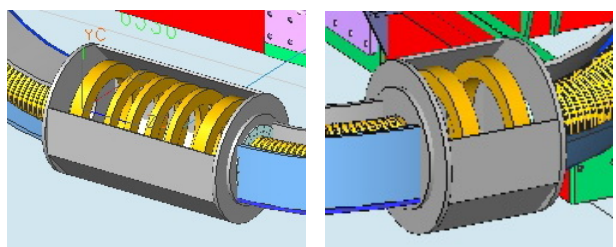

Figure 6: Straight sections.

The purpose of the insertions is to provide easy access to vacuum system in order to: install vacuum pumps, provide assembly and disassembly of vacuum system, simplify output from pickup electrodes. Therefore the insertions consist of three types of relatively big coils. Two types for producing of magnetic field in the beginning and in the end of insertion and one type in center. Using the coils, linear parts with appropriate uniformity of magnetic field can be made.

CORRECTION

It was said that we need two types of correctors to decrease transverse motion of electron beam in the cooling section. One type for correction of dipole motion

of the beam and another type for correction of beam galloping.

First one is supposed to be made of two independent dipoles. Every dipole consists of two coils connected in series. Using the corrector one can decrease both V_x and V_y components of transverse velocity independently.

In order to correct beam galloping the same coils which are installed in the matching section are supposed to be used. Changing current in one coil one can make axial magnetic lens. Using several coils, beam galloping can be decreased.

Supposing that beam diagnostic system allows us to measure transverse Larmor radius with resolution 0.1 mm [5], resulting transverse angle for 2 MeV electrons is about $2.5 \cdot 10^{-3}$. It corresponds to temperature of the beam 1 eV.

ENERGY RANGES

It is clear that it is possible to set one value of energy of electron beam and to adjust cooler optics for this energy in order to avoid high temperature of the electron beam in cooling section. But wide range of operating electron energy means that optics of the cooler must be easily adjustable for all energies. One method of realization of such system is to adjust optics manually for every value of energy. Number of parameters and correctors in our system allow us to do this, but this method is very time consuming. There is easier method which was proposed for this system. The idea of the method is to change magnetic field in the cooler synchronously with beam energy. For example: if magnetic system was adjusted for 2 MeV electron beam, then after decreasing of energy for value U, we must decrease magnetic field (longitudinal and transverse) in α times where α is equal to ratio of momentums for 2 MeV and for U:

$$\alpha = \frac{p_{2MeV}}{p_E} \approx \sqrt{\frac{(2+0.511)^2 - 0.511^2}{(U[MeV]+0.511)^2 - 0.511^2}} . \qquad (8)$$

It is impossible to use this formula for full range of energy. Because of this we divided the range for 4 smaller ranges (fig. 6).

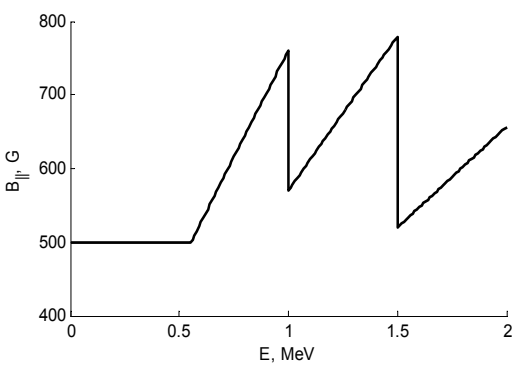

Figure 7: Longitudinal magnetic field in bends for different energies.

From the fig. 6 one can see that there are three regions with independent adjustment of optics (0.55~1.0 MeV, 1.0~1.5 MeV, 1.5~2.0 MeV). The idea of the division is to have integer number of Larmor length in a 90° bend. The numbers are 4, 3 and 2 for regions 0.55~1.0 MeV, 1.0~1.5 MeV and 1.5~2.0 MeV correspondingly. After adjustment, magnetic field in the cooler must be changed synchronously with energy. For energy lower than 0.55 MeV Larmor length is small, because of this motion of electrons is adiabatic and excitation of transverse motion of the beam is small.

CONCLUSION

So complicated shape of the cooler and so wide range of operating energy force us to adjust optics of the cooler in order to make transverse temperature of electron beam in the cooling section as small as it is required.

In some elements (bends, matching sections, straight sections) resulting transverse temperature is decreased adjusting some parameters of the elements. Otherwise, after transition of these elements resulting temperature can be very high. In other elements, in which resulting temperature is not very high, special adjustment isn't used.

Resulting transverse motion of the beam is sum of dipole motion and beam galloping. In order to correct it two types of correctors (two perpendicular dipoles and axial magnetic lens in matching sections) are used.

ACKNOWLEGMENTS

Authors thank Dr. J. Dietrich from COSY (Juelich, Germany) and head of electron cooling laboratory V.V. Parkhomchuk (Novosibirsk, Russia) for useful consultations. Also thank to V.K. Gosteev for help in printing of the article.

REFERENCES

[1] J. Dietrich, M.I. Bryzgunov, A.D. Goncharov, V.V. Parkhomchuk, V.B. Reva, D.N. Skorobogatov, "Prototype of the high voltage section for the 2 MeV electron cooler at COSY-Juelich", EPAC'08, Genoa, Italy, p. 3467.

[2] V. Bocharov, A. Bubley, S. Konstantinov, V. Panasyuk, V. Parkhomchuk, "Precision measurements and compensation for the transverse components of the solenoids magnetic field", Instruments and Experimental Techniques, Vol. 48, Number 6, 2005, p. 772.

[3] V. Parkhomchuk, I. Ben-Zvi, "Electron cooling for RHIC", C-A/AP/47, http://www.agsrhichome.bnl.gov/AP/ap_notes/ap_note_47.pdf, April, 2001, p. 59.

[4] Ya.S. Derbenev, "Advanced optical concepts for electron cooling", ECOOL'99, Uppsala, Sweden, p. 223.

[5] "HESR electron cooler. Design study", http://www5.tsl.uu.se/hesr/public/D32_HESR_EC.pdf, Uppsala, Sweden, 2009.

SIMULATION STUDY OF SIMULTANEOUS USE OF STOCHASTIC COOLING AND ELECTRON COOLING WITH INTERNAL TARGET AT COSY AND HESR

Takashi Kikuchi*, Nagaoka University of Technology, Nagaoka 940-2188, Japan
Jürgen Dietrich, Rudolf Maier, Dieter Prasuhn, Hans Stockhorst, FZJ, Jülich, Germany
Takeshi Katayama, GSI, Darmstadt, Germany

Abstract

The small momentum spread of proton or anti-proton beam has to be realized and kept in the storage ring during the experiment with dense internal target such as pellet target. The stochastic cooling alone cannot compensate the mean energy loss by the internal target, and the barrier bucket cavity will help this energy loss. In addition the further small momentum spread can be realized with use of electron cooling. In the present study, the simulation results on the simultaneous use of stochastic cooling and electron cooling at COSY and HESR are presented.

INTRODUCTION

A stochastic cooling is useful tool to cool a hot beam with smaller number of beam particles even in the high kinetic energy regime. While an electron cooling is useful for lower energy and cold beam, and has also advantage for effective cooling even in the large number of beam ions.

In HESR of FAIR project [1] a large number of anti-protons with high kinetic energy should be stored in the storage ring. The small momentum spread of anti-proton beam has to be realized and kept in the storage ring during the experiment with dense internal target such as pellet target.

In this study, we propose the simultaneous use of the stochastic cooling and electron cooling. The stochastic cooling can collect the protons or anti-protons with large momentum spread into the central energy regime, in addition the further small momentum spread can be realized with use of electron cooling.

SIMULATION MODEL

A Fokker-Planck equation is often used as an investigation tool in the stochastic momentum cooling process. The simplified Fokker-Planck equation for a model of a stochastic momentum cooling is given by [2]

$$\frac{\partial \Psi}{\partial t} + \frac{\partial}{\partial E}\left(F\Psi - D\frac{\partial \Psi}{\partial E}\right) = 0, \qquad (1)$$

where $\Psi \equiv \Psi(E,t) \equiv dN/dE$ is the particle distribution function, $F \equiv F(E)$ is the coefficient for the cooling force, and $D \equiv D(\Psi(E),t)$ is the coefficient for the diffusion process.

* tkikuchi@nagaokaut.ac.jp

The coherent and incoherent terms in the Fokker-Planck equation mean the cooling force and the diffusion process, respectively. The terms are derived by the electrical characteristics of the feedback system for the stochastic cooling [3]. Also the coherent term coefficient includes the electron cooling force as

$$F = F_{scool} + F_{ecool}, \qquad (2)$$

where F_{scool} is the cooling force due to the stochastic cooler and F_{ecool} is the cooling force caused by the electron cooler. For the calculation model of the electron cooling drag force, we carry out the Parkhomchuk empirical formula [4].

In this study, we simulate numerically the particle distribution during the cooling process using the Fokker-Planck equation solver [5] based on a constrained interpolation profile (CIP) method with a rational function [6].

Table 1 shows the parameters for COSY simulation [7] including the electron cooler option [8].

Table 2 shows the parameters for HESR simulation [1].

NUMERICAL SIMULATION RESULTS

COSY

Figure 1 shows the energy spread history during the cooling in COSY parameters. Here the energy spread σ is calculated by

$$\sigma^2(t) = \frac{1}{N}\int_{-\infty}^{\infty} E^2 \Psi(E,t)\, dE, \qquad (3)$$

where N is the total particle number in the ring.

As shown in Fig. 1, the energy spread can be improved well by the stochastic cooling in the case without the internal target. In the case with the internal target, the stochastic cooling does not compensate the energy loss, and the energy spread increases. When the electron cooling is simultaneously applied with the stochastic cooling, the energy spread can be improved until 500 sec in the case with the internal target. However even if in cooperation of the electron cooling of 0.25 A, the energy loss due to the internal target is not compensated in the later stage.

HESR

Figure 2 shows the particle distributions as a function of energy during the stochastic cooling in HESR at each cooling time. The anti-protons can be collected into the

Table 1: Parameters for COSY Simulation

Beam	
Momentum	3.224 GeV/c
Kinetic energy	2.42 GeV
Particle number	10^{10}
Energy spread (1σ)	0.774 MeV
Ring Dispersion	-0.1
Momentum acceptance	+/- 1.5 $\times$ 10^{-3}
Stochastic cooling system	
Band width	1 $\sim$ 1.8 GHz
Gain	96 dB
Effective temperature	80 K
Electrode length	32 mm
Electrode width	20 mm
Gap height	20 mm
Impedance	50 Ω
Number of pickup and kicker	24
TOF from pickup to kicker	0.3229 μsec
System delay	-0.04 ns
Electron cooling system	
Beta function at cooler	6 m
Dispersion at cooler	0 m
Beam current	0.1 or 0.25 A
Effective energy spread	0.001 eV
Beam diameter	0.01 m
Cooler length	2 m

Table 2: Parameters for HESR Simulation

Beam	
Kinetic energy	8 GeV
Particle number	10^{11}
Ring circumference	573.1 m
Stochastic cooling system	
Band width	2 $\sim$ 4 GHz
Gain	105 dB
Effective temperature	80 K
Electrode length	25 mm
Electrode width	25 mm
Gap height	26 mm
Impedance	50 Ω
Number of pickup and kicker	64
Electron cooling system	
Beta function at cooler	100 m
Dispersion at cooler	0 m
Beam current	0.1 A
Effective energy spread	0.001 eV
Beam diameter	0.01 m
Cooler length	25 m

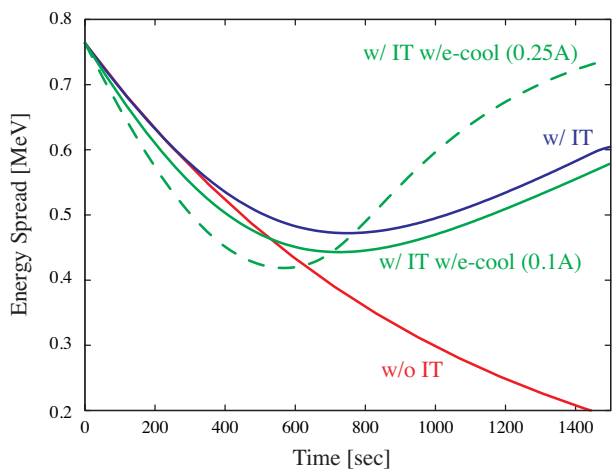

Figure 1: Energy spread history during cooling in COSY. The red curve shows the stochastic cooling result without the internal target, the blue line shows the stochastic cooling result with the internal target, the green lines indicate the internal target results with the stochastic and electron coolers for the electron beam current of 0.1 A (solid) and 0.25 A (dashed), respectively.

central energy of the beam due to the stochastic cooling.

Figure 3 shows the energy spread history during the stochastic cooling in HESR at each initial energy spread. The final energy spread is 0.35 MeV, which is as the momentum spread $\Delta p/p = 4 \times 10^{-5}$.

Figure 4 shows the energy spread history during cooling in HESR parameters at each cooling option. Here "s" means the stochastic cooling, "e" indicates the electron cooling, "s+e" indicates the simultaneous use of the stochastic cooling and electron cooling, "s→e" implies the switching from the stochastic cooling to electron cooling at each time, and "s+e→e" indicates the switching from the simultaneous use of the stochastic cooling and electron cooling to electron cooling alone at each time, respectively.

The smallest final energy spread is obtained with the electron cooling after the simultaneous use of the stochastic cooling and electron cooling, "s+e→e". Because in the smaller momentum spread beam, the diffusion term D of the stochastic cooling affects the collected protons around the central beam energy. For this reason, it is favorable to switch off the stochastic cooler in the later stage of the simultaneous use of the two cooling schemes. As shown in Fig. 4, the scheme also gives the fastest cooling speed.

The simulation results for the initial energy spread $\sigma_0 = 2.8$ MeV with the different cooling methods are summarized as Table 3. In the table, the cooling time to attain the energy spread of σ_0/e, $\sigma_0/10$, and $\sigma_0/20$ are given for each cooling method. From Table 3, "s+e→e at 600 s" case is best situation in the condition. As a result, the switching method from the simultaneous use of the stochastic cooling and electron cooling to electron cooling alone has advantage for the fast cooling, and the switching time has the optimal value.

Figure 5 shows the energy spread history during the cooling in HESR with and without the internal target. The

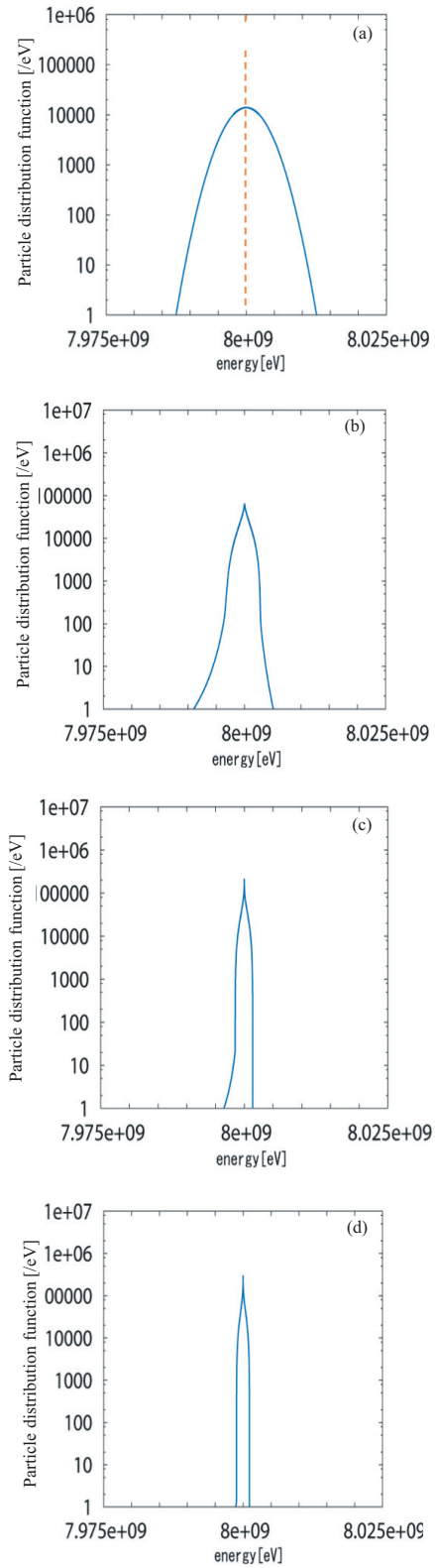

Figure 2: Particle distribution as a function of energy during stochastic cooling in HESR for the initial energy spread in $\sigma_0 = 2.8$ MeV, (a) for the initial condition, (b) for 400 sec, (c) for 800 sec, and (d) for 1200 sec, respectively.

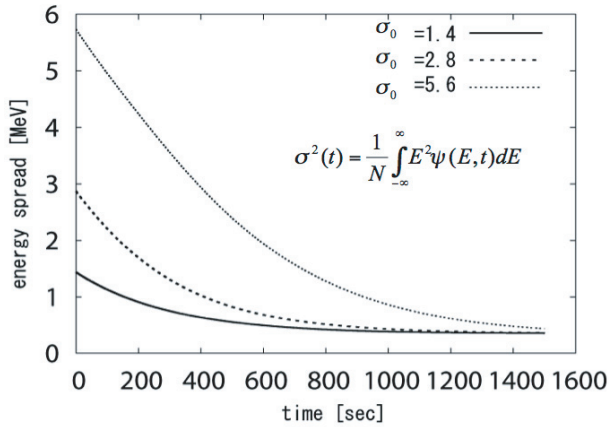

Figure 3: Energy spread history during stochastic cooling in HESR for the initial energy spread $\sigma_0 = 1.4$ MeV (solid), for $\sigma_0 = 2.8$ MeV (dashed), for $\sigma_0 = 5.6$ MeV (dotted), respectively.

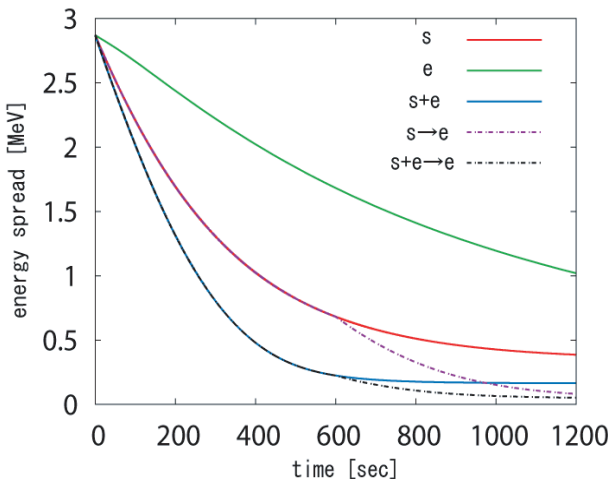

Figure 4: Energy spread history during cooling in HESR at each cooling combination method. The red curve shows the stochastic cooling result, the green line indicates the electron cooling result, the blue line shows the result with stochastic cooling and electron cooling, the red and dashed curve indicates the result for the electron cooling after the stochastic pre-cooling, and the black and dashed line shows the electron cooling result after the stochastic cooling and electron cooling, respectively.

stochastic cooling is carried out as the main beam cooler. Here if the barrier bucket voltage can be applied to compensate the mean energy loss at the internal target, the coherent term does not include the energy loss [9]. As shown in Fig. 5, the energy spread increase is not prevented by the stochastic cooling alone in the case with the internal target. On the other hand, the mean energy loss compensation by the barrier bucket voltage is a useful option. The simultaneous use of the electron cooler has an advantage for the energy loss compensation with fast cooling.

Table 3: Required Time for Cooling in HESR at each Method. The symbol "–" means that those values cannot be achieved.

Cooling method	Time [sec] for σ_0/e	for $\sigma_0/10$	for $\sigma_0/20$
s	400	–	–
e	1200	–	–
s+e	250	530	–
s→e at 400 s	400	850	1050
s→e at 600 s	400	880	1050
s→e at 800 s	400	950	1150
s+e→e at 400 s	250	580	810
s+e→e at 600 s	250	530	730
s+e→e at 800 s	250	530	860

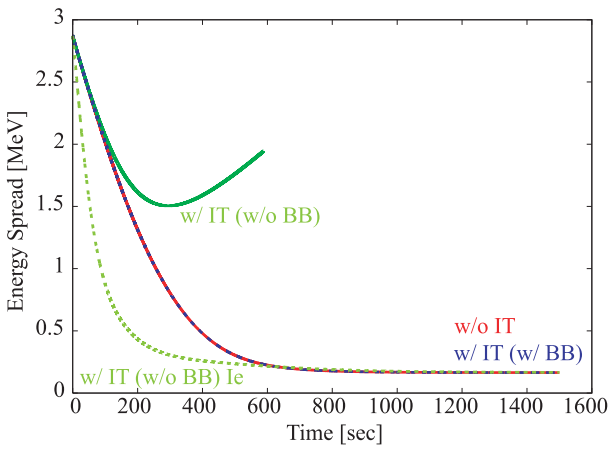

Figure 5: Energy spread history during stochastic cooling in HESR. The red curve shows the result without the internal target, the green line indicates the result with the internal target, the blue line shows the result with the internal target and the barrier bucket voltage, and the green dashed curve shows the result with the internal target and the electron cooling for the current of 0.1A, respectively.

CONCLUSION

The simultaneous use of the stochastic cooling and electron cooling was proposed and was investigated numerically using the Fokker-Planck equation with the rational function CIP solver in this study. The small momentum spread of proton beam has to be realized and kept in the storage ring during the experiment with dense internal target. The stochastic cooling alone could not compensate the mean energy loss by the internal target, and the barrier bucket cavity will help this energy loss. In addition the further small momentum spread could be realized with use of electron cooling. Since the diffusion term of the stochastic cooling affects the collected particles around the central beam energy, it is favorable to switch off the stochastic cooler in the later stage of the simultaneous use of the two cooling schemes. The optimal switching time exists for the smallest momentum spread and the fast cooling. The simulation results showed that the simultaneous use method of the stochastic cooling and the electron cooling is useful scheme even in the case with the internal target.

REFERENCES

[1] HESR, "Baseline Technical Report", http://www.fzjuelich.de/ikp/hesr.

[2] T. Katayama and N. Tokuda, Part. Accel. 21, 99 (1987).

[3] T. Katayama, *private communications*.

[4] V.V. Parkhomchuk, NIM A441 (2000) 9.

[5] T. Kikuchi, S. Kawata, T. Katayama, "Numerical solver with CIP method for Fokker Planck equation of stochastic cooling", PAC'07, Albuquerque, New Mexico, June 2007, pp.3336-3338, THPAN048, http://jacow.org.

[6] F. Xiao, "Numerical schemes for advection equation and multi-layered fluid dynamics"", Ph.D. Thesis, Tokyo Institute of Technology, (1996).

[7] H. Stockhorst, T. Katayama, R. Stassen, R. Maier and D. Prasuhn, "Longitudinal Stochastic Cooling Simulations in Comparison with Cooling Experiments of COSY", Annual Report, IKP, Forschungzentrum, (2007).

[8] J. Dietrich, et al., "Status of the 2 MeV Electron Cooler for COSY Jülich", COOL'09, Lanzhou, China, FRM1MCIO03, http://jacow.org.

[9] H. Stockhorst, et al., "Compensation of Mean Energy Loss due to an Internal Target by Application of a Barrier Bucket and Stochastic Momentum Cooling at COSY", COOL'09, Lanzhou, China, TUM2MCIO01, http://jacow.org.

IMPLEMENTATION OF LONGITUDINAL DYNAMICS WITH BARRIER RF IN BETACOOL AND COMPARISON TO ESME

A. Smirnov#, A. Sidorin, D. Krestnikov, JINR, Dubna, Russia
C. Bhat, L. Prost, Fermilab, Batavia, USA
A.Fedotov, BNL, Upton, USA

Abstract

The barrier bucket RF system is successfully used on Recycler storage ring at Fermilab. The special program code ESME [1] was used for numerical simulation of longitudinal phase space manipulations. This program helps optimizing the various regimes of operation in the Recycler and increasing the luminosity in the colliding experiments. Electron and stochastic cooling increases the phase space density in all degrees of freedom. In the case of a small phase space volume the intrabeam scattering introduces coupling between the transverse and longitudinal temperatures of the antiproton beam. For numerical simulations of the cooling processes at the Recycler, a new model of the barrier buckets was implemented in the BETACOOL code [2]. The comparison between ESME and BETACOOL codes for a stationary and moving barrier buckets is presented.

This article also includes an application of the barrier bucket numerical model for simulation of the luminosity distribution for RHIC colliding experiments. These simulations take into account the specific longitudinal distribution of the bunch and the vertex size of the detector.

BARRIER BUCKET MODELS IN THE BETACOOL PROGRAMM

Currently, the BETACOOL code has three algorithms that describes the synchrotron motion of the particles and which can be used for the simulation of the barrier bucket (BB) models. The first algorithm solves the standard equations of motion in the longitudinal phase space(s-s_0, $\delta=\Delta p/p$). The equations are:

$$\begin{cases} \dfrac{d(s-s_0)}{dt} = |\eta|\beta c\,\delta \\ \dfrac{d\delta}{dt} = -\dfrac{ZeV(t)}{Cp_0} \end{cases} \qquad (1)$$

where βc is the ion velocity, η is the ring off-momentum factor, Ze – the particle charge, $V(t)$ – the dependence of RF voltage on time, C – the ring circumference and p_0 – the momentum of the particles.

In the context of this algorithm the longitudinal motion any arbitrary RF voltage shape can be simulated. However, the problem of this algorithm is the calculation time because the integration step should be much smaller than the synchrotron period.

To avoid this problem, the analytical solution of the longitudinal motion between two square barrier buckets was introduced. In this case, the integration step can be independent on the synchrotron period. When the ion passes through the cavity gap at voltage $\pm V_0$ it gains (losses) an equal amount of energy ZeV_0, i.e.

$$\frac{d(\Delta E)}{dt} = \pm\frac{ZeV_0}{T_0} \qquad (2)$$

where ΔE is the energy deviation from the synchronous one, T_0 – the revolution period. The ion trajectory in the longitudinal phase space (t-t_0, ΔE) inside the bucket can be written in the following form:

$$(\Delta E)^2 = \begin{cases} A_E^2, & if\ |t-t_0| \le T_2/2 \\ A_E^2 - \left(|t-t_0| - \dfrac{T_2}{2}\right)\dfrac{2\beta^2 E_0 ZeV_0}{T_0|\eta|}, & \\ \qquad if\ T_2/2 \le |t-t_0| \le (T_2/2)+T_1 & \end{cases} \qquad (3)$$

where A_E is the maximum energy deviation from the synchronous energy E_0, V_0 is the voltage height, T_1 is the pulse width, T_2 is the gap duration. The phase space trajectory is composed of a straight line in the RF gap region and a parabola in the square RF wave region

The analytical model has static potentials for the barrier bucket with a rectangular shape which is resolved analytically in the longitudinal phase space. However, using of the analytical model is very difficult for the case of a moving bucket with an arbitrary shape.

A numerical model of the RF bucket is implemented in the BETACOOL code where the motion of one particle through each barrier is calculated independently. After crossing of the barrier the particle energy can increase (Fig.1a), decrease (Fig.1b) or the particle can be reflected by the barrier (Fig.1c).

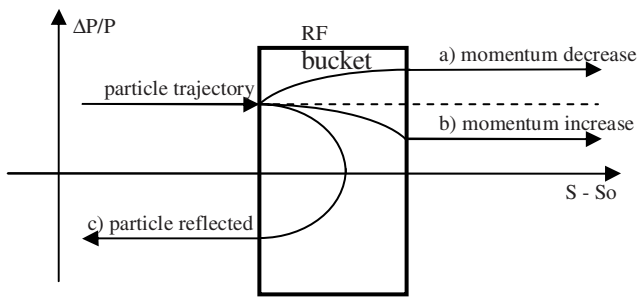

Figure 1: Particle trajectories trough a RF barrier in longitudinal phase space.

For the description of the individual synchrotron motion of each particle one can use a series of the barriers and numerical integration over the longitudinal phase

#smirnov@jinr.ru

space. If the integration step is larger than the synchrotron period, we can assume that for the static barriers the synchrotron period is random.

COMPARISON WITH ESME

The first example shows a comparison of longitudinal particle dynamics for stationary BB without any cooling or heating processes. The initial distribution of particles was generated by the ESME program (Fig.2) and translated into the BETACOOL units (Fig.3). In BETACOOL (Fig.3), the red line is the barrier distribution in units of momentum spread and the blue line is the average momentum spread over each barrier length.

Figure 2: Longitudinal distribution of model particles in ESME.

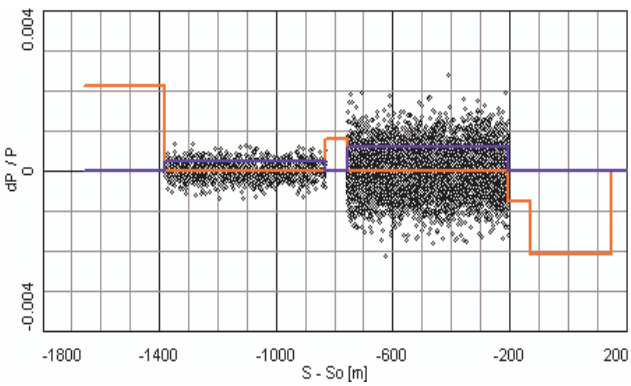

Figure 3: Longitudinal distribution of model particles and barrier bucket in momentum space in BETACOOL.

The beam profile along the longitudinal coordinate shows the particle density normalized to the line density of a coasting beam (Fig.4). This value is used for the simulation of IBS over each barrier length. The black line is the integral of particles normalized to the maximum value of the longitudinal profile.

The simulation consisted in letting evolve the initial distribution which was not in equilibrium, without any other effects. The final distributions after 15 sec (real time) have good agreement with ESME results (Fig.5,6). For BETACOOL, two sets of data with different integration steps are shown.

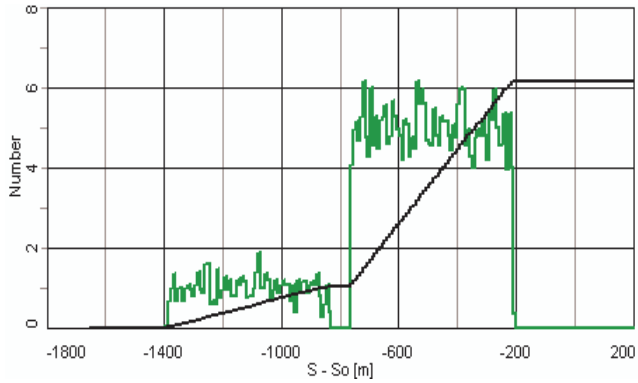

Figure 4: Longitudinal beam profile along longitudinal coordinate in BETACOOL.

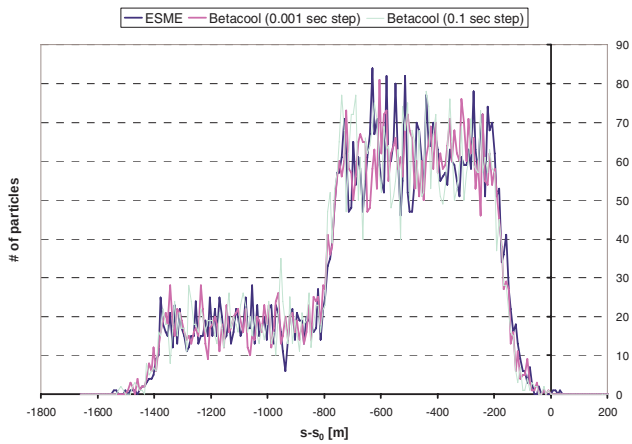

Figure 5: Longitudinal beam profiles along the longitudinal coordinate.

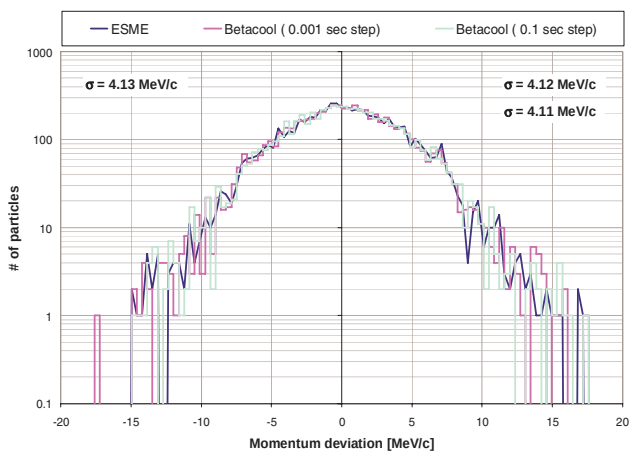

Figure 6: Momentum spread distributions. Final distributions.

The moving barrier option can be used for manipulation of particles in the longitudinal phase space in the case of adiabatic expansion or compression of the bunch. Input

files for moving barriers can have any number of columns: the first column is the time in seconds; each other pairs define the position of the barriers in circumference units and the amplitude in volts. Consecutive rows determine the initial and final conditions (for both the position and the amplitude). Increments of the position and amplitude for each integration step are linear.

The initial distribution of particles was generated by the ESME program and was translated into BETACOOL (Fig.7).

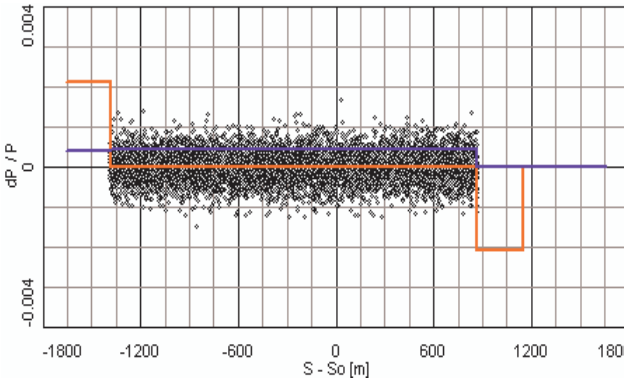

Figure 7: Longitudinal distribution of model particles and barrier buckets in momentum space in BETACOOL. Initial distribution.

In this example, the simulation entailed reproducing a 'squeeze', where the beam bunch length is reduced relatively slowly. The time sequence was the following: wait for 5 seconds (from initial distribution), squeeze for 5 seconds, and wait for 10 seconds. Longitudinal beam profiles and momentum spread distributions in the final state are shown in Fig.8.

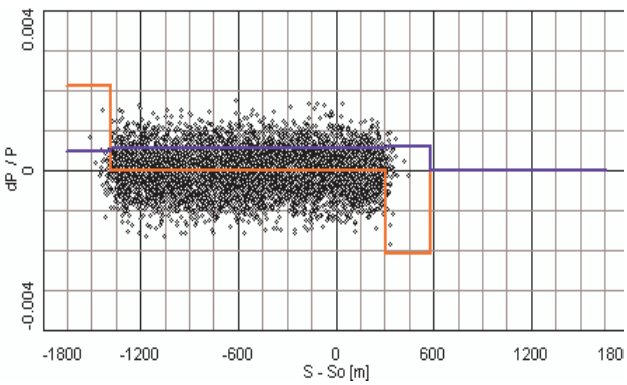

Figure 8: Longitudinal distribution of model particles and barrier bucket in momentum space in BETACOOL. Final distribution after 25 sec.

Although the agreement appears to be pretty good, a slightly more quantitative analysis shows bigger discrepancies than for the stationary bucket case. The bunch length (defined as twice the rms) is 1438 m in ESME while it is 1479 m in BETACOOL (a ~3% relative difference). This is actually visible in Fig.9 in which one can see that the edges of the beam fall more rapidly in the BETACOOL case than in the ESME simulation, hence extending the 'flat-top'. Also, even though the momentum distributions overlap very well in Fig.10, the rms momentum spreads are somewhat different: 4.67 MeV/c in ESME and 4.49 MeV/c in BETACOOL. The relative difference here is 4%, while the momentum spread agreed almost exactly for the stationary bucket case.

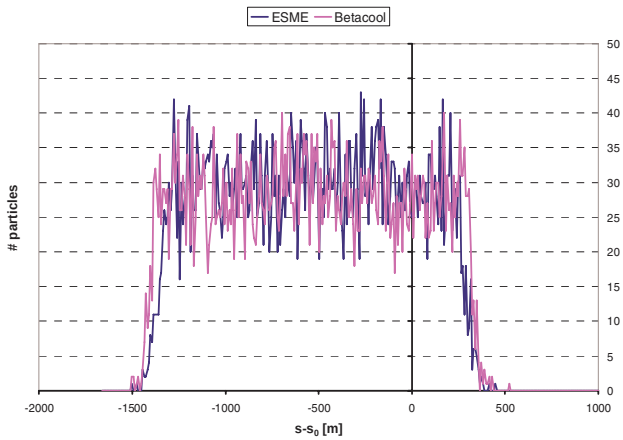

Figure 9: Longitudinal beam profiles along the longitudinal coordinate. Final distribution.

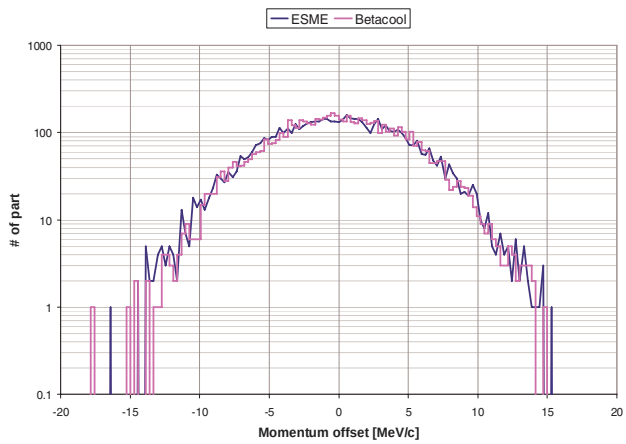

Figure 10: Momentum spread distributions. Final distribution.

The two examples above illustrate that the implementation of longitudinal dynamics in BETACOOL is appropriate and agrees with the well established (and more advanced) code ESME, even in the case of moving barriers, which is more difficult to reproduce correctly (for instance, it is important to make sure that the integration step size is much smaller than the synchrotron period).

USING BARRIER BUCKET MODEL FOR RHIC COLLIDING EXPERIMENT

The longitudinal synchrotron motion realized in the BETACOOL program can be used for different tasks. The specific particle distribution in RHIC colliding experiments is formed when the initial momentum spread

is much higher than the amplitude of the RF voltage. Note that in real RHIC experiments satellites are not as strongly pronounced as in Fig. 11 [3]. In Fig. 11, the distribution was intentionally strongly cooled to produce clearly pronounced satellites for illustration purposes.

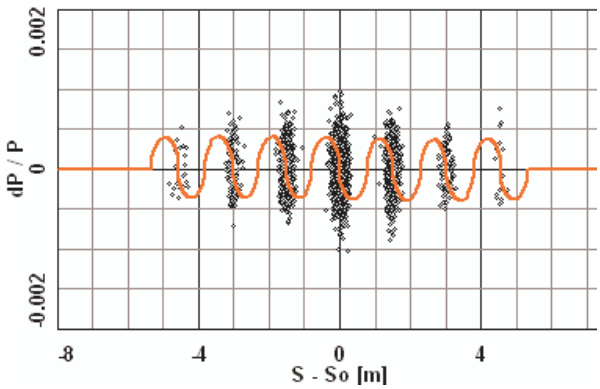

Figure 11: Particle distribution with satellites in longitudinal phase space.

Additional satellites are produced in neighbouring potential wells are due to the sum of two harmonics of the RF system (Fig.12). The luminosity calculation for such a specific particle distribution was implemented in the BETACOOL program (Fig.13). The time dependence can be calculated via the particle velocity. Note that the interaction region is twice smaller than the total bunch length.

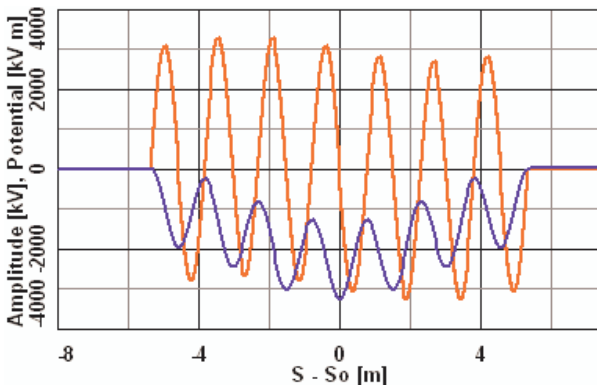

Figure 12: Distribution of the RF voltage as the sum of low and high RF harmonics (red line) and corresponding potential distribution (blue line).

The vertex cut defines as the interaction region where the colliding events can be registered (Fig.14). This algorithm permits to numerically calculate the hourglass effect for an arbitrary particle distribution in the longitudinally phase space. For example for Fig.13 and Fig.14 the hourglass effect factors are 0.76 and 0.75, respectively.

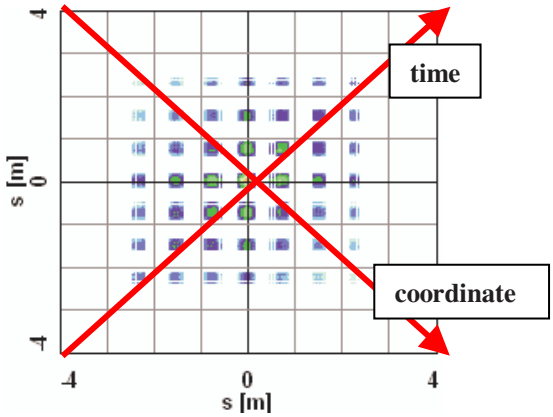

Figure 13: Luminosity distribution for colliding experiments without vertex cut.

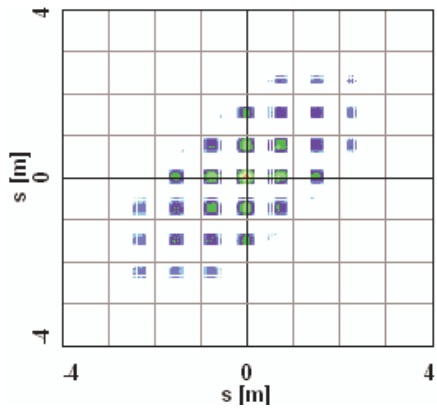

Figure 14: Luminosity distribution for colliding experiments with vertex cut (±100 cm).

REFERENCES

[1] J.MacLachlan, J.-F.Ostiguy. Enhancements to the Longitudinal Dynamics Code ESME. Proceeding of PAC'97. http://jacow.org

[2] A.Sidorin, I.Meshkov, I.Seleznev, A.Smirnov, E.Syresin, and G. Trubnikov. BETACOOL program for simulation of beam dynamics in storage rings. NIM, A, 558, 325 (2006).

[3] M.Blaskiewicz, J.M.Brennan. Bunched Beam Stochastic Cooling Simulations and Comparison With Data. Proceeding of COOL'07. http://jacow.org

ADVANCE IN THE LEPTA PROJECT*

E. Ahmanova, V. Bykovsky, M. Eseev*, V. Kaplin, V. Karpinsky, A. Kobets#,
V. Lokhmatov,V. Malakhov, I. Meshkov, V. Pavlov, R. Pivin, A. Rudakov, A.A.Sidorin,
S. Yakovenko, JINR, Dubna

Abstract

The Low Energy Positron Toroidal Accumulator (LEPTA) at JINR is close to be commissioned with circulating positron beam. The LEPTA facility is a small positron storage ring equipped with the electron cooling system and positron injector. The maximum positron energy is of 10 keV. The main goal of the project is generation of intensive flux of Positronium (Ps) atoms - the bound state of electron and positron, and setting up experiments on Ps in-flight. The report presents an advance in the project: up-grade of LEPTA ring magnetic system, status of the construction of positron transfer channel, and the electron cooling system, first results of low energy positron beam formation with ^{22}Na radioactive positron source of radioactivity of 25 mCi.

LEPTA RING DEVELOPMENT

The Low Energy Particle Toroidal Accumulator (LEPTA) is designed for studies of particle beam dynamics in a storage ring with longitudinal magnetic field focusing (so called "stellatron"), application of circulating electron beam to electron cooling of antiprotons and ions in adjoining storage electron cooling of positrons and positronium in-flight generation.

For the first time a circulating electron beam was obtained in the LEPTA ring in September 2004 [1]. First experience of the LEPTA operation demonstrated main advantage of the focusing system with longitudinal magnetic field: long life-time of the circulating beam of low energy electrons. At average pressure in the ring of 10^{-8} Torr the life-time of 4 keV electron beam of about 20 ms was achieved that is by 2 orders of magnitude longer than in usual strong focusing system. However, experiments showed a decrease of the beam life-time at increase of electron energy. So, at the beam energy of 10 keV the life time was not longer than 0.1 ms. The possible reasons of this effect are the magnetic inhomogeneity and resonant behaviors of the focusing system.

Magnetic and Vacuum System Improvements

During March-May 2009 new measurements of the longitudinal magnetic field at solenoids connections were performed. According to the measurement results water cooled correction coils have been fabricated and mounted. As result, the inhomogeneity has been decreased down to $\Delta B/B \leq 0{,}02$ (Fig.1).

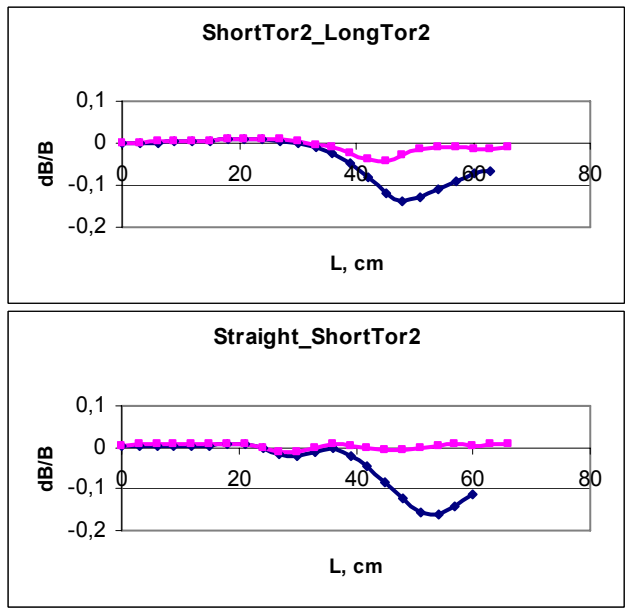

Figure 1: Magnetic field distribution along the toroidal solenoid axis.

The new water cooled helical quadrupole lens was designed and fabricated (Fig.2) that allowed us to improve significantly the vacuum conditions in the straight section.

Figure 2: The water cooled helical qudrupole.

To improve vacuum condition the evaporating titanium getter pumps manufactured at Budker INP have been mounted at the entrance and the exit of the straight section (Fig.3). First run of the pumps showed the average pressure decrease down to $5 \cdot 10^{-9}$ Tor at least.

* M.V.Lomonosov Pomor State University, Russia.
# kobets@jinr.ru

Figure 3: The evaporating getter pump.

Testing after Upgrading

After all the improvements and modifications the ring has been reassembled, the electron beam circulation has been obtained again and its life time has been remeasured.

Typical life time dependence on electron energy, τ_e(Ee), has two slopes (Fig.4). The left one, where τ_e increases with Ee, is defined by electron scattering on residual gas. The right slope, descending with Ee, relates to violation of electron motion adiabaticity on inhomogeneities of solenoid magnetic field.

The curves 1 and 2 were obtained in 2005, whereas the curves 3, 4 and the point 5 have been measured in June 2008. The curve 6 was measured in August 2009, after all modifications of the ring described above. One can see significant increase of the electron life time. Of the main importance is the increase of the life time (comparing with the values of the year 2005, 2008) in the energy range above 4 keV by 6÷10 times. It proves the necessity of a further improvement of the solenoid field homogeneity.

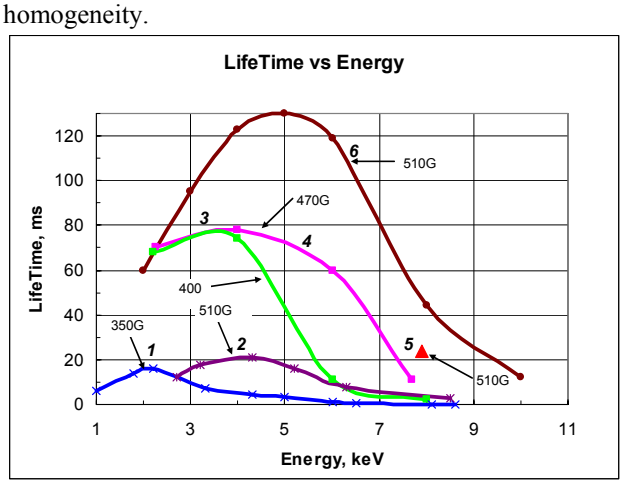

Figure 4: LifeTime vs electron energy.

An essential influence of magnetic field quality on τ_e value is demonstrated in Fig.5: the lifetime of 8 keV electrons increases significantly with correction coil current enhancement.

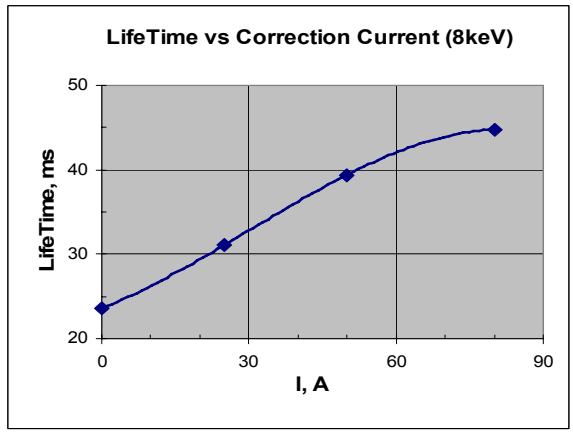

Figure 5: Lifetime vs correction coil current at electron energy of 8 keV.

Electron Cooling System Construction

The manufacturing of the system for generation, transportation and energy recovering of single pass electron beam has been completed at the beginning of the current year. Test of the electron beam transportation from the gun to collector was done in pulsed mode of the gun operation. The regime of the transportation system corresponded to the design one.

Positron Transfer Channel

The channel is aimed to transport positrons extracted from the trap of the injector (see below) and accelerate them up to 10 keV (maximum) in electrostatic field in the gap between the trap and the channel entrance. The designing of the channel elements is completed, their manufacturing is in progress.

TEST OF THE NEW POSITRON SOURCE

The slow monochromatic positron flux is formed from broad spectrum of positrons from radioactive isotope ^{22}Na (Fig.6). The positrons with energy up to 0,54 MeV are moderated to the energy of few eV in the solid neon [2]. The neon is frozen on the copper cone surface where capsule with isotope is located (Fig.7).

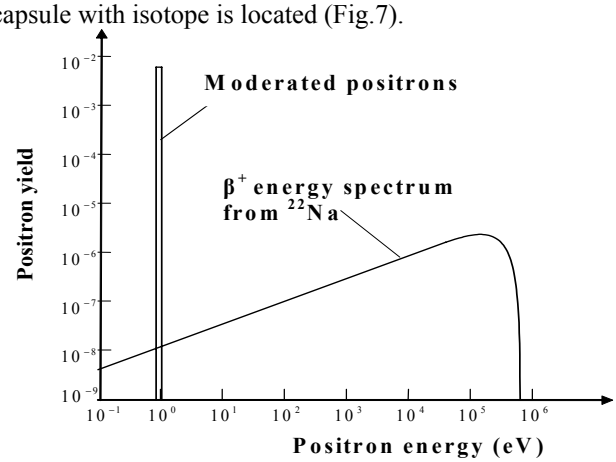

Figure 6: Positron spectrum from radioactive isotope ^{22}Na and moderated one.

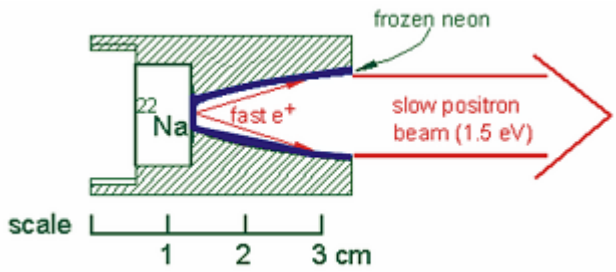

Figure 7: Positron moderation principle.

^{22}Na positron source of activity of 25mCi for LEPTA facility has been donated by iThemba LABS (RSA) and transferred to JINR in Febrary 2008. After completion of the very long procedure of formalities it was mounted in the LEPTA injector and tested (Fig.8).

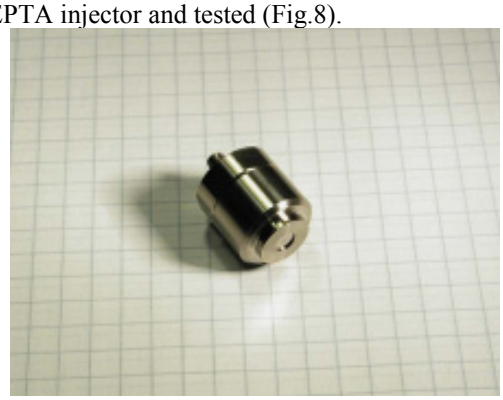

Figure 8: The positron source of iThemba Labs production.

To detect slow positron flux we used microchannel plate (MCP) detector and scintillater detector both working by coincidence scheme and independently. Efficiency of both detectors and maximum flux of slow positrons have been determined by standard method of analysis of a coincidence scheme counts. Integral spectra of slow positrons were measured with MCP and electrostatic analyzer - a short drift tube suspended at variable positive potential. The fitting of the experimental results are presented (Fig. 9).

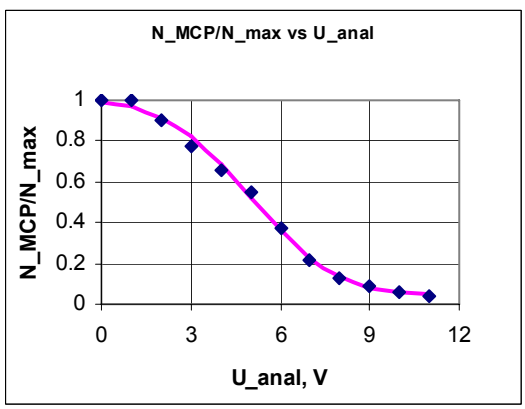

Figure 9: Gaussian fitting of positron energy spectrum curve measured at T = 7,35 K, d = 10 mcm, $(dN/dE)_{max}$ = 5.5 eV, spectrum width σ = 2.3 eV.

Maximum flux of slow positrons determined by standard method for coincidence scheme was equal:

$$N_{max} \approx 1.5 \cdot 10^5 \text{ positrons/ sec.}$$

THE POSITRON TRAP

When slow positron beam is formed, it enters the Penning-Malmberg trap where the positron cloud is accumulated [3]. The trap is a device which uses static electric and magnetic fields to confine charged particles using the principle of buffer gas trapping. The confinement time for particles in the Penning-Malmberg traps can be easily extended into hours allowing for unprecedented measurement accuracy. Such devices have been used to measure the properties of atoms and fundamental particles, to capture antimatter, to ascertain reaction rate constants and in the study of fluid dynamics. The JINR positron trap (Fig. 10) was constructed to store slow positrons and inject positron bunch into the LEPTA ring.

The research of the accumulation process was carried out using electron flux. For this purpose the test electron gun allowing to emit $dN/dt = 1*10^6$ electrons per second with energy 50 eV and spectrum width of a few eV was made. These parameters correspond to slow monochromatic positron beam which we expect from a radioactive source at activity of 50 mCi.

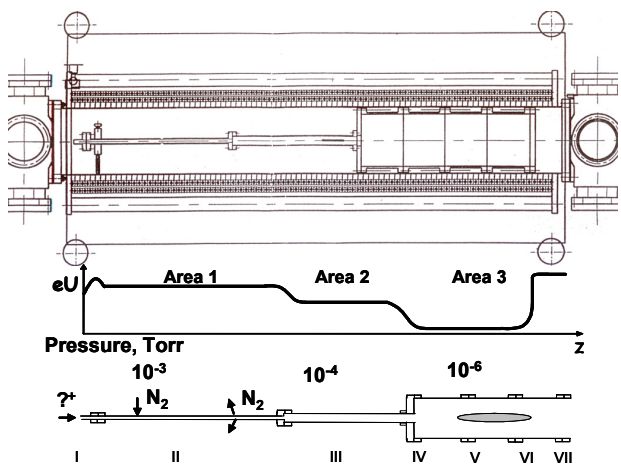

Figure 10: Assembly drawing of the positron trap (upper picture), potential and pressure distributions along the electrode system.

Electron accumulation in the trap with application of rotating electrical field [4] was studied during December 2006 and repeated in July 2009. One of the trap electrodes (Fig. 10, electrode IV) consists of four isolated segments, which are connected with sine voltage generator of amplitude A and frequency f (Fig.11). The phases of the voltage applied to each segment are shifted by 90^0 one to another one that forms rotating transverse electric field.

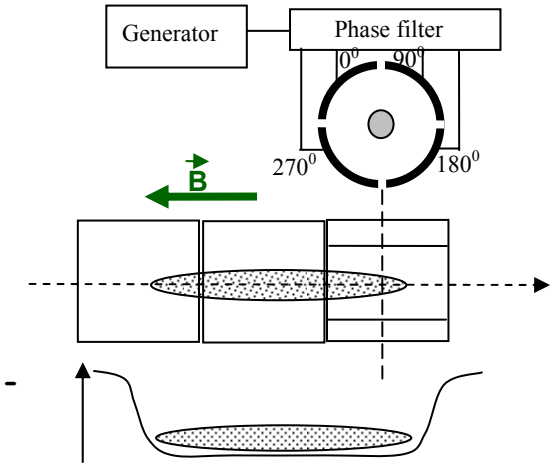

Figure 11: The rotating electrical field method.

The dependence of the accumulated electron number *N(t)* on accumulation time has been measured at different conditions (Fig.12). The curve 1 presents the function *N(t)* after optimization of distribution of pressure and electrode potentials. The curve 2 presents *N(t)* after optimization of the transverse correction magnetic field. The rotating field is OFF in both cases. The curve 3 gives *N(t)* after optimization of frequency and amplitude of the rotating electric field. The optimum frequency of rotation has been found equal to 650 кHz at the amplitude of 1V.

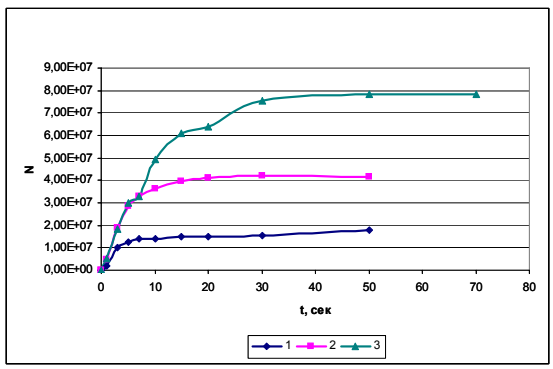

Figure 12: The trapped electron number as a function of storage time

CONCLUDING REMARKS

The development of the LEPTA project is approaching the stage of experiments with circulating positron beam. All main elements of the ring and the injector are ready and have been tested. The positron transfer channel is expected to be commissioned by the end of this year, that will allow us to start the experiments with positrons.

REFERENCES

[1] A. Kobets, et. al., Status of the LEPTA project, proceeding of Beam Cooling and Related Topics, http://accelconf.web.cern.ch/accelconf/.

[2] A.P. Mills, Jr. and E.M. Gullikson, “Solid Neon Moderator for Producing Slow Positrons”. Appl. Phys. Lett. 49, 1121 (1986).

[3] M. Amoretti et al., The ATHENA antihydrogen apparatus, Nucl. Inst.Meth. Phys. Res. A 518 (2004) 679-711.

[4] C.M. Surko, R.G. Greaves, Radial compression and inward transport of positron plasmas using a rotating electric field, Physics of Plasmas, 8 (2001), 1879-1885.

MUON COOLING IN A RACETRACK FFAG USING SUPERFLUID HELIUM WEDGE ABSORBERS

A. Sato , Osaka University, Osaka, Japan;
S. Ishimoto, KEK, Ibaraki, Japan

Abstract

A fixed field alternating gradient (FFAG) lattice with racetrack-shape has been proposed to cool muon beams. The ring has straight sections with FFAG magnets. Wedge absorbers using superfluid helium and RF cavities are installed to the straight section. This paper describes the first result of simulation study and R&D status of the superfluid helium wedge absorber.

INTRODUCTION

The 6D-emittance reduction of a muon beam is essential for future neutrino factories and muon colliders. Ionization cooling was proposed to achieve a quick muon cooling, since the muon lifetime is 2.2 s in its rest frame. The emittance reduction in the muon ionization cooling is achieved by repeated channels of an absorber and an RF cavity [1]. In order to demonstrate this cooling method, the MICE is in preparation at Rutherford Appleton Laboratory (RAL) [2]. A long muon cooling channel is necessary to achieve a required emittance reduction for a neutrino factory and a muon collider. Such channels need a high cost of construction. A cooling section using a ring (ring cooler) would be more cost-effective than that consists of straight channels, since a number of RF and absorbers would be reduced. Some designs for the ring cooler have been proposed [3]. These designs, however, have some issues must be solved: injection/extraction and its kicker system, effects of windows for absorbers and RFs.

The study in this paper is the first attempt to design a ring cooler using the following ideas:

- racetrack FFAG ring and
- superfluid helium wedge absorbers.

The racetrack FFAG can be realized by new ideas of a straight beamline consists of FFAG type magnets, which was proposed recently by Y. Mori and S. Machida, *et.al.* [7]. These ideas bring new possibilities to design of the scaling type FFAGs such as dispersion suppressing section in a FFAG ring and an enough space to install devices for kicker systems. New ideas with the racetrack FFAG are actively discussed for example in the PRISM task force [4] and FFAG workshops [5]. FFAG as a muon ring cooler is not well studied yet. Papers by H. Schönauer report the study on ionization cooling in Japan's FFAG-based neutrino facility [6]. However, there is no other papers on the muon ionization cooling in FFAGs.

A typical absorber material proposed in the muon cooling channels is liquid hydrogen, since it has the lowest multiple scattering due to its lowest Z and sufficient ionization loss. Since the liquid hydrogen is an explosive material, its mechanical and engineering design and cooling of the liquid hydrogen are very finicky [8]. On the other hand, helium has no explosion risk and the second lowest Z of any materials. For the superfluid helium, there are more advantages as the absorber material: a lower pressure than the liquid hydrogen and a high thermal conductivity. All of these properties would make the absorber design easier than that with the liquid hydrogen. A thinner absorber window can be used, and a cooling system for the absorber material can be simpler, for instance.

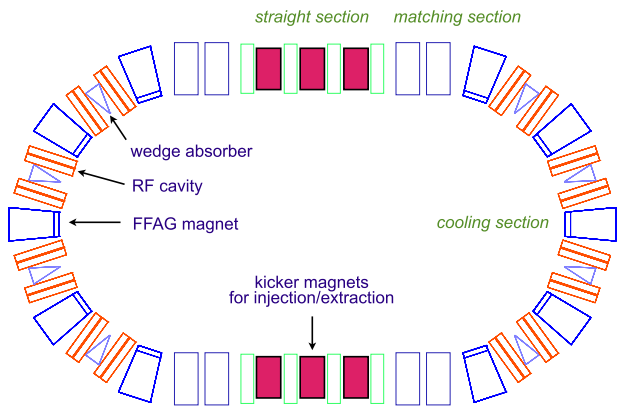

Figure 1: Concept of the muon ring cooler with a racetrack FFAG.

CONCEPT OF RACETRACK FFAG COOLER

Figure 1 illustrates a concept of the muon ring cooler with a racetrack FFAG. The ring is designed as a scaling type FFAG, since it can achieve a large transverse acceptance and a large momentum acceptance simultaneously. The ring consists of three sections: arc sections for the cooling, which has RF cavities and wedge absorbers; straight sections, which have an enough space to install kicker magnets for injection and extraction; and matching sections between the arc section and the straight section.

Zero-chromaticity and large momentum dispersion in a

sato@phys.sci.osaka-u.ac.jp

scaling FFAG would enable effective longitudinal cooling with wedge absorbers. Choosing cooling parameters carefully, 6-D cooling would be possible in this racetrack FFAG cooler.

MUON COOLING IN PRISM-FFAG BASED LATTICE

As the first step of study for the racetrack FFAG cooler, muon cooling in a FFAG ring cooler based on the PRISM-FFAG [9] lattice have been studied. Figure 2 shows a ring used in this study. Parameters for the ring are summarized in Table 1. A set of lattice parameters of the PRISM-FFAG ring is used for this study except for the central momentum of the muon beam and the magnitude of magnetic field. The central momentum is 308 MeV/c, since the momentum region of 200-300 MeV/c is suitable for the ionization cooling. Magnetic fields of FFAG magnets are calculated by Opera-3d. The beta function and dispersion function are shown in Fig.3 and Fig.4, respectively. This ring cooler lattice would show a possibility of PRISM-FFAG type FFAG ring as a muon ring cooler and can be considered as a racetrack FFAG without straight sections: an ultimate case of the racetrack. Eight set of four RF cavities and four liquid hydrogen wedge absorbers is installed to the ring as shown in Fig.2. Parameters of the RF cavities and the absorbers are listed in Table 2. The opening angle of the wedge absorbers is adjusted to achieve the minimum momentum spread of the muon beam after 15 turns in the ring. A muon beam is injected to the ring at the point A in Fig.2. The beam eminence at the injection point is summarized in Table 3. The g4beamline [10] is used as a tracking code in this study. The beam information is recorded at the point A at every turn until the 15th turn.

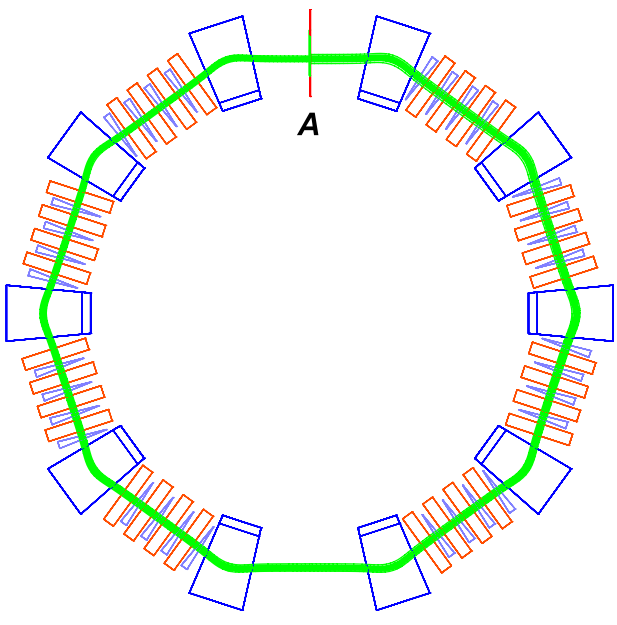

Figure 2: A PRISM-FFAG based lattice for muon ionization cooling used in this simulation study.

Table 1: Parameters of the PRISM-FFAG based lattice for muon ionization cooling.

Circumstance (m)	38
Number of cells	10
Field index k	4.6
F/D ratio	6.0
Maximum field (T)	1.6
Central momentum (MeV/c)	308
Magnet type	DFD triplet
Magnet aperture	H:100 cm V: 30 cm
Horizontal tune	2.73
Vertical tune	1.58

Table 2: Parameters of the RF cavities and the absorbers.

Circumstance (m)	38
Total number of cells	10
Cell with RF cavities and absorbers	8
Central momentum P_0 (MeV/c)	308
Number of wedge absorbers per cell	4
Wedge thickness on r_0 for P_0(cm)	8.672
Wedge opening angle (degree)	3.86
Absorber material	LH_2
Number of cavities per cell	4
Cavity length (cm)	28.75
RF gradient (MV/m)	8.709

Table 3: Beam emittance of the injected muon beam.

E_0^{kin}		220	MeV
P_0		308	MeV/c
σ_x		4	cm
σ_{p_x}		15.4	MeV/c
$\sigma_{x'}$	$=\sigma_{p_x}/P_0$	0.05	
ε_x^{norm}	$=\sigma_x\sigma_{x'}$	0.582	cm
σ_y		4	cm
σ_{p_y}		4.6	MeV/c
$\sigma_{y'}$	$=\sigma_{p_y}/P_0$	0.015	
ε_y^{norm}	$=\sigma_y\sigma_{y'}$	0.175	cm
σ_{cT}		8	cm
σ_T		0.2667	ns
σ_{dE}		20	MeV
σ_{p_z}		21.1	MeV/c
ε_L^{norm}	$=\sigma_{cT}(\sigma_{p_z}/P_0)$	1.591	cm
ε_{6D}	$=\varepsilon_x^{norm}\varepsilon_y^{norm}\varepsilon_L^{norm}$	0.16	cm^3

Figure 5, 6, and 7 show the tracking results of horizontal, vertical, and longitudinal phase space, respectively. No emittance reduction was observed in every phase space in this study, although the momentum spread was converted to the time spread as shown in Fig.7. The number of survived muon at each turn was quickly reduced as shown in the figures. These results would be caused by a large beta func-

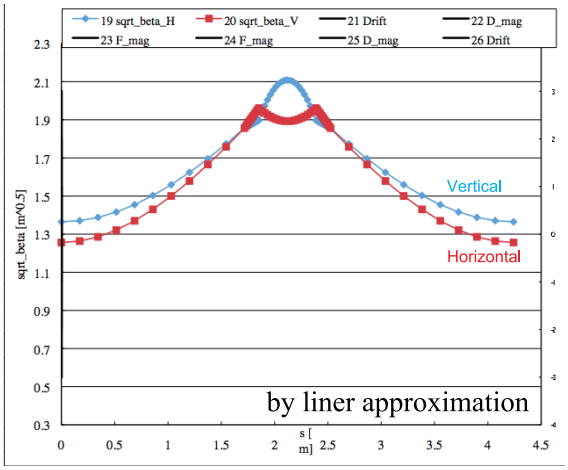

Figure 3: Beta function of the PRISM-FFAG based lattice.

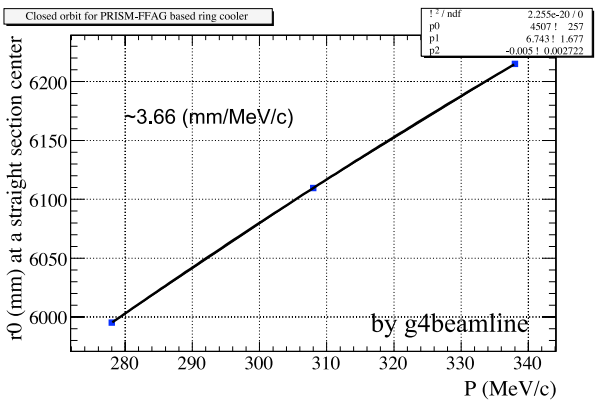

Figure 4: Dispersion function of the PRISM-FFAG based lattice.

tion of this lattice: $\sqrt{\ }$ [$\sqrt{m}$]=1.25 for horizontal and 1.37 for vertical at the center of straight sections and probably improper parameters of RF and absorbers. In order to improve the cooling efficiency, much detailed studies will be performed. Using this system, cooling tests with a heater in the absorber will be carried out in the coming year.

R&D ON SUPERFLUID HELIUM WEDGE ABSORBER

The superfluid helium is safer than liquid hydrogen as an absorber material for the muon cooling and has a high thermal conductivity, which is useful to reduce heat from the muon beam. A superfluid helium absorber, however, is never developed yet so far. A cryostat and a prototype of the wedge absorber for superfluid helium have been constructed in KEK. Figure 8 is a picture of the prototype wedge absorber.

SUMMARY AND FUTURE PROSPECTS

A new muon ring cooler using a racetrack FFAG and wedge absorbers with superfluid helium have been proposed. Its R&D has just been started. As the first attempt, the PRISM-FFAG based lattice was studied. The lattice with the RF and absorber parameters in Table 2 was, however, not suitable for a ring cooler. Possible causes are large beta functions, not enough acceptance, and improper parameters of RF and absorbers. In order to improve the cooling efficiency, much detailed studies will be performed. A new lattice for the ring cooler must be designed. Then matching and straight section including a kicker system for injection and extraction will be studied to complete a racetrack FFAG ring cooler. A cooling test of a superfluid helium wedge absorber will be performed soon.

ACKNOWLEDGEMENT

This work was supported by Grant-in-Aid for Scientific Research (B) No.18340065 from the Ministry of Education, Science, Sports, and Culture, Japan.

REFERENCES

[1] D. Neuffer, Nucl. Instrum. and Meth. A 532 (2004) 26–31,

[2] `http://mice.iit.edu/`,

[3] R.B. Palmer, Nucl. Instrum. and Meth. A 532 (2004) 255–259,

[4] `http://www.hep.ph.ic.ac.uk/muec/meetings/20090701/`,

[5] Web site for FFAG09: `http://conferences.fnal.gov/ffag09/`,

[6] H. Schönauer, Nucl. Instrum. and Meth. A 503 (2003) 318–321; H. Schönauer, J. Phys. G: Nucl. Part. Phys. 29 (2003) 1739–1742,

[7] J. B. Lagrange, *et.al.*, "Straight Section in Scaling FFAG Accelerator", Proceedings of PAC09, FR5PFP002; Y. Mori, " Advanced Scaling FFAG for Muon Accel- eration, " presented at NuFact09 (op. cit.); T. Planche, " Scaling FFAG Straight Lines and their Applications, " ; S. Machida, "Beam Transport Line with a Scaling Type FFAG Magnet", Proceedings of PAC09, FR5PFP026,

[8] M. A. C. Cummings *et.al.*, "PROGRESS ON THE LIQUID HYDROGEN ABSORBER FOR THE MICE COOLING CHANNEL", Proceedings of PAC05, pp.1772–1774,

[9] A. Sato *et al.*, "R&D Status of the High-intense Monochromatic Low-energy Muon Source: PRISM", EPAC'06, Edinburgh, UK, June 2006, WEPLS056, (2006) ,

[10] T. Roberts *et al.*, "G4Beamline Simulation Program for Matter-dominated Beamlines", PAC07, Albuquerque, New Mexico, USA 2007, THPAN103, p. 3468 (2007),

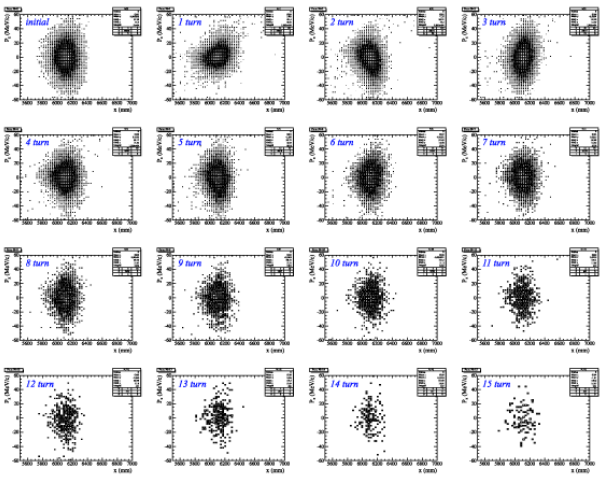

Figure 5: Tracking result: Vertical phase space.

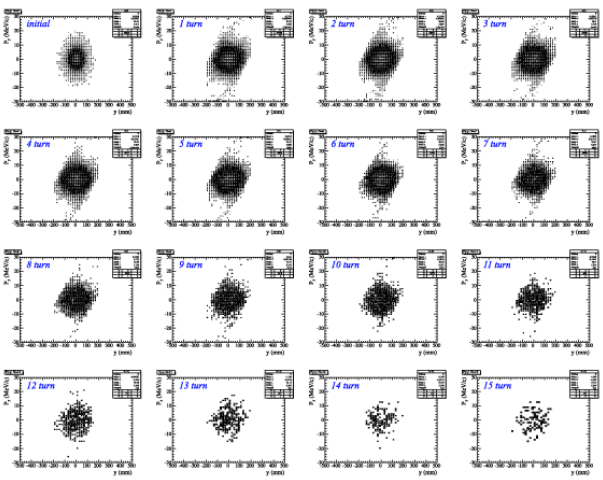

Figure 6: Tracking result: Horizontal phase space.

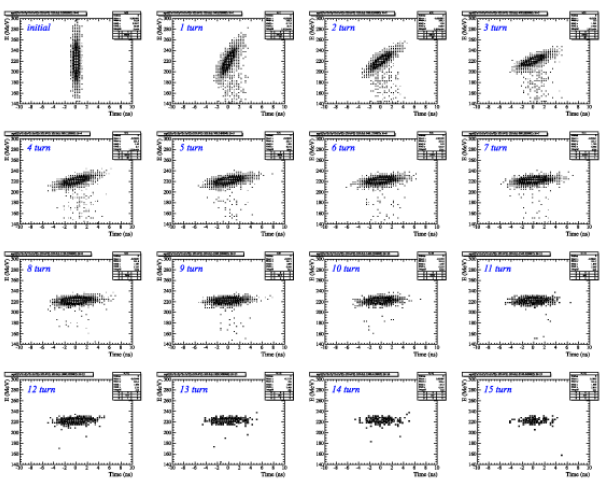

Figure 7: Tracking result: Longitudinal phase space.

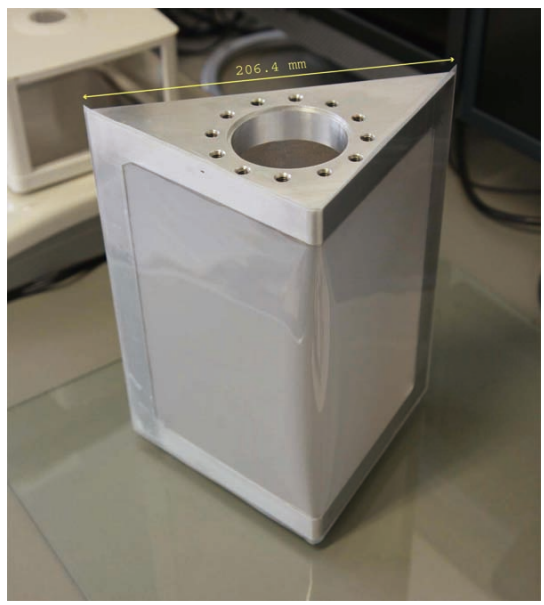

Figure 8: Container of the first prototype of the Superfluid Helium Wedge Absorber.

COOLING STACKING EXPERIMENTS AT HIMAC

T. Shirai#, T. Furukawa, K. Mizushima, K. Noda,
National Institute of Radiological Sciences (NIRS), 4-9-1 Anagawa, Inage, Chiba 263-8555, Japan.
S. Shibuya,
Accelerator Engineering Corporation (AEC), 2-12-1 Konakadai, Inage, Chiba 263-8555, Japan.
T. Nakamura, K. Kobayashi, JASRI/SPring-8, 1-1-1 Kouto, Sayo-cho, Hyogo, 679-5198, Japan

Abstract

^{11}C beam acceleration has been studied in order to form and verify a three-dimensional irradiation field for cancer radiotherapy at HIMAC. In the project, the ^{11}C beam is generated in the ion source and injected to HIMAC synchrotron. The cooling stacking technique plays an important role because of the low intensity of ^{11}C (several 10^7 /injection). The numerical target of the stored ^{11}C is 10^9 in the ring, which is a sufficient number to irradiate a single slice in the 3D scanning irradiation method. We have preceded the cooling stacking experiments using ^{12}C. The issues of the cooling stacking at HIMAC are the cooling time and the coherent instability. The cooling time becomes 2 sec after the improvements of the ion trapping. The coherent instability can be suppressed by the digital beam feedback system. The stacking of 8×10^9 particles is achieved with the feedback.

INTRODUCTION

Since 1994, the carbon beam treatment has been continued at the Heavy Ion Medical Accelerator in Chiba (HIMAC) [1]. The total number of patients reaches more than 4000. Based on the experience of the treatment, we have constructed the new facility for the further therapeutic developments [2]. The research subjects are the fast 3D scanning system toward the adaptive therapy and a gantry system for the intensity modulated carbon therapy. Another future subject is the radioactive beam irradiation such as ^{11}C in order to confirm the dose distribution directly.

Figure 1 (a) shows the treatment plan for head phantom by the carbon beam irradiation [3]. The irradiation shape is concave. Figure 1 (b) shows the PET-CT image after 1 Gy irradiation of ^{12}C. The positron emitter is created along the beam track and the image shows the irradiation area. But it is difficult to compare it with the treatment plan quantitatively. On the other hand, Fig. 1 (c) shows the PET-CT image after 1 Gy irradiation of ^{11}C, which is the positron emitter beam. It was carried out in the secondary beam line at HIMAC. The image clearly shows the stop point of the ^{11}C beam. It is possible to compare with the treatment plan without model calculation. The event rate of PET is also higher than the ^{12}C irradiation. However, the fragment reaction is used for the present ^{11}C irradiation at HIMAC and the beam rate is less than 10^7 pps. It is too low for the normal treatment, because the particle number of 10^{10} is necessary even by the scanning irradiation.

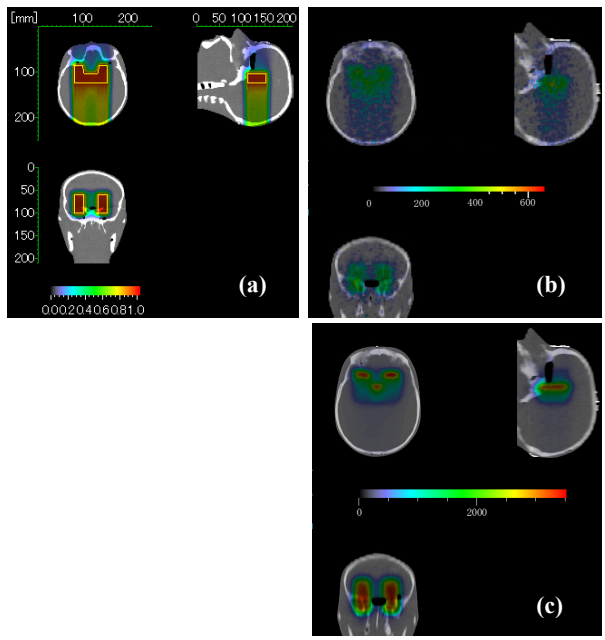

Figure 1: Dose distribution of the treatment planning for head phantom (a) and the measured image by PET-CT after the beam irradiation of ^{12}C , 1 Gy (b) and ^{11}C , 1 Gy (c) [3].

In order to increase the ^{11}C beam intensity for the treatment, we are planning to use the direct ^{11}C beam acceleration scheme from ion source to synchrotron [4]. Figure 2 shows the schematic diagram of the system. It is the application of the drug generation technique for PET. The separation of ^{11}C is carried out with liquid Ar using the difference of the melting point. The separation efficiency is around 50 % [4]. The atoms of ^{11}C are provided to ECR ion source.

Although the sufficient numbers of ^{11}C atoms are generated by the proton beam irradiation, the number of the injected ^{11}C to the synchrotron is rather limited due to the low efficiency of the compression and the ionization processes. The expected number of ^{11}C is less than 10^8 per one injection. Typically, the 10^{10} particles are necessary for the treatment but the ^{11}C particles are sufficient for one slice irradiation by the 3D scanning method. If we can irradiate a slice with the single injection, the non-uniformity of the dose distribution can be avoided. We

t_shirai@nirs.go.jp

have proposed to use the cooling stacking in order to increase the ^{11}C beam intensity from several 10^7 to 10^9.

The main specifications of HIMAC and the HIMAC electron cooler are shown in Table 1. We discuss here two issues for the cooling stacking at HIMAC, the cooling time and the coherent instability.

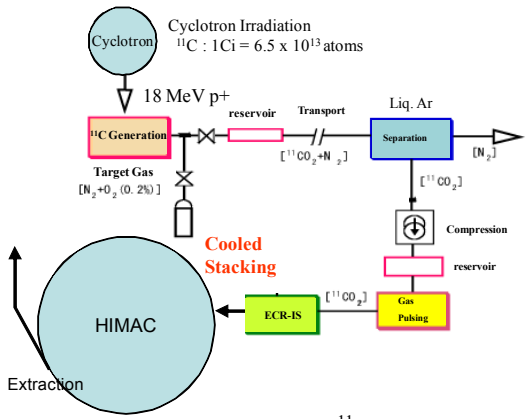

Figure 2: Schematic diagram of the ^{11}C beam acceleration system [4].

Table 1: HIMAC Parameters at Cooling Stacking

HIMAC Ring	
Circumference	129 m
Stack intensity	$10^9 \sim 10^{10}$
Ion Species, Energy	^{12}C, 6 MeV/n
Betatron tunes	3.73 / 3.11
Injection Repetition	3.3 sec
Electron Cooler	
Current	50 mA ~ 300 mA
Cathode Diameter	35 mm
Magnetic Field	500 Gauss
Magnetic Expansion Factor	3.3

COOLING TIME

The injection repetition rate at HIMAC is 3.3 sec and the beam lifetime at the injection energy is around 30 seconds. If the cooling time is less than 3.3 sec, the cooling stacking gain of 10 is expected. The calculated cooling time by BETACOOL [5] is almost consistent with the electron current of 50 mA. However, the cooling time was not shortened with the higher current in the past.

We have measured the cooling time with the various parameters of the ion clearing potential. The cooling time is measured by the sheet beam profile monitor [6]. The ion clearing electrode is a quadratic one and the location is shown in Fig.3. When the quadratic electric potential (+-+-) of +/-1 kV is applied, the cooling time becomes constant with the electron current of higher than 100 mA. It is improved with the dipole electric potential (++--). Figure 4 shows the relation between the electron current and the cathode voltage of the electron, when the ion velocity is kept constant. The ion clearing potential is dipole pattern and the voltage is -1 kV, 0 kV and +/-1 kV. With the voltage of -1 kV and 0 kV, the drop of the cathode voltage is observed, which shows the ion trapping. It is improved with the voltage of +/-1 kV.

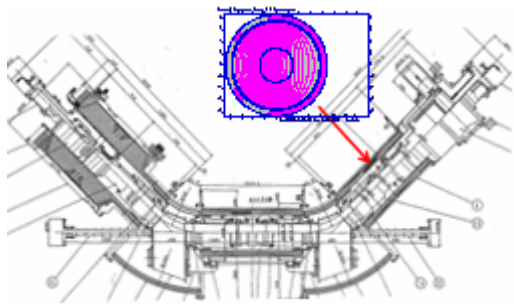

Figure 3: Cut view of the HIMAC electron cooler and the field distribution of the ion clearing electrode.

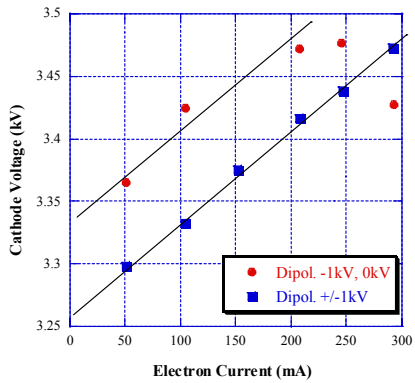

Figure 4: Relation between the electron current and the cathode voltage of the electron, when the ion velocity is kept constant.

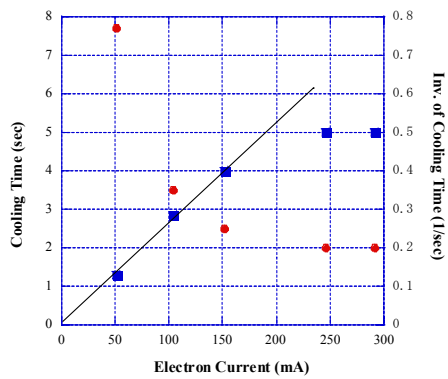

Figure 5: Cooling time and the reciprocal number as a function of the electron current. The clearing voltage is dipole pattern of +/-1 kV.

Figure 5 shows the cooling time and the reciprocal number of it as a function of the electron current. The ion clearing voltage is dipole pattern of +/-1 kV. The reciprocal of the cooling time is proportional to the electron current up to 150 mA, but it shows the plateau with the higher current. The improvements are still necessary to reach the cooling time of 1 sec, which corresponds to the maximum injection rate at HIMAC.

COHERENT BEAM INSTABILITY

Another issue of the cooling stacking is a coherent instability. Figure 6 (a) is the typical trend of the DC-CT signal. The maximum stored particle is $2x10^9$ with the electron cooling. It corresponds to the ion current of 480 eμA. The source of the beam loss is the coherent vertical oscillation. Even below 10^9 particles, the oscillation is observed. The oscillation frequency is around 10 MHz with the revolution frequency of 0.25 MHz.

We applied the digital feedback system for the beam orbit [7]. The pickup signal is processed by the digital filtering and the delay and gain unit in FPGA box and applied to the electrostatic kicker through 10 W power amplifier. The processing cycle is 100 MHz and enough faster than the typical oscillation period. The digital feedback system has some advantages compared with the analogue one. It can suppress the horizontal and vertical oscillation from the single input and subtract the offset signal by the filter. Figure 6 (b) shows the DC-CT with the feedback. The maximum particle number is increased to 8 x 10^9 and the coherent oscillation is not observed below 10^9 particles.

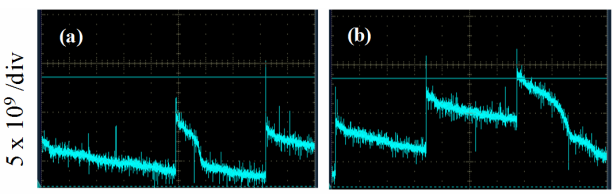

Figure 6: Trend of the DC-CT signal during the cooling stacking without feedback (a) and with feedback (b).

In the compact cooler ring, S-LSR at Kyoto University, the similar vertical coherent oscillation has been observed in the cooling stacking [8]. The maximum particle number without feedback is around $1.5x10^9$ protons in the ring, which corresponds to 400 eμA. The oscillation frequency is around 90 MHz with the revolution frequency of 1.6 MHz. Table 2 shows the comparison of the results between HIMAC and S-LSR. The threshold current of the instability and the ratio between the oscillation and the revolution frequency are similar in the two rings. The ring size and the vacuum pressure are different but the cooler parameters are similar, such as the electron energy and the magnetic field.

Figure 7 shows the demonstration of the low current cooling stacking of ^{12}C. The injection beam current is $3x10^8$ and after the 10 times injection, the beam current reaches 2.5 $x10^9$. The maximum current is limited by the coherent oscillation.

Table 2: Comparison of the Coherent Oscillation Measurements between HIMAC and S-LSR

HIMAC Ring	HIMAC	S-LSR
Circumference	129 m	22.6 m
Ion Species, Energy	^{12}C, 6 MeV/n	p, 7 MeV
Betatron tunes	3.73 / 3.11	1.64 / 1.21
Threshold Number	$2x10^9$ $^{12}C^{6+}$	$1.5x10^9$ p^+
Threshold Current	480 μA	400 μA
Oscillation Frequency	10 MHz	90 MHz
Revolution Frequency	0.25 MHz	1.6 MHz
Vac. Pressure	10^{-6} Pa	10^{-8} Pa
Solenoid Field	500 Gauss	500 Gauss

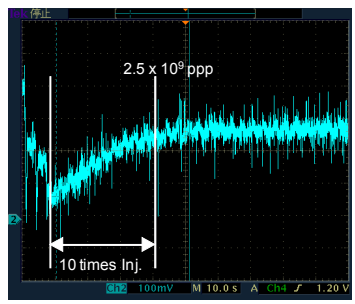

Figure 7: Trend of the DC-CT signal during the cooling stacking.

CONCLUSION

We have improved the ion trapping at HIMAC electron cooler and studied the cooling stacking of ^{12}C toward the future ^{11}C stacking. The cooling time is still longer than our target number of 1 sec but we can confirm the feasibility. We go forward the ^{11}C ion source development in parallel and will evaluate the actual particle number from the ECR ion source.

REFERENCES

[1] Y. Hirao et al., Nucl. Phys. **A538** (1992) 541c-550c.
[2] K. Noda et al., Nucl. Instrum. and Meth. in Phys.Res. B **266** (2008) p.2182.
[3] T. Inaniwa, private communication.
[4] S. Hojo et al., Nucl. Instrum. and Meth. in Phys.Res. B **240** (2005) p.75.
[5] http://lepta.jinr.ru/betacool.htm.
[6] Y. Hahimoto et al., Nucl. Instrum. and Meth. in Phys.Res. A **527** (2007) p.289.
[7] T. Nakamura, K. Kobayashi,Proc. of ICALEPCS, (2005) p.3022.
[8] T. Shirai et al., Proc. of HB2006, Tsukuba, Japan (2006).

APPLICATION OF BPM IN HIRFL-CSR ELECTRON COOLER

Guohong Li#, Xiaodong Yang, Lijun Mao, Jie Li, Tailai Yan, Xiaoming Ma
Institue of Modern Physics, CAS, Lanzhou, China

Abstract

In order to measure the positions of ion beam and electron beam at the same time, two sets of capacitive cylinder beam position monitors were installed in the two ends of electron cooling section. The NI-5105 (8 channel High-Density Digitizer) was adopted as main data acquisition and the data was processed by the special code of LabView. With the help of these systems, the positions of electron beam and ion beam were measured during the process of accumulation and acceleration in CSRm. The movement of cooling force was observed in the case of different relative position (angle) in CSRe.

INTRODUCTION

CSR is a double cooler-storage-ring with a main ring (CSRm) and an experimental ring (CSRe). Two electron coolers located in the long straight sections of CSRm and CSRe.

In CSRm e-cooling is used for the beam accumulation. In CSRe e-cooling is used to compensate the growth of beam emittance during internal-target experiments or to provide high-quality beams for the high-resolution mass measurements of nuclei. For the two e-coolers, the hollow e-beam can be obtained to partially solve the problem due to space charge effect of recombination between the ions and the e-beam.[1]

The parameters of CSR coolers are listed in Table 1.

Table 1: Parameters of CSR Coolers

Parameters	CSRm	CSRe
Energy Ion [MeV/u]	10-50	25-500
E [keV]	4-35	10-300
Ion beam momentum spread	$\pm1.5\times10^{-3}$	$\pm1.5\times10^{-3}$
Ion beam divergences [mrad]	4.7, 1.3	2.0, 1.4
Ion beam emittance [π·mm·mrad]	150, 20	30, 30
e-beam radius at cooling section [cm]	2.9	2.9
Magnetic expansion factor	1- 4	1- 10
Length of cooling section [m]	4.0	4.0
Effective cooling section length [m]	3.4	3.4
β at cooling section [m]	10.0,17.0	12.5, 16.0
Parallelity of cooling solenoid field	$\leq1\times10^{-4}$	$\leq1\times10^{-4}$
Electron loss rate	$\leq3\times10^{-4}$	$\leq3\times10^{-4}$
HVPS stability	$\pm1\times10^{-5}$	$\pm1\times10^{-5}$
Electron beam current [A]	3 (1.0A@5.5keV)	

ligh@impcas.ac.cn

BPM SYSTEM

The basic principle of electron cooling requires the ion beam is parallel with the electron beam. In order to measure the positions of ion beam and electron beam at the same time, a beam position measurement system was developed for the HIRFL-CSR electron cooling device, which is consist of some capacitive cylinder linear-cut probes, a NI-5105 (8 channel High-Density Digitizer) and some PET-amplifier (AM-4A-000110-11030N).

Due to the electron beam is direct current, this monitor can not get the signal, and the electron beam was modulated by an external 3MHz signal. The system was illustrated in Fig.1.

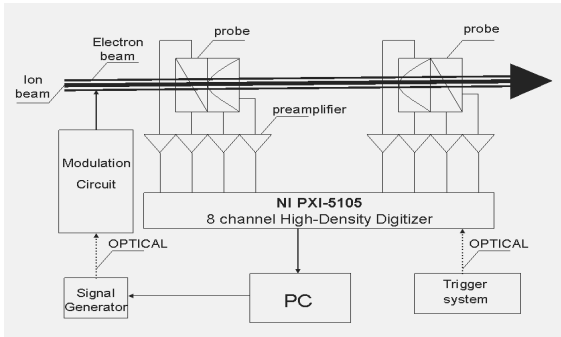

Figure 1: Layout of BPM system for HIRFL-CSR COOLER.

Probes were made of cylinder stainless steel, which specs are 80mm (length), 100mm (radius) and 1mm (thickness). They are sensitive and linearizing due to their induction and linear-cut configuration. Signal processing system consisted of preamplifiers and high-density digitizer. Preamplifier is PET P/N AM-4A-000110-11030N, which specs are 1MHz-1000MHz (BW), 54dB (gain) and 50Ω (input\output impedance). High-Density Digitizer is NI 12-bits and 8-channel PXI-5105, which specs are 60MS/s (sampling rate), 60MHz (BW), $150mV_{pp}$-$30V_{pp}$ (input voltage range) and 50Ω\1MΩ (input impedance).

The electron beam was modulated by an external 3MHz signal in electron gun-side. In order to prevent electromagnetic interference resulted from high voltage device, the external modulation signal was converted to optical signals and transmitted to the modulator module via fiber.[2]

The signals picked up by probes were magnified by independent preamplifiers. The data was processed by the special code of LabView. The both beam position were derived from the picking up signals of electrodes with the help of FFT method. The positions of electron and ion

beam at the same time were distinguished by different frequency spectrum. Fig.2 shows the mixed signal of electron and ion beam. The 'a' means mixed signal in time domain. The 'b' and 'c' mean the analysis of electron and ion beam mixed signal in frequency domain.

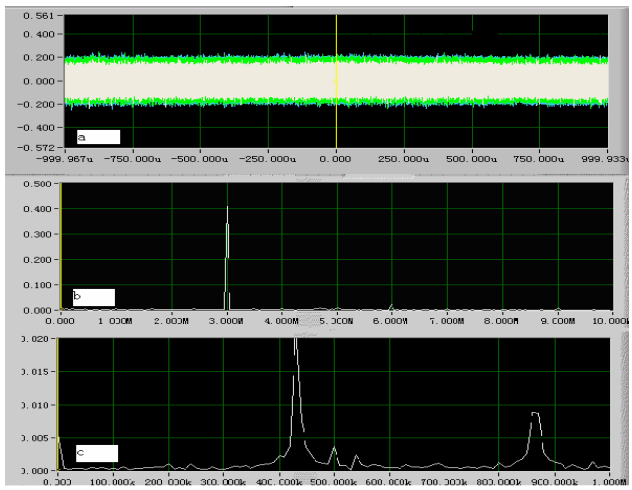

Figure 2: Electron and ion beam mixed signal analysis.

POSITION MEASUREMENT

CSRm

The positions of electron and ion beam at the same time are important parameters during an accumulation and acceleration period because e-cooling was used for ion beam accumulation.

Figure 3 illuminates the C^{4+} beam current situation during an accumulation and acceleration period 7~25~175MeV/u. The mark 'a' means the first RF capture after 19 accumulations and the mark 'b' means the second RF capture when the C^{4+} energy is 25MeV/u. The mark 'c' means the end of acceleration when the C^{4+} energy is 175MeV/u.

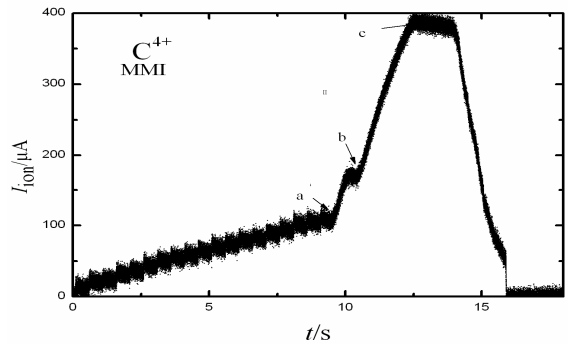

Figure 3: C^{4+} beam current during an accumulation and acceleration period.

The positions of ion beam and electron beam at different time of mark 'a', 'b' and 'c' were obtained by the help of BPM system in CSRm cooler. Fig.4 shows the electron beam and ion beam positions in two ends cooler at mark times. The ion beam is parallel with the electron beam by adjustment correct coils which was installed in cooling device and correct magnet near the cooler.

CSRe

In order to compensate the growth of beam emittance during internal-target experiments and provide high-quality beams for the high-resolution mass measurements of nuclei, the cooler in CSRe must keep a better cooling effect. With the help of the BPM system for cooler, positions of electron beam and ion beam was obtained. And the ion beam is parallel with the electron beam after adjustment of correct coils for electron and correct magnet for ion. Fig.5 illuminates the electron beam and ion beam positions in CSRe cooler after adjustment.

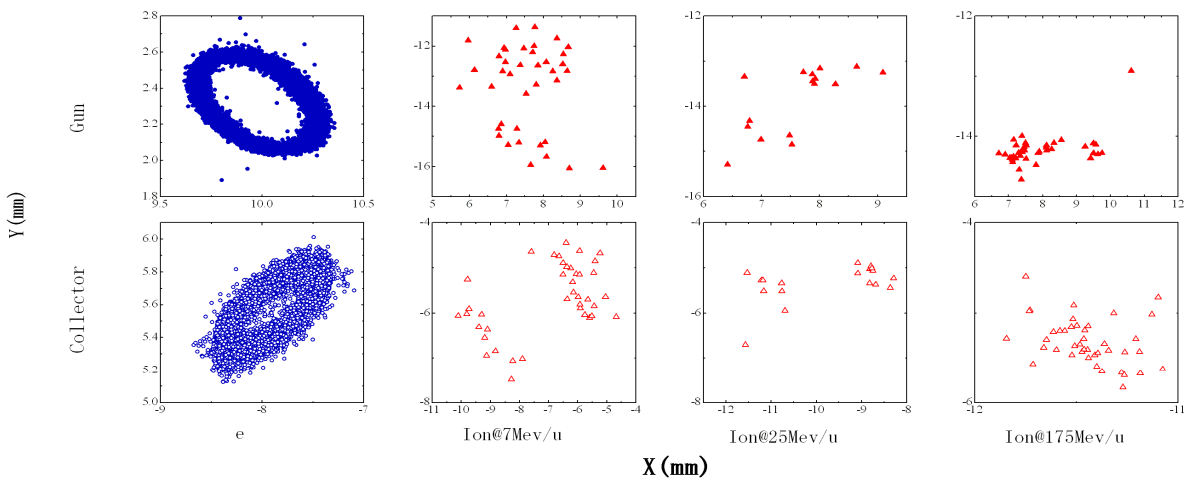

Figure 4: An accumulation and acceleration period for C^{4+} ion beam.

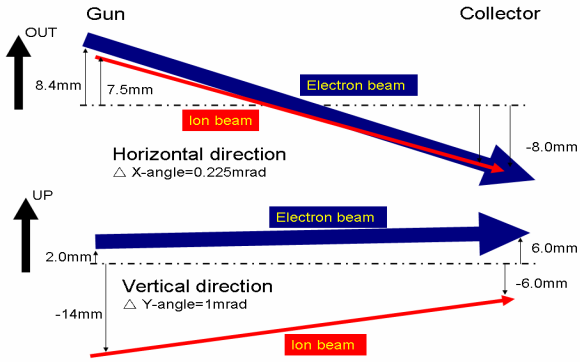

Figure 5: Beam positions in CSRe cooler.

COOLING FORCE MEASUREMENT RESULT

Cooling force is important parameter in cooling process. The fast shift of electron gun cathode voltage will leads to distinct speed different between electron and ion when the cooling effect is good. And cooling force can be measured by a frequency analysis from Schottky signals.

Longitudinal cooling force movement will be observed when the angle between electron and ion beam was changed. Figure 6 [3] shows the cooling force measurement results when the vertical angle between electron beam and ion beam was changed about 21.6MeV/u Ar^{18+} in CSRm. Fig.7 shows the cooling force measurement results when the electron beam horizontal and vertical position was changed by correct coils CX6 and CY6 which were installed in the middle of cooling section of 400MeV/u C^{6+} in CSRe.

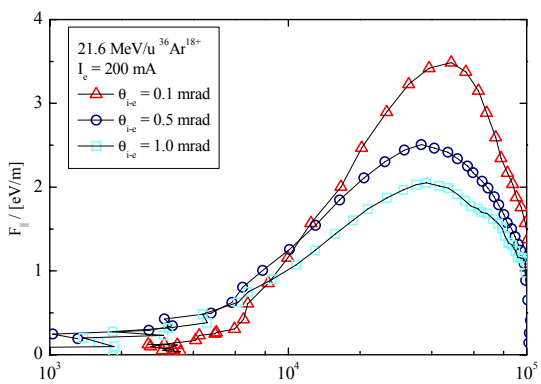

Figure 6: Ar^{18+} beam cooling force measurement at different angle between ion and electron beam in CSRm.

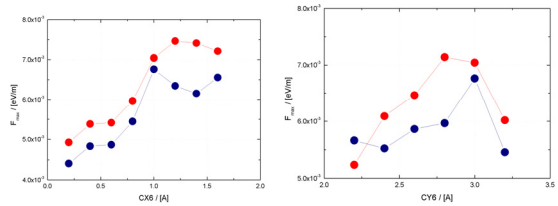

Figure 7: C^{6+} beam cooling force measurement at different angle between ion and electron beam in CSRe.

CONCLUSION

BPM system in HIRFL-CSR can measure the ion beam and electron beam positions at the same time. With the system's help the angle between ion beam and electron beam will be adjusted to decrease and the cooling effect will be better. Cooling force was measured at different angle between ion beam and electron beams.

REFERENCES

[1] Xia J.W, Zhan W.L, Wei B.W, et al. Nucl Instr and Meth. 2002, A488:11.
[2] E. Bekhtenev. Problems of Atomic Science and Technology. 2006(46):108.
[3] Mao Lijun. Doctoral Dissertation. 2006(46):108.

STUDY ON THE OXIDE CATHODE FOR HIRFL-CSR ELECTRON COOLER

Xianheng Liao, Xiaoxia Wang,Qinglan Zhao, Mingfeng Meng,Yun Li
R&D Center Microwave for Device and Technology,
Institute of Electronics, Chinese Academy of Sciences, Beijing 100190 P.R. China

Abstract

The oxide cathode is still wildly used in vacuum electronic devices as electron sources. With the ongoing development of electronic devices, the requirements for the emission characteristics of the cathode have to be enhanced to suit the new applications. It is a promising research direction improving the emission characteristics of the cathode at a low operating temperature and simple manufacture technology.

This paper studied the manufacture technology and properties of the oxide cathode and its emission mechanism. Then a new type of oxide cathode is developed and tested for its emission properties and lifetime. Its emission characteristic is better than that of the conventional oxide cathode. Part of properties of the cathode used in HIRFL-CSR Electron cooler is tested. The results show that the new oxide cathode is suitable to the electron cooler applications.

Keywords: Electron cool, Oxide cathode, Emission current

INTRODUCTION

The oxide cathode is a cathode coated $BaSrCa(CO_3)$ on the surface of Ni base or W filament. When heated it in vacuum, the $BaSrCa(CO_3)$ is decomposed into BaSrCaO, and Ba is produced when BaO reacted with the activators like Si and Mg in the Ni base, which make the cathode emit electrons. The oxide cathode has been developed more than 100 years. It is widely applied in electric light source, transmitter-receiver tube, grid control tubes, CRTs, space TWTs, high power klystrons[1,2,3,4] and electron cooler[5,6] because of its low operating temperature, large pulse emission current density, simple manufacture technology and low cost. However, the application of the oxide cathode is restricted in dc and wide pulse, high duty ratio pc emission tube because of its coating resistance and the interface layer resistance produced during the cathode operating process. For many years, worldwide scholars have programed a great deal of research to solve this problem.

In 1986, Saito[7] developed the rare-earth doped oxide cathode, doping 0.12-0.20% rare-earth oxide (Sc_2O_3 or Y_2O_3) in the coating of the conventional oxide cathode. The emission capability and lifetime of the rare-earth oxide cathode exceed that of the conventional oxide cathode because of its high coating electrical conductivity with the free Sc released by $BaSc_2O_4$'s reaction with the oxide in the coating. In the 1970's, a new type of oxide cathode has been developed in IECAS[8]. With the low coating resistance and little interface layer resistance, the cathode has high reliability, large current and long lifetime and has been applied to high power klystrons, long lifetime satellite TWTs and some special devices.

This paper analyzed the material composition of the oxide Cathode for HIRFL-CSR Electron cooler, and the emission characteristic such as dc, pc and the lifetime of this cathode is compared with that of the new oxide cathode developed by us through diode testing. The result shows that the lifetime and reliability of the electron gun for HIRFL-CSR electron cooler can be improved.

THE CATHODE STRUCTURE IN ELECTRON COOLER

The main parameters of the cathode: the convex radius of the cathode is 48mm, the diameter is Φ30mm, the Ni sponge is sintered on the cathode surface and its diameter is 28mm, a layer carbonates is sprayed on the Ni sponge. This kind of cathode is Ni sponge oxide cathode. The Ni sponge oxide cathode has ever been used in gird-control emission tube with 3% duty ratio in our insititute, but it was not succeed. However, this gird-control emission tube using the new oxide cathode operated successfully with 4～6% duty ratio in radar.

ELECTRON EMISSION PHYSICAL PROCESSES OF THE CATHODE

The Conventional Oxide Cathode

The basic structure of the conventional oxide cathode is shown in figure1. The process of the electron emission of the oxide cathode is following three steps:

A.By heating, the carbonate on the Ni base decomposes into oxide:

$$(BaSrCa)CO_3 \rightarrow (BaSrCa)O+CO_2\uparrow$$

B.The activator (Si, Mg, W) in the Ni base diffuses to cathode's surface which reacts with the BaSrCaO and produces excess Ba:

$$BaO+Si \rightarrow SiO_2+Ba$$
$$BaO+W \rightarrow WO_3+Ba$$

C. The excess Ba diffuses to the surface of the (BaSrCa)O grain and is activated by SrO, then releases two electrons and emit vacuum through micro-ostium in the coating. The excess Ba loses two electrons and becomes Ba^{++} which needs obtaining electron and keeps its electric charge balance. At the same time, the interface layer ($BaSiO_3$) is produced by the reaction between SiO_2 to BaO:

$$BaO+SiO_2 \rightarrow BaSiO_3$$

The interface layer prevents the diffusing of the electron from Ni base to its surface. So the conventional oxide cathode can not provide large dc emission current and pc emission current with wide pulse.

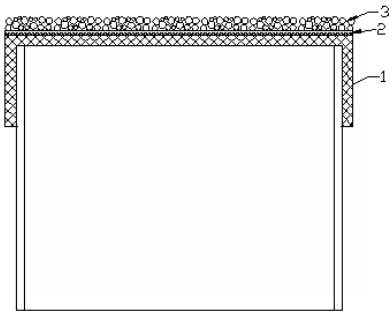

Figure 1: The structure of the conventional oxide cathode. 1. Ni base 2. Interface layer 3. Carbonates.

New Type of Oxide Cathode

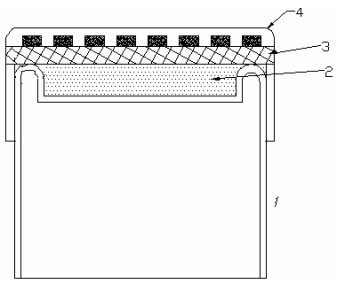

Figure 2: The structure of the reservoir oxide cathode. 1. Ni base 2. Reservoir material 3. Ni net 4.Carbonates

The structure of the new type of reservoir oxide cathode is shown in Fig. 2. Based on the process of production, diffusion and emission electrons of the excess Ba of the cathode, the structure and the emission material of this oxide cathode was devised. This type of oxide cathode is a reservoir dispenser oxide cathode. Its excess Ba comes from the reservoir emission material in a cell of the cathode:

$$Ba_5Ca_3Al_2O_4+2Ti \rightarrow 2BaAl_2O_4+2Ba+Ca$$

The excess Ba diffuses to the surface of the cathode to emit electrons through the Ni sponge, which avoids producing the interface resistance layer and has very low coating resistance, then can provide high emission current density.

EMISSION CHARACTERISTICS OF THE CATHODE

A diode test was done for detecting the characteristics of the Ni sponge oxide cathode and the new type of oxide cathode applied in cooler devices. The characteristics included dc emission, pc emission and lifetime.

A cathode with diameter of 3 mm and a Mo anode with diameter of 30 mm and thickness of 0.4 mm are used in the test. The distance between the cathode and the anode is 1.2–1.5 mm. The operating temperature of the cathode is measured by a Ni–Mo thermocouple spot-welded on the cathode cap, which is 0.5 mm away from the cathode emission surface. After decomposing, activating and aging of the cathode for 50h, we tested their emission current and lifetime.

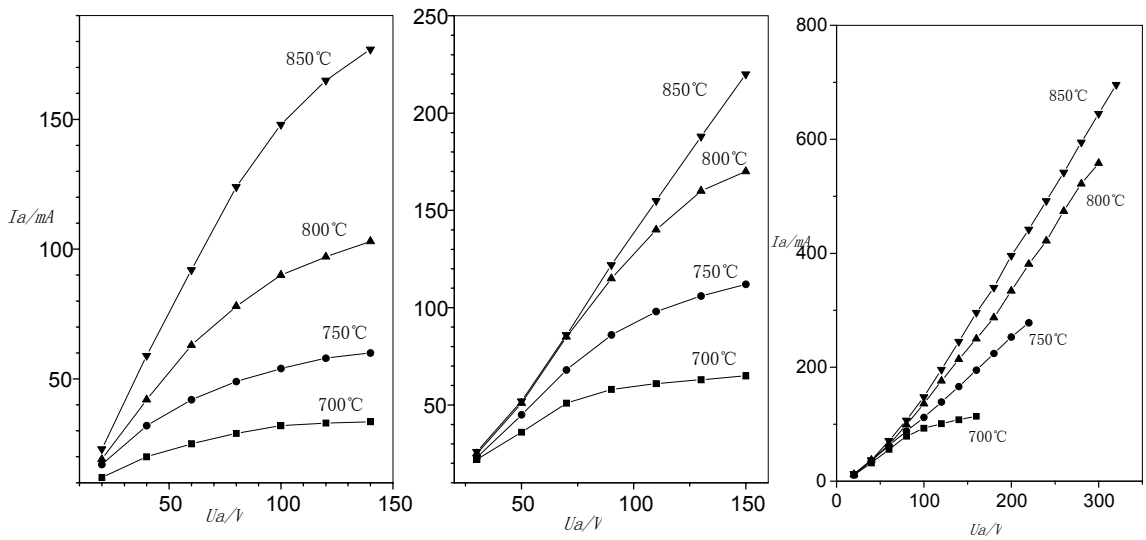

Figure 3: The emission characteristics in dc mode.（a）Ni sponge oxide cathode （b）new type of oxide cathode （c）improved new type of oxide cathode

Direct Emission Current Density

The dc emission characteristics of the Ni sponge oxide cathode, the new type of oxide cathode and the improved new oxide cathode under different temperatures are respectively given in Fig.3(a), Fig.3(b), Fig.3(c). The emission current density of the Ni sponge oxide cathode is 250mA/cm2 at 700 ℃, 500mA/cm2 at 750 ℃, 1000mA/cm2 at 800℃ and 1600mA/cm2 at 850℃. The emission current density of the new type of oxide cathode is 500mA/cm2 at 700 ℃, 1100mA/cm2 at 750 ℃,

2000mA/cm2 at 800℃ and 3000mA/cm2 at 850℃. The emission current density of the improved new type of oxide cathode is 1300mA/cm2 at 700℃, 3000mA/cm2 at 750℃, 5000mA/cm2 at 800℃ and over7000mA/cm2 at 850℃.

The dc emission characteristics of three kinds oxide cathode results show that the dc current density of the new type of oxide cathode is 2 times that of Ni sponge oxide cathode at same operating temperature, the dc current density of the improved new oxide cathode is 4 times that of the new oxide cathode under same condition, and the dc emission current of the Ni sponge is sensitive on its operating temperature.

Pulse Emission Current Density

The pulse emission current density at short pulse width of the Ni sponge oxide cathode and the new type of oxide cathode is shown in Table 1 for three different operating temperatures with pulse duration of 10μs and a repetition rate of 100Hz, which shows that the short pulse emission current density of the new type of oxide cathode is lower than that of the Ni sponge oxide cathode at same temperature.

Table 1: The Pulse Emission Current Density （A/ cm2）

	750℃	800℃	850℃
New type of oxide cathode	7	13	28
Ni sponge oxide cathode	9.1	15.7	30.6

Figure 4 shows the relation of emission current with the pulse widths. It is clear that the pulse emission of the new type of oxide cathode is very steady with the increase of pulse duration. In contrast, the pulse emission current of the Ni sponge oxide cathode increases with the increase of its pulse width, which shows that the temperature of the cathode surface increase with the increase of its pulse width due to the high interface resistance. The two different results indicate that the Ni sponge oxide cathode has good emission capability at short pulse, but the new type of oxide cathode has good emission capability at long pulse because of its low interface resistance.

Lifetime Testing

The results of the lifetime testing for two kinds of cathodes in a temperature range of 800～820℃ and dc load of 1.5A/ cm2 are given in Fig.5, which shows that the emission current of the Ni sponge oxide cathode decreases to 80% of the preliminary emission current at 1800h lifetime, but the emission current of the new type of oxide only decreases 5% after 3000h lifetime.

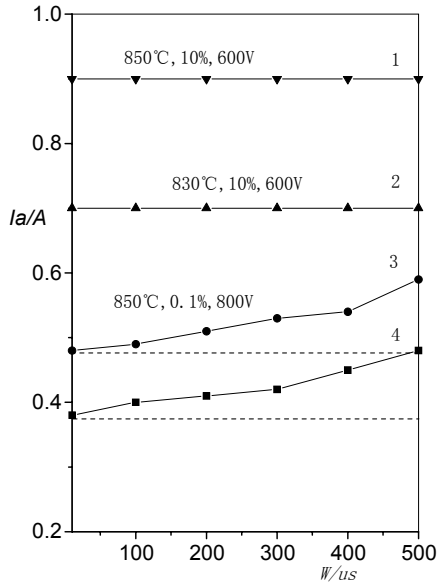

Figure 4: The emission current versus pulse width of cathode. 1,2 new type of oxide cathode, 3,4 Ni sponge oxide cathode.

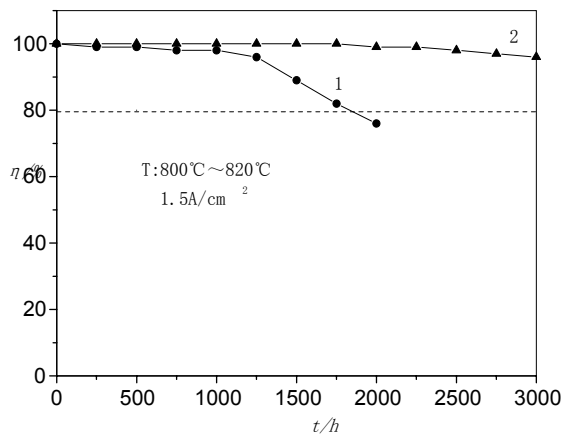

Figure 5: The lifetime curve of the cathode. 1. Ni sponge oxide cathode, 2.new type of oxide cathode.

Application of the Cathode in Microwave Devices

In order to rationally appraise the characteristics of a cathode, the cathode should be applied to a vacuum device so as to test how much current density it can provide, how long its lifetime is in practical applications and so on. Several application examples for the cathode in microwave device are given in this subsection.

(a) High power grid-controlled transmitting tube: The cathode provides an emission current density of 3A/ cm2 with 4～6% duty ratio at 820℃ and a lifetime of over 3000h.

(b) TWT for space satellite communications: The cathode provides a dc emission current density of 0.3A/cm2 at 820℃ and a lifetime of 3 years.

(c) Moderate power TWT: The cathode provides a dc emission current density of 0.5A/cm2 at 750℃ and a lifetime of 12000h.

THE APPLICATION OF THE NEW OXIDE CATHODE USED IN HIRFL-CSR ELECTRON COOLER

The main characteristics of the cathode for HIRFL-CSR electron cooler: the dc emission current density of the cathode is 0.5A/ cm2, the heating power is 36W～100W, and the lifetime is 5000h. The main parameters of the cathode: the convex radius of the cathode is 48mm, the diameter is Φ30mm, the Ni sponge diameter is 28mm and no emission current on cathode edge. The cathode high is 5mm and uphold by a indium steel strip. The cathode picture shows in Fig.6.

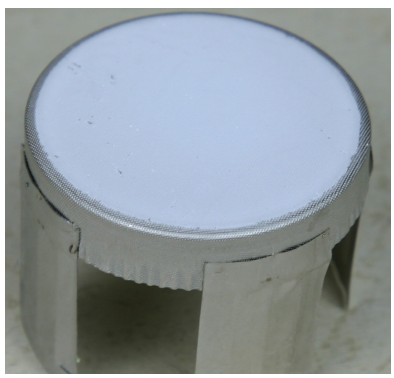

Figure 6: The cathode picture in HIRFL-CSR Electron cooler.

The temperatures of the cathode under different heating power are given in table 2. The results show that the surface temperature of the cathode is uniform, which will be beneficial to the uniform of the electron bind during the process of the electron cooler.

Table 2: The cathode temperature under different heating power (℃)

Heating power	1	2	3	4	5
13V/3.5A	703	699	701	704	703
14V/3.7A	733	730	730	737	740
15V/3.9A	751	759	760	754	761
17V/4.1A	837	838	842	835	842

CONCLUSION

Comparing to Ni sponge oxide cathode, the above-mentioned results for the experiments and applications of the new oxide cathode show that the new oxide cathode has good emission characteristics with high reliability and long lifetime. And it also has good resistance to poisoning, low evaporation and good resistance to shaking and shock, which will not be discussed in detail here. The new oxide cathode can not only substitute completely for Ni sponge oxide cathode in electron cooler but also enhance emission current, prolong operating lifetime, and improve of reliability of the electron gun in electron cooler.

ACKNOWLEDGEMENTS

The author wish to thanks Li Yutao and Lü Yanjie for fruitful discussion and experimental supports.

REFERENCES

[1] Georg G, Daniel D E 2005 *Appl.Sur.Sci.***251** 24
[2] Zalm P 1968 *Adv.Electron.Electron phys.***25** 211
[3] Liao X H, Wang X X, Zhao Q L, Meng M F 2005 *Appl.Sur.Sci.***251** 64
[4] Wang X X，Liao X H，Luo J R，Zhao Q L 2008 *Acta Phys. Sin.* **57** 3990
[5] Bubiey A.V, Panasyuk V.M. et al *Nuclear Instruments and Methods in physics Research* 2004 **A532** 413
[6] Li J, Yang X D et al *Atomic Energy science and Technology 2007* **41** 94
[7] M.Saito *IVESC2004* 104
[8] Liao X H，Huang H F，Tang B Y, Wan X W 1984 *J.Electron* **1** 205

DESIGN OF STOCHASTIC COOLING SYSTEM AT HIRFL-CSRe *

J.X. Wu#, Y.J. Yuan, J.W. Xia, J.C. Yang, R.S. Mao, T.C. Zhao, H.S.Xu, IMP, China.

T. Katayama and F.Nolden, GSI, Germany

Abstract

In the CSRm synchrotron, the beam is accelerated to energies of 500-1000 MeV/u. It can be fast extracted at energies of 200-700 MeV/u to produce radioactive ion beams (RIBs) or high Z beams at the target in the beam line. The secondary beams can be stored in the CSRe ring for internal-target experiments or β decay measurements. The secondary beams are very hot. Electron cooling to such beams would take several minutes, which is too long for experiments with short-lived ions. Stochastic cooling is very efficient for such hot beams. The large phase space after injection will be reduced to values which are well-suited for the subsequent e-cooling.

We report here the proposal and primary design of the stochastic cooling system at CSRe. The simulation results of the Palmer cooling and bunch rotation will be presented.

INTRODUCTION

HIRFL-CSR [1], a heavy ion synchrotron and cooler-storage ring system in Lanzhou, consists of a main synchrotron ring (CSRm) and an experimental storage ring (CSRe). The two existing cyclotrons SFC (K=69) and SSC (K=450) of the Heavy Ion Research Facility in Lanzhou (HIRFL) are used as its injector system. The heavy ion beams from the HIRFL with energies of 7-25MeV/u are injected into the CSRm. Electron cooling supports the accumulation at injection energy. The beams are accelerated and extracted slowly at energies of 500-1000MeV/u for external-target experiments, or fast extracted at energies of 200-700MeV/u to produce RIBs or high Z beams at an external production target for rare isotope beams. These beams are stored or decelerated in the CSRe for internal-target experiments or high precision spectroscopy with beam cooling. The radioactive fragments emerging from the target occupy a large transverse and longitudinal phase space which would lead to the e-cooling times of several minutes. This is too long for the experiments with rare isotope beams of short lifetime. Stochastic cooling at the CSRe would be very efficient to cool such hot beams and it will be used mainly for pre-cooling of RIBs. It is planned to reduce the momentum spread of ±1% and the horizontal and vertical emittances of 30 π mm mrad to the values which are well-suited for the subsequent e-cooling. The beam energy for stochastic cooling will be in the range of 350-500MeV/u.

CSRE RING

The layout of CSRe ring is shown in Fig. 1. It has a race-track shape and consists of two quasi-symmetric parts. One is the internal target part and another is the e-cooler part. Each part is a symmetric system and consists of two identical arc sections. Each arc consists of four dipoles, two quadruple triplets or one triplet and one doublet. Two long dispersion free straight sections house the internal target and the e-cooler. The major parameters of the CSRe are listed in table 1.

Table 1 Major parameters of CSRe

	CSRe
Circumference (m)	128.80
Ion species	Stable nuclei: C~U, RIB(A<238)
Max. energy (MeV/u)	600 (C^{6+}), 400 (U^{90+})
Intensity (Particles)	$10^{3\sim9}$
$B\rho_{max}$ (Tm)	8.40
B_{max} (T)	1.4
Ramping rate (T/s)	0.01~0.4
E-cooler	
Ion energy (MeV/u)	25~400
Length (m)	4.0
RF system	Capture
Harmonic number	1
f_{min}/f_{max} (MHz)	0.5 / 2.0
Voltages (n × kV)	2 × 10.0
Vacuum pressure (mbar)	6.0×10^{-11}

In CSRe three lattice modes are adopted for different requirements. The first one is the internal-target mode with small β-amplitude at the target point, large transverse acceptance (A_h=150πmm mrad, A_v=75πmm mrad) and γ_{tr} = 2.457 for internal-target experiments. The second one is the normal mode with a large momentum acceptance of $\Delta P/P$ = 2.6% and γ_{tr} = 2.629 used for high-precision mass spectroscopy. The third one is the isochronous mode with a small transition γ_{tr} that equals the energy γ of beam in order to measure the mass of those short-life-time RIB. Figure 2 and Figure 3 show the distribution of the β-functions and the dispersions for those modes.

*Work supported by NSFC (10705039)

#wujx@impcas.ac.cn

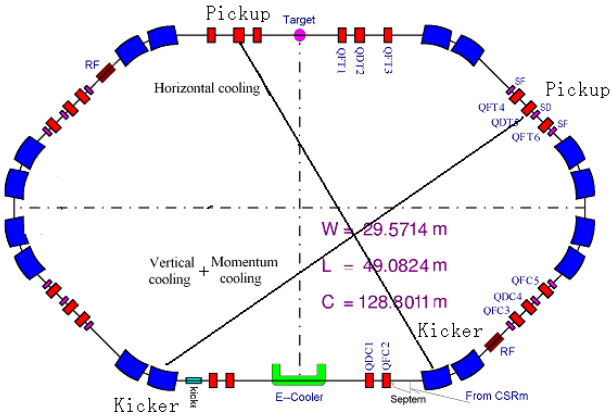

Figure 1: CSRe layout.

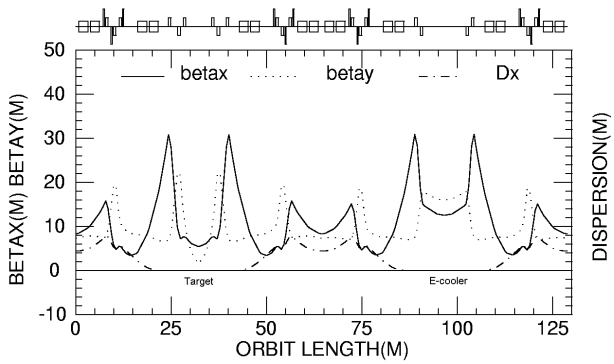

Figure 2: Distribution of the β-functions and the dispersion for the normal mode

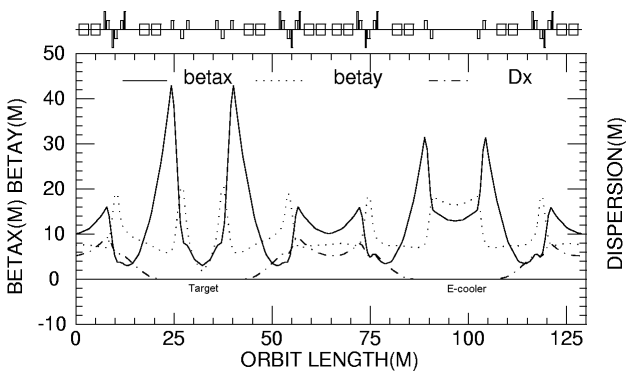

Figure 3: Distribution of the β-functions and the dispersion for the internal target mode

Because of space restrictions, all pickups and kickers will be installed inside the gaps of dipole and quadruple magnets. We plan to use Palmer cooling for longitudinal cooling and share the same pickup and kicker tank with vertical cooling. Twiss parameters at the pickups and kickers are shown in Table 2, where θ is the betatron phase advance between the pickup and kicker, L is the distance between them. The length of the quadruple is 750mm and 2.4m for the dipole. The vacuum cross sections in the quadruple and dipole magnets of CSRe are shown in Fig.4 and Fig.5.

Table 2 Twiss parameters for stochastic cooling (normal mode)

	Horizontal		Vertical+Momentum	
	Pickup	Kicker	Pickup	Kicker
β_x(m)	9.7-30.9	9.7-17	15.1-4.6	17.6-9.7
β_y(m)	22.2-6.7	7.6-6.9	8.9-18.4	6.9-7.6
D_x(m)	0	0-0.457	4.9-7.4	0-0.457
θ	68^0		92^0	
L(m)	57.8		54.2	

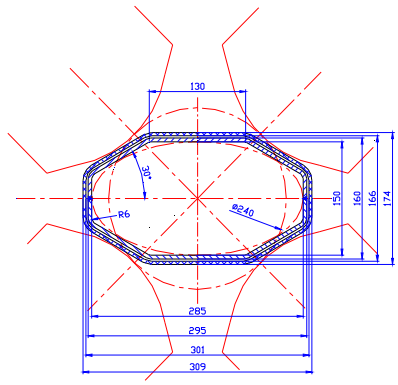

Figure 4: Vacuum cross section in the quadruple magnet

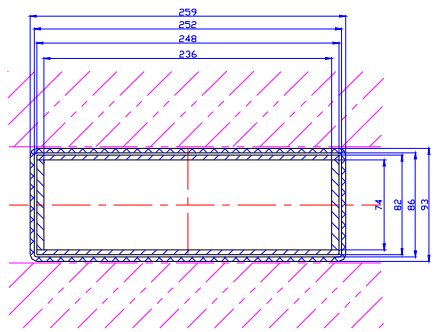

Figure 5: Vacuum cross section in the dipole magnet

SIMULATION RESULTS OF COOLING

Stochastic cooling will be used for internal target mode and normal mode which have large η values (0.25-0.36) with beam energy of 350 MeV/u - 510 MeV/u. As the injected momentum spread of RIB is as large as $\pm 1\%$, the maximum frequency of the stochastic cooling will be limited below 460 MHz due to the unwanted mixing effect from the pickup to the kicker. If the bandwidth is chosen to be 200 MHz – 400 MHz and $\lambda/4$ loop couplers are used, the electrode length will be about 262 mm and only two electrodes can be installed inside a quadruple. The signal to noise ratio will be poor in this case and the cooling speed will be slow. Figure 6 and figure 7 are the simulated results for Palmer cooling with initial momentum spread of ±1% (uniform) (All the simulations in this paper are for $^{132}Sn^{50+}$ beam with the particle number of 1.0e5 and the energy of 380MeV/u). From the results we can see that the best case is with 2 pickups and 8 kickers, with the gain of 150 dB and with the cryogenic

pickup electrodes, then the microwave power needed is 230 W and the stochastic cooling will reduce the momentum spread to 1/5 of initial value within 10 s.

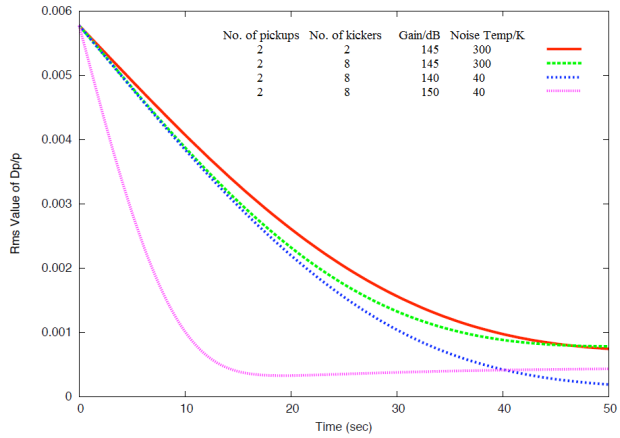

Figure 6 Rms value of $\Delta p/p$ & time

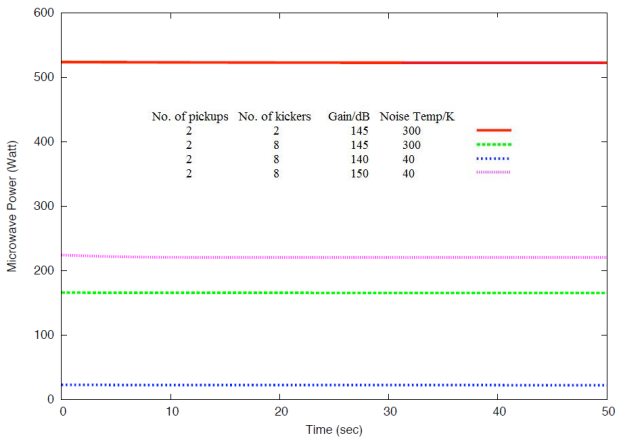

Figure 7 Microwave power

But for the rare isotope beams with short life, the cooling time should be as short as possible. There are several possibilities to improve this situation. One is to choose slot type pickups [2] and kickers. More of those by unit length could be installed, leading to an improved signal-to-noise ratio. Details of how to build such electrodes are not yet clear at such a low bandwidth. They would have to be installed into the quadruple with elliptic cross section. Furthermore there is still some flexibility to change the lattice mode to make η small. Then the bandwidth could be increased, but the acceptance would be decreased also. If the bunch length at extraction from the CSRm is not too large, one could install an additional bunch rotation system to decrease the initial momentum spread, so the bandwidth can be increased. Figure 8 is one simulated result during the bunch rotation with the initial bunch length of 100 ns and with 100 kV RF voltage applied during quarter synchrotron oscillation period and switched off. In a very short time the rms momentum spread can be reduced from 5.76e-3 to 1.44e-3, and the bandwidth can be increased to 0.5 - 1.0 GHz. With this initial momentum spread and bandwidth, the cooling time is shorter and the equilibrium momentum spread is smaller, which is shown in Fig.9.

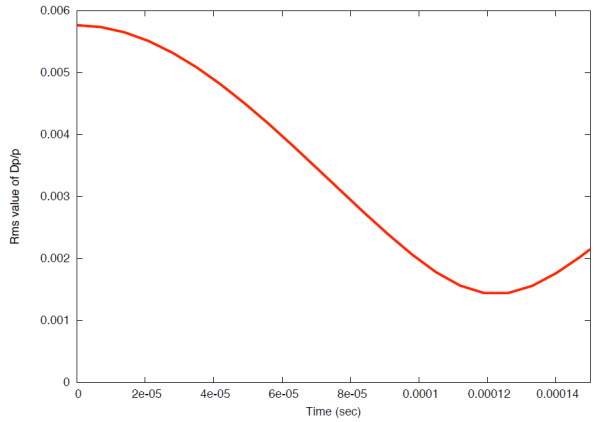

Figure 8 Rms value of $\Delta p/p$ & time during bunch rotation

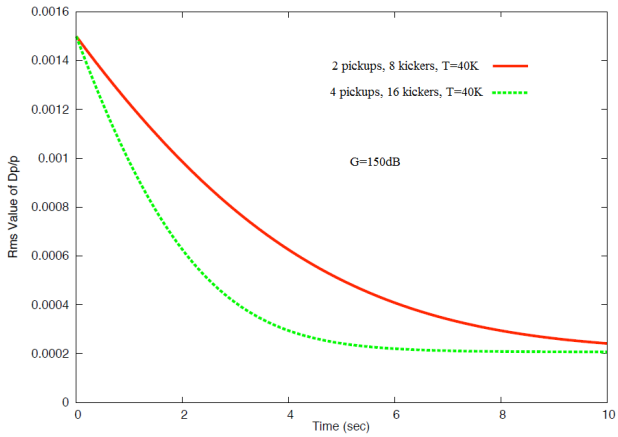

Figure 9 Rms value of $\Delta p/p$ & time

Table 3 shows a comparison for Palmer cooling with and without bunch rotation. There is no doubt that with bunch rotation we can get lower momentum spread in shorter time, which is better for the subsequent electron cooling. But the bunch rotation is effective only if the bunch length is less than 100 ns. The next step is to measure the bunch length after CSRm extraction.

Table 3 Palmer cooling with and without bunch rotation

Bunch rotation	Yes	No
$\Delta p/p$ (initial)	±1%	±1%
$\Delta p/p$ (after bunch rotation)	1.5e-3 (RMS)	±1% (uniform)
Bandwidth	0.5–1.0GHz	0.2-0.4GHz
Amplifier gain	150 dB	155 dB
Microwave power	540 W	750 W
$\Delta p/p$ (after 5 s)	2.2e-4	1.5e-3
N_{pu}/N_k	4/16	2/8

We also calculated the cooling process of e-cooling alone, e-cooling after stochastic cooling with and without the bunch rotation, shown in Figs.10, 11 and 12, where red line is the momentum spread, green and blue are transverse emittances. The e-cooling time is 900 s for initial momentum spread of ±1% and transverse emittance

of 30π mm mrad, while they are 2.7 s for 2.2e-4 and 5 π mm mrad, 7 s for 1.5e-3 and 5 π mm mrad.

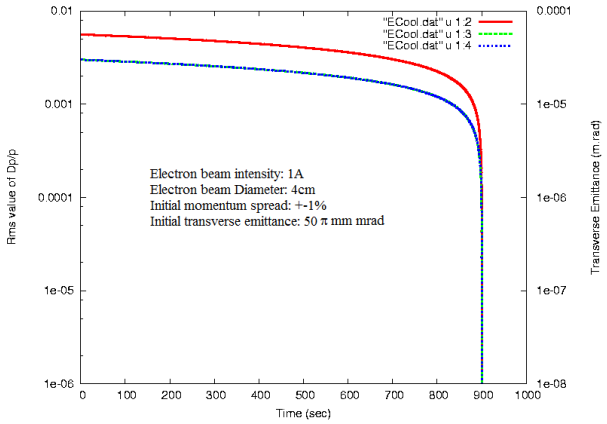

Figure 10: E-cooling process alone

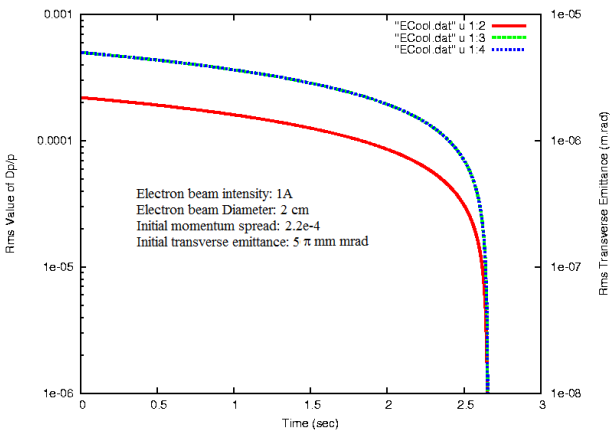

Figure 11: E-cooling process after stochastic cooling and bunch rotation

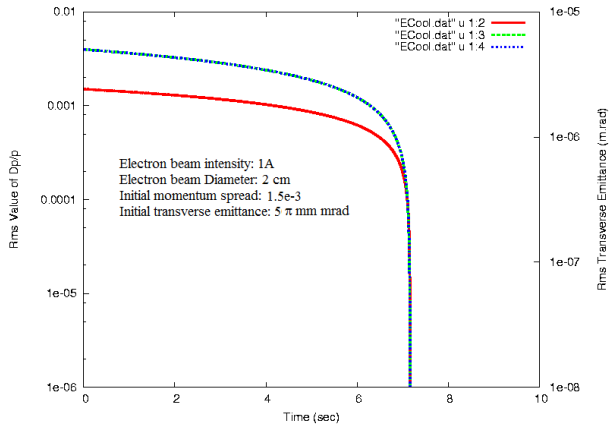

Figure 12: E-cooling process after stochastic cooling

SUMMARY ACKNOWLEDGMENTS

To get the same final cooled values with the same initial conditions, the cooling time is 900 s for the e-cooling alone, 7.7 s for the combination of the e-cooling and stochastic cooling after the bunch rotation, 12 s for the e-cooling and stochastic cooling without the bunch rotation. So the pre-cooling of stochastic cooling is quite helpful at CSRe for hot RIBs with short life time.

The authors gratefully acknowledge the helpful discussions about pickups with C. Peschke.

REFERENCES

[1] J.W. Xia, et al, "Construction and commissioning of the HIRFL-CSR", APAC'04, Indore, India, Feb. 2007, THXMA03, p.534.

[2] R. Stassen, P. Brittner, et al, "Recent developments for the HESR stochastic cooling system", Proceedings of COOL 2007, JACoW, http://www.jacow.org/cl07

ELECTRON COOLING FOR THE THERAPY ACCELERATOR COMPLEX

V.V. Parkhomchuk, V.B. Reva, A.V. Bubley, V.M. Panasyuk
BINP, Novosibirsk, Russia

Abstract

Institute of Nuclear Physics (BINP, Novosibirsk) is engaged in R&D of the new therapy accelerator system based on the electron cooling. The electron cooling is used for the ion beam accumulation in process of repeated multi turn injection into the main ring from the fast cycling booster synchrotron. After acceleration of the carbon ions up to 200-400 MeV/u the electron cooling is used for shrinking the beam emittance to minimal value and for further extraction and distribution of small fractions of the ion beam according to the irradiation program. The extraction systems base on the electron cooling is discussed in the report. The computer simulation results are in a good agreement with the experimental data of the electron cooling of the carbon ion beam with energy 400 MeV/u obtained resently during the CSRe commissioning (May 2009).

INTRODUCTION

Heavy ion beam therapy is one of the most advanced and effective cancer treatments. It is more accurate, caused less damage to healthy tissue and has a higher cure rate in comparison with conventional kinds of radiotherapy with x-ray. Traditional therapy systems with carbon ion beam consist of following parts: ion source, linear accelerator up to 30 MeV/u, synchrotron for ions acceleration up to the energy of 100-400 MeV/u and irradiation channels including (in most radiotherapy centers) the gantry system intended for irradiation a tumor from different directions [1]. The application of the achievements of the ion beam cooling science to this therapy system can fundamentally improve the characteristic of beams used for therapy. If we discuss just adding the electron cooling to existing system [2] it looks like additional cost about 2 M$ to the existing equipment with total price about 70-100 M$. But new system based on the electron cooling from the very beginning (from stage of design) opens many unique possibilities unachievable for conventional systems namely:

1. Accumulation primary ion beams by means of repeating injection that relieves requirements on injection system.
2. Possibility to accumulate secondary positrons emitting nuclei that can be used for precise diagnostic of the radiation dose distribution in and around a tumor with the help of standard PET apparatus.
3. After acceleration with further cooling the ion beam has very small emitance that allow the extraction system to be less powerful and has failure-free operation
4. Possibility of the precise beam extraction by a recombination.

These advantages make it possible to construct therapy system more reliable and cheaper. According to a contract with Chinese company BINP works on development of the project for carbon therapy. But after the economic crisis begun the project got strong problems with financing. Initial construction of prototype of elements and calculation of the cooling process showed high level perspectives. This year experiments with cooling 400 MeV/u carbon ions at CSRe demonstrate very interesting results.

PRIMARY BEAM ACCUMULATION

Injector comprises the ion sources, tandem accelerator, the fast-cycling booster synchrotron and low energy beam transport lines. A multi-turn injection from the tandem accelerator into the booster synchrotron is performed in a horizontal plane. The booster synchrotron accelerates protons up the maximum energy of 250 MeV and the carbon ions $^{12}C^{+4}$ up to 430 MeV/u. The booster circumference is of 27 m, repetition rate is 10 Hz. The maximal energy of booster synchrotron is 30 MeV/u which is optimal for accumulation the carbon ions in the main synchrotron with period 0.1 sec. After injection into the main synchrotron, the ion beam is stored, cooled and accelerated up to the energy required for therapy then extracted into the high energy beam transport system. The ion beam is stored during 10 booster cycles with electron cooling.

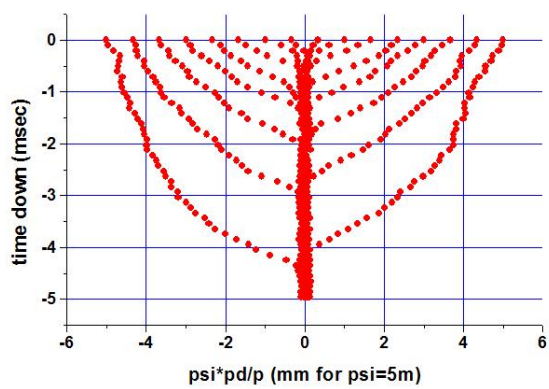

Figure 1: The computer simulation of initially injected beam cooling (momentum): electron current 0.5 A, electron energy 16 kV, time range arrow is shown from up to down in milliseconds.

Radioactive Isotopes Accumulation

The electron cooling can be used for an accumulation of radioactive nuclei which could be useful for cancer

therapy. For example, treatment by the use of ^{11}C with life time about 20 min looks very effective for the dose diagnostic as far as all dose measurements after irradiation could be performed with normal Positron Emission Tomography. This is similarly to the process of proton treatment [3,4] where radioactive nuclei arise in considerable amount (about 1000-2000 1/cm) that also can be used for diagnostic. The cross section of the ^{11}C ions production has a maximum value 100 mb at proton energy near 30-40 MeV. The first estimations of production yield for ^{11}C nuclei on the special external hydrogen target gives hope to reach efficiency about 0.01 for transformation buster intensity ^{12}C to ^{11}C. This technology opens the possibility to combine the results of standard PET diagnostic which detects cancer tumor after taking isotopes medicine with the irradiation zone visualization after irradiation with the short life time isotopes. The points of stopping ^{11}C ions with known energy and initial space distribution gives precise information about the stopping ions power of the real muscular tissue.

EXTRACTION OF ION BEAM FROM MAIN SYNCHROTRON

Pellet Extraction

The presence of electron cooling in the synchrotron provides a small size and energy spread of the cooled beam thus enabling the realization of the original beam extraction scheme by small precisely dosed portions, the so-called pellet extraction. Electron cooling allows concentrating a portion of the ion beam in a given place of the phase space and then getting the ion beam low density in the neighboring regions for decreasing the "tails" of the distribution and losses at the extraction septum [5]. The operation scheme is the following. Upon the ion beam acceleration up to the required energy, RF voltage is off and the beam is de-bunched. In the period of 50-200 ms (depending on the extraction energy) the beam is cooled down to the relevant equilibrium state. Then the beam is prepared for its extraction, for example, by scanning the electron beam energy with respect to the mean energy of the ion beam we produce the flat distribution of ions with $\Delta p / p = \pm 2 \div 2.5 \cdot 10^{-3}$. Then it is necessary to separate a portion of particles with energy deviation from the main beam. The portion intensity should be controlled in the range of N = $10^6 \div 10^7$ particles. The neighbouring ions are concentrated under the friction force action. The intensity of obtained portion is controlled by the time of storage and de-tuning of the electron beam energy from the distribution edge. By placing the kicker at the azimuth of the ion orbit where the dispersion is sufficient to separate the main beam from the portion the single turn extraction of the portion is realized. It is clear that ions concentrate in a portion but close to the storage portion region there are many ions nearing the ion cooling region, which will be bombarded the septum knife. In order to improve the extraction efficiency, it is necessary to clean the septum knife region. One of simplest solutions is to use the betatron core for accelerating the ion beam and "separating" the main beam from the region where the beam is prepared for its extraction. The magnet field in the core slowly increases so that the energy of the ion beam also increases on every turn moving the beam aside the septum. In this case, the maximum electron cooling force should be sufficient for the confinement and cooling the ions in the extraction region (Fig.1). It is seen that the main beam is moving away from the storage region and the left side portion is concentrated in the extraction area. Such an ion energy swiping accelerates noticeably the beam preparation for its extraction and cleans the "knife" region from the lost particles.

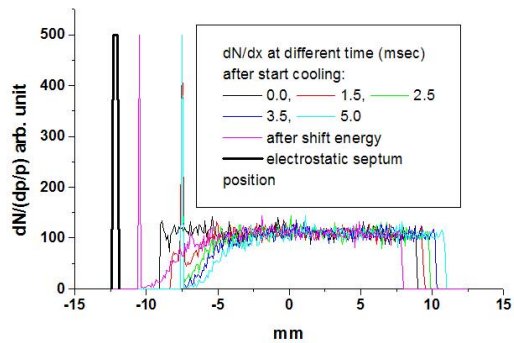

Figure 2: The 5 msec cycle of carbon ions extraction with electron cooling.

Upon completion of the extracted portion storage and cooling, the betatron core exchanges polarity rapidly enough and the stored portion is rapidly moving to the kicker and the main beam distribution tail returns again in the cooling region for storing a new portion. In the scheme of using swiping, the extraction efficiency is much higher for the system repetition frequency up to 500 Hz. In the region of 1-2 kHz, the losses are still high 20-30 % for the septum knife with thickness 0.5 mm.

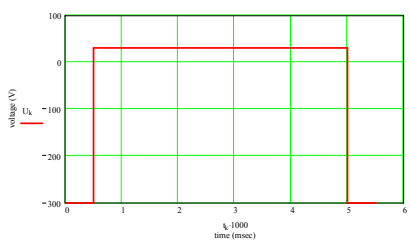

Figure 3: The voltage on betatron core versus time at cycle.

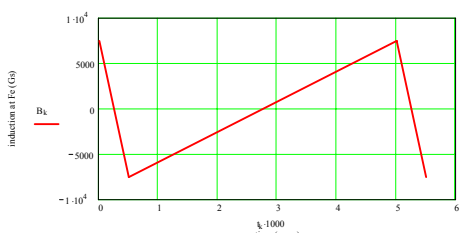

Figure 4: Magnet field at betatron core versus time.

For the beam extraction the fast kicker, electrostatic septum and permanent septum of the Lambertson type are used. Since the dispersion function at the kicker azimuth and electrostatic septum has the maximum value of 4.3 m, the main beam orbit and portions are separated by $\Delta X \approx$ 10 mm. After kick, the portion reaches the electrostatic septum aperture and acquiring an additional deflection along radius reaching the aperture of the Lambertson-type septum magnet, by which it is extracted vertically at the angle φ_y = 13.5° with respect to the equilibrium orbit. The beam deflection angle corresponds to the ΔX =10 mm beam drop to the electrostatic septum aperture and, correspondingly, the electrostatic septum drops the beam into the septum magnet at the value of ΔX = 14 mm. The kicker kicks the beam by purely electric field and has the pulse duration of 80 ns with the fronts about 10 ns by order of magnitude. The presence of the cut in the inner plate causes the stray field and field non-uniformity inside the kicker aperture. With the separation of orbits by 10 mm, the main beam perturbation is $\Delta\varphi \le 5 \cdot 10^{-6}$.

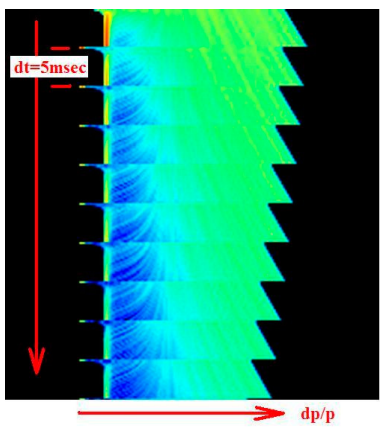

Figure 5: The computer simulation of 10 cycles of extraction with period 5 msec (full time 50 msec.), initial momentum spread ∆p/p=±0.001.

Figure 5 shows the 10 cycles of extraction when main beam during each 200 Hz cycles linearly moved to right and just before extraction jumped to the left (the time of the magnetic field polarity exchange). Slow moving to the left is connected with action of the cooling force which shifts the main beam to extraction zone.

Slow Extraction by Recombination

The project of the storage ring for the cancer therapy proposed by BINP team proposes using recombination reaction C^{+6}+e->C^{+5} for the extraction of the ion beam. The charge states C^{+6} and C^{+5} have difference 20% in momentum, so it is possible to organize the strong shift between primary and extracted beam by the proper choice of the dispersion with very low ion density in the gap between these two orbits. So, the flow of the particles on the septum elements can be low according the extraction scheme. It leads to small leakage of the particles during extraction and liberalizes the requirement to the power supply of the storage ring because the ripple of the magnetic field doesn't produce the interference of the primary and extraction beam in the space. The ion beam after cooling on high energy 100-400 MeV/u very small (see Fig.6) and beam after recombination too very small. For example, fig. 6 show photo of nuclear emulsion after exposition at hydrogen beam on distance 10 m from the electron cooler NAP-M.

Figure 6: The first photo of hydrogen atoms beam after recombination at NAP-M cooler [6].

The recombination coefficient is proportional to electron density. This enables to operate by the dose of the extraction beam. The electron gun as an electron tube can modulate the electron current in the megahertz frequency range. This frequency is certainly enough for any regime of the tumor scanning. The presence of the diagnostic of the extraction dose enables to have a feedback for the stabilization dose in the tumor. Moreover the recombination extraction is more safety because it is very difficult to have breakdown extraction of all stored ion beam during very short time. Protection system can quickly switch off the electron current and stop the extraction. The main disadvantage of the recombination extraction is relatively small rate of the extraction namely 10^7 /s at the number of the ions in the storage ring 10^{10} and the electron density 10^8 1/cm^3 in the cooling section. But this value is enough for the treatment of the small cancer tumor. For example, the tumor with diameter 30 mm should be irradiated ions those have the rest kinetic energy near 50 MeV/u. For accumulation doze of 5 Gy with ion flux 10^7 /s required exposition time is near 1 min.

FIRST EXPERIMENTS ON CSRE WITH 400 MEV/U

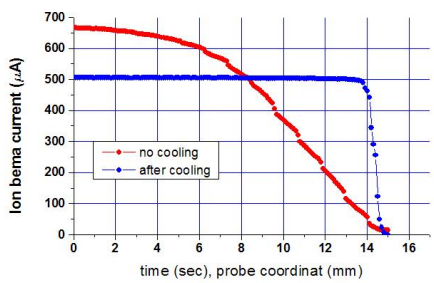

Figure 7: The scraping the ion beam at CSRe.

The first experiments at **CSRe** with cooling of carbon beam showed perspectives of this type of extraction. Fig.7 shows results of the carbon ion beam current measurement during moving the mechanical scraper inside vacuum chamber (with velocity 1 mm/sec) before cooling and after the electron cooling. As we can see, the ion beam size is near 15 mm in the case of absence of the cooling but after cooling it becomes less than 1 mm. It is more interesting that we can see many seconds of the ion beam life time when the scraper is located in less then 2 mm from the centre of the ion beam orbit. There is direct situation what was used for kick extraction simulation shown in fig.2 (just before stored portion of the beam was kicked out). The kicker voltage amplitude is required to excite the beam oscillations with amplitude about 2 mm. This corresponds to the angle about 2×10^{-4} at the point with a beta function value of 10 m. For producing so small kick we are going to use low power transistor generator instead of powerful gas-filled triode generator.

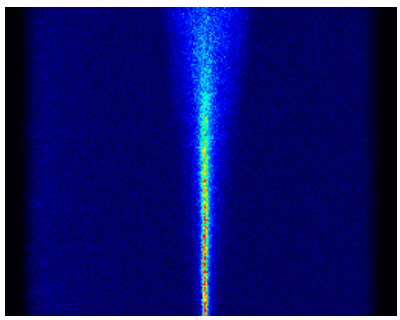

Figure 8: Schotky signal of carbon beam during cooling at CSRe with energy 400 MeV/u.

The cooling process of the ions with initial momentum spread $\delta p_{r.m.s.}/p = 2\times10^{-4}$ is shown in fig.8. Initial momentum spread is cooled down to equilibrium spread 1×10^{-5} with the exponential cooling time 20 sec. The electron beam diameter was about 50 mm and density of 1 A electron beam very low at these experiments. The alignment of ion and electron beams was far from optimum (was $\theta_{eff} \approx 5\times10^{-4}$) and the calculation of the cooling time with the same code as for fig.1 gives about 20 sec. In the case of using the electron beam with diameter of 1 cm and careful alignment with accuracy $\theta_{eff} \approx 1\times10^{-4}$ cooling rate should increase at factor $g \approx 1/a_e^2 \times 1/\theta_{eff}^3 \approx 3000$ that decreases the cooling time down to 5 msec.

ELECTRON COOLER DESIGN

Electron cooler consists of the following subsystems: the support and the vacuum system, the magnetic system comprising the focusing solenoids, toroids and correction magnets, the system of electrostatics including 300 kV accelerating tubes and electrodes, the high voltage power supply system, diagnostics, the gas vessel (SF6) system and the oil cooling system for collector and high voltage terminal. The electron cooler after acceleration should fast increased the high voltage and cooled ion on top energy. The electron beam from electron gun (14) move at gun solenoid (13), toroid solenoid (15), the cooling straight section (11) with ion beam and after turn at toroid (9) to collector solenoid (6) damped at collector (5). The high voltage system at pressed vessel (1) connected pressed high voltage lines (4) with the electron gun and collector (5). All the solenoids are mounted on the frame made of the magnetic soft steel. The frame closes the magnetic flux and serves as the magnetic shield.

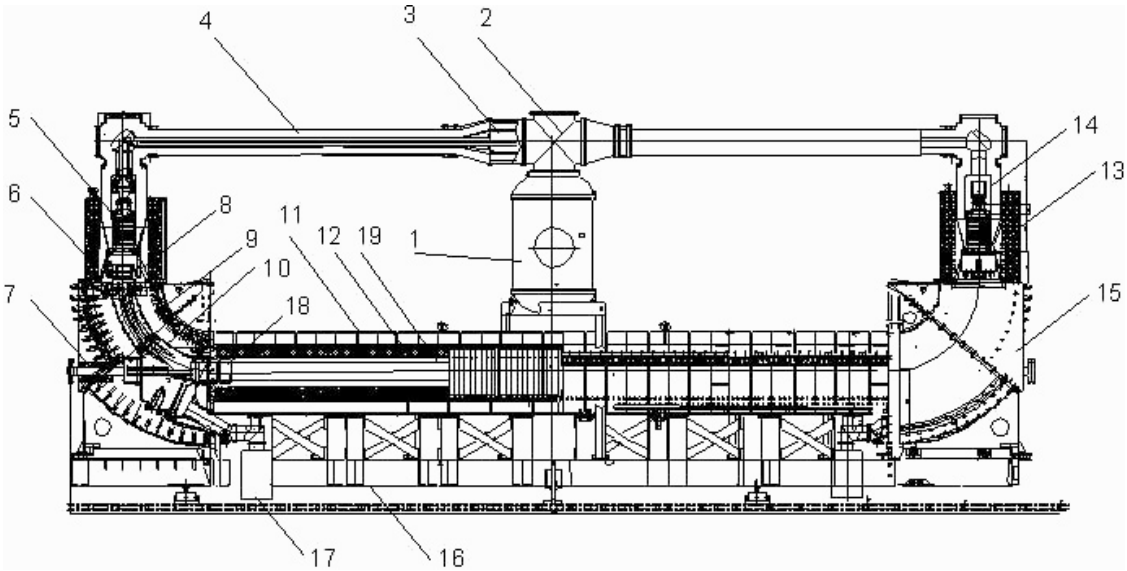

Figure 9: Design plot of the electron cooler for the therapy accelerator complex. The main parameters of cooler: electron beam energy up to 250 keV, total length 8 m, cooling length 4.8 m, magnetic field at cooling section 0.1-0.15 T,magnetic field straightness $\Delta H_{\perp} / H < 10^{-4}$, Pressure at vacuum chamber10^{-8}·10^{-9} Pa, SF6 gas pressure at the high voltage vessel 2-3 bar, the electric power consumption near 350 kWt, total weight 30 t, water consumption (5 bar) 1 m^3/minut, occupied area 10*10*5 m^3.

In the ion beam input/output places the dipole corrections are located (7) that compensates the ion beam displacements caused by the vertical component of the magnetic field in the toroidal section (9). The vacuum chamber is pumped off with two ion pumps placed near (17). An addition pumping is provided by the titanium pump placed near the accelerating tube of the decelerating column (8). The residual pressure is·10^{-8}-10^{-9} Pa.

CONCLUSION

The carbon ion beam system is based on a few approved key innovations historically came from BINP (Novosibirsk) such as: electron cooling, using negative ions for stripping injection, storage rings. Electron cooling helps to make operation of the system easier by decreasing the beam emittance which results in stable ions energy and easy extraction. Example of CSRm operation shows that electron cooler can stable operates many months without switching off

ACKNOWLEDGMENTS

This report is only small part of BINP team work for development of the carbon ion treatment accelerator system. Authors are gratefully acknowledged A.N. Skrinsky, E.B. Levichev, V.A. Vostrikov for fruitful discussions.

REFERENCES

[1] The clinical facility in Heidelberg http://www.gsi.de/portrait/Broschueren/Therapie/Klinikanlage_e.html

[2] K. Noda, S. Shibuya, NIM and Methods in Physics Research A 532 (2004) 129-136. COOL-03.

[3] J. Beebe-Wang, F.A Dilmanian, S. Peggs, D.J. Schlyer, P. Vaska, "Feasibility of Positron Emission Tomography of Dose Distribution in Proton Beam Cancer Therapy". Proceedings of EPAC 2002, p. 2721-2723 (2002).

[4] J. Beebe-Wang, S. Peggs, L. Smith, "Dependence of the Production Yields of Positron Emitters in Proton Therapy on the Cross Section Data Variations", preprint C-A/AP/#109, Sep. 2003, BNL.

[5] Radiation Therapy Facility based on Carbon Ion Cooler Synchrotron, V. Kiselev , V. Vostrikov, S. Konstantinov, G. Kurkin, E. Levichev, V. Parkhomchuk , Yu. Pupkov, V. Reva, R. Salimov, A. Semenov, S. Sinyatkin, A. Skrinsky, Proceedings RuPAC08. http://cern.ch/AccelConf/r08/papers/THBAU01.pdf

[6] G.I. Budker, A.N.Skrinsky, Electron cooling and new perspective at physic of particles, UFN, 1978, 124, #4, p.561.

COMMISSIONING OF ELECTRON COOLING IN CSRe*

X.D. Yang#, L.J. Mao, G.H. Li, J. Li, X.M. Ma, T.L. Yan, Y.J. Yuan, M.T. Song, J.C. Yang, Y. Liu,T.C. Zhao, J.W. Xia, W. Zhang, D.Q. Gao, Z.Z. Zhou, H.B. Yan, R.S. Mao, Y. H, S.F. Han, J.H. Zheng, X. T. Yang, H.W. Zhao, G.Q Xiao, C. Xiao, D.Y. Yin, P. Li, H. Jia, Institute of Modern Physics, 730000 Lanzhou, CAS, China
V.V. Parkhomchuk, V.B. Reva, D.N. Skorobogatov,Budker institute of Nuclear Physics,630090 Novosibirsk, RAS, Russia

Abstract

The 400MeV/u $^{12}C^{6+}$ ion beam was successfully cooled by the intensive electron beam near 1 Ampere in CSRe. The momentum cooling time was estimated near 15 seconds. The cooling force was measured in the cases of different electron beam profiles, and the different angles between ion beam and electron beam. The lifetime of ion beam in CSRe was over 80 hours. The dispersion in the cooling section was confirmed as positive close to zero. The beam sizes before cooling and after cooling were measured by the moving screen. The beam diameter after cooling was about 1 millimeter. The bunch length was measured with the help of BPM signals. The diffusion was studied in the absent of electron beam.

INSTRUCTION

HIRFL-CSR[1] is a new ion cooler-storage-ring system in IMP China. It consists of a main ring (CSRm) and an experimental ring (CSRe). The two existing cyclotrons SFC (K=69) and SSC (K=450) of the Heavy Ion Research Facility in Lanzhou (HIRFL) are used as its injector system. The heavy ion beams from HIRFL is injected into CSRm, then accumulated, e-cooled and accelerated, finally extracted to CSRe for internal-target experiments and other physics experiments.

Table 1: Lattice Parameters of CSRe

Lattice Parameter	Value
Transition gamma	$\gamma_{tr} = 2.629$
Betatron Tune	Q_x / Q_y =2.53/2.57
Max. Betatron amplitude	β_x / β_y =17.6/8.2m(Dipole) β_x / β_y =30.9/22.3m(Quadruple)
Max. Dispersion	D_x =6.5m(Dipole β_x=13m) D_x =7.8m(Quadruple β_x=16m)
Injection section	β_x=30.4m, D_x =0m(Septum) β_x=30.9m, D_x =0m(Quadruple)
Electron cooling section	β_x / β_y =12.5/16.0m, D_x =0
Internal target	β_x / β_y =5.4/1.5m, D_x =0
RF station	β_x / β_y =4.0/8.4m, D_x =4.5m

* supported by the central government of China
1) E-mail:yangxd@impcas.ac.cn

CSRe is a 128.8m circumference cooler storage ring with sixteen 22.5 degree C-type bending dipole magnets. The maximum Betatron functions are 30.9m and 22.3m in horizontal and vertical respectively. The maximum dispersion is 7.8m, and the dispersion at injection point is zero, the Betatron function is 30.4m in the Septum. The Betatron functions at electron cooler are 12.5m and 16m in the two transverse directions respectively, the dispersion is near zero here. The tunes are about 2.53 and 2.57, the transition gamma is 2.629, and the transverse acceptance of CSRe is about 150πmmmrad, and the longitudinal one is $\pm 5\times10^{-3}$.

Accelerated ion beam from the CSRm through the radioactive beam separator line with the length of 100m was injected into the CSRe. Generally the CSRe operated with the DC mode. A gas jet internal target was installed in the opposite side of electron cooler.

Table 2: Parameters of the CSRe Electron Cooler

Maximum electron energy	300 keV
Maximum electron current	3A
Gun perveance	29 μP
Cathode diameter	29mm
Current collection efficiency	≥99.99%
Maximum magnetic field in gun section	0.5T
Maximum magnetic field in cooling section	0.15T
Field parallelism in cooling section	4×10^{-5}
Effective length of cooling section	3.4m
Vacuum pressure	$\leq 3\times10^{-11}$mbar

The electron cooling device plays an important role in HIRFL-CSR experimental ring for the heavy ion beam. Continuous electron cooling is applied to the stored ion beam for the compensation of the heating by various scattering. The most important is the ability to cool ion beams to highest quality for physics experiments with stored highly charged ions. The new state-of-the-art electron cooling device was designed and manufactured in the collaboration between BINP and IMP, it has three distinctive characteristics, namely high magnetic field parallelism in cooling section, variable electron beam profile and electrostatic bending in toroids. The main parameters are listed in table 2. It was reported in many conferences[2],[3],[4],[5],[7]The previous commissioning results have been given in the COOL05-P02[6] and COOL07-TUM1I02[8]

BEAM COOLING EXPERIMENTS

Beam Position Monitor

The basic principle of electron cooling requires the ion beam is parallel with the electron beam. In this case, two sets of capacitive cylinder beam position monitors were installed in the ends of electron cooling section. The electron beam was modulated by an external 3MHz signal. The signals picked up by four probes were magnified by four independent preamplifiers. The NI-5105 (8 channel High-Density Digitizer) was employed as main data acquisition and the data was processed by the special code of LabView.

The ion beam becomes bunched one after RF capture, the ion beam position was measured at this moment.

From these results, the angles and displacements between ion and electron beams in horizontal and vertical planes were derived. According to the information, the closed-orbit of ion beam in the ring was corrected, ion beam positions at the ends of cooling section were close to parallel with the electron beam, the electron beam was slightly adjusted with the help of correction coils of cooler in the cooling section, finally the ion beam and electron beam were matched well, the cooling was observed. A small displacement between two beams was not critical due to the bigger size of the electron beam.

Beam Cooling Results

Due to the electron cooler located near the injection point and just before the injection septum kicker. The injection efficiency and the closed-orbit correction should be compromised. In this case, four additional correction coils in the dipoles before and after electron cooler operated as ramping mode. In the injection interval, these coils were ramped to the proper value, and then return to the normal value to keep the correct orbit in the cooling section. During the commission, the electron beam was set as plat profile.

At the beginning, 200MeV/u $^{12}C^{6+}$ was injected into CSRe, the magnetic field of electron cooler was set as quarter of maximum value. In this case, the magnetic field in cooling section is 0.0385T, the electron beam current was set as 300mA. After orbit correction and regulation of electron beam angle, the cooling was observed, but the cooling process is not fast enough. It could be caused by poor quality of the high energy electron beam confined by a weak magnetic field in toroid, additional transverse temperature was introduced. For lack of proper transverse beam profile monitor, the moving screen was employed as scrapper to measure the profile of cooled ion beam. After the screen was moved near the centre of ion beam, the DCCT signal of ion beam became not recognized from the noise, but the Schottky signal was clear to observe the ion beam. The momentum spread in the range of 10^{-6} was observed in the case of low ion intensity.

At given value of the stored particle number, the momentum spread is determined by the equilibrium between the electron cooling and various heating effects, main of which is an intrabeam scattering. At large intensity the momentum spread $\Delta P/P$ is scale with the stored particle number N in accordance with a power law $\Delta P/P \propto N^{\kappa}$, where the power coefficient κ depends on the settings of a storage ring and cooling system[9], the value is determined by the misalignment angle between the ion beam and electron beam during the cooling. The minimum momentum spread at low intensity is determined by the stabilities of the magnetic field of the ring dipole and the electron beam energy, it is also limited by the detection technique.

Schottky signal in the electron cooling process is illustrated in Fig. 1, The momentum spread vary as the time in cooling is shown in Fig. 2, The Schottky signal distribution before and after electron cooling is shown in Fig. 3.

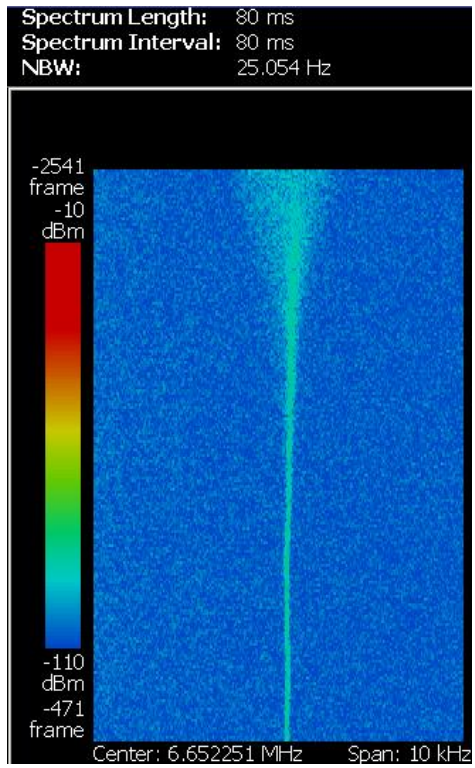

Figure 1: Schottky signal of electron cooling process.

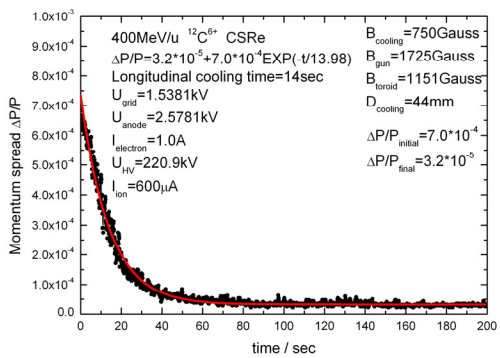

Figure 2: The momentum spread vary as the time in cooling.

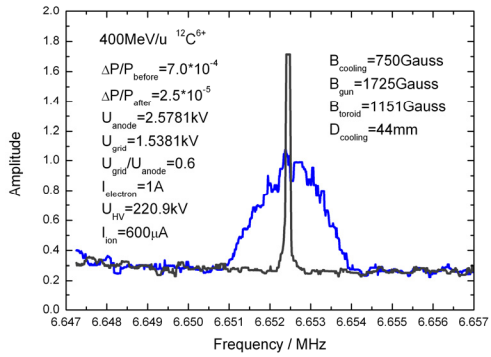

Figure 3: The momentum spread before and after electron cooling.

Longitudinal cooling force measurement

The electron energy-step[10] method is one of the straightforward techniques for measuring the longitudinal cooling force. Ion beam has been cooled firstly, the ion and electron velocities was been matched well. The electron energy was jumped rapidly by changing the cathode potential, a well defined velocity difference between ions and electrons was created. The ions will be accelerated or decelerated toward the new electron velocity. The acceleration is determined via Schottky signal from the change in revolution frequency per unit time.

The Tektronix RSA3303A real-time spectrum analyzer was used in experiments. The 4th harmonic centre frequency shift will be calculated using the spectra files recorded by analyzer. This method was applicable to relative velocities from 10^3 to 10^6 m/sec. The behavior of a cooled $^{12}C^{6+}$ beam after applying a step of 410eV was illustrated in fig 4.

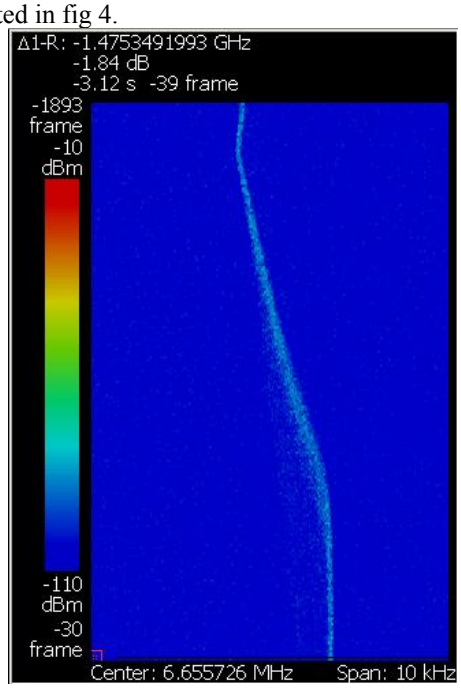

Figure 4: Schottky signal after 410eV electron energy step.

The experiments were performed using the electron energy-step method described above. The experimental conditions were summarized as table 2. These standard operational parameters were determined by HIRFL-CSRe optimization. The profile of electron beam was controlled by the ratio between potential of grid and anode.

Table 2: Parameters of Electron Cooler in Experiments

Items	200.0MeV/u	400MeV/u
B_{gun} [T]	0.1428	0.1725
B_{toroid}[T]	0.073	0.1151
$B_{cooling\ section}$ [T]	0.075	0.075
$I_{electron}$ [A]	0.3~0.5	1.0
Energy step [eV]	200	410

Further experiments studied the influence of the electron beam intensity on the longitudinal cooling force for $^{12}C^{6+}$ beam. Fig 5 shows that the force increases with increased electron beam centre density.

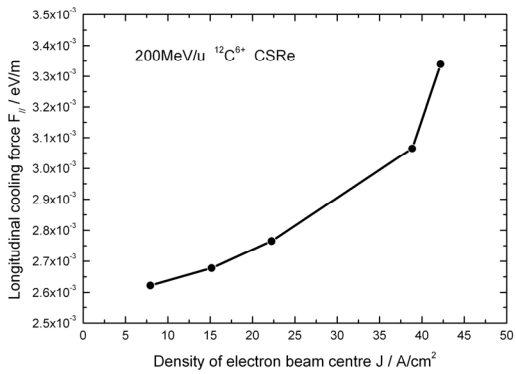

Figure 5: Longitudinal cooling force measured for $^{12}C^{6+}$ ion as a function of different centre density of different electron beam profiles

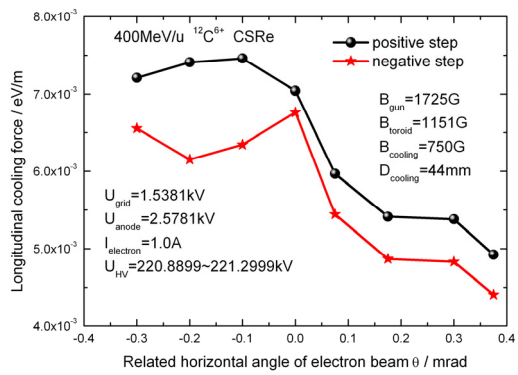

Figure 6: Longitudinal cooling force for different relative horizontal angle of electron beam

The dependence of the longitudinal cooling force on the alignment angles between the ion and the electron beam in horizontal direction was measured for $^{12}C^{6+}$ ions. The longitudinal cooling force as function of the alignment angle was shown in Fig. 6 and Fig 7. It's obvious that perfect alignment is helpful for obtaining maximum longitudinal cooling force.

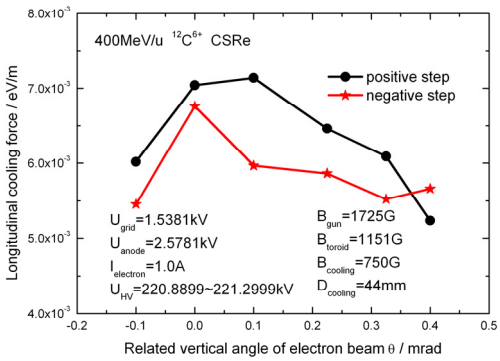

Figure 7: Longitudinal cooling force for different relative vertical angle of electron beam.

Longitudinal cooling forces were obtained for 200 MeV/u $^{12}C^{6+}$ and 400 MeV/u $^{12}C^{6+}$ by electron energy-step method. The experimental results were best agreement with semi-empirical formula. The longitudinal cooling force increases with increasing electron beam current or decreasing the alignment angle between ion and electron beams. According the experiment results, the momentum cooling time of 15sec for 400MeV/u $^{12}C^{6+}$ was obtained in HIRFL-CSRe.

Beam Lifetime

After one injection to CSRe, the injection was stopped and CSRe operated in the mode of DC. The lifetime was measured with the help of DCCT signal. At the beginning, due to the influence of the kicker and other ramping elements, ion beam decayed fastly in the range of , after the field of the kicker and other element disappeared completely, the ion beam decay very slow. The lifetime of 400MeV/u $^{12}C^{6+}$ in CSRe was shown in Fig. 8. From the fitting results, the lifetime was over 80 hours.

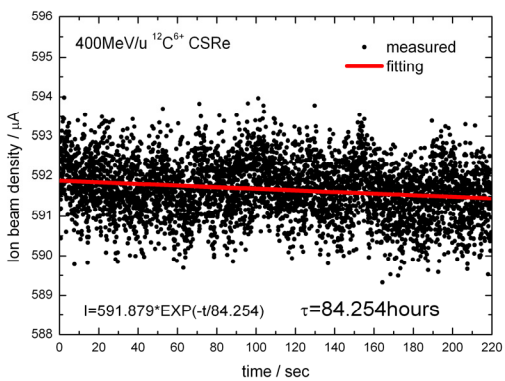

Figure 8: The ion beam lifetime after electron cooling.

Intrabeam Scattering

The electron beam was turn off after the ion beam was cooled to the equilibrium. The Intrabeam Scattering and the diffusion of residual gas were investigated. All particle suffer from the action of vacuum, this caused the energy loss, and the momentum shift. But IBS happened in certain condition, it caused the momentum spread became bigger(longitudinal blow-up). If the electron beam was switched off after cooling, these two processes happened synchronously, after some time the IBS disappear, and only vacuum action still exist. The momentum spread vary with the time was shown in Fig. 9. At the beginning, the momentum spread increase very fast, it is caused by the IBS, after this the scattering of residual gas was dominated, the slide of change became smaller than beginning. The centre frequency shift was shown in Fig. 10. Compared with the simulation results, two results were good agreement each other.

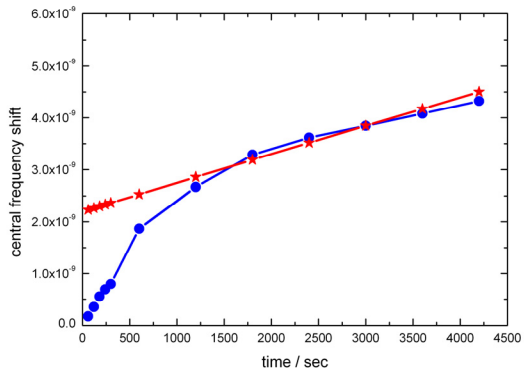

Figure 9: The central frequency shift due to IBS and vacuum.

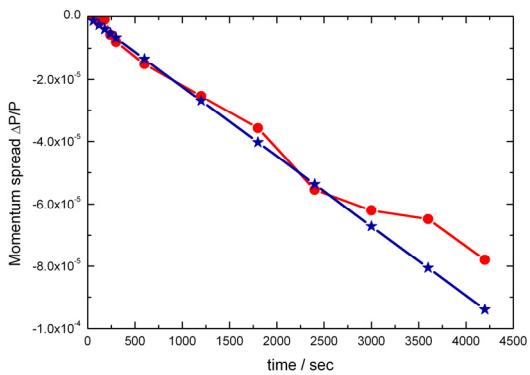

Figure 10: The momentum spread vary as time after switch off electron beam.

Stability of High Voltage

From those results after the electron beam was switched off, the stability of high voltage system of CSRe cooler was derived. The data of HV was recorded as one file, the high voltage value was derived from the ion beam revolution frequencies, Fig. 11 shows the results of stability of HV of CSRe cooler, one can find that due to the electron beam energy slightly decreased, the ion beam was moved from the initial point to the another point with the change of electron energy. From this point of view, the stability of HV system of CSRe cooler should be improved.

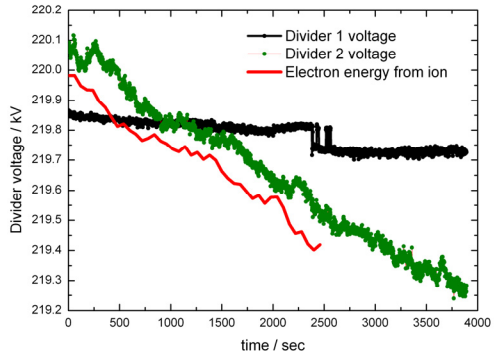

Figure 11: The stability of HV system of CSRe electron cooler.

Beam Transverse Dimension Measurement

Due to the transverse profile monitors were not available in CSRe, a screen drove by step motor was used to measure the transverse dimension of ion beam. The average moving speed is about 1mm/sec, during the screen moving, the ion density signal was recorded by the DCCT in CSRe Fig. 12, the loss rate of ion information was gotten by this way, and the transverse dimension of ion beam was derived from this signal. The transverse dimension was about 24mm before cooling, it reduce to 1mm after cooling. The measurement results were shown in the Fig. 13.

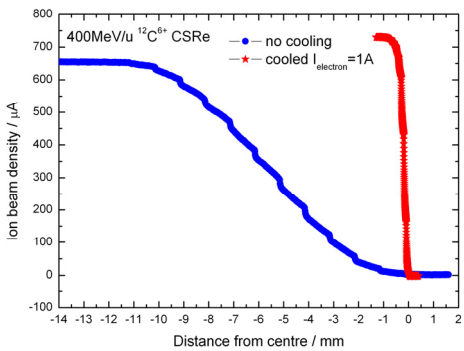

Figure 12: The DCCT signal during the moving the screen.

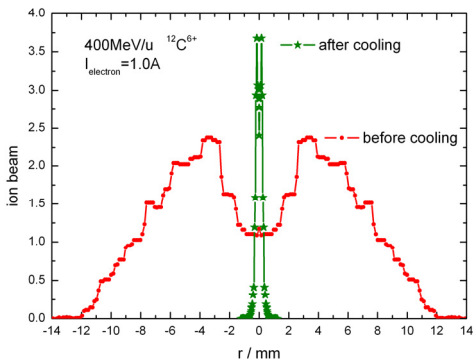

Figure 13: The transverse ion beam size.

SUMMARY AND OUTLOOK

The CSRe electron cooler has come to the routine operation for experiments with stored heavy ion beams in HIRFL-CSR. The cooling process of 400MeV/u $^{12}C^{6+}$ ion beam was studied in CSRe, the main parameters such as momentum spread, transverse ion beam size, and lifetime of stored ion beam was measured. The longitudinal cooling force was measured in the cases of different electron beam profiles, and the different angles between ion beam and electron beam. Some initial results of IBS and residual gas scattering were investigated base on the experimental results.

REFERENCES

[1] J.W Xia et al. “Heavy ion cooler-storage-ring synchrotron in Lanzhou”, High Power Laser & Particle Beams, 2008, Vol.20, No. 11, 1787-1794.

[2] E. I. Antokhin, V.N. Bocharov., A. V. Bubley., et al “Conceptual project of an electron cooling system at an energy of electron of 350kV” NIM.A, 2000,441:87.

[3] V. N. Bocharov, A. V. Bubley, Y. Boimelstein et al “HIRFL-CSR electron cooler commissioning” NIM.A, 2004,532:144.

[4] E. Behtenev, V.N. Bochanov, A.V. Bubley, et al “Commission of electron cooler EC-300 for HIRFL-CSR”, RuPAC XIX Dubna Russia 2004 506-510.

[5] E. Behtenev, V.N. Bochanov, A.V. Bubley,, et al “Commission of electron cooler EC-300 for HIRFL-CSR”, EPAC 2004 Lucerne Switzerland, 1419-1421.

[6] E. Behtenev, V.N. Bochanov, A.V. Bubley,, et al “Commission of electron cooler EC-300 for HIRFL-CSR”, COOL’05, Galena, Illinois, U.S.A 18-23 September 2005, AIP Conference Proceedings 821 334-340.

[7] V.M.Veremeenko, R.V. Voskoboynikov, A.D. Gonchanov, et al “High voltage power supplies for ion beams electron coolers” , RuPAC 2006, Novosibirsk, Russia 97-99.

[8] [8] X.D.Yang et al. “Commissioning of electron cooling in CSRm”, COOL’07, Bad Kreuznach, Germany, September, 2007, 59-63.

[9] M. Steck et al. NIM.A, 2004,532:357.

[10] J. Bosser Electron cooling[A], CAS CERN accelerator school, fifth advanced accelerator physics course[C], CERN95-06, 1995. 673-730.

[11] I. Meshkov, A. Sidorin, A. Smirnov, et al “Necessary condition for beam ordering” COOL’07, Bad Kreuznach, Germany, September, 2007, 87-90 http://accelconf.web.cern.ch/AccelConf/cl07/PAPERS/TUA1C03.PDF.

STATUS OF THE 2 MEV ELECTRON COOLER FOR COSY JUELICH

J. Dietrich#, V. Kamerdzhiev, FZJ, Juelich, Germany
M.I. Bryzgunov, A.D. Goncharov, V.V. Parkhomchuk, V.B. Reva, D.N. Skorobogatov, BINP, Novosibirsk, Russia

Abstract

The design and construction of the 2 MeV electron cooling system for COSY-Juelich is proposed to further boost the luminosity in presence of strong heating effects of high-density internal targets. In addition the 2 MeV electron cooler is an important step towards the high energy electron cooler for the High Energy Storage Ring (HESR) in the FAIR project. The design of the 2 MeV electron cooler will be accomplished in cooperation with the Budker Institute of Nuclear Physics in Novosibirsk, Russia. A newly developed prototype of the high voltage (HV) section, consisting of a gas turbine, magnet coils and HV generator was successfully tested. Special emphasis is given to voltage stability which must be better than 10^{-4}. First experiments with three HV sections, installed in a pressure vessel filled with SF_6 gas are reported.

INTRODUCTION

The new generation of particle accelerators operating in the energy range of 1-8 GeV/u for nuclear physics experiments requires very powerful beam cooling to obtain high luminosity. For example, the investigation of meson resonances with PANDA detector requires an internal hydrogen target with effective thickness 4×10^{15} atoms per cm^2 and $10^{10}-10^{11}$ antiprotons at 15 GeV circulating in the HESR. In this case the peak luminosities ranging from 2×10^{31} to 2×10^{32} $cm^{-2}s^{-1}$ are achievable. These experiments allow to study meson resonances in proton-antiproton annihilations. Resolution of the experiments is limited only by momentum spread in antiproton beam, which must be better than 10^{-4}.

The average momentum losses *dp/pdt* on such a target (for 4 GeV antiprotons) will be about $4\cdot10^{-6}s^{-1}$ and the heating rate of momentum spread by fluctuation of ionization losses will be near $dp^2/p^2dt = 2\times10^{-9}s^{-1}$ To obtain momentum spread of $10^{-5}-10^{-4}$ cooling time in the range $\tau_{cool} = 2(dp/p)^2/(dp^2/dt/p^2) = 0.1\div10s$ is needed. The 4 MeV electron cooler at the RECYCLER ring (FNAL) [1] achieves cooling time about 1 hour. The new cooler for COSY should provide a few orders of magnitude more powerful cooling that requires new technical solutions. The basic idea of this cooler is to use high magnetic field along the orbit of the electron beam from the electron gun to the electron collector. In this case high enough electron beam density at low effective temperature can be achieved in the cooling section. For example the electron beam density of 2×10^8 cm^{-3} (6 mm beam diameter and 1.5 A of current) magnetized with longitudinal magnetic field of 2 kG will have 2.7×10^6 cm/s drift velocity in the beam reference frame. This velocity allows (in principle) to have cooling time near 0.1 s for the low angular spread ($\Delta p_\perp / p = 10^{-5}$) beam.

BASIC DESIGN FEATURES

The basic parameters for the COSY cooler are listed in Table 1. The restrictions are given by the space available in the COSY ring. The height is limited to 7 m by the building.

Table 1: Basic Parameters and Requirements

COSY 2 MeV Electron Cooler	Parameter
Energy Range	0.025 ... 2 MeV
High Voltage Stability	$< 10^{-4}$
Electron Current	0.1 ... 3 A
Electron Beam Diameter	10 ... 30 mm
Length of Cooling Section	2-3 m
Toroid Radius	1.25 m
Magnetic Field (cooling section)	0.5 ... 2 kG
Vacuum at Cooler	10^{-8} ... 10^{-9} mbar
Available Overall Length	6 m
Maximum Height	7 m
COSY Beam Axis above Ground	1.8 m

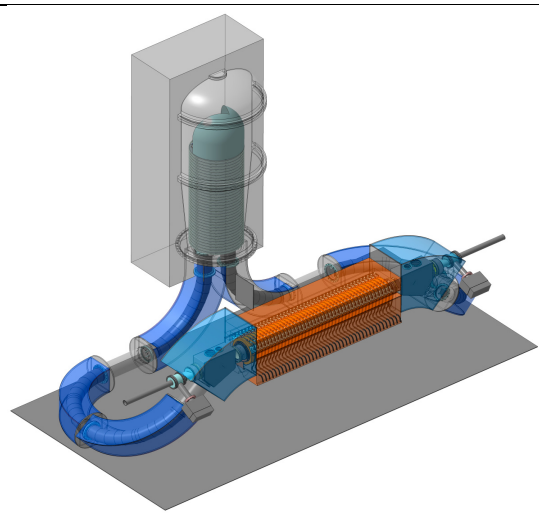

Figure 1: Layout of the 2 MeV electron cooler for COSY.

In Fig. 1 the layout of the COSY 2 MeV cooler is shown. The cooler HV terminal is installed inside the pressure vessel filled with SF_6 gas. The main features of the cooler are:

1. The design of the cooling section solenoid is similar to the ones of CSR (IMP) and LEIR (CERN) coolers designed by BINP [2,3]. However, for the 2 MeV cooler the requirement on the straightness of magnetic field lines is so high ($\Delta\theta < 10^{-5}$) that a system for monitoring the magnetic field lines in vacuum becomes necessary.

#j.dietrich@fz-juelich.de

2. For suppression of high energy electron beam losses at IMP and LEIR coolers electrostatic bending was used [4]. The shape of the 2 MeV transport lines, however, dictates a different approach. The collector (inside the HV terminal) will be modified to suppress return flux. A new low energy line in front of the collector with electrostatic field or 180 degree bending can be used .

PROTOTYPE ELEMENTS STUDY

For the last few years the COSY-BINP collaboration was studying prototype elements for the magnetized cooler. The turbine electro generator driven by compressed gas feeding magnet coils along the HV column was tested. This gas is used to produce power for individual sections and, at the same time, to cool the 500 Gauss coils (Fig. 2).

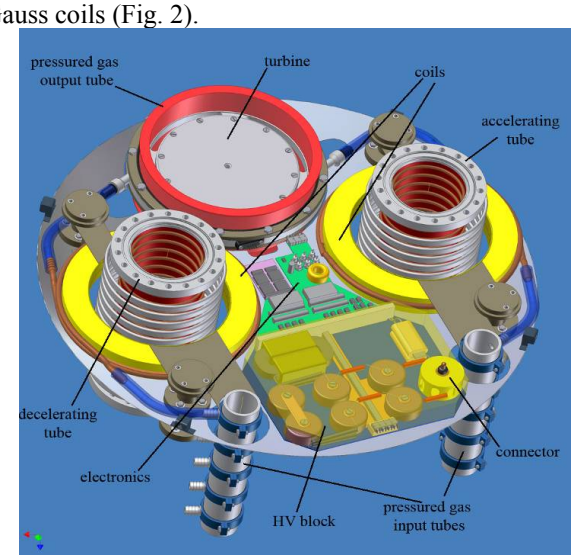

Figure 2: Preliminary design of the HV section with magnet coils around the acceleration and deceleration tubes.

For experiments with HV sections in pressurized SF_6 gas we used the same vessel as used for 1-1.5 MeV industrial accelerator of ELV type (Fig. 3 and Fig. 4). The height of a single HV section equals 4 cm while the gap between them is 2 cm. The results of HV tests are shown in Fig. 5 and Fig. 6.

Figure 3: Pressure vessel used for HV section testing.

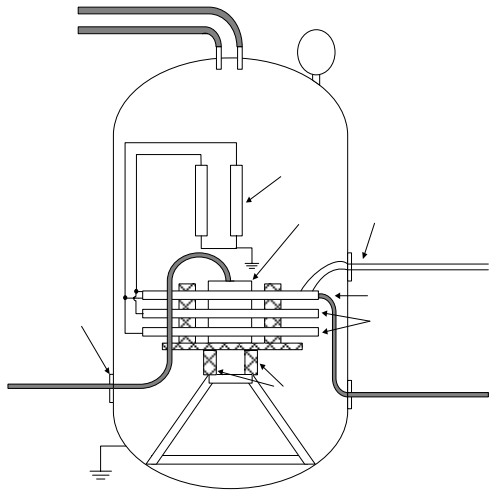

Figure 4: HV test setup.

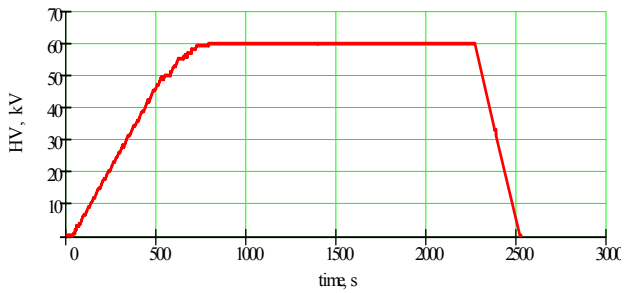

Figure 5: Voltage between sections in SF_6 (1.6 atm.).

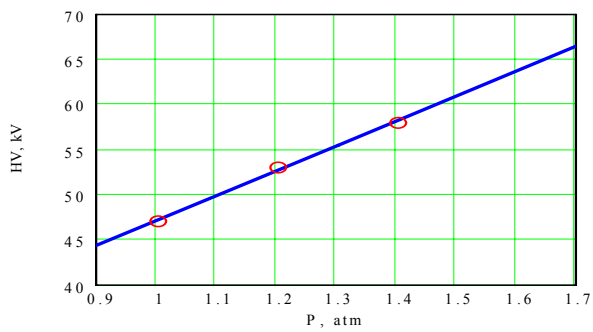

Figure 6: Discharge voltage versus SF_6 pressure.

Fig. 6 shows the measurement of discharge voltage between HV sections for different SF_6 pressure. Linear extrapolation (blue line) shows that the discharge voltage at 1.6 atm is 63 kV which is higher than the design output of the HV source (60 kV). From these experiments it is clear that SF_6 gas isolation works well for the chosen HV section design. HV stability was measured using an ADC installed in the HV terminal. In Fig. 7 relative HV stability is shown.

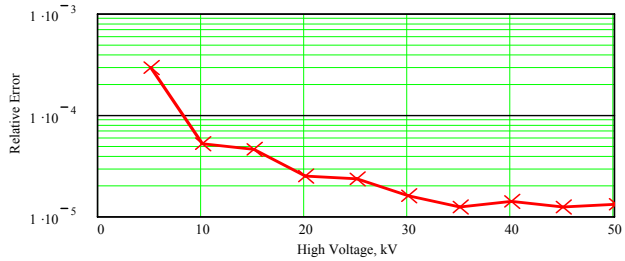

Figure 7: Relative HV stability versus HV value.

In Fig. 8 voltage between sections at 1.2 atm. of SF_6 is shown.

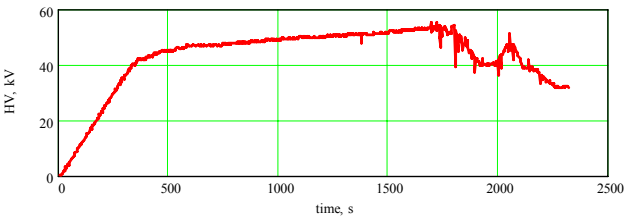

Figure 8: Voltage between sections in SF6 (1.2 atm.).

There is ripple which appears at higher voltage and does not vanish when the voltage is decreased. The most probable explanation of the effect is the appearance of regions of ionized gas after the first spark. After that sparks in this region appear more often and at lower voltages. Similar behavior can be observed at 1.4 atm. (Fig. 9).

At high values of voltage, which are close to maximum, sparks appear. Maximum voltage reached for this pressure (1.4 atm) is 58 kV. Stable operation is possible at 56-57 kV. To estimate the coil temperature, the coil resistance was measured during the experiments. Using the equation for dependence of coil resistance on temperature $R = R_0(1+\alpha\Delta T)$ one can estimate the average coil temperature (for copper α=0.0038 [1/K]).

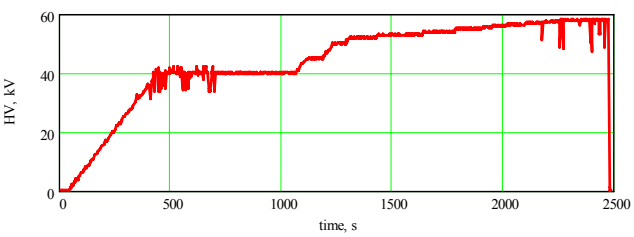

Figure 9: Voltage between sections in SF_6 (1.4 atm.).

The evolution of the coil temperature is shown in Fig. 10. The coil temperature increase (reconstructed from coil resistance) is acceptable. There is no dependence of the temperature on conditions in the vessel. It proves that coil cooling provided by gas flowing in tubes is much stronger than cooling by convection.

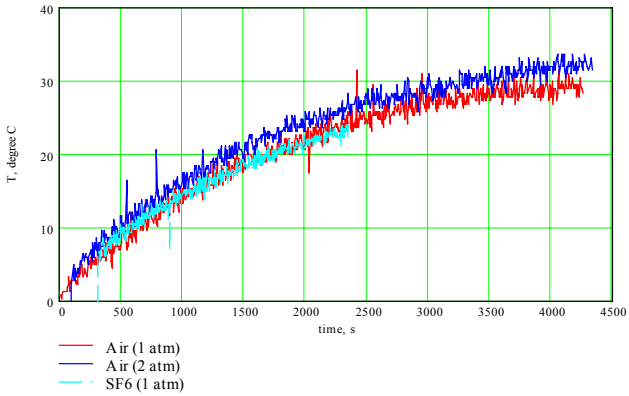

Figure 10: Average coil temperature calculated from resistance minus room temperature for different conditions in the vessel. I=1.3 A.

SUMMARY

The HV section prototype was successfully tested under different gas mixtures and pressures in a test bench at BINP. The specified voltage stability of better 10^{-4} was reached. The magnetic field in the coils of a single section reached the required value of 500 G. The specified high voltage of 60 kV per section was reached with required stability under SF_6 pressure of 1.6 atm. In the next step more of such high voltage sections will be combined and long life time and reliability will be investigated.

ACKNOWLEDGEMENTS

The authors would like to thank the colleagues who recently joined the project team at BINP, especially the mechanical design team members V. K. Gosteev, A. M. Kruchkov, A. A. Putmakov and V. A. Poluhin.

REFERENCES

[1] L.R. Prost, A. Burov, K. Carlson, A. Shemyakin, M. Sutherland, A. Warner, Electron Cooling Status and Characterization at Fermilab's Recycler, Proceeding of COOL07, Bad Kreuznach, Germany p.49-54.

[2] X.D. Yang et al., Commissioning of Electron Cooling in CSRm, Proceeding of COOL07, Bad Kreuznach, Germany p.59-61.

[3] G. Tranquille, Cooling results from LEIR, Proceeding of COOL07, Bad Kreuznach, Germany p.55-58.

[4] E.I. Antokhin et al., Conceptual Project of an Electron Cooling System at an Energy of Electrons of 350 keV, ECOOL'99, NIM A 441 (2000) 87-91.

ELECTRON COOLING FOR ELECTRON-ION COLLIDER AT JLAB*

Ya. Derbenev and Y. Zhang
Thomas Jefferson National Accelerator Facility, Newport News, VA23606, U.S.A

Abstract

A critical component of a conceptual design of a high luminosity electron-ion collider at JLab is an electron cooling facility which consists of a 10 mA, 33 MeV energy recovery linac and a circulator ring. A fast kicker has been conceptually designed for switching electron bunches between the linac and the circulator ring. To alleviate space charge impact on cooling, we developed a concept of *helical* electron cooling in which the cooled ion beam has a large round size but a low 4D emittance by matching the *circular eigenmodes* of the ion ring with solenoid in the cooling section. The collider luminosity could be restored by transforming the round ion beam to a flat one in the collision area. In this paper, design parameters of this cooling facility and a scenario of forming and cooling of the ion beam will be presented.

INTRODUCTION

The CEBAF recirculating SRF linac, currently under an energy doubling upgrade, will provide up to 12 GeV polarized CW electron beam with 3x499 MHz bunch repetition rates and excellent beam quality for fixed target nuclear science programs at JLab. The upgraded CEBAF will also open a great opportunity for a high luminosity electron-ion collider (ELIC) which can be achieved by adding an ion complex. [1] Such a collider could provide collisions between polarized electrons and polarized light ions or non-polarized heavy ions in a wide center-of-mass (CM) energy range, delivering a luminosity up to 10^{35} $cm^{-2}s^{-1}$. Electron cooling (EC) is essential both during the process of forming high intensity ion beams as well as at a collision mode for maintaining good beam quality. A conceptual design of the ELIC electron cooler was first reported in a previous paper of the same workshop series. [2] Here we will present an update of the design and also discuss several key technology R&D issues required for realizing this design.

ELECTRON-ION COLLIDER AT JLAB

JLab has been engaged in conceptual design of ELIC for nearly a decade. After several major design iterations, the latest ELIC design, as shown in Figure 1, focuses on a low-to-medium energy collider with CM energy up to 52 GeV. [3] There are three vertically stacked figure-8 shape storage rings, namely, the electron ring and two ion rings for low (up to 12 GeV/c) or medium (up to 60 GeV/c) momentum per proton respectively, in a small tunnel (red line in Fig.1a) of approximately 640 m, and crossed at four collision points as shown in Fig. 1b. Two large figure-8 rings (the grey line in Fig.1a) are for future upgrade to a high energy collider. Table 1 summarizes the design parameters for the low to medium energy ELIC.

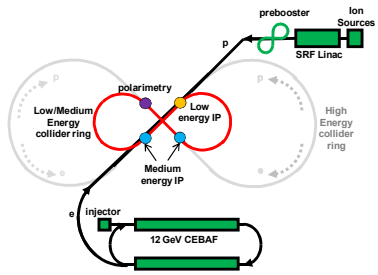

Figure 1a. Schematic drawing of a ring-ring electron collider based on CEBAF at JLab.

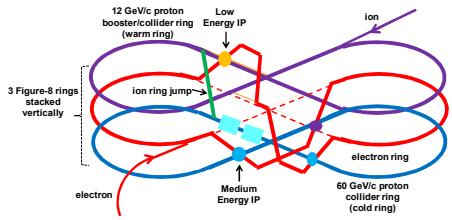

Figure 1b. Three figure-8 shape storage rings for electron, low and medium energy ions are stacked vertically and crossed at four collision points.

Table 1. ELIC main parameters

Beam energy	GeV	60/5	60/3	12/3
Collision frequency	MHz	499		
Beam current	A	0.6/2.3	1.1/6	0.5/2.3
Particles/bunch	10^{10}	0.7/2.9	0.86/4.8	0.47/2.3
Energy spread	10^{-4}	~3		
RMS bunch length	mm	5	5	50
Hori. emit., norm.	mm	0.56/85	0.8/75	0.2/80
Verti. emitt, norm	mm	0.11/17	0.16/15	0.18/80
Hori. beta-star	mm	25	25	5
Verti. beta-star	mm	5		
Verti. b-b tune shift		.01/.03	.015/.08	.015/.013
Laslett tune shift		0.1	0.054	0.1
Peak lumi./IP, 10^{34}	$cm^{-2}s^{-1}$	1.9	4	0.6

The ELIC high luminosity concept is based on the following design features: very high bunch collision rate (0.5 GHz), large beam-beam parameters, and very small bunch spot sizes at collision points. The very small β_y^* value (~5 mm) requires a very short ion bunch (~5 mm RMS) which is achievable due to not only electron cooling but also a relatively small bunch charge, a fraction of 10^{10} protons per bunch, compared to typical super bunches (of 10^{12} protons or more) with much longer bunch lengths (10 cm RMS or larger) in all existing hadron colliders.

* Authored by Jefferson Science Associates, LLC under U.S. DOE Contract No. DE-AC05-06OR23177. The U.S. Government retains a non-exclusive, paid-up, irrevocable, world-wide license to publish or reproduce this manuscript for U.S. Government purposes

FORMING AND COOLING OF ION BEAM

One important task for the ELIC ion complex is forming a high intensity beam with high bunch repetition rate and short bunch length. The present design utilities ion sources, an SRF linac (0.2 to 0.3 GeV/c) and a pre-3 GeV/c booster ring as shown in Figure 2 for achieving this goal. The ion beam is stacked at the pre-booster which also acts as an accumulator ring with multi-turn injections from the SRF linac and phase space damping through a cooling procedure. Negative ion beams such as H^- or D^- can be accumulated directly in the pre-booster without cooling due to their relatively small phase space footprints. The accumulated beam then fills the low energy collider ring for acceleration up to 12 GeV/c for proton or appropriate momentum per nucleon of ions. The beam can be either RF bunched and cooled for low CM energy collisions in this ring or injected into the medium energy ring for further energy boost in order to enable collisions at medium CM energies. Table 2 lists accelerating procedures of ion beams and appropriate cooling schemes at various stages.

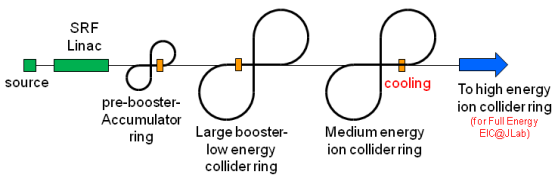

Figure 2. A flow chart for ELIC ion beam formation.

Table 2. Ion beam formation and acceleration scheme

	Length	Max. Energy	Cooling Scheme	Processes
	M	GeV/c		
Source/Linac		0.2		
Prebooster/ accumulator ring	~100	3	DC electron	Stacking Energy boost
Low energy collider ring (large booster)	~630	12	ERL electron	Fill ring Energy boost RF bunching
Medium energy collider ring	~630	60	ERL electron	Energy boost RF bunching
High energy collider ring	~630	250	ERL electron	Energy boost RF bunching

Electron Cooling at the Pre-booster

For stacking positive ions in the ELIC pre-booster, an efficient cooling mechanism must be introduced during the accumulating process. This reduces the phase space area the accumulated beam occupies in order to allow injection of new ions from the linac. Both stochastic and electron cooling were considered for this task and are still under evaluation. While the stochastic cooling option was reported earlier [2], table 3 shows the parameters for a DC electron cooling option.

Staged Electron Cooling in the Collider Ring

Immediately after an ion beam is injected into a collider ring, either low energy or medium energy, electron cooling is called to provide an initial cooling for phase space footprint reduction before the ion beam is accelerated to the final colliding energy and bunched by SRF cavities. Then electron is called again for minimizing 6D emittance of the ion beam to the design values. After the machine is switched on for collisions, electron cooling must be continued all the time in order to suppress heating of ion beams by intra-beam scatterings and to maintain beam quality. The three columns in Table 4 are design parameters for EC in the medium energy collider ring at initial and final stages of ion beam formation as well as at collision mode. In making this table, we have assumed the electron cooler is able to deliver up to 3 A CW electron beam with energy up to 33 MeV. The cooling rates are obtained using analytic formulas based on a simplified EC model. [4]

Table 3. Parameters for EC in the pre-booster

Circumference	m	~80
Arc radius	m	~3
Crossing straight length	m	2 x 15
Energy/u	GeV	0.2 -0.4
Electron current	A	1
Electron energy	MeV	0.1 - 0.2
Cooling time for protons	ms	10
Stacked ion current	A	1
Norm. emit. after stacking	μm	16

Table 4. Parameters for staged EC at ELIC medium energy collider ring.

		Initial cooling	After bunching	Colliding mode
Momentum	GeV/MeV	12/6.6	60/33	60/33
Beam current	A	0.6/3	0.6/3	0.6/3
Particle/bunch	10^{10}	0.7/3.8	0.7/3.8	0.7/3.8
Bunch length	mm	200/200	10/30	5/15
Energy spread	10^{-4}	5/1	5/1	3/1
Hori. Emit. norm.	mm	4	1	0.56
Vert. emtt. norm.	mm	4	1	0.11
Laslett tune shift		0.002	0.006	0.1
Cooling length	m	15	15	15
Cooling time	s	92	162	0.2
IBS growth time (longitudinal)	s			0.9

ERL BASED CIRCULATOR COOLER

The present ELIC electron cooler design, first described in a previous paper [2] and shown in Figure 3, is based on ERL and circulator ring (CR) technologies. Electron bunches from an injector and an SRF linac are arranged to circulate a number of times in a small (~ 50 m) ring while cooling ion bunches in each evolution in a 15 m long channel immersed inside a superconducting solenoid before being ejected and sent to the same SRF linac for energy recovery. The recovered energy will be used to accelerate new cooling electron bunches from the injector. The choice of ERL technology is aimed at overcoming the challenge of very high average RF power, up to 100 MW, drawn from klystrons in order to deliver a 3 A CW 33 MeV electron beam. With state-of-the-art ERL technology, the required power from wall plugs could be

reduced to one MW or less (roughly beam power from an injector). The choice of CR solves the other challenge of the ELIC cooler design, namely, the photocathode lifetime due to demand of unprecedented high average current from a photocathode injector. With a 3 A CW operation, the cooler would draw about 260 kC electrons from the cathode each day. By recirculating electron bunches 100 to 300 times in a CR and assuming the cooling efficiency is still satisfactory, the amount of charge from a photocathode could be reduced by a factor of 100 to 300, to a level very much manageable with the present state-of-the-art photocathode injectors.

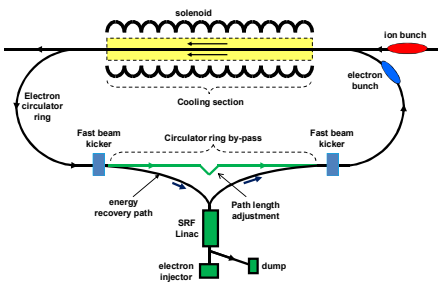

Figure 3. ERL based circulator electron cooler for ELIC.

Alternatively, one can use a grid-operated thermionic gun for producing a high average current electron beam with large bunch charge and long bunch length. Such guns normally have a much longer cathode lifetime, and are able to deliver thousands of kC charge before requiring a service of their cathode surfaces, therefore a circulator ring may only be needed for either avoiding high average current ERL or for reducing the bunch repetition rate of the injector.

A classical scheme with a magnetized electron beam can also be used for high energy electron cooling for ELIC. [5-7] After the gun which is immersed inside a solenoid, an electron beam can be transported for acceleration in RF or SRF cavities in the injector and in the ERL with axial-symmetric and quadrupole focusing lenses. The solenoids in the cooling section should be matched with the rest of the circulator ring optics to provide a magnetized parallel beam required for efficient cooling. [6]

MATCHED ELECTRON COOLING

In principle, equilibrium emittances of a high intensity low energy ion beam under cooling could be limited by Coulomb repulsion. A circulator ring whose optics is matched with solenoids in a cooling section prompts a possible way to reduce the space charge effect on ion transverse emittance.

Assuming such an optically matched ring is used for a low energy hadron collider, one principal feature of such optics design is that two components of a hadron particle's motion in solenoids, namely drift and cyclotron, are not mixed by optics outside of the solenoids. In other words, the radial fringe field of the solenoids transforms the cyclotron and drift motion into two circular modes of opposite helicities, and such modes can be transported around the ring by an axial-symmetric optics as well as quadrupoles. Tunes of two modes can also be split in order to prevent resonance exchange between them.

Further, if there is no organized redistribution of cooling decrements of emittances, only the cyclotron mode will experience the cooling. Thus, space charge cannot stop cooling of the cyclotron mode since the beam size will not shrink, being related to the drift mode. As a consequence, one of the two emittances can be cooled to a very low equilibrium, especially taking into account the magnetization effect on the cooling process [5,8]. The emittance associated to drift can be cooled to the space charge limit using the dispersive mechanism [5,9]. Since the cyclotron motion and momentum spread will already be cooled, the beam will shrink quickly.

A minimum spot of a cooled ion beam with an appropriate aspect ratio for matching with a flat electron beam at collision points can be obtained using round to flat beam transformers [9]. Other benefit of such optics concept is drastic reduction of the space charge impact on particle dynamics in low energy hadron beams for avoiding decrease of luminosity of the collider.

FAST KICKER FOR ERL-CCR

One key element in the ERL based circulator cooler for ELIC is an ultra fast kicker that will be used to switch electron bunches in and out of the circulator ring. Table 5 shows the basic parameters for the required kicker. A conceptual design of a RF kicker was developed and presented in a previous paper. [2]

Table 5: Estimated parameters for a RF kicker

Beam energy	MeV	125
Kick angle	10^{-4}	3
Integrated BdL	GM	1.25
Frequency BW	GHz	2
Kicker Aperture	cm	2
Peak kicker field	G	3
Kicker Repetition Rate	MHz	15
Peak power/cell	kW	10
Average power/cell	W	15
Number of cells		20

Beam-beam Kicker

An innovative idea recently under active investigation utilizes a non-relativistic sheet beam for providing transverse kicking to a flat electron bunch. [10] This idea of a beam-beam kicker was first proposed by Shiltsev [11] for two round Gaussian beams. Here we consider a case of two flat beams as shown in Figure 4, though analytical treatments for these two cases are quite similar. We present here final results plus considerations of cooling electron bunch requirement in order to have an effective kicker scheme. Two technical issues will be also briefly discussed.

Since the target flat (cooling) beam is moving at the speed of light, it passes through the non-relativistic kicking flat beam in a period of time determined by the

length of the kicker beam l_k under condition $l_k<(\lambda-l)v_k/c$ where v_k, λ and l are speed, bunch spacing and bunch length of the target beam, respectively. At a close distance to the kicking beam, an electron in the target beam receives an instant angle kick determined by integration of the transverse force over that passing time

$$\delta\theta_y = \frac{2\pi N_k r_e}{\gamma\sigma_{xk}}$$

under conditions $\delta\theta_y >> \sigma_{\theta y}$ and $\sigma_{xk} >> \sigma_{yk}$, where N_k, σ_{xk} and σ_{yk} are number of electrons, horizontal and vertical RMS size of the kicker bunch, $\sigma_{\theta y}$ is the RMS angle spread of the cooling bunch, r_e is the electron classical radius.

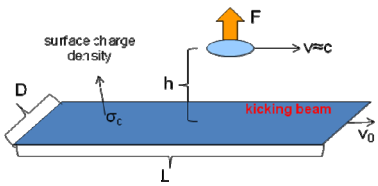

Figure 4. A schematic drawing of beam-beam fast kicker

In order to reducing the required kick, the cooling beam should have large vertical beta function at the kicker section. Combining this with the flatness condition, we find the following requirements to the cooling beam

$$1 << \frac{\beta_y}{\beta_x} << \frac{\varepsilon_x}{\varepsilon_y}$$

Table 6 summarizes the design parameters for a beam-beam kicker for the ELIC CR cooler design. It should be noted that, with 100 to 300 revolutions of cooling electron bunches in the CR, the repetition frequency of the kicking beam can be a factor of 100 to 300 smaller than the repetition rate of the CW cooling beam.

Table 6. Design parameters for beam-beam kicker

Circulating beam energy	MeV	33
Kicking beam energy	MeV	~0.3
Kicking Repetition frequency	MHz	5 – 15
Kicking angle	mrad	0.2
Kicking bunch length	cm	15 – 50
Kicking bunch width	cm	0.5
Kicking bunch charge	nC	2

Making of a Flat Kicker Beam

A flat kicker beam can be produced utilizing a grid-operated DC (thermionic) electron gun with a round magnetized cathode. While maintaining the beam in solenoid, one can impose a constant quadrupole field that causes beam shrinking in one plane while enlarging in the other plane due to the drift motion of particles. The process should be adiabatic relative to the particles' cyclotron motion in the solenoid [6]. The beam current density could be specifically profiled at the cathode to create uniform distribution in a homogenous field in a direction transverse to in the "plane" of flattened beam.

Obtaining a Flat Cooling Beam

While the magnetized state of a cooling beam is transplanted from the gun to the solenoids in the cooling section, the beam can be made flat at a kicker section of the circulator ring applying round-to-flat beam transformation proposed for an angular momentum dominated beam. [12] Such transformation can be performed by a special group of skew-quadrupoles matched with optics of the circulator ring. This will create flat beam with two very different emittances [7]:

$$\frac{\varepsilon_y}{\varepsilon_x} = \frac{r_c^2}{r_0^2}, \quad \varepsilon_x\varepsilon_y = \varepsilon_0^2$$

where r_0, r_c and ε_0 are the space and thermal cyclotron radii respectively and the normalized emittance of round beam at the cathode.

CONCLUSIONS

ELIC relies on staged cooling for making and maintaining small transverse emittance and short bunch colliding ion beams. Its cooler design is based on ERL and CR technologies for delivering high average current electron beam. This design can be easily scaled to higher electron energy to serve the cooling needs of a high energy electron-ion collider based on CEBAF. All key technology elements, namely a 10 to 30 mA average current injector, ERL and fast beam kicker, are either already existing and mature, or with promising conceptual designs. Our future R&D effort will be concentrated on the proto-typing of fast kickers, studies of high average current circulating electron beam dynamics, stability and precision control of coupled ion and cooling electron systems required for efficient electron cooling.

ACKNOWLEDGEMENT

We would like to thank P. Evtushenko for suggestion of a beam based kicker.

A note from the authors

The ELIC conceptual design is done by the JLab ELIC study group, of which both authors of this paper are members. It is presented here in unusual detail mainly for the purpose of self sufficiency of the paper since the latest design of a low-to-medium ELIC has never been documented anywhere else.

REFERENCES

[1] For example, A. Bogacz, et al, Proc. EPAC08, P2634
[2] Ya. Derbenev, et al, Proc. Cool 2007, P187
[3] For example, Y. Zhang, presentation at Common ENC/EIC Workshop at GSI, May 2009
[4] Ya. Derbenev, BIM A 532 (2004) P307
[5] Ya. Derbenev, NIM A 441 (2000) P223
[6] Yu. Martirosyan et al., Proc. EPAC 2000
[7] A. Burov et al.,Phys. Rev. STAB, 3,094002 (2000)
[8] A. Burov et al., Phys. Rev. E, 016503 (2002)
[9] Ya. Derbenev, et al., Sov. Phys. Rev., 1 (1981) 165
[10] P. Evtushenko, Private communication
[11] V.Shiltsev, NIM. A374 (1996) 137
[12] I.Meshkov, Private communication

STATUS OF HIRFL-CSR PROJECT*

Y.J. Yuan#, H.W. Zhao, J.W. Xia, X.D. Yang, H.S. Xu and CSR Group

Institute of Modern Physics(IMP), CAS, Lanzhou, 730000, P.R. China.

Abstract

The HIRFL-CSR project is a national mega project of China, which concentrates on heavy ion synchrotrons and cooling storage rings. It is finished recently. The present commissioning results, testing experiments and new development are introduced in this paper. The future improvement of the machine is also discussed in this paper.

INTRODUCTION

The HIRFL-CSR project consists of CSRm (main synchrotron), RIBLL2 (RIB production and transfer line), CSRe(experimental storage ring) and experimental terminals (see Fig. 1). Its injector is a two cyclotrons complex. Its total budget is around 27 million euro. The main parameters are listed in Table 1.

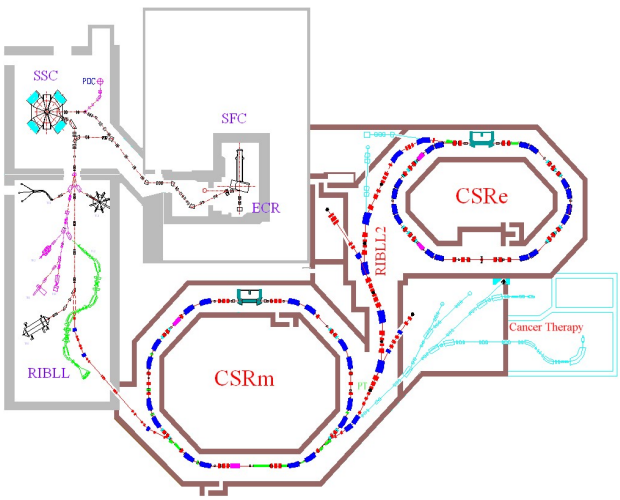

Figure 1: Layout of HIRFL-CSR.

The project starts in Apr. 2000 and gets the first stored beam in CSRm in Jan. 2006. By end of 2007, the commission and official tests are done successfully.

Up to now, several species of beam are commissioned at CSR, including Carbon, Argon, Krypton and Xeon. The intensity of them reached 7×10^9, 4×10^8, 1×10^8 and 1×10^8 pps respectively. The energy of Carbon and Argon reached 1AGeV, which surpassed the designed magnet rigidity value 10.64Tm. The Carbon, Argon and Krypton beams are injected into CSRe, and two mass measurement experiments are done with Argon and Krypton beams.

The slow extraction is realized for CSRm, it's the first step towards external target experiments and cancer therapy study.

Table 1: Major Parameters of CSR

	CSRm	CSRe
Ion species	Carbon~Uranium	Carbon~Uranium
Magnet rigidity	0.7~11.5Tm	0.6~9Tm
Max. Energy	$^{12}C^{6+}$-1000MeV/u $^{238}U^{72+}$-460MeV/u	$^{12}C^{6+}$-700MeV/u $^{238}U^{91+}$-460Mev/u
Beam intensity	$^{12}C^{6+}$- 7×10^9ppp $^{129}Xe^{27+}$-1×10^8ppp	$^{12}C^{6+}$- 7×10^9ppp $^{129}Xe^{27+}$-1×10^8ppp
Emittance	~1π mm mrad	~1π mm mrad
Tunes	3.63/2.62	2.53/2.58
e-cooler energy	35keV (50MeV/u)	300keV (400MeV/u)
Vacuum Pressure	$<6\times10^{-11}$mbar	$<6\times10^{-11}$mbar
RF cavity	0.24~1.7MHz 7kV	0.5~2MHz 2×10kV
Injection	Multi-turn Charge exchange	Single turn
Extraction	Fast Slow(RF KO)	-

COMMISSIONING AND OPERATION

At beginning of 2005, the commission of CSRm started. The first beam passed CSRm in Feb. 2005. During 2005, a lot of work was done to improve the beam diagnosis system, power supply system and local control system. The first stored beam was obtained by charge stripping injection (CSI) method in Jan. 2006(Fig. 2).

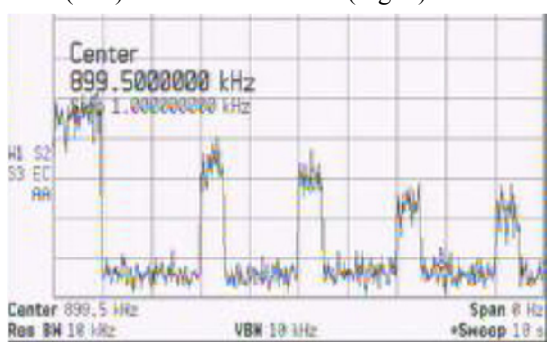

Figure 2: The first stored beam observed by periodical RF capture and release.

Later, the remote control system, the beam current monitor, and tune measurement were available. The magnet field measurement data is investigated and

*Work supported by HIRFL-CSR project
#yuanyj@impcas.ac.cn

repaired to fit the system error. The RF harmonic transfer technique was realized In Oct. 2006, the $^{12}C^{6+}$ beam was accelerated from 7MeV/u (0.76Tm/0.1T) to 1000MeV/u (11.3Tm/1.5T) with a beam intensity of 2.8×10^8 pps (Fig. 3). The main goals of CSRm were fully finished.

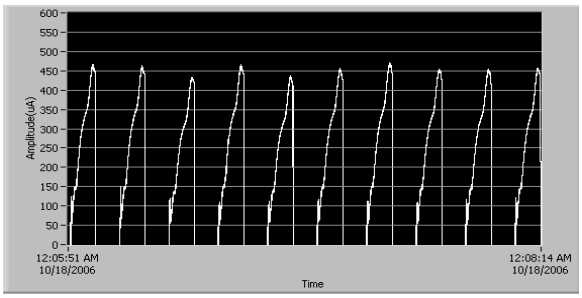

Figure 3: Beam current observed for 10 periods of acceleration of $^{12}C^{6+}$ beam from 7MeV/u to 1000MeV/u.

The beam intensity is improved dramatically to 2×10^9 pps (Fig. 4) with e-cooling in CSRm[2]. The record was renewed to 7×10^9 pps in Sep. 2007.

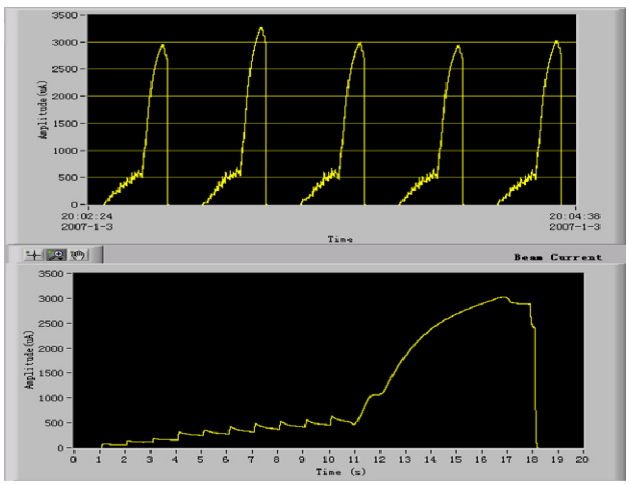

Figure 4: Accumulation and acceleration of $^{12}C^{6+}$ beam with electron cooler.

The charge stripping injection method is fit for elements lighter than argon, only. To accumulate heavy ions, multi-multi-turn injection (MMI) method is the major scheme. The MMI was first realized in Apr. 2007 with carbon beam. After that the first argon (4×10^8 pps) and xenon (1×10^8 pps) beam was accumulated and accelerated in CSRm(Fig. 5).

In Aug. 2007 the first fast extracted beam was available. After struggling with the beam line the first beam was stored in CSRe in October. The stored beam reached 7×10^9pps for $^{12}C^{6+}$ and 1.2×10^8pps for $^{36}Ar^{18+}$.

The first slow extracted beam is seen on detector in Jan. 2008. The time structure of first slow extracted beam ($^{36}Ar^{18+}$-368AMeV) is shown in Fig. 6. The spill length is about 1s. The effect of 50Hz ripple of power supply is obvious, estimated to be around 5×10^{-4}. Recent results also show similar structure.

During commissioning and about one year operation, HIRFL-CSR provided $^{12}C^{6+}$, $^{36}Ar^{18+}$, $^{129}Xe^{27+}$ and $^{78}Kr^{36+}$ beams for experiments and cancer therapy research. The maximum rigidity reached 11.3Tm.

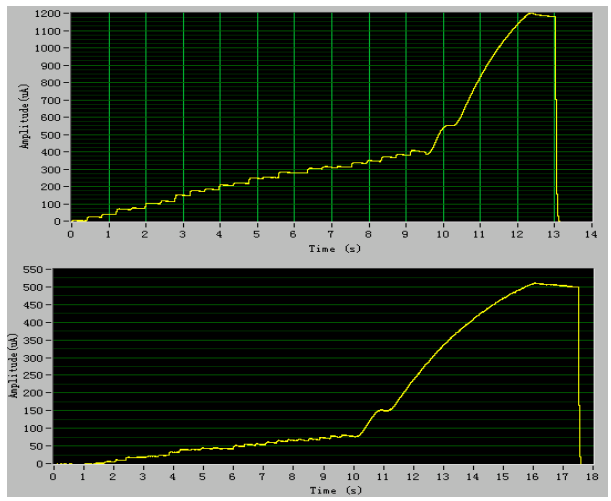

Figure 5: Accumulation and acceleration of $^{36}Ar^{18+}$(up) and $^{129}Xe^{27+}$ beam by MMI.

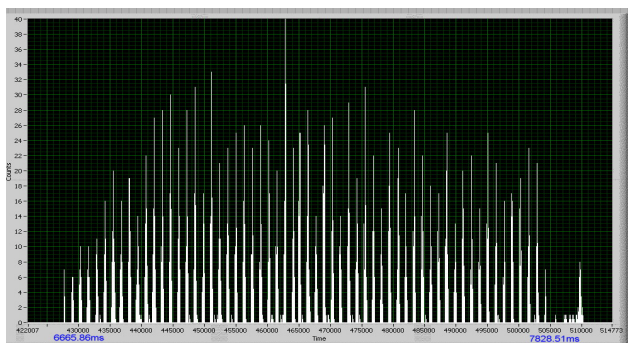

Figure 6: Time structure of first slow extracted beam from CSRm, detected by plastic scintillator.

E-COOLER COMMISSIONING

The e-coolers play essential role in CSR project. As a new generation of e-cooler developed by BINP, the coolers can provide controlled electron beam density distribution [5, 6].

The e-cooler for CSRm was in function by the end of 2006[2]. The study of e-cooler is done during the commissioning for official tests. Up to now, the grid to anode voltage ratio is set around 0.2 to get a pizza-like density distribution, which is the "best" to reach high ion current at present condition of the ring.

Although the profile and closed orbit monitoring system are not in function properly, many tests are done to test the operation condition of e-cooler in CSRm. Most of the results show the "big" crossing angle between the ion beam and electron beam.

By using of single wire scanning profile monitor, the transverse emittances are estimated to be around 35 π mm mrad after cooling($\Delta p/p\sim2\times10^{-4}$), which indicates that the crossing angle is about 1.9 mrad. According to ref.[7], the beam phase space is hollow with misalignment angle.

The relation of momentum spread to number of particles (N) is proportional to $N^{0.11\sim0.2}$(Fig.7), which is

different from theory prediction. Some other results also hints to the effect of misalignment to beam cooling(Fig.8).

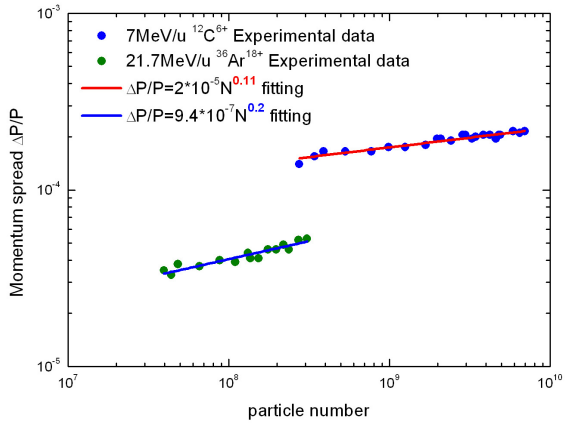

Figure 7: Measured relation of momentum spread to number of particles of cooled beam

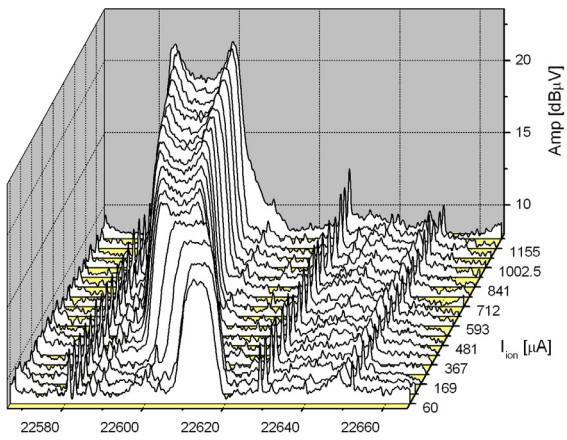

Figure 8: Spectrum of longitudinal beam signal during decay of beam intensity. The increase of frequency centre during decay is reverse from IBS theory.

The longitudinal cooling force is measured. Some results are shown in Fig. 9 and Fig. 10. The result in Figure 10 is an authentic evidence of the misalignment.

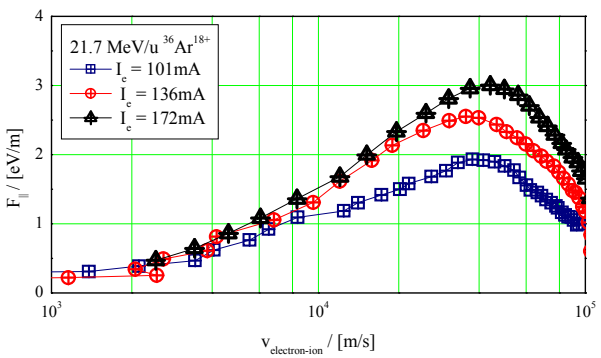

Figure 9: Measured cooling force relative to electron beam intensity.

The cooler for CSRe is ready to cool beams up to 400MeV/u.[8]

For both cooler precise and reliable closed orbit measurement and correction will be improved, the cooling force will be enhanced.

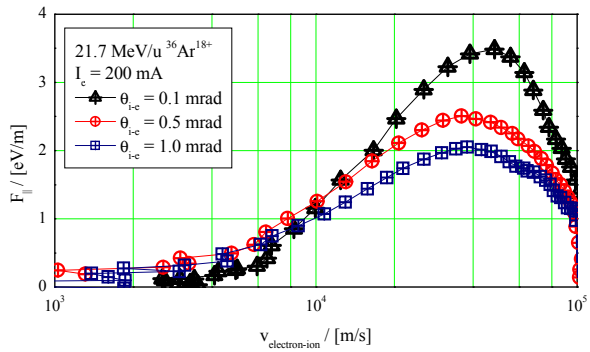

Figure 10: Measured cooling force relative to changing of crossing angle between ion beam and electron beam.

EXPERIMENTS

Mass Measurement Testing

For CSRe, to measure the mass of RIBs produced in the beam line, isochronous mode[3] is designed. The transition energy is reached to γ_{tr} =1.395. When the primary beam from CSRm matches the condition, the frequency spread from momentum spread can be neglected (see Eq. 1).

$$\frac{\delta f}{f} = \left(\frac{1}{\gamma^2} - \frac{1}{\gamma_{tr}^{\ 2}} \right) \frac{\delta P}{P} \tag{1}$$

The measured frequency spread in CSRe for primary beam is 1×10^{-7}, which proves the isochronous mode is reached. After RIBs are produced on the target, the fragments with the same magnetic rigidity can be accepted by CSRe. Additional frequency shifts relative to the frequency of primary beam can be observed for fragments with different mass to charge ratio(see Eq. 2).

$$\frac{\delta f}{f} = -\frac{1}{\gamma_{tr}^{\ 2}} \frac{\delta(m/q)}{m/q} \tag{2}$$

Using $^{36}Ar^{18+}$ 368MeV/u as primary beam, the fragments(A=2Z) are measured and identified in CSRe. The resolution of mass reaches 10^{-5}(Fig. 11)[4].

To measure the fragments with A=2Z+1, the energy of primary beam is increased to 400MeV/u. Similar resolution is reached.

Recently another mass measurement experiment is done using Krypton beam. The data analysis are in processing (Fig. 12).

Testing of Atomic Physics Experimental Platform

The atomic physics experimental platform is installed in both CSRm and CSRe. The hardware installed passed vacuum test and motor driven motion test. The data acquisition system passed primary test.

This platform is now ready to study the RR and DR procedure of H+ like and naked atoms. It's also possible to be used in beam profile monitor after improvements.

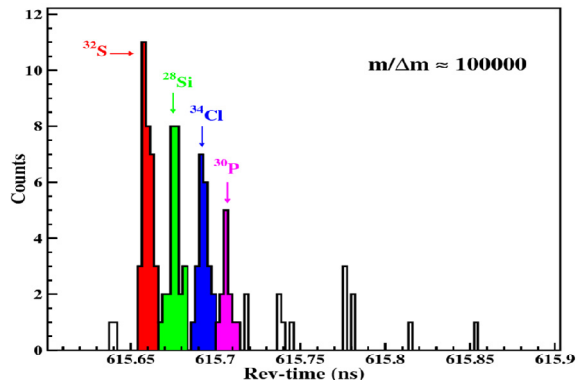

Figure 11: Mass measurement result for A=2Z.

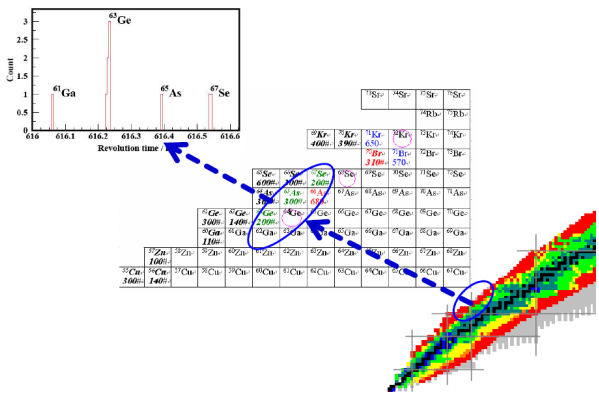

Figure 12: Mass measurement of nuclei near drip-line.

Research of Tumor Therapy with Carbon Beam

IMP puts efforts to do research of tumour therapy for several years. Before the new project is finished, low energy carbon beam(<100MeV/u) is used to do research on superficially-placed tumour therapy. Since autumn 2008, IMP extends the research to deep-seated tumour therapy by using the slow extracted carbon beam from CSRm.

There is only one horizontal terminal recently. By using of SOBP, multi-leaf collimator, large area ionization chamber and other techniques, two runs of research study were done recently. Based on the virtual accelerator concept, the energy switching between cycles is tested.

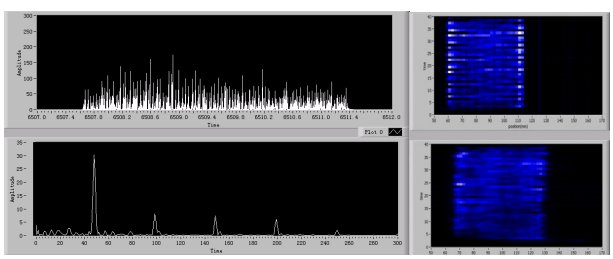

Figure 13: The time structure and X-Y scanned distribution of slow extracted beam

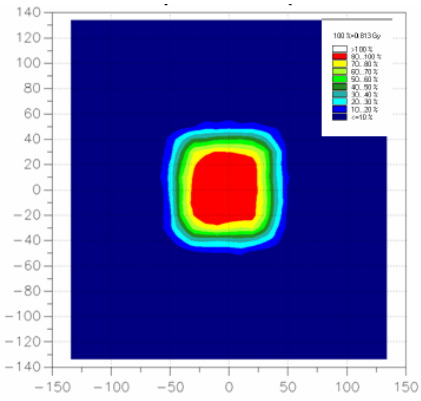

Figure 14: The measured dose distribution at therapy site

FUTURE IMPROVEMENT

Many aspects of the HIRFL-CSR need to be optimized to improve the performance of machine and convenience of commission. Some major requirements are listed in the following subsections.

Hardware Aspects

Power supply system should be improved to reduce ripple to about 10^{-6}, which is needed for stable slow extraction for external target experiments and therapy study.

The control system is being improved to reduce data flow, to realize multiple virtual machine operation and to reduce noise disturbance induced from environments. The realization of multiple virtual machine operation makes it possible to change energy from pulse to pulse. There are still some devices are controlled using temporary local computers, which should be made to join the system.

New sets of controller for power supplies and RF system are installed recently to match the requirement from cancer therapy study. The application software are revised and improved accordingly.

For diagnosis system, new devices should be introduced to observe beam intensity and position of the extracted beam. They are urgently needed to improve commission efficiency of the beam line between CSRm and CSRe. Two sets of ICT are installed recently at the beam line.

Software Aspects

The application software is developed based on intra-network for HIRFL-CSR project. For making the commission convenient and systematic, it's necessary to devote manpower and budget to develop software for automatic data generation, feedback commission and operation data collection. The structure of database based on ORACLE should be studied in detail to fulfil the demand from beam physics.

For diagnosis system, status monitoring, real time data collection and analysis software should be developed.

Experiment Aspects

The mass measurement in CSRe with cooled secondary beams is being studied.

The internal target is installed in CSRe, but detectors and data acquisition system is not finished. The external targets are being developed.

The possibility of acceleration of molecular beams in CSRm is been studied.

ACKNOWLEDGMENTS

The authors wish to thank the international advisory committee members: N. Angert, V.V. Parkhomchuk, D. Reistad, Y. Yano, T. Katayama, A. Goto, M. Steck, A.N. Skrinsky, J. Xu, S. Fang et al for their enthusiastic contributions to the project.

Thanks to BINP and JINR for the enthusiastic cooperation in design and construction of electron coolers, RF systems and internal target.

Thanks also to the official delegations for their help and advices during commission.

REFERENCES

[1] J.W. Xia et al, "The heavy ion cooler-storage-ring project (HIRFL-CSR) at Lanzhou", NIMA, 2002, vol. 488, no1-2, pp. 11-25.

[2] X.D.Yang, V.V. Parkhomchuk et al, Proceedings of COOL 2007, Bad Kreuznach, Germany, pp.59-63.

[3] B. Schlitt, "Mass spectrometry at the heavy ion storage ring ESR", DISS 97-01(Heidelberg)

[4] Tu Xiaolin et al, IMP&HIRFL Annual Report, 2008, preprint.

[5] A. Bubley et al, "The Electron Gun with Variable Beam Profile for Optimization of Electron Cooling", Proceedings of EPAC 2002, Paris, France. pp. 1356-1358.

[6] Behtenev, E. et al, "Comission of Electron Cooler EC-300 for HIRFL-CSR", COOL05, AIP Conference Proceedings, Volume 821, pp. 334-340 (2006).

[7] H. Danared et al, "Studies of Transverse Electron Cooling", Proceedings of EPAC 2000, Vienna, Austria, pp. 301-303.

[8] X.D. Yang, "Commissioning of Electron Cooling in CSRe", This conference.

List of Authors

Italic papercodes indicate primary authors

— A —

Ahmanova, E.V. MOM2MCIO02

— B —

Bao, Y. *TUM1MCCO03*
Ben-Zvi, I. MOM2MCIO01
Bessonov, E.G. *TUM1MCIO02*, *TUA2MCIO02*
Bhat, C.M. MOM1MCIO01, THPMCP006
Birkl, G. MOA1MCIO01
Blaum, K. THM2MCCO03
Blume, C. TUM1MCCO03
Bojtar, L. *MOM1MCIO02*
Broemmelsiek, D.R. MOM1MCIO01
Bross, A.D. *TUM1MCIO01*
Bryzgunov, M.I. *THPMCP004*, FRM1MCIO03
Bubley, A.V. FRM1MCIO01
Burov, A.V. MOM1MCIO01
Bussmann, M.H. *MOA1MCIO01*
Bykovsky, V. MOM2MCIO02, THPMCP007

— C —

Caldwell, A. TUM1MCCO03
Carlson, K. MOM1MCIO01
Chang, X. MOM2MCIO01
Crisp, J.L. MOM1MCIO01

— D —

Danared, H. *THM2MCIO01*
Derbenev, Y.S. *FRM2MCCO01*
Derwent, P. MOM1MCIO01
Dietrich, J. MOM2MCIO02, MOM2MCIO03, THPMCP005, *FRM1MCIO03*
Dimopoulou, C. MOA1MCIO01, TUM2MCIO02, *THM2MCIO02*
Dolinskyy, A. MOA2MCIO02, THM2MCIO02

— E —

Eddy, N. MOM1MCIO01

— F —

Fedotov, A.V. *MOM2MCIO01*, THPMCP006
Franzke, B. MOA2MCIO02
Furukawa, T. THPMCP010

— G —

Gattuso, C. MOM1MCIO01
Geer, S. TUM1MCIO01
Geppert, Ch. MOA1MCIO01
Goncharov, A.D. FRM1MCIO03
Greenwald, D.E. TUM1MCCO03
Grieser, M. THM2MCCO03

— H —

Hanson, G.G. TUM1MCIO04
Heine, R.G. THM2MCIO02
Hettrich, R. MOA1MCIO03
Hojo, S. THPMCP010
Hu, M. MOM1MCIO01
Huang, D. *TUA1MCIO02*

— I —

Ishimoto, S. THPMCP008

— J —

Jandewerth, U. MOA1MCIO03, THPMCP003

— K —

Källberg, A. THM2MCIO01
Kamerdzhiev, V. THM1MCCO02, FRM1MCIO03
Katayama, T. MOM2MCIO02, *MOA2MCIO02*, TUM2MCIO01, THM2MCIO02, THPMCP005
Kayran, A. MOM2MCIO01
Kikuchi, T. *THPMCP005*
Kirk, H.G. TUM1MCIO01
Kobets, A.G. MOM2MCIO02, *THPMCP007*
Kozhuharov, C. MOA1MCIO01
Krestnikov, D.A. MOM2MCIO02, TUM2MCIO02, THPMCP002, THPMCP006
Kuehl, T. MOA1MCIO01

— L —

Laier, U. THM2MCIO02
Lebedev, V.A. *MOA1MCCO02*
Li, D. *TUA1MCIO01*
Li, G.H. THM1MCCO03, *THPMCP011*
Li, J. THM1MCCO03, THPMCP011
Li, X.-P. TUA2MCIO01
Li, Y. THPMCP012
Liao, X.H. *THPMCP012*
Litvinenko, V. MOM2MCIO01
Litvinov, S.A. MOA2MCIO02
Liu, Y. THM1MCCO03
Lokhmatov, V.I. THPMCP007

— M —

Ma, X.M. THM1MCCO03, THPMCP011
Maier, R. MOM2MCIO03, TUM2MCIO01, THPMCP005
Mao, L.J. *THM1MCCO03*, THPMCP011

Meng, M.F. THPMCP012
Meshkov, I.N. MOM2MCIO02, TUM2MCIO02, THPMCP007
Mikhailichenko, A.A. TUM1MCIO02
Mizushima, K. THPMCP010
Möhl, D. MOA2MCIO02

— N —

Nakamura, T. THPMCP010
Ng, K.Y. TUA1MCIO02
Noda, K. THPMCP010
Noertershaeuser, W. MOA1MCIO01
Nolden, F. *MOA1MCIO03*, MOA2MCIO02, THM2MCIO02, *THPMCP001*, THPMCP003
Novotny, C. MOA1MCIO01

— O —

Okamoto, H. TUA2MCIO01
Orlov, D. THM2MCCO03

— P —

Panasyuk, V.M. THPMCP004, FRM1MCIO01
Parkhomchuk, V.V. *FRM1MCIO01*, FRM1MCIO03
Pasquinelli, R.J. MOA1MCCO02, *MOA2MCIO01*
Pavlov, V. THPMCP007
Pendzick, A. MOM2MCIO01
Peschke, C. MOA1MCIO03, *THPMCP003*
Petri, P. MOA1MCIO03, THPMCP003
Pivin, R. MOM2MCIO02, TUM2MCIO02, THPMCP007
Prasuhn, D. *MOM2MCIO03*, TUM2MCIO01, THPMCP005
Prost, L.R. *MOM1MCIO01*, THPMCP006
Pruss, S.M. MOM1MCIO01

— R —

Reva, V.B. THPMCP004, FRM1MCIO01, FRM1MCIO03
Roberts, T.J. TUA1MCIO02
Rogers, C.T. *TUA2MCCO03*
Romanov, A.L. THM1MCCO02
Rudakov, A.Yu. MOM2MCIO02, THPMCP007

— S —

Sato, A. *THPMCP008*
Satogata, T. MOM2MCIO01
Schramm, U. MOA1MCIO01
Schreiber, G. TUM2MCIO02, THM2MCIO02
Sessler, A. TUA2MCIO01
Shemyakin, A.V. MOM1MCIO01
Shibuya, S. THPMCP010
Shiltsev, V.D. TUM1MCIO01, THM1MCCO02
Shirai, T. *THPMCP010*
Shornikov, A. *THM2MCCO03*
Sidorin, A.A. THPMCP007
Sidorin, A.O. MOM2MCIO02, TUM2MCIO02, THPMCP002, THPMCP006
Simonsson, A. THM2MCIO01
Skorobogatov, D.N. FRM1MCIO03
Smirnov, A.V. *MOM2MCIO02*, *TUM2MCIO02*, *THPMCP002*, *THPMCP006*
Snopok, P. *TUM1MCIO04*, TUA2MCCO03
Stassen, R. MOM2MCIO03, TUM2MCIO01
Steck, M. MOA1MCIO01, MOA1MCIO03, MOA2MCIO02, TUM2MCIO02, *THM1MCIO01*, THM2MCIO02, THPMCP003
Stockhorst, H. MOM2MCIO03, *TUM2MCIO01*, THPMCP005
Stoehlker, T. MOA1MCIO01
Sutherland, M. MOM1MCIO01

— T —

Thorndahl, L. MOA2MCIO02, TUM2MCIO01

— V —

Valishev, A. THM1MCCO02

— W —

Walther, T. MOA1MCIO01
Wang, X.X. THPMCP012
Warner, A. MOM1MCIO01
Wei, J. *TUA2MCIO01*
Werkema, S.J. MOA1MCCO02
Winters, D.F.A. MOA1MCIO01
Wolf, A. THM2MCCO03
Wu, J.X. *THPMCP013*

— X —

Xia, J.W. THM1MCCO03, THPMCP013, FRM2MCIO02
Xiao, M. MOM1MCIO01
Xu, H.S. FRM2MCIO02

— Y —

Yakovenko, S. MOM2MCIO02, THPMCP007
Yan, T.L. THM1MCCO03, THPMCP011
Yang, J.C. THM1MCCO03
Yang, X.D. THM1MCCO03, THPMCP011, *FRM1MCIO02*, FRM2MCIO02
Yonehara, K. *TUA1MCIO03*
Yu, P.-CH. TUA2MCIO01
Yuan, Y.J. THM1MCCO03, THPMCP013, FRM1MCIO02, *FRM2MCIO02*
Yuri, Y. TUA2MCIO01

— Z —

Zhang, X. THM1MCCO02
Zhao, H.W. FRM2MCIO02
Zhao, Q.L. THPMCP012
Zisman, M.S. TUM1MCIO01

Institutes List

AEC
Chiba
- Shibuya, S.

BINP SB RAS
Novosibirsk
- Bryzgunov, M.I.
- Goncharov, A.D.
- Panasyuk, V.M.
- Parkhomchuk, V.V.
- Reva, V.B.
- Romanov, A.L.
- Skorobogatov, D.N.

BINP
Novosibirsk
- Bubley, A.V.

BNL
Upton, Long Island, New York
- Ben-Zvi, I.
- Chang, X.
- Fedotov, A.V.
- Kayran, A.
- Kirk, H.G.
- Litvinenko, V.
- Pendzick, A.
- Satogata, T.

CERN
Geneva
- Bojtar, L.
- Möhl, D.
- Thorndahl, L.

CLASSE
Ithaca, New York
- Mikhailichenko, A.A.

FZD
Dresden
- Bussmann, M.H.
- Schramm, U.

FZJ
Jülich
- Dietrich, J.
- Kamerdzhiev, V.
- Maier, R.
- Prasuhn, D.
- Stassen, R.
- Stockhorst, H.

Fermilab
Batavia
- Bhat, C.M.
- Broemmelsiek, D.R.
- Bross, A.D.
- Burov, A.V.
- Carlson, K.
- Crisp, J.L.
- Derwent, P.
- Eddy, N.
- Gattuso, C.
- Geer, S.
- Hu, M.
- Lebedev, V.A.
- Ng, K.Y.
- Pasquinelli, R.J.
- Prost, L.R.
- Pruss, S.M.
- Shemyakin, A.V.
- Shiltsev, V.D.
- Sutherland, M.
- Valishev, A.
- Warner, A.
- Werkema, S.J.
- Xiao, M.
- Yonehara, K.
- Zhang, X.

GSI
Darmstadt
- Dimopoulou, C.
- Dolinskyy, A.
- Franzke, B.
- Heine, R.G.
- Hettrich, R.
- Jandewerth, U.
- Katayama, T.
- Kozhuharov, C.
- Kuehl, T.
- Laier, U.
- Litvinov, S.A.
- Noertershaeuser, W.
- Nolden, F.
- Peschke, C.
- Petri, P.
- Schreiber, G.
- Steck, M.
- Stoehlker, T.
- Winters, D.F.A.

HU/AdSM
Higashi-Hiroshima
- Okamoto, H.

IIT
Chicago, Illinois

- Huang, D.

IMP
Lanzhou
- Li, G.H.
- Li, J.
- Liu, Y.
- Ma, X.M.
- Mao, L.J.
- Wu, J.X.
- Xia, J.W.
- Xu, H.S.
- Yan, T.L.
- Yang, J.C.
- Yang, X.D.
- Yuan, Y.J.
- Zhao, H.W.

Institute of Electronics, Chinese Academy of Sciences
Beijing
- Li, Y.
- Liao, X.H.
- Meng, M.F.
- Wang, X.X.
- Zhao, Q.L.

JAEA/TARRI
Gunma-ken
- Yuri, Y.

JASRI/SPring-8
Hyogo-ken
- Nakamura, T.

JINR
Dubna, Moscow Region
- Ahmanova, E.V.
- Bykovsky, V.
- Kobets, A.G.
- Lokhmatov, V.I.
- Meshkov, I.N.
- Pavlov, V.
- Pivin, R.
- Rudakov, A.Yu.
- Sidorin, A.A.
- Sidorin, A.O.
- Smirnov, A.V.
- Yakovenko, S.

JINR/DLNP
Dubna, Moscow region
- Krestnikov, D.A.

JLAB
Newport News, Virginia
- Derbenev, Y.S.

Johannes Gutenberg University Mainz
Mainz
- Geppert, Ch.

Johannes Gutenberg University Mainz, Institut für Physik
Mainz
- Novotny, C.

KEK
Ibaraki
- Ishimoto, S.

LBNL
Berkeley, California
- Li, D.
- Sessler, A.
- Zisman, M.S.

LPI
Moscow
- Bessonov, E.G.

MPI für Physics
Muenchen
- Bao, Y.
- Blume, C.
- Greenwald, D.E.

MPI-K
Heidelberg
- Blaum, K.
- Grieser, M.
- Orlov, D.
- Shornikov, A.
- Wolf, A.

MPI-P
München
- Caldwell, A.

MSL
Stockholm
- Danared, H.
- Källberg, A.
- Simonsson, A.

Muons, Inc
Batavia
- Roberts, T.J.

NIRS
Chiba-shi
- Furukawa, T.
- Hojo, S.
- Mizushima, K.
- Noda, K.
- Shirai, T.

Nagaoka University of Technology
Nagaoka, Niigata
- Kikuchi, T.

Osaka University
Osaka
- Sato, A.

STFC/RAL/ASTeC
Chilton, Didcot, Oxon
- Rogers, C.T.

Skyworks Solutions, Inc.
Newbury Park. California
- Li, X.-P.

TU Darmstadt
Darmstadt
- Birkl, G.
- Walther, T.

TUB
Beijing
- Wei, J.
- Yu, P.-CH.

UCR
Riverside, California
- Hanson, G.G.
- Snopok, P.

Participants List

— B—

Yu Bao
MPI fuer Physics
Munich
Germany

Evgeniy G. Bessonov
LPI RAS
Moscow
Russia

Lajos Bojtar
CERN, AB
CH-1211 Geneva 23
Switzerland

Alan David Bross
Fermilab
Batavia, IL 60510,
USA

Maxim I. Bryzgunov
BINP SB RAS
630090 Novosibirsk
Russia

Michael Bussmann
FDR
D-01328 Dresden
Germany

— D —

Håkan Danared
Manne Siegbahn Laboratory
S-10405 Stockholm
Sweden

Jürgen Dietrich
FZ Jülich
D-52425 Jülich
Germany

Christina Dimopoulou
GSI
D-64291 Darmstadt
Germany

— F —

Alexei Fedotov
Brookhaven National Laboratory
11973 Upton, NY
USA

— K —

Vsevolod Kamerdzhiev
FZ Jülich
D-52425 Jülich
Germany

Takeshi Katayama
GSI
188-0004，5-507, 4-4-17,
Nishihara, NishiTokyo,
Tokyo
Japan

Takashi Kikuchi
Nagaoka University of Technology
1603-1 Kamitomioka,
Nagaoka
Japan

Masayuki Kumada
Institute of Physics
Academia Sinica
Taipei，China

— L—

Valeri A Lebedev
Accelerator Division
Fermi National Accelerator Laboratory
60510 Batavia, IL
USA

Derun Li
LBNL
Berkeley, California 94720
USA

Guohong Li
Institute of Modern Physics
Chinese Academy of Sciences
730000 Lanzhou, Gansu
P.R. China

Xianheng Liao
Institute of Electronics, CAS
Beijing 100190
P.R. China

— M —

Lijun Mao
Institute of Modern Physics
Chinese Academy of Sciences
730000 Lanzhou, Gansu
P.R. China

— N —

King Yuen Ng
Fermi National Accelerator Laboratory
60510 Batavia, IL
USA

Fritz Nolden
GSI
D-64291 Darmstadt
Germany

— P —

Vasily V. Parkhomchuk
Budker Institute of Nuclear Physics
630090 Novosibirsk
Russia

Ralph J Pasquinelli
AD/RF Department
Fermi National Accelerator Laboratory
60510 Batavia, IL
USA

Claudius Peschke
GSI
D-64291 Darmstadt
Germany

Christine Petit-Jean-Genaz
CERN
CH-1211 Geneva 23
Switzerland

Dieter Prasuhn
FZ Jülich
D-52425 Jülich
Germany

Lionel R Prost
Fermi National Accelerator Laboratory
60510 Batavia, IL
USA

— S —

Akira Sato
Osaka University
Osaka
Japan

Volker RW Schaa
GSI
D-64291 Darmstadt
Germany

Toshiyuki Shirai
NIRS
Chiba 263-8555
Japan

Andrey Shornikov
MPI-K
D-69117 Heidelberg
Germany

Alexander V Smirnov
Joint Institute for Nuclear Research
141980 Dubna
Russia

Pavel Snopok
University of California
Riverside, CA 92521
USA

Markus Steck
GSI
D-64291 Darmstadt
Germany

— W —

Xiaoxia Wang
Institute of Electronics, CAS
Beijing 100190
P.R. China

Jie Wei
Tsinghua University & BNL
Beijing 100084
P.R. China

Junxia Wu
Institute of Modern Physics
Chinese Academy of Sciences
730000 Lanzhou, Gansu
P.R. China

— Y —

Xiaodong Yang
Institute of Modern Physics
Chinese Academy of Sciences
730000 Lanzhou, Gansu
P.R. China

Katsuya Yonehara
Fermi National Accelerator Laboratory
60510 Batavia, IL
USA

Youjin Yuan
Institute of Modern Physics
Chinese Academy of Sciences
730000 Lanzhou, Gansu
P.R. China

— Z —

Xiaolong Zhang
Fermi National Accelerator Laboratory
60510 Batavia, IL
USA

Yuhong Zhang
Thomas Jefferson National Accelerator Facilty
23606 Newport News,Va
USA

Hongwei Zhao
Institute of Modern Physics
Chinese Academy of Sciences
730000 Lanzhou, Gansu
P.R. China